2015 AAAS ANNUAL MEETING San Jose, CA

Science

$10
24 OCTOBER 2014
sciencemag.org

AAAS

Innovations in imaging

Advanced techniques elucidate the processes of life

CONTENTS

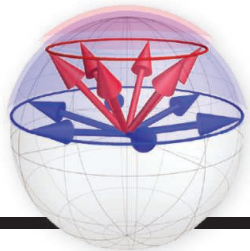

422 & 448
Driving valley currents in graphene

24 OCTOBER 2014 • VOLUME 346 • ISSUE 6208

NEWS

IN BRIEF

402 Roundup of the week's news

IN DEPTH

404 **U.S. HALTS TWO DOZEN RISKY VIRUS STUDIES**
One-year "pause" to develop new policy on controversial research *By J. Kaiser*

405 **IN PRAISE OF TAMENESS**
We may have domesticated ourselves into the cooperative species we are today *By A. Gibbons*

406 **EPIC PRE-COLUMBIAN VOYAGE SUGGESTED BY GENES**
South American DNA found in Easter Islanders *By A. Lawler*

407 **TAIWAN'S OCEAN PROGRAM REELS FROM LOSS OF SHIP, SCIENTISTS**
New vessel was sparking international collaborations *By D. Normile*

408 **ELECTION STAKES GO BEYOND CONTROL OF THE SENATE**
Funding, peer review, water, and fusion are some of the issues on tap after the vote *By J. Mervis*

408 **Does science suffer an 'innovation deficit'?**
By J. Mervis

410 **SEARCHING FOR SCIENCE IN INDIA'S TRADITIONAL MEDICINE**
Critics say ayurgenomics is at best a quixotic quest *By P. Pulla*

FEATURE

411 **SHOW ME THE MONEY**
A bitter dispute lays bare questionable practices in China's foreign-talent programs *By M. Hvistendahl*

INSIGHTS

PERSPECTIVES

416 **BEYOND THE RAINBOW**
Dinosaur color vision may have been key to the evolution of bird feathers *By M.-C. Koschowitz* et al.

418 **TERMINATING THE REPLISOME**
Multiple proteins modify and dismantle a key enzyme after DNA replication terminates *By S. P. Bell*
▸ RESEARCH ARTICLE P. 440; REPORT P. 477

420 **BOUNDLESS NO MORE**
Ending illegal, unregulated, and unreported fishing would bring hope for ocean wildlife *By A. C. J. Vincent and J. M. Harris*

422 **HARNESSING CHIRALITY FOR VALLEYTRONICS**
Artificial magnetic fields bend electron trajectories in gapped graphene *By M. B. Lundeberg and J. A. Folk*
▸ REPORT P. 448

423 **SEX AND THE SINGLE FERN**
Separation of the synthesis and sensing of a signaling molecule controls sex in ferns *By T. Sun*
▸ REPORT P. 469

424 **BREATHING THE UNBREATHABLE**
A crystal structure reveals how some bacteria break down organohalide pollutants *By E. A. Edwards*
▸ REPORT P. 455

426 **RATCHETING THE EVOLUTION OF MULTICELLULARITY**
Traits that entrench cells in a group lifestyle may pave the way for complexity *By E. Libby and W. C. Ratcliff*

427 **UNANCHORED UBIQUITIN IN VIRUS UNCOATING**
Components of a cellular degradation system are exploited by influenza virus during infection *By R. Rajsbaum and A. García-Sastre*
▸ REPORT P. 473

429 **COPING WITH THE CURSE OF FRESHWATER VARIABILITY**
Institutions, infrastructure, and information for adaptation *By J. W. Hall* et al.

BOOKS *ET AL.*

431 **SURGEON GENERAL'S WARNING**
By M. Stobbe, reviewed by J. M. Samet

432 **JACKSON HOLE SCIENCE MEDIA AWARDS**
Reviewed by C. Ash

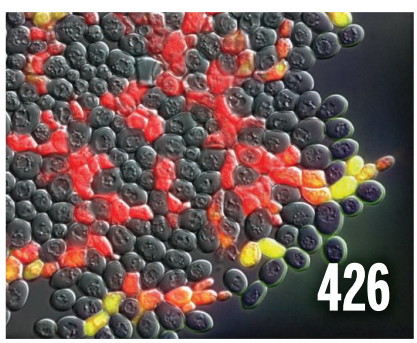

LETTERS

433 **EBOLA: MOBILITY DATA**
By M. E. Halloran et al.

433 **EBOLA: PUBLIC-PRIVATE PARTNERSHIPS**
By L. A. Reperant et al.

434 **EBOLA: SOCIAL RESEARCH OVERLOOKED**
By G. Guerrier

434 **TECHNICAL COMMENT ABSTRACTS**

DEPARTMENTS

401 **EDITORIAL**
China's private universities
By Huiqing Jin

510 **WORKING LIFE**
A double dose of advice
By Huan Wang

Science Staff 400
New Products 489
AAAS Meeting Program 490
Science Careers 500

Published by AAAS

CONTENTS

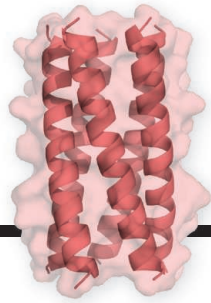

481 & 485

Using helices to design bundles and barrels

24 OCTOBER 2014 • VOLUME 346 • ISSUE 6208

RESEARCH

IN BRIEF

435 From *Science* and other journals

REVIEW

438 **MICROBE ANALYSIS**
Zooming in to see the bigger picture: Microfluidic and nanofabrication tools to study bacteria *F. J. H. Hol and C. Dekker*
REVIEW SUMMARY; FOR FULL TEXT: dx.doi.org/10.1126/science.1251821

RESEARCH ARTICLES

439 **ADVANCED IMAGING**
Lattice light-sheet microscopy: Imaging molecules to embryos at high spatiotemporal resolution *B.-C. Chen* et al.
RESEARCH ARTICLE SUMMARY; FOR FULL TEXT: dx.doi.org/10.1126/science.1257998

440 **DNA REPLICATION**
Cdc48 and a ubiquitin ligase drive disassembly of the CMG helicase at the end of DNA replication *M. Maric* et al.
RESEARCH ARTICLE SUMMARY; FOR FULL TEXT: dx.doi.org/10.1126/science.1253596
▸ PERSPECTIVE P. 418; REPORT P. 477

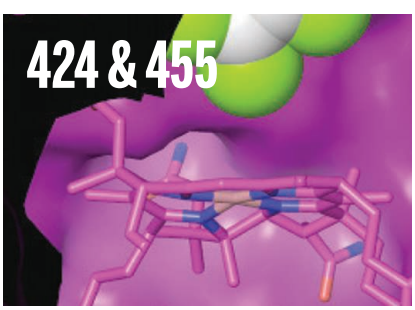

REPORTS

441 **SOLAR CELLS**
Fulleropyrrolidine interlayers: Tailoring electrodes to raise organic solar cell efficiency *Z. A. Page* et al.

445 **ULTRAFAST DYNAMICS**
A photoinduced metal-like phase of monoclinic VO_2 revealed by ultrafast electron diffraction *V. R. Morrison* et al.

448 **VALLEYTRONICS**
Detecting topological currents in graphene superlattices *R. V. Gorbachev* et al.
▸ PERSPECTIVE P. 422

451 **ASYMMETRIC CATALYSIS**
Room-temperature enantioselective C–H iodination via kinetic resolution *L. Chu* et al.

455 **METALLOPROTEINS**
Structural basis for organohalide respiration *M. Bommer* et al.
▸ PERSPECTIVE P. 424

458 **WORKING MEMORY**
Medial prefrontal activity during delay period contributes to learning of a working memory task *D. Liu* et al.

463 **EVOLUTIONARY BIOLOGY**
Rapid evolution of a native species following invasion by a congener *Y. E. Stuart* et al.

466 **NEW WORLD ARCHAEOLOGY**
Paleoindian settlement of the high-altitude Peruvian Andes *K. Rademaker* et al.
▸ PODCAST

469 **PLANT SCIENCE**
Antheridiogen determines sex in ferns via a spatiotemporally split gibberellin synthesis pathway *J. Tanaka* et al.
▸ PERSPECTIVE P. 423

473 **VIRAL CELL BIOLOGY**
Influenza A virus uses the aggresome processing machinery for host cell entry *I. Banerjee* et al.
▸ PERSPECTIVE P. 427

477 **DNA REPLICATION**
Polyubiquitylation drives replisome disassembly at the termination of DNA replication *S. Priego Moreno* et al.
▸ PERSPECTIVE P. 418; RESEARCH ARTICLE P. 440

PROTEIN DESIGN

481 High thermodynamic stability of parametrically designed helical bundles *P.-S. Huang* et al.

485 Computational design of water-soluble α-helical barrels *A. R. Thomson* et al.

ON THE COVER

Image from the laboratory of the 2014 Nobel Prize winner for chemistry, Eric Betzig, showing neurons in the brain of a live zebrafish embryo. Sample-induced aberrations often degrade imaging quality in multicellular specimens, but a clear view was obtained here by using adaptive optics, the same technology used to view distant astronomical objects through Earth's turbulent atmosphere. For more on imaging, see page 439 and dx.doi.org/10.1126/science.1257998. *Image: Kai Wang, Eric Betzig, Janelia Research Campus; Jeff Mumm, Johns Hopkins University*

SCIENCE (ISSN 0036-8075) is published weekly on Friday, except the last week in December, by the American Association for the Advancement of Science, 1200 New York Avenue, NW, Washington, DC 20005. Periodicals mail postage (publication No. 484460) paid at Washington, DC, and additional mailing offices. Copyright © 2014 by the American Association for the Advancement of Science. The title SCIENCE is a registered trademark of the AAAS. Domestic individual membership and subscription (51 issues): $153 ($74 allocated to subscription). Domestic institutional subscription (51 issues): $1282; Foreign postage extra: Mexico, Caribbean (surface mail) $55; other countries (air assist delivery) $85. First class, airmail, student, and emeritus rates on request. Canadian rates with GST available upon request, GST #1254 88122. Publications Mail Agreement Number 1069624. **Printed in the U.S.A.**
Change of address: Allow 4 weeks, giving old and new addresses and 8-digit account number. **Postmaster:** Send change of address to AAAS, P.O. Box 96178, Washington, DC 20090–6178. **Single-copy sales:** $10.00 current issue, $15.00 back issue prepaid includes surface postage; bulk rates on request. **Authorization to photocopy** material for internal or personal use under circumstances not falling within the fair use provisions of the Copyright Act is granted by AAAS to libraries and other users registered with the Copyright Clearance Center (CCC) Transactional Reporting Service, provided that $30.00 per article is paid directly to CCC, 222 Rosewood Drive, Danvers, MA 01923. The identification code for *Science* is 0036-8075. *Science* is indexed in the *Reader's Guide to Periodical Literature* and in several specialized indexes.

Published by AAAS

Science
AAAS
1200 New York Avenue, NW, Washington, DC 20005
Bateman House, 82-88 Hills Road, Cambridge, UK CB2 1LQ

Editor-in-Chief Marcia McNutt
Executive Editor Monica M. Bradford **News Editor** Tim Appenzeller
Managing Editor, Research Journals Katrina L. Kelner
Deputy Editors Barbara R. Jasny, Andrew M. Sugden(UK), Valda J. Vinson, Jake S. Yeston

Research and Insights

SR. EDITORS Caroline Ash(UK), Gilbert J. Chin, Lisa D. Chong, Maria Cruz(UK), Julia Fahrenkamp-Uppenbrink(UK), Pamela J. Hines, Stella M. Hurtley(UK), Paula A. Kiberstis, Marc S. Lavine(Canada), Kristen L. Mueller, Ian S. Osborne(UK), Beverly A. Purnell, L. Bryan Ray, Guy Riddihough, H. Jesse Smith, Jelena Stajic, Peter Stern(UK), Phillip D. Szuromi, Brad Wible, Nicholas S. Wigginton, Laura M. Zahn **ASSOCIATE EDITORS** Brent Grocholski, Melissa R. McCartney, Margaret M. Moerchen, Sacha Vignieri **ASSOCIATE BOOK REVIEW EDITOR** Valerie B. Thompson **ASSOCIATE LETTERS EDITOR** Jennifer Sills **CHIEF CONTENT PRODUCTION EDITOR** Cara Tate **SR. CONTENT PRODUCTION EDITORS** Harry Jach, Trista Wagoner **CONTENT PRODUCTION EDITORS** Jeffrey E. Cook, Chris Filiatreau, Cynthia Howe, Lauren Kmec, Barbara P. Ordway **SR. EDITORIAL COORDINATORS** Carolyn Kyle, Beverly Shields **EDITORIAL COORDINATORS** Ramatoulaye Diop, Joi S. Granger, Lisa Johnson, Anita Wynn **PUBLICATIONS ASSISTANTS** Aneera Dobbins, Jeffrey Hearn, Dona Mathieu, Le-Toya Mayne Flood, Shannon McMahon, Scott Miller, Jerry Richardson, Rachel Roberts(UK), Alice Whaley(UK), Brian White **EXECUTIVE ASSISTANT** Anna Bashkirova **ADMINISTRATIVE SUPPORT** Janet Clements(UK), Lizanne Newton(UK), Maryrose Madrid, John Wood(UK)

News

NEWS MANAGING EDITOR John Travis **INTERNATIONAL EDITOR** Richard Stone **DEPUTY NEWS EDITORS** Daniel Clery(UK), Robert Coontz, Elizabeth Culotta, David Grimm, David Malakoff, Leslie Roberts **CONTRIBUING EDITORS** Martin Enserink(Europe), Mara Hvistendahl (Asia) **SR. CORRESPONDENTS** Jeffrey Mervis, Elizabeth Pennisi **NEWS WRITERS** Adrian Cho, Jon Cohen, Jennifer Couzin-Frankel, Carolyn Gramling, Eric Hand, Jocelyn Kaiser, Kelly Servick, Robert F. Service, Erik Stokstad, Emily Underwood **INTERNS** David Shultz, Jia You **CONTRIBUTING CORRESPONDENTS** Pallava Bagla(South Asia), Michael Balter(Paris), John Bohannon, Ann Gibbons, Sam Kean, Richard A. Kerr, Eli Kintisch, Kai Kupferschmidt(Berlin), Andrew Lawler, Christina Larson(Beijing), Mitch Leslie, Charles C. Mann, Eliot Marshall, Virginia Morell, Dennis Normile(Tokyo), Heather Pringle, Tania Rabesandratana(Brussels), Gretchen Vogel(Berlin), Lizzie Wade(Mexico City) **CAREERS** Jim Austin(Editor), Donisha Adams **COPY EDITORS** Kara Estelle, Nora Kelly, Jennifer Levin **ADMINISTRATIVE SUPPORT** Scherraine Mack

Executive Publisher Alan I. Leshner
Publisher Beth Rosner **Chief Digital Media Officer** Rob Covey

BUSINESS OPERATIONS AND ADMINISTRATION DIRECTOR Deborah Rivera-Wienhold **BUSINESS SYSTEMS AND FINANCIAL ANALYSIS DIRECTOR** Randy Yi **MANAGER OF FULFILLMENT SYSTEMS** Neal Hawkins **SYSTEMS ANALYST** Nicole Mehmedovich **ASSISTANT DIRECTOR, BUSINESS OPERATIONS** Eric Knott **MANAGER, BUSINESS OPERATIONS** Jessica Tierney **BUSINESS ANALYSTS** Cory Lipman, Cooper Tilton, Celeste Troxler **FINANCIAL ANALYST** Jeremy Clay **RIGHTS AND PERMISSIONS ASSISTANT DIRECTOR** Emilie David **PERMISSIONS ASSOCIATE** Elizabeth Sandler **RIGHTS, CONTRACTS, AND LICENSING ASSOCIATE** Lili Kiser

MARKETING DIRECTOR Ian King **MARKETING MANAGER** Julianne Wielga **MARKETING ASSOCIATE** Elizabeth Sattler **SR. MARKETING EXECUTIVE** Jennifer Reeves **SR. ART ASSOCIATE, PROJECT MANAGER** Tzeitel Sorrosa **ART ASSOCIATE** Seil Lee **ASSISTANT COMMERCIAL EDITOR** Selby Frame **MARKETING PROJECT MANAGER** Angelissa McArthur **SR. WRITER** Bill Zimmer **PROGRAM DIRECTOR, AAAS MEMBER CENTRAL** Peggy Mihelich **FULFILLMENT SYSTEMS AND OPERATIONS** membership@aaas.org **MANAGER, MEMBER SERVICES** Pat Butler **SPECIALISTS** LaToya Casteel, Javia Flemmings, Latasha Russell **MANAGER, DATA ENTRY** Mickie Napoleoni **DATA ENTRY SPECIALISTS** JJ Regan, Jaimee Wise, Fiona Giblin

DIRECTOR, SITE LICENSING Tom Ryan **DIRECTOR, CORPORATE RELATIONS** Eileen Bernadette Moran **SR. PUBLISHER RELATIONS SPECIALIST** Kiki Forsythe **PUBLISHER RELATIONS MANAGER** Catherine Holland **PUBLISHER RELATIONS, EASTERN REGION** Keith Layson **PUBLISHER RELATIONS, WESTERN REGION** Ryan Rexroth **MANAGER, SITE LICENSE OPERATIONS** Iquo Edim **FULFILLMENT ANALYST** Lana Guz **ASSOCIATE DIRECTOR, MARKETING** Christina Schlecht **MARKETING ASSOCIATES** Thomas Landreth, Minah Kim

DIRECTOR OF WEB TECHNOLOGIES Ahmed Khadr **SR. DEVELOPER** Chris Coleman **DEVELOPER** Dan Berger **SR. PROJECT MANAGER** Trista Smith **SYSTEMS ENGINEER** Luke Johnson **PRODUCT MANAGER** Walter Jones

CREATIVE DIRECTOR, MULTIMEDIA Martyn Green **DIRECTOR OF ANALYTICS** Enrique Gonzales **SR. WEB PRODUCER** Sarah Crespi **WEB PRODUCER** Alison Crawford **VIDEO PRODUCER** Nguyen Nguyen **SOCIAL MEDIA PRODUCER** Meghna Sachdev

DIRECTOR OF OPERATIONS PRINT AND ONLINE Lizabeth Harman **PRINT PRODUCTION DIRECTOR** Wendy K. Shank **PREFLIGHT MANAGER** Marcus Spiegler **ASSISTANT MANAGER ONLINE** Lisa Stanford **ASSISTANT MANAGER PRINT** Rebecca Doshi **SR SPECIALISTS** Steve Forrester, Jason Hillman, Antoinette Hodal, Tara Kelly, Anthony Rosen **SPECIALISTS** Jacob Hedrick, Nichele Johnston, Lori Murphy, Kimberley Oster

DESIGN DIRECTOR Beth Rakouskas **ASSOCIATE ART DIRECTOR** Laura Creveling **SR. ILLUSTRATORS** Chris Bickel, Katharine Sutliff **ILLUSTRATOR** Valerie Altounian **SR. ART ASSOCIATES** Holly Bishop, Preston Huey **ART ASSOCIATES** Kay Engman, Garvin Grullón, Chrystal Smith **SR. PHOTO EDITOR** William Douthitt **PHOTO EDITOR** Leslie Blizard

DIRECTOR, GLOBAL COLLABORATION, CUSTOM PUBLICATIONS, ADVERTISING Bill Moran **EDITOR, CUSTOM PUBLISHING** Sean Sanders: 202-326-6430 **ASSISTANT EDITOR, CUSTOM PUBLISHING** Tianna Hicklin: 202-326-6463 **ADVERTISING MARKETING MANAGER** Justin Sawyers: 202-326-7061 science_advertising@aaas.org **ADVERTISING MARKETING ASSOCIATE** Javia Flemmings **ADVERTISING SUPPORT MANAGER** Karen Foote: 202-326-6740 **ADVERTISING PRODUCTION OPERATIONS MANAGER** Deborah Tompkins **SR. PRODUCTION SPECIALIST/GRAPHIC DESIGNER** Amy Hardcastle **PRODUCTION SPECIALIST** Yuse Lajiminmuhip **SR. TRAFFIC ASSOCIATE** Christine Hall **SALES COORDINATOR** Shirley Young **ASSOCIATE DIRECTOR, COLLABORATION, CUSTOM PUBLICATIONS/CHINA/TAIWAN/KOREA/SINGAPORE** Ruolei Wu: +86-186 0822 9345, rwu@aaas.org **COLLABORATION/CUSTOM PUBLICATIONS/JAPAN** Adarsh Sandhu + 81532-81-5142 asandhu@aaas.org **EAST COAST/E. CANADA** Laurie Faraday: 508-747-9395, FAX 617-507-8189 **WEST COAST/W. CANADA** Lynne Stickrod: 415-931-9782, FAX 415-520-6940 **MIDWEST** Jeffrey Dembksi: 847-498-4520 x3005, Steven Loerch: 847-498-4520 x3006 **UK EUROPE/ASIA** Roger Goncalves: TEL/FAX +41 43 243 1358 **JAPAN** Katsuyoshi Fukamizu(Tokyo): +81-3-3219-5777 kfukamizu@aaas.org **CHINA/TAIWAN** Ruolei Wu: +186-0082-9345

WORLDWIDE ASSOCIATE DIRECTOR OF SCIENCE CAREERS Tracy Holmes: +44 (0) 1223 326525, FAX +44 (0) 1223 326532 tholmes@science-int. co.uk **CLASSIFIED** advertise@sciencecareers.org **U.S. SALES** Tina Burks: 202-326-6577, Nancy Toema: 202-326-6578 **SALES ADMINISTRATOR** Marci Gallun **EUROPE/ROW SALES** Axel Gesatzki, Sarah Lelarge **SALES ASSISTANT** Kelly Grace **JAPAN** Hiroyuki Mashiki(Kyoto): +81-75-823-1109 hmashiki@aaas.org **CHINA/TAIWAN** Ruolei Wu: +86-186 0082 9345 rwu@aaas.org **MARKETING MANAGER** Allison Pritchard **MARKETING ASSOCIATE** Aimee Aponte

AAAS BOARD OF DIRECTORS RETIRING PRESIDENT, CHAIR Phillip A. Sharp **PRESIDENT** Gerald R. Fink **PRESIDENT-ELECT** Geraldine (Geri) Richmond **TREASURER** David Evans Shaw **CHIEF EXECUTIVE OFFICER** Alan I. Leshner **BOARD** Bonnie L. Bassler, May R. Berenbaum, Carlos J. Bustamante, Claire M. Fraser, Laura H. Greene, Elizabeth Loftus, Raymond Orbach, Inder M. Verma

SUBSCRIPTION SERVICES For change of address, missing issues, new orders and renewals, and payment questions: 866-434-AAAS (2227) or 202-326-6417, FAX 202-842-1065. Mailing addresses: AAAS, P.O. Box 96178, Washington, DC 20090-6178 or AAAS Member Services, 1200 New York Avenue, NW, Washington, DC 20005

INSTITUTIONAL SITE LICENSES 202-326-6755 **REPRINTS:** Author Inquiries 800-635-7181 **COMMERCIAL INQUIRIES** 803-359-4578 **PERMISSIONS** 202-326-6765, permissions@aaas.org **AAAS Member Services** 202-326-6417 or http://membercentral.aaas.org/discounts

Science serves as a forum for discussion of important issues related to the advancement of science by publishing material on which a consensus has been reached as well as including the presentation of minority of conflicting points of view. Accordingly, all articles published in *Science*—including editorials, news and comment, and books reviews—are signed and reflect the individual views of the authors and not official points of view adopted by AAAS or the institutions with which the authors are affiliated.

INFORMATION FOR AUTHORS See pages 680 and 681 of the 7 February 2014 issue or access www.sciencemag.org/about/authors

SENIOR EDITORIAL BOARD
A. Paul Alivisatos, *Lawrence Berkeley Nat'l. Laboratory,* **Ernst Fehr,** *U. of Zürich*
Susan M. Rosenberg, *Baylor College of Medicine,* **Michael S. Turner,** *U. of Chicago*

BOARD OF REVIEWING EDITORS (Statistics board members indicated with **(S)**)
Adriano Aguzzi, *U. Hospital Zürich*
Takuzo Aida, *U. of Tokyo*
Leslie Aiello, *Wenner-Gren Foundation*
Judith Allen, *U. of Edinburgh*
Sonia Altizer, *U. of Georgia*
Virginia Armbrust, *U. of Washington*
Sebastian Amigorena, *Institut Curie*
Kathryn Anderson, *Memorial Sloan-Kettering Cancer Center*
Peter Andolfatto, *Princeton U.*
Meinrat O. Andreae, *Max-Planck Inst. Mainz*
Paola Arlotta, *Harvard U.*
Johan Auwerx, *EPFL*
David Awschalom, *U. of Chicago*
Jordi Bascompte, *Estación Biológica de Doñana CSIC*
Facundo Batista, *London Research Inst.*
Ray H. Baughman, *U. of Texas, Dallas*
David Baum, *U. of Wisconsin*
Mark Bear, *Massachusetts Inst. of Technology*
Kamran Behnia, *ESPCI-ParisTech*
Yasmine Belkaid, *NIAID, NIH*
Philip Benfey, *Duke U.*
Stephen J. Benkovic, *Penn State U.*
Gabriele Bergers, *U. of California, San Francisco*
Christophe Bernard, *Aix-Marseille U.*
Bradley Bernstein, *Massachusettes General Hospital.*
Peer Bork, *EMBL*
Bernard Bourdon, *Ecole Normale Supérieure de Lyon*
Chris Bowler, *École Normale Supérieure*
Ian Boyd, *U. of St. Andrews*
Emily Brodsky, *U. of California, Santa Cruz*
Ron Brookmeyer, *U. of California Los Angeles* **(S)**
Christian Büchel, *U. Hamburg-Eppendorf*
Joseph A. Burns, *Cornell U.*
William P. Butz, *Population Reference Bureau*
Gyorgy Buzsaki, *New York U. School of Medicine*
Blanche Capel, *Duke U.*
Mats Carlsson, *U. of Oslo*
David Clapham, *Children's Hospital Boston*
David Clary, *U. of Oxford*
Joel Cohen, *Rockefeller U., Columbia U.*
Jonathan D. Cohen, *Princeton U.*
James Collins, *Boston U.*
Robert Cook-Deegan, *Duke U.*
Alan Cowman, *Walter & Eliza Hall Inst.*
Robert H. Crabtree, *Yale U.*
Roberta Croce, *Vrije Universiteit*
Janet Currie, *Princeton U.*
Jeff L. Dangl, *U. of North Carolina*
Tom Daniel, *U. of Washington*
Frans de Waal, *Emory U.*
Stanislas Dehaene, *Collège de France*
Robert Desimone, *MIT*
Claude Desplan, *New York U.*
Ap Dijksterhuis, *Radboud U. of Nijmegen*
Dennis Discher, *U. of Pennsylvania*
Gerald W. Dorn II, *Washington U. School of Medicine*
Jennifer A. Doudna, *U. of California, Berkeley*
Bruce Dunn, *U. of California, Los Angeles*
Christopher Dye, *WHO*
Todd Ehlers, *U. of Tuebingen*
David Ehrhardt, *Carnegie Inst. of Washington*
Tim Elston, *U. of North Carolina at Chapel Hill*
Gerhard Ertl, *Fritz-Haber-Institut, Berlin*
Barry Everitt, *U. of Cambridge*
Ernst Fehr, *U. of Zurich*
Anne C. Ferguson-Smith, *U. of Cambridge*
Michael Feuer, *The George Washington U.*
Peter Fratzl, *Max-Planck Inst.*
Elaine Fuchs, *Rockefeller U.*
Daniel Geschwind, *UCLA*
Andrew Gewirth, *U. of Illinois*
Karl-Heinz Glassmeier, *TU Braunschweig*
Julia R. Greer, *Caltech*
Elizabeth Grove, *U. of Chicago*
Kip Guy, *St. Jude's Children's Research Hospital*
Taekjip Ha, *U. of Illinois at Urbana-Champaign*
Christian Haass, *Ludwig Maximilians U.*
Steven Hahn, *Fred Hutchinson Cancer Research Center*
Michael Hasselmo, *Boston U.*
Martin Heimann, *Max-Planck Inst. Jena*
Yka Helariutta, *U. of Finland*
James A. Hendler, *Rensselaer Polytechnic Inst.*
Janet G. Hering, *Swiss Fed. Inst. of Aquatic Science & Technology*
Michael E. Himmel, *National Renewable Energy Lab.*
Kai-Uwe Hinrichs, *U. of Bremen*
Kei Hirose, *Tokyo Inst. of Technology*
David Hodell, *U. of Cambridge*
David Holden, *Imperial College*
Lora Hooper, *UT Southwestern Medical Ctr. at Dallas*
Thomas Hudson, *Ontario Inst. for Cancer Research*
Raymond Huey, *U. of Washington*
Steven Jacobsen, *U. of California, Los Angeles*
Kai Johnsson, *EPFL Lausanne*
Peter Jonas, *Inst. of Science & Technology (IST) Austria*
Matt Kaeberlein, *U. of Washington*
William Kaelin Jr., *Dana-Farber Cancer Inst.*
Daniel Kahne, *Harvard U.*
Daniel Kammen, *U. of California, Berkeley*
Masashi Kawasaki, *U. of Tokyo*
Joel Kingsolver, *U. of North Carolina at Chapel Hill*
Robert Kingston, *Harvard Medical School*
Alexander Kolodkin, *Johns Hopkins U.*
Roberto Kolter, *Harvard Medical School*
Alberto R. Kornblihtt, *U. of Buenos Aires*
Leonid Kruglyak, *UCLA*
Thomas Langer, *U. of Cologne*
Mitchell A. Lazar, *U. of Pennsylvania*
David Lazer, *Harvard U.*
Thomas Lecuit, *IBDM*
Virginia Lee, *U. of Pennsylvania*
Stanley Lemon, *U. of North Carolina at Chapel Hill*
Ottoline Leyser, *Cambridge U.*
Marcia C. Linn, *U. of California, Berkeley*
Jianguo Liu, *Michigan State U.*
Luis Liz-Marzan, *CIC biomaGUNE*
Jonathan Losos, *Harvard U.*
Ke Lu, *Chinese Acad. of Sciences*
Christian Lüscher, *U. of Geneva*
Laura Machesky, *CRUK Beatson Inst. for Cancer Research*
Anne Magurran, *U. of St. Andrews*
Oscar Marin, *CSIC & U. Miguel Hernández*
Charles Marshall, *U. of California, Berkeley*
C. Robertson McClung, *Dartmouth College*
Graham Medley, *U. of Warwick*
Yasushi Miyashita, *U. of Tokyo*
Richard Morris, *U. of Edinburgh*
Alison Motsinger-Reif, *NC State U.* **(S)**
Sean Munro, *MRC Lab. of Molecular Biology*
Thomas Murray, *The Hastings Center*
James Nelson, *Stanford U. School of Med.*
Karen Nelson, *J. Craig Venter Institute*
Daniel Neumark, *U. of California, Berkeley*
Timothy W. Nilsen, *Case Western Reserve U.*
Pär Nordlund, *Karolinska Inst.*
Helga Nowotny, *European Research Advisory Board*
Ben Olken, *MIT*
Luke O'Neill, *Trinity College, Dublin*
Joe Orenstein, *U. of California Berkeley & Lawrence Berkeley National Lab*
Harry Orr, *U. of Minnesota*
Andrew Oswald, *U. of Warwick*
Steve Palumbi, *Stanford U.*
Jane Parker, *Max-Planck Inst. of Plant Breeding Research*
Giovanni Parmigiani, *Dana-Farber Cancer Inst.* **(S)**
Donald R. Paul, *U. of Texas, Austin*
John H. J. Petrini, *Memorial Sloan-Kettering Cancer Center*
Joshua Plotkin, *U. of Pennsylvania*
Philippe Poulin, *CNRS*
David Randall, *Colorado State U.*
Colin Renfrew, *U. of Cambridge*
Felix Rey, *Institut Pasteur*
Trevor Robbins, *U. of Cambridge*
Jim Roberts, *Fred Hutchinson Cancer Research Ctr.*
Barbara A. Romanowicz, *U. of California,Berkeley*
Jens Rostrup-Nielsen, *Haldor Topsoe*
Mike Ryan, *U. of Texas, Austin*
Mitinori Saitou, *Kyoto U.*
Shimon Sakaguchi, *Kyoto U.*
Miquel Salmeron, *Lawrence Berkeley National Lab*
Jürgen Sandkühler, *Medical U. of Vienna*
Alexander Schier, *Harvard U.*
Randy Seeley, *U. of Cincinnati*
Vladimir Shalaev, *Purdue U.*
Robert Siliciano, *Johns Hopkins School of Medicine*
Joseph Silk, *Institut d'Astrophysique de Paris*
Denis Simon, *Arizona State U.*
Alison Smith, *John Innes Centre*
Richard Smith, *U. of North Carolina* **(S)**
John Speakman, *U. of Aberdeen*
Allan C. Spradling, *Carnegie Institution of Washington*
Jonathan Sprent, *Garvan Inst. of Medical Research*
Eric Steig, *U. of Washington*
Paula Stephan, *Georgia State U. and National Bureau of Economic Research*
Molly Stevens, *Imperial College London*
V. S. Subrahmanian, *U. of Maryland*
Ira Tabas, *Columbia U.*
Sarah Teichmann, *Cambridge U.*
John Thomas, *North Carolina State U.*
Christopher Tyler-Smith, *The Wellcome Trust Sanger Inst.*
Herbert Virgin, *Washington U.*
Bert Vogelstein, *Johns Hopkins U.*
Cynthia Volkert, *U. of Göttingen*
Douglas Wallace, *Dalhousie U.*
David Wallach, *Weizmann Inst. of Science*
Ian Walmsley, *U. of Oxford*
David A. Wardle, *Swedish U. of Agric. Sciences*
David Waxman, *Fudan U.*
Jonathan Weissman, *U. of California, San Francisco*
Chris Wikle, *U. of Missouri* **(S)**
Ian A. Wilson, *The Scripps Res. Inst.* **(S)**
Timothy D. Wilson, *U. of Virginia*
Rosemary Wyse, *Johns Hopkins U.*
Jan Zaanen, *Leiden U.*
Kenneth Zaret, *U. of Pennsylvania School of Medicine*
Jonathan Zehr, *U. of California, Santa Cruz*
Len Zon, *Children's Hospital Boston*
Maria Zuber, *MIT*

BOOK REVIEW BOARD
David Bloom, *Harvard U.,* **Samuel Bowring,** *MIT,* **Angela Creager,** *Princeton U.,* **Richard Shweder,** *U. of Chicago,* **Ed Wasserman,** *DuPont*

Published by AAAS

EDITORIAL

China's private universities

China's expansion of universities has not been on a level playing field. Earlier this year, Education Minister Guiren Yuan declared that the government must treat both public and private universities equally. As founder and president of one of China's largest private universities, I wholeheartedly agree. China's private universities can help usher in new opportunities for social and economic development, but they must be enabled to launch robust education programs and compete for research grants. Unless the government loosens restrictions on such endeavors, private universities could enter a tailspin, and such an erosion of higher education could threaten social stability.

China is no newcomer to private higher education. More than 2000 years ago, Confucian, Taoist, and Buddhist private schools, among others, prospered. With the establishment of modern China in 1949, the young nation embraced public ownership, and private higher education was abolished. As China embarked on an era of reform in the 1970s, the cash-strapped central government gradually enabled the reestablishment of private universities to meet the demand for skilled workers. Today, private universities account for 19.3% of higher education institutions, and 19.7% of all university students matriculate there.

Unfortunately, the rapid expansion of private universities has not received adequate support from the government. In 2011, of the $114 billion that the central government spent on higher education, only 0.44% went to private universities, primarily for destitute-student stipends. Because private universities receive almost no financial support from the government, they find it hard to compete with public universities in faculty recruitment and for infrastructure and equipment funds. Only public universities can enjoy government direct or indirect subsidies for mandatory laboratory equipment, for example, and for dormitory amenities (such as air conditioners). In addition, private universities face many restrictions in launching graduate degree programs and deciding how many students may enroll. Private universities have had no choice but to tolerate such unfair treatments.

"Any private institution of learning that cannot obtain government funding for research will never obtain international prestige..."

But private universities have several advantages over public universities. The latter tend to be overstaffed, follow rigid rules, and support a unified salary system, whereas private universities are guided by market and social needs. At any time, the skills and talents cultivated by private universities can be adjusted to match emerging industries, and management can be changed according to policy trends. Private universities also focus on the quality of accomplishments in faculty performance appraisals.

The biggest advantage of private universities is the system of responsibility that separates management from ownership, which limits the profit-seeking of investors and the casualness of operators. The board of directors at a private university has more decision-making power, chooses the university's president, and has substantial oversight to curtail inept or corrupt university leadership. The president of a public university must obey the government's rigid management model, which in almost any institution can breed the conditions for dereliction of duty, corruption, and other bad behaviors.

Any private institution of learning that cannot obtain government funding for research will never obtain international prestige, and their graduates will suffer an even greater disadvantage in landing jobs, which could exacerbate social problems. That is precisely why Minister Yuan's message is heartening. He offers a radical and new perspective. He has vowed to set up special funds consistent with the nature of private university operating funds and property rights to promote curriculum development and quality control, feature coursework and programs consistent with local needs and university culture, support academic research and public services, and incorporate information technology to enhance and improve the university mission. It's time to implement these uplifting intentions. The central government must enshrine, in legislation, equal treatment for public and private universities. – **Huiqing Jin**

Huiqing Jin is the president of Anhui Sanlian University, Hefei, China. E-mail: jinhuiqing@sanliangroup.com.cn

10.1126/science.1262035

IMAGES: (INSET) G.GRULLÓN/*SCIENCE*/ISTOCKPHOTO.COM; (RIGHT) ANHUI SANLIAN UNIVERSITY

Downloaded from www.sciencemag.org on October 24, 2014

Published by AAAS

$4,500,000

Legal fees paid by the University of California, Los Angeles, to defend chemistry professor Patrick Harran in a case involving a fatal laboratory fire in 2008. The case was settled in June. **http://scim.ag/Harrancase**

IN BRIEF

Siding Spring comet snapped

Siding Spring buzzed by Mars this week (*above*), but left orbiting NASA and ESA probes unscathed.

Planetary scientists have lifted the veil from comet Siding Spring, which brushed past Mars on 19 October. The image of the comet's nucleus at left—usually hidden in a cloud of gas and dust—was taken by NASA's Mars Reconnaissance Orbiter at a distance of 138,000 kilometers, or nearly a third of the distance between Earth and the moon. It is the first resolved picture of a long-period comet, one with an orbit of a million years or more and originating from the Oort cloud, a shell of icy planetesimals at the edge of the solar system. Siding Spring's nucleus is smaller than expected—about half a kilometer across—and the comet is half the size of a typical short-period comet (hailing from the Kuiper belt past Neptune). The size difference might point to different formation mechanisms in the different parts of the solar system more than 4.5 billion years ago.

AROUND THE WORLD

Icy worlds for post-Pluto visit

WASHINGTON, D.C. | Members of NASA's New Horizons team can breathe a sigh of relief: The mission won't have to end with its July 2015 visit to Pluto. On 15 October, NASA announced that the Hubble Space Telescope had identified three candidate Kuiper belt objects (KBOs) for a follow-on mission after the Pluto flyby. Finding target KBOs—small icy worlds that circle the sun in orbits beyond Neptune—was a challenge, both because the objects are so faint and because telescopes had to find them against the bright, cluttered backdrop of the center of the Milky Way galaxy. Hubble has identified one target that is definitely within reach given New Horizons' remaining fuel, and two others that are potentially so. They are 1% to 2% the size of Pluto.

Lockheed's new fusion machine

BETHESDA, MARYLAND | Defense firm Lockheed Martin caused a stir last week when it revealed it was working on a fusion reactor that could power a small city, fit on a truck, and would be ready for commercialization in a decade. Twitter was abuzz, and researchers likened it to the 1980s frenzy over cold fusion. At a 20 October press conference, team leader Thomas McGuire revealed plans for a device that combined techniques known as cusp confinement and magnetic mirrors, both approaches that were tested by fusion researchers and largely abandoned last

> "Everything is slowed down. But I wouldn't make that statement."

National Institute of Allergy and Infectious Diseases head Anthony Fauci on *Meet the Press* 19 October, contradicting National Institutes of Health (NIH) head Francis Collins's statement that an Ebola vaccine would have been available were it not for NIH budget cuts.

PHOTOS: (TOP TO BOTTOM) SEN/D. PEACH; NASA/JPL-CALTECH/UNIVERSITY OF ARIZONA

Downloaded from www.sciencemag.org on October 24, 2014

Published by AAAS

Few common midwife toads remain healthy.

Virus killing Europe's amphibians

A type of ranavirus (RV) is being blamed for gruesome deaths and declining populations of a wide range of species in the Picos de Europa National Park in northern Spain, according to research published online last week in *Current Biology*. The virus was first noticed in 2005; park biologists tracking six common species of amphibians there have seen sick animals with necrotic tissue, open sores, and internal hemorrhages. The common midwife toad has been most severely affected, as well as the common toad and the alpine newt. The virus, named the common midwife toad virus, adds to the woes of the world's amphibians, which have been declining at a worrying rate. A major culprit, the chytrid fungus *Batrachochytrium dendrobatidis*, has apparently driven many species of frogs extinct in the tropics. The new RV, in contrast, seems to be a problem for temperate species. **http://scim.ag/toadvirus**

century. "We have an idea that makes us very excited," he told reporters, but declined to reveal any results on the device's performance. That will come next year. The team is now looking for technology partners. **http://scim.ag/Lockheedreactor**

India boosts students' stipend

NEW DELHI | As a "special gift" on the holiday of Diwali, in which Hindus honor the goddess of wealth, the Indian government announced on 21 October that the monthly stipend for state-funded graduate students and postdoctoral students, amounting to about 71,000 researchers, will go up by 60% on average. Researchers had protested the low pay for months. "No doubt this is long overdue … but what is really required is a policy by which there are periodic and predictable revisions in scholarships," says evolutionary biologist Raghavendra Gadagkar, the president of the Indian National Science Academy. "The demand was legitimate and the science ministry worked doubly hard to get this pay hike implemented," says India's science minister, Jitendra Singh. **http://scim.ag/Indiastipend**

Yucca Mountain passes hurdle

NYE COUNTY, NEVADA | Remember Yucca Mountain? A 781-page report, published 16 October by the Nuclear Regulatory Commission (NRC), on the proposed nuclear waste repository has given the site a thumbs up, concluding that it has "multiple barriers to isolate radioactivity from the environment" for hundreds of thousands of years. The report is the second of five assessment volumes to be published on Yucca. The site was designated in 1987 legislation as a repository and has faced political opposition in Nevada ever since. In 2008, the Department of Energy submitted a license application to open the repository, but withdrew it 2 years later. Last year, a court ordered NRC to move forward with its review and licensing process. **http://scim.ag/Yuccahurdle**

Fusion road map criticized

WASHINGTON, D.C. | U.S. fusion scientists are blasting a Department of Energy (DOE) report outlining a 10-year plan for their field. Drafted in double-quick time by a subcommittee of the Fusion Energy Sciences Advisory Committee (FESAC) that, at DOE's request, included no members from existing U.S. fusion labs, the report proposes less basic plasma physics and more technology for future power reactors. It recommends that the United States be ready to build a large new reactor in 10 years' time. Fusion researchers attacked the report, calling it "flawed" and rife with conflicts of interest. Of the 23 FESAC members who voted on the report on 10 October, 14 recused themselves for connections to a lab that might benefit from the report's recommendations. The nine remaining voters voted 6 to 3 to approve the report. **http://scim.ag/USfusionplan**

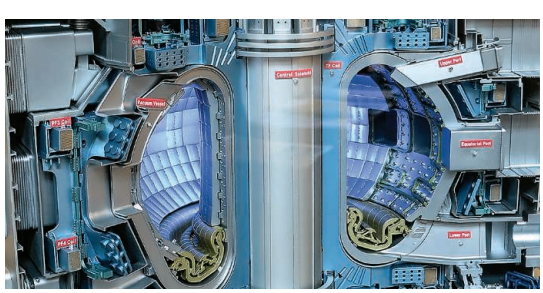

Mock-up of the ITER fusion reactor, under construction in France with U.S. and other international support.

NEWSMAKERS

Obama names Ebola czar

Last week the Obama administration named lawyer **Ron Klain** to coordinate Ebola efforts. Lawmakers had called on the president to designate an Ebola czar in the wake of the mishandling of the first U.S. case, and Klain, former chief of staff to two Democratic vice presidents, is a battle-scarred veteran of Washington policy crises. At the same time, Klain's appointment highlighted the absence of a Senate-confirmed U.S. surgeon general. The 15-month vacancy is the result of Republican opposition to Vivek Murthy, a 36-year-old physician and health care advocate who was nominated in November 2013.

PHOTOS: (TOP TO BOTTOM) © LAURENT LEBOIS/FLICKR; CONLETH BRADY/IAEA

Published by AAAS

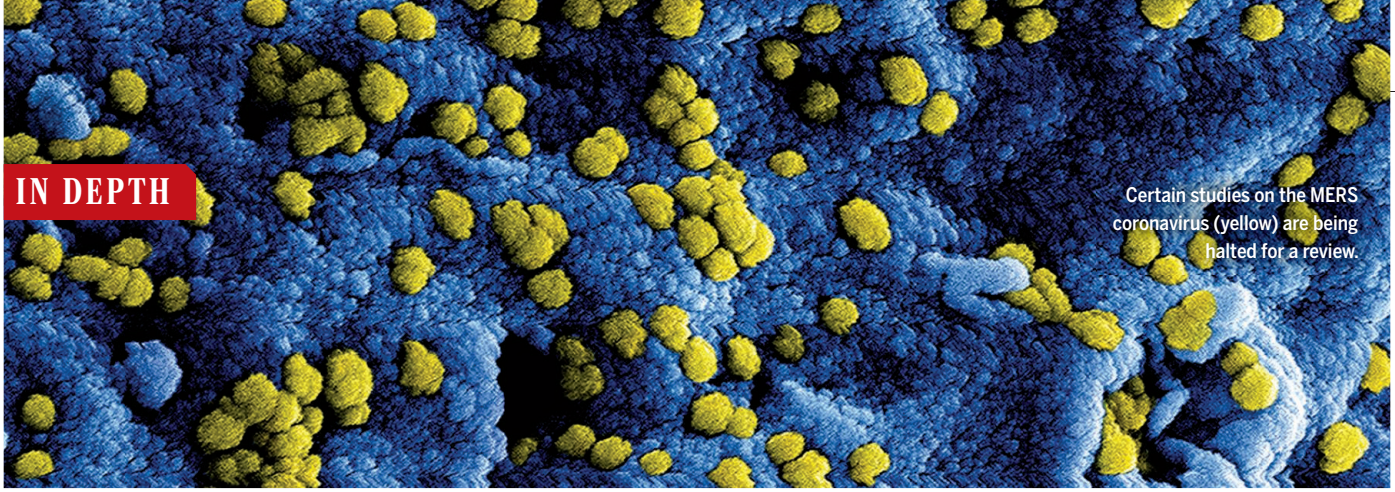

IN DEPTH

Certain studies on the MERS coronavirus (yellow) are being halted for a review.

BIOSECURITY

U.S. halts two dozen risky virus studies

One-year "pause" to develop new policy on controversial research that enhances pathogens

By **Jocelyn Kaiser**

Ebola isn't the only virus scaring the U.S. government. It is also worrying about a hypothetical threat: a deadly virus created in a lab. On 17 October, in an unprecedented step, federal officials moved to stop so-called gain-of-function (GOF) studies on three kinds of viruses. To buy time for experts to work out a government-wide policy for weighing the risks and benefits of such work, officials are halting all new funding for the studies and are asking researchers doing ongoing work to agree to a voluntary moratorium.

Although the microbiology community had expected some sort of "pause" for weeks, the move took some researchers by surprise because it potentially covers studies on any influenza strain—not just two bird strains that are already tightly restricted—as well as two coronaviruses: SARS, which panicked Asia in 2003, and MERS, now spreading from camels to people in the Middle East. The funding pause affects about two dozen projects supported by the National Institutes of Health (NIH), but the voluntary moratorium could put the brakes on more. As *Science* went to press, researchers were scrambling to consult with their program officers at NIH to find out whether they would have to halt their work.

The debate kicked off 3 years ago when two separate research teams revealed that they had altered the H5N1 avian influenza strain, which doesn't normally transmit among mammals, so that it could spread between ferrets. Many scientists worried that if the new lab strains were accidentally or deliberately released, they could spark a deadly pandemic. But proponents argued that such studies will help public health researchers detect an impending flu pandemic and prepare vaccines.

After researchers agreed to a 1-year voluntary moratorium on GOF H5N1 studies and the U.S. government issued new rules, the work resumed last year. But concerns have reignited as new papers on risky human-made flu strains have come out in recent months. Meanwhile, reports of mishandled samples at the U.S. Centers for Disease Control and Prevention have raised questions about safety at U.S. high-containment labs. Scientists known as the Cambridge Working Group collected nearly 300 signatures on a July statement calling for studies on "potential pandemic pathogens" to be "curtailed" until the risks and benefits could be evaluated; another large group, Scientists for Science, defended the studies as safe but also called for a meeting to discuss the issues (*Science*, 5 September, p. 1112).

The funding pause, developed by the White House Office of Science and Technology Policy and the Department of Health and Human Services, applies to new studies "that may be reasonably anticipated to confer attributes to influenza, MERS, or SARS viruses such that the virus would have enhanced pathogenicity and/or transmissibility in mammals via the respiratory route." The government also "encourages" those now doing this work, even if not with federal funding, to stop. Testing of naturally occurring forms of these pathogens can continue as long as the tests don't increase risks.

During the pause, U.S. officials plan to evaluate the risks and benefits of GOF experiments and to develop a policy for approving new studies. The process was scheduled to begin this week with a meeting of the National Science Advisory Board for Biosecurity (NSABB), an advisory group that has not convened for 2 years. The National Academies' National Research Council and Institute of Medicine will also hold a workshop to discuss the scientific issues; they will later review NSABB's recommendations, which are due within 6 months. The plan is to have a final policy in place within a year, when the pause will end—except, presumably, for studies that don't pass the new risk assessment process.

Two researchers who led the original H5N1 studies—Yoshihiro Kawaoka of the University of Wisconsin, Madison, and Ron Fouchier of Erasmus MC in the Netherlands—said they are ready to comply.

Coronavirus researcher Stanley Perlman of the University of Iowa in Iowa City said his lab's efforts to generate a new MERS strain will have to stop for now. His goal is to develop a virus that sickens mice, making possible a mouse model for testing MERS drugs and vaccines. Adapting a virus to mice usually makes it less pathogenic in humans, he notes. He's hoping to qualify for an exception in the policy for studies "urgently necessary to protect the public health." Says Perlman: "I think it [the policy] caught a fish that wasn't meant to be caught."

Despite the confusion over exactly which studies will be affected, those who think GOF studies need more scrutiny are celebrating. Harvard University epidemiologist Marc Lipsitch, who co-organized the Cambridge Working Group, says he is "very pleased." Boston University microbiologist Paul Duprex, a leader of Scientists for Science, says that although he is "not a fan of blanket bans," there is "precedent" because of the earlier voluntary moratorium. He looks forward to "the presentation of hard evidence." The debate will continue before NSABB this week, where both Lipsitch and Duprex are expected to speak. ■

IMAGE: NIAID/FLICKR/CREATIVE COMMONS

Downloaded from www.sciencemag.org on October 24, 2014

Published by AAAS

HUMAN EVOLUTION

How we tamed ourselves—and became modern

'Self-domestication' turned humans into the cooperative species we are today

By **Ann Gibbons**, *in San Diego, California*

Call a man "tame" or "domesticated" and he's not likely to take it as a compliment. But all of us, male and female, may have to get used to it: Some scientists believe that "self-domestication" was key to the evolution of our species. At a meeting here earlier this month, they argued that with our reduced jaws, flat faces, and lower male aggression, humans are as tame as many of the animals we live with. Like dogs, cows, and horses, we show many of the physical traits that emerge during animal domestication. The accompanying changes in behavior, especially among men, might have helped humans evolve more complex language, live atop each other in cities, and work together to create sophisticated cultures.

No one set out to domesticate humans, of course. But at the first-ever symposium on self-domestication of humans (see http://carta.anthropogeny.org/symposia/past_list), held here at the Salk Institute for Biological Studies, researchers outlined a set of linked behavioral and anatomical changes seen in animals that humans have tamed as well as in creatures that have tamed themselves. In the course of evolution, some animals have overcome the fear and stress they feel when encountering humans or unfamiliar members of their own species and become less aggressive. Bonobos, for example, are much less aggressive with each other than are their chimpanzee relatives, researchers noted. Other species may have tamed themselves to live alongside humans, such as seals and ancient cats.

Researchers at the symposium proposed that something similar happened as human ancestors began to live in closer quarters, relying more on each other and on wider social networks to survive. By favoring more tolerant, less antagonistic individuals, natural selection reshaped both our behavior and our appearance. "The hypothesis that humans may have domesticated themselves … has the potential to solve many of the long-standing problems of human evolution," says linguist Robert Kluender of the University of California, San Diego.

The view of humans as domesticated dates back to 1871, when Charles Darwin wrote that "[m]an in many respects may be compared with those animals which have long been domesticated." Darwin also was the first to discover that selective breeding for tameness produced similar side effects in different animals, including smaller brains.

Since Darwin's time, others have confirmed and expanded upon his observations, identifying the elements of a "domestication syndrome." In a renowned study started back in the 1950s, Russian researchers found that captive silver foxes bred for tameness also exhibited a suite of other traits, such as white patches of fur on their heads, curly tails, "feminized" faces with shorter snouts and floppy ears, and skulls in males that weren't much larger than in females. "Just by choosing foxes that were less nasty, they got a suite of other changes," says cognitive biologist Tecumseh Fitch of the University of Vienna.

In a study in *Current Anthropology* in August, paleoanthropologist Robert Franciscus of the University of Iowa in Iowa City and his colleagues identified some of the same changes in recent human evolution. The team analyzed the projection of the brow ridge, facial shape, and cranial volume of 13 early *Homo sapiens* that lived before 80,000 years ago; 41 modern humans that lived 38,000 to 10,000 years ago; and skulls from a global sample of 1367 recent humans. They found that brow ridges shrank and faces shortened during the past 80,000 years, as our ancestors began to exhibit symbolic behavior and spread around the world. Cranial volume also diminished, particularly after the invention of agriculture about 10,000 years ago.

All of these changes tend to make male faces look more like female ones, Franciscus noted at the meeting, and are linked to lower testosterone levels. He and his colleagues proposed that selection for higher levels of social tolerance led to lower levels of testosterone and stress hormones, especially in males, and thus facial feminization. Studies of dog DNA have shown that the genes that regulate aggression affect development of facial shape, he reported at the meeting.

Other speakers proposed that all of these traits, from hormone levels to craniofacial features, have a common root in early embryonic development. Fitch and co-authors Richard Wrangham of Harvard University and Adam Wilkins of Humboldt University in Berlin, who proposed their theory in July in *Genetics*, point out that these traits are controlled by so-called neural crest cells, which in vertebrate embryos form a neural tube along the spine. As development proceeds, neural crest cells break away, migrating from head to toe to form tissues involved in pigmentation, muscles, teeth, bone, cartilage, and adrenal glands, which produce stress hormones as well as testosterone.

The team proposed that this process is

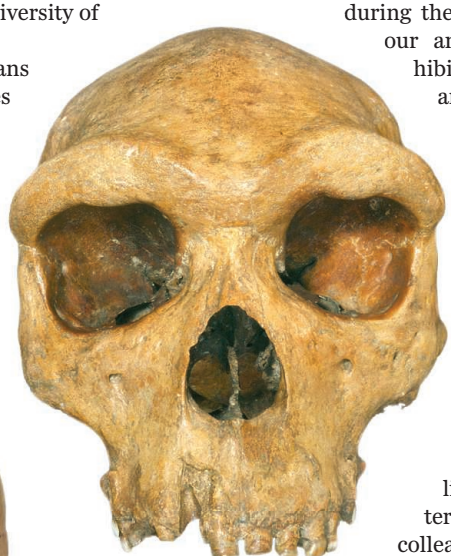

Big brow ridges and teeth suggest that ancient *Homo heidelbergensis* (*above*) may have had more testosterone than modern *Homo sapiens* (*left*).

PHOTOS: THE NATURAL HISTORY MUSEUM/ALAMY (2)

Downloaded from www.sciencemag.org on October 24, 2014

Published by AAAS

drawn out in domesticated animals, because domestication selects for animals that develop more slowly. Very young animals—2- to 3-month-old puppies, for example—are naturally less fearful and produce less stress hormones. During that time, puppies exposed to friendly humans can learn to cooperate with people. Prolonging that period of development favors such learning, crucial to domestication. Other studies at the meeting confirmed that domestication lengthens development, with important consequences for behavior. For example, young domesticated Bengalese finches have a longer window of song learning and so can learn more complicated songs than their wild progenitors, reported biopsychologist Kazuo Okanoya of the University of Tokyo.

But slower development also means that fewer neural crest cells reach their destinations, Fitch and colleagues argue. This affects everything from the adrenal glands to coloration of the fur on the face or tail and lengthening of the snout, creating the domestication syndrome, Fitch said. It would also explain why so many domesticated animals exhibit "neoteny": They retain juvenile traits as adults. Mature dogs look like wolf pups, and humans look more like chimp infants than chimp adults, researchers noted at the meeting.

In his talk, Wrangham argued that natural selection triggered just such a process of delayed development and reduced aggression in humans. Ethnologists have observed that hunter-gatherers kill men who steal wives or kill others. As social ties became more important to survival, Wrangham thinks, human ancestors may have inflicted the same kind of capital punishment, weeding out males who acted with intense and confrontational aggression. This doesn't mean that humans are not "a dastardly species," capable of war and torture, he noted, only that selection favored males who could work together, whether for peaceable ends or to carry out "low-arousal" or coalitional aggressive acts such as war.

Others were intensely interested in this idea, but urged more tests. Fitch was among the first to point out the problems with his own team's theory: Humans and bonobos don't seem to have all the traits of the domestication syndrome—no floppy ears or white facial patches for us. A mechanism other than delayed development of the neural crest therefore may explain some features of domestication in humans and bonobos. "It's very daring to talk about the self-domestication syndrome," Fitch says. "The hard work is figuring out how to test it." ■

MIGRATIONS

Epic pre-Columbian voyage suggested by genes

South American DNA found in Easter Islanders

By **Andrew Lawler**

Polynesians from Easter Island and natives of South America met and mingled long before Europeans voyaged the Pacific, according to a new genetic study of living Easter Islanders. In this week's issue of *Current Biology*, researchers argue that the genes point to contact between Native Americans and Easter Islanders before 1500 C.E., 3 centuries after Polynesians settled the island also known as Rapa Nui, famous for its massive stone statues. Although circumstantial evidence had hinted at such contact, this is the first direct human genetic evidence for it.

In the genomes of 27 living Rapa Nui islanders, the team found dashes of European and Native American genetic patterns. The European genetic material made up 16% of the genomes; it was relatively intact and was unevenly spread among the Rapa Nui population, suggesting that genetic recombination, which breaks up segments of DNA, has not been at work for long. Europeans may have introduced their genes in the 19th century, when they settled on the island.

Native American DNA accounted for about 8% of the genomes. Islanders enslaved by Europeans in the 19th century and sent to work in South America could have carried some Native American genes back home, but this genetic legacy appeared much older. The segments were more broken and widely scattered, suggesting a much earlier encounter—between 1300 C.E. and 1500 C.E.

But did Polynesians land on South American beaches, or did Native Americans sail 3500 kilometers into the Pacific to reach Rapa Nui? "Our studies strongly suggest that Native Americans most probably arrived [on Rapa Nui] shortly after the Polynesians," says team member Erik Thorsby, an immunologist at the University of Oslo. He thinks that could support the controversial theory, posited by Norwegian adventurer Thor Heyerdahl more than a half-century ago, that Native Americans had the skills to move west across the Pacific.

But many scientists say that Pacific currents and Polynesian mastery of the waves make it more likely that the Polynesians were the voyagers. They may have sailed to South America, swapped goods for sweet potatoes and other novelties—and returned to their island with South American women.

Sweet potato was domesticated in the Andean highlands, and researchers recently determined that the crop spread west across Polynesia before Europeans arrived (*Science*, 11 June 2010, p. 1344). Another hint of trans-Pacific exchange comes from chicken bones—unknown in the Americas before 1500 C.E.—excavated on a Chilean beach, which some believe predate Christopher Columbus.

Skeptics say that genetic evidence from modern human populations is not enough to prove ancient contact. The genetic clock is often uncertain, says anthropologist Carl Lipo Lipo of California State University, Long Beach. "We need ancient DNA from skeletal evidence—not modern evidence—to resolve this question." ■

Wooden canoes like this one from Easter Island may have brought Native Americans and Polynesians together.

ILLUSTRATION: © MARY EVANS PICTURE LIBRARY/ALAMY

Published by AAAS

Taiwan's *Ocean Researcher V* was in service for less than 2 years when it sank on 10 October.

OCEAN RESEARCH

Taiwan's ocean program reels from loss of ship, scientists

New vessel was sparking international collaborations

By **Dennis Normile**

The sinking of Taiwan's *Ocean Researcher V* on 10 October, barely a day into a cruise to study atmospheric pollution, not only claimed the lives of two scientists but also dealt the nation's ocean research program a devastating blow.

The 2700-ton, 72.6-meter-long ship, in service for less than 2 years, had "put Taiwan's oceanography on the map," says Shaw-Chen Liu, an atmospheric chemist at Academia Sinica's Research Center for Environmental Changes in Taipei. Colleagues overseas, too, are mourning. "This loss is felt by the international community," says Kirk McIntosh, a geophysicist at the University of Texas Institute for Geophysics in Austin, a veteran of collaborations with Taiwan.

The Ministry of Science and Technology, which owns the ship through its National Applied Research Laboratories, has found itself on the defensive over its decision to hire a private shipping company to supply a crew. According to local press reports, Science and Technology Minister San-Cheng Chang has promised to review the outsourcing policy pending the results of an accident investigation. Meanwhile, the Taiwan Ocean Research Institute (TORI) in Kaohsiung, which managed the ship's scientific operations, is hoping to rebound quickly. "We are trying to get a ship as a temporary replacement," says TORI Director Hui-Ling Lin.

The accident's cause is unclear. *Ocean Researcher V* had departed Tainan, a city in southern Taiwan, on the morning of 9 October, carrying 27 researchers and students and an 18-member crew on a planned 8-day mission. Around noon on 10 October, the crew decided to return to port because of worsening weather. In the late afternoon, the ship apparently struck a reef and started taking on water. It sank shortly after 8 p.m. that evening near the Penghu Islands, about 260 kilometers southwest of Taipei in the Taiwan Strait.

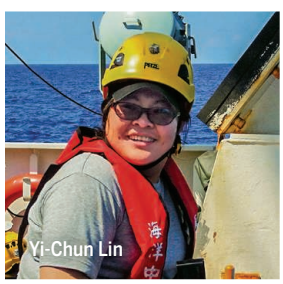
Yi-Chun Lin

Shih-Chieh Hsu

The cruise's chief scientist, 47-year-old Shih-Chieh Hsu, remained aboard the listing vessel until the rest of the researchers and students were swimming in the choppy water toward rescuers. "He helped others before jumping [off the] ship," Liu says. His body was recovered later that evening; he had drowned despite wearing a life jacket.

Hsu, an environmental scientist, "was outstanding. I have rarely seen anyone work as hard," says Liu, who recruited Hsu in 2001. The institute, Liu says, built a program on air quality and air-sea interactions around Hsu's expertise in aerosols. The other victim was Yi-Chun Lin, a TORI engineering assistant. "Yi-Chun was a sweet angel. We all miss her," says Hui-Ling Lin, who is no relation.

The $48 million ship had been a dream of researchers since the late 1990s. Taiwan's marine scientists had been using three small vessels that were limited to coastal waters. In 2007, after years of appeals, the government appropriated funds for a deep-sea vessel with state-of-the-art features: a computer-controlled dynamic positioning system for keeping the vessel in one place or on track despite winds, waves, and currents; the capacity to launch a remotely operated vehicle and tow a 6-kilometer-long seismic survey streamer to probe seafloor geology; and onboard labs for biology and chemistry analyses. Institutes across Taiwan ramped up programs in anticipation of the enhanced capabilities.

Despite its short life, *Ocean Researcher V* was racking up a solid record of accomplishments, says Shu-Kun Hsu, a marine geophysicist at National Central University in Jhongli: From the sea floor southwest of Taiwan, the ship scooped methane hydrate—methane trapped in a crystal lattice of ice—perhaps a future energy source for the resource-poor nation. It also mapped the many poorly charted low islands, reefs, and atolls in the Dangerous Ground region of the South China Sea, which is the focus of long-simmering territorial disputes. Taiwan has wanted to strengthen research in the area for strategic as well as scientific reasons, Lin notes.

Other nations took notice of Taiwan's new asset. This past summer, researchers from several Philippine institutes joined a cruise aboard *Ocean Researcher V* to investigate the complex geology of the subduction zone where the Philippine plate is diving beneath Eurasia. McIntosh says the chance to study this tectonic collision had sparked collaborations among scientists from the United States, Europe, and Taiwan that stretch back at least a decade. McIntosh hopes to revive plans for further cooperation after his Taiwanese colleagues "get past this disaster."

Hsu says that it could take several months to unravel the sinking's cause, negotiate with insurers, and decide whether to salvage the craft, which now lies 30 to 40 meters deep. "Even if the ship is recovered, I don't think it could be repaired," Lin says.

The long-term hope is to build a new deep-sea ship, Lin says. In the meantime, she says, the institute might lease a retired vessel from another country. She vows to keep TORI's deep-sea research program alive. ■

PHOTOS: (TOP TO BOTTOM) TAIWAN OCEAN RESEARCH INSTITUTE (2); RESEARCH CENTER FOR ENVIRONMENTAL CHANGES

Downloaded from www.sciencemag.org on October 24, 2014

Published by AAAS

U.S. POLICY

Election stakes go beyond control of the Senate

Funding, peer review, water rules, fusion, and other science issues on tap after the vote

By **Jeffrey Mervis**

For many political junkies, the 4 November U.S. election is about whether Republicans can win control of the U.S. Senate and rule both houses of Congress. If they succeed, Republicans would have even more leverage to block anything that President Barack Obama wants to do during his final 2 years in office.

For many science advocates, however, the Senate's fate is merely a sideline in their continued campaign to reverse stagnating science budgets and ward off new automatic, across-the-board budget cuts like last year's sequester. They are also waiting to see how the next Congress and the White House resolve a bevy of science-related policy controversies.

The drama will play out in two acts. The first opens when the current Congress returns to Washington, D.C., for a 6-week lame-duck session. The second will begin in January after members of the 114th Congress are sworn in and get down to business.

In the lame duck, the spotlight will be on budget issues. That's because Congress couldn't agree on a spending plan for the 2015 fiscal year, which began 1 October. Instead, it froze budgets at existing levels before recessing for the fall campaign. A final 2015 budget is more likely to happen if the election preserves the status quo, observers predict. In contrast, if Republicans capture the Senate, they may be more inclined to wait until the new session to act on spending issues. And their victory could well be seen as a mandate for fiscal restraint.

Whatever the makeup of the next Congress, lawmakers will need to confront the specter of automatic, across-the-board cuts. This budget-cutting mechanism is enshrined in a 2011 law called the Budget Control Act (BCA), which requires a $1 trillion reduction in the deficit through 2021 by means of some combination of cuts and additional revenue. When Congress couldn't agree on how to allocate the cuts, the so-called sequester took effect in March 2013 for the rest of that year's budget. It meant a 5% cut to the National Institutes of Health and many other civilian science agencies. A budget deal last December suspended the mandatory cuts for 2014 and 2015, but they will come roaring back in 2016.

Both Democrats and Republicans have said they despise the sequester (often for different reasons), and Obama has already hinted that the White House's 2016 budget request, expected in February, will propose lifting the BCA's spending caps. The 2011 law has done its job, the administration argues: The annual budget deficit for 2014 was $483 billion, the lowest since 2008; at 2.8% of the gross domestic product, it's below the average for the past 40 years. It's time to reinvest in science and other national needs, White House officials argue, if necessary by trimming some mandatory spending programs.

Does science suffer an 'innovation deficit'?

By **Jeffrey Mervis**

Behold the "innovation deficit." U.S. science lobbyists coined the phrase last year to help make an economic argument for increasing federal funding of basic research, namely, that the current spending levels are too low for the United States to remain a global leader in innovation. Given political and budget realities, erasing this "deficit" anytime soon will take a minor miracle. But the phrase seems to be catching on, despite the fact that a one-time surge of funds could create its own problems.

The chair of the powerful Senate Appropriations Committee, Senator Barbara Mikulski (D–MD), used the phrase three times in her opening remarks at a hearing last spring on how to spur U.S. innovation by boosting science budgets. Lawmakers have also embraced its logic in pending legislation to pump up the budget of the National Institutes of Health (NIH). NIH supports roughly half of all federally funded basic research, so a sizable increase for that agency would go a long way toward meeting the community's goal.

But is the innovation deficit real? The argument rests on two claims: Research has paid handsome societal dividends, and current spending has fallen behind some past long-term rate of growth. The first premise is undeniable. But there's no clear evidence to support the second.

Trends in federal spending over the past 20 years for what amounts to basic research suggest that the supposedly predictable and steady support for research may be illusory (see graph). In the case of NIH's budget, for instance, the last 2 decades include two

What's your line?

Four scenarios for future U.S. spending on basic science

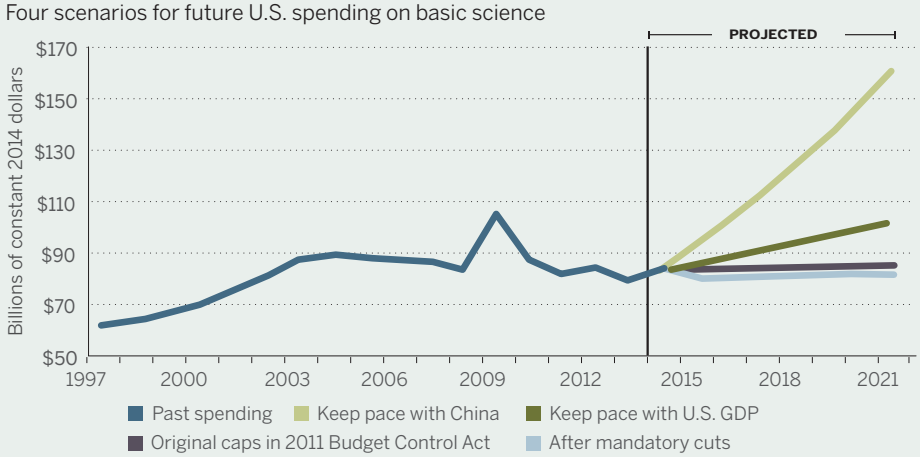

DATA: M. HOURIHAN/AAAS

Downloaded from www.sciencemag.org on October 24, 2014

Published by AAAS

Representative David McKinley (R–WV), *right*, shakes hands with Jon Retzlaff, a government affairs official with the American Association for Cancer Research.

It's too early to know whether the new Congress will agree to tweak the BCA or how much of any "new" money would go to science. Research advocates are ready with a new catch phrase, the "innovation deficit," to help them make a case for a funding boost (see sidebar, p. 408). But that's just one issue that science advocates will be following closely. Here are others:

NSF POLICY: The current session saw a bitter fight between the community and Republicans on the House of Representatives science committee over the panel's plan to revise peer review, cut social science funding, and make other operational changes at the National Science Foundation (NSF). The legislation never came to a vote on the House floor, however, and research advocates are hoping the next version hews closer to current NSF policies.

WATERWAYS: A draft rule from the Environmental Protection Agency defining what kinds of waters federal agencies have the power to protect has upset farm groups, who fear it could give the federal government greater control over private land. Last month, the House passed a bill that would block it. But the White House says the president would veto the measure if it were to pass Congress.

RESEARCH REGULATIONS: Universities say they are making progress in persuading Congress to ease what they consider burdensome and unnecessary research regulations, such as grant-reporting requirements. In July, the House passed a bipartisan bill (H.R. 5056) creating a White House task force to review the rules. The Senate has yet to act.

FUSION: Ballooning costs and slipping schedules for ITER, an experimental fusion reactor being built in France, have led the Senate to propose a U.S. pullout, with its contribution—$200 million this year—redirected to domestic fusion programs. The House so far has stood behind the multinational project despite its problems.

IMMIGRATION: Efforts to enact comprehensive reform of the nation's immigration system have collapsed in Congress, but the White House may bypass Congress and move administratively to expand the number of high-skill workers eligible for a green card work permit. Another option is legislation focused narrowly on that elite population. ■

sharp rises—a 5-year doubling between 1998 and 2003 and a one-time bolus of money in 2009 that increased NIH's budget by roughly one-third. Those peaks stand out among stretches of essentially flat budgets, aside from a dip in 2013 because of mandatory cuts under the Budget Control Act (BCA), or "the sequester," and a partial rebound this year.

Another funding dip is coming in 2016 under the BCA, unless Congress and the White House strike a new long-term spending deal. In the meantime, a few Democratic legislators have offered a novel solution: Exempt NIH's budget from the BCA on the grounds that biomedical research is too important to be subject to arbitrary reductions in the name of fiscal responsibility.

Legislation sponsored by Senator Tom Harkin (D–IA) and Representative Rosa DeLauro (D–CT) would give lawmakers emergency powers under the BCA to boost NIH's budget by 10% annually in 2015 and 2016 and by 5% for each of the next 5 years—without having to take the money from another federal agency. "This bill will put a plan in place for the Appropriations Committee to reverse the 10-year retrenchment in biomedical research funding over the remaining years of the Budget Control Act," Harkin said in July in introducing the Accelerating Biomedical Research Act. A second bill, by Senator Richard Durbin (D–IL), would create a trust fund that would provide a 5% annual increase after inflation for NIH, the Centers for Disease Control and Prevention, and several military biomedical research programs. However, Durbin hasn't explained how the trust fund would be financed.

The bills stand almost no chance of becoming law this year. Still, some lobbyists hope that Harkin, who is retiring in December after 40 years in Congress, will make a last-ditch push to apply the exemption for NIH to the 2015 bill covering the entire federal budget that lawmakers will take up in their lame-duck session. Harkin's proposal might be attractive to legislators, because it allows them to be generous to NIH without squeezing elsewhere.

If adopted, however, Harkin's approach to closing the innovation deficit could trigger yet another dramatic budget swing for NIH, especially if it were adopted only for 2015. Scientific leaders have long bemoaned such sudden fluctuations, saying they are disruptive and make long-range planning nearly impossible. And upturns send false messages of hope that the good times will extend into the foreseeable future.

The potential downsides don't seem to bother science lobbyists. "We're advocating for the [Harkin] bill because of the need to get NIH back on track," says Jennifer Poulakidas of the Association of Public and Land-grant Universities in Washington, D.C. "If there's the possibility of expanding that approach to all federally funded research, then we'd be in favor of that, too. But the key is to take that first step. And you can make a special case for NIH because of the importance of finding cures and better treatments."

Jennifer Zeitzer, a lobbyist for the Federation of American Societies for Experimental Biology in Bethesda, Maryland, puts it simply. "We support anything that helps NIH. It's our No. 1 priority."

Lobbyists outside of the biomedical field say such fervent support for the Harkin approach is understandable. "Biomedical advocates are so beaten down by a decade of flat funding," says Joel Widder of Federal Science Partners, a boutique government relations firm in Washington, D.C., "that they will grab for anything they can get." ■

PHOTO: ALAN LESSIG/AMERICAN ASSOCIATION FOR CANCER RESEARCH

Published by AAAS

BIOMEDICAL RESEARCH

Searching for science in India's traditional medicine

Critics say ayurgenomics is at best a quixotic quest

By **Priyanka Pulla**, *in Bangalore, India*

For centuries, practitioners of Indian traditional medicine, or Ayurveda, have followed a standard protocol for sizing up patients. They don't start with symptoms, family history, or vital signs. Instead they identify a person's *prakriti*, or body type, which reflects a combination of three mystical humors: windy, bilious, and phlegmatic. To assign a *prakriti*, an Ayurvedic physician uses a questionnaire to assess more than 100 attributes, from joint strength and cold sensitivity to temperament and stress tolerance. Depending on the *prakriti*, treatment for the same illness can differ markedly.

The approach is alien to Western medicine, but the Indian government is pushing hard to show that Ayurveda, which remains popular throughout India, is based on sound science. With hefty government support, the nascent field of "ayurgenomics" has roped in dozens of researchers from leading institutions such as the Indian Institute of Science here and the Centre for Cellular & Molecular Biology in Hyderabad. And it has published papers on the genetic bases of Ayurvedic traits, some of them in leading journals. "We are trying to contemporize Ayurveda," explains Mitali Mukerji, a molecular biologist who leads ayurgenomics research at the Institute of Genomics & Integrative Biology in New Delhi.

The effort has also stirred a rising chorus of criticism. Skeptics point to failed attempts to derive drugs from the herbal concoctions used in Ayurveda and other schools of traditional medicine. Ayurveda itself got a black eye several years ago after heavy metals were detected in some over-the-counter preparations. Another issue, says Satyajit Rath, an immunologist at the National Institute of Immunology in New Delhi, is that the biomedical industry has a tough time unraveling complex herbal preparations. To David Gorski, a cancer biologist at Wayne State University in Detroit, Michigan, the premise of *prakritis* is unscientific, which undermines any studies that rely on them. "You can do genomics on samples collected in studies of pseudoscience," he says, "but that doesn't make it science."

India's central government, on the other hand, has shown ample enthusiasm. It provided seed funding for ayurgenomics in 2007, and then in 2012 earmarked $16 million to the field for the 5-year plan ending in 2017. That support is unlikely to abate: In a campaign manifesto, the current ruling party cited ayurgenomics as a priority. "There is no shortage of funding," says ayurgenomics adherent Samir Brahmachari, former director-general of the Council of Scientific and Industrial Research.

Ayurvedic medicines like these herbs to treat the eye remain popular in India.

PHOTO: M. A. PUSHPA KUMARA/EPA/CORBIS

Ayurgenomics drew attention in 2008, when Mukerji's team reported that people categorized into the three "extreme" *prakritis*—body types dominated by a single humor—showed differences in expression of several genes implicated in metabolic, cardiovascular, immune, and psychiatric diseases. Biochemical markers such as lipid profiles were also strikingly different across the three body types. People with a *kapha prakriti*, in particular, had higher levels of triglycerides, cholesterol, and other known markers for cardiovascular disease, which jibes with Ayurvedic texts linking *kapha prakriti* with a higher susceptibility to heart disease. Skeptics, however, were quick to point out that people with that *prakriti* tend to be obese, thus explaining any propensity for heart disease.

Undeterred, Mukerji's group followed up with a 2010 report in the *Proceedings of the National Academy of Sciences* showing that a gene variant linked to an acute form of altitude sickness occurs more frequently in the *kapha prakriti*. Another variant that helps people tolerate high altitudes was more prevalent in a different *prakriti*, the group found. But skeptics argue that the concept of *prakriti* is at best too broad for gene-association studies. Analabha Basu, a population geneticist at the National Institute of Biomedical Genomics in West Bengal state, says that although Mukerji's team does solid work, their findings could be more insightful if they were to hunt for associations between gene variants and individual traits. "If you could directly characterize the gene with one of the traits of *kapha*, you might find a stronger association with better predictive power," Basu argues.

The latest report from the ayurgenomics frontier raises another concern: whether studies are receiving adequate peer review. Last month, a team including one of the field's most visible backers, cardiac surgeon M. S. Valiathan of Manipal University, published the first attempt to yoke *prakriti* classification to scientific measures such as body mass index. But the report appeared in the *Journal of Ayurveda and Integrative Medicine*, and some of the authors are also editors of the journal. "Couldn't they find another journal to publish it in?" asks K. Somasundaram, a cancer biologist at the Indian Institute of Science. That criticism is unfair, responds Bhushan Patwardhan, a biochemist at the University of Pune. "My being a co-author is incidental," he says. "The submission to the journal was done by the lead author of the paper, which has been processed through the routine peer-review process."

Proponents of ayurgenomics are used to facing skepticism. But Mukerji insists that "striking" parallels between predictions in ancient Ayurvedic texts and genetic propensities of *prakritis* will prove important. In modern medicine, she says, "you aren't able to look at a healthy person and say he may be prone to a particular disease, because there is no way of stratifying healthy people." Brahmachari, a well-respected genome biologist, says the accumulation of findings leaves him optimistic that ayurgenomics will win over critics. "We hope more people will start working in this field and it will become a movement," he says. ■

Downloaded from www.sciencemag.org on October 24, 2014

Published by AAAS

FEATURES

Show me the money

A bitter dispute lays bare questionable practices in China's foreign-talent programs

By **Mara Hvistendahl**, *in Guangzhou, China*

In a hotel room on the sidelines of a conference in China in 2011, theoretical physicist Ulf Leonhardt says he got an offer that was too good to refuse. The Centre for Optical and Electromagnetic Research (COER) here at South China Normal University (SCNU) invited him to spend 3 months a year at the center, during which COER would pay him a monthly salary of 133,333 RMB ($21,762): three times greater than at his tenured position at the University of St. Andrews in the United Kingdom.

A prominent figure in theoretical physics who had made headlines by outlining a theoretical framework for an invisibility cloak, Leonhardt had no shortage of career prospects. But the offer from Guangzhou came at a moment when he was hard up for flexible funding that would allow him to travel and bring in visitors. And Leonhardt had watched, impressed, as China's huge investment in science had begun to reap dividends. Since his first visit in 2008, he'd noted "a really steep increase both in the quantity and quality" of papers in his field, he says. A longer stay made sense.

To supplement Leonhardt's COER salary, photonics expert Sailing He and colleagues at COER helped him apply to two government programs for attracting foreign talent: the Recruitment Program of Foreign Experts, or "Thousand Talents" plan, which offers a one-time 500,000 RMB ($81,642) resettlement subsidy for a minimum of 3 years of part-time work, and a program offshoot called the Guangdong Province Leading Talent award, which brings an additional one-time subsidy of 1 million RMB plus up to 5 million RMB in research funds over 5 years. (The full-time Thousand Talents program, which Leonhardt did not participate in, includes research funding as well as a subsidy.)

Thousand Talents and similar programs had struggled to attract candidates of international caliber (*Science*, 31 July 2009,

ILLUSTRATION: © DAVIDE BONAZZI

Published by AAAS

Downloaded from www.sciencemag.org on October 24, 2014

ILLUSTRATION: © DAVIDE BONAZZI

p. 534), and Leonhardt, who was applying at the peak of his career, seemed a shoo-in. By September 2012, he had snagged acceptances from both programs and had signed a 5-year contract with COER. The center offered his partner, Jana Silberg, a part-time job, too.

But Leonhardt and Silberg would come to suspect that a substantial portion of his grant money and the salary due to Silberg were being diverted to other uses. After hiring lawyers to investigate, they uncovered a web of misinformation, including incorrectly translated agreements and covert purchases of equipment at COER. "The fraud they committed was so brazen," charges Leonhardt, who bailed out of his contract after spending just one summer in Guangzhou.

Sailing He flatly denies that COER diverted any funds, and others at COER say that Leonhardt agreed up front to an arrangement in which the bulk of his grant would be administered by others. Sailing He calls Leonhardt ungrateful for COER's help in securing the lucrative arrangement: "He was getting $20,000 USD a month. He doesn't need to care about the details."

At a time when China is spending heavily to recruit talented overseas scientists, the dispute between COER and Leonhardt is a cautionary tale. Interviews with other foreign-born recipients of Thousand Talents awards reveal that host institutions in several instances have seized the reins, controlling everything from the application process to grant administration. Among Thousand Talents awardees interviewed by *Science*, ignorance of the program's nuts and bolts—even at the most basic level, such as the amount of money they are due—is the norm.

Both sides in the dispute blame the other for failing to live up to expectations. Sailing He says it boils down to cultural differences: "In China, you have to be flexible," he says. Things are "not always [done] according to the regulations. But it's not with bad intentions."

BORN IN SCHLEMA, in former East Germany, Leonhardt, 49, studied at Humboldt University in Berlin and elsewhere before moving over to the University of St. Andrews. (He now works at the Weizmann Institute of Science in Rehovot, Israel.) His theoretical research focuses on novel optical effects such as so-called transformation optics—bending light in curious ways with metamaterials, or assemblages of rods and rings smaller than a wavelength of electromagnetic radiation. In 2006, he showed how metamaterials could be fashioned into a circular shell capable of funneling light around any object placed inside, rendering it invisible—as did, independently, John Pendry of Imperial College

Published by AAAS

London and colleagues (*Science*, 23 June 2006, pp. 1777 and 1780).

Since then, Leonhardt has continued to study other novel optical phenomena, such as making an analog of a white hole—sort of the opposite of a black hole—in an optical fiber (*Science*, 7 March 2008, p. 1321). "Leonhardt is definitely one of the top scientists in our field," says Xiang Zhang, a physicist at the University of California, Berkeley.

Sailing He, meanwhile, had made a name for himself in photonics, the effort to develop technologies that manipulate light much as electronic devices control the flow of electricity. Like many talented Chinese researchers, he left the country in the 1980s to study overseas. In 1992, he earned a Ph.D. from the Royal Institute of Technology in Stockholm, and in 1996 he received tenure and, he says, Swedish citizenship. Since then, He has authored or co-authored more than 400 peer-reviewed publications.

In 1999, He returned to China as one of the first recruits under the prestigious Changjiang Scholars Program, which entitled him to a premium-level salary at Zhejiang University in Hangzhou and optional research funding. He took advantage of his pedigree to build crucial ties overseas, boasting of importing international standards to China: "With finances we use a transparent style of administration, dropping the bad habits of the past," he wrote in an article published on Zhejiang University's website in 2001.

COER was "smuggling in an alien research project in the grant proposal they wrote in my name."

Ulf Leonhardt, Weizmann Institute of Science

In 2011, He took a part-time post at SCNU, devoting himself to the newly created COER. Early on, the center landed a respected Swedish couple as part-timers: physicist Sune Svanberg, an expert in spectrometry, and oncologist Katarina Svanberg, who studies laser light interactions in biological tissue. The center's staff also includes physicist Liu Liu, a recipient of a Young Thousand Talents award, which is available to scientists under age 40. In recruiting Leonhardt, Sailing He told *Science* that he hoped to "raise the local level of research in metamaterials."

In August 2011, He and colleagues at COER began assembling application materials for Leonhardt's Thousand Talents and Leading Talent submissions. (*Science* reviewed documents and e-mails provided by COER and by Leonhardt.) Ma Yungui, who works with He at Zhejiang University, says he wrote most of the two applications, which were in Chinese. Leonhardt says the center never sent him either the Chinese version or an English translation of either document (COER says he never asked); he later obtained the Leading Talent application through his lawyers.

In July and September 2012, after Leonhardt won acceptance to both programs, he and Silberg signed contracts with COER. She was hired as an assistant in international affairs for COER during the 3 months of the year that the couple would spend in Guangzhou. Leonhardt's contract specified that he was to "publish some high quality papers in top journals (like *Science*, *Nature*, or *Nature* series) with the first affiliation of COER."

Leonhardt's contract is bilingual, with English and Chinese versions of clauses side by side. But the versions differ in content: Silberg, who has a Ph.D. in business administration and is accustomed to scrutinizing such documents, spotted a numeral in the Chinese version that was missing from the English: 6. In fact, the Chinese document contained an extra clause stating that Leonhardt's "total amount of time" working for the center would "reach 6 months": 3 months in Guangzhou and 3 months overseas. The English version said the work abroad was "limited to" 3 months and did not mention 6 months. Leonhardt and Silberg asked He to remove the extraneous clause from the Chinese contract, and after what they describe as a heated debate, COER offered Leonhardt an amended contract.

Copies of the second contract, which Leonhardt alleges COER did not ratify until July 2013, show that COER inserted a statement saying that the English text would take precedence over the Chinese version. But the center did not delete the disputed clause, instead merely replacing the Roman numeral 6 with the Chinese character. The clause was likely inserted to maintain the Leading Talent grant, which does not offer a part-time option; the minimum time commitment required by the grant is 6 months.

Leonhardt would later learn that the contract had other inconsistencies. It mentioned the 1 million RMB ($164,000) resettlement subsidy from the Leading Talent award but omitted the additional subsidy due to him from the Thousand Talents program. Liu, the young researcher at COER, wrote in an e-mail to *Science* that the center didn't address the subsidy in the contract because "we did not know" that the part-time Thousand Talents program included a subsidy. COER told *Science* in an e-mail that Leonhardt "should be able to find out all the details pertinent to this title by himself." In a subsequent e-mail to *Science*, COER claimed that it was Leonhardt's idea to apply for the Thousand Talents grant and that COER professors merely helped him as a favor.

THE THOUSAND TALENTS plan, or *Qianren Jihua*—aimed at recruiting up to 2000 leading scientists, entrepreneurs, and financial experts over 5 to 10 years—was launched in 2008 by the Communist Party of China's powerful Organization Department. With the party backing the program, provincial governments dove in, setting targets for the number of recipients they would attract and starting competitive local programs like the Leading Talent award. "If a guy becomes a Thousand Talent, there are cases where that guy is getting multiple local benefits—local incentives, local grants," says Wang Huiyao, director of the Center for China & Globalization (CCG) in Beijing.

As an incentive for recruiting scholars, some universities are also given rewards, says David Zweig, a political scientist at the Hong Kong University of Science and Technology who studies the international flow of talent. At one university in northern China, attracting a recipient for either the full-time or part-time Thousand Talents program earns the institution 12 million RMB ($1.96 million), according to a paper Zweig and Wang published in *The China Quarterly* in September 2013. A portion of that payment is supposed to go to salary for the recruited scholar, with the rest distributed to other faculty. Some local talent programs, meanwhile, offer an 8 million RMB ($1.31 million) payment to universities that recruit full-time candidates, Zweig and Wang found.

Despite such incentives, the program has struggled. Scholars who hold tenured positions in Europe or North America are unlikely to drop everything to take on full-time 5-year contracts in China, notes Cong Cao, an expert on Chinese science policy at the University of Nottingham in the United Kingdom: "That's something wrong with the program design from the beginning." As a result, some institutions resort to recruiting scholars already in China. Others hire scientists with full-time commitments overseas, and then assure them that no one will strictly review their time sheets, Cao says. Some scholars "drop in for 2 weeks of the year, and that's it," says Neil Foster, a chemical engineer at the University of New South Wales in Sydney, Australia, who in 2010 received a Thousand Talents award to work part-time at the

PHOTO: WEIZMANN INSTITUTE OF SCIENCE

Published by AAAS

Beijing University of Chemical Technology.

The scope for abuses grew as the Thousand Talents program, which originally landed mainly high-profile overseas Chinese, cast a wider net. In 2011, the Organization Department launched the Recruitment Program of Foreign Experts and published program requirements—but not application materials—in English. Many candidates now don't speak or read Chinese. According to Cao, that could allow institutions to cheat the government "without the knowledge of the person they are going to hire."

COER AND SILBERG originally agreed that her salary would be paid monthly, even when she wasn't in Guangzhou. But in November 2012, 2 months after her contract began, she still had not received any money. Earlier, Wendy Huang, COER's administrative assistant, had written Leonhardt that the university's personnel department had decided not to pay Silberg until she was in Guangzhou and that Huang was "too busy" with an upcoming conference to help with the situation right away. Now Leonhardt raised the issue again.

Sailing He chimed in by e-mail to say he had a "quick solution" and suggested that he and Leonhardt hash out the details on Skype. In that call, Leonhardt says the Chinese scientist explained that he had a sum of money that might be used to pay Silberg. (Sailing He denies this.) Soon after, He e-mailed Huang instructions to have 500,000 RMB ($81,637) transferred to Leonhardt's bank account. Sailing He called the sum a "tax-free subsidy" but did not explain in the e-mail that it was the resettlement money owed Leonhardt under the Thousand Talents award.

Silberg and Leonhardt were confused. Her contract prescribed a salary of 80,000 RMB ($13,061) a year; even if COER were to pay her for all 5 years at once, she would be due only 400,000 RMB ($65,303), and that would have been taxable. "We did not want to take it," Leonhardt recalls. "It smelled very unkosher." But he hadn't yet received his resettlement subsidy from the Leading Talent award, and he says they needed the money. In December 2012, he e-mailed Sailing He that he would accept the money only as "an advance on the housing payment" from the Leading Talent grant. He's e-mailed reply was cryptic: "One needs to be a bit flexible in China in order to fix things effectively (instead of spending too much time/effort on it)." About 3 months later, when Leonhardt received his Leading Talent subsidy, he returned the money as promised, transferring it to Huang's account on her instructions.

In June 2013, Silberg and Leonhardt arrived in Guangzhou for 9 weeks of work. Leonhardt describes the research environment at the institute that houses COER as uninspiring. Apart from one team working on optical fibers for linking supercomputers and the work done by the Svanbergs, the institute appeared moribund, he says: "I'd see students in seminars, and they were falling asleep." But his hosts had reason to be pleased. The month he arrived, Leonhardt published an article in *Nature*'s "News & Views" section, commenting on the cloaking of heat and listing COER as his primary affiliation, as his contract required. SCNU plugged the piece on its website, calling it the "first paper published in *Nature*" to prominently name the university, and later including it as one of the university's top 10 "big research achievements" of 2013.

DURING HIS TIME IN GUANGZHOU, Leonhardt planned to work on the theory of Casimir forces, a strange pull or push between two closely spaced objects that arises because of quantum mechanical fluctuations in the vacuum of empty space. He thought much of the 5 million RMB research funding he was due from the Leading Talent program would go to paying his salary and overhead. That would leave up to 1.5 million RMB ($244,917) in funding for traveling and hosting visitors in connection with this theoretical research.

> ***"He was getting $20,000 USD a month. He doesn't need to care about the details."***
>
> **Sailing He**, South China Normal University

In fact, Leonhardt was paid out of COER's budget, as is standard with China's foreign-talent programs, freeing up to 3.5 million RMB ($571,508) in research funds for other uses. The Chinese version of a document he had signed the year before had given Jun Li, the center's deputy director for administration, wide-ranging authority to spend Leonhardt's funding on equipment whenever he was away from Guangzhou. Yet the English translation COER gave Leonhardt stated only that Li would be able to "sign some papers about financial affairs for my funding when I am out for business."

Before he had even started working in Guangzhou, COER ordered a linear motor stage and controller, monochromators, lasers, and four laptop computers—for a total of $116,741—using Leonhardt's Leading Talent research money. Leonhardt says that he didn't need any of the equipment for his planned theoretical work.

A document that Li gave *Science* shows Leonhardt heading up a team of four researchers and explains that one of the laptops, along with several other computers, workstations, and a printer that the center later purchased, were for these scientists, who would together work on "Casimir force, etc." But Liu, one of the scientists pictured in the presentation, laughed when asked about the project: "I don't know anything about Casimir forces."

A copy of Leonhardt's Leading Talent application in Chinese describes, along with cloaking, a very different line of research: military stealth technology. "At microwaves and other low-frequency waves, absorbent materials can lower the scattering of electromagnetic waves for aircraft and other military targets, so as to achieve antiradar stealth," it reads. The application goes on to suggest that such research is based on transformation optics. In fact, absorption is effectively the enemy of many applications of transformation optics—cloaking in particular. Cloaking aims to funnel light around an object. Absorption, which Leonhardt does not study, subverts that process by making the cloak cast a shadow.

Leonhardt charges that COER was "smuggling in an alien research project in the grant proposal they wrote in my name." A budget estimate prepared for the Leading Talent project suggests that fully 2.7 million RMB ($440,826) of his 5 million RMB in research funds would be spent on equipment for a third topic outlined in the Leading Talent proposal: "super-resolution display and metamaterials," including spectroscopic tools. Leonhardt says he saw neither the application nor the budget estimate until his lawyers procured them and that he assumed the entire grant would focus on theoretical research.

COER has a different take. An e-mail from Huang on behalf of COER says that, "Even though Ulf is the PI [principal investigator] for the leading talent project, this project is a team work requiring both his theoretical part and the experimental efforts from some COER full-time faculty members."

Leonhardt suspects that the Leading Talent documents emphasize absorption and spectroscopy because that is what Sailing He studies. This past July, for example, He and colleagues described in *Applied Physics Letters* a metamaterial coating that works as a perfect absorber of microwaves of a particular frequency. "They seem to have sold me to the Chinese military, like a Greek slave to the Roman legions in a different era," Leonhardt contends.

SCNU professor Ao Xianyu, writing on behalf of COER, says that work on absorption and cloaking aren't really so disparate,

Published by AAAS

arguing that the mathematical tools of transformation optics are applicable to designing better absorbers. Ao also says that the work on absorbers was included in the Leading Talent proposal to satisfy a requirement to produce something that could be commercialized. "Otherwise, there is no chance to get this project approved at all," Ao says. "Leonhardt knew this reason quite well and agreed to this from the draft preparation to the final presentation."

Leonhardt insists he never saw a draft. When he began to have concerns, he e-mailed administrators for both programs, along with officials at the Ministry of Science and Technology; the Chinese Academy of Sciences; the Central Commission for Discipline Inspection, the Communist Party's anticorruption watchdog; and the National Natural Science Foundation of China. None responded directly to him, he says.

Representatives of the Leading Talent program reached by phone by *Science* declined to discuss the details of Leonhardt's grant, which was canceled on 9 October. The State Administration of Foreign Experts Affairs (SAFEA), which administers the Thousand Talents program for the Organization Department, did not respond to repeated interview requests.

Interviews with other foreign Thousand Talents recipients suggest that ignorance of award conditions is common. For example, Geoff Gadd, a geomicrobiologist at the University of Dundee in the United Kingdom, who has a part-time award for work at the Xinjiang Institute of Ecology and Geography in Urumqi, wrote *Science* that he has not received a resettlement subsidy or any information about the program in English. "I am not sure who administers the grant," Gadd wrote. "I received no details about this kind of thing." Fuel cell expert Subhash Singhal, a fellow emeritus at the Pacific Northwest National Laboratory in Richland, Washington, says he had a similar experience at the China University of Mining and Technology in Beijing, where he received a short-term Thousand Talents award: "[With] the grant process, I had absolutely no idea what they were doing or how they were doing it." His host institution's lack of transparency about award money issued in his name would probably deter him from returning to China, he says.

Several grant recipients say that the program has proven fruitful, and they were keen to renew the terms of their stay in China. "The networking is going to be long-term huge for me," says Michael Arnold, who received a Thousand Talents grant to work at the Kunming Institute of Zoology. "I can just see ripples going out through the rest of my career." But even those who were happy

A PowerPoint presentation prepared to accompany Leonhardt's Leading Talent grant application depicts a research team that he says didn't exist.

with their experience were not clued in to grant administration. Four out of the five researchers interviewed by *Science* say that they did not receive a resettlement subsidy. Foster says he received no money at all; his university in China paid for his accommodation, but he did not earn a salary and says he "didn't claim" a subsidy.

CCG's Wang concedes that the program has had growing pains. "There could be problems, there could be fake [scholars], there could be scandals." But he maintains, "The general picture and the message they're sending to attract talent is good."

WHEN ASKED ABOUT Leonhardt's allegations, other foreign scientists who work with Sailing He profess disbelief. Sune Svanberg says he and his wife felt "very appreciated" at COER: "We never felt that anything was different from what was said. I'm just astonished that something like this would develop."

Sailing He and others insist the dispute boils down to a personality conflict. They note that Leonhardt sued the University of St. Andrews in 2013 over pay for vacation days he never took. Leonhardt responds that his claim was justified, and he won compensation for most of the days he contested. (The University of St. Andrews declined to comment, citing privacy laws.)

Leonhardt and Silberg never returned to China for the second year of their 5-year terms. For months, they tried through lawyers to figure out what exactly had happened with the grant money due to Leonhardt, while attempting to terminate their contracts. Last December, COER still hoped to woo Leonhardt back; in an e-mail, Sailing He offered him a sum equal to the amount spent on the disputed equipment for "whatever equipment you tell SCNU to buy." Leonhardt refused. COER terminated their contracts in June.

COER now argues that Leonhardt was not in Guangzhou for the amount of time agreed upon in his contract, that he tried to abuse his travel funds while at SCNU, and that "he did not show any interest or intent in either building a lab or a research group," Li wrote in an e-mail. "Introducing [Leonhardt] to South China Normal University was the biggest mistake of my academic career," says Sailing He, who recently proposed to SAFEA that the Thousand Talents program dole out the resettlement subsidy over the course of a grant, rather than provide a lump sum up front.

Early last month, COER sent *Science* Leonhardt's Thousand Talents application, which Leonhardt had tried in vain to obtain through his lawyers. The date on the application—18 August 2011—predates his initial trip to Guangzhou to discuss the award. The document, in Chinese, describes research on Casimir forces, which Leonhardt says he didn't suggest until a year after the application was purportedly submitted.

Leonhardt suspects the document is a fake. COER acknowledges it doctored the date because it submitted the application after the deadline passed, but the center maintains that its researchers prepared the document at Leonhardt's request as a "personal favor." In an e-mail to *Science*, Li explained it this way: "We were just passively helping him." ■

With reporting by Adrian Cho.

CREDIT: COURTESY OF COER

Published by AAAS

Good sex for ferns is all about signal timing *p. 423*

Any hope for ocean wildlife? *p. 420*

PERSPECTIVES

EVOLUTION

Beyond the rainbow

Dinosaur color vision may have been key to the evolution of bird feathers

By **Marie-Claire Koschowitz,[1,2] Christian Fischer,[2] and Martin Sander[1,3]**

Once believed to be a diagnostic feature of birds, feathers are now known to have evolved in dinosaurs well before the first birds. In birds, feathers serve several functions: Down feathers insulate the body, whereas planar or pennaceous feathers are necessary for flight, communication, camouflage, and brooding (see the first figure). What was their original function in nonavian dinosaurs? Based on a specimen of *Archaeopteryx* that preserves a spectacular plumage of pennaceous feathers, Foth *et al.* (*1*) recently hypothesized that pennaceous feathers did not evolve for flight but for display. Together with insights into body size evolution in dinosaurs along the line to birds (*2*) and the discovery of protofeathers in early dinosaurs (*3*), these results contribute to an emerging understanding of why pennaceous feathers may have been superior to filamentous protofeathers.

Protofeathers presumably evolved in early dinosaurs (see the second figure) (*4*). Their main function must have been to insulate, because an increase in growth rate was facilitated by a faster metabolism early

[1]*Division of Paleontology, Steinmann Institute for Geology, Mineralogy and Paleontology, University of Bonn, Nussallee 8, 53115 Bonn, Germany.* [2]*Institute for Zoology and Anthropology, Department of Morphology, Systematics and Evolutionary Biology with Zoological Museum, Georg-August-Universität Göttingen, Berliner Strasse 28, 37073 Goettingen, Germany.* [3]*Natural History Museum of Los Angeles County, 900 Exposition Boulevard, Los Angeles, CA 90007, USA. E-mail: m.koschowitz@uni-bonn.de*

Vulturine guineafowl (*Acryllium vulturinum*) plumage. Structural colors like blue and violet are displayed in concert with intricate, high-resolution ornamentation. The close-up shows a specimen in the collection of the Museum Alexander Koenig. The full-size bird is from the Zoological Museum of the University of Göttingen.

PHOTO CREDITS: CHRISTIAN FISCHER (GUINEA FOWL) AND GEORG OLESCHINSKI (CLOSE-UP)

Published by AAAS

in dinosaur evolution (*5*). A faster metabolism necessitates body insulation because without an insulated skin, metabolic energy would be lost as heat instead of being available for growth. This is particularly true for small- to medium-sized animals such as early dinosaurs and their juveniles because of their poor ratio of body volume to body surface. A recent study (*2*) suggests that body size decreased much faster in the bird stem lineage than in other dinosaurs. For fast-growing, presumably warm-blooded animals (*5*), such miniaturization would only have been possible with sufficient body insulation.

However, protofeathers came at a price: the loss of structural color signaling capabilities. Structural color signaling is limited in a body cover of flexible hairlike structures such as the filamentous feathers of some birds. The display of structural colors (including iridescence, vivid blues and greens, and ultraviolet reflection) requires the precise arrangement of light-scattering elements at nanometer scales (*6*–*8*). In modern bird feathers, these elements consist of keratin, air, and melanosome-based nanostructures (*7*), producing iridescence and saturated color displays that are central to communication and sexual selection (see the first figure) (*9*).

Like every signaling system, structural color signaling involves a receiver: the eye of the (nonhuman) beholder. This raises the question of the visual capabilities of dinosaurs. Differentiated color vision, much superior to that of humans and other mammals (*10*), is known from virtually all extant reptiles (see the second figure) and in many taxa includes ultraviolet vision. Phylogenetic inference suggests that dinosaurs were endowed with the highly differentiated color vision of birds (*11*, *12*), termed "tetrachromacy" (the ability to discriminate hues ranging from ultraviolet to turquoise via a fourth, short-wavelength receptive cone cell; the other three cone cell types are sensitive to blue, green, and red). Tetrachromacy is a basal characteristic of land vertebrates and widely found in other vertebrates and invertebrates (*6*, *10*).

In addition to protofeathers, several nonavian maniraptoran dinosaurs independently evolved pennaceous feathers that clearly did not serve in flight (*13*, *14*). Pennaceous feathers may have been the solution to the evolutionary trade-off faced by these dinosaurs between insulation by protofeathers (*4*), increased metabolic rate (*5*), and miniaturization (*2*) on the one hand, and the loss of structural color signaling caused by protofeathers on the other. Instructive parallels can be found in early mammalian evolution, when fur starts to appear in the fossil record.

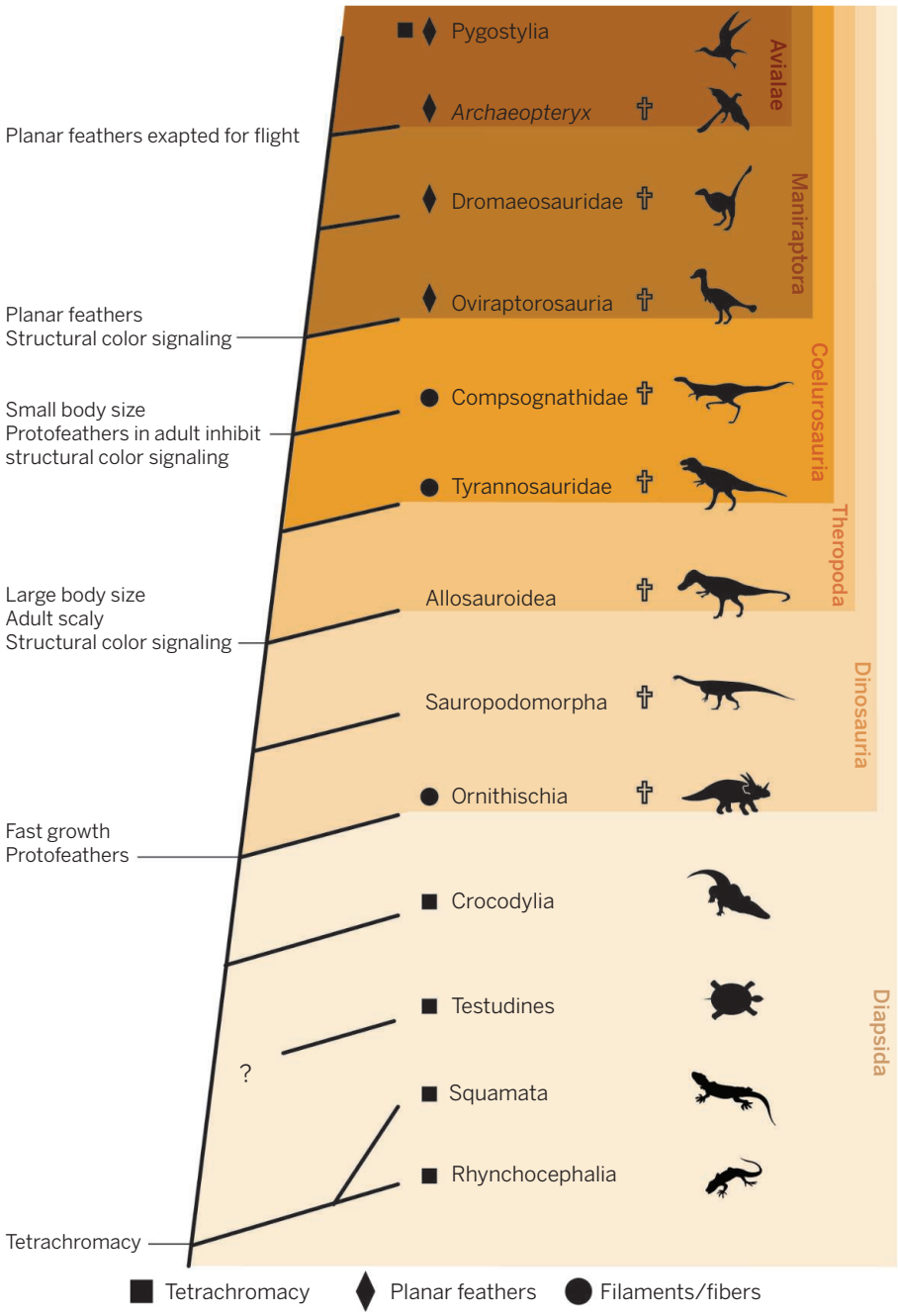

Color vision and feather evolution. Extant lizards, tuatara (Rhynchocephalia), turtles, crocodiles, and birds possess four cone cell types (tetrachromacy), enabling highly differentiated color vision that presumably was also present in dinosaurs. Protofeathers probably evolved in early dinosaurs for insulation and preceded planar feathers in coelurosaurians. Planar feathers, in turn, preceded flight or gliding. Miniaturization along the bird stem line led to a trade-off between color display and insulation, which could have been solved by the evolution of planar feathers serving both functions.

Here, coloration depends on the absence or presence of pigments ranging from reddish brown to black. Lacking a coherent surface, fur did not allow directed light scattering and severely impaired structural color display. Nocturnal activity patterns and body size reduction once again mandated body insulation, but sophisticated color perception and signaling lost their importance at night and differentiated color vision was lost (*15*).

It appears that in advanced maniraptoran dinosaurs, this trade-off was solved through the evolution of a new type of skin outgrowth that served insulation and display needs at the same time: the planar feather. Planar feathers would have covered up and partially replaced the filamentous protofeathers, thus leading to the evolution of contour feathers (the smooth feathers that form the outer covering of

Published by AAAS

the plumage), as preserved in the *Archaeopteryx* specimen studied in (*1*).

Planar feathers consist of a network of multiple interlocking branches of two orders (barbs and barbules) that are arranged into two sheetlike vanes horizontally protruding from a central shaft. Because both the precise arrangement of light scattering elements and the optimal exposition to light are mandatory for structural colors and iridescence, flattened branching filaments offer several benefits. They provide more surface area, maximizing structural color signaling at a macroscopic level. Also, sheetlike surfaces provide optimal physical conditions for iridescence and saturated color production. Finally, a "zip-lock" mechanism created by barbules generates a canvas for detailed ornamentation (see the first figure), a substantial advantage over less coherently ordered furlike filaments. A case in point are birds with furlike plumages, such as ostriches, cassowaries, and kiwis, that have reduced feather complexity and only display drab feather colors (but bright structural skin colors in the cassowary).

Because of their structural color signaling function and sophisticated three-dimensional architecture, planar feathers could easily have outperformed other integumentary structures such as scales, filamentous feathers, and hair in visually driven sexual selection in dinosaurs, leading to the highly diverse plumage seen in modern birds. The development of quantitative methods for estimating degrees of barb-barbule adhesiveness in fossil dinosaur feathers would allow testing of planarity resilience and the accompanying display capabilities in dinosaurs.

REFERENCES

1. C. Foth, H. Tischlinger, O. W. M. Rauhut, *Nature* **511**, 79 (2014).
2. M. S. Y. Lee, A. Cau, D. Naish, G. J. Dyke, *Science* **345**, 562 (2014).
3. P. Godefroit *et al.*, *Science* **345**, 451 (2014).
4. P. Chen, Z. Dong, S. Zhen, *Nature* **391**, 147 (1998).
5. J. Cubo, N. Le Roy, C. Martinez-Maza, L. Montes, *Paleobiology* **38**, 335 (2012).
6. S. M. Doucet, M. G. Meadows, *J. R. Soc. Interface* **6**, S115 (2009).
7. J. T. Bagnara, P. J. Fernandez, R. Fujii, *Pigment Cell Res.* **20**, 14 (2007).
8. B. D. Wilts, K. Michielsen, H. De Raedt, D. G. Stavenga, *Proc. Natl. Acad. Sci. U.S.A.* **111**, 4363 (2014).
9. G. E. Hill, K. J. McGraw, Eds., *Bird Coloration. Vol. 2: Function and Evolution* (Harvard Univ. Press, Cambridge, MA, 2006).
10. J. K. Bowmaker, *Vision Res.* **48**, 2022 (2008).
11. M. P. Rowe, *Palaeontol. Electron.* **3**, 43 (2000).
12. B. S. W. Chang, *Integr. Comp. Biol.* **43**, 500 (2003).
13. X. Xu, Y. Guo, *Vertebrata PalAsiatica* **47**, 311 (2009).
14. J. Clarke, *Science* **340**, 690 (2013).
15. K. D. Angielczyk, L. Schmitz, *Proc. Biol. Sci.* **281**, 20141642 (2014).

10.1126/science.1258957

DNA REPLICATION

Terminating the replisome

Multiple proteins modify and dismantle a key enzyme after DNA replication terminates

By **Stephen P. Bell**

In a eukaryotic cell, DNA replication begins with the unwinding of double-stranded DNA at an origin, followed by the synthesis of complementary strands that grow bidirectionally along the original DNA strands (forming a replication fork) from the origin. This synthesis is carried out by a complex structure called a replisome, the heart of which is a ring-shaped DNA helicase that unwinds the DNA. Two key events occur when replication forks arising from two different origins converge. The DNA associated with each fork first must be fully replicated and

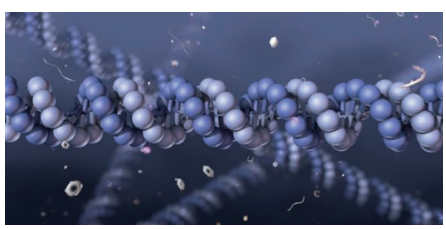

separated from each other; topoisomerases facilitate both fork convergence and this decatenation (*1*–*3*). Then, the replisome associated with each converging fork must be dismantled. Because the DNA helicase cannot be reloaded onto DNA once it is removed, the processivity of replication demands that these enzymes associate tightly with substrate DNA. On pages 440 and 477 of this issue, Maric *et al.* (*4*) and Priego Moreno *et al.* (*5*), respectively, demonstrate that disassembly of the eukaryotic replicative DNA helicase is actively controlled.

In eukaryotic cells, loading and activation of the replicative DNA helicase are temporally separated to ensure that no origin reinitiates during the cell division cycle. Helicase loading occurs during the G_1 phase of the cell cycle, resulting in a dimer of the hexameric ring-shaped minichromosome maintenance (MCM) 2-7 helicase encircling the origin DNA (*6*). Upon entry into S phase, two helicase-activating proteins—cell division cycle 45 (Cdc45) and go-ichi-ni-san (GINS)—are recruited to each Mcm2-7 hexamer, forming the active replicative helicase, the Cdc45–Mcm2-7–GINS (CMG) complex (*7*). DNA unwinding at the origin results in the active CMG complex encircling the single-stranded "leading-strand" DNA template. The CMG complex forms the foundation upon which the DNA polymerases and other replisome proteins assemble. The resulting replisome replicates the associated DNA until it encounters another replisome and terminates replication. Although the proteins and events involved in eukaryotic helicase loading and activation have been intensively studied, how the replisome is disassembled upon replication termination has been unknown.

Maric *et al.* and Priego Moreno *et al.* gained their first insights into replication termination by studying ubiquitylation of the replisome. Each group discovered that a specific Mcm2-7 subunit (Mcm7) is modified by a chain of ubiquitin proteins (polyubiquitylated), with lysine 48 (K48) linkages between ubiquitins. This modification was only observed under conditions that allowed replication to be completed. Prevention of CMG formation, treatment with replication inhibitors, or blocking replication termination prevented Mcm7 ubiquitylation. Blocking Mcm7 ubiquitylation caused replication defects consistent with inhibition of replication termination (*5*). A member of the Skp1–Cullin–F-box (SCF) family of ubiquitin ligases mediates the observed Mcm7 ubiquitylation, and in budding yeast, the F-box protein (which controls substrate specifity) is Dia2 (*4*). Intriguingly, SCF^{Dia2} was previously identified as a replisome component (*8*).

Maric *et al.* and Priego Moreno *et al.* observed that polyubiquitylation of Mcm7 is required for the disassembly and release of the CMG complex from DNA upon termination of synthesis. Maric *et al.* show that elimination of SCF^{Dia2} results in the retention of DNA-associated CMG even after cells enter the next G_1 phase. Similarly, Priego Moreno *et al.* report that inhibition of polyubiquitin chain formation prevents release of CMG complexes from chromatin after replication is completed. Because the CMG complex is the foundation of the replisome, release of the CMG from chromatin results in replisome disassembly.

Howard Hughes Medical Institute, Department of Biology, Massachusetts Institute of Technology, Cambridge, MA 02139, USA. E-mail: spbell@mit.edu

CREDIT: C. BICKEL/*SCIENCE*

Published by AAAS

Both Maric *et al.* and Priego Moreno *et al.* show that Cdc48 (also called p97), a AAA+ adenosine triphosphatase (ATPase) that forms a hexameric ring, disassembles the CMG complex (see the figure). Adenosine 5′-triphosphate (ATP) binding and hydrolysis power conformational changes in Cdc48 that can drive protein unfolding (*9*). Both groups found that elimination of Cdc48 activity resulted in retention of CMG on the chromatin. Both groups also show that Cdc48 specifically associates with ubiquitylated CMG complexes. Despite the well-known role of K48-linked ubiquitin chains in protein degradation by the 26*S* proteasome, inhibiting this mechanism of proteolysis did not prevent CMG disassembly. Instead, Mcm7 is probably removed from the CMG by partial or complete ATP-dependent translocation through the narrow pore of the Cdc48 hexamer ring. Loss of Mcm7 would open the Mcm2-7 ring, providing an exit for DNA. Although Mcm7 does not interact with Cdc45 or GINS (*10*), Maric *et al.* show that associations between multiple Mcm2-7 subunits are disrupted during CMG release, presumably resulting in release of Cdc45 and GINS. It remains unclear whether these released subunits can participate in a new round of replication; however, previous studies have suggested that synthesis of new Mcm subunits is required for the subsequent round of replication (*11*).

Cdc48 typically requires adaptors to facilitate substrate recognition. Indeed, adaptors are required for the Cdc48-dependent chromatin release of Cdc45 and GINS in *Caenorhabditis elegans* (*12*). This study suggested that the Cdc48-dependent degradation of the replication factor Cdt1 is required for release of Cdc45 and GINS from chromatin during embryogenesis, but the findings of Maric *et al.* and Priego Moreno *et al.* suggest that these events are independent in most cells.

The attributes of terminated replisomes that direct Mcm7 ubiquitylation by SCF^{Dia2} remain to be determined. Maric *et al.* show that formation of the CMG complex is one essential requirement, but additional determinants must distinguish elongating from terminated replisomes. An inactive replisome is not sufficient for targeting because treatments that stall or stop the replisome did not lead to Mcm7 ubiquitylation. It is possible that interactions between two converging replisomes activate Mcm7 ubiquitylation, although there is no evidence for a stable interaction between replisomes during termination. An intriguing alternative is that the DNA bound by the CMG complex dictates its recognition. The CMG complex encircles single-stranded DNA during replication, but upon termination, it must encircle the fully replicated double-stranded DNA. Recent studies suggest that Mcm2-7 complexes surrounding double-stranded DNA and single-stranded DNA have different conformations (*13*). Consistent with a DNA-mediated signal, Maric *et al.* show that CMG disassembly is not cell-cycle regulated. SCF^{Dia2} can target CMG complexes that remain on chromatin in the next cell cycle (due to mutation). It is also possible that additional proteins acting during termination direct SCF^{Dia2} targeting. For example, MCM-binding protein facilitates Mcm2-7 chromatin release in metazoan cells (*14*).

This mechanism of replisome disassembly may not be specific to termination events. The breast cancer 1 (BRCA1) ubiquitin ligase is required for CMG release at intrastrand cross-links, although the BRCA1 target is unknown (*15*). It is also clear that Cdc48 functions in the removal of many proteins from chromatin (*16*). The robust systems described by Maric *et al.* and Priego Moreno *et al.* promise rapid progress toward a full understanding of the replisome disassembly and the role of SCF and Cdc48 in this event.

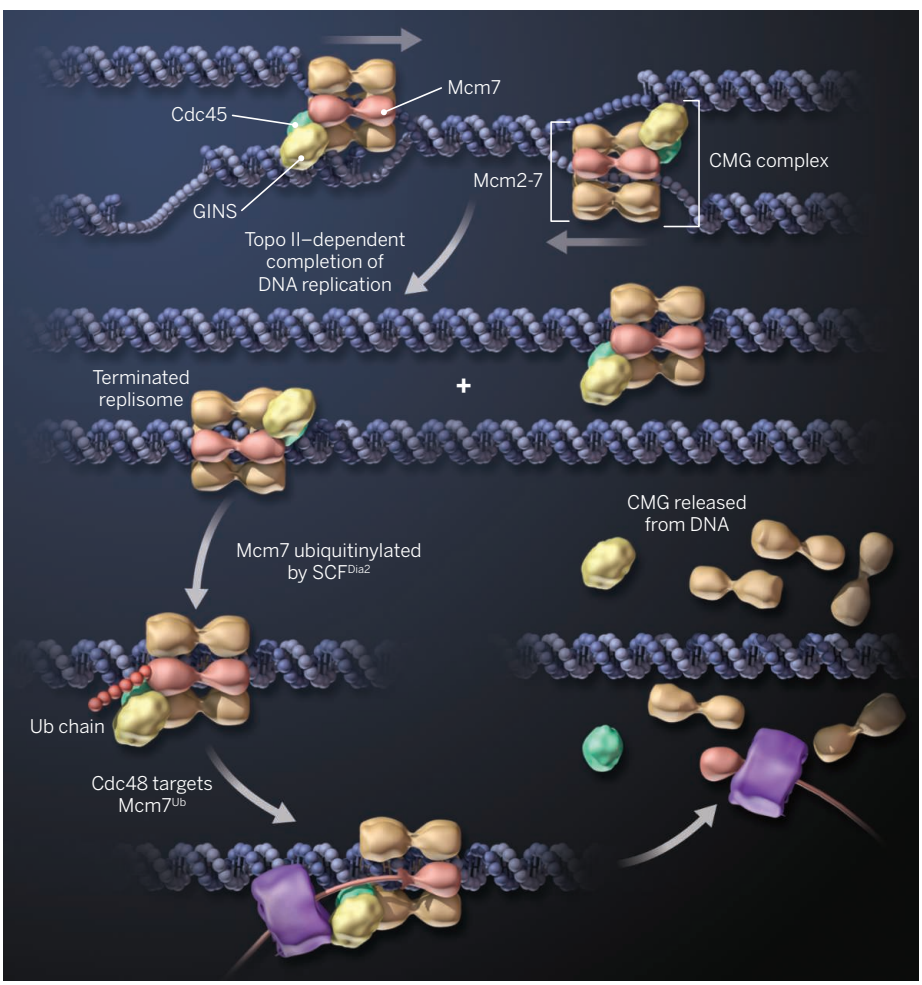

Disassembly required. Once two converging replisomes complete DNA replication, they are targeted sequentially by SCF^{Dia2} and Cdc48, resulting in CMG disassembly. For simplicity, parts of the replication machinery and DNA polymerases are not shown. Topo-II, Type II topoisomerase; Ub, ubiquitin.

CREDIT: C. BICKEL/*SCIENCE*

REFERENCES

1. J. Baxter, J. F. X. Diffley, *Mol. Cell* **30**, 790 (2008).
2. O. Cuvier, S. Stanojcic, J.-M. Lemaitre, M. Méchali, *Genes Dev.* **22**, 860 (2008).
3. D. Fachinetti *et al.*, *Mol. Cell* **39**, 595 (2010).
4. M. Maric, T. Maculins, G. De Piccoli, K. Labib, *Science* **346**, 1253596 (2014).
5. S. Priego Moreno, R. Bailey, N. Campion, S. Herron, A. Gambus, *Science* **346**, 477 (2014).
6. H. Yardimci, J. C. Walter, *Nat. Struct. Mol. Biol.* **21**, 20 (2014).
7. S. Tanaka, H. Araki, *Cold Spring Harb. Perspect. Biol.* **5**, a010371 (2013).
8. H. Morohashi, T. Maculins, K. Labib, *Curr. Biol.* **19**, 1943 (2009).
9. D. Barthelme, J. Z. Chen, J. Grabenstatter, T. A. Baker, R. T. Sauer, *Proc. Natl. Acad. Sci. U.S.A.* **111**, E1687 (2014).
10. D. Komander, M. Rape, *Annu. Rev. Biochem.* **81**, 203 (2012).
11. K. A. Braun, L. L. Breeden, *Mol. Biol. Cell* **18**, 1447 (2007).
12. A. Franz *et al.*, *Mol. Cell* **44**, 85 (2011).
13. A. Costa *et al.*, *eLife* **3**, e03273 (2014).
14. A. Nishiyama, L. Frappier, M. Méchali, *Genes Dev.* **25**, 165 (2011).
15. D. T. Long, J. C. Walter, *Mol. Cell* **46**, 111 (2012).
16. N. P. Dantuma, T. Hoppe, *Trends Cell Biol.* **22**, 483 (2012).

10.1126/science.1261245

Published by AAAS

MARINE SCIENCE

Boundless no more

Ending illegal, unregulated, and unreported fishing would bring hope for ocean wildlife

By **Amanda C. J. Vincent**[1] *and* **Jean M. Harris**[2]

Historically, many scientists considered marine fishes too fecund and wide-ranging to go extinct. Indeed, this view sometimes persists, not least at the Convention on International Trade in Endangered Species of Wild Fauna and Flora (CITES), where the few decisions to control export of marine fishes—including the recent restrictions on sharks and rays—have been hard won (*1*). Increasingly, however, there is recognition that the metrics for overfishing and conservation threat largely agree (*2*) and that remedial action is urgently needed. Given today's unprecedented threats to marine species, it is critical that rapid action be taken to conserve ocean wildlife.

Of all the problems that beset marine species, misjudged exploitation is the most egregious but may also be one of the more tractable. Marine life is used for food, but also for many other purposes such as medicines, construction materials, and ornamental display. Almost 30% of the relatively few assessed fish stocks are fished at unsustainable levels (*3*). Fishing impacts are exacerbated by other stressors, such as habitat degradation, pollution, aquaculture, invasive species, and climate change. The full scale and rate of loss of marine life over the past few centuries are scarcely noticed by society at large, as each generation adapts to the new "natural" baseline of ever fewer and smaller animals.

CONSERVATION SERIES

ILLEGAL, UNREGULATED, UNREPORTED FISHING. Some of the greatest risks to species conservation come from illegal, unregulated, and unreported (IUU) fishing (*4*). Considerable attention is focused on the serious problem of illegal fisheries that use large boats and advanced technology, often on the high seas. Many other fisheries have been largely overlooked, particularly those that are unregulated and unreported.

Small-scale fisheries that cumulatively involve about 90% of the world's fishers (*5*) are ubiquitous in the world's coastal waters but generally operate without controls or records. Most of these 100 million or so fishers depend on the ocean for livelihoods and exploit marine resources persistently and intensely. Such relentless pressure has led to fisheries collapse and serial depletion—overfishing one species then another—until fishers extract virtually any marine life that might provide food or generate cash.

Small-scale fisheries by women are so little recognized or documented as to be effectively invisible. Yet women fish all over the world and can account for up to half of the family catch (*6*). Much of their extraction involves gathering ocean life in the intertidal areas or very shallow waters that are important nurseries for marine species. Often limited to what men do not take, women remove a wide array of marine species (mainly invertebrates), commonly unsustainably. Obliviousness to women's fisheries disadvantages both women and marine species.

Apart from a handful of commercial species, most of the expanding fisheries for invertebrates globally (*7*) are unregulated and unreported, even where they involve men and industrial gear. Invertebrates constitute 95% of ocean species. We know the conservation status of very few, but the evidence is that exploitation is contributing to their decline (*7*). Moreover, some invertebrate fisheries are particularly indiscriminate, destroying marine ecosystems.

BOTTOM TRAWLING. Of all indiscriminate fisheries, bottom trawling is the most catastrophic for both species and habitats. It also contributes substantially to IUU take, mainly through bycatch. Even where a trawl fishery for the target species is legal—and they often are not—the other marine life it captures is very rarely regulated or reported. Yet thousands of animal, plant, and algal species are taken incidentally. Cumulatively, they often constitute 85 to 90% of the total biomass of the catch in the net. Trawl pressure is so intense that bycatch of about one seahorse per vessel per night (see the photos) led to annual exports of 2.2 million individuals from Vietnam (*8*).

A dearth of constraints on trawl fisheries means that some boats—for example, in Thailand—no longer target particular species. They grab any and all life forms for use in animal feed and fishmeal, emptying the ocean and laying waste to the ocean floor. Such strip mining threatens both conservation and food security. Worse, such appalling degradation is powered by widespread government subsidies that make these abusive practices economically feasible.

CREDIT: SARAH FOSTER/PROJECT SEAHORSE

Published by AAAS

Unintended consequences. Seahorses are mainly taken as bycatch but also caught by small-scale fishers, including women. Their future will depend on protected areas, co-management, and the removal of perverse incentives for bottom trawling.

The enormity of trawl bycatch is creating worldwide concern. The European Union now requires landing of all bycatch, hoping to encourage reduction of such take. These landings may, however, instead promote businesses that process bycatch into fishmeal, thus perversely promoting "dirty fishing."

TAKING ACTION. Given the patent inadequacy of marine management to date, much depends on effective use of promising tools that address multiple IUU issues: marine protected areas, co-management, joined-up governance, and broader societal and scientific engagement with policy.

Marine protected areas

Marine protected areas (MPAs) that exclude or severely limit fishing are critical in addressing IUU fishing. They can be set up with limited data and provide vital species refuges, including from fisheries—such as bottom trawls—that damage habitats. No-take zones, in particular, are often easier to enforce than complex management regimes. Their role in fostering recovery of marine life has been well documented.

More proof that MPAs also improve fisheries could goad nations to meet their commitment to protect 10% of the ocean by 2020; the current total is less than 3%. For example, Kerwath *et al.* have reported that catches of sea-bream in South Africa rapidly improved near a new MPA without increasing fishers' costs (*9*).

Establishment of MPAs can be accelerated—and enforcement enhanced—by placing them quickly where local people want them. Implementation has too often been delayed while perfect data are sought, but immediate action can be very effective. As Hansen *et al.* have shown, rapid and cheap ad hoc placement in areas selected by communities resulted in the necessary representative protection of most habitats (*10*).

Co-management

Government alone cannot control IUU fishing. Co-management systems, where government partners engage directly with community members or industry, offer real hope for improved conservation (*11*).

The sustainability of fisheries can increase where fishers own access rights to marine resources or otherwise take responsibility. In South Africa, a pilot venture to involve subsistence fishers in co-management of mussels was successful in stabilizing marine populations; consequently, it expanded to 18 more communities and was institutionalized in the provincial system (*12*). In western Canada, industrialized groundfish (bottom) trawlers forged innovative relationships with government and environmental groups that include sizable reductions in fishing area and restrictions on accidental capture from sensitive sponge habitats (*13*).

Reducing the damage from IUU fisheries may simply depend on fostering leaders and strong local advocates. A global analysis of 130 fisheries from diverse social, ecological, and political settings revealed that strong leadership best predicted success in co-management (*11*). Local leaders help cope with changes of government, influence users' compliance, and enhance conflict resolution. They could be critical to ensuring attention to gender equity and empowering women to rebuild target stocks.

Joined-up governance

One of the best hopes of ending IUU fisheries lies in mobilizing all layers of government. Communities and local managers acting together at scales of 1 to 10 km need to contrive workable rules and recordkeeping to aid recovery of the ocean. Municipal and provincial governments working at scales of hundreds of kilometers provide a critical bridge between local and national initiatives. They must be brought to their full potential in regulating and enforcing fisheries laws, through serious investment in technical capacity and governance skills.

National governments working at scales of thousands of kilometers need to fully implement laws and practices that minimize IUU exploitation. This includes removing subsidies for fuel and other incentives that encourage bottom trawlers to mine the ocean unsustainably. The funds used to subsidize fisheries globally—estimated at over US$25 billion annually (*14*)—could better be applied to marine conservation.

Pacific seahorse (*Hippocampus ingens*)

CREDIT: ERIC RIESCH/GUYLIAN SEAHORSES OF THE WORLD

Public and scientific engagement

The indispensable political will to conserve marine species and spaces will only truly emerge when public opinion insists on action for ocean protection. Eco-certification offers a way to involve consumers and fishers in making choices that foster sustainable fishing. Among the many useful seafood report cards, the Marine Stewardship Council is an internationally recognized scheme that generates measurable improvements in fish biomass and fisheries practices (*15*). Further public engagement is fostered by citizen science schemes for the ocean. Linking people directly to the future of their ocean is probably the most vital step in marine species conservation.

A combination of public commitment and bold input by scientists can be powerful in reducing threats to marine life, particularly when a government is failing to protect. In Australia this year, such joint action reversed government decisions to dump tons of spoil on the Great Barrier Reef and to cull threatened sharks in Western Australia (*16*). One key in both cases was that scientists deployed their knowledge without delaying to gather more data. More data are often valuable, but available knowledge must be used now to guide decisions that affect ocean health.

[1]*Project Seahorse, Fisheries Centre, The University of British Columbia, Vancouver, BC V6T 1Z4, Canada.* [2]*Scientific Services, Ezemvelo KwaZulu-Natal Wildlife, Pietermaritzburg 3202, South Africa. E-mail: a.vincent@fisheries.ubc.ca*

REFERENCES AND NOTES

1. A. C. J. Vincent, Y. J. Sadovy de Mitcheson, S. L. Fowler, S. Lieberman, *Fish Fish.* 10.1111/faf.12035 (2013).
2. T. D. Davies, J. K. Baum, *Sci. Rep.* **2**, 561 (2012).
3. FAO, *State of World Fisheries and Aquaculture* (U.N. Food and Agriculture Organization, Rome, 2014), www.fao.org/3/a-i3720e.pdf.
4. A. M. Miller, S. R. Bush, A. P. J. Mol, *Mar. Policy* **45**, 138 (2014).
5. J. Kolding, C. Béné, M. Bavinck, in *Governance for Marine Fisheries and Biodiversity Conservation. Interaction and Coevolution*, S. Garcia, J. Rice, A. Charles, Eds. (Wiley-Blackwell, Hoboken, NJ, 2014), pp. 317–331.
6. D. Kleiber, L. M. Harris, A. C. J. Vincent, *Fish Fish.* 10.1111/faf.12075 (2014).
7. S. C. Anderson, J. M. Flemming, R. Watson, H. K. Lotze, *PLOS ONE* **6**, e14735 (2011).
8. B. G. Giles, S. K. Truong, H. H. Do, A. C. J. Vincent, *Biodivers. Conserv.* **15**, 2497 (2006).
9. S. E. Kerwath, H. Winker, A. Götz, C. G. Attwood, *Nat. Commun.* **4**, 2347 (2013).
10. J. A. Hansen *et al.*, *Biol. Conserv.* **144**, 1866 (2011).
11. N. L. Gutiérrez, R. Hilborn, O. Defeo, *Nature* **470**, 386 (2011).
12. J. M. Harris, G. M. Branch, B. M. Clark, S. C. Sibiya, in *Fisheries Management: Progress Towards Sustainability*, T. R. McClanahan, J. C. Castilla, Eds. (Blackwell, Oxford, 2007), pp. 112–138.
13. D. P. Dupont, *Mar. Policy* **44**, 60 (2014).
14. R. U. Sumaila *et al.*, *J. Bioecon.* **12**, 201 (2010).
15. N. L. Gutiérrez *et al.*, *PLOS One* **7**, e43765 (2012).
16. See, for example, www.abc.net.au/news/2014-09-11/wa-dumps-shark-drum-lines-after-epa-review/5737526.

10.1126/science.1255923

Published by AAAS

PHYSICS

Harnessing chirality for valleytronics

Artificial magnetic fields bend electron trajectories in gapped graphene

By **Mark B. Lundeberg**[1] *and* **Joshua A. Folk**[2]

One of the unusual electronic characteristics of graphene is that the direction of motion of its charge carriers is locked to an extra quantum mechanical degree of freedom, known as pseudospin. Graphene is in this way similar to the conducting surface layer of a topological insulator, where the direction of motion of the carriers is locked to their true spin—that is, to their magnetic moment. Whereas the true spin state of an electron can be described as a superposition of spin-up and spin-down components, pseudospin in graphene is a superposition of electron orbitals of the two carbon atoms in a hexagonal lattice unit cell. To date, graphene's pseudospin has played only a subtle role in carrier scattering, and in phenomena that are directly sensitive to the phase of a quantum mechanical wave function. On page 448 of this issue, Gorbachev *et al.* (*1*) show that pseudospin, modified in the right way, can be used to drive a so-called valley current in a graphene device. That is, a voltage applied across the device gives rise to counter-propagating streams of carriers in graphene's two band structure valleys. By harnessing its built-in chirality, an all-electrical valleytronic circuit using graphene is demonstrated.

Valleytronics is the name given to a paradigm for information processing that stores information in the crystal momentum of a carrier—that is, in its freedom to exist in one band structure valley or another. The name draws an analogy to spintronics, where information is stored in the carrier spin. Valleytronics may offer lower dissipation of energy for classical circuits, as well as reduced decoherence in quantum processors. A roadblock to practical circuits, however, is that charge carriers in most materials react to external fields independently of their valley, thereby preventing the efficient generation and detection of valley currents.

The experiment reported by Gorbachev *et al.* removes the symmetry between the two valleys in graphene by giving each a different pseudospin texture. These valleys, labeled K and K', appear as inverted Dirac cones in the band structure (see the figure). Precisely aligned boron nitride (BN) substrates are used to bend the pseudospin up out of the plane of the momentum at the tip of the K valley and down out of the plane at the tip of the K' valley. Electrons in the modified valley tips are driven perpendicular to applied electric fields, left or right depending on their valley. This valley Hall effect is analogous to the ordinary Hall effect, where transverse voltages are generated by charge currents in a magnetic field. But the valley Hall effect does not require a magnetic field. Instead it relies on nontrivial pseudospin texture within each valley, similar to spin-orbit–based anomalous or spin Hall effects (*2*–*4*). The valley Hall effect was first observed via an identical pseudospin-based mechanism in molybdenum disulfide (MoS_2) (*5*).

The relation of the valley Hall effect to pseudospin is easier to understand by comparison with quantum and classical effects of a magnetic field. The vector potential associated with a magnetic field adds phase (Aharonov-Bohm or AB phase) into the wave function of a charge moving along the vector potential lines. Interference of different AB phases for slightly different paths provides a quantum explanation of the classical Lorentz force on a moving charge, which ultimately depends only on the local magnetic field. Vector potentials can be finite even in regions where the field is zero, as in the space surrounding a long solenoid, so the AB phase and Lorentz force do not need to go together. For example, a particle traveling in a loop around a solenoid experiences no Lorentz force but accumulates an AB phase set by the amount of magnetic flux in the solenoid and independent of the path itself.

The present experiment is understood in terms of an analogous kind of quantum mechanical phase, known as Berry's phase, involving paths through momentum space (following the band structure) rather than through real space. Carriers in graphene accumulate a Berry's phase of 180° for a momentum-space circumnavigation of either valley, due to the 360° rotation of pseudospin locked to momentum. This situation resembles the AB phase from a path in the field-free region around a solenoid, in that the amount of phase is independent of details of the path; it is visible to experiment only through subtle signatures such as modifications to the quantum Hall effect. The Berry's phase does not alter the motion of charge carriers because the Berry's flux core

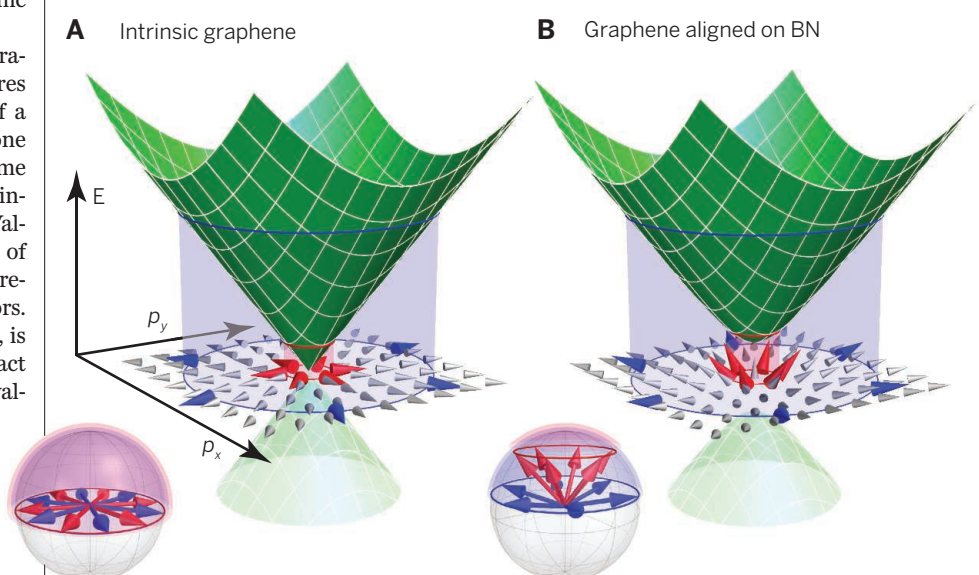

Into the valley. (**A** and **B**) The tips of graphene's Dirac cones are modified by an aligned boron nitride (BN) substrate. A small energy gap is introduced, and the pseudospin vectors (shown here for upper Dirac cone, K valley) are tilted out of the plane on BN. Blue circles show paths in momentum space circumnavigating the Dirac cone for larger magnitudes of momentum; red circles show these paths for smaller magnitudes of momentum. (Insets) Pseudospin vectors along blue and red paths trace out identical solid angles on a Bloch sphere for the intrinsic case (A) but different solid angles, leading to different Berry's phases, for graphene on BN (B).

[1]*Institute of Photonic Sciences (ICFO), Mediterranean Technology Park, 08860 Castelldefels, Barcelona, Spain.* [2]*Department of Physics and Astronomy, University of British Columbia, Vancouver, BC V6T1Z1, Canada. E-mail: jfolk@physics.ubc.ca*

Published by AAAS

is locked inside a topological singularity at the tip of the cone.

For graphene-on-BN, the tips of the Dirac cones are rounded, and the pseudospin is tilted out of the graphene plane but is still locked to momentum. As a result, the pseudospin traces out a smaller solid angle (a smaller Berry's phase is accumulated) when circumnavigating the cone close to the tip. It is as if there were a Berry's flux spread across the tip of the Dirac cone, so larger circles in momentum space accumulate more Berry's phase. Carriers accelerated through this region of Berry's flux then experience direct classical effects, analogous to the Lorentz force for a charge moving through regions with magnetic flux. The acceleration leads to a transverse velocity that is opposite for the two valleys, spatially separating K and K' carriers.

The experiment can also be viewed from the point of view of conservation laws. Although pseudospin is often thought of as an abstract quantity, it is believed that the pseudospin vector itself encodes a (valley-dependent) angular momentum that, together with orbital angular momentum, must be conserved (*6*). For graphene-on-BN, accelerating a carrier from the bottom of the Dirac cone (pseudospin up or down) to the sides (pseudospin in the plane) requires a transfer of angular momentum that can only be accomplished by a shift transverse to the direction of acceleration. This experiment thus offers a real physical connection to the pseudospin in graphene.

Gorbachev *et al.* make two important steps toward practical valleytronics. Theirs is the first demonstration of valley current generation and detection by purely electrical means, in a material that is well suited to electronics (stable in air, easy to contact, offering high mobilities). Moreover, the valley degree of freedom is usually invisible to experiment in graphene—an advantage from the point of view of quantum coherence. The authors have created a tiny region in the band structure, accessed by small changes in gate voltage, where the valley influence is profound. This offers promise for a device in which valley freedom can be long-lived but still controlled electrically on a fast time scale.

REFERENCES

1. R. V. Gorbachev *et al.*, *Science* **346**, 448 (2014).
2. D. Xiao, M.-C. Chang, Q. Niu, *Rev. Mod. Phys.* **82**, 1959 (2010).
3. N. Nagaosa, J. Sinova, S. Onoda, A. H. MacDonald, N. P. Ong, *Rev. Mod. Phys.* **82**, 1539 (2010).
4. S. O. Valenzuela, M. Tinkham, *Nature* **442**, 176 (2006).
5. K. F. Mak, K. L. McGill, J. Park, P. L. McEuen, *Science* **344**, 1489 (2014).
6. M. Mecklenburg, B. C. Regan, *Phys. Rev. Lett.* **106**, 116803 (2011).

10.1126/science.1260989

CREDIT: BLICKWINKEL/ALAMY

PLANT SCIENCE

Sex and the single fern

Separation of the synthesis and sensing of a signaling molecule controls sex in ferns

By **Tai-ping Sun**

Unlike animals, plants have two alternating generations: a diploid sporophyte and a haploid gametophyte. Through meiosis, the sporophyte produces haploid spores, which then give rise to gametophytes, a multicellular haploid structure that produces gametes for sexual reproduction. All seed plants and some non–seed plants are heterosporous, producing spores of different sizes: large female spores and small male spores. Most ferns, on the other hand, are homosporous; they produce a single type of spore. After germination, each fern spore has the potential to develop into a male, female, or hermaphrodite gametophyte. The developmental decision that determines the sex of a particular gametophyte depends on an interplant communication system mediated by chemical signals, termed antheridiogens (*1*, *2*). On page 469 of this issue, Tanaka *et al.* (*3*) show that an antheridiogen in the Japanese climbing fern (*Lygodium japonicum*) functions as more than a simple chemical signal. Covalent modification of the antheridiogen is required to trigger the fern's response to form male gametophytes. Temporal and spatial separation of the biosynthetic pathway between the early- and late-maturing gametophytes ensures the production of the antheridiogen, and the active male-inducing chemically modified form, at just the right time and place.

In a fern population, the early-maturing gametophytes (from spores that germinated first) produce and secrete into the aqueous environment antheridiogens, which promote differentiation of the neighboring younger gametophytes into males. These early-maturing antheridiogen-producing gametophytes will mainly develop the egg-forming female sex organ. This mechanism results in a small number of female gametophytes being surrounded by male gametophytes, promoting out-crossing and the maintenance of genetic diversity. Although this phenomenon was first discovered in 1950 (*4*), very little is known about how antheridiogen production is regulated and how this signal is perceived.

Tanaka *et al.* (*3*) show that an antheridiogen gibberellin (GA) A_9 methyl ester (GA_9-Me) is C3 hydroxylated and de-methylated to become an active GA (GA_4). This antheridiogen is produced via the conserved gibberellin biosynthetic pathway in plants (*3*, *5*, *6*), although the methyl transferase and methyl esterase for the conversion between GA_9 and GA_9-Me have not yet been identified. Importantly, Tanaka *et al.* find that genes encoding several enzymes for the production of GA_9 are more highly expressed in the early-maturing gametophyte than in the late-maturing young gametophytes. In contrast, the gene encoding the enzyme (GA 3-oxidase) for the conversion of GA_9 to the active GA_4 is preferentially expressed in the late-maturing young gametophytes, which are known to be highly sensitive to antheridiogens. This gene expression partitioning explains why only the early-maturing gametophytes produce the antheridiogen GA_9-Me and only the late-maturing younger gametophytes can respond to this pheromone to become males (see the figure).

In seed plants, GA_4 is an active hormone that plays a key role in regulating both vegetative and reproductive development (*5*, *6*). However, GA_9-Me is inactive. GA_4 turns on the GA signaling pathway by activating its nu-

Department of Biology, Duke University, Durham, NC 27705, USA. E-mail: tps@duke.edu

Published by AAAS

clear receptor GIBBERELLIN INSENSITIVE DWARF1 (GID1) to interact with and induce degradation of the DELLA master growth repressors (*7*, *8*). Tanaka *et al.* find that GA_4 in the Japanese climbing fern (a non–seed plant) activates the GA response pathway in a similar manner: GA_4, but not GA_9-Me, induces the GID1-DELLA interaction. Moreover, GID1 is preferentially expressed in the late-maturing young gametophyte, and treatment of such a gametophyte with a GID1 inhibitor blocks the male-inducing effect of GA_9-Me, supporting the idea that the GA-GID1-DELLA signaling module controls sex organ differentiation in this fern.

An outstanding critical question is how the fern is able to respond to a signal made endogenously at low levels and which is then further diluted upon secretion into the environment. Tanaka *et al.* measured the biochemical properties of the key enzyme GA 3-oxidase and the GA receptor GID1 and found that these proteins have up to 24- and 100-fold higher affinity, respectively, for substrate and ligand than their seed plant counterparts, facilitating the necessarily highly sensitive response to the scarce antheridiogen. Another key question the authors addressed is why ferns do not simply produce GA_4 as an antheridiogen. Tanaka *et al.* show that GA_9-Me is more efficiently taken up than GA_4 by the young gametophytes, likely because the hydrophobic GA_9-Me can easily diffuse through the cell membrane. However, how GA_9-ME is transmitted through the aqueous environment is unknown; Tanaka *et al.* suggest that a protein transporter may facilitate this process.

Sex determination in plants can be controlled by genes located on the sex chromosomes or by chemical signals, such as hormones in seed plants, and pheromones (such as antheridiogens) in non–seed plants, such as ferns (*2*). However, the detailed molecular mechanisms of sex determination in plants are presently largely unknown. The identification of the conserved GA-GID1-DELLA signaling module as the central regulator in sex organ differentiation in the fern is important, especially because GA also controls sex determination in some seed plants, such as *Zea mays* (corn) and *Cucumis sativa* (cucumber). Future studies of the downstream signaling pathways from DELLA in different plant species will reveal whether the GA-regulated sex determining process is conserved more broadly across plants.

REFERENCES AND NOTES

1. H. Yamane, *Int. Rev. Cytol.* **184**, 1 (1998).
2. M. Tanurdzic, J. A. Banks, *Plant Cell* **16** (suppl.), S61 (2004).
3. J. Tanaka *et al.*, *Science* **346**, 469 (2014).
4. W. Döpp, *Ber. Deut. Bot. Ges.* **63**, 139 (1950).
5. P. Hedden, S. G. Thomas, *Biochem. J.* **444**, 11 (2012).
6. S. Yamaguchi, *Annu. Rev. Plant Biol.* **59**, 225 (2008).
7. T. P. Sun, *Curr. Biol.* **21**, R338 (2011).
8. M. Ueguchi-Tanaka, M. Nakajima, A. Motoyuki, M. Matsuoka, *Annu. Rev. Plant Biol.* **58**, 183 (2007).

ACKNOWLEDGMENTS

I thank K. Preyer and A. Silverstone for helpful discussions.

10.1126/science.1260948

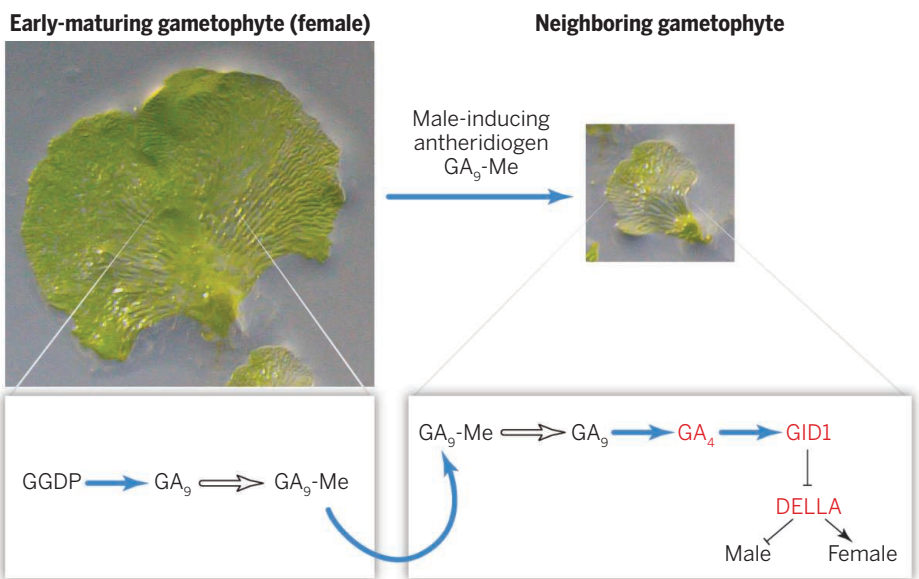

Sorting out sexual differentiation. Interplant communication via antheridiogen between early- and late-maturing gametophytes is achieved by physical separation of the GA biosynthetic pathway in these individuals. The antheridiogen (GA_9-Me) is produced and secreted by the early-maturing gametophyte (left). Once taken up by the neighboring late-maturing young gametophyte (right), GA_9-Me is converted to the active GA_4. GA_4 activates its receptor GID1, which in turn promotes male sex organ formation by inhibiting the GA signaling repressor DELLA. The open arrows represent steps catalyzed by unidentified enzymes. GGDP, geranylgeranyl diphosphate.

MICROBIOLOGY

Breathing the unbreathable

A crystal structure reveals how some bacteria break down organohalide pollutants

By **Elizabeth Anne Edwards**

Organohalides are highly versatile chemicals containing at least one carbon atom bound to a halogen atom such as chlorine, bromine, fluorine, or iodine. They include the dry-cleaning solvent tetrachloroethene (PCE), the industrial degreaser trichloroethene (TCE), ozone-depleting refrigerants such as chlorofluorocarbons (CFCs), and anti-stick compounds like Teflon. Organohalides are also produced by volcanic emissions and lightning strikes; plants, animals, and microbes produce them as hormones, as signaling molecules, and for self-defense (*1*). Certain microbes can break down organohalide pollutants. On page 455 of this issue, Bommer *et al.* (*2*) report the crystal structure of an enzyme from the bacterium *Sulfurospirillum multivorans* that catalyzes the cleavage of the carbon-halogen bond in PCE and TCE. This structure opens the door to a full mechanistic and predictive understanding of this important detoxifying reaction.

Some organohalides are toxic at sufficient concentration. Their industrial emissions are now controlled and drinking water levels are regulated. These chemicals tend to be highly stable and poorly soluble in water and thus persist in the environment, where they accumulate in sediments, cell membranes, and fatty tissues. Many synthetic organohalides are produced in large quantities, and historical, accidental, or inadvertent releases have created an enormous legacy of contaminated sites around the world. TCE and its carcinogenic daughter products are among the most common organic groundwater pollutants, necessitating often expensive cleanup efforts.

Hints that anaerobic microbial communities could reductively dehalogenate organohalides and might be used to detoxify these pollutants first emerged almost 50 years ago (*3*). Evidence that anaerobic microbes could grow using the energy in a

IMAGE: M. MATSUOKA

Published by AAAS

carbon-halogen bond was reported 30 years ago (*4*). Soon after, the microbes responsible were identified thanks to a remarkable alignment of scientific discovery and rising concern over the extent of TCE contamination (*5*–*9*). The industrial application of these organohalide-respiring microbes for bioremediation is arguably one of the fastest translations of scientific discovery into practice. A decade after the first small field trials (*10*), remediation efforts now widely rely on specific organohalide-respiring bacteria to accelerate reductive dechlorination of PCE and TCE in situ (*11*).

At the heart of this successful application of bioremediation are fascinating microbes that use organohalides as terminal electron acceptors in their metabolism: They breathe these molecules as we do oxygen (*12*). During this process, the halogen substituents are sequentially removed from the organic backbone. Complete dehalogenation typically renders the molecule nontoxic, but even partial dehalogenation increases water solubility and accelerates natural attenuation. Organohalide-respiring microbes are phylogenetically diverse and are found around the planet in both freshwater aquifers and marine sediments; new genera continue to be discovered. For some, such as *Sulfurospirillum* and *Desulfitobacterium*, organohalides are just one of several options for anaerobic respiration. For others, such as *Dehalococcoides* and *Dehalobacter*, organohalide respiration is the only way of life, oxygen is lethal, and strictly anaerobic conditions are required for cultivating them. All these microbes grow best in complex communities with fermenting and methane-producing microbes. Such anaerobic environments are commonly found in nature and are readily established in sediments and in the subsurface to enhance dehalogenation reactions.

Within the genomes of these remarkable microbes is an equally extraordinary diversity of genes coding for the enzymes that catalyze reductive dehalogenation. Hundreds of thousands of genes for putative reductive dehalogenases are present in GenBank, with as many as 36 dehalogenase genes in a single *Dehalococcoides* genome, yet for most of these enzymes, the substrates remain completely unknown (*13*). Scientists have been able to determine a few substrates for only a handful of these enzymes, because it is so difficult to grow and manipulate the organisms and their genomes. Reductive dehalogenase enzymes require several cofactors to help bring about the reaction, including variants of vitamin B_{12} that harbor a reactive cobalt atom critical to breaking the carbon-halogen bond. Some organisms depend on other organisms to synthesize vitamin B_{12} for their survival.

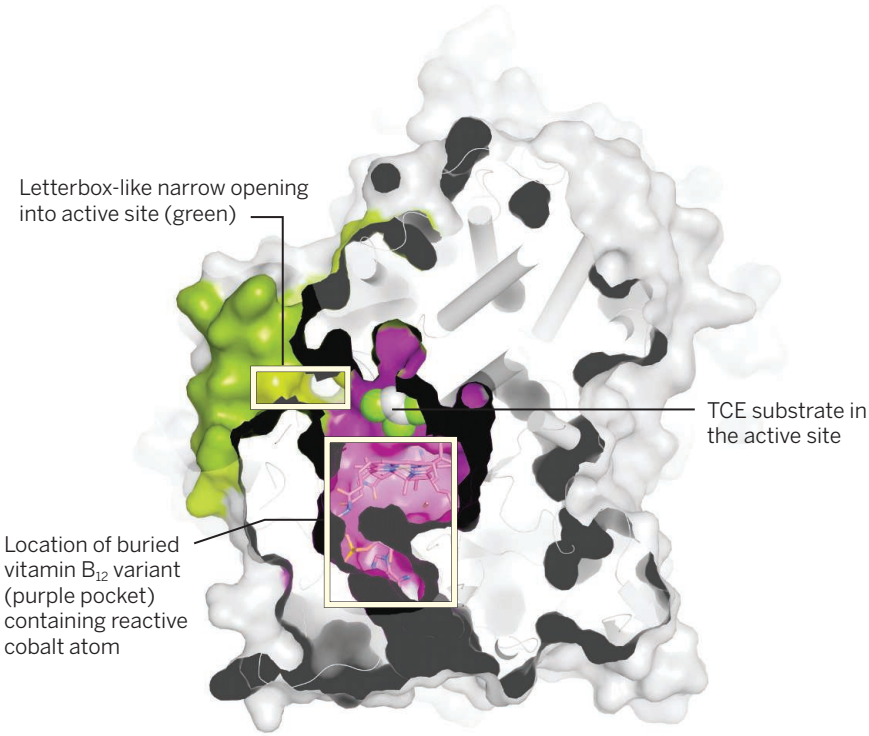

Deeply buried—safely destroyed. In Bommer *et al*.'s dehalogenase structure, a deep substrate binding pocket (purple) contains the reactive vitamin B_{12} variant as well as the substrate, TCE. Access to the active site is limited to a narrow hydrophobic "letterbox" opening (green). The structure helps to clarify how dehalogenating microbes are able to break down organohalide pollutants such as TCE.

Bommer *et al.* now show that the highly reactive cobalt-containing vitamin is in fact deeply buried—and thus protected—in the enzyme (see the figure). The structure allows mechanistic questions to be answered that could previously only be approached tangentially using experiments with crude cell extracts, partially purified proteins, chemical inhibitors, isotopes, and vitamin B_{12} analogs. Knowledge of the active site of the enzyme will facilitate structure-based remodeling to new substrates, including some of the most toxic or persistent organohalides.

A complementary paper published very recently in *Nature* (*14*) describes the structure and inferred mechanism for a distinct yet similar class of B_{12}-dependent reductive dehalogenases found more typically in aerobic microbes. Together, these new structures begin to reveal the relationship between sequence and substrate preferences, helping to predict the fate of synthetic and naturally occurring chemicals in the environment based on the resident populations of dehalogenating microbes. Such fundamental understanding is crucial for effective management of contaminated sites. Finally, these seminal pieces of work have implications beyond environmental problems. The wide variety of naturally occurring organohalides and the diversity of genes encoding putative reductive dehalogenases gleaned from environmental DNA studies portend a central role for these enzymes in the global halogen cycle.

Department of Chemical Engineering and Applied Chemistry, University of Toronto, Toronto, Ontario M5S 3E5, Canada. E-mail: elizabeth.edwards@utoronto.ca

CREDIT: ADAPTED FROM (*2*)

REFERENCES

1. G. W. Gribble, *Chemosphere* **52**, 289 (2003).
2. M. Bommer *et al.*, *Science* **346**, 455 (2014).
3. D. W. Hill, P. L. McCarty, *J. Water Pollut. Control Fed.* **39**, 1259 (1967).
4. D. R. Shelton, J. M. Tiedje, *Appl. Environ. Microbiol.* **48**, 840 (1984).
5. D. L. Freedman, J. M. Gossett, *Appl. Environ. Microbiol.* **55**, 2144 (1989).
6. C. Holliger *et al.*, *Arch. Microbiol.* **169**, 313 (1998).
7. X. Maymó-Gatell, Y. Chien, J. M. Gossett, S. H. Zinder, *Science* **276**, 1568 (1997).
8. H. Scholz-Muramatsu, A. Neumann, M. Meßmer, E. Moore, G. Diekert, *Arch. Microbiol.* **163**, 48 (1995).
9. K. A. DeWeerd, L. Mandelco, R. S. Tanner, C. R. Woese, J. M. Suflita, *Arch. Microbiol.* **154**, 23 (1990).
10. D. W. Major *et al.*, *Environ. Sci. Technol.* **36**, 5106 (2002).
11. H. F. Stroo, A. Leeson, C. H. Ward, Eds., *Bioaugmentation for Groundwater Remediation* (Springer, New York, 2013).
12. D. Leys, L. Adrian, H. Smidt, *Philos. Trans. R. Soc. B* **368**, 20120316 (2013).
13. L. A. Hug *et al.*, *Philos. Trans. R. Soc. B* **368**, 20120322 (2013).
14. K. A. P. Payne *et al.*, *Nature* 10.1038/nature13901 (2014).

10.1126/science.1261194

Published by AAAS

EVOLUTION

Ratcheting the evolution of multicellularity

Traits that entrench cells in a group lifestyle may pave the way for complexity

By **Eric Libby**[1] *and* **William C. Ratcliff**[2]

Multicellularity is one of the major transitions that allowed the evolution of large, complex organisms, fundamentally reshaping Earth's ecology (*1*). Early steps in this process remain poorly resolved, because known transitions occurred hundreds of millions of years ago (*2*) and few transitional forms persist. It is generally accepted that the first steps toward multicellularity were the formation of cellular clusters, followed by the success or failure of those clusters depending on their traits. As clusters of cells adapted, cells lost their evolutionary autonomy, becoming mutually reliant parts in a new higher-level whole (*1*, *3*). This transition may be facilitated by a "ratcheting" process in which cells adopt traits that entrench them in a group lifestyle, stabilizing the group and paving the way for the evolution of multicellular complexity.

The transition to multicellularity is thought to be stabilized by the evolution of traits that export fitness from cells to newly formed groups of cells (*3*, *4*). But conflicts between levels of selection can be problematic, as cell-level selection can easily overwhelm the generally slower process of group-level selection (*5*). For example, groups of microbes that produce costly extracellular metabolites can grow faster than those that do not, but within groups, free-riding cheats usually grow fastest of all (*6*). Such cell-level evolution can also lead to cancer and is a potential problem for all multicellular organisms.

Making matters more complicated, many primitive multicellular life cycles likely included both uni- and multicellular stages with heritable variation in traits that affect the fitness of each stage. Such dual-stage life cycles readily evolve de novo from unicellular starting points in the lab. For example, experiments selecting for multicellularity in the unicellular green alga *Chlamydomonas reinhardtii* produced a strain that formed sessile multicellular clusters that reproduced via motile unicellular propagules (*7*). Reliance on a unicellular stage, however, provides opportunity to forego group formation. As an example, the bacterium *Pseudomonas fluorescens* rapidly evolves to produce multicellular mats on the surface of static growth media to gain better access to oxygen. Once a mat has formed, selection then favors unicellular cheats that do not produce the glue responsible for mat formation, ultimately leading to the mat's destruction (*8*). The unicellular cheats that escape the mat's collapse may not evolve into mat formers again without suitable selective conditions. This experimental work reveals that a key problem in the transition to multicellularity is not how multicellular clusters evolve in the first place, but rather how multicellularity persists when the balance of selection tilts toward single cells.

One solution to stabilizing multicellularity is the evolution of traits that increase cell-level fitness in a group context, but come at a cost to free-living fitness. Accumulation of these traits would ratchet cells into a group lifestyle, ultimately preventing unicellular reversion. For example, in a yeast model of multicellularity (*9*), selection for fast sedimentation in a liquid culture of unicellular yeast results in the evolution of multicellular clusters composed of hundreds of clonal cells (see the figure). These clusters quickly evolve a secondary trait: elevated rates of programmed cell death (apoptosis) (*9*). At first glance, it is hard to see how cellular suicide could be beneficial, but mathematical modeling reveals that higher rates of apoptosis allow clusters to circumvent growth constraints imposed by volume and nutrient flow limitations (*10*). Specifically, apoptotic cells act as "weak links" in a chain of cells within a cluster. Breaking these links produces proportionally smaller, faster-growing propagules. Indeed, high rates of apoptosis repeatedly evolved in independent replicate populations of lineages that form large clusters (*9*). This contrasts with a unicellular context where apoptosis should be maladaptive. If any of the yeast that evolved high rates of apoptosis within clusters were to leave the group and revert to a unicellular lifestyle, they would find themselves at a competitive disadvantage relative to other, low-apoptosis unicellular strains. Moreover, if the balance of selection favored single cells over groups, then cells that leave the group would enjoy less of a fitness benefit due to the cost of apoptosis in free-living cells. Thus, the accumulation of ratcheting traits, such as apoptosis, makes the successful reversion to unicellularity a many-step process (i.e., the traits evolved in a group context would need to be counterbalanced). This stabilizes multicellularity by limiting evolutionary reversion, even when the environment favors unicellular growth.

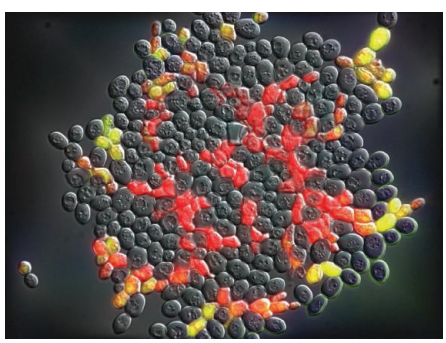

Apoptosis as a ratchet. Apoptotic cells (green) and dead cells (red) act as weak links within a cluster of yeast cells. Breaking these links allows the cluster to dodge growth constraints (volume and nutrient flow limitations), producing smaller, faster-growing groups of cells.

CREDIT: W. C. RATCLIFF

For traits to act as ratchets, they must have opposite effects on fitness in multi- and unicellular contexts. This dichotomy is clear in traits such as apoptosis. Premature death of the organism is, after all, an almost universally costly trait. However, other traits that ratchet the evolution of multicellular complexity may be more subtle. For instance, a division of labor over the production of metabolites could provide a ratcheting function. Recent experiments with bacteria have shown that strains engineered to cooperatively cross-feed grow faster than the unicellular ancestor capable of autonomous growth, but this benefit requires coculture (*11*). In general, the more a trait makes cells in a cluster mutually reliant, the more it serves as a ratchet. This raises the intriguing hypothesis that division of labor might be common in multicellular organisms not only because of the adaptive benefits of specialization, but also because multicellular lineages with this ratcheting trait may be more evolutionarily persistent.

Ratcheting may also play a role in other major evolutionary transitions, leading to the establishment of new types of biological "individuals." For example, symbiosis between free-living prokaryotes led to the origin of eukaryotic cells—a new type of biological individual—capable of photosynthesis and oxidative metabolism. The evolution of host cell dependence on the metabolic utility of their symbionts acts as a ratchet

[1]Santa Fe Institute, Santa Fe, NM 87501, USA. [2]School of Biology, Georgia Institute of Technology, Atlanta, GA 30332, USA. E-mail: elibby@santafe.edu

Published by AAAS

by limiting opportunity for reversion. For example, *Paramecium* experimentally deprived of their photosymbiont *Chlorella* pay a substantial fitness cost when grown under bright conditions (*12*). Likewise, the symbiont's loss of genes required for life outside of the host cell acts as a ratchet (*13*). During the evolution of eusocial "superorganisms" from multicellular individuals, reproductive division of labor (*14*) acts as a ratchet, limiting the ability of individuals to return to an asocial, solitary state. Honey bee workers, for instance, are incapable of sexual reproduction and can only lay male eggs, making it difficult to start a solitary nest.

The ratcheting theory may also help solve a "chicken and egg" problem of multicellular evolution. It has been argued that a key step in the evolution of multicellularity is the export of fitness from cells to groups—"Darwinizing" groups while "deDarwinizing" cells (*3*, *15*). This would allow groups to adapt as individuals. But how do groups evolve multicellular traits when the traits that facilitate multicellular adaptation are themselves multicellular adaptations? For example, reproductive division of labor through germ cell–somatic cell differentiation resolves conflicts between cell and group fitness interests during the evolution of large, long-lived organisms like animals. But germ-soma differentiation is a complex multicellular adaptation whose origin requires that the balance of selection tilts firmly toward groups, not cells. By stabilizing life in early multicellular groups, ratcheting facilitates further multicellular adaptation and, in so doing, may play a key role in the evolution of multicellular complexity.

REFERENCES

1. J. Maynard Smith, E. Szathmáry, *The Major Transitions in Evolution* (Oxford Univ. Press, New York, 1995).
2. R. K. Grosberg, R. R. Strathmann, *Annu. Rev. Ecol. Evol. Syst.* **38**, 621 (2007).
3. R. E. Michod, *Proc. Natl. Acad. Sci. U.S.A.* **104** (suppl. 1), 8613 (2007).
4. H. J. Folse 3rd, J. Roughgarden, *Q. Rev. Biol.* **85**, 447 (2010).
5. G. C. Williams, *Adaptation and Natural Selection* (Princeton Univ. Press, Princeton, NJ, 1966).
6. K. M. Sandoz, S. M. Mitzimberg, M. Schuster, *Proc. Natl. Acad. Sci. U.S.A.* **104**, 15876 (2007).
7. W. C. Ratcliff *et al.*, *Nat. Commun.* **4**, 2742 (2013).
8. P. B. Rainey, B. Kerr, *BioEssays* **32**, 872 (2010).
9. W. C. Ratcliff, R. F. Denison, M. Borrello, M. Travisano, *Proc. Natl. Acad. Sci. U.S.A.* **109**, 1595 (2012).
10. E. Libby, W. C. Ratcliff, M. Travisano, B. Kerr, *PLOS Comput. Biol.* **1**, e1003803 (2014).
11. S. Pande *et al.*, *ISME J.* **8**, 953 (2014).
12. S. J. Karakashian, *Physiol. Zool.* **36**, 52 (1963).
13. J. P. McCutcheon, N. A. Moran, *Nat. Rev. Microbiol.* **10**, 13 (2012).
14. B. J. Crespi, D. Yanega, *Behav. Ecol.* **6**, 109 (1995).
15. P. Godfrey-Smith, *Darwinian Populations and Natural Selection* (Oxford Univ. Press, New York, 2009).

10.1126/science.1262053

CREDIT: V. ALTOUNIAN/*SCIENCE*

VIROLOGY

Unanchored ubiquitin in virus uncoating

Components of a cellular degradation system are exploited by influenza virus during infection

By **Ricardo Rajsbaum**[1] *and* **Adolfo García-Sastre**[2,3,4]

Misfolded proteins in eukaryotic cells can be modified with the small protein ubiquitin (Ub). The conjugation of a chain of Ub proteins [polyubiquitin (poly-Ub)] targets a substrate for destruction by complexes called proteasomes (*1*). But unanchored poly-Ub chains are emerging as key factors in multiple cellular responses, including innate antiviral pathways (*2*, *3*). Such free chains can also activate the aggresome pathway, another mechanism that degrades unwanted proteins when the proteasome system is overwhelmed or inhibited (*4*). On page 473 of this issue, Banerjee *et al.* (*5*) report that influenza virus engages the host cell's aggresome system by carrying unanchored poly-Ub chains. The strategy allows the virus to "uncoat" and replicate after its escape from the endosome during entry into the host cell.

Polyubiquitylation of proteins occurs post-translationally. The free carboxyl-terminal glycine residue of Ub can be conjugated to lysine residues of specific substrates. Ub itself can be covalently attached to other Ub proteins through one of its seven lysines (K6, K11, K27, K29, K33, K48, and K63) to form poly-Ub chains (*1*). Proteins modified with poly-Ub at K48 are usually targeted for the proteasome. In addition, a deubiquitylating enzyme, Poh1, releases K63-linked poly-Ub chains from protein aggregates (*6*). These freed chains are recognized by the enzyme histone deacetylase 6 (HDAC6), a component of the aggresome pathway. HDAC6 is a predominantly cytoplasmic protein deacetylase, but acts as an adaptor protein between unanchored Ub chains and dynein motor complexes in the aggresome-autophagy pathway (*7*–*9*). Thus, these unanchored poly-Ub chains function to recruit protein aggregates to the aggresome for degradation (*4*) (see the first figure).

Unanchored poly-Ub chains also have antiviral functions. Unanchored K63-linked poly-Ub chains bind to and activate retinoic acid–inducible gene I (RIG-I), a protein that induces the expression of type I interferons, potent antiviral cytokines (*3*). Additionally, unanchored K48-linked poly-Ub chains bind and activate the enzyme inhibitor of κB kinase ε (IKKε) and a downstream signaling cascade that stimulates the expression of antiviral genes (*2*).

Influenza A viruses (IAVs) are highly infectious pathogens that have caused major pandemics and annual epidemics. Successful virus infection requires crossing the host cell membrane. IAV is an enveloped virus that attaches to a target cell and gets internalized by the endocytosis pathway. Acidification of the endosome causes a conformational change in the viral surface protein hemagglutinin (HA), which triggers fusion of the viral and endosomal membranes. As a result, viral ribonucleoproteins (RNPs), consisting of the viral RNAs, nucleoprotein (NP), and polymerase, are released into the cytoplasm. RNPs are then transported into the nucleus where viral RNA replication takes place (*10*). But for this passage to occur, RNPs must lose an associated viral matrix M1 protein. This process, called uncoating, is facilitated by the viral M2 protein, a small ion channel in the viral membrane (*11*) (see the second figure).

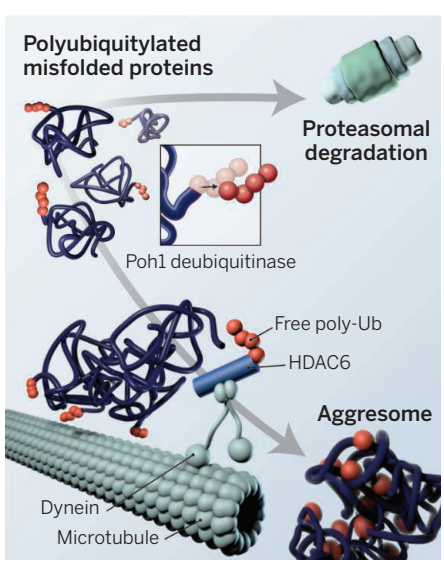

Aggresome pathway. Misfolded proteins that are tagged with poly-Ub, but are not destroyed in the proteasome, are recognized by HDAC6. HDAC6 binds to free ubiquitin chains and to dynein motor complexes in the aggresome-autophagy degradation pathway.

Published by AAAS

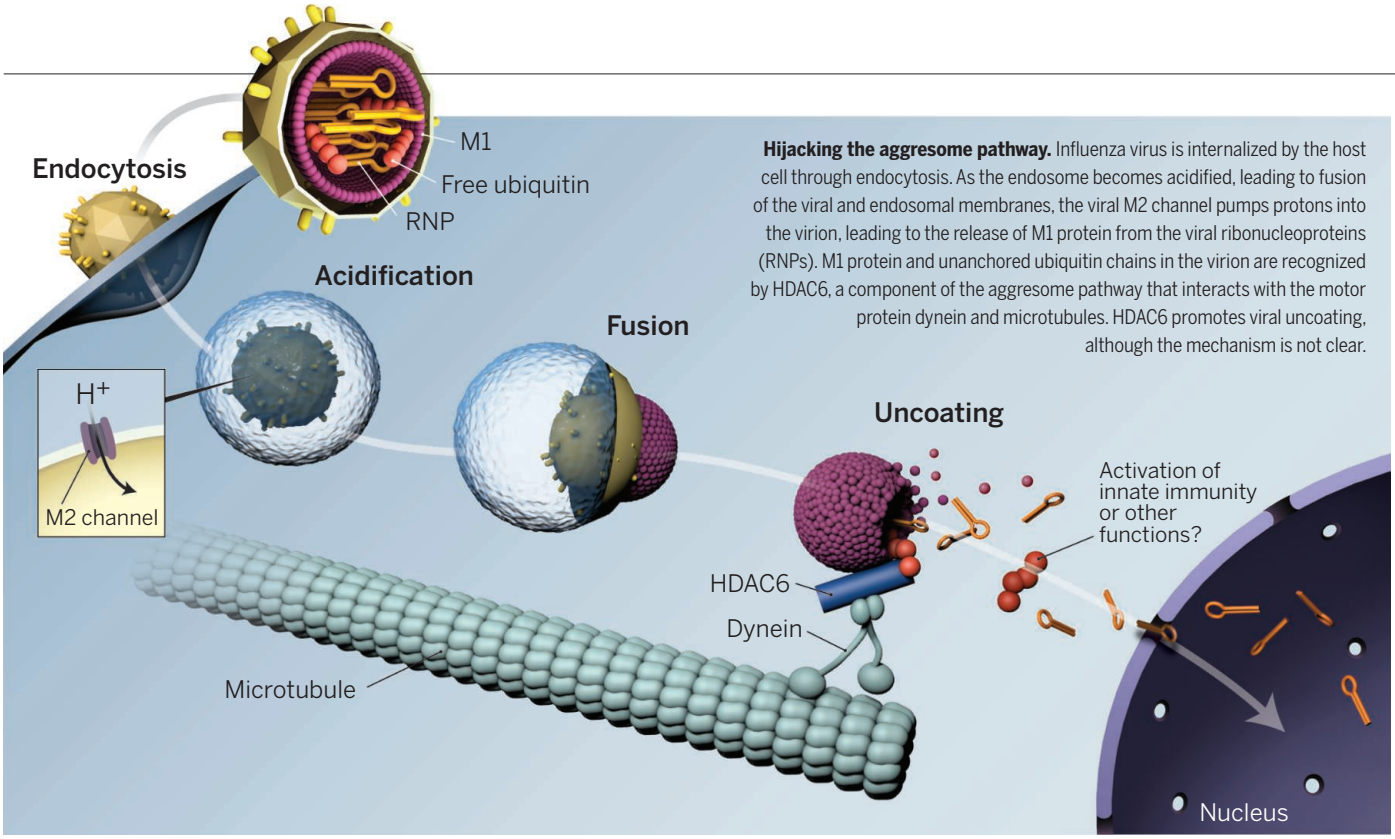

Hijacking the aggresome pathway. Influenza virus is internalized by the host cell through endocytosis. As the endosome becomes acidified, leading to fusion of the viral and endosomal membranes, the viral M2 channel pumps protons into the virion, leading to the release of M1 protein from the viral ribonucleoproteins (RNPs). M1 protein and unanchored ubiquitin chains in the virion are recognized by HDAC6, a component of the aggresome pathway that interacts with the motor protein dynein and microtubules. HDAC6 promotes viral uncoating, although the mechanism is not clear.

Endosomal acidification not only triggers membrane fusion, but also activates the M2 ion channel. M2 pumps protons from the endosome into the virion, creating an acidic bath that debilitates M1 interaction with the viral RNP. Amantadine and rimantadine (*12*), two approved drugs for treating influenza, block M2 activity. Banerjee *et al.* reveal a new requirement for optimal influenza virus uncoating.

Banerjee *et al.* tested the biological role of aggresomes during influenza virus infection of mice lacking HDAC6. Although these mice are viable, they show slightly reduced immune response and bone homeostasis (*13*). The authors found decreased virus replication in bronchoalveolar lavages in these infected mice. However, markers of cellular immune response were not affected, in contrast to a previous report (*13*). No differences were observed in viral endocytic uptake, acid-induced HA conversion, or fusion between wild-type cells and cells lacking HDAC6. However, uncoating and nuclear import of viral RNPs were reduced in cells lacking HDAC6. The requirement of HDAC6 clearly depended on its capacity to bind unanchored poly-Ub, because cultured cells reconstituted with a version of HDAC6 containing a mutation in the Ub-binding domain showed reduced viral uncoating and replication compared to wild-type HDAC6 or HDAC6 with point mutations in the deacetylase domain. Banerjee *et al.* also observed that HDAC6 binds to NP and M1 and that influenza A virions carry free mono-Ub and poly-Ub. Collectively, these findings point to a role of the aggresome in promoting viral uncoating.

HDAC6 mediates the transport of misfolded protein aggregates along microtubules to aggresomes through its interactions with the motor protein dynein and dynactin, the protein complex that links cargo to dynein (*7*). Banerjee *et al.* show that depletion of dynactin 2 (by RNA interference), inhibition of dynein by ciliobrevin D, and induction of actin depolymerization by cytochalasin D and nocodazole all prevented viral uncoating. However, whether the motor protein and cytoskeleton provide a physical force that drives the uncoating is not known. Nevertheless, these data, along with the ability of HDAC6 to bind to free poly-Ub chains, NP, and M1, all suggest aggresome pathway-mediated viral uncoating.

How is unanchored ubiquitin loaded into the virion? Although Banerjee *et al.* did not identify the type of Ub linkage (i.e., K63, K48, or others) that is bound to both the virus capsid and HDAC6, previous studies have shown that K63-linked unanchored poly-Ub is associated with HDAC6 (*6*). Banerjee *et al.* detected unanchored di-, tri-, and tetra-Ub inside the virion, raising the question as to whether these different lengths of Ub chains activate different functions when released into the cell. It is also unclear how the aggresome pathway promotes viral uncoating. Whether the aggresome pathway is involved in uncoating other enveloped viruses, including ebola virus and HIV-1, becomes an interesting new avenue of investigation.

The study of Banerjee *et al.* highlights another example of virus adaptation to exploit cellular machinery for its replication. It also underscores the recently emerging roles of free poly-Ub in activating different cellular pathways. As viral uncoating is a proven target for treating influenza virus infection, blocking the aggresome pathway may present a strategy for discovering antivirals. If such inhibitors are not toxic, they have a better chance of overcoming the development of resistance that is inherent to the M2 ion channel inhibitors.

[1]*Department of Microbiology and Immunology, The University of Texas Medical Branch, 301 University Boulevard, Galveston, TX 77555, USA.* [2]*Department of Microbiology, Icahn School of Medicine at Mount Sinai, One Gustave L. Levy Place, New York, NY 10029, USA.* [3]*Global Health and Emerging Pathogens Institute, Icahn School of Medicine at Mount Sinai, One Gustave L. Levy Place, New York, NY 10029, USA.* [4]*Department of Medicine, Icahn School of Medicine at Mount Sinai, One Gustave L. Levy Place, New York, NY 10029, USA. E-mail: adolfo.garcia-sastre@mssm.edu; rirajsba@utmb.edu*

REFERENCES

1. J. F. Trempe, *Curr. Opin. Struct. Biol.* **21**, 792 (2011).
2. R. Rajsbaum *et al.*, *Immunity* **40**, 880 (2014).
3. W. Zeng *et al.*, *Cell* **141**, 315 (2010).
4. H. Ouyang *et al.*, *J. Biol. Chem.* **287**, 2317 (2012).
5. I. Banerjee *et al.*, *Science* **346**, 473 (2014).
6. R. Hao *et al.*, *Mol. Cell* **51**, 819 (2013).
7. Y. Kawaguchi *et al.*, *Cell* **115**, 727 (2003).
8. J. Y. Lee *et al.*, *EMBO J.* **29**, 969 (2010).
9. L. S. Chin, J. A. Olzmann, L. Li, *Biochem. Soc. Trans.* **38**, 144 (2010).
10. T. O. Edinger, M. O. Pohl, S. Stertz, *J. Gen. Virol.* **95**, 263 (2014).
11. L. H. Pinto, L. J. Holsinger, R. A. Lamb, *Cell* **69**, 517 (1992).
12. A. G. Bukrinskaya, N. K. Vorkunova, G. V. Kornilayeva, R. A. Narmanbetova, G. K. Vorkunova, *J. Gen. Virol.* **60**, 49 (1982).
13. Y. Zhang *et al.*, *Mol. Cell. Biol.* **28**, 1688 (2008).

10.1126/science.1261509

CREDIT: V. ALTOUNIAN/*SCIENCE*

Published by AAAS

WATER SECURITY

Coping with the curse of freshwater variability

Institutions, infrastructure, and information for adaptation

By J. W. Hall,[1]* D. Grey,[1] D. Garrick,[2] F. Fung,[3] C. Brown,[4] S. J. Dadson,[1] C. W. Sadoff[5]

Coping with variable and unpredictable freshwater resources represents a profound challenge to climate adaptation. Rainfall, snowmelt, soil moisture, and runoff can vary from zero to large quantities, over a range of time scales and in ways not well predicted by climate models. Extreme floods and droughts are the most obvious manifestations, but hydrologic variability can also have chronic impacts. Water security involves managing these risks so that they do not place an intolerable burden on society and the economy (*1*). We discuss interlinked roles of institutions, infrastructure, and information in managing those risks.

Economic output [Gross Domestic Product (GDP)] can be sensitive to hydrologic variability (*2*), especially in agriculture-dependent societies. Droughts, floods, and extreme variability affect output directly and have ripple effects through the economy, depending on the severity of the hydrologic hazard and the vulnerability of socioeconomic systems. For example, hydrologic variability in Ethiopia accounts for there having been 38% less economic growth than would have been expected based on average rainfall (*3*). Multiyear drought in Syria has triggered migration into cities by unemployed farmers, contributing to conflict (*4*).

POLICY

Even the perceived risk of future losses can create disincentives for investment, which inhibits growth. The $43 billion in economic losses and $16 billion insured losses due to the 2011 flooding in Thailand (see the photo) shook the insurance industry and threatened continued foreign direct investment (*5*).

UNDERSTANDING VARIABILITY. With hydrologic variability poorly understood (*6*), extreme events can be hard to predict. Future changes in variability are highly uncertain. At least three dimensions of hydrologic variability can cause harm: intra-annual (seasonal and monthly), interannual (year-to-year), and unpredictable timing and intensity of extremes. Strong seasonal variability, experienced in monsoonal and tropical climates, limits the productive portion of the year. In parts of India, 50% of annual precipitation falls in just 15 days, and over 90% of annual river flows are concentrated in only 4 months of the year (*7*). Arid regions, like the southwestern United States, Australia, Middle East, North Africa, and Central Asia, are characterized by strong interannual variability, increasing the likelihood of multiyear droughts and also of intense rainfall that far exceeds the average and can lead to catastrophic flash flooding.

When these dimensions are combined, the situation is most challenging—a wicked combination of hydrology that confronts the world's poorest people. Of the 35 river basins with a population greater than one million that are classified by the World Bank as "low income," 19 have variability of runoff that is greater than both the interannual and intra-annual medians (across all populous river basins globally), and only two have variability of runoff that is less than both the interannual and intra-annual medians (see supplementary materials).

The scale of economic losses depends on factors that are difficult to isolate. Coping capacity increases with wealth (*8*), with more resources invested to manage risk. Yet, increasing wealth can increase economic exposure to extreme events, with more assets in harm's way. The Intergovernmental Panel on Climate Change (IPCC) reports that losses from climate-related hazards were 1% of GDP for middle-income countries during the years 2001–2006, but only 0.1% of GDP for high-income countries (*8*). Major investments in risk reduction, often triggered by catastrophic losses, e.g., the 1926–27 Mississippi River floods and 1953 floods in the Netherlands, have proved to be effective in managing economic impacts of climate hazards. Yet deteriorating infrastructure and changing frequency of extreme events can push losses beyond the tolerability threshold, as seen from U.S. impacts of hurricanes Katrina and Sandy.

Countries have little control over their hydrologic endowment: when and where it rains and how much water evaporates, infiltrates, and runs off. Countries that have managed to grow economically, notwithstanding complex hydrology, have invested heavily to reduce risk. In river basins where there has been low investment to cope with complex hydrology, economic output is overwhelmingly low (see the chart, lower right) (Fig. 2). By contrast, countries along river basins with benign hydrology are more wealthy, even though investments in water management have sometimes been quite modest (see the chart, left side). Additional investment required to transition from water-insecure to secure is greatest in river basins with highly variable hydrology (see the chart, right side). This is least affordable and hardest to deliver in the poorest countries. Although investment in institutions and infrastructure can shift river basins upward in the chart, reflecting improved water security, climate change may shift them rightward, adding to the threat in societies already underequipped to cope with risk.

PATHWAYS TO WATER SECURITY. Adapting to hydrologic variability, building resilience to risk, involves "the three 'I's": institutions, infrastructure, and information. Institutions and governance (including river basin organizations, legal systems, national governments, and nongovernmental organizations) support proactive planning and development of legal and economic in-

Floods in Thailand in 2011 caused $43 billion in losses (*5*). Rojana Industrial Park, Ayutthaya, Thailand, October 2011 (*14*).

CREDIT: WIKIMEDIA COMMONS

Downloaded from www.sciencemag.org on October 24, 2014

Published by AAAS

Linking economic growth, hydrologic variability, and investment in risk mitigation

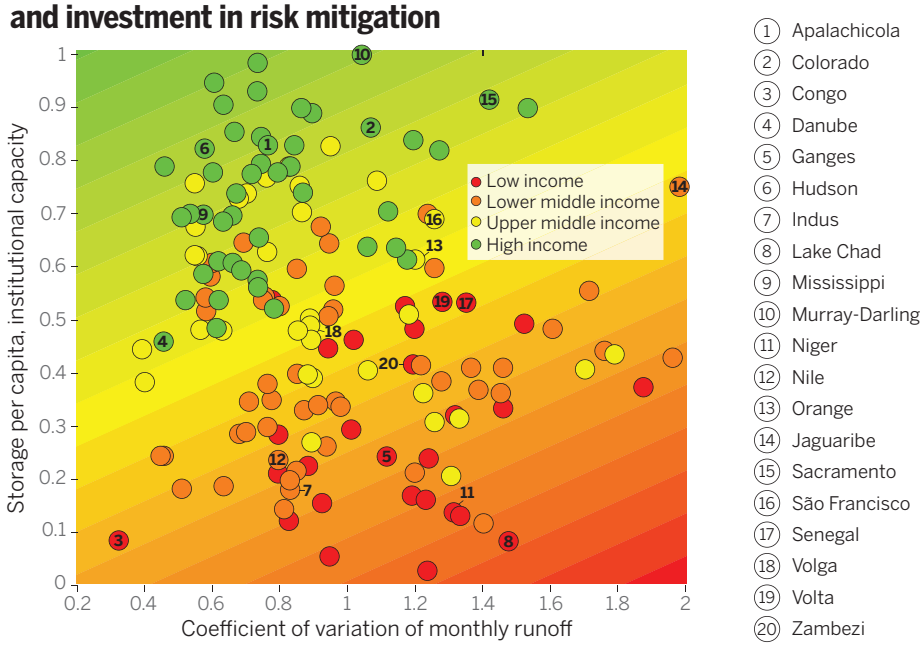

Linking economic growth, hydrologic variability, and investment in risk mitigation. The world's river basins with a population >2 million, colored according to GDP per capita of the population in the basin. The horizontal axis summarizes hydrologic variability. The vertical axis is a composite indicator of investment in infrastructure and institutional capacity. The colored contours are a linearly interpolated surface reflecting the association between variability, water security investments, and GDP. See supplementary materials for details.

struments to manage and share risks (water allocation and property rights, land zoning, watershed protection, water pricing and trading, insurance, and food trade liberalization) (*9*). Investments in infrastructure buffer variability and minimize risks (storage, transfers, groundwater wells, levees, wastewater treatment, and desalination). Information collection, analysis, and transfer (monitoring, forecast and warning systems, expert know-how, simulation models, and decision-support systems) are essential for operating institutions and infrastructure.

Coping with variability involves combinations of the three I's—seldom do they yield their full benefits in isolation. Thus, although individual projects have typically been the "unit of currency" in investment decision-making, this needs to be replaced by a more systemic view of the pathway to water security, sequencing investments along a pathway that can most cost-effectively and equitably reduce risk. Benefits of water security may not fully materialize until some way along the pathway when systems are nearing completion. Unwise choices can lock in unsustainable pathways, storing up future costs, for example, of environmental restoration.

Investment in hydraulic infrastructure is not consistently productive. Investments may be wasteful and inefficient, and perhaps socially and ecologically harmful, causing political disruption and undermining the catchment's capacity to deliver ecosystem services (*10*). A transformation in investment appraisal is therefore required, focused on risks, trade-offs, and uncertainties associated with alternative investment pathways. There are promising cases of analysis of costs and benefits of water resources management in a changing climate [e.g., in the Great Lakes (*11*) and the Dutch Delta Programme] and of long-term planning for water security in a rapidly urbanizing world (e.g., in Singapore). Even in these advanced-economy settings, the analysis of risks, exploration of uncertainties, and development of long-term investment plans have generally not been integrated in the way that we believe water security requires.

In practice, this requires (i) accounting for what is known about variability (from the observed record and model evidence) and taking proportionate risk-based decisions (*12*), (ii) extensive sensitivity testing of residual uncertainties (known and unknown) to identify key vulnerabilities and select robust options, and (iii) promotion of adaptive approaches and system resilience that can cope with unexpected change (*13*).

There is increasing capability for modeling runoff, water resources, and extreme events, but there has been disinvestment in observation systems that are essential for validation of simulations and to provide evidence for risk managers on the ground (*6*). Embracing nonstationarity requires more observations over space and time, not fewer, exploiting the possibilities of new sensors and data sources—from crowd-sourcing to Earth observation.

Understanding the evolution of risk also means tracking and predicting processes of demographic, economic, social, institutional, and environmental change. Global socioeconomic data sets and scenarios are an exciting advance but provide a limited picture of vulnerability and exposure, often at coarse resolution. Records of impacts of risks rely heavily on reported events, which provide an incomplete picture. Scarcest of all are the data to quantify the effectiveness of investments in institutions and infrastructure to reduce risk. We know that successful investments are path dependent, i.e., that context matters. But we do not know, for different basins and development paths, what are the critical balance and sequencing of investments in institutions, infrastructure, and information.

[1]*University of Oxford, Oxford OX1 3QY UK.* [2]*Department of Political Science and Walter G. Booth School of Engineering Practice, McMaster University, Hamilton, Ontario L8S 0A3, Canada.* [3]*Environment Agency, Bristol BS1 5AH, UK.* [4]*Department of Civil and Environmental Engineering, University of Massachusetts, Amherst, MA 01003, USA.* [5]*World Bank, Washington, DC 20433, USA. E-mail: jim.hall@eci.ox.ac.uk*

SUPPLEMENTARY MATERIALS

www.sciencemag.org/content/346/6208/429/suppl/DC1

REFERENCES AND NOTES

1. D. Grey *et al.*, *Philos. Trans. R. Soc. London* **371**, 1471 (2013).
2. C. Brown, U. Lall, *Nat. Resour. Forum* **30**, 306 (2006).
3. World Bank, *Ethiopia: Managing Water Resources to Maximize Sustainable Growth* (Agricultural and Rural Development Department, World Bank, Washington, DC, 2006).
4. P. H. Gleick, *Weather Clim. Soc.* **6**, 331 (2014).
5. Munich Re, *Severe Weather in Asia: Perils, Risks, Insurance* (Munich Re, Munich, 2013).
6. C. Lorenz, H. Kunstmann, *J. Hydrometeorol.* **13**, 1397 (2012).
7. J. Briscoe, R. P. S. Malik, *India's Water Economy. Bracing for a Turbulent Future* (Oxford Univ. Press, New Delhi, 2006).
8. IPCC, *Managing the Risks of Extreme Events and Disasters to Advance Climate Change Adaptation: A Special Report of Working Groups I and II of the Intergovernmental Panel on Climate Change* (Cambridge Univ. Press, Cambridge, 2012).
9. R. Q. Grafton *et al.*, *Nat. Clim. Change* **3**, 315 (2012).
10. C. J. Vörösmarty *et al.*, *Nature* **467**, 555 (2010).
11. P. Moody, C. Brown, *Water Resour. Res.* **48**, W10524 (2012).
12. J. W. Hall, S. Brown, R. J. Nicholls, N. F. Pidgeon, R. T. Watson, *Nat. Clim. Change* **2**, 833 (2012).
13. M. A. Janssen, J. M. Anderies, E. Ostrom, *Soc. Nat. Resour.* **20**, 307 (2007).
14. Flooding of Rojana Industrial Park, Ayutthaya, Thailand, October 2011, U.S. Marine Corps photo by Cpl. Robert J. Maurer—Defense Video and Imagery Distribution System: III Marine Expeditionary Force/Marine Corps Installation Pacific.

ACKNOWLEDGMENTS

The analysis described in this article forms part of the Global Water Partnership/Organisation for Economic Cooperation and Development global dialogue on Water Security and Sustainable Growth and the Oxford Martin Programme on Resource Stewardship.

10.1126/science.1257890

Published by AAAS

BOOKS *et al.*

HISTORY OF MEDICINE

The rise and fall of the nation's doctor

By **Jonathan M. Samet**

In lectures to medical and public health professionals, I often ask audiences if they can identify the current U.S. surgeon general. Typically, few know the answer (the current acting surgeon general is Rear Admiral Boris Lushniak). If the surgeon general is the trusted voice on health—the "nation's doctor"—how can he be unknown to a room full of physicians and other medical professionals?

PHOTO: FEVERPITCHED/ISTOCKPHOTO.COM

Journalist Mike Stobbe provides answers in *Surgeon General's Warning*, which describes the rise and fall of this presidentially appointed official over the past century and a half. He traces the origins of the office and its continually changing duties and describes the men and women who have held the office. The book is organized into four eras: *Rise*, *1871–1948*; *Decline*, *1949–1980*; *Struggle*, *1981–2001*; and *Plummet, 2002 to Present*, which weave together stories of personality, power, and politics.

Throughout the history of the office, power and politics have been closely linked. Early surgeons general sought to enlarge their reach, but ultimately, politics shifted the authority for public health elsewhere within the growing federal health bureaucracy. Today, the surgeon general has some responsibilities for the Commissioned Corps, a group of health professionals within the Public Health Service, but no others, and the office has no direct budget. Politics continue nonetheless. The current nominee for the position of surgeon general, Vivek Murthy, is a young physician who has already made a name for himself on the political scene as the founder of Doctors for Obama, now Doctors for America, a nonprofit that has advocated in support of both the president and the Affordable Care Act. He stands to be the youngest physician to be appointed to the role, but final confirmation hearings have been delayed following comments he made concerning guns as a public health issue (he thinks they are).

Of the 18 surgeons general, many were colorful personalities, as nicely captured by Stobbe. Some readers will remember surgeon general Everett Koop, appointed by President Reagan, who unexpectedly became a vigorous public health advocate and spokesperson to the nation after being appointed largely because of his views against abortion. He is still regarded as a model for his credibility, communication skills, and use of the "bully pulpit"—a role not yet stripped away—while he held the office. Antonia Novello, appointed by George H. W. Bush, was the first woman to hold the office of surgeon general. A controversial figure while in office, she was later indicted on charges related to abuses of her position as commissioner of health for the State of New York. Readers may also remember Joycelyn Elders, appointed by President Clinton and dismissed within a year for her frank discussion of masturbation. Surgeon general Richard Carmona, appointed by George W. Bush, was a former medic and Green Beret with a colorful history as a feisty trauma surgeon and leader of the Pima County SWAT team. Since leaving, he has unsuccessfully run for the Senate and joined the board of a company that manufactures electronic cigarettes.

Stobbe gives equal weight to the early surgeons general as well, including John Woodworth, the first to hold the position, which was then known as the supervising surgeon of the Marine Hospital Service; John Hamilton, who created the Commissioned Corps, which still operates today; and Walter Wyman, under whose leadership the position saw a substantial expansion in responsibilities. He devotes an entire chapter to Thomas Parran, who held office from 1936 to 1948 and campaigned vigorously against sexually transmitted diseases. While he was involved with the establishment of the World Health Organization, Parran's legacy was tarnished by his role in the Tuskegee Syphilis Study and another set of experiments in Guatemala in which nearly 1300 soldiers, prisoners, and mental health patients were deliberately exposed to syphilis and other sexually transmitted diseases without their consent.

The reviewer is in the Department of Preventive Medicine, Keck School of Medicine of USC, and the USC Institute for Global Health, University of Southern California, Los Angeles, CA 90089-9239, USA. E-mail: jsamet@med.usc.edu

Surgeon General's Warning: How Politics Crippled the Nation's Doctor

Mike Stobbe
University of California Press, 2014. 393 pp.

Since 1964, the surgeon general has been tightly linked to tobacco control, having prepared a number of authoritative reports on smoking and health. The first report (1), released by Luther Terry in 1964, stands as a landmark model of systematic review, evidence synthesis, and causal inference, reaching the then momentous conclusion that smoking causes lung cancer. Subsequent reports on secondhand smoke and addiction (2, 3) have had wide policy effects.

Now, as Stobbe notes, the office is largely vestigial, gaining attention only with the release of a report. When this occurs, the surgeon general briefly holds a national stage and is granted the opportunity to communicate to the nation on public health issues. But otherwise, the bully pulpit has effectively been taken away from the office.

Although Stobbe tells the history of the office, he only partially details the public health context that is the backdrop. The historical sweep of the office spans from an era when a few infectious diseases dominated the public health sphere to today, where factors including chronic, noncommunicable diseases; antibiotic resistance; and the politicization of public health issues such as vaccination have significantly increased the breadth and complexity of this arena. Given the complicated nature of today's health challenges, does it really make sense to have one national voice on health? Stobbe thinks not and proposes eliminating the office altogether. Alternatively, I believe that the status of the office could be rebuilt and the bully pulpit restored. Only then might health professionals and the public once again know and trust the surgeon general.

REFERENCES

1. Public Health Service, *Smoking and Health: Report of the Advisory Committee to the Surgeon General* (Public Health Service, Washington, DC, 1964).
2. Office on Smoking and Health, *The Health Consequences of Involuntary Smoking: A Report of the Surgeon General* (Public Health Service, Washington, DC, 1986).
3. Office on Smoking and Health, *The Health Consequences of Smoking: Nicotine Addiction: A Report of the Surgeon General* (Public Health Service, Washington, DC, 1988).

10.1126/science.1260189

Downloaded from www.sciencemag.org on October 24, 2014

Published by AAAS

FILM

Science on the silver screen

By **Caroline Ash**

There is a renewed interest in raising the profile of science in the filmmaking industry but a relative lack of venues to showcase this type of material. Recognizing this, the organizers of the prestigious Jackson Hole Wildlife Film Festival have initiated the biannual Science Media Awards, held most recently in September 2014 in Boston. The goal of the festival is to recognize the best offerings in the range of internationally available science film–making. Of the films on show at this year's gathering—and, as a judge, I saw them all—some were exquisite and some distinctly under par, but a few stood out as exceptional.

Jabbed: Love, Fear and Vaccines (Genepool Productions) is one in the exceptional category. This film explores the science behind vaccinations and investigates the costs of opting out. What made the film stand out was how the producer, Sonya Pemberton, was able to earn the trust of families afflicted by both the consequences of vaccination and of infection. The cultivation of these relationships yielded extraordinary and honest insights into individual lives and decisions, as well as revealing the great public good that vaccines bring. For its courageous and balanced consideration of an emotionally charged topic, *Jabbed* was recognized as the Best Medical Sciences Program.

Another bold analysis of a common, but underappreciated, medical problem was presented by student filmmaker Ingrid Pfau in her debut production, *Seizing the Unrecorded*. Using sound, clever cinematography, and animation, she shows what it might feel like to experience seizures. Pfau, who herself suffers from epilepsy, uses her own experiences, as well as those of several others whom she meets during the course of her treatment, to show the debilitating range of symptoms suffered by individuals with this disease, from the physical to the emotional. Pfau was recognized as the Best Student and Emerging Filmmaker for this personal and moving film, completed as part of her thesis project at Montana State University.

A crowd favorite, and the ultimate winner of the Best of Festival award (1), the film *Particle Fever* (PF Productions, LLC, and Anthos Media, LLC) presents the story of the discovery of the Higgs boson—the so-called "God particle"—at CERN, the European Organization for Nuclear Research. Featuring a cast of charismatic scientists, a big question (does this fundamental particle really exist?), high emotion, near disaster (the equipment failed early on, halting experiments for more than a year), and crisp editing, this film hit all of the right notes.

Jackson Hole Science Media Awards
Boston, MA
17 to 19 September 2014
www.jhfestival.org

A short series of films called *Your Inner Fish* (Tangled Bank Studios and Windfall Films, for PBS) was recognized as the Best Limited Series. Featuring the anatomist Neil Shubin, the series uses fossils, genetics, and embryonic data to reveal clues about our ancient ancestors that are hidden in our bodies.

In *Miracles of Nature: Super-Bodies* (Terra Mater Factual Studios GmbH), Richard Hammond (of *Top Gear* fame) lends his characteristic enthusiasm to an exploration of extraordinary animal abilities that have inspired unlikely inventions—for example, a laser-based navigation technology inspired by the whiskers of the harbor seal. Throughout the program, Hammond demonstrates that he is willing to literally throw himself into grand-scale demonstrations of the principles being discussed. Gamely working with bizarre props in exotic locations, Hammond stole the award for Best Hosted or Presenter-led Program.

The winner of the Best Technological Sciences Program, *Zeppelin Terror Attack* (Windfall Films, Ltd., for NOVA/WGBH, Channel 4, and National Geographic Channel) tells the harrowing tale of the technological arms race that unfolded during World War I as Britain scrambled to neutralize the enormous German aircraft. Although the technology was historical, the science was clear and precisely presented. Besides, what's not to like about a man standing in a field with an airship balanced on his head?

Featuring a glittering cast of Hollywood heavyweights and top journalists, the Showtime documentary series *Years of Living Dangerously* (Roaring Fork Films) received a special consideration for its confrontational examination of the growing consequences of anthropogenic climate warming.

Many more films won many more awards, and many others were close contenders for accolades, but they cannot all be described here. The full list of winners can be found at www.jhfestival.org/science-media-awards.html.

The reviewer is on staff at Science *magazine, AAAS Science International, Cambridge CB2 1LQ, UK. E-mail: cash@science-int.co.uk*

REFERENCES

1. AAAS, the publisher of *Science*, sponsored the Best of Festival Award.

10.1126/science.1261999

PHOTOS: MARINARAZUMOVSKAYA; JACKSON HOLE SCIENCE MEDIA AWARDS

Downloaded from www.sciencemag.org on October 24, 2014

Published by AAAS

Edited by **Jennifer Sills**

Ebola: Mobility data

UNDERSTANDING HUMAN movement and mobility is important for characterizing, forecasting, and controlling the spatial and temporal spread of infectious diseases. Unfortunately, the current West African Ebola outbreak is taking place in a region where mobility has changed considerably in recent years. Efforts must be made to better understand these mobility patterns. For example, mobile phone call records provide insight into how people move within countries, particularly if they move from hotspots of disease. Analyses of Orange Telecom data have produced initial maps of movement in Senegal and Ivory Coast (*1*, *2*), and endeavors are under way to obtain similar data for Sierra Leone, Guinea, and Liberia.

Additional sources are needed to gain a more complete picture of mobility and infer patterns of disease spread. For example, information on land border crossings would elucidate regional movement. Genomic surveillance data can genetically link cases across time and space ("Genomic surveillance elucidates Ebola virus origin and transmission during the 2014 outbreak," S. K. Gire *et al.*, Reports, 12 September, p. 1369; published online 28 August). More complete data are needed on the routes taken by trucks and buses, which have been implicated in disease spread. Quantifying recurrent seasonal migration in response to climate, harvest cycles, or cultural events is important for anticipating fluctuations in transmission rates (*3*).

All these types of data can be used in dynamic transmission models to provide case projections, help focus resources and interventions, and assess the success of interventions. However, modeling efforts are limited in the absence of good mobility data. Existing data sources for West Africa include air transportation data, which have been used to model the local, regional, and global spread of Ebola (*4*) and newly updated world population data sets (*5*). However, newer census data are vital to underpin the mobility data. Keeping this information up to date while developing more comprehensive mobility data sets will greatly benefit intervention planning and resource allocation.

Such data should not necessarily lead to travel restrictions, such as flight route cancellations and border closures, which hamper relief efforts. Rather, the information should be used to create more valid models of transmission, which can then be used to plan and evaluate potential interventions. Better quantification of the impact of potential interventions will be critical in the coming weeks as the outbreak continues to grow.

M. Elizabeth Halloran,[1,2]* Alessandro Vespignani,[3] Nita Bharti,[4] Leora R. Feldstein,[1,5] K. A. Alexander,[6] Matthew Ferrari,[4] Jeffrey Shaman,[7] John M. Drake,[8] Travis Porco,[9] Joseph N. S. Eisenberg,[10] Sara Y. Del Valle,[11] Eric Lofgren,[12] Samuel V. Scarpino,[13] Marisa C. Eisenberg,[10] Daozhou Gao,[9] James M. Hyman,[14] Stephen Eubank,[12,15] Ira M. Longini Jr.[16]

[1]Fred Hutchinson Cancer Research Center, University of Washington, Seattle, WA 98109, USA. [2]Department of Biostatistics, University of Washington, Seattle, WA 98195, USA. [3]Department of Physics, Northeastern University, Boston, MA 02115, USA. [4]Department of Biology, Pennsylvania State University, University Park, PA 16802, USA. [5]Department of Epidemiology, University of Washington, Seattle, WA 98195, USA. [6]Department of Fish and Wildlife Conservation, Virginia Polytechnic Institute and State University, Blacksburg, VA 24061, USA. [7]Department of Environmental Health Sciences, Mailman School of Public Health, Columbia University, New York, NY 10032, USA. [8]Odum School of Ecology, University of Georgia, Athens, GA 30602, USA. [9]Francis I. Proctor Foundation, University of California, San Francisco, CA 94143, USA. [10]Department of Epidemiology, University of Michigan, Ann Arbor, MI 48109, USA. [11]Los Alamos National Laboratory, Los Alamos, NM 87545, USA. [12]Virginia Bioinformatics Institute, Virginia Polytechnic Institute and State University, Blacksburg, VA 24061, USA. [13]Santa Fe Institute, Santa Fe, NM 87501, USA. [14]Department of Mathematics, Tulane University, New Orleans, LA 70118, USA. [15]Department of Population Health Sciences, Virginia Polytechnic Institute and State University, Blacksburg, VA 24061, USA. 16Department of Biostatistics, University of Florida, Gainesville, FL 32611, USA.

*Corresponding author. E-mail: betz@u.washington.edu

Liberian health care workers collect the body of an Ebola victim.

PHOTO: EPA/AHMED JALLANZO

REFERENCES

1. Flowminder.org (www.flowminder.org).
2. A. Wesolowski *et al.*, *PLOS Curr. Outbreaks* 10.1371/currents.outbreaks.0177e7fcf52217b8b634376e2f3efc5e (2014).
3. N. Bharti *et al.*, *Science* **334**, 1424 (2011).
4. M. F. C. Gomes *et al.*, *PLOS Curr. Outbreaks* 10.1371/currents.outbreaks.cd818f63d40e24aef769dda7df9e0da5 (2014).
5. WorldPop, Ebola (www.worldpop.org.uk/ebola).

ACKNOWLEDGMENTS

The authors of this letter are all in the MIDAS Network supported by the National Institute of General Medical Sciences of the National Institutes of Health.

Ebola: Public-private partnerships

ACCORDING TO THE World Health Organization, the current Ebola epidemic is unlikely to be controlled in the coming months (*1*). With the exception of the compassionate use of unregistered compounds (*2*), no specific medical interventions, including the use of antiviral drugs, antibodies, or vaccines, are available. Some candidate compounds and vaccines have entered into limited clinical trials for safety and immunogenicity in healthy individuals. Most of these trials have been carried out by governmental organizations, such as the National Institute of Allergy and Infectious Diseases (NIAID), or by small or medium-size biotechnology companies with public funding. Private-sector investment has been very limited because past filovirus outbreaks were largely self-limiting and therefore believed to provide insufficient financial return on investment. We argue that this is a misconception of the very nature of emerging viruses.

Effective medical intervention strategies against the Ebola and other emerging viruses should address the following needs: local or regional antiviral treatment or vaccination of a limited number of individuals, including health care workers, while prepandemic conditions continue to be observed; stockpiling of antiviral treatments or vaccines to address the potential threat of a large-scale epidemic or pandemic; and antiviral treatments or vaccines for travelers and humanitarian volunteers. These needs can be addressed

Downloaded from www.sciencemag.org on October 24, 2014

Published by AAAS

by the private sector in the context of public-private partnerships and fast-track regulatory procedures.

Public-private partnerships include a range of Innovative Medicines Initiative projects in Europe and programs of the Defense Advanced Research Projects Agency and National Institutes of Health in the United States. For example, a public-private partnership has been formed between the NIAID and the pharmaceutical company GlaxoSmithKline for the accelerated clinical trial of a vaccine candidate against the Ebola virus. Meanwhile, regulatory agencies, including the European Medicines Agency and the U.S. Food and Drug Administration, are dedicated to implementing fast-track regulatory procedures and adaptive licencing programs (*3*). Rethinking the mechanisms to involve the private sector in developing antiviral compounds and vaccines before the onset of an emerging epidemic would not only benefit the pharmaceutical industry but also society at large.

L. A. Reperant,[1,2] L. H. M. van de Burgwal,[3] E. Claassen,[1,3] A. D. M. E. Osterhaus[1,2]*

[1]Artemis One Health Research Foundation, 3584 CL Utrecht, Netherlands. [2]Department of Viroscience, Erasmus MC, 3000 CA Rotterdam, Netherlands. [3]Athena Institute, Vrije Universiteit Amsterdam, 1081 HV Amsterdam, Netherlands.

*Corresponding author. E-mail: a.osterhaus@erasmusmc.nl

REFERENCES

1. WHO, "Barriers to rapid containment of the Ebola outbreak" (11 August 2014).
2. WHO, "Ethical considerations for use of unregistered interventions for Ebola virus disease (EVD)" (12 August 2014).
3. Tekmira Pharmaceuticals Corportation, "FDA modifies Tekmira's TKM-Ebola clinical hold to partial hold" (7 August 2014).

Ebola: Social research overlooked

INTENSIVE RESEARCH ON potential therapies and vaccine candidates to control Ebola ("Ebola vaccines racing forward at record pace," J. Cohen, In Depth, 12 September, p. 1228) should not overlook the urgent need for instructions on how to implement curative strategies in non-Western settings. Recurrent incidents targeting health care providers and counterproductive behaviors leading to preventable infections clearly demonstrate that control of such an outbreak cannot be effective without the local population's cooperation.

Culturally tailored procedures should be elaborated and based on the expertise of medical anthropologists. We must prioritize research on such strategies to enrich the few resources already available on the subject (*1*). We need more data on the best ways to incorporate local beliefs and practices into patient care and response efforts, limit the mistrust regarding experimental vaccines and therapies in affected communities, and ease the informed consent collecting process.

Gilles Guerrier

Hôtel-Dieu and Cochin Hospitals, Assistance Publique des Hôpitaux de Paris (AP-HP), Paris Descartes University, 75679, Paris, France. E-mail: guerriergilles@gmail.com

REFERENCE

1. B. S. Hewlett, A. Epelboin, B. L. Hewlett, P. Formenty, *Bull. Soc. Pathol. Exot.* **98,** 230 (2005).

TECHNICAL COMMENT ABSTRACTS

Comment on "A Jurassic ornithischian dinosaur from Siberia with both feathers and scales"

Theagarten Lingham-Soliar

Godefroit *et al.* (Reports, 25 July 2014, p. 451) reported scales and feathers, including "basal plates," in an ornithischian dinosaur. Their arguments against the filaments being collagen fibers are not supported because of a fundamental misinterpretation of such structures and underestimation of their size. The parsimonious explanation is that the filaments are support fibers in association with badly degraded scales and that they do not represent early feather stages.

Full text at http://dx.doi.org/10.1126/science.1259983

Response to Comment on "A Jurassic ornithischian dinosaur from Siberia with both feathers and scales"

Pascal Godefroit, Sofia M. Sinitsa, Danielle Dhouailly, Yuri L. Bolotsky, Alexander V. Sizov, Maria E. McNamara, Michael J. Benton, Paul Spagna

Lingham-Soliar questions our interpretation of integumentary structures in the Middle-Late Jurassic ornithischian dinosaur *Kulindadromeus* as feather-like appendages and alternatively proposes that the compound structures observed around the humerus and femur of *Kulindadromeus* are support fibers associated with badly degraded scales. We consider this hypothesis highly unlikely because of the taphonomy and morphology of the preserved structures.

Full text at http://dx.doi.org/10.1126/science.1260146

Published by AAAS

the dense packing above the β face of the corrin ring (fig. S4A). The same steric constraints would disable an initial nucleophilic attack of Co^{I} on PCE. Instead, the short substrate-cofactor distances would allow the second electron transfer to occur either directly from the proximal [4Fe-4S] cluster or via the Co ion (Fig. 4). The strictly conserved Tyr^{246} is pointing with its phenolic hydroxyl group toward C1 and could donate the required proton to neutralize the carbanion (*20*). Deprotonation of Tyr^{246} could be stabilized by the neighboring positive charge of Arg^{305}. Equally, a role of Tyr^{246} in a radical route (*18*) cannot be excluded.

REFERENCES AND NOTES

1. C. Holliger, G. Wohlfarth, G. Diekert, *FEMS Microbiol. Rev.* **22**, 383–398 (1998).
2. B. Kräutler *et al.*, *Helv. Chim. Acta* **86**, 3698–3716 (2003).
3. L. A. Hug *et al.*, *Philos. Trans. R. Soc. London Ser. B* **368**, 20120322 (2013).
4. A. Mac Nelly, M. Kai, A. Svatoš, G. Diekert, T. Schubert, *Appl. Environ. Microbiol.* **80**, 4313–4322 (2014).
5. A. Neumann, G. Wohlfarth, G. Diekert, *J. Biol. Chem.* **271**, 16515–16519 (1996).
6. H. Scholz-Muramatsu, A. Neumann, M. Messmer, E. Moore, G. Diekert, *Arch. Microbiol.* **163**, 48–56 (1995).
7. Materials and methods are available on *Science* Online
8. T. Goris *et al.*, *Environ. Microbiol.* 10.1111/1462-2920.12589 (2014).
9. E. Miller, G. Wohlfarth, G. Diekert, *Arch. Microbiol.* **166**, 379–387 (1996).
10. L. Ye, A. Schilhabel, S. Bartram, W. Boland, G. Diekert, *Environ. Microbiol.* **12**, 501–509 (2010).
11. C. L. Drennan, S. Huang, J. T. Drummond, R. G. Matthews, M. L. Ludwig, *Science* **266**, 1669–1674 (1994).
12. F. Mancia *et al.*, *Structure* **4**, 339–350 (1996).
13. J. Kim, C. Gherasim, R. Banerjee, *Proc. Natl. Acad. Sci. U.S.A.* **105**, 14551–14554 (2008).
14. D. S. Froese *et al.*, *Biochemistry* **51**, 5083–5090 (2012).
15. H. B. Gray, J. R. Winkler, *Proc. Natl. Acad. Sci. U.S.A.* **102**, 3534–3539 (2005).
16. T. Svetlitchnaia, V. Svetlitchnyi, O. Meyer, H. Dobbek, *Proc. Natl. Acad. Sci. U.S.A.* **103**, 14331–14336 (2006).
17. M. John, R. P. H. Schmitz, M. Westermann, W. Richter, G. Diekert, *Arch. Microbiol.* **186**, 99–106 (2006).
18. J. Shey, W. A. van der Donk, *J. Am. Chem. Soc.* **122**, 12403–12404 (2000).
19. R. P. H. Schmitz *et al.*, *Environ. Sci. Technol.* **41**, 7370–7375 (2007).
20. G. Glod, W. Angst, C. Holliger, R. P. Schwarzenbach, *Environ. Sci. Technol.* **31**, 253–260 (1997).
21. W. Schumacher, C. Holliger, A. J. Zehnder, W. R. Hagen, *FEBS Lett.* **409**, 421–425 (1997).
22. K. M. McCauley *et al.*, *J. Am. Chem. Soc.* **127**, 1126–1136 (2005).

ACKNOWLEDGMENTS

H.D. acknowledges support by the Cluster of Excellence "Unifying Concepts in Catalysis (UniCat)." G.D. and T.S. were supported by the Deutsche Forschungsgemeinschaft (DFG) (Research Unit FOR 1530). M.B. was funded by the DFG through grant SFB 1078-A5. We are grateful for the funding of C.K. by the Ernst Abbe Foundation; in addition, we thank the staff at the Helmholtz-Zentrum Berlin (HZB) MX beamlines and DESY PETRA III beamline P11 for their assistance. We acknowledge access to beamlines of the BESSY II storage ring (Berlin, Germany) via the Joint Berlin MX-Laboratory. The authors thank O. Einsle for critical reading of the manuscript. Structure factors and models have been deposited in the Protein Data Bank under accession numbers 4UQU (empty), 4UR0 (TCE bound), 4UR1 (*cis*-DBE bound), 4UR2 (iodide bound), and 4UR3 ($P2_1$ crystal form).

SUPPLEMENTARY MATERIALS

www.sciencemag.org/content/346/6208/455/suppl/DC1
Materials and Methods
Figs. S1 to S6
Table S1
References (*23*–*35*)

30 June 2014; accepted 18 September 2014
Published online 2 October 2014;
10.1126/science.1258118

WORKING MEMORY

Medial prefrontal activity during delay period contributes to learning of a working memory task

Ding Liu,[1,2]* Xiaowei Gu,[1,2]* Jia Zhu,[1,2]* Xiaoxing Zhang,[1] Zhe Han,[1,2] Wenjun Yan,[1,2] Qi Cheng,[1,2] Jiang Hao,[1]† Hongmei Fan,[1] Ruiqing Hou,[1] Zhaoqin Chen,[1] Yulei Chen,[1] Chengyu T. Li[1]‡

Cognitive processes require working memory (WM) that involves a brief period of memory retention known as the delay period. Elevated delay-period activity in the medial prefrontal cortex (mPFC) has been observed, but its functional role in WM tasks remains unclear. We optogenetically suppressed or enhanced activity of pyramidal neurons in mouse mPFC during the delay period. Behavioral performance was impaired during the learning phase but not after the mice were well trained. Delay-period mPFC activity appeared to be more important in memory retention than in inhibitory control, decision-making, or motor selection. Furthermore, endogenous delay-period mPFC activity showed more prominent modulation that correlated with memory retention and behavioral performance. Thus, properly regulated mPFC delay-period activity is critical for information retention during learning of a WM task.

Working memory (WM) is essential for cognition by allowing active retention of behaviorally relevant information over a short duration known as the delay period (*1*–*3*). Previous studies have shown that the prefrontal cortex (PFC) is crucial for WM, because perturbation of PFC activity impaired WM (*3*) and WM-related activity was observed during the delay period in neurons of dorsal-lateral PFC (DL-PFC) in primates and medial PFC (mPFC) in rodents (*3*–*10*). Nevertheless, the functional role of PFC delay-period activity in WM remains unclear. Memory retention and attentional control are leading candidates (*2*, *3*, *11*). However, PFC is also critical for other brain functions (*3*, *12*, *13*) and has been suggested to be important for inhibitory control (*14*), decision-making (*15*), or motor selection (*16*). These roles cannot be distinguished by a delayed-response task, in which decision-making precedes the delay period (*3*, *12*). In addition, traditional methods for perturbing neural activity (*3*), including transcranial magnetic stimulation (*17*) and electrical stimulation (*18*), do not provide the temporal resolution and cell-type specificity required for delineating the functional role of PFC delay-period activity in WM. We addressed these issues by using a WM task with a delay period designed to temporally separate memory retention from other functions (*5*, *6*, *19*, *20*) and optogenetic approaches (*21*) to bidirectionally manipulate mPFC activity of excitatory and inhibitory neurons during the delay period.

Head-fixed mice were trained to perform an olfactory delayed nonmatch to sample (DNMS) task (Fig. 1, A and B; fig. S1; and movie S1), a modified version of the behavioral paradigms previously used in rats (*19*, *20*). For each trial, an olfactory stimulus (ethyl acetate, EA, or 2-pentanone, 2P) was presented as the sample, followed by a delay period (4 to 5 s) and then a testing olfactory stimulus, either matched or nonmatched to the sample. Water-restricted mice were rewarded with water if they licked within a response time window in the nonmatch but not match trials (Fig. 1B and fig. S2). During the delay period, mice need to retain the information associated with the odor sample. The performance correct rate (referred to hereafter as performance), correct rejection rate, discriminability (d'), and lick efficiency steadily increased throughout the training, but there was a ceiling effect for the hit rate (Fig. 1, C and D, and fig. S3). The potential involvement of visual, auditory, or somatosensory cues was excluded (fig. S4A). The performance decreased with increasing duration of the delay period (fig. S4B), a typical hallmark of WM paradigms (*1*, *3*). For a genuine WM task, subjects should be able to perform beyond two cues (*19*, *20*), which was indeed observed (fig. S4C). We next expressed hM4Di, a designer receptor exclusively activated by designer drug (DREADD) (*22*), in mPFC with adeno-associated virus (AAV). Suppression of neural activity (fig. S5) by intraperitoneal injection of clozapine-N-oxide (CNO) significantly impaired the performance of the mice during the learning phase (days 1 to 5, Fig. 1E; statistics shown in table S1).

It is essential that mice were using WM instead of residual odor during the delay period to perform the task. Photoionization detector (PID)

[1]Institute of Neuroscience and Key Laboratory of Primate Neurobiology, Shanghai Institutes for Biological Sciences, Chinese Academy of Sciences, Shanghai 200031, China. [2]University of Chinese Academy of Sciences, Beijing 100049, China.
*These authors contributed equally to this work. †Present address: Friedrich Miescher Institute for Biomedical Research, Maulbeerstrasse 66, 4058 Basel, Switzerland. ‡Corresponding author.
E-mail: tonylicy@ion.ac.cn

measurements were used to ensure minimal residual odor in the construction of the olfactometry system (fig. S6A). In addition, a behavioral control experiment (nonmatch to long duration sample, NMLS) was performed to further exclude possible involvement of residual odor undetectable by PID. In this task, odor samples were provided during a period corresponding to the delay period in the standard DNMS task to simulate potential delay-period residual odor (fig. S6B). The sample concentration for the chance level performance of the NMLS task was well above the PID-detected residual level during the delay period in the standard DNMS task (fig. S6C).

We then suppressed the delay-period activity of pyramidal neurons with optogenetic methods. It was first achieved through activating γ-aminobutyric acid–releasing (GABAergic) inhibitory neurons expressed with channel rhodopsin (ChR2). We stereotactically and bilaterally injected AAV carrying a Cre-inducible gene encoding ChR2 [pAAV-Ef1a-DIO-ChR2(H134R)-mCherry (*21*); referred hereafter as DIO-ChR2] or mCherry (pAAV-Ef1a-DIO-mCherry, hereafter DIO-mCherry) into mPFC of vesicular GABA transporter (VGAT)–Cre transgenic mice (*23*). Expression and activity-suppression efficiency were verified by immunostaining and op-tetrode recording (fig. S7 and Fig. 2B). Optogenetic manipulation could influence neurons within 1.4 mm from an optical fiber (fig. S8) and affect all subregions of mPFC (fig. S7). Behavioral and optogenetic experiments were performed in a blind design. Step laser illumination (473 nm, 2 mW) was applied in the last 4 s of the 5-s delay period in all trials throughout the learning (Fig. 2A). Suppressing the delay-period activity of mPFC pyramidal neurons in the learning phase impaired behavioral performance, as manifested by the deficits in performance, correct rejection rate, *d'*, lick efficiency, number of trials to criterion (performance above 80% for consecutive 40 trials), and consecutive false choice (Fig. 2, A and B; figs. S9 and S10; and table S2), but not hit rate (Fig. 2B). Optogenetic suppression of mPFC delay-period activity failed to impair WM performance in well-trained mice (based on the averaged results from day 8, Fig. 2, A and B, and table S2), although session-based analysis revealed a small degree of relearning at the initial sessions, which was significantly influenced by suppressing delay-period activity (fig. S11). The results were consistent with the suggested role of PFC in performing novel and attention-demanding, rather than routine and well-rehearsed, tasks (*2*, *3*, *12*, *24*).

To directly suppress activity of mPFC pyramidal neurons, we expressed halo-rhodopsin (NpHR) (*21*) or enhanced yellow fluorescent protein (eYFP) in pyramidal neurons by injecting AAV-CaMKIIα-eNpHR3.0-eYFP or AAV-CaMKIIα-eYFP into mPFC. The expression and functionality of NpHR were verified by immunostaining and op-tetrode recording (fig. S12 and Fig. 2D). Direct suppression of delay-period activity of pyramidal neurons in mPFC by step laser illumination (532 nm, 10 mW) impaired WM performance during the learning phase but not after the mice were well trained (Fig. 2, C and D; figs. S13 and S14; and table S3).

To examine whether optogenetic manipulation influenced WM on a trial-by-trial basis, we suppressed mPFC delay-period activity in an interleaved laser on/off design (Fig. 2E). Performance was indeed impaired in laser-on trials (Fig. 2, E and F; fig. S15; and table S4). To examine the regional specificity of the behavioral effects of optogenetic manipulation, we suppressed delay-period activity in somatosensory cortex (S1) and found no impairment in WM performance (fig. S16).

To further determine whether elevating activity of mPFC pyramidal neurons during the delay period could affect the learning of a WM task, we expressed AAV-CaMKIIα-ChR2-mCherry or AAV-CaMKIIα-mCherry in mPFC of wild-type mice (Fig. 3A and fig. S17). We then applied step laser illumination (473 nm, 0.8 mW) throughout learning. When optogenetic activation was performed during the learning phase, CaMKIIα-ChR2 mice performed worse than the control group (Fig. 3A and table S5). Both hit and correct rejection rates were modulated (Fig. 3B). By contrast, optogenetic activation during the well-trained phase had no effect on the performance, although the correct rejection rate was significantly decreased. Similar results were obtained by enhancing mPFC

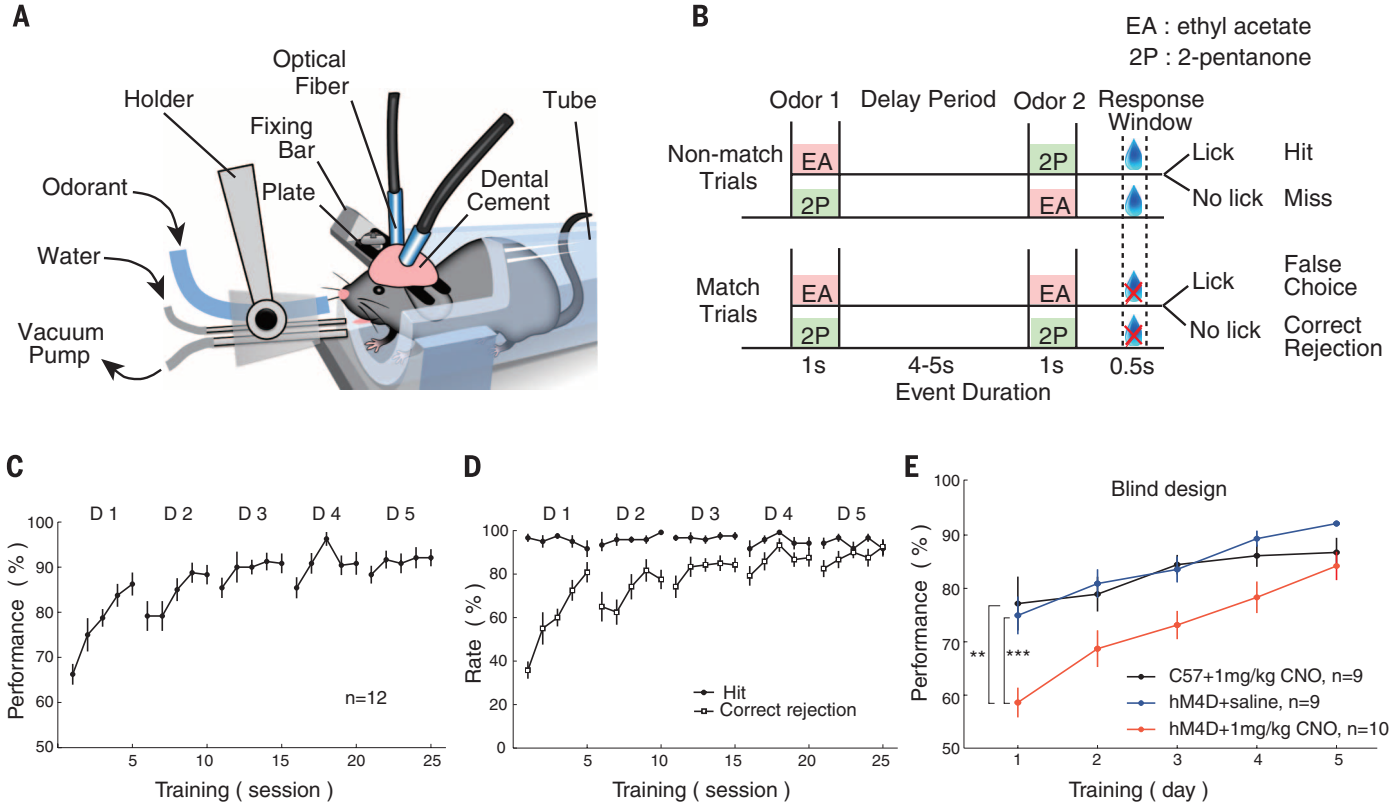

Fig. 1. WM paradigm. (**A** and **B**) Behavioral diagram. (**C**) Performance during learning. Five sessions per day, 20 trials per session. Error bars indicate SEM unless stated otherwise. (**D**) Hit rates and correct rejection rates in learning. (**E**) Performance in experiments of suppressing mPFC activity by hM4Di. $^{**}P$ = 0.003; $^{***}P < 0.001$; two-way analysis of variance with mixed design (Tw-ANOVA-md).

delay-period activity with laser illumination in an odor-sample specific manner (fig. S18). Thus, elevating mPFC activity during the delay period interfered with the learning of the WM task.

In further experiments, we suppressed mPFC activity through NpHR in the second odor-delivery period, during which decision-making behavior occurred. Behavioral performance was unaffected early in learning (days 1 and 2) but was impaired after day 3 (fig. S19). Therefore, the contribution of mPFC delay-period activity in learning of the WM task was temporally specific, a result distinct from but not contradictory to the previous findings of behavioral deficits in well-trained subjects using classic techniques to perturb mPFC activity (*3*, *15*).

To study the functional specificity of optogenetic manipulation, we used behavioral experiments of a nonmatch to sample task without the delay period (NMS-WD, Fig. 3C) and a go/no-go odor discrimination task (GNG, Fig. 3E). Both tasks required sensory encoding, inhibitory control, decision-making, and motor selection (fig. S20A) but not memory retention. In the NMS-WD task, laser illumination covered the entire period for odor perception, decision-making, and motor selection (Fig. 3C). In the GNG task with random intertrial intervals, laser illumination was applied after a trial-starting cue and before the decision-making behavior occurred (Fig. 3E),

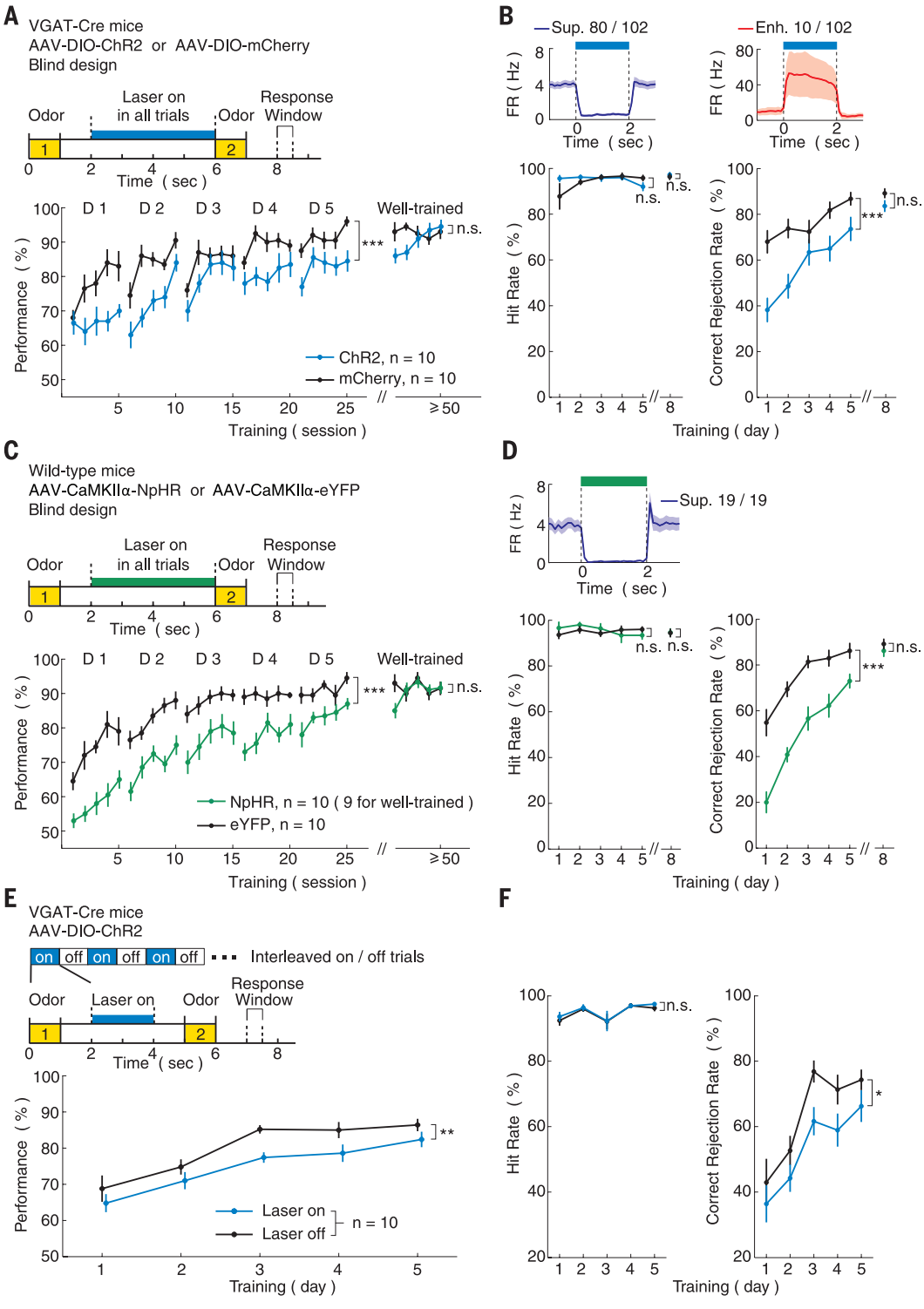

Fig. 2. Suppressing mPFC delay-period activity impaired performance in learning of the WM task. (**A** and **B**) Performance, hit rates, and correct rejection rates for experiments, in which activity of pyramidal neurons was suppressed by activating GABAergic neurons. Top in (A): paradigm information. Top in (B): activity-suppression efficiency revealed by awake op-tetrode recording in vivo. FR, firing rate. (**C** and **D**) As in (A) and (B) with NpHR in pyramidal neurons. (**E** and **F**) As in (A) and (B) with interleaved laser on/off design. *P = 0.016; **P = 0.003; ***P < 0.001; n.s., not significant; learning: Tw-ANOVA-md; well-trained: Mann-Whitney U test.

simulating the delay period in the DNMS task (fig. S20B). We found that behavioral performance was not affected by laser illumination in all trials, in either the NMS-WD (Fig. 3, C and D, and table S6) or GNG (Fig. 3, E and F, and table S7) task. In separate sets of experiments with an interleaved laser on/off design, the same results were obtained (figs. S21 and S22). Therefore, mPFC delay-period activity appeared to be more important in memory retention than sensory encoding, inhibitory control, decision-making, and motor selection.

To examine the neural correlates throughout learning the WM task, we recorded single-unit activity of mPFC by using custom-made tetrodes (Fig. 4, A to C, and figs. S23 and S24). By lowering recording electrodes each day, we recorded 564 neurons during the learning phase (days 1 to 5) from 15 mice and 95 neurons from seven well-trained (days 10 to 15) mice. Similar results were obtained from 636 neurons of nine mice without daily lowering of electrodes (figs. S25 to S28). The delay-period activity was more prominently modulated during the learning than the well-trained phase (Fig. 4D and fig. S29). The delay-period firing rates during the learning phase were significantly higher for neurons with enhanced delay-period activity and lower for suppressed neurons, as compared with those in the well-trained phase (Fig. 4E and table S8).

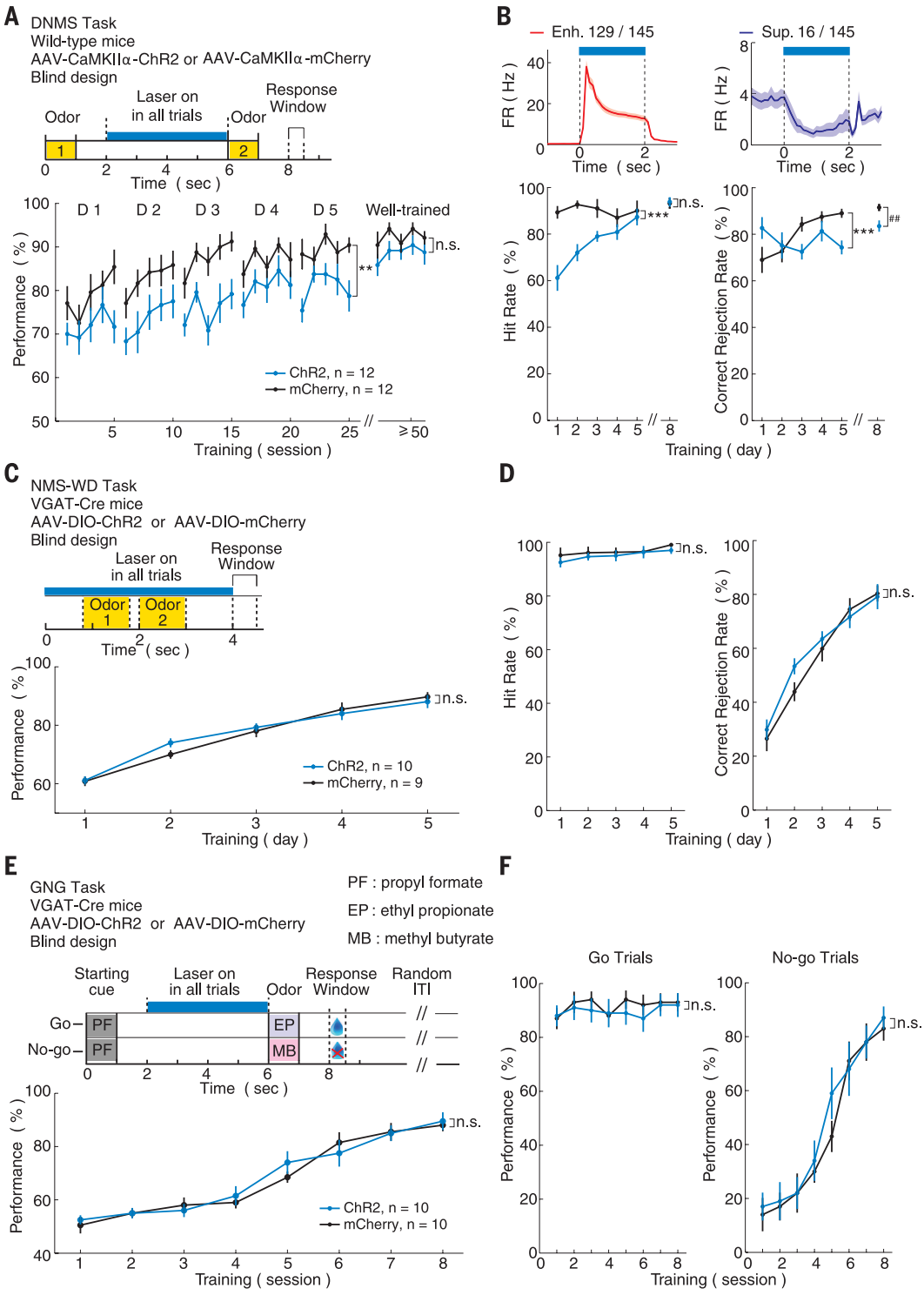

Fig. 3. Importance of properly regulated mPFC delay-period activity and its functional role in the WM task. (**A** and **B**) Performance, hit rates, and correct rejection rates in experiments with elevated mPFC activity during the delay period. (**C** and **D**) Paradigm and performance for NMS-WD experiments with suppressed mPFC activity. (**E** and **F**) As in (C) and (D) for the GNG task. $^{**}P = 0.002$; $^{***}P < 0.0001$; learning: Tw-ANOVA-md. $^{\#\#}P = 0.0048$; well-trained: Mann-Whitney U test.

To retain odor-related information, delay-period population activity should be different after distinct odor samples. We therefore visualized population activity by principal component analysis (PCA) (*25*). The first three PCs captured the majority of variance (72%). The trajectories during the delay period after two different odor samples were separated during the learning but not the well-trained phase (Fig. 4F, fig. S30, and movie S2), as quantified by the trajectory distance (Fig. 4G). The results remained robust by only using half of the neurons (fig. S31). We further analyzed the sensitivity of delay-period population trajectories to behavioral outcome and found that trajectories in correct trials were more separated than in error trials during the learning but not well-trained phase (fig. S32). In decoding analysis (*26*), delay-period activity

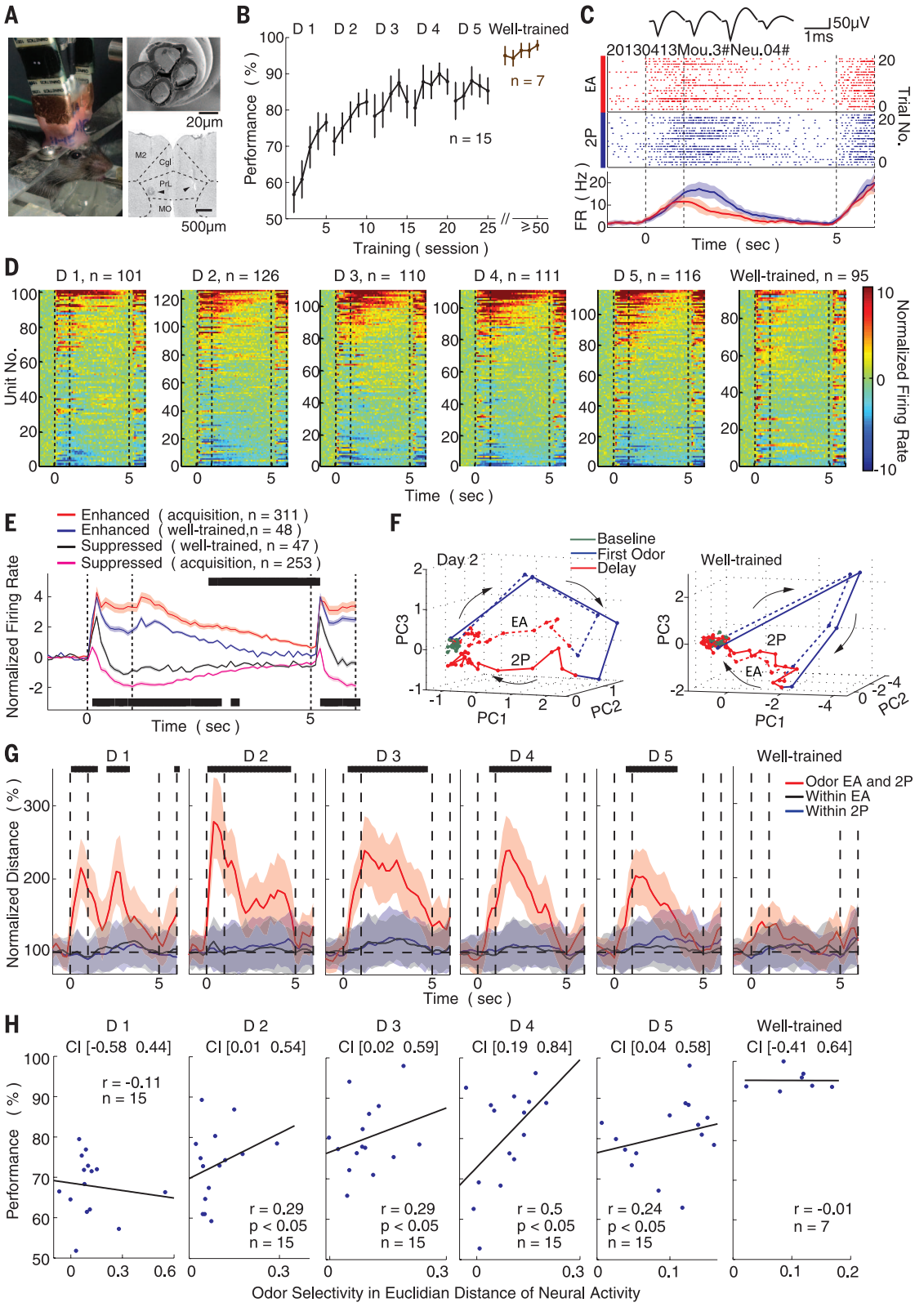

Fig. 4. Modulation of mPFC delay-period activity in learning the WM task. (**A**) Images of microdrive (left), tetrode (right top, electron microscopy), and recording sites (right bottom, indicated by arrowheads). M2, secondary motor area; Cg1, cingulate cortex, area 1; PrL, prelimbic cortex; MO, medial orbital cortex. (**B**) Performance for the recorded mice, 40 trials per session. (**C**) Spike-raster and peristimulus time histogram of an example neuron; trials sorted by odor samples. (Top) Spike waveforms. Shadows indicate SEM. (**D**) Modulation of population activity, which was normalized in *Z*-score and averaged across all trials for each neuron. Results from all the mice recorded with daily lowering of electrodes were presented in (D) to (H). (**E**) Averaged firing rates for neurons with enhanced and suppressed delay-period activity (bin of 100 ms). Black blocks indicate bins with enhanced delay-period activity and significant difference between learning and well-trained phases, $P < 0.05$, Mann-Whitney U test. Black blocks below indicate significant bins for neurons with decreased delay-period activity. Shadows, SEM. (**F**) PCA trajectories of population activity after different odor samples (bin of 200 ms). Arrows: time. (**G**) Distance in PCA trajectories. Shadows indicate 95% confidence interval (CI) from bootstrap of 100 times. (**H**) Correlations between behavioral performance and neuronal odor selectivity. Each dot represents averaged results from one mouse. Statistics: 95% CI from bootstrap of 100 times.

during the learning phase exhibited higher decoding power for odor samples than in the well-trained phase (fig. S33), which critically depended on the neurons with significant delay-period activity (fig. S34).

We then analyzed whether the delay-period odor selectivity of neurons is correlated with the behavioral performance of mice. The Euclidean distance between delay-period activity after different odor samples was calculated for a given neuron and then averaged for all neurons simultaneously recorded to represent neuronal selectivity for each mouse in one day. Although only 2 to 13 neurons (median of 8) were simultaneously recorded each day from a mouse, significant correlation between behavioral performance and neuronal selectivity was observed during the learning (days 2 to 5) but not well-trained phase (Fig. 4H and fig. S35).

The importance of mPFC delay-period activity in the learning phase of a WM task is consistent with its central role in flexible cognitive control in changing environments (*2*, *3*, *12*). However, the DL-PFC activity in primates is important in WM tasks after subjects are well trained (*3*, *12*). Because mPFC appeared earlier than DL-PFC during evolution (*12*), the functional difference between mPFC and DL-PFC suggests that memory retention in novel situations may represent an evolutionarily more primitive function. It is not clear which brain region in rodents is homologous or analogous to DL-PFC in primates (*3*, *12*), but delay-period activity in brain regions other than mPFC (*3*, *5*, *19*, *27–30*) could mediate WM in well-trained mice. Activity of mPFC in other periods during the behavioral task may underlie inhibitory control (*14*), decision-making (*15*), and motor selection (*16*). Nevertheless, the present finding underscores the notion that properly regulated delay-period activity of mPFC is critical for memory retention in attention-demanding WM tasks in novel situations.

REFERENCES AND NOTES

1. A. D. Baddeley, *Working Memory* (Oxford Univ. Press, Oxford, 1986).
2. E. K. Miller, J. D. Cohen, *Annu. Rev. Neurosci.* **24**, 167–202 (2001).
3. J. M. Fuster, *The Prefrontal Cortex* (Academic Press, London, ed. 4, 2008).
4. J. M. Fuster, G. E. Alexander, *Science* **173**, 652–654 (1971).
5. E. K. Miller, C. A. Erickson, R. Desimone, *J. Neurosci.* **16**, 5154–5167 (1996).
6. R. Romo, C. D. Brody, A. Hernández, L. Lemus, *Nature* **399**, 470–473 (1999).
7. E. H. Baeg *et al*., *Neuron* **40**, 177–188 (2003).
8. S. Fujisawa, A. Amarasingham, M. T. Harrison, G. Buzsáki, *Nat. Neurosci.* **11**, 823–833 (2008).
9. J. C. Erlich, M. Bialek, C. D. Brody, *Neuron* **72**, 330–343 (2011).
10. E. M. Meyers, X. L. Qi, C. Constantinidis, *Proc. Natl. Acad. Sci. U.S.A.* **109**, 4651–4656 (2012).
11. R. Desimone, *Proc. Natl. Acad. Sci. U.S.A.* **93**, 13494–13499 (1996).
12. R. E. Passingham, S. P. Wise, *The Neurobiology of the Prefrontal Cortex: Anatomy, Evolution, and the Origin of Insight* (Oxford Univ. Press, Oxford, ed. 1, 2012).
13. S. H. Wang, R. G. Morris, *Annu. Rev. Psychol.* **61**, 49–79, C1–C4 (2010).
14. R. Dias, J. P. Aggleton, *Eur. J. Neurosci.* **12**, 4457–4466 (2000).
15. D. R. Euston, A. J. Gruber, B. L. McNaughton, *Neuron* **76**, 1057–1070 (2012).
16. K. Matsumoto, W. Suzuki, K. Tanaka, *Science* **301**, 229–232 (2003).
17. E. A. Allen, B. N. Pasley, T. Duong, R. D. Freeman, *Science* **317**, 1918–1921 (2007).
18. S. Sobotka, M. D. Diltz, J. L. Ringo, *J. Neurophysiol.* **93**, 128–136 (2005).
19. T. Otto, H. Eichenbaum, *Hippocampus* **2**, 323–334 (1992).
20. X.-C. M. Lu, B. M. Slotnick, A. M. Silberberg, *Physiol. Behav.* **53**, 795–804 (1993).
21. L. Fenno, O. Yizhar, K. Deisseroth, *Annu. Rev. Neurosci.* **34**, 389–412 (2011).
22. B. N. Armbruster, X. Li, M. H. Pausch, S. Herlitze, B. L. Roth, *Proc. Natl. Acad. Sci. U.S.A.* **104**, 5163–5168 (2007).
23. H. T. Chao *et al*., *Nature* **468**, 263–269 (2010).
24. S. B. Ostlund, B. W. Balleine, *J. Neurosci.* **25**, 7763–7770 (2005).
25. M. Rabinovich, R. Huerta, G. Laurent, *Science* **321**, 48–50 (2008).
26. E. M. Meyers, D. J. Freedman, G. Kreiman, E. K. Miller, T. Poggio, *J. Neurophysiol.* **100**, 1407–1419 (2008).
27. M. Stopfer, G. Laurent, *Nature* **402**, 664–668 (1999).
28. C. D. Harvey, P. Coen, D. W. Tank, *Nature* **484**, 62–68 (2012).
29. Z. V. Guo *et al*., *Neuron* **81**, 179–194 (2014).
30. J. Yamamoto, J. Suh, D. Takeuchi, S. Tonegawa, *Cell* **157**, 845–857 (2014).

ACKNOWLEDGMENTS

We thank M. P. Stryker for communication on head-fixed mice preparation; Z. F. Mainen and N. Uchida for communication on behavioral design; G. Laurent for communication on population analysis; L. P. Wang for help in optogenetics; L. N. Lin for help in tetrode drive manufacturing; H. L. Hu for help in electrophysiological recordings; Y. Dan and J. F. Erlich for communication on spike sorting; H. Y. Zoghbi for VGAT-Cre mice; B. L. Roth for DREADD vectors; Z. L. Qiu, H. L. Hu, and X. Yu for help on AAV virus packaging and transgenic mice; A. K. Guo for help in PID experiments; Q. Hu for help in imaging experiments; Y. G. Sun for histochemistry experiments; Y. F. Li for help in drawing diagrams; and M. M. Poo and R. Desimone for critical comments on the manuscript. The work was supported by Chinese 973 Program (2011CBA00406), the State Key Laboratory of Neuroscience, and Chinese Academy of Sciences Hundreds of Talents Program (to C.T.L.). All the behavioral, optogenetic, electrophysiological, and histochemical data are archived in Institute of Neuroscience, Shanghai Institutes for Biological Sciences, Chinese Academy of Sciences.

SUPPLEMENTARY MATERIALS

www.sciencemag.org/content/346/6208/458/suppl/DC1
Materials and Methods
Figs. S1 to S35
Tables S1 to S8
References (*31–42*)
Movies S1 and S2

27 May 2014; accepted 16 September 2014
10.1126/science.1256573

EVOLUTIONARY BIOLOGY

Rapid evolution of a native species following invasion by a congener

Y. E. Stuart,[1]*†‡ T. S. Campbell,[2]* P. A. Hohenlohe,[3] R. G. Reynolds,[1,4] L. J. Revell,[4] J. B. Losos[1]

In recent years, biologists have increasingly recognized that evolutionary change can occur rapidly when natural selection is strong; thus, real-time studies of evolution can be used to test classic evolutionary hypotheses directly. One such hypothesis is that negative interactions between closely related species can drive phenotypic divergence. Such divergence is thought to be ubiquitous, though well-documented cases are surprisingly rare. On small islands in Florida, we found that the lizard *Anolis carolinensis* moved to higher perches following invasion by *Anolis sagrei* and, in response, adaptively evolved larger toepads after only 20 generations. These results illustrate that interspecific interactions between closely related species can drive evolutionary change on observable time scales.

In their classic paper, Brown and Wilson (*1*) proposed that mutually negative interactions between closely related species could lead to evolutionary divergence when those species co-occurred. In the six decades since, this idea has been debated vigorously, with support that has vacillated, depending on the latest set of theoretical treatments and comparative studies [reviewed in (*2–5*)]. However, tests of interaction-driven evolutionary divergence have been slow to capitalize on the growing recognition that evolutionary change can occur rapidly in response to strong divergent natural selection [but see (*6–9*)]; thus, evolutionary hypotheses about phenomena once thought to transpire on time scales too long for direct observation can be tested in real time while using replicated statistical designs.

An opportunity to study such real-time divergence between negatively interacting species has been provided by the recent invasion of the Cuban brown anole lizard, *Anolis sagrei*, into the southeastern United States, where *Anolis carolinensis* is the sole native anole. These species have potential to interact strongly [e.g., (*10*)], being very similar in habitat use and ecology (*11*). We investigated the eco-evolutionary consequences of this interaction on islands in Florida (*12*) using an *A. sagrei* introduction experiment, well-documented natural invasions by *A. sagrei*, genomic analyses of population structure, and a common garden experiment. This multifaceted approach can rule against several of the most

[1]Museum of Comparative Zoology and Department of Organismic and Evolutionary Biology, Harvard University, Cambridge, MA, USA. [2]Department of Biology, University of Tampa, Tampa, FL, USA. [3]Department of Biological Sciences and Institute for Bioinformatics and Evolutionary Studies, University of Idaho, Moscow, ID, USA. [4]Department of Biology, University of Massachusetts, Boston, MA, USA.
*These authors contributed equally to this work. **†Corresponding author. E-mail: yestuart@utexas.edu** ‡Present address: Department of Integrative Biology, University of Texas, Austin, TX, USA.

TECHNICAL COMMENT

DINOSAUR EVOLUTION

Comment on "A Jurassic ornithischian dinosaur from Siberia with both feathers and scales"

Theagarten Lingham-Soliar

Godefroit *et al*. (Reports, 25 July 2014, p. 451) reported scales and feathers, including "basal plates," in an ornithischian dinosaur. Their arguments against the filaments being collagen fibers are not supported because of a fundamental misinterpretation of such structures and underestimation of their size. The parsimonious explanation is that the filaments are support fibers in association with badly degraded scales and that they do not represent early feather stages.

Godefroit *et al.* (*1*) attempt to dismiss the hypothesis of collagen fibers versus that of feathers in the ornithischian dinosaur *Kulindadromeus* with three main lines of arguments, which necessitate a reply.

1) "First, integumentary collagen fibers typically occur in layered arrays of parallel, densely packed fibers where fibers in successive layers are oblique to one another" [supplementary materials (SM) for (*1*)]. They are not typical but form a highly specialized design architecture associated with special biomechanical functions—for example, enabling stiffness and mobility either of the whole body (*2*–*6*) or of organ systems such as arteries (*7*), rectal sheaths, and linea alba (*8*). In humans, as in many other vertebrates, the dermal fibers are randomly (here, nonopposing orientations) organized. Even in animals with this specialist design, numerous layers of fibers may have the same orientation in one location of the animal and an alternating crossed-fiber orientation in another, dependent on function. Furthermore, fiber angles are rarely consistent but may change from low angles to high depending on the tension required in different parts of the body (*4*, *8*). In fact, rather than consistent angles as alleged (*1*), in different zones in *Kulindadromeus* [figure 2, F and I, in (*1*)] varied filament angles are evident. As emphasized (*6*), the unique exposure of a crossed-fiber architecture in a 130-million-year-old *Psittacosaurus* fossil could only emanate "from freak combinations of circumstances."

2) "[I]ntegumentary collagen fibers are typically on the order of several microns in diameter; the structures we describe are at least two orders of magnitude larger" [SM for (*1*)]. The integumental structures identifiable at light microscopy level in dinosaurs and ichthyosaurs and many extant vertebrates are not just several microns thick and are collagen fiber bundles, not fibers. Although most experts in this field refer to the components of the cross-fiber architecture as fibers, it is clear to workers involved that they are fiber bundles [see Pabst's (*3*) table 2, "diameter of collagen fibres" in dolphin hypodermis range "208-469 μm" and white shark (*Carcharodon carcharias*) and ichthyosaur (*Stenopterygius*) dermis (*4*, *5*), up to 1000 μm]. However, anticipating that workers unfamiliar with histological research might misinterpret the vernacular term of fibers, I consequently clearly defined its use (*9*) and reiterated it in a study (*6*) the authors attest knowledge of: "Note that as with most studies in which dermal fibre architectures have been investigated [e.g. sharks and dolphins in Motta (1977) and Pabst (1996), respectively], reference to the term 'collagen fibre' is one of convenience because, strictly speaking, observations at the light microscopic level show fibre bundles (approx. 50–250 μm across) rather than fibres (approx. 4–20 μm across)." Hence, it is of concern that the authors misinterpret the size of the integumental structures that they imply familiarity with by "at least two orders of magnitude" [SM for (*1*)].

3) "[M]orphology of the compound and ribbon-like integumentary filaments (Fig. 3D-H) is unknown for integumentary collagen" [SM for (*1*)]. Generally, figures allegedly showing feather-like structures are low-resolution images of badly degraded sections, confirmed by the need for interpretive drawings on the alleged vital structures (figure 3, C, F, and I, and figure S9C), which are highly subjective. Beyond alleging what the ribbon-like filaments are not—i.e., collagen—the authors do not say what they are (besides unsupported speculation). Notwithstanding, they have not explained why they cannot be among a multitude of alternatives—e.g., ribbon-like structures occur as structural collagen in blood vessels (*7*), linea alba, and rectal sheaths (*8*) and in connective tissue, the most abundant collagenous material in vertebrates (Fig. 1F). They could be plant or inorganic material in the proximity of the dead animal or even the degraded remains of very thin (highly degradable) ribbon-like scales—e.g., found in the ventral regions (aiding distension)

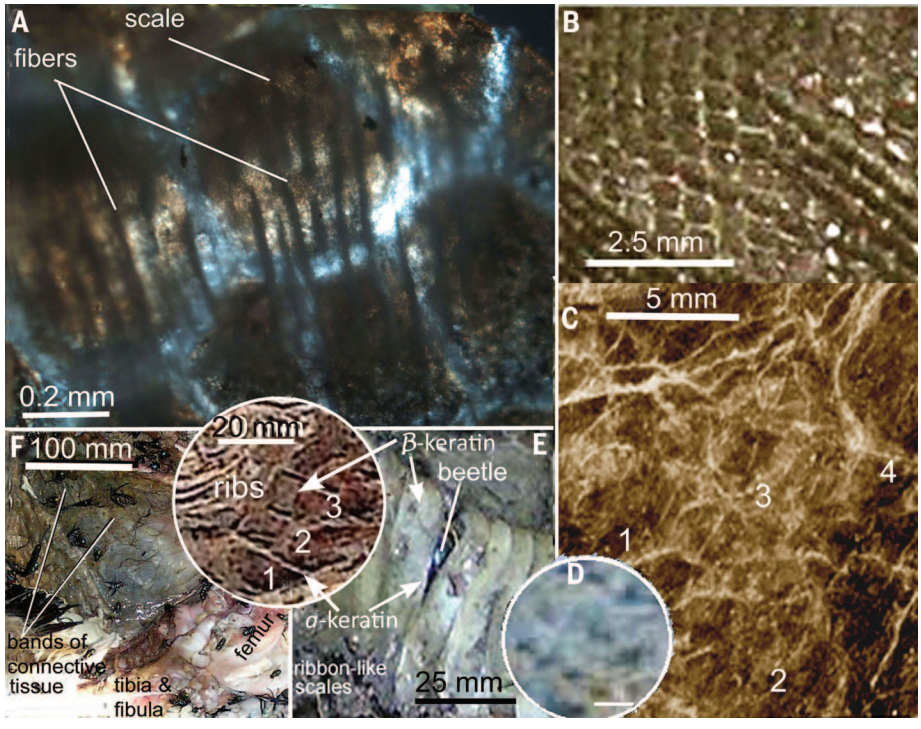

Fig. 1. Integument and decomposition. Integument: (**A** and **B**) Scales of Jesus lizard along skin flap (A), back-lit, showing underlying collagen fibers. (**C**) Severely eroded scales (ghosts) in *Psittacosaurus* [also figure 2 in (*6*)] showing underlying fibers. (**D**) Pebble-like scales in *Kulindadromeus*, adjacent to "basal plates." Decomposition: (**E**) Ribbon-like scales in ventral regions in *Naja* and *Sinosauropteryx* (inset) (*10*). (**F**) Bifurcating connective tissue bands around the gut of a juvenile ostrich, *Struthio camelus*.

Nelson Mandela Metropolitan University, Port Elizabeth, South Africa. **E-mail: theagarajen.soliar@nmmu.ac.za**

of, for example, *Naja mossambica* (cobra) and *Sinosauropteryx* (*10*) (Fig. 1E and inset).

Poor preservation renders the interpretation of filaments arising from a "basal plate" (*1*), given the enormous evolutionary implications, unsound. A parsimonious explanation is evident in figure 3A in (*1*). On the left are filaments associated with "basal plates" (both poorly preserved). On the right are somewhat less poorly preserved scales without filaments. The "basal plates" on the left are in fact severely degraded scales, but otherwise they resemble in size the scales on the right and the size class given by the authors for small scales, <3.5 mm, given variability of scale size in reptiles, even in close proximity (Fig. 1A). The explanation being self-evident, that more severe degradation and erosion have exposed the underlying filaments and resulted in loss of scales—and hence apparent greater spacing—in contrast to the reasons for proposing basal plates (*1*). In some places, all that may remain are the pigment impressions from the overlying scales (*11*) around the underlying filaments (*1*). We know that such filaments underlie scales in *Basiliscus*, the Jesus lizard (Fig. 1, A and B), and in *Psittacosaurus* R 497 [Fig. 1C; also figure 1B in (*6*)].

Given the severe level of degradation and distortion of soft-tissue structures in *Kulindadromeus*, the authors' proposals of primary preservations of unprecedented structures allegedly depicting finite filament lengths, filament groups threaded through single and sometimes multiple "basal plates," and filaments and plates preserved in three dimensions (*1*) are unjustified. The proposals are further weakened by a disregard for taphonomic tribulations (*12*) of a more than 150-million-year-old fossil and the complexities of tissue histology.

REFERENCES

1. P. Godefroit *et al.*, *Science* **345**, 451–455 (2014).
2. P. J. Motta, *Copeia* **1977**, 454–464 (1977).
3. D. A. Pabst, *J. Zool.* **238**, 35–52 (1996).
4. T. Lingham-Soliar, *J. Morphol.* **263**, 1–11 (2005).
5. T. Lingham-Soliar, *Lethaia* **34**, 287–302 (2001).
6. T. Lingham-Soliar, *Proc. Biol. Sci.* **275**, 775–780 (2008).
7. T. Reichlin *et al.*, *Struct. Biol* **152**, 52–63 (2005).
8. H. Axer, D. G. Keyserlingk, A. Prescher II, *J. Surg. Res.* **96**, 127–134 (2001).
9. T. Lingham-Soliar, *Naturwissenschaften* **90**, 563–567 (2003).
10. T. Lingham-Soliar, *J. Ornithol.* **153**, 699–711 (2012).
11. T. Lingham-Soliar, G. Plodowski, *Naturwissenschaften* **97**, 479–486 (2010).
12. T. Lingham-Soliar, J. Glab, *Palaeogeogr. Palaeoclimatol. Palaeoecol.* **291**, 481–487 (2010).

13 August 2014; accepted 17 September 2014
10.1126/science.1259983

RESEARCH

How vanadium dioxide switches from semiconductor to metallic

Morrison et al., *p. 445*

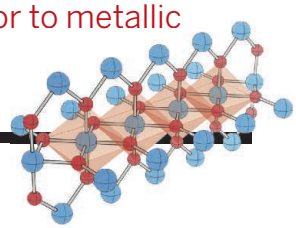

IN *SCIENCE* JOURNALS

Edited by **Stella Hurtley**

Anolis carolinensis (green) moves up for *Anolis sagrei* (brown)

EVOLUTIONARY BIOLOGY

Making adjustments for a new neighborhood

Competition between species drives the acquisition of diversity. Stuart *et al.* introduced a non-native anole lizard to natural experimental islands. In response, the original inhabitants adopted higher perches in the trees, where the larger invader was at a disadvantage. Within about 3 years—or 20 generations—the shift led to inherited morphological changes in the native lizards, including their growing larger toepads. — SNV

Science, this issue p. 463

IMMUNOLOGY

Digital amplification of T cell receptor signals

The kinase PKD2 is activated in T cells of the immune system when a peptide antigen binds to and stimulates the T cell receptor (TCR). Navarro *et al*. found that low concentrations of a peptide antigen activated PKD2 in a small proportion of T cells. In response to increased amounts of peptide antigen, a greater proportion of T cells exhibited maximal PKD2 activation. Thus, PKD2 may act as a digital amplifier of TCR signals, so that T cells mount an immune response tailored to the strength of the stimulus. —JFF

Sci. Signal. **7**, ra99 (2014).

NEW WORLD ARCHEOLOGY

Mountain dwellers of the Pleistocene

Humans colonized the inhospitable high Andes at least 11.5 thousand years ago. Rademaker *et al.* unearthed evidence of hunter-gatherer occupation at heights of almost 4500 m in Peru in two open-air sites. The sites contained more than 750 tools, including likely spearheads and scrapers. A nearby rockshelter with sooted ceilings and floor detritus may have been a campsite. The sites were probably used seasonally for hunting vicuña and other high-altitude prey. — AMS

Science, this issue p. 466

Stone artifacts from mountain camp

VIRAL CELL BIOLOGY

Flu mimics damaged proteins during entry

Viruses are master manipulators. The early stages of how flu viruses enter cells are very well understood, but Banerjee *et al.* describe a new wrinkle (see the Perspective by Rajsbaum and García-Sastre). It seems that the virus carries with it into the cell ubiquitin: a molecule involved in marking proteins for destruction. The virus then exploits host cell machinery involved in recognizing and dealing with damaged proteins to uncoat its own RNA genome, ready to continue its path toward successful infection. — SMH

Science, this issue p. 473; see also p. 427

VALLEYTRONICS

Making use of graphene's valleys

Graphene has two distinct valleys in its electronic structure, in which the electrons have the same energy. Theorists have predicted that creating an asymmetry between the two valleys will coax graphene into exhibiting the so-called valley Hall effect (VHE). In this effect, electrons from the two valleys move across the sample in opposite directions when the experimenters run current along the sample. Gorbachev *et al.* achieved this asymmetry

PHOTOS: (TOP TO BOTTOM) MORRISON *ET AL.*; © CHRIS MATTISON/ALAMY; © MICHEL GUNTHER/BIOSPHOTO/CORBIS; ERICA COOPER

Downloaded from www.sciencemag.org on October 24, 2014

Published by AAAS

by aligning graphene with an underlying layer of hexagonal-boron nitride (hBN) (see the Perspective by Lundeberg and Folk). The authors measured the transport characteristics of the sample, which were consistent with the theoretical predictions for the VHE. The method may in the future lead to information processing using graphene's valleys. — JS

Science, this issue p. 448; see also p. 422

SOLAR CELLS

Layering on solar cell power and stability

Solar cells made from carbon-based polymers are helpfully flexible. However, there's been a frustrating tradeoff between cell stability and efficiency when converting solar power to electrical power. Page *et al.* offer a strategy to partially resolve this dilemma by inserting a layer of polar organic compound (a fullerene derivative) between the cathode (the positive pole in the circuit) and the rest of the cell. Aluminum is an efficient cathode material but is prone to oxidative degradation. The easily applied polar layer enables the use of more stable metals, such as silver and copper, for the cathode, while counteracting their tendencies to diminish power conversion efficiency. — JSY

Science, this issue p. 441

PROTEIN DESIGN

Building with alpha-helical coiled coils

Understanding how proteins fold into well-defined three-dimensional structures has been a longstanding challenge. Increased understanding has led to increased success at designing proteins that mimic existing protein folds. This raises the possibility of custom design of proteins with structures not seen in nature. Thomson *et al.* describe the design of channel-containing α-helical barrels, and Huang *et al.* designed hyperstable helical bundles. Both groups used rational and computational design to make new protein structures based on α-helical coiled coils but took different routes to reach different target structures. — VV

Science, this issue p. 485, p. 481

CANCER

Anticancer drug coming out on TOPK

The TOPK protein is found in a wide range of human cancers and is believed to promote tumor growth. Matsuo *et al.* developed a drug that can inhibit TOPK and be delivered by multiple routes. The oral form of this drug was well tolerated by mice, which allowed convenient and effective treatment. An intravenous form was even more effective, and providing it as a liposomal formulation eliminated hematological side effects and promoted the complete regression of tumors. The inhibitor may thus be a viable anticancer agent, although human trials will be required before it can be used in the clinic. — YN

Sci. Transl. Med. **6**, 259ra145 (2014).

METALLOPROTEINS

How bacteria break down organohalides

Anaerobic bacteria can break down a range of organohalide pollutants. To do so, they use unusual reductive dehalogenase enzymes that remove the halogen ion from the molecule, making the pollutants less toxic. Bommer *et al.* describe x-ray crystal structures of one such enzyme from *Sulfurospirillum multivorans* (see the Perspective by Edwards). Vitamin B_{12}, present near the substrate binding site, catalyzes the reduction of trichloroethylene in concert with two iron-sulfur clusters. The structures provide mechanistic clues for how to engineer enzymes to recognize other pollutants. — NW

Science, this issue p. 455; see also p. 424

IN OTHER JOURNALS

Edited by **Kristen Mueller** *and* **Jesse Smith**

A leaf from a tobacco plant

PHOTO: © WAYNE HUTCHINSON/ALAMY

PLANT CELL DIVISION

Actin reins in plant cell division

When plant cells divide, they must make a new cell wall between the daughter cells. Microtubules of the mitotic spindle generate a structure called the phragmoplast, which helps cells to do this. The phragmoplast directs vesicles carrying cell wall components to the cell plate: the growing disc that will physically separate the two daughter cells. Although scientists know that the protein actin aids in this process, they do not know its precise role. Wu and Bezanilla now demonstrate that the molecular motor protein myosin VIII and actin steer phragmoplast expansion during moss and tobacco cell division. Myosin VIII's motor activity along actin filaments physically pulls the growing phragmoplast toward the edges of the cell. — SMH

eLife **3**, e03498 (2014).

Published by AAAS

ALSO IN *SCIENCE* JOURNALS

Edited by **Stella Hurtley**

MICROBE ANALYSIS

Experimental platforms for probing bacteria

Bacteria respond to a host of changing cues provided by their environment. Hol and Dekker review how microfluidic and nanofabricated devices can provide a platform to deliver different stimuli in a variety of environments. Bacterial quorum sensing and electron transport are among the problems that can be studied in this way. — PDS

Science, this issue p. 438

ADVANCED IMAGING

From single molecules to embryos in living color

Animation defines life, and the three-dimensional (3D) imaging of dynamic biological processes occurring within living specimens is essential to understand life. However, in vivo imaging, especially in 3D, involves inevitable tradeoffs of resolution, speed, and phototoxicity. Chen *et al.* describe a microscope that can address these concerns. They used a class of nondiffracting beams, known as 2D optical lattices, which spread the excitation energy across the entire field of view while simultaneously eliminating out-of-focus excitation. Lattice light sheets increase the speed of image acquisition and reduce phototoxicity, which expands the range of biological problems that can be investigated. The authors illustrate the power of their approach using 20 distinct biological systems ranging from single-molecule binding kinetics to cell migration and division, immunology, and embryonic development. — SMH

Science, this issue p. 439

DNA REPLICATION

How to stop after copying the genome

Replication is highly regulated: Failure to copy any part of the genome or copying parts of it more than once can cause genome instability with potentially disastrous consequences. Maric *et al.* and Priego Moreno *et al.* show that the DNA replication machinery, which stably encircles DNA during the duplication process, is actively disassembled once replication is complete (see the Perspective by Bell). The protein ring encircling the DNA is covalently modified, which allows it to be opened and the whole replication complex to be removed from DNA by a special disassembly complex. — GR

Science, this issue p. 440, p. 477; see also p. 418

ULTRAFAST DYNAMICS

How to make vanadium dioxide metallic

At about 70°C, the material vanadium dioxide (VO_2) switches from being a semiconductor to a metal. The switch happens so fast that it may be useful in electronic devices, but it is not clear whether the switch is primarily caused by enhanced interactions between electrons or by a change in the crystal structure. Morrison *et al.* shone laser light on a sample of VO_2, initially in a semiconducting state. They used electron diffraction to monitor the changes in the material's crystal structure and simultaneously measured its optical properties to monitor the electronic state. For certain laser powers, VO_2 switched to a long-lived metallic state even though it preserved its initial crystal structure. — JS

Science, this issue p. 445

ASYMMETRIC CATALYSIS

Ensuring handedness when breaking C-H bonds

Many organic compounds are chiral: They manifest two distinct mirror-image variants, or enantiomers. Kinetic resolution can transform one enantiomer to a desired product while leaving its mirror image unmodified. Chu *et al.* applied this strategy to a reaction that replaces aryl carbon–hydrogen bonds with carbon-iodine bonds. They used a chiral palladium catalyst that reacts selectively with just one of two enantiomers of various benzylamine derivatives. In medicinal chemistry, such selective synthesis of individual enantiomers is essential for screening interactions with chiral biomolecules such as proteins. — JSY

Science, this issue p. 451

WORKING MEMORY

Identifying the workhorse of working memory

Working memory allows us to keep behaviorally relevant information in mind over a short period of time. Liu *et al.* trained mice to remember a smell for a short period after it had been removed. Manipulating nerve cell activity in the mouse medial prefrontal cortex during this period interfered with the mice's performance when learning what they were supposed to do when they then smelled the same or a different odor. Once the animals were well trained on the task, the same manipulations did not affect performance. — PRS

Science, this issue p. 458

PLANT SCIENCE

Sex determination driven by community cooperation

An optimized ratio of male and females in a sexually reproducing population helps to generate the genetic diversity useful to a species in a changing world. Tanaka *et al*. studied a fern in which the sex ratio is adjusted not by individual identity, but by signaling between individual plants (see the Perspective by Sun). Early-maturing individual ferns express some of the biosynthetic genes needed to make a precursor of the plant hormone gibberellin, which they secrete into the environment. Younger ferns, which express the enzymes needed to finalize synthesis of gibberellin, take up the signal and in response develop the organs that produce male gametes. — PJH

Science, this issue p. 469; see also p. 423

MARINE CONSERVATION

Addressing fishing threats to ocean wildlife

Marine ecosystems are under pressure. In a Perspective, Vincent and Harris highlight the particular problems of illegal, unregulated, and unreported fishing. In coastal areas worldwide, millions of people fish without controls or records, including many women who gather marine species from intertidal areas or shallow waters. Deep-sea habitats and species are also under threat from bottom trawlers that may legally trawl for target species but capture much other marine life incidentally. Marine protected areas, comanagement, and other policy measures can help to reduce these pressures on ocean wildlife. — JFU

Science, this issue p. 420

EVOLUTION

Dinosaur color vision and the evolution of feathers

The first feathers that evolved in early dinosaurs had a simple hairlike structure and probably served to insulate the body. How did these simple protofeathers evolve into the more complex feathers found in today's birds? In a Perspective, Koschowitz *et al.* argue that dinosaur color vision played a key role in this evolution. Dinosaur color vision, like that of birds, is likely to have been superior to that of humans. The evolution of complex feathers would have enabled color signaling; for example, during sexual selection. — JFU

Science, this issue p. 416

Published by AAAS

REVIEW SUMMARY

MICROBE ANALYSIS

Zooming in to see the bigger picture: Microfluidic and nanofabrication tools to study bacteria

Felix J. H. Hol and Cees Dekker*

BACKGROUND: Nanotechnology and bacteriology at first sight may seem like two disparate worlds, but a rapidly moving field of research has formed at the interface of these disciplines in the past decade. Bacteria experience spatial structure at many scales: Individual bacteria interact with nanoscale surface features, whereas bacterial communities are shaped by landscape structure down to the microscale. Nanofabrication and microfluidics are ideally suited to define and control the environment at those scales, allowing us to zoom in on the peculiarities of individual cells and to broaden our understanding of the processes that shape multi-species communities. Recently developed nanotools provide unprecedented control over the bacterial microenvironment and have been key to the discovery of new phenomena in bacteriology.

ADVANCES: Nanofabrication and microfluidics have expanded our view on a myriad of bacterial phenomena. Microfluidics provides ways to study individual bacteria in dynamic and well-defined environments and has been used to address long-standing questions concerning bacterial aging and antibiotic persistence. Biological insights have been gained by exploring bacterial growth and movement in nanofabricated constrictions and revealed that bacteria can penetrate constrictions as narrow as only half their width. Furthermore, nanofabrication has been used to discriminate between competing hypotheses regarding the mechanisms that underlie intercellular electron transport. Confinement of single bacteria in tiny volumes has provided an individualistic perspective on collective phenotypes and demonstrated that density-dependent behaviors can even be exhibited by individuals. Bacteria growing in nanofabricated chambers adopt predefined shapes and have been used to study the geometry dependence of intracellular processes. Microfluidics and nanofabrication have been combined to create synthetic ecosystems in which the spatial eco-evolutionary dynamics of bacterial communities can be explored. Various approaches to mimic the intricate spatial structure of natural bacterial habitats now contribute to our understanding of competition and cooperation within bacterial populations. Microfluidic platforms have boosted research on unculturable environmental species by eliminating the need for pre-analysis culturing. On-chip whole-genome amplification of environmental isolates has recently provided a first genotypic glimpse on this "dark matter of biology."

ON OUR WEB SITE

Read the full article at http://dx.doi.org/10.1126/science.1251821

OUTLOOK: Looking ahead, it is clear that the doors that nanofabrication and microfluidics have opened will continue to make important contributions to basic bacteriology research. A comprehensive investigation of the uncultured majority with microfluidic technologies, for instance, may uncover the vast potential of currently unknown species. Practical applications such as microbial fuel cells or antibacterial surfaces will benefit from the understanding of bacterial behavior at the nanoscale. Microfluidic devices are now beginning to be commonly used in microbiology labs because of a demand for precise measurements in complex environments that can be controlled at the microscale. This trend will undoubtedly continue as scientists delve deeper into the complex lives of bacteria. ■

Department of Bionanoscience, Kavli Institute of Nanoscience, Delft University of Technology, Delft, Netherlands.
*Corresponding author. E-mail: c.dekker@tudelft.nl
Cite this article as: F. J. H. Hol, C. Dekker, *Science* 346, 1251821 (2014). DOI: 10.1126/science.1251821

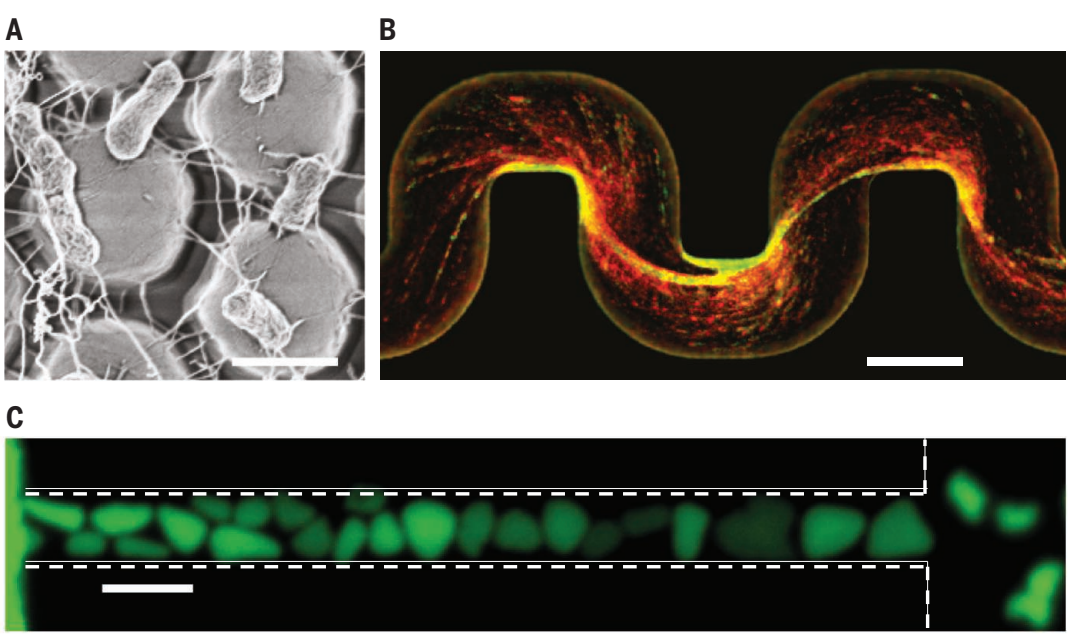

Studying bacteria using nanofabrication and microfluidics. (**A**) *Escherichia coli* bacteria use their flagella to exploit submicrometer crevices for surface attachment [Reprinted with permission from (*5*) (reference list of full paper online)]. (**B**) Biofilm streamers form in a meandering flow channel (*Pseudomonas aeruginosa*, red; extracellular polymeric substances, green) [Reprinted with permission from (*93*)]. (**C**) *E. coli* undergo a shape transition when squeezing into a nanofabricated channel as shallow as half their width [Reprinted with permission from (*26*)]. Scale bars, (A) 2 μm; (B) 200 μm; and (C) 5 μm.

Published by AAAS

REVIEW

MICROBE ANALYSIS

Zooming in to see the bigger picture: Microfluidic and nanofabrication tools to study bacteria

Felix J. H. Hol and Cees Dekker*

The spatial structure of natural habitats strongly affects bacterial life, ranging from nanoscale structural features that individual cells exploit for surface attachment, to micro- and millimeter-scale chemical gradients that drive population-level processes. Nanofabrication and microfluidics are ideally suited to manipulate the environment at those scales and have emerged as powerful tools with which to study bacteria. Here, we review the new scientific insights gained by using a diverse set of nanofabrication and microfluidic techniques to study individual bacteria and multispecies communities. This toolbox is beginning to elucidate disparate bacterial phenomena—including aging, electron transport, and quorum sensing—and enables the dissection of environmental communities through single-cell genomics. A more intimate integration of microfluidics, nanofabrication, and microbiology will enable further exploration of bacterial life at the smallest scales.

At first glance, nanotechnology and bacteriology may seem like two disparate worlds. However, in the past decade a dynamic and rapidly expanding field of research has formed at the interface of these two disciplines. Many "nanotools" have been developed to study individual bacteria as well as multispecies communities in complex yet well-defined environments. In addition to a host of exciting new techniques, the confluence of nanotechnology and bacteriology has yielded new biological insights that would have been inaccessible without the merging of these disciplines.

Natural bacterial habitats, ranging from volcanic soil to our gastrointestinal tract, are spatially structured at multiple scales. The soil matrix, for instance, consists of a three-dimensional (3D) network of micrometer-sized patches (*1*, *2*), and habitats ranging from the gut to the ocean contain chemical gradients down to the microscale (*3*, *4*). At even smaller scales, bacteria can squeeze through submicrometer constrictions and exploit nanosized crevices for surface attachment.

In these spatially structured habitats, multispecies consortia form organized communities. Understanding how these bacterial communities assemble and function is a grand challenge that requires an interdisciplinary approach. The fundamental units of communities are cells, and the typical dimensions of a bacterial cell match well with the scales at which micro- and nanotechnology can shape and manipulate the environment (Fig. 1A). Traditional methods to culture bacteria—test tubes and petri dishes—are not compatible with long-term monitoring of an individual cell or the precise manipulation of its microenvironment. As a result, seemingly simple questions such as "How long can a bacterium live?" or "What is the smallest constriction a bacterium can pass through?" remained unanswered until recently. Answers to such long-standing questions are now emerging at the interface of microbiology and microfluidics.

Nanofabrication provides unprecedented control over the local environment of cells and allows researchers to visualize the mechanical role of flagella in surface attachment (*5*) or to investigate individual bacteria donating electrons to electrodes (*6*). To study population-level processes, microfluidics and nanofabrication can create well-defined on-chip ecosystems that mimic the complexity of the natural environment. Experiments with such synthetic ecosystems are revealing how the microscopic spatial structure of bacterial habitats affects the cooperation, competition, and evolution of bacteria (*7*–*11*).

Here, we review the development and use of novel nanofabrication and microfluidics tools that provide detailed insight into the complex lives of bacteria, and we highlight some of the exciting microbiological discoveries that have been made with those techniques. We first review several approaches to study bacterial growth and shape at the single-cell level. Subsequently, we discuss how single-cell studies of bacterial electron transport and quorum-sensing provide insight into population-level manifestations of those phenomena. We then discuss efforts to understand bacterial community dynamics by using synthetic ecosystems, and to dissect natural communities by using microfluidics. We finish with a brief outlook on new opportunities at the interface of bacteriology and nanotechnology.

Department of Bionanoscience, Kavli Institute of Nanoscience, Delft University of Technology, Delft, Netherlands.
*Corresponding author. E-mail: c.dekker@tudelft.nl

Bacterial growth and shape

Microfluidics and nanofabrication provide powerful tools to control, shape, and manipulate the environment of individual bacteria. In this section, we describe microfluidic approaches that address long-standing questions concerning bacterial growth, and we discuss how nanofabrication opens doors to studying bacterial growth and shape.

Mysteries of bacterial growth solved with microfluidics

Monitoring an individual cell for extended periods in a well-defined environment is crucial to answer fundamental growth and aging-related questions. However, long-term imaging of a single cell in a constant environment is challenging; because of exponential growth rates and resource consumption, a bacterial colony creates internal chemical gradients and reaches an unmanageable size within a few generations, precluding the tracking of a single cell for long periods. One model species for bacterial aging, *Caulobacter crescentus*, helps to solve this problem by only dividing as long as it is attached to a surface. While the dividing mother cell is stuck to the bottom of a channel, the planktonic progeny can get flushed out (*12*). In many other species, however, growth and dispersal are not mutually exclusive, hence their aging process remained a mystery until recent microfluidic innovations allowed the long-term (in principle, indefinite) monitoring of an individual bacterium in a constant environment. To accomplish this, Wang *et al.* immobilized bacteria in dead-end channels having a width and height matched to that of the cell body (*13*). The device is designed to flush out the offspring after division (Fig. 1B). Using this device (dubbed "the mother machine"), single *Escherichia coli* bacteria were monitored for more than 200 cell divisions, constituting a marked improvement compared with earlier work in which aging *E. coli* could typically be followed up to seven generations (*14*, *15*). Long-term monitoring revealed that the division rate of *E. coli* remained constant for more than 200 generations, but the death rate increased after 50 divisions. These results suggest that growth and death in *E. coli* are uncoupled processes—a property not previously found in model organisms used to study aging.

Norman *et al.* recently used a similar microfluidic device to investigate cell-fate switching between an individual planktonic state and a sessile multicellular state by individual *Bacillus subtilis* bacteria and characterized the underlying regulatory circuit (*16*). In order to observe single *B. subtilis* differentiate, Norman *et al.* fabricated long dead-end channels connected to 500-nm-shallow medium reservoirs. These shallow reservoirs prevent gradients from developing along the length of the channel and ensure a constant environment over the long time scales associated with cell-fate switching (Fig. 1C). Tracking

of individual cells revealed that switching from the motile state is "memoryless"—the probability to switch to the multicellular state is independent of how long a cell has been planktonic. Switching back to the motile state, however, is tightly controlled, resulting in a low variability of the lifetime of multicellular growth. Differences in lifetime regulation of the two states likely reflect the necessity to coordinate behavior over multiple generations in the multicellular state and the absence of such coordination in the motile state.

The phenomenon of bacterial persistence presents another long-standing question of bacterial growth physiology that was addressed by using microfluidics. More than seven decades ago, it was observed that a small fraction of a clonal nonresistant population of bacteria can survive antibiotic treatment—an observation of obvious clinical relevance (*17*). Upon regrowth, these persistent bacteria ("persisters") give rise to a population that remains susceptible to the antibiotic used, showing that resistance is not genetically acquired.

The mechanism that allows a fraction of the susceptible population to remain refractory to antibiotic treatment remained obscure until the phenomenon was investigated at the single-cell level (*18*), which revealed that a heterogeneity in growth rates is key. *E. coli* growing in open-ended channels [a single-cell chemostat (Fig. 1B)] showed the presence of two subpopulations: The vast majority of cells grew at a rate identical to the growth rate in batch culture, whereas a small fraction of the population was dormant. The use of a microfluidic device permitted tracking of the growth and death of individual *E. coli* bacteria upon transient exposure to ampicillin (medium and antibiotics were applied from above through a membrane covering the bacterial channels) and revealed that the cells that were dormant before antibiotic exposure survived the treatment. On-chip observations of single persister cells furthermore revealed stochastic growth-resumption of persisters when antibiotic-free medium was supplied after exposure. Later studies showed that persisters may transiently exhibit metabolic activity, resulting in a short-lived state of antibiotic susceptibility (*19*).

A recent microfluidics study reported a different mechanism underlying persistence in populations of *Mycobacterium smegmatis* exposed to the antibiotic isoniazid. Here, persistence was found to relate to the stochastic expression of KatG, an enzyme necessary for activation of the antibiotic. Cells that infrequently expressed *katG* continued to grow and divide, whereas cells that were frequently pulsing *katG* were prone to die. This balanced growth and death rates and resulted in a population of "dynamic persisters" (*20*). A thorough characterization of the various mechanisms underlying persistence is key to identifying the weaknesses of persister cells that may facilitate their clinical management.

Although arranging individual bacterial cells in single file is conceptually simple, the ability to monitor the same cell for unlimited periods of time while having accurate temporal control over its chemical environment is a powerful new tool in microbiology (*21*–*24*). In particular, studies of phenotypes that exhibit temporal

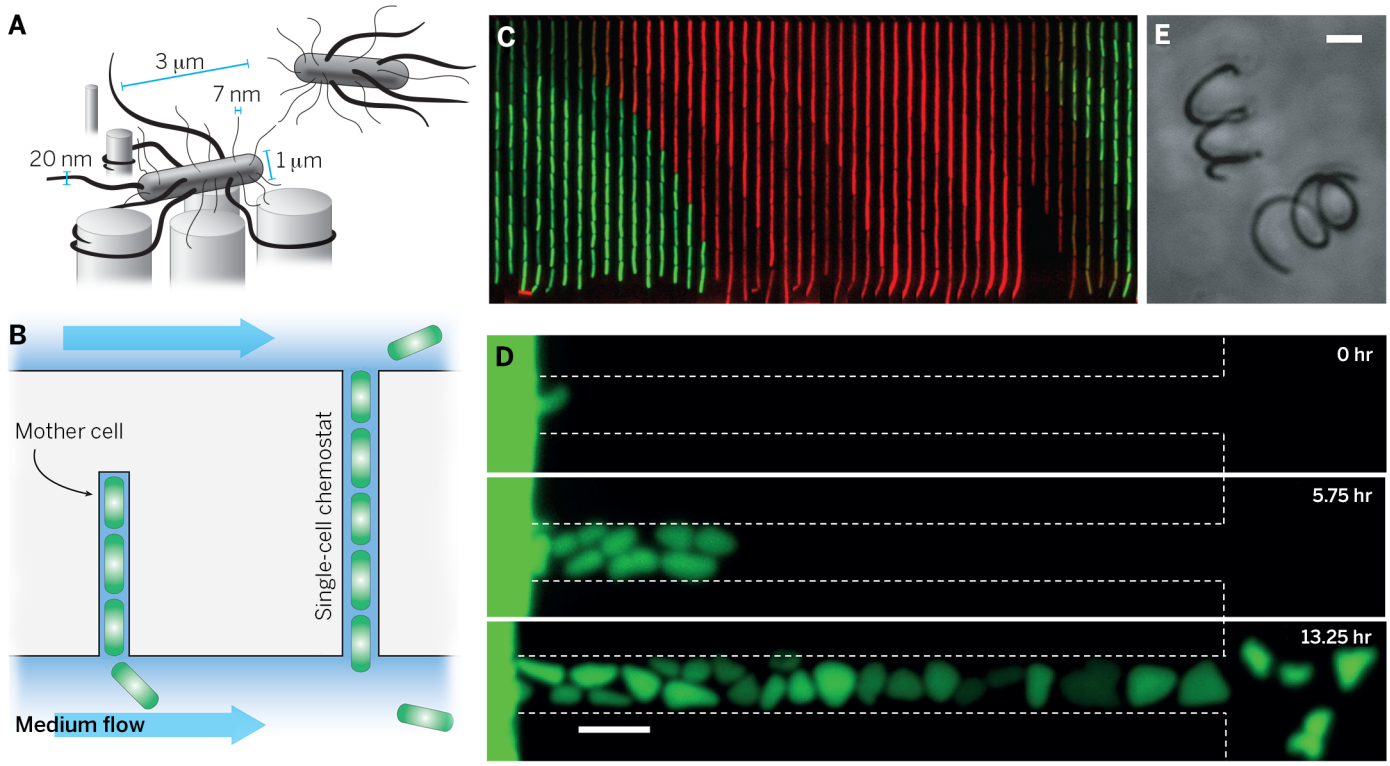

Fig. 1. Bacterial growth and shape in microstructures. (**A**) The scales at which nanofabrication and microfluidics can shape and control the environment matches well to the characteristic size scales of a bacterium (0.3 to 10 μm) and its subcellular components (for example, flagella and pili are ~20 and ~7 nm wide, respectively). (**B**) A cell immobilized in a dead-end channel (left) pushes its offspring out through growth and division. The mother cell remains in the same location and can be observed indefinitely. A linear colony growing in a channel open at both ends (right) is a continuous culture technique (chemostat) that allows single-cell imaging. In both designs, the growth channel abuts a larger flow channel that washes out offspring, supplies fresh nutrients, and can be used to change medium conditions. (**C**) Kymograph of *B. subtilis* in a dead-end channel. Switching from motile growth (green) to chained growth (red) by an individual cell can be seen; frames are taken 10 min apart and stacked horizontally. [Reprinted by permission from Macmillan Publishers, *Nature* (*16*) copyright (2013)] (**D**) *E. coli* squeezing through a 300-nm-shallow nanochannel (50 μm long and 5 μm wide) connecting two deep chambers. Dashed lines mark the lateral edges of the channel. Scale bar, 5 μm. Cells that squeeze into the nanochannel undergo a shape transition and become flat and aberrantly shaped upon confined growth and division. The population of squeezing cells traverses the nanochannel through growth and division. Once cells enter the deep chamber on the right, they adopt various globular shapes (bottom right). [Reprinted with permission from (*26*)] (**E**) A filamentous *E. coli* cell adopted a spiral shape after growth in a circular channel. Scale bar, 10 μm. [Reprinted with permission from (*28*) copyright (2005) American Chemical Society]

dynamics spanning many generations, such as cell-fate switching (*16*) and circadian oscillations (*25*), benefit from this innovation.

Shape-shifting bacteria

In their natural habitats, bacteria often encounter submicrometer holes and crevices that are smaller than the cell body. Indeed, in clinical and industrial settings submicrometer-pore filters are readily used to sterilize liquids. In order to investigate whether constrictions narrower than a cell indeed rigorously prevent bacteria from penetrating, Männik *et al.* fabricated nanochannels of a range of widths and determined the narrowest constriction through which bacteria could pass. Surprisingly, *E. coli*—which have a diameter of 800 to 900 nm—could penetrate channels as narrow as only half their width (*26*). Shown in Fig. 1D are *E. coli* cells that squeeze into a 300-nm-shallow channel, which demonstrates that a population of squeezing cells can traverse a shallow nanochannel of several hundred micrometers in length by means of growth and division. Cells popping out on the other end are aberrantly shaped but readily give rise to a population of normal rod-shaped cells. In contrast, the Gram-positive bacterium *B. subtilis* could not penetrate channels of a width narrower than its cell body, suggesting that cell-wall rigidity and turgor-pressure differences between Gram-negative (such as *E. coli*) and Gram-positive bacteria may have implications regarding their ability to penetrate submicrometer constrictions.

In a follow-up study, the squeezing *E. coli* were used as a model system with which to study the shape-dependent functioning of *E. coli*'s cell-division machinery (*27*). Despite their irregular shape, squeezed *E. coli* produce equally sized daughter cells with a high division accuracy that is nearly identical to normal rod-shaped cells. Visualizing various components of the cell-division machinery in these squeezed cells demonstrated the importance of the nucleoid in positioning the divisome (the contractile ring that divides the cell) and showed that nucleoid occlusion provides a robust mechanism for division-site selection in aberrantly shaped cells.

Shaping bacteria into diverse morphologies can enhance our understanding of the spatial organization and geometry dependence of intracellular processes. The squeezed cells shown in Fig. 1D, however, adopt irregular and undefined shapes and as such are not ideal to systematically study the shape-dependence of intracellular processes. Bacteria confined in nanofabricated chambers with a specified geometry can adopt a predefined shape through growth. An example of a cell that adopted a spiral shape after being cultivated in a circular chamber is shown in Fig. 1E (*28*). A similar approach has been used to manipulate the local curvature of cell membranes, showing that curvature has a regulatory role in localizing cardiolipin and various membrane-associated proteins (*28*–*30*). We anticipate that new nanofabrication approaches to grow bacteria into predefined shapes will prove to be valuable in appreciating the adaptive virtue of cellular shapes and enhance our understanding of the geometry dependence of intracellular processes (*31*).

Hydrodynamic flow presents another method to deform bacterial cells. Two studies have recently investigated the bending dynamics of filamentous bacteria protruding from growth channels by using flow perpendicular to the growth direction of the cells (*32*, *33*). These studies showed that rapid mechanical perturbations lead to elastic bending, whereas constantly applied forces lead to growth-induced plastic deformations of the cell body. When the bending force is removed, plastically deformed cells eventually recover their rod shape through dislocation-mediated cell-wall growth.

Motility and adhesion: Bacteria-surface interactions

In contrast to their laboratory counterparts in a test tube or a chemostat, bacteria living in natural habitats are often in close contact with a surface. The surfaces on which bacteria grow and move are structured at the nanoscale, which has implications for surface adhesion and motility. In this section, we discuss how visualizing the interactions of bacteria with nanofabricated structures is revealing the mechanisms that bacteria use to migrate and settle into a biofilm lifestyle.

Settling down

Surface-attached growth is a common lifestyle among bacteria, and genetic analyses have suggested important roles for flagella and pili in the initial stages of biofilm formation (*34*). Mechanical insight into the interaction of bacteria with nanoscale features, however, was lacking. Recently, Friedlander *et al.* (*5*) visualized the interaction of *E. coli* with nanofabricated structures and elegantly showed how *E. coli* use their flagella to "reach" into submicrometer crevices to enhance surface attachment (Fig. 2, A and B) (*5*). Imaging this process demonstrated that bacterial flagella do not only function in bacterial motility but also facilitate surface attachment by allowing bacteria to grasp submicrometer objects. A further characterization of the structural mechanisms underlying bacterial attachment to nanoscale surface

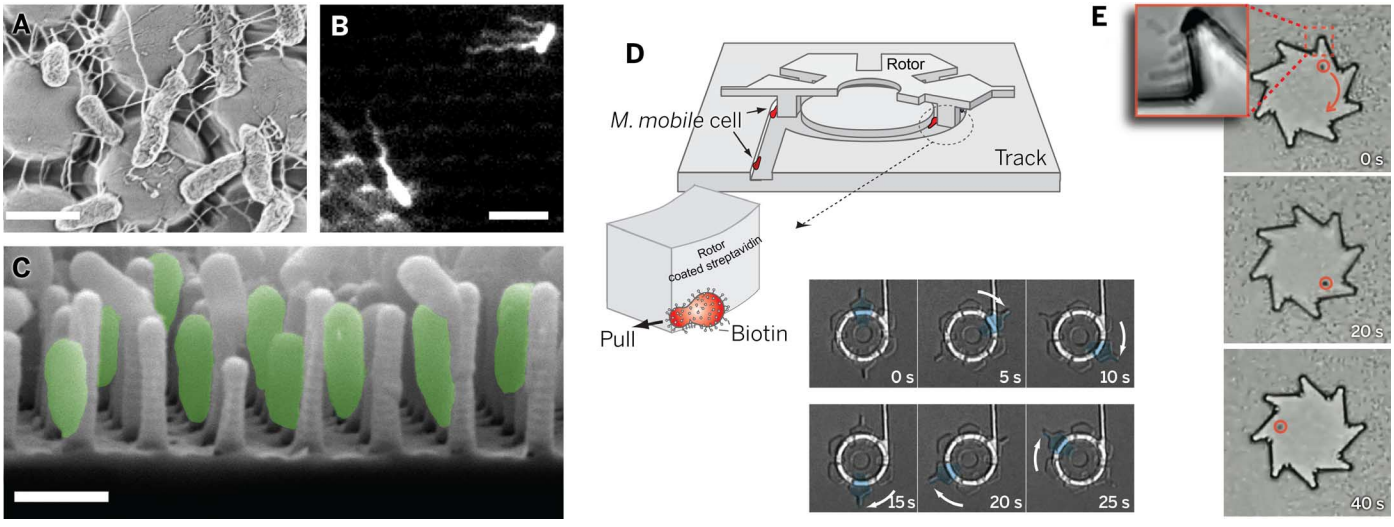

Fig. 2. Bacterial attachment and motility probed with nanofabricated structures. (**A** and **B**) Flagella "grasp" submicrometer crevices to improve surface attachment. (A) Scanning electron microscopy image (scale bar, 2 μm) and (B) fluorescence microscopy image (scale bar, 5 μm) of several *E. coli* on an array of hexagonal posts separated by 440-nm-wide trenches. Flagella nestled in the trenches facilitate surface attachment. [Reprinted with permission from (*5*)] (**C**) *P. aeruginosa* cells attach to 300-nm-diameter posts. An array of nanoposts induces the self-organization of an ordered colony in which the majority of cells stands upright between the posts. Cells are false-colored in green to enhance visibility. Scale bar, 1 μm. [Reprinted with permission from (*42*) copyright (2010) American Chemical Society] (**D**) Schematic of a microrotor powered by *M. mobile*. Gliding cells attach to the 20-μm-diameter rotor and rotate it, as can be seen from microcopy images (bottom right). [Reprinted with permission from (*58*) copyright (2006) National Academy of Sciences, USA] (**E**) Swimming bacteria rotate a gear at 1 rpm (48 μm in diameter) by bumping into its asymmetric teeth. [Reprinted with permission from (*59*)]

features is necessary to elucidate how bacteria lay the foundation for biofilm growth.

A better understanding of bacterial surface attachment at the nanoscale is relevant to prevent biofouling. At the scale of 10 to 100 nm, surface roughness can promote the adhesion of certain species while inhibiting attachment of others. Such species-specific interactions are suggested to depend on the size and shape of a cell (spherical or rodlike). For example, depending on how their shapes matched nanofabricated surface features, spherical *Staphylococcus aureus* cells attached to nanostructured surfaces, whereas rod-shaped *Pseudomonas aeruginosa* did not, and vice versa (*35*). The systematic characterization of bacterial surface-attachment at the nanoscale has attracted strong interest, and general principles relating surface characteristics to adhesion are currently emerging (*36*–*38*). Addressing the many questions that remain, however, is of clear importance for designing next-generation antibacterial surfaces (*39*, *40*).

Posts measuring 300 nm in width guide swimming motility and have been suggested to induce preferential attachment to the posts instead of to the flat surface that supports them (*41*). *P. aeruginosa* cells standing upright between posts are shown in Fig. 2C. Remarkably, periodic arrays of such nanoposts can facilitate the self-organization of bacterial populations into spatially patterned colonies (*42*). Arrays of nanostructures can be used to form highly ordered colonies in which cells assume different orientations, depending on the periodic post spacing. This behavior is exhibited by several species and does not depend on the action of flagella or pili because defective mutants show similar behavior.

On the move

Larger fabricated structures (an order of magnitude larger than the nanofeatures involved in surface attachment) can have an intriguing effect on bacterial motility. When swimming near surfaces, bacteria become hydrodynamically trapped and continue swimming along the surface (*43*, *44*). This effect can have interesting consequences when bacteria navigate microfluidic channels and can be used to sort or direct cells. Playing with the hydrodynamic properties of the floor and ceiling of a microfluidic channel, DiLuzio *et al.* made *E. coli* "swim on the right-hand side" and take a right turn when approaching intersecting channels (*45*). In contrast, the traffic rules are reversed when *E. coli* swims near a liquid-air interface, where it takes left turns (*46*). In addition to steering swimming bacteria, the hydrodynamic effects of bacteria swimming near surfaces can be exploited to concentrate randomly swimming bacteria by using nanofabricated funnels (*47*, *48*) or sort them according to their size by using microfluidic ratchets (*49*).

Bacterial chemotaxis, the ability of motile cells to sense and navigate chemical gradients, has been studied extensively by using microfluidics to create defined chemical gradients (*50*). The opportunity to track individual cells in arbitrarily shaped gradients that are continuous or time-variant has provided insight into the coherence of chemotactic populations (*51*), the remarkable sensitivity of chemotaxis (*52*), and the various strategies that marine bacteria adopt to optimize their foraging (*53*, *54*). The use of microfluidic platforms to study chemotaxis has been reviewed extensively in (*55*) and (*56*).

An interesting potential of motile bacteria that interact with microstructures is the possibility to extract useful work from them. Besides motility, bacteria have many capabilities—such as self-reproduction and sensing of the environment—that make them interesting candidates to propel or transport micrometer-sized objects (*57*). Several studies have provided proof-of-concept experiments that bacterial motility may be used to power microscale rotors (*58*–*60*). A design by Hiratsuka *et al.* is shown in Fig. 2D, in which gliding *Mycoplasma mobile* cells attach to a 20-μm-diameter rotor running on a silicon track (*58*). In this approach, *M. mobile* cells collectively managed to rotate the motor at 2 rotations per min (rpm). Recent studies demonstrated conceptually simpler designs in which asymmetric rotors suspended in a bacterial population were rotated by swimming bacteria that bumped into the asymmetric teeth (Fig. 2E) (*59*, *60*). Asymmetric environments have also been used to let randomly swimming bacteria that bump into colloids deliver the particles to the center of a structure consisting of asymmetric barriers (*61*). Although the prospect of using nanofabricated structures to harness the power of bacteria is still remote, these studies illustrate the potential of hybrid micromachines.

Zooming in on single cells to learn about population-level phenomena

In nature, cells rarely live in isolation. Microbial communities are often composed of many interacting cells from various species. The functions of bacterial interactions are as stunningly diverse as the communities in which they occur. For example, interactions serve to assess whether it is beneficial to induce costly collective behaviors, or give rise to peculiar phenomena such as long-range electron transport through biofilms. Below, we discuss two examples—electron transport and quorum-sensing—that show how zooming in on the building blocks of populations (individual cells) enhances our understanding of population-level phenomena.

Bacterial electricity

To facilitate respiration, various bacterial species exchange electrons with their external environment. The mechanisms that underlie bacterial electron transport are not well understood. A detailed understanding of these processes is, however, imperative to exploit the potential of electricity-generating bacterial populations in the development of microbial fuel cells or the processing of organic waste (*62*–*64*). In theory, bacteria can donate electrons to extracellular insoluble acceptors (such as electrodes) in various ways: Soluble redox-active molecules can transport electrons by means of diffusion, redox-active molecules on the outer cell surface may transfer electrons upon contact, and biofilms perhaps may facilitate long-range electron transport through contacts formed by conductive pili (*65*). It remains a matter of debate which of these mechanisms bacteria use to transport electrons (*66*, *67*).

To distinguish between the three modes of electron transport mentioned above, Jiang *et al.* fabricated electrodes patterned with an insulating layer (*68*). The insulating layer was designed to prevent direct cell-electrode contact while allowing diffusing molecules to reach the electrode through nanoscale holes. Using this approach, it was shown that the cell body of *Shewanella oneidensis* does not need to be in direct contact with an electrode in order for it to generate a detectable current, suggesting that electron transport takes place through pili or diffusing mediators. Pili of *S. oneidensis* were previously demonstrated to be radially conductive (*69*) and later also suggested to transport electrons along their long axis (*70*). Two observations by Jiang *et al.*, however, argue against an important role for pili in mediating electron transfer: Simultaneous optical imaging and current recording showed that a current can be detected before cells are in the proximity of the electrodes. Furthermore, the removal of diffusible redox mediators after a layer of cells had formed on the electrode abolished the current. These observations suggest that *S. oneidensis* mainly relies on diffusible molecules for electron transport and that pili may only have a minor role (*68*).

Experiments on *Geobacter sulfurreducens* suggested that it uses a different mechanism to transport electrons (*6*). Simultaneous imaging and current detection of single *G. sulfurreducens* in contact with a nanofabricated electrode is shown in Fig. 3A. Stepwise current increases can be observed when individual cells come into contact with the electrodes, and in contrast to *S. oneidensis*, the removal of diffusible redox mediators did not reduce the current produced by *G. sulfurreducens*. These observations suggest that *G. sulfurreducens* exchanges electrons through redox-active molecules on its cell surface or along conductive pili.

The spatial scale over which bacterial electron transport occurs becomes vastly larger when multiple cells form a biofilm (*71*) or in cables composed of filamentous bacteria (*72*). Such multicellular assemblies have been shown to transport electrons over centimeter distances. Where studies at the level of single cells suggest a minor role for pilus-mediated transport in *S. oneidensis* and focused on cell-body contact for *G. sulfurreducens*, pili were reported to be crucial for the conductivity in biofilms of *G. sulfurreducens* (*71*, *73*), which were claimed to exhibit a high conductivity, approaching that of synthetic metals (*71*).

The above studies illustrate that the use of nanofabrication is valuable for enhancing our understanding of electron transfer at the single-cell and biofilm levels. However, many open questions remain, and a thorough investigation of the diverse mechanisms that single bacteria use to transport electrons is warranted to estimate the

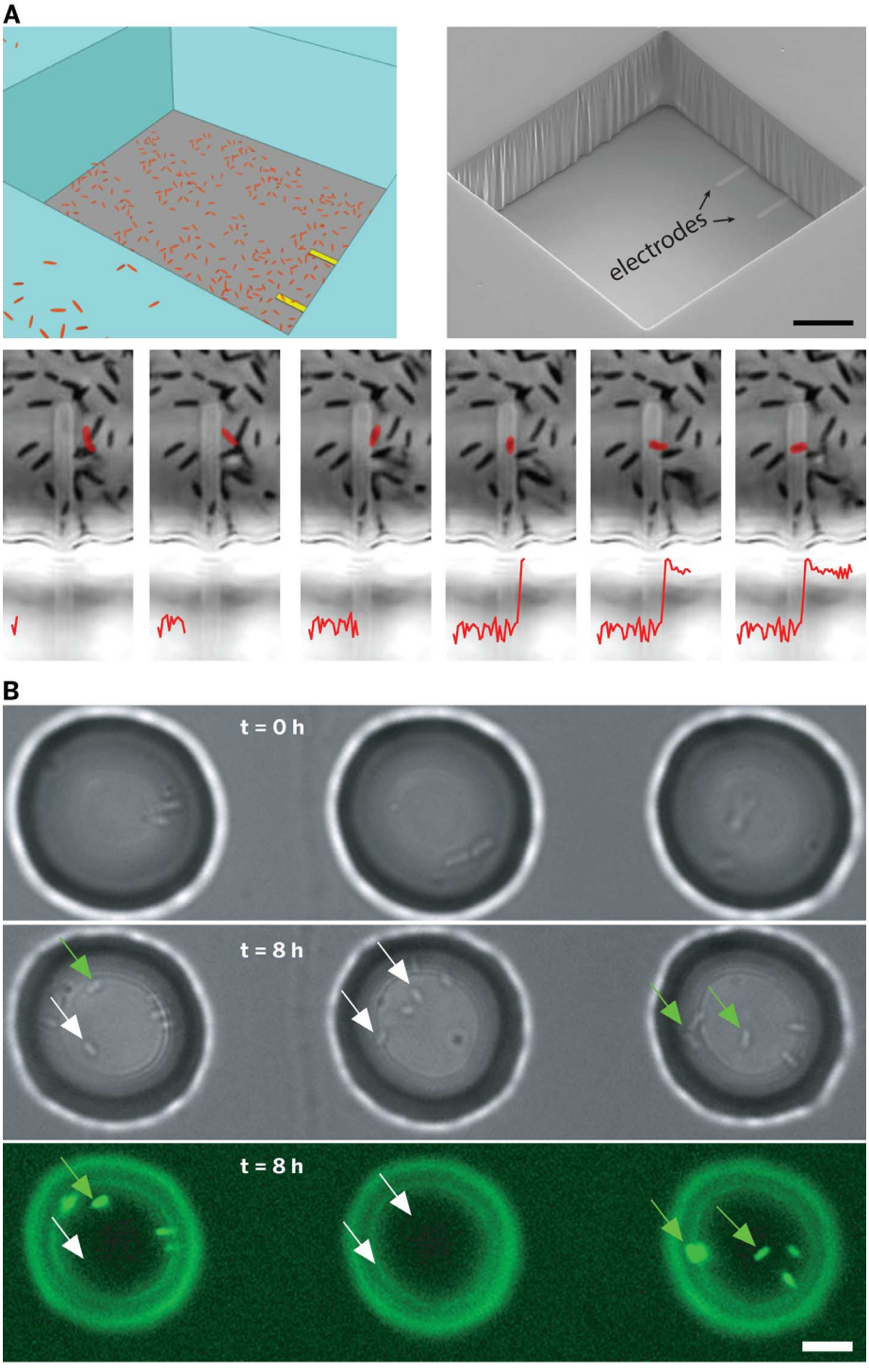

Fig. 3. Single-cell measurements of electron transport and quorum-sensing. (**A**) Schematic (top left) and scanning electron microscopy image (top right) of a well containing two electrodes. Scale bar, 20 μm. A time sequence of *G. sulfurreducens* bacteria interacting with an electrode is shown at bottom. When the cell labeled in red comes in contact with the electrode, a stepwise current increase is measured (current is plotted in red). [Reprinted by permission from Macmillan Publishers, *Nature Communications* (*6*) copyright (2013)] (**B**) Small groups of *P. aeruginosa* are confined in 100-fl droplets. (Top and middle) Bright-field images demonstrating growth of cells. Scale bar, 5 μm. Not all cells in the same droplet initiate quorum sensing, showing that quorum sensing initiation is heterogeneous (green arrows point to cells that induced quorum-sensing; white arrows point to cells that did not). [Reprinted with permission from (*79*) copyright (2009) Wiley]

full potential of bacteria populations as tools to turn waste into energy.

Lonely quorums

Quorum-sensing is a phenomenon in which bacteria sense secreted molecules and undergo genetic reprogramming when these molecules reach threshold densities (*74*). For example, this form of density-dependent signaling allows bacterial populations to induce "expensive" collective behaviors when a critical population density (a quorum) makes those worthwhile. Quorum-sensing has mainly been investigated in traditional assays by using well-mixed cultures grown in flasks. However, the mediation of quorum-sensing by diffusible molecules makes it evident that the geometry of an environment and the spatial arrangement of cells are key to these processes (*75*). A lively debate (*76*–*78*) on what bacteria are actually sensing—such as population density or medium diffusibility—spurred basic questions regarding the induction of quorum-sensing.

Two parallel efforts focused on the question of whether a single bacterium can quorum-sense—whether it can induce density-dependent pathways in response to a self-secreted signal. This can be probed by confining individuals or small groups of cells in a femtoliter- to picoliter-sized droplet (Fig. 3B). Boedicker *et al.* developed a microfluidic device in which *P. aeruginosa* were encapsulated in droplets created in microstructured wells (*79*), whereas Carnes *et al.* used a self-assembly process in which lipid/silica nanostructures encapsulated *S. aureus* bacteria (*80*–*82*). The small droplets provide the opportunity to have individual bacteria at a "density" that in essence is similar to a population approaching stationary phase in a test tube (~10^9 cells/mL). Both studies confirmed that individual cells could indeed induce quorum-sensing pathways that were previously only observed in large, high-density populations. The observations revealed that the initiation of quorum-sensing is heterogeneous; cells in identical droplets (equal cell density) did not necessarily exhibit similar quorum-sensing induction kinetics. The induction of quorum-sensing pathways substantially increased the viability of wild-type *S. aureus* compared with their non–quorum-sensing counterparts.

Recent efforts that encapsulate *E. coli* bacteria in 2D arrays of microdroplets open doors to investigate the effect of the spatial arrangement of cells on quorum-sensing (*83*). Arrays of droplets may similarly be used to spatially organize multispecies consortia in an effort to unravel the various inter- and intraspecies languages that bacteria speak (*74*).

Unraveling bacterial communities

Natural bacterial habitats have in common that they are spatially structured and chemically heterogeneous environments. Bacteria usually live in multispecies communities of which the majority is unculturable (*84*). Two distinct approaches aimed at understanding the complexity of bacterial communities are currently gaining ground. First, synthetic ecosystems are used in a "bottom-up"

approach in which the ecology of bacterial populations is explored in well-controlled on-chip ecosystems. This approach allows researchers to build a laboratory landscape from scratch and populate it with a defined multispecies consortium. Secondly, "top-down" approaches to dissect naturally occurring bacterial communities are facilitated by technological advancements that allow the isolation and characterization of unculturable bacteria directly isolated from environmental samples.

Building up bacterial communities

Approximately a decade ago, researchers first created on-chip ecosystems to study the spatial dimension of bacterial community dynamics in detail. Nanofabrication and microfluidics have the potential to transform the way bacterial ecology is studied by providing the tools to create ecosystems that mimic characteristics of natural environments. In the absence of external mixing (which occurs in shaken flasks), dispersal, chemotaxis, and aggregation become key drivers of bacterial community dynamics. As a result of these factors, the population expansion of bacteria that colonize a structured habitat does not obey the statistics of an ideal gas; instead, high-density demographic clusters form in close proximity to unoccupied territory (*7*, *85*–*88*). Keymer *et al.* demonstrated that these processes allow *E. coli* to organize into a structured metapopulation (a population of populations) when colonizing an array of coupled habitat patches (*7*).

The spatial structure of a community affects the competitive interactions between different cell types (*8*). The microscale diffusion of nutrients (*53*, *54*), secreted public goods (*10*, *89*), and toxins, for example, set the spatial scale at which cooperative or spiteful interactions emerge. Synthetic ecosystems (Fig. 4) provide the opportunity to study the interaction between competing bacteria in different ecological scenarios (such as varying geometry and medium composition) and track the resulting community dynamics at high spatiotemporal resolution. Such approaches provide insight into the eco-evolutionary interaction of bacteria with their environment and have shed light on the strategies bacteria use to solve social dilemmas concerning resource management (*9*, *90*) and the exploitation of public goods (*10*). A two-strain community is shown in Fig. 4A consisting of cooperator and cheater *E. coli* that inhabit a microfabricated habitat. These two strains do not stably coexist when cocultured in a well-mixed flask where resource competition (due to mixing) is global. However, in a habitat that is spatially structured by microfabrication, cooperator and cheater bacteria only compete with their local neighbors and self-organize into a structured community in which cooperators and cheaters coexist (*90*).

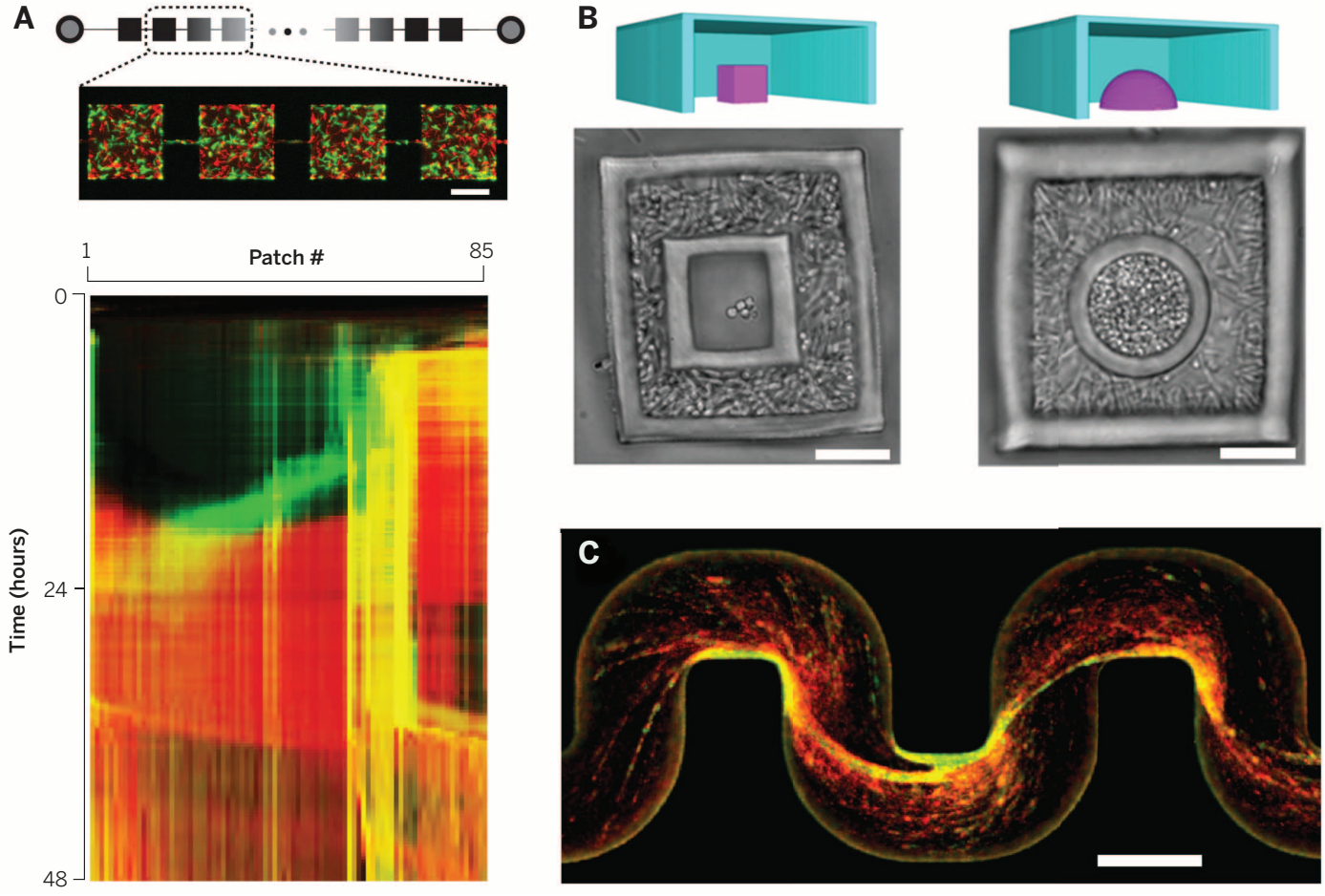

Fig. 4. Bacterial communities in synthetic ecosystems. (**A**) Kymograph of cooperator and cheater *E. coli* colonizing a microfabricated habitat consisting of 85 habitat patches (100 by 100 by 10 μm) connected by corridors. Space is depicted horizontally, and time is depicted vertically. Each pixel represents a habitat patch that is color-coded according to its cooperator (green) and cheater (red) occupancy; yellow indicates coexistence. Lateral population shifts occur readily, and the community remains dynamic for days. A schematic of the microhabitat, and a zoom-in of fluorescently labeled bacteria inhabiting four patches, are shown above the kymograph. Scale bar, 50 μm. [Adapted from (*90*)] (**B**) Two examples of nested communities in 3D-printed ecosystems. *S. aureus* populations confined in rectangular (left) and hemispherical (right) structures are surrounded by *P. aeruginosa*. Scale bars, 10 μm. The 3D-printed structures are porous. [Reprinted with permission from (*95*)] (**C**) *P. aeruginosa* (labeled in red) form biofilm streamers in a microfluidic flow channel. A sievelike network consisting of bacteria and extracellular polymeric substances (labeled in green) can be discerned. Over time, the build-up of cells and EPS forms a network that eventually clogs the flow channel. Scale bar, 200 μm. [Reprinted with permission from (*93*)]

An important aspect of bacterial life is the formation of biofilms. Microfluidics have been used to investigate how bacteria form biofilm streamers to enhance their survival in porous habitats (*91*–*93*). Streamers formed by *P. aeruginosa* growing in a meandering flow channel are shown in Fig. 4C. Biofilms that initially grow on the channel walls secrete extracellular polymeric substances (EPS) that form a sievelike network spanning the full width of the channel. As the biofilm constantly sheds bacteria, those planktonic cells get "caught" in the EPS network. The gradual build-up of biofilm streamers eventually leads to a catastrophic clogging event and the abrupt cessation of flow. Such an extraordinary ability of bacterial communities to self-structure, organize, and modify their environment is a central theme that emerges in various studies that use synthetic ecosystems.

A promising recent innovation is provided by the 3D printing of bacterial ecosystems by use of multiphoton lithography (*94*, *95*). Connell *et al.* confined defined bacterial populations within 3D-printed containers consisting of photo-crosslinked gelatin and protein. These ecosystems can have arbitrary 3D shapes, while the gelatin matrix allows diffusion through the walls, facilitating chemical interactions between confined populations. A population of *S. aureus* is shown in Fig. 4B contained in a 3D-printed structure embedded within a population of *P. aeruginosa*. This technique can potentially be used to reproduce the spatial structure and species-composition of complex natural communities in an experimentally accessible manner.

Studies such as (*93*, *95*, *96*) are examples of the move toward laboratory experiments that strive to be a realistic representation of the natural environment while retaining a high degree of experimental control and permitting visualization at high spatiotemporal resolution. This development will not only continue to enhance our understanding of the intricacies of bacterial communities but will also prove to be beneficial for the development of new approaches to manage bacteria in clinical and industrial settings.

Breaking down bacterial communities

Microfluidic platforms enable researchers not only to perform controlled ecological experiments in well-defined ecosystems but also facilitate the characterization of naturally occurring communities. It is estimated that less than 1% of all existing bacterial species is culturable (*84*). The vast majority of Earth's bacterial diversity—the so-called "dark matter of biology"—can thus currently not be analyzed from pure culture and hence remains mysterious (*97*). In addition to satisfying our curiosity about the natural world, analyzing and culturing these species may unlock a vast repertoire of useful, but currently unknown, chemical compounds.

Microfluidic techniques are currently unveiling various secrets of the unculturable majority by enabling the isolation and analysis of individual bacteria from environmental samples. The ability to confine individual cells in microfluidic chambers eliminates the need for pre-analysis culturing and provides the opportunity to do single-cell genomics on cells that are obtained directly from natural communities. Target genes of interest, or the presence of phage, are identified from multiplex digital polymerase chain reaction (PCR) on individual cells. This approach has proven to be useful for characterizing environmental communities by allowing researchers to link specific species to specific community functions or identify new host-page interactions (*98*, *99*).

Owing to recent advances in on-chip, single-cell, whole-genome amplification, DNA can be obtained directly from individual cells isolated on-chip. The use of nano- or picoliter volumes in such platforms overcomes challenges posed by the amplification of contaminants when working with larger volumes (*100*–*102*). The obtained DNA can subsequently be used for off-chip analyses such as genome sequencing. Such approaches have resulted in the genome sequence of various unculturable species coming from habitats including the human mouth (*97*) and various aquatic ecosystems (*103*, *104*). In earlier work using microfluidic devices to isolate bacteria, single cells were usually obtained probabilistically by dispersing cells over many isolation chambers. The integration of micro- and optofluidics, however, now facilitates targeted isolation of single cells and allows for additional selection criteria such as morphology or size.

Apart from enabling the analysis of single isolated bacteria, microfluidic techniques may also be used to develop new platforms that permit the culturing of the uncultured (*105*, *106*). A bottleneck that is prohibiting the culturing of certain species is the dependence on factors secreted by other microbes that are part of their natural ecology (*107*). Microfluidic approaches are ideally suited to physically separate cells or small populations while allowing chemical communication to take place between them. Approaches that allow several species to collectively define the chemical complexity of the medium while retaining the contributing cells in pure culture could, for instance, be implemented by using the on-chip ecosystems or 3D-printing technique described above. Other techniques that establish the physical segregation of populations while allowing chemical interactions rely on coupling separate culturing wells through a porous membrane (*8*) or hydrogel (*108*) or use shallow slits that prevent cellular migration from one compartment to the other (*87*, *109*). We expect that these and other (*110*) approaches will prove to be valuable tools to unravel the complexity of natural bacterial communities.

Looking ahead

Microfluidic devices are beginning to be common in microbiology laboratories. This trend undoubtedly will continue because microbiologists have a need for tools that allow precise measurements in environments that can be manipulated at the microscale. Reproducible and controlled experiments are needed to enhance our understanding of bacterial individuality and to unravel complex processes that rely on the coordinated action of many cells, such as biofilm formation. In addition to the techniques reviewed above, imaging mass spectrometry approaches [for example, reviewed in (*56*) and (*111*)] have reached subcellular resolution. Although the required sample preparation currently complicates the integration of such approaches with microfluidic platforms, the possibility to add high-resolution spatial information about the chemical composition of a sample to the phenotypes observed on-chip is promising.

Another emerging trend is the use of bacterial communities inhabiting engineered landscapes as model systems for sociomicrobiology (*9*, *10*, *90*, *112*). The ability to track large numbers of individual cells competing in complex landscapes makes synthetic ecosystems ideally suited to test ecological predictions concerning the environmental conditions that favor cooperation or the implications of habitat structure for biodiversity. The opportunity to probe the same community in diverse ecological scenarios undoubtedly will be valuable to elucidate bacterial social behaviors. Single-cell genomics approaches using novel microfluidic platforms will likely be key to uncover the dark matter of biology. Efforts aimed at dissecting natural bacterial communities are currently only scratching the surface of the vast repertoire of useful substances that presumably are produced by unculturable species. Among those, new classes of antibiotics may, for example, be identified. Other areas of research in which nanotechnology-driven basic research may find important practical applications are the development of microbial fuel cells and the production of nanostructured antibacterial surfaces.

It has been approximately a decade since nanotechnology and microfluidics gained a foothold in microbiology laboratories as new tools with which to study bacteria. This endeavor led to the development of powerful new tools and yielded fundamental biological insights. However, many open questions remain, and exciting times lie ahead at the crossroads of microbiology, microfluidics, and nanofabrication. A further integration of these disciplines will facilitate a deeper understanding of bacterial life by focusing on the details of single cells and broadening our perspective on complex multispecies communities.

REFERENCES AND NOTES

1. M. Vos, A. B. Wolf, S. J. Jennings, G. A. Kowalchuk, Micro-scale determinants of bacterial diversity in soil. *FEMS Microbiol. Rev.* **37**, 936–954 (2013). pmid: 23550883
2. X. Raynaud, N. Nunan, Spatial ecology of bacteria at the microscale in soil. *PLOS ONE* **9**, e87217 (2014). doi: 10.1371/journal.pone.0087217; pmid: 24489873
3. R. Stocker, Marine microbes see a sea of gradients. *Science* **338**, 628–633 (2012). doi: 10.1126/science.1208929; pmid: 23118182
4. L. Dethlefsen, P. B. Eckburg, E. M. Bik, D. A. Relman, Assembly of the human intestinal microbiota. *Trends Ecol. Evol.* **21**, 517–523 (2006). doi: 10.1016/j.tree.2006.06.013; pmid: 16820245
5. R. S. Friedlander *et al.*, Bacterial flagella explore microscale hummocks and hollows to increase adhesion. *Proc. Natl. Acad. Sci. U.S.A.* **110**, 5624–5629 (2013). doi: 10.1073/pnas.1219662110; pmid: 23509269

6. X. Jiang *et al*., Probing single- to multi-cell level charge transport in *Geobacter sulfurreducens* DL-1. *Nat. Commun.* **4**, 2751 (2013). doi: 10.1038/ncomms3751; pmid: 24202068
7. J. E. Keymer, P. Galajda, C. Muldoon, S. Park, R. H. Austin, Bacterial metapopulations in nanofabricated landscapes. *Proc. Natl. Acad. Sci. U.S.A.* **103**, 17290–17295 (2006). doi: 10.1073/pnas.0607971103; pmid: 17090676
8. H. J. Kim, J. Q. Boedicker, J. W. Choi, R. F. Ismagilov, Defined spatial structure stabilizes a synthetic multispecies bacterial community. *Proc. Natl. Acad. Sci. U.S.A.* **105**, 18188–18193 (2008). doi: 10.1073/pnas.0807935105; pmid: 19011107
9. J. E. Keymer, P. Galajda, G. Lambert, D. Liao, R. H. Austin, Computation of mutual fitness by competing bacteria. *Proc. Natl. Acad. Sci. U.S.A.* **105**, 20269–20273 (2008). doi: 10.1073/pnas.0810792105; pmid: 19074280
10. K. Drescher, C. D. Nadell, H. A. Stone, N. S. Wingreen, B. L. Bassler, Solutions to the public goods dilemma in bacterial biofilms. *Curr. Biol.* **24**, 50–55 (2014). doi: 10.1016/j.cub.2013.10.030; pmid: 24332540
11. Q. Zhang *et al*., Acceleration of emergence of bacterial antibiotic resistance in connected microenvironments. *Science* **333**, 1764–1767 (2011). doi: 10.1126/science.1208747; pmid: 21940899
12. M. Ackermann, S. C. Stearns, U. Jenal, Senescence in a bacterium with asymmetric division. *Science* **300**, 1920 (2003). doi: 10.1126/science.1083532; pmid: 12817142
13. P. Wang *et al*., Robust growth of *Escherichia coli*. *Curr. Biol.* **20**, 1099–1103 (2010). doi: 10.1016/j.cub.2010.04.045; pmid: 20537537
14. E. J. Stewart, R. Madden, G. Paul, F. Taddei, Aging and death in an organism that reproduces by morphologically symmetric division. *PLOS Biol.* **3**, e45 (2005). doi: 10.1371/journal.pbio.0030045; pmid: 15685293
15. A. B. Lindner, R. Madden, A. Demarez, E. J. Stewart, F. Taddei, Asymmetric segregation of protein aggregates is associated with cellular aging and rejuvenation. *Proc. Natl. Acad. Sci. U.S.A.* **105**, 3076–3081 (2008). doi: 10.1073/pnas.0708931105; pmid: 18287048
16. T. M. Norman, N. D. Lord, J. Paulsson, R. Losick, Memory and modularity in cell-fate decision making. *Nature* **503**, 481–486 (2013). doi: 10.1038/nature12804; pmid: 24256735
17. J. Bigger, Treatment of staphylococcal infections with penicillin by intermittent sterilisation. *Lancet* **244**, 497–500 (1944). doi: 10.1016/S0140-6736(00)74210-3
18. N. Q. Balaban, J. Merrin, R. Chait, L. Kowalik, S. Leibler, Bacterial persistence as a phenotypic switch. *Science* **305**, 1622–1625 (2004). doi: 10.1126/science.1099390; pmid: 15308767
19. O. Gefen, C. Gabay, M. Mumcuoglu, G. Engel, N. Q. Balaban, Single-cell protein induction dynamics reveals a period of vulnerability to antibiotics in persister bacteria. *Proc. Natl. Acad. Sci. U.S.A.* **105**, 6145–6149 (2008). doi: 10.1073/pnas.0711712105; pmid: 18427112
20. Y. Wakamoto *et al*., Dynamic persistence of antibiotic-stressed mycobacteria. *Science* **339**, 91–95 (2013). doi: 10.1126/science.1229858; pmid: 23288538
21. J. R. Moffitt, J. B. Lee, P. Cluzel, The single-cell chemostat: An agarose-based, microfluidic device for high-throughput, single-cell studies of bacteria and bacterial communities. *Lab Chip* **12**, 1487–1494 (2012). doi: 10.1039/c2lc00009a; pmid: 22395180
22. M. C. Moolman, Z. Huang, S. T. Krishnan, J. W. J. Kerssemakers, N. H. Dekker, Electron beam fabrication of a microfluidic device for studying submicron-scale bacteria. *J. Nanobiotechnol.* **11**, 12 (2013). doi: 10.1186/1477-3155-11-12; pmid: 23575419
23. Z. Long *et al*., Microfluidic chemostat for measuring single cell dynamics in bacteria. *Lab Chip* **13**, 947–954 (2013). doi: 10.1039/c2lc41196b; pmid: 23334753
24. P. Chen *et al*., Nanoscale probing the kinetics of oriented bacterial cell growth using atomic force microscopy. *Small* **10**, 3018–3025 (2014). doi: 10.1002/smll.201303724; pmid: 24706390
25. S.-W. Teng, S. Mukherji, J. R. Moffitt, S. de Buyl, E. K. O'Shea, Robust circadian oscillations in growing cyanobacteria require transcriptional feedback. *Science* **340**, 737–740 (2013). doi: 10.1126/science.1230996; pmid: 23661759
26. J. Männik, R. Driessen, P. Galajda, J. E. Keymer, C. Dekker, Bacterial growth and motility in sub-micron constrictions. *Proc. Natl. Acad. Sci. U.S.A.* **106**, 14861–14866 (2009). doi: 10.1073/pnas.0907542106; pmid: 19706420
27. J. Männik *et al*., Robustness and accuracy of cell division in *Escherichia coli* in diverse cell shapes. *Proc. Natl. Acad. Sci. U.S.A.* **109**, 6957–6962 (2012). doi: 10.1073/pnas.1120854109; pmid: 22509007
28. S. Takeuchi, W. R. DiLuzio, D. B. Weibel, G. M. Whitesides, Controlling the shape of filamentous cells of *Escherichia coli*. *Nano Lett.* **5**, 1819–1823 (2005). doi: 10.1021/nl0507360; pmid: 16159230
29. L. D. Renner, D. B. Weibel, Cardiolipin microdomains localize to negatively curved regions of *Escherichia coli* membranes. *Proc. Natl. Acad. Sci. U.S.A.* **108**, 6264–6269 (2011). doi: 10.1073/pnas.1015757108; pmid: 21444798
30. L. D. Renner, P. Eswaramoorthy, K. S. Ramamurthi, D. B. Weibel, Studying biomolecule localization by engineering bacterial cell wall curvature. *PLOS One* **8**, e84143 (2013). doi: 10.1371/journal.pone.0084143; pmid: 24391905
31. K. D. Young, The selective value of bacterial shape. *Microbiol. Mol. Biol. Rev.* **70**, 660–703 (2006). doi: 10.1128/MMBR.00001-06; pmid: 16959965
32. Y. Caspi, Deformation of filamentous *Escherichia coli* cells in a microfluidic device: A new technique to study cell mechanics. *PLOS One* **9**, e83775 (2014). doi: 10.1371/journal.pone.0083775; pmid: 24392095
33. A. Amir, F. Babaeipour, D. B. McIntosh, D. R. Nelson, S. Jun, Bending forces plastically deform growing bacterial cell walls. *Proc. Natl. Acad. Sci. U.S.A.* **111**, 5778–5783 (2014). doi: 10.1073/pnas.1317497111; pmid: 24711421
34. L. A. Pratt, R. Kolter, Genetic analysis of *Escherichia coli* biofilm formation: Roles of flagella, motility, chemotaxis and type I pili. *Mol. Microbiol.* **30**, 285–293 (1998). doi: 10.1046/j.1365-2958.1998.01061.x; pmid: 9791174
35. E. P. Ivanova *et al*., Differential attraction and repulsion of *Staphylococcus aureus* and *Pseudomonas aeruginosa* on molecularly smooth titanium films. *Sci. Rep.* **1**, 165 (2011). doi: 10.1038/srep00165; pmid: 22355680
36. K. A. Whitehead, J. Colligon, J. Verran, Retention of microbial cells in substratum surface features of micrometer and sub-micrometer dimensions. *Colloids Surf. B Biointerfaces* **41**, 129–138 (2005). doi: 10.1016/j.colsurfb.2004.11.010; pmid: 15737538
37. E. Fadeeva *et al*., Bacterial retention on superhydrophobic titanium surfaces fabricated by femtosecond laser ablation. *Langmuir* **27**, 3012–3019 (2011). doi: 10.1021/la104607g; pmid: 21288031
38. A. V. Singh *et al*., Quantitative characterization of the influence of the nanoscale morphology of nanostructured surfaces on bacterial adhesion and biofilm formation. *PLOS One* **6**, e25029 (2011). doi: 10.1371/journal.pone.0025029; pmid: 21966403
39. L. D. Renner, D. B. Weibel, Physicochemical regulation of biofilm formation. *MRS Bull.* **36**, 347–355 (2011). doi: 10.1557/mrs.2011.65; pmid: 22125358
40. J. Hasan, R. J. Crawford, E. P. Ivanova, Antibacterial surfaces: The quest for a new generation of biomaterials. *Trends Biotechnol.* **31**, 295–304 (2013). doi: 10.1016/j.tibtech.2013.01.017; pmid: 23434154
41. H. E. Jeong, I. Kim, P. Karam, H.-J. Choi, P. Yang, Bacterial recognition of silicon nanowire arrays. *Nano Lett.* **13**, 2864–2869 (2013). doi: 10.1021/nl401205b; pmid: 23682751
42. A. I. Hochbaum, J. Aizenberg, Bacteria pattern spontaneously on periodic nanostructure arrays. *Nano Lett.* **10**, 3717–3721 (2010). doi: 10.1021/nl102290k; pmid: 20687595
43. M. A.-S. Vigeant, R. M. Ford, M. Wagner, L. K. Tamm, Reversible and irreversible adhesion of motile *Escherichia coli* cells analyzed by total internal reflection aqueous fluorescence microscopy. *Appl. Environ. Microbiol.* **68**, 2794–2801 (2002). doi: 10.1128/AEM.68.6.2794-2801.2002; pmid: 12039734
44. A. P. Berke, L. Turner, H. C. Berg, E. Lauga, Hydrodynamic attraction of swimming microorganisms by surfaces. *Phys. Rev. Lett.* **101**, 038102 (2008). doi: 10.1103/PhysRevLett.101.038102; pmid: 18764299
45. W. R. DiLuzio *et al*., *Escherichia coli* swim on the right-hand side. *Nature* **435**, 1271–1274 (2005). doi: 10.1038/nature03660; pmid: 15988531
46. R. Di Leonardo *et al*., Swimming with an image. *Phys. Rev. Lett.* **106**, 038101 (2011). doi: 10.1103/PhysRevLett.106.038101
47. P. Galajda, J. Keymer, P. Chaikin, R. Austin, A wall of funnels concentrates swimming bacteria. *J. Bacteriol.* **189**, 8704–8707 (2007). doi: 10.1128/JB.01033-07; pmid: 17890308
48. P. Galajda *et al*., Funnel ratchets in biology at low Reynolds number: Choanotaxis. *J. Mod. Opt.* **55**, 3413–3422 (2008). doi: 10.1080/09500340802495826
49. S. Elizabeth Hulme *et al*., Using ratchets and sorters to fractionate motile cells of *Escherichia coli* by length. *Lab Chip* **8**, 1888–1895 (2008). doi: 10.1039/b809892a; pmid: 18941690
50. T. Ahmed, T. S. Shimizu, R. Stocker, Bacterial chemotaxis in linear and nonlinear steady microfluidic gradients. *Nano Lett.* **10**, 3379–3385 (2010). doi: 10.1021/nl101204e; pmid: 20669946
51. J. Saragosti *et al*., Directional persistence of chemotactic bacteria in a traveling concentration wave. *Proc. Natl. Acad. Sci. U.S.A.* **108**, 16235–16240 (2011). doi: 10.1073/pnas.1101996108; pmid: 21918111
52. H. Mao, P. S. Cremer, M. D. Manson, A sensitive, versatile microfluidic assay for bacterial chemotaxis. *Proc. Natl. Acad. Sci. U.S.A.* **100**, 5449–5454 (2003). doi: 10.1073/pnas.0931258100; pmid: 12704234
53. R. Stocker, J. R. Seymour, A. Samadani, D. E. Hunt, M. F. Polz, Rapid chemotactic response enables marine bacteria to exploit ephemeral microscale nutrient patches. *Proc. Natl. Acad. Sci. U.S.A.* **105**, 4209–4214 (2008). doi: 10.1073/pnas.0709765105; pmid: 18337491
54. J. R. Seymour, R. Marcos, R. Stocker, Resource patch formation and exploitation throughout the marine microbial food web. *Am. Nat.* **173**, E15–E29 (2009). doi: 10.1086/593004; pmid: 19053839
55. T. Ahmed, T. S. Shimizu, R. Stocker, Microfluidics for bacterial chemotaxis. *Integr. Biol. (Camb)* **2**, 604–629 (2010). doi: 10.1039/c0ib00049c; pmid: 20967322
56. A. K. Wessel, L. Hmelo, M. R. Parsek, M. Whiteley, Going local: Technologies for exploring bacterial microenvironments. *Nat. Rev. Microbiol.* **11**, 337–348 (2013). doi: 10.1038/nrmicro3010; pmid: 23588251
57. D. B. Weibel *et al*., Microoxen: Microorganisms to move microscale loads. *Proc. Natl. Acad. Sci. U.S.A.* **102**, 11963–11967 (2005). doi: 10.1073/pnas.0505481102; pmid: 16103369
58. Y. Hiratsuka, M. Miyata, T. Tada, T. Q. P. Uyeda, A microrotary motor powered by bacteria. *Proc. Natl. Acad. Sci. U.S.A.* **103**, 13618–13623 (2006). doi: 10.1073/pnas.0604122103; pmid: 16950878
59. R. Di Leonardo *et al*., Bacterial ratchet motors. *Proc. Natl. Acad. Sci. U.S.A.* **107**, 9541–9545 (2010). doi: 10.1073/pnas.0910426107; pmid: 20457936
60. A. Sokolov, M. M. Apodaca, B. A. Grzybowski, I. S. Aranson, Swimming bacteria power microscopic gears. *Proc. Natl. Acad. Sci. U.S.A.* **107**, 969–974 (2010). doi: 10.1073/pnas.0913015107; pmid: 20080560
61. N. Koumakis, A. Lepore, C. Maggi, R. Di Leonardo, Targeted delivery of colloids by swimming bacteria. *Nat. Commun.* **4**, 2588 (2013). doi: 10.1038/ncomms3588; pmid: 24100868
62. D. R. Bond, D. E. Holmes, L. M. Tender, D. R. Lovley, Electrode-reducing microorganisms that harvest energy from marine sediments. *Science* **295**, 483–485 (2002). doi: 10.1126/science.1066771; pmid: 11799240
63. D. R. Lovley, Bug juice: Harvesting electricity with microorganisms. *Nat. Rev. Microbiol.* **4**, 497–508 (2006). doi: 10.1038/nrmicro1442; pmid: 16778836
64. B. E. Logan, K. Rabaey, Conversion of wastes into bioelectricity and chemicals by using microbial electrochemical technologies. *Science* **337**, 686–690 (2012). doi: 10.1126/science.1217412; pmid: 22879507
65. D. R. Lovley, Electromicrobiology. *Annu. Rev. Microbiol.* **66**, 391–409 (2012). doi: 10.1146/annurev-micro-092611-150104; pmid: 22746334
66. A. G. Smart, Two experiments, two takes on electric bacteria. *Phys. Today* **63**, 18–20 (2010). doi: 10.1063/1.3529396
67. N. S. Malvankar, D. R. Lovley, Microbial nanowires: A new paradigm for biological electron transfer and bioelectronics. *ChemSusChem* **5**, 1039–1046 (2012). doi: 10.1002/cssc.201100733; pmid: 22614997
68. X. Jiang *et al*., Probing electron transfer mechanisms in *Shewanella oneidensis* MR-1 using a nanoelectrode platform and single-cell imaging. *Proc. Natl. Acad. Sci. U.S.A.* **107**, 16806–16810 (2010). doi: 10.1073/pnas.1011699107; pmid: 20837546
69. Y. A. Gorby *et al*., Electrically conductive bacterial nanowires produced by *Shewanella oneidensis* strain MR-1 and other microorganisms. *Proc. Natl. Acad. Sci. U.S.A.* **103**, 11358–11363 (2006). doi: 10.1073/pnas.0604517103; pmid: 16849424
70. M. Y. El-Naggar *et al*., Electrical transport along bacterial nanowires from *Shewanella oneidensis* MR-1. *Proc. Natl. Acad. Sci. U.S.A.* **107**, 18127–18131 (2010). doi: 10.1073/pnas.1004880107; pmid: 20937892
71. N. S. Malvankar *et al*., Tunable metallic-like conductivity in microbial nanowire networks. *Nat. Nanotechnol.* **6**, 573–579 (2011). doi: 10.1038/nnano.2011.119; pmid: 21822253

72. C. Pfeffer *et al*., Filamentous bacteria transport electrons over centimetre distances. *Nature* **491**, 218–221 (2012). doi: 10.1038/nature11586; pmid: 23103872
73. G. Reguera *et al*., Extracellular electron transfer via microbial nanowires. *Nature* **435**, 1098–1101 (2005). doi: 10.1038/nature03661; pmid: 15973408
74. B. L. Bassler, R. Losick, Bacterially speaking. *Cell* **125**, 237–246 (2006). doi: 10.1016/j.cell.2006.04.001; pmid: 16630813
75. T. Danino, O. Mondragón-Palomino, L. Tsimring, J. Hasty, A synchronized quorum of genetic clocks. *Nature* **463**, 326–330 (2010). doi: 10.1038/nature08753; pmid: 20090747
76. R. J. Redfield, Is quorum sensing a side effect of diffusion sensing? *Trends Microbiol.* **10**, 365–370 (2002). doi: 10.1016/S0966-842X(02)02400-9; pmid: 12160634
77. B. A. Hense *et al*., Does efficiency sensing unify diffusion and quorum sensing? *Nat. Rev. Microbiol.* **5**, 230–239 (2007). doi: 10.1038/nrmicro1600; pmid: 17304251
78. S. A. West, K. Winzer, A. Gardner, S. P. Diggle, Quorum sensing and the confusion about diffusion. *Trends Microbiol.* **20**, 586–594 (2012). doi: 10.1016/j.tim.2012.09.004; pmid: 23084573
79. J. Q. Boedicker, M. E. Vincent, R. F. Ismagilov, Microfluidic confinement of single cells of bacteria in small volumes initiates high-density behavior of quorum sensing and growth and reveals its variability. *Angew. Chem. Int. Ed. Engl.* **48**, 5908–5911 (2009). doi: 10.1002/anie.200901550; pmid: 19565587
80. E. C. Carnes *et al*., Confinement-induced quorum sensing of individual *Staphylococcus aureus* bacteria. *Nat. Chem. Biol.* **6**, 41–45 (2010). doi: 10.1038/nchembio.264; pmid: 19935660
81. Y. Lu *et al*., Aerosol-assisted self-assembly of mesostructured spherical nanoparticles. *Nature* **398**, 223–226 (1999). doi: 10.1038/18410
82. H. K. Baca *et al*., Cell-directed assembly of lipid-silica nanostructures providing extended cell viability. *Science* **313**, 337–341 (2006). doi: 10.1126/science.1126590; pmid: 16857936
83. M. Weitz *et al*., Communication and computation by bacteria compartmentalized within microemulsion droplets. *J. Am. Chem. Soc.* **136**, 72–75 (2014). doi: 10.1021/ja411132w; pmid: 24358940
84. M. S. Rappé, S. J. Giovannoni, The uncultured microbial majority. *Annu. Rev. Microbiol.* **57**, 369–394 (2003). doi: 10.1146/annurev.micro.57.030502.090759; pmid: 14527284
85. S. Park *et al*., Motion to form a quorum. *Science* **301**, 188 (2003). doi: 10.1126/science.1079805; pmid: 12855801
86. S. Park *et al*., Influence of topology on bacterial social interaction. *Proc. Natl. Acad. Sci. U.S.A.* **100**, 13910–13915 (2003). doi: 10.1073/pnas.1935975100; pmid: 14623970
87. S. van Vliet, F. J. Hol, T. Weenink, P. Galajda, J. E. Keymer, The effects of chemical interactions and culture history on the colonization of structured habitats by competing bacterial populations. *BMC Microbiol.* **14**, 116 (2014). doi: 10.1186/1471-2180-14-116; pmid: 24884963
88. F. J. H. Hol, M. J. Voges, C. Dekker, J. E. Keymer, Nutrient-responsive regulation determines biodiversity in a colicin-mediated bacterial community. *BMC Biol.* **12**, 68 (2014). doi: 10.1186/s12915-014-0068-2; pmid: 25159553
89. T. Julou *et al*., Cell-cell contacts confine public goods diffusion inside *Pseudomonas aeruginosa* clonal microcolonies. *Proc. Natl. Acad. Sci. U.S.A.* **110**, 12577–12582 (2013). doi: 10.1073/pnas.1301428110; pmid: 23858453
90. F. J. H. Hol *et al*., Spatial structure facilitates cooperation in a social dilemma: Empirical evidence from a bacterial community. *PLOS ONE* **8**, e77042 (2013). doi: 10.1371/journal.pone.0077042; pmid: 24167557
91. R. Rusconi, S. Lecuyer, L. Guglielmini, H. A. Stone, Laminar flow around corners triggers the formation of biofilm streamers. *J. R. Soc. Interface* **7**, 1293–1299 (2010). doi: 10.1098/rsif.2010.0096; pmid: 20356880
92. R. Rusconi, S. Lecuyer, N. Autrusson, L. Guglielmini, H. A. Stone, Secondary flow as a mechanism for the formation of biofilm streamers. *Biophys. J.* **100**, 1392–1399 (2011). doi: 10.1016/j.bpj.2011.01.065; pmid: 21402020
93. K. Drescher, Y. Shen, B. L. Bassler, H. A. Stone, Biofilm streamers cause catastrophic disruption of flow with consequences for environmental and medical systems. *Proc. Natl. Acad. Sci. U.S.A.* **110**, 4345–4350 (2013). doi: 10.1073/pnas.1300321110; pmid: 23401501
94. J. L. Connell *et al*., Probing prokaryotic social behaviors with bacterial "lobster traps". *MBio* **1**, e00202-10 (2010). doi: 10.1128/mBio.00202-10; pmid: 21060734
95. J. L. Connell, E. T. Ritschdorff, M. Whiteley, J. B. Shear, 3D printing of microscopic bacterial communities. *Proc. Natl. Acad. Sci. U.S.A.* **110**, 18380–18385 (2013). doi: 10.1073/pnas.1309729110; pmid: 24101503
96. H. J. Kim, D. Huh, G. Hamilton, D. E. Ingber, Human gut-on-a-chip inhabited by microbial flora that experiences intestinal peristalsis-like motions and flow. *Lab Chip* **12**, 2165–2174 (2012). doi: 10.1039/c2lc40074j; pmid: 22434367
97. Y. Marcy *et al*., Dissecting biological "dark matter" with single-cell genetic analysis of rare and uncultivated TM7 microbes from the human mouth. *Proc. Natl. Acad. Sci. U.S.A.* **104**, 11889–11894 (2007). doi: 10.1073/pnas.0704662104; pmid: 17620602
98. E. A. Ottesen, J. W. Hong, S. R. Quake, J. R. Leadbetter, Microfluidic digital PCR enables multigene analysis of individual environmental bacteria. *Science* **314**, 1464–1467 (2006). doi: 10.1126/science.1131370; pmid: 17138901
99. A. D. Tadmor, E. A. Ottesen, J. R. Leadbetter, R. Phillips, Probing individual environmental bacteria for viruses by using microfluidic digital PCR. *Science* **333**, 58–62 (2011). doi: 10.1126/science.1200758; pmid: 21719670
100. Y. Marcy *et al*., Nanoliter reactors improve multiple displacement amplification of genomes from single cells. *PLOS Genet.* **3**, 1702–1708 (2007). doi: 10.1371/journal.pgen.0030155; pmid: 17892324
101. K. Leung *et al*., A programmable droplet-based microfluidic device applied to multiparameter analysis of single microbes and microbial communities. *Proc. Natl. Acad. Sci. U.S.A.* **109**, 7665–7670 (2012). doi: 10.1073/pnas.1106752109; pmid: 22547789
102. P. C. Blainey, The future is now: Single-cell genomics of bacteria and archaea. *FEMS Microbiol. Rev.* **37**, 407–427 (2013). doi: 10.1111/1574-6976.12015; pmid: 23298390
103. P. C. Blainey, A. C. Mosier, A. Potanina, C. A. Francis, S. R. Quake, Genome of a low-salinity ammonia-oxidizing archaeon determined by single-cell and metagenomic analysis. *PLOS One* **6**, e16626 (2011). pmid: 21364937
104. N. H. Youssef, P. C. Blainey, S. R. Quake, M. S. Elshahed, Partial genome assembly for a candidate division OP11 single cell from an anoxic spring (Zodletone Spring, Oklahoma). *Appl. Environ. Microbiol.* **77**, 7804–7814 (2011). doi: 10.1128/AEM.06059-11; pmid: 21908640
105. K. Zengler *et al*., Nonlinear partial differential equations and applications: Cultivating the uncultured. *Proc. Natl. Acad. Sci. U.S.A.* **99**, 15681–15686 (2002). doi: 10.1073/pnas.252630999; pmid: 12438682
106. E. J. Stewart, Growing unculturable bacteria. *J. Bacteriol.* **194**, 4151–4160 (2012). doi: 10.1128/JB.00345-12; pmid: 22661685
107. T. Kaeberlein, K. Lewis, S. S. Epstein, Isolating "uncultivable" microorganisms in pure culture in a simulated natural environment. *Science* **296**, 1127–1129 (2002). doi: 10.1126/science.1070633; pmid: 12004133
108. S. T. Flickinger *et al*., Quorum sensing between *Pseudomonas aeruginosa* biofilms accelerates cell growth. *J. Am. Chem. Soc.* **133**, 5966–5975 (2011). doi: 10.1021/ja111131f; pmid: 21434644
109. A. Groisman *et al*., A microfluidic chemostat for experiments with bacterial and yeast cells. *Nat. Methods* **2**, 685–689 (2005). doi: 10.1038/nmeth784; pmid: 16118639
110. D. Nichols *et al*., Use of ichip for high-throughput in situ cultivation of "uncultivable" microbial species. *Appl. Environ. Microbiol.* **76**, 2445–2450 (2010). doi: 10.1128/AEM.01754-09; pmid: 20173072
111. J. D. Watrous, P. C. Dorrestein, Imaging mass spectrometry in microbiology. *Nat. Rev. Microbiol.* **9**, 683–694 (2011). doi: 10.1038/nrmicro2634; pmid: 21822293
112. J. L. Connell, M. Whiteley, J. B. Shear, Sociomicrobiology in engineered landscapes. *Nat. Chem. Biol.* **8**, 10–13 (2012). doi: 10.1038/nchembio.749; pmid: 22173344

ACKNOWLEDGMENTS

We acknowledge invaluable discussions with J. Keymer, P. Galajda, J. Mannik, F. Wu, S. van Vliet, M. Voges, and B. Beaumont. F.J.H.H. acknowledges J. Keymer for sage advice and mentoring. This work was supported by the European Research Council Advanced Grant 247072 and the Netherlands Organisation for Scientific Research (NWO/OCW), as part of the Frontiers of Nanoscience program.

10.1126/science.1251821

RESEARCH ARTICLE SUMMARY

ADVANCED IMAGING

Lattice light-sheet microscopy: Imaging molecules to embryos at high spatiotemporal resolution

Bi-Chang Chen, Wesley R. Legant, Kai Wang, Lin Shao, Daniel E. Milkie, Michael W. Davidson, Chris Janetopoulos, Xufeng S. Wu, John A. Hammer III, Zhe Liu, Brian P. English, Yuko Mimori-Kiyosue, Daniel P. Romero, Alex T. Ritter, Jennifer Lippincott-Schwartz, Lillian Fritz-Laylin, R. Dyche Mullins, Diana M. Mitchell, Joshua N. Bembenek, Anne-Cecile Reymann, Ralph Böhme, Stephan W. Grill, Jennifer T. Wang, Geraldine Seydoux, U. Serdar Tulu, Daniel P. Kiehart, Eric Betzig*

INTRODUCTION: In vivo imaging provides a window into the spatially complex, rapidly evolving physiology of the cell that structural imaging alone cannot. However, observing this physiology directly involves inevitable tradeoffs of spatial resolution, temporal resolution, and phototoxicity. This is especially true when imaging in three dimensions, which is essential to obtain a complete picture of many dynamic subcellular processes. Although traditional in vivo imaging tools, such as widefield and confocal microscopy, and newer ones, such as light-sheet microscopy, can image in three dimensions, they sacrifice substantial spatiotemporal resolution to do so and, even then, can often be used for only very limited durations before altering the physiological state of the specimen.

RATIONALE: To address these limitations, we developed a new microscope using ultrathin light sheets derived from two-dimensional (2D) optical lattices. These are scanned plane-by-plane through the specimen to generate a 3D image. The thinness of the sheet leads to high axial resolution and negligible photobleaching and background outside of the focal plane, while its simultaneous illumination of the entire field of view permits imaging at hundreds of planes per second even at extremely low peak excitation intensities. By implementing either superresolution structured illumination or by dithering the lattice to create a uniform light sheet, we imaged cells and small embryos in three dimensions, often at subsecond intervals, for hundreds to thousands of time points at the diffraction limit and beyond.

RESULTS: We demonstrated the technique on 20 different biological processes spanning four orders of magnitude in space and time, including the binding kinetics of single Sox2 transcription factor molecules, 3D superresolution photoactivated localization microscopy of nuclear lamins, dynamic organelle rearrangements and 3D tracking of microtubule plus ends during mitosis, neutrophil motility in a collagen mesh, and subcellular protein localization and dynamics during embryogenesis in *Caenorhabditis elegans* and *Drosophila melanogaster*. Throughout, we established the performance advantages of lattice light-sheet microscopy compared with previous techniques and highlighted phenomena that, when seen at increased spatiotemporal detail, may hint at previously unknown biological mechanisms.

ON OUR WEB SITE

Read the full article at http://dx.doi.org/10.1126/science.1257998

CONCLUSION: Photobleaching and phototoxicity are typically reduced by one to two orders of magnitude relative to that seen with a 1D scanned Bessel beam or the point array scanned excitation of spinning disk confocal microscopy. This suggests that the instantaneous peak power delivered to the specimen may be an even more important metric of cell health than the total photon dose and should enable extended 3D observation of endogenous levels of even sparsely expressed proteins produced by genome editing. Improvements of similar magnitude in imaging speed and a twofold gain in axial resolution relative to confocal microscopy yield 4D spatiotemporal resolution high enough to follow fast, nanoscale dynamic processes that would otherwise be obscured by poor resolution along one or more axes of spacetime. Last, the negligible background makes lattice light-sheet microscopy a promising platform for the extension of all methods of superresolution to larger and more densely fluorescent specimens and enables the study of signaling, transport, and stochastic self-assembly in complex environments with single-molecule sensitivity. ■

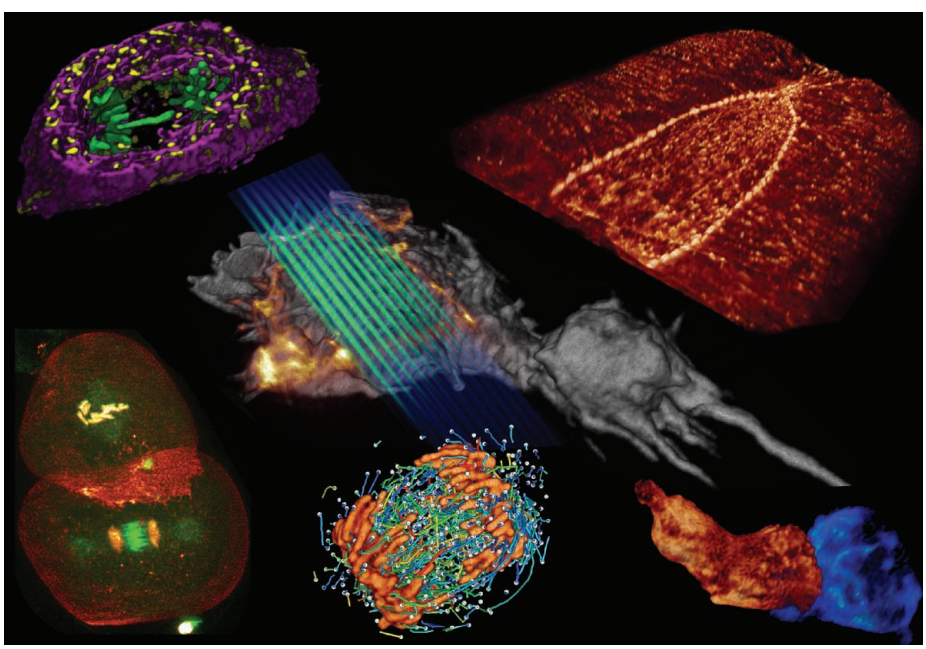

Lattice light-sheet microscopy. An ultrathin structured light sheet (blue-green, center) excites fluorescence (orange) in successive planes as it sweeps through a specimen (gray) to generate a 3D image. The speed, noninvasiveness, and high spatial resolution of this approach make it a promising tool for in vivo 3D imaging of fast dynamic processes in cells and embryos, as shown here in five surrounding examples.

The list of author affiliations is available in the full article online.
***Corresponding author. E-mail: betzige@janelia.hhmi.org**
Cite this article as B.-C. Chen *et al.*, *Science* **346**, 1257998 (2014). DOI: 10.1126/science.1257998

Published by AAAS

RESEARCH ARTICLE

ADVANCED IMAGING

Lattice light-sheet microscopy: Imaging molecules to embryos at high spatiotemporal resolution

Bi-Chang Chen,[1*†] Wesley R. Legant,[1*] Kai Wang,[1*] Lin Shao,[1] Daniel E. Milkie,[2] Michael W. Davidson,[3] Chris Janetopoulos,[4] Xufeng S. Wu,[5] John A. Hammer III,[5] Zhe Liu,[1] Brian P. English,[1] Yuko Mimori-Kiyosue,[6] Daniel P. Romero,[7] Alex T. Ritter,[8,9] Jennifer Lippincott-Schwartz,[8] Lillian Fritz-Laylin,[10] R. Dyche Mullins,[10] Diana M. Mitchell,[11‡] Joshua N. Bembenek,[11] Anne-Cecile Reymann,[12,13§] Ralph Böhme,[12,13] Stephan W. Grill,[12,13§] Jennifer T. Wang,[14] Geraldine Seydoux,[14] U. Serdar Tulu,[15] Daniel P. Kiehart,[15] Eric Betzig[1||]

Although fluorescence microscopy provides a crucial window into the physiology of living specimens, many biological processes are too fragile, are too small, or occur too rapidly to see clearly with existing tools. We crafted ultrathin light sheets from two-dimensional optical lattices that allowed us to image three-dimensional (3D) dynamics for hundreds of volumes, often at subsecond intervals, at the diffraction limit and beyond. We applied this to systems spanning four orders of magnitude in space and time, including the diffusion of single transcription factor molecules in stem cell spheroids, the dynamic instability of mitotic microtubules, the immunological synapse, neutrophil motility in a 3D matrix, and embryogenesis in *Caenorhabditis elegans* and *Drosophila melanogaster*. The results provide a visceral reminder of the beauty and the complexity of living systems.

The hallmark of life is that it is animate. Every living thing is a complex thermodynamic pocket of reduced entropy through which matter and energy flow continuously. Thus, although structural imaging is certainly informative, a more-complete understanding of how inanimate molecules assemble to create animate life requires high-resolution imaging across all four dimensions of spacetime simultaneously.

The problem is that the twin goals of high spatial resolution to see fine structural detail and high temporal resolution to follow fast dynamical processes are mutually opposed to one another: Increased spatial resolution requires more measurements, takes more time, and pumps more potentially damaging radiation into the specimen.

Fortunately, the most common tools used for in vivo molecular and organelle-specific imaging, widefield and confocal fluorescence microscopy (*1*, *2*), leave substantial room for improvement, because they each illuminate the entire thickness of the specimen, even though high-resolution information is obtained from only a single focal plane. This results in premature photobleaching and phototoxicity, limiting the duration of the imaging and altering the physiological state of the specimen.

A notable exception in this regard is light-sheet microscopy (*3*, *4*), which uses a separate excitation lens perpendicular to the widefield detection lens to confine the illumination to the neighborhood of the focal plane. This approach has proven powerful for noninvasive four-dimensional (4D) imaging of embryos at single-cell resolution (*5*, *6*); however, conventional light sheets created with Gaussian beams (Fig. 1A) are too thick over cellular dimensions to benefit subcellular imaging. In response, we introduced (*7*) "nondiffracting" Bessel beams to light sheet microscopy (Fig. 1B): When swept across the imaging focal plane, such a beam creates a virtual light sheet of submicrometer thickness well suited to noninvasive high-speed 4D live cell imaging.

In a more-recent implementation (*8*) that exploits the principles of 3D superresolution structured illumination microscopy (SIM) (*9*) for further resolution enhancement, we used a linear array of seven parallel, noninteracting Bessel beams to compensate for the additional acquisition time that SIM requires. To our surprise, we found this multiple-beam approach to be much less phototoxic than a single beam for the same total power delivered to the sample. Similar effects have been observed in spinning disk confocal microscopy (*10*), where the excitation is spread across many foci, greatly reducing the intensity at any single focus and in turn reducing the effect of nonlinear photodamage mechanisms. We therefore decided to explore means to create a thin, nondiffracting light sheet of low intensity, spread across a broad area, which would offer further gains in speed and noninvasiveness.

Lattice light sheets: Theory and performance

Our approach begins with a 2D optical lattice. Optical lattices are periodic interference patterns in two or three dimensions created by the coherent superposition of a finite number of plane waves traveling in certain well-defined directions (*11*, *12*) (fig. S1) and have been used to trap and cool atoms (*13*) or to fabricate nanolithographic structures (*14*). Like an ideal Bessel beam, an ideal 2D lattice is nondiffracting in the sense that it propagates indefinitely in a direction y without changing its cross-sectional profile, which extends infinitely in x and z. In either case, this is accomplished by confining the illumination at the rear pupil plane of the excitation objective to points on an infinitesimally thin ring. In practice, it is necessary to replace this ring with an annulus of finite thickness and to control the thickness of the annulus to confine the pattern in z, thereby producing a sheet rather than a block of light. However, this also reduces the extent in y over which the pattern is uniform, so there is a tradeoff between the thinness of the light sheet and its effective field of view in y. In the case of a Bessel beam restricted in y to cover the field of view of a typical cultured cell, there is enough energy remaining in side lobes concentric to the central beam to create substantial out-of-focus background in z when the beam is swept in x (Fig. 1B). On the other hand, we have identified (supplementary note 1) numerous 2D optical lattices that, over a similar field of view, can be optimized to either confine the excitation (*15*) tightly to the xy plane (Fig. 1C), maximize the z resolution (Fig. 1D and fig. S2) defined by the overall point spread function (PSF) of the microscope, or provide superresolution in the xz plane by SIM (fig. S3).

To create these lattices, we started with an optical path that is (fig. S4) conceptually similar to our earlier Bessel microscope (*7*, *8*). To this, we added a fast switching spatial light modulator (SLM) conjugated to the sample plane and placed before the annular mask. We write the xz cross-sectional electric field amplitude of the desired theoretical

[1]Janelia Research Campus, Howard Hughes Medical Institute, Ashburn, VA 20147, USA. [2]Coleman Technologies, Incorporated, Newtown Square, PA 19073, USA. [3]National High Magnetic Field Laboratory and Department of Biological Science, Florida State University, Tallahassee, FL 32310, USA. [4]Department of Biological Sciences, University of the Sciences, Philadelphia, PA 19104, USA. [5]Laboratory of Cell Biology, National Heart, Lung, and Blood Institute, National Institutes of Health, Bethesda, MD 20892, USA. [6]Optical Image Analysis Unit, RIKEN Center for Developmental Biology, Kobe 650-0047, Japan. [7]Department of Pharmacology, University of Minnesota, Minneapolis, MN 55455, USA. [8]Cell Biology and Metabolism Program, National Institute of Child Health and Human Development, National Institutes of Health, Bethesda, MD 20892, USA. [9]Cambridge Institute for Medical Research, Addenbrooke's Hospital, Cambridge CB2 0XY, England, UK. [10]Department of Cellular and Molecular Pharmacology, University of California, San Francisco, San Francisco, CA 94158, USA. [11]Department of Biochemistry and Cellular and Molecular Biology, University of Tennessee, Knoxville, TN 37996, USA. [12]Max Planck Institute for Molecular Cell Biology and Genetics, 01307 Dresden, Germany. [13]Max Planck Institute for the Physics of Complex Systems, 01307 Dresden, Germany. [14]Department of Molecular Biology and Genetics, Howard Hughes Medical Institute, Center for Cell Dynamics, Johns Hopkins School of Medicine, Baltimore, MD 21205, USA. [15]Department of Biology, Duke University, Durham, NC 27708, USA.
*These authors contributed equally to this work. †Present address: Research Center for Applied Sciences, Academica Sinica, Taipei 115-29, Taiwan. ‡Present address: Department of Biological Sciences, University of Idaho, Moscow, ID 83844, USA. §Present address: BIOTEC, Technische Universität Dresden, 01307 Dresden, Germany. ||Corresponding author. E-mail: betzige@janelia.hhmi.org

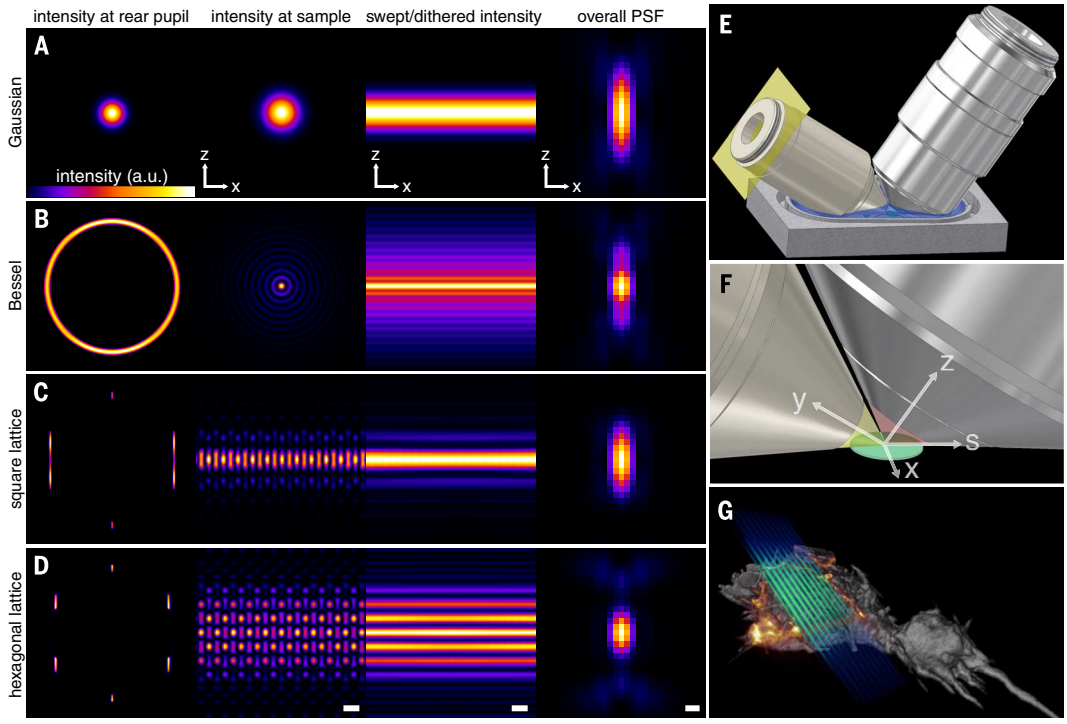

Fig. 1. Methods of light-sheet microscopy. (**A**) The traditional approach, where a Gaussian beam is swept across a plane to create the light sheet. a.u., arbitrary units. (**B**) A Bessel beam of comparable length produces a swept sheet with a much narrower core but flanked by sidebands arising from concentric side lobes of the beam. (**C** and **D**) Bound optical lattices (compare with movie S1) create periodic patterns of high modulation depth across the plane, greatly reducing the peak intensity and, as we have found, the phototoxicity in live cell imaging. The square lattice in (C) optimizes the confinement of the excitation to the central plane, and the hexagonal lattice in (D) optimizes the axial resolution as defined by the overall PSF of the microscope. The columns in (A) to (D) show the intensity pattern at the rear pupil plane of the excitation objective; the cross-sectional intensity of the pattern in the *xz* plane at the focus of the excitation objective (scale bar, 1.0 μm); the cross-sectional intensity of the light sheet created by dithering the focal pattern along the *x* axis (scale bar, 1.0 μm); and the *xz* cross section of the overall PSF of the microscope (scale bar, 200 nm). (**E**) Model showing the core of our microscope, with orthogonal excitation (left) and detection (right) objectives dipped in a media-filled bath (compare with fig. S4). (**F**) Higher magnification view, showing the excitation (yellow) and detection (red) light cones, which meet at a common focus within a specimen that is either mounted or cultured onto a cover glass within the media. The *x*, *y*, and *z* directions are indicated. The *s*-axis defines the direction the specimen moves from image plane to image plane. (**G**) Representation of a lattice light sheet (blue-green) intersecting a cell (gray) to produce fluorescence (orange) in a single plane. The cell is swept through the light sheet to generate a 3D image (compare with movie S2).

lattice light sheet as a binary phase pattern on the SLM (fig. S5). Incident laser light is then diffracted by the SLM, filtered by the mask, and focused by the excitation objective to produce a light sheet and corresponding PSFs in good agreement with theoretical predictions (fig. S6).

To apply such light sheets to in vivo imaging, the excitation objective and an orthogonal detection objective were suspended from above with their ends dipped in a shallow media-filled and temperature-controlled bath (Fig. 1E), at an angle (Fig. 1F) in the *yz* plane such that their light cones of excitation (yellow) and detection (red) lie on one side of a horizontally mounted cover slip upon which the specimen rests. The lattice light sheet created in the *xy* plane at their common foci intersects the specimen obliquely (Fig. 1G). As the specimen is moved through the light sheet, the fluorescence thereby generated is recorded as series of 2D images on a camera. These are then assembled into a 3D image, and the process is repeated to build a 4D data set of cellular dynamics.

We operated the microscope in one of two different modes: a superresolution SIM mode or a high-speed dithered mode. In the SIM mode, we recorded F images at every z plane as we stepped the lattice light sheet in the x direction in F equal fractions of the lattice period. These data were then used to reconstruct a 3D image (*9*) with resolution extended beyond the diffraction limit in x and z. In the dithered mode, we used a galvanometer (fig. S4) to oscillate the lattice pattern back and forth in x at an amplitude larger than the lattice period and a speed fast compared with the camera exposure time, providing time-averaged uniform illumination across the *xy* plane. In this mode, we needed to capture only one 2D image at each z plane, but the resolution remained diffraction-limited.

We imaged the dynamics of filopodia on HeLa cells transiently expressing mEmerald-Lifeact and found that lattice light-sheet microscopy substantially outperformed our earlier Bessel beam approach. We chose cells of similar morphology and expression level for all trials and imaged each at the same excitation power. In the SIM mode, the resolution of the two approaches (Fig. 2, A and B) and the *xz* extension beyond the diffraction limit (Fig. 2, E and F) were similar. However, in nine trials of 100 3D image volumes acquired by each approach, all cells imaged by lattice SIM exhibited minimal bleaching or changes in morphology indicative of stress, whereas all but one of the cells imaged by Bessel SIM retracted (e.g., Fig. 2B, inset), six of them within the first 50 volumes. This is likely due to the much lower intensity across the lattice light sheet, as well as the much higher signal-to-noise ratio (SNR) obtained because of its coherent modulation, versus the incoherent modulation produced with a stepped Bessel beam. In practice, this led to an ~75% reduction in the total radiation delivered and ~three times faster imaging for patterns of similar period. It also allowed us to use finer patterns (fig. S3A) that require fewer steps F per plane. As a result, over 200 3D volumes could be acquired at 4.0-s intervals by lattice SIM, 6.6 times faster than with our previous Bessel approach.

In the dithered mode, we could construct low background lattices (e.g., Fig. 1C) where nearly all the excitation is within the narrow depth of focus of a high numerical aperture ($NA_{det} = 1.1$) detection objective (fig. S7). This affords high-resolution, high-contrast 2D imaging within multicellular specimens at up to 100 frames per second for thousands of time points (movie S6). In comparison, a swept Bessel light sheet exhibited substantial out-of-focus background (Fig. 1B) over a similar field of view.

Another advantage of the dithered mode is that we can craft high-resolution lattices (e.g., Fig. 1D and fig. S2) with an even more tightly confined excitation plane, although unavoidably flanked by several progressively weaker parallel planes. However, by choosing the spacing of these planes to match the nodes of the detection PSF (fig. S7), such lattices yield 3D images of substantially higher axial resolution (Fig. 2, C and G) than can be obtained with a swept Bessel light sheet (Fig. 2, D and H). In fact, the dithered lattice resolution [as defined by the optical transfer function (OTF)] (Fig. 2G) is 230 nm in x and ~370 nm in z, assuming green fluorescent protein (GFP) excitation and emission. This is only

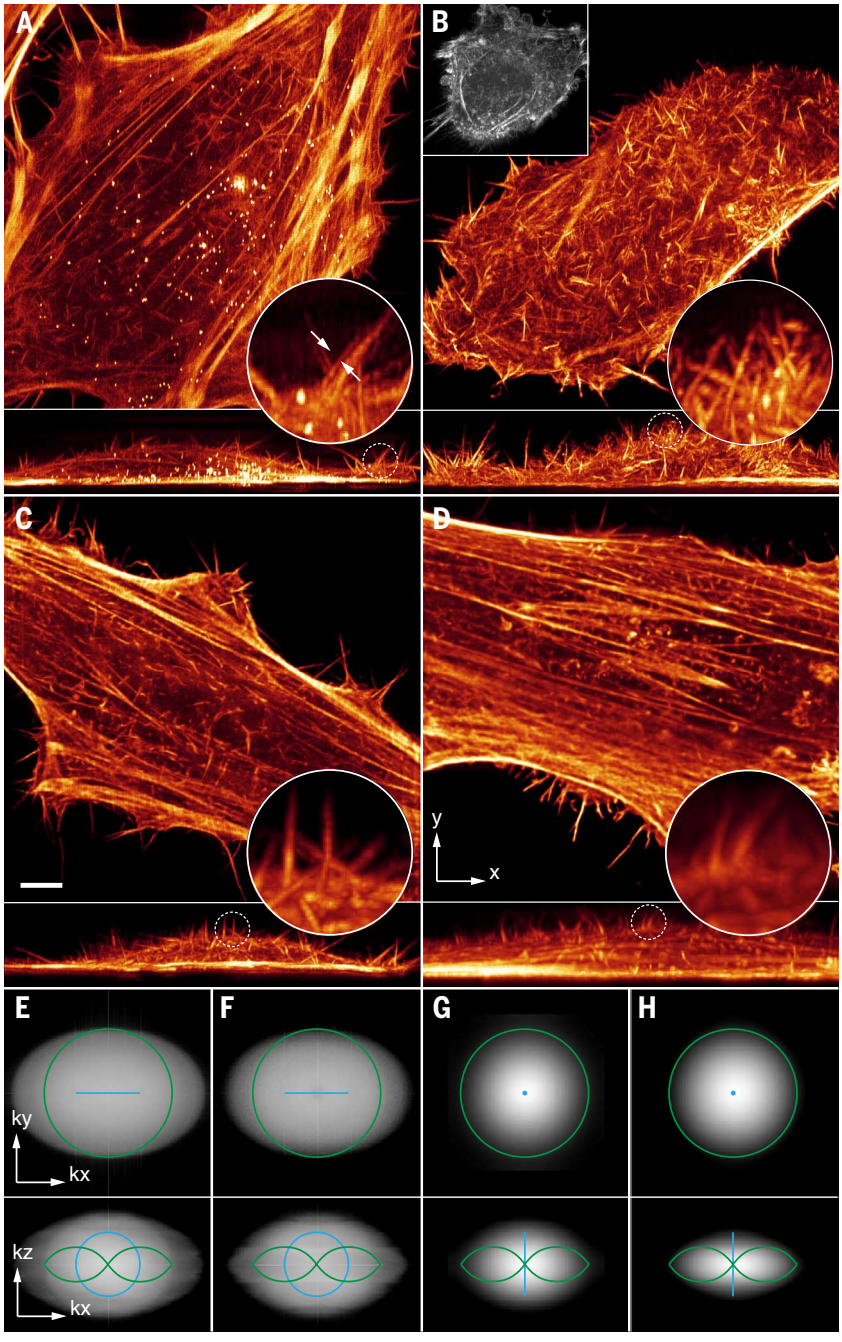

Fig. 2. Experimental comparisons of Bessel beam and lattice light-sheet microscopy. (**A**) Three-dimensional renderings in the *xy* (top) and *xz* (bottom) directions of the 300th time point of a 4D data set of a living HeLa cell transfected with mEmerald-Lifeact, taken in the SIM mode with a five-phase hexagonal lattice at 7.5-s intervals. (**B**) First time point from a different live HeLa cell imaged with a stepped Bessel beam and five-phase SIM at 30-s intervals. Square inset shows the same cell, retracted at the 32nd time point (compare with movie S3). The coherent lattice light sheet generates a pattern of much greater modulation depth (compare with movie S4), requiring less power and generating less damage to produce an image of comparable SNR. It also allows finer, three-phase patterns to be used for SIM mode imaging as fast as 4 s per volume (compare with movie S5). (**C**) The 300th time point from a third HeLa cell, acquired with a hexagonal lattice in the dithered mode at 1.5 s intervals (compare with Movie 1). Scale bar, 5 μm. The low photoxicity of this mode permits even light-sensitive specimens such as *D. discoideum* to be imaged for long periods (compare with movie S7 and Movie 3). (**D**) First time point from a fourth HeLa cell, acquired with a swept Bessel beam at 1.5-s intervals. Circular insets in (A) to (D) show magnified *xz* views of filopodia. (**E**) OTFs in log scale showing amplitudes of spatial frequencies for the hexagonal lattice SIM mode used in (A). (**F**) OTFs for the Bessel SIM mode used in (B). (**G**) OTFs for the dithered hexagonal lattice used in (C). (**H**) OTFs for the swept Bessel mode used in (D). Green curves in (E) to (H) represent the diffraction limit of the detection. Blue curves in (E) to (H) represent the diffraction limit of the excitation.

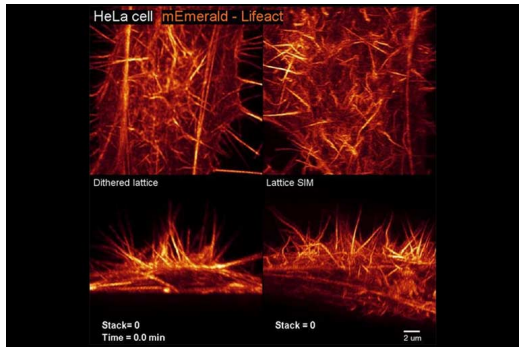

Movie 1. Top and side view volume renderings of filopodia in a HeLa cell expressing mEmerald-Lifeact. The high speed of the dithered mode of lattice light-sheet microscopy (**left**) is compared against the high resolution of the SR-SIM mode (**right**).

~1.3 to 1.5 times poorer in each direction than the 150 nm–by–280 nm *xz* resolution we obtain in the SIM mode (Fig. 2E), yet these lattices allow us to image ~7.5 times faster at comparable SNR (Movie 1). Furthermore, in the dithered mode, we can image many specimens indefinitely in 3D without photobleaching or noticeable phototoxicity. This includes even notoriously light-sensitive specimens such as *Dictyostelium discoideum*, in which we have imaged for hundreds of time points the rapid 3D dynamics of microtubules in multinucleate cells (*16*), (Movie 2, 2.0 seconds per volume); the contractile vacuole network, an extremely light-sensitive organelle composed of interconnected tubules and bladders (*17*); and filamentous cortical actin (*18*) (Movie 3, 1.0 s per volume). Thus, in practice we have found that, unless the additional resolution of the SIM mode is absolutely essential, the dithered lattice light sheet is the preferred option for most biological systems.

Single-molecule tracking and superresolution

The ability to detect and determine to nanometer precision the positions of single fluorescent molecules in vivo (*19*), either bound or diffusing, is essential to understand the molecular basis of cellular physiology. To cover cellular volumes with sufficient time resolution, widefield excitation is typically used, but the resulting out-of-focus background often limits observations to the thinner regions of single cells or confined subregions such as the plasma membrane. Light-sheet microscopy has been applied to address this issue (*20*, *21*) but with conventional Gaussian light sheets that are, over cellular dimensions, at least ~two to five times thicker than the depth of focus of a high-NA detection objective. Consequently, the majority of the illuminated molecules are still out of focus and produce large, blurred spots that cannot be localized precisely. Furthermore, very low molecular concentrations are needed to ensure that these out-of-focus spots do not overlap with the much smaller spots of in-focus molecules, compromising the localization of the latter. As a result, Gaussian light sheets substantially limit the number of molecules that can be studied per unit time and therefore the density as well as the

precision of the localization map obtained for a given total radiation dose to the specimen.

We used dithered lattice light sheets in the low-background configuration (Fig. 1C) to overcome these problems; even over a 50-μm field of view, we can still confine the excitation to a band with a full width at half maximum (FWHM) of ~1.0 μm. This is comparable to the ~1.1-μm depth of focus of the detection objective, and thus nearly all illuminated molecules are in focus. This allowed us to study the diffusion and binding kinetics of single TMR-HaloTag (Promega)–labeled Sox2 transcription factors at high SNR not in just single isolated cells at low density (*22*, *23*) but across a densely labeled ~35-μm-diameter spheroid of mouse embryonic stem cells (Fig. 3, A and B), where epi-illumination revealed nothing and single Bessel beam plane illumination exhibited much lower SNR because of side lobe excitation. Analyzed within four nuclei (Fig. 3C), the diffusion of Sox2 fit well to a biexponential curve (Fig. 3, D and E) having a fast coefficient of 0.89 ± 0.07 $\mu m^2/s$ and a slow coefficient of 0.13 ± 0.01 $\mu m^2/s$. It had been shown previously that these two diffusion coefficients represent nonspecific and DNA-specific binding interactions (*22*). In contrast, within the cytoplasm, high-speed imaging revealed that the diffusion was 10-fold greater: 8.4 ± 0.2 $\mu m^2/s$ for a coefficient representing free diffusion or directed transport into the nucleus and 0.74 ± 0.03 $\mu m^2/s$ for a coefficient related to transient, nonspecific interactions.

Another important application of single-molecule localization is superresolution microscopy (*24*). As above, this has been most often applied to single cells in order to have sufficient SNR for precise localization, although Gaussian light sheets have also been used (*25*) to extend the approach to multicellular specimens. However, in either case, out-of-focus molecules substantially reduce the median localization precision, the localization rate, and the fraction of molecules localized rather than lost to photobleaching, which together reduce the speed and resolution of the technique. These problems are exacerbated when the method is extended to 3D, where the axial position of each molecule is inferred from the shape of its image, either directly from defocus (*26*) or with applied astigmatism (*27*). Here, even under ideal circumstances, the lateral localization precision decreases rapidly with distance from the focal plane, and minute background variations resulting from neighboring molecules can render the localization inaccurate in all three dimensions.

With a dithered lattice light sheet, on the other hand, we could extend 3D localization-based superresolution to thick specimens without sacrificing the localization precision, localization rate, or fraction of total molecules localized that is achievable in the optimal limit of a thin specimen. To demonstrate, we used photoactivated localization microscopy (PALM) (*28*) with applied astigmatism to image Dendra2–lamin A at the nuclear envelope of a fixed U2OS cell. We scanned a region around the nucleus of the cell 31,600 times through the 1.1-μm-thick light sheet in 61 steps of 0.50 μm each to ensure that every molecule would be detected at high SNR and that fluorescent bead fiducial markers would be visible across multiple steps. This allowed us to accurately assemble the narrow slab of 3D localization data from each 2D image at each sample position into a much larger 3D picture encompassing the entire field of view. At each step, we applied an 8-ms pulse of 405-nm light and then imaged the molecules thereby activated for 95 ms under 560-nm excitation.

In the end, we localized 4.2×10^6 molecules with a median emission of 645 photons to a median precision of $\sigma_x = 10.4$ nm, $\sigma_y = 8.2$ nm, and $\sigma_z = 45.4$ nm (Cramer Rao lower bound) across a volume of 51 μm by 26 μm by 30 μm. Compared with a diffraction-limited, deconvolved 3D image acquired with the dithered lattice light sheet before PALM imaging (Fig. 3F), the resulting 3D PALM image (Fig. 3, G and H) reveals far more structural detail in the nuclear envelope, such as a twisted braid of lamin A on the inner surface (Fig. 3, G and H, inset). The mean localization density within this feature is 2.2×10^4 localizations/μm^3, corresponding to a resolution limit defined by the Nyquist criterion of 71 nm. An exploded view in three sections (Fig. 3H) also reveals at high resolution envelope invaginations (*29*) that form channels spanning the entire thickness of the nucleus.

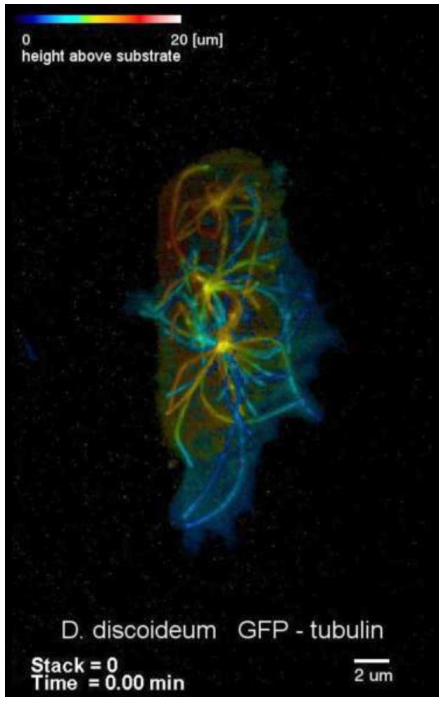

Movie 2. Top view of microtubule dynamics in multinucleate *D. discoideum* cells expressing GFP-tubulin. Cells are color-coded based on their height above the substrate, over 1430 time points at 2.0-s intervals. Rapid translational movements present in the movie represent a recentering of the organism within the microscope field of view.

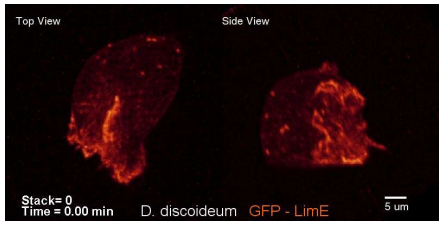

Movie 3. Top- and side-view volume renderings of actin-associated GFP-LimE in a *D. discoideum* cell. Images taken over 150 time points at 1.0-s intervals, highlighting a transient, extremely rapid "lightning bolt" of actin-rich material in the cell cortex.

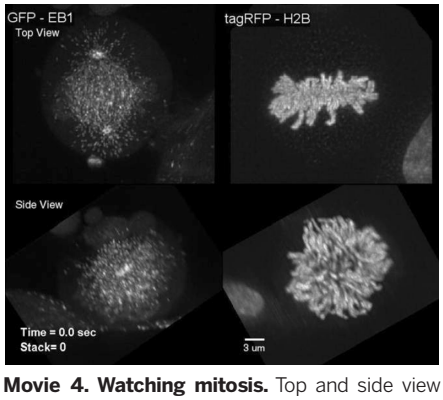

Movie 4. Watching mitosis. Top and side view maximum-intensity projections after deconvolution of GFP-EB1 at growing microtubule ends (**left**) and TagRFP-H2B highlighting chromosomes (**right**) in a HeLa cell at three different stages of mitosis.

Noninvasive 3D imaging of intracellular dynamics

The dividing cell is a spatially complex, highly dynamic environment. This is perhaps nowhere more evident than in the dynamic instability of microtubules (MTs), which undergo rapid, stochastically switched phases of growth and shrinkage during mitosis. Growing MT ends are decorated with the accessory protein EB1, which, when fluorescently labeled, provides a punctuate marker of the growing end (*30*). In interphase, it is relatively straightforward to apply 2D single-particle tracking algorithms to widefield or confocal live cell data and quantify this growth in space and time. In mitosis, however, the thickness of the cell and density and speed of these punctae (Movie 4) demand a much higher level of 4D spatiotemporal resolution to allow them to be isolated and tracked precisely. Such resolution is afforded by the dithered lattice light sheet.

To demonstrate, we imaged HeLa cells stably expressing GFP-EB1 and mTagRFP-H2B throughout mitosis, identified the stage of mitosis by the morphology of the chromosomes (from H2B), and quantified the EB1 tracks with a 2D algorithm (*31*) that we modified for 3D. From these data, we were able to extract the 3D microtubule tip positions, growth phase lifetimes, and growth velocities across the entire cell. In a typical experiment (Fig. 4A and Movie 5), we recorded ~100 two-color 3D volumes at 1.5-s intervals, waited 5 to 10 min for the cell to recover from the excitation while it advanced to a later stage, and then repeated this process through cytokinesis. Despite the extreme sensitivity of the cell during mitosis (*32*), we could often record ~500 3D volumes in each trial, yet still each cell would pass through its mitotic checkpoints and divide

normally. Quantification from 12 cells (fig. S8) revealed that microtubule (MT) growth accelerates during the early stages of mitosis, doubling velocity by prometaphase/metaphase, and then gradually decelerates until reaching the original interphase velocity distribution in cytokinesis. Although harder to quantify, 3D images also suggest a higher mean velocity for kinetochore MT growth than astral MT growth during anaphase/telophase (fig. S8 and Movie 5).

We also imaged the spatiotemporal relationship of the endoplasmic reticulum (ER), mitochondria,

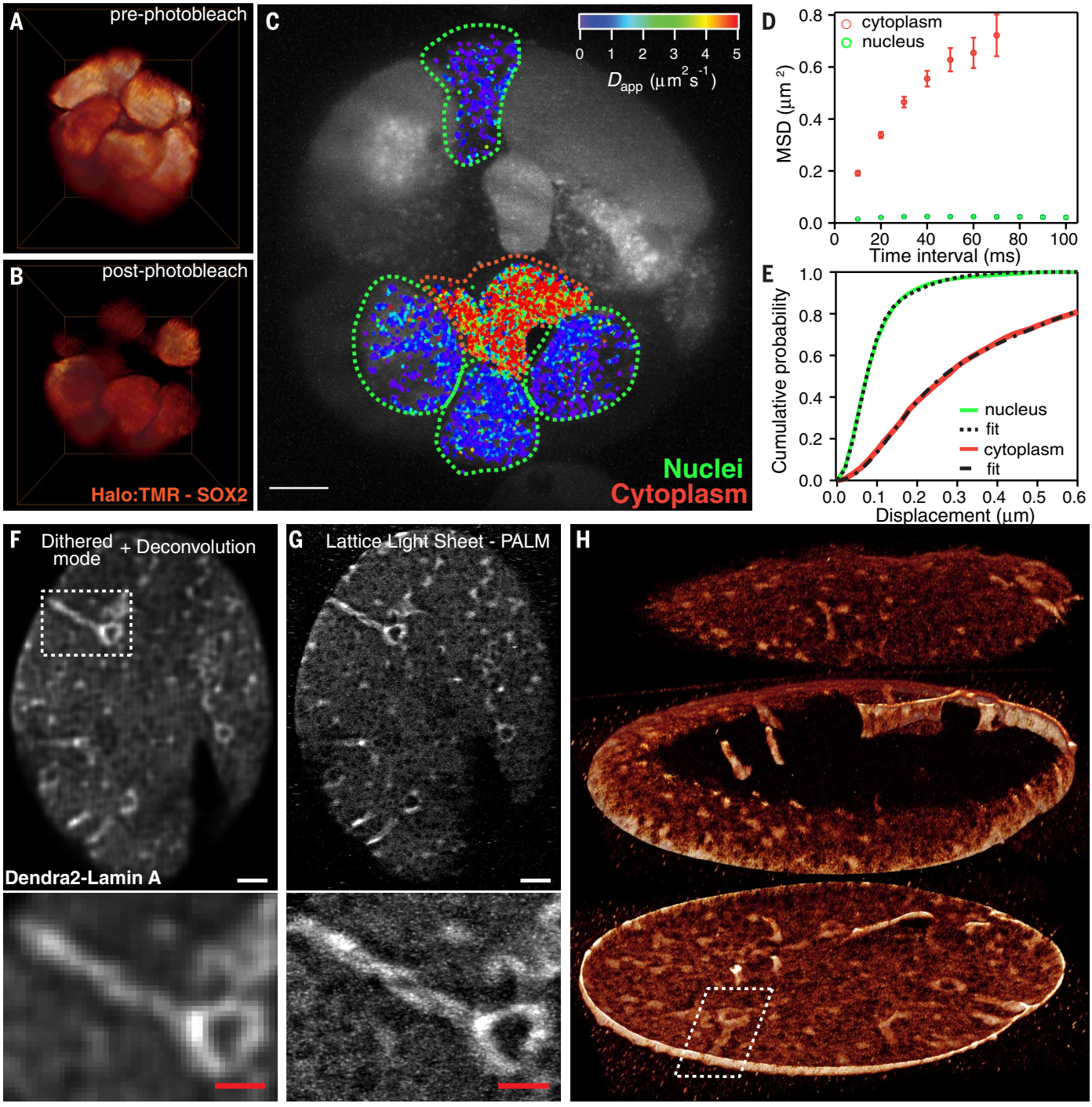

Fig. 3. Single-molecule tracking and superresolution. (**A**) Lattice light sheet 3D rendering of a ~35-μm-diameter spheroid of mouse embryonic stem cells containing TMR-labeled Sox2 transcription factors. (**B**) Same spheroid, showing bleached region after single-molecule imaging with the light sheet dithered at a fixed plane (compare with movies S8 and S9). (**C**) Local apparent diffusion coefficients of Sox2 molecules. Scale bar, 5 μm. (**D**) MSDs of molecules in the nuclei (7608 trajectories) or cytoplasm (2339 trajectories) with error bars indicating the standard errors of the means. (**E**) Corresponding cumulative distribution functions (CDFs) representing the fraction of all tracked molecules at a given MSD or below. (**F**) Diffraction-limited maximum intensity projection (MIP) from a 600-nm-thick slab cut through the bottom of the nuclear membrane of a fixed U2OS cell expressing Dendra2–lamin A, taken in the dithered lattice mode. (**G**) Super-resolution MIP from the same slab, taken with 3D PALM, where molecules in successive planes are excited with a dithered lattice light sheet. Scale bars, 2 μm in upper views of (F) and (G), 1 μm in zoomed boxes below. (**H**) Exploded view of the full 3D rendering of the nuclear envelope by PALM (compare with movie S10).

and chromosomes during mitosis by using three-color lattice light sheet microscopy. We labeled LLC-PK1 cells stably transfected with mEmerald-ER and mApple-H2B with MitoTracker Deep Red dye (Life Technologies) and recorded 300 3D volumes in each color at 3.8-s intervals by acquiring a 2D image in each color at each z plane before moving on to the next (Fig. 4B and Movie 6). As reported elsewhere, in mitosis the mitochondria fragment (*33*) and the ER reorganizes into large, extended cisternae (*34*) with little remaining of the reticular network familiar to interphase. However, with the lattice light sheet we additionally see that the mitochondrial fragments nestle within and are corralled by the ER cisternae as they move fluidly within and between these pockets. We observed no exchange of fluorophore between mitochondria and the ER, which would be suggestive of their mutual fusion. Last, both organelles were excluded from the region occupied by the chromosomes and the mitotic spindle during anaphase/telophase.

Whereas our current system is capable of imaging at up to 200 planes per second in multiple colors and up to 1000 planes per second in a single color over a 100 μm–by–20 μm *xy* field of view, biological systems still exist for which even higher speed is desired. An example is the model protozoan *Tetrahymena thermophila* (*35*): We imaged a GFP-scramblase expressing specimen that was trapped in a pocket of 0.5% low melting point agarose for 1250 time points at 3.2 volumes per second (Fig. 4C and Movie 7). However, the temporal resolution was insufficient to continuously follow the rapid morphological changes that we observed or allay the fear of motion-induced artifacts. We then transitioned to 2D imaging of a single plane on the same specimen at 3 ms per frame. We were then able to smoothly track for 18,000 frames the motion of even the fastest processes falling within the image plane, such as the beating of motile cilia (fig. S10), raising the possibility of quantifying their bending and the forces they generate to elucidate their roles in signal transduction and locomotion. The combination of 3D and 2D imaging represented more than 200,000 images obtained from a single living, motile specimen within the time span of about 7.4 min. During this time, we observed no change in organism dynamics or protein distribution that would be indicative of phototoxicity.

Imaging cell-cell and cell-matrix interactions

The vast majority of cells do not live in isolation, but rather in contact with neighboring cells or an extracellular matrix (ECM). We investigated both scenarios with the dithered lattice light sheet. In one example, we imaged the initial 3D aggregation of starved *D. discoideum* cells as they rapidly chemotaxed toward one another and began the transition from unicellular to multicellular behavior (fig. S11). In another, we added a suspension of cytotoxic T cells expressing GFP-Lifeact to a field of peptide-pulsed EL4 target cells stably expressing plasma membrane markers fused to TagRFP on a cover slip and observed the processes of T cell/target cell engagement and the formation of the immunological synapse (*36*). Across dozens of trials, a stereotypic behavior emerged: A T cell, blunt at

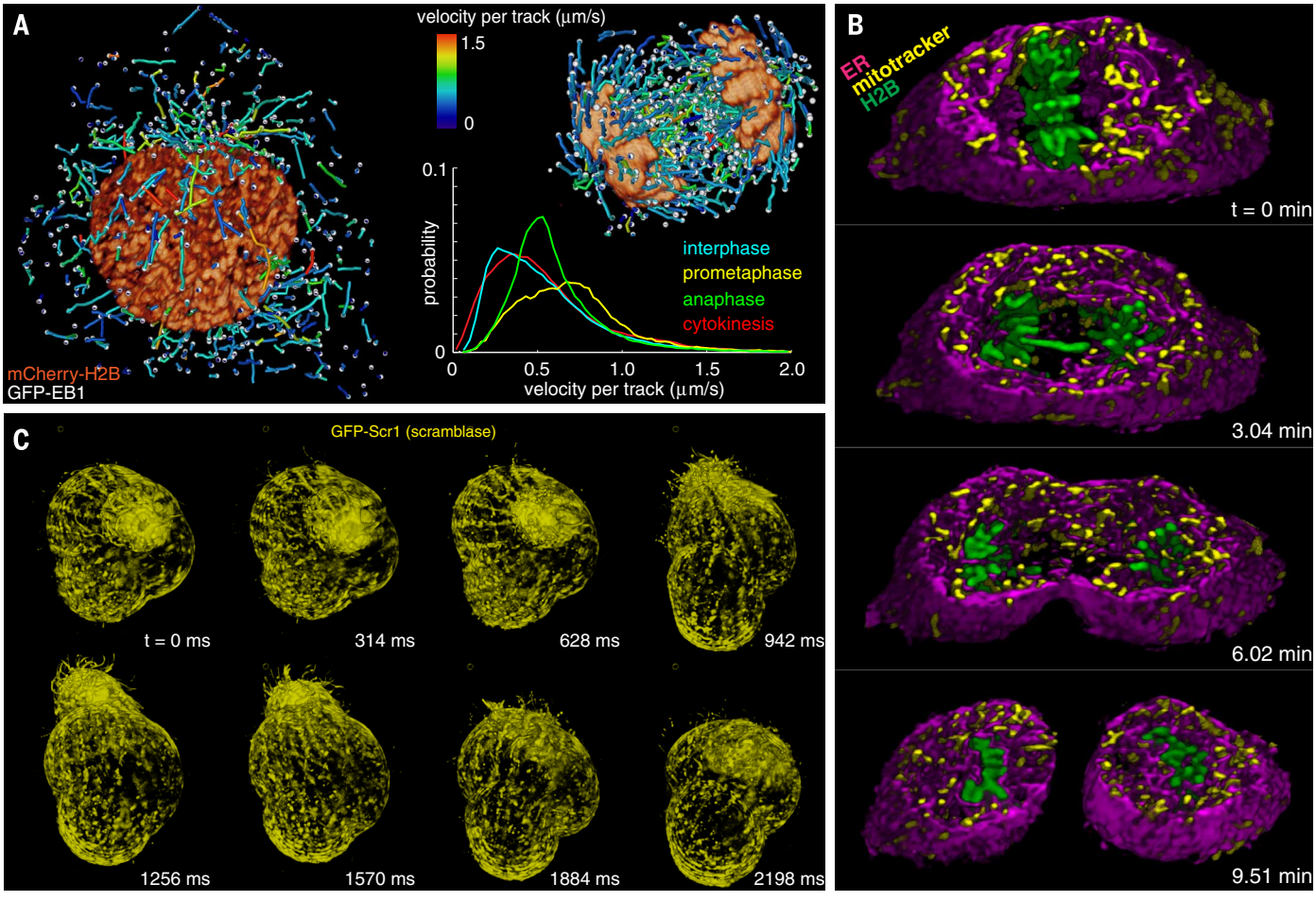

Fig. 4. Intracellular dynamics in three dimensions. (**A**) Cells in prophase (left) and anaphase (right), showing histones and 3D tracks of growing microtubule ends, color-coded by velocity. Color-coding of each track by height (movie S11) or growth-phase lifetime (movie S12) is also possible. Each image in (A) represents a distillation of a few time points from a 4D, two-color data set typically covering hundreds of time points per cell (compare with Movie 5). Graph shows the distribution of growth rates at different stages of mitosis, averaged across 9 to 12 cells (compare with figs. S8 and S9). (**B**) The 3D spatial relationship of histones (green), mitochondria (yellow), and ER (magenta) at four time points during mitosis in a slab extracted from a larger 4D, three-color data set of HeLa cells imaged for 300 time points (compare with Movie 6). (**C**) Volume renderings at eight consecutive time points of a single specimen of the protozoan *T. thermophila* taken from a 4D data set spanning 1250 time points (compare with Movie 7). Imaging at 3 ms per frame in a single plane (compare with movie S13) reveals the motions of individual cilia.

the leading end and trailing a small uropod, migrated toward a target cell while extending probing lamellipodia (Fig. 5A). Upon initial contact with the target cell, the T cell begins to establish a synapse rich in actin as the T cell rounds up (Fig. 5, B and C). Lamellipodial protrusion and movement of 3D actin structures are observed along the T cell body (Movie 8) that would be difficult to observe without the speed and resolution of the lattice microscope.

Mammalian cells typically migrate not on a 2D substrate but through a complex 3D meshwork of ECM proteins. However, because of the limitations of conventional imaging modalities, the majority of studies of cell motility have focused on the locomotion of cells on planar surfaces (*37*). Recent extensions into 3D geometries have used slowly moving mesenchymal cells such as fibroblasts (~1 μm/min) (*38*), where the speed is amenable to current technologies. However, less is known about migration of neutrophils, which must navigate at ~10-times faster speeds (~8 to 12 μm/min) (*39*) through complex 3D microenvironments in infected tissues. We studied this process by adding neutrophil-like human HL-60 cells (*40*) expressing mCherry-utrophin to a 3D, fluorescently labeled collagen mesh (Fig. 5D and Movie 9). Cells embedded in the mesh migrated at speeds comparable to cells on cover slips (Movie 10), despite the added physical constraints. They also exhibited a similar polarized morphology, with leading lamella and a trailing uropod (Fig. 5E). However, the embedded cells sent lamellar-like protrusions in a greater variety of directions as they probed alternative pathways through the mesh. We also recorded the displacement of the collagen filaments by the cells (Fig. 5F), and in the future these data might be combined with 3D traction force microscopy (*41*) to create high-spatiotemporal-resolution maps of the forces generated by the cells as they migrate through their surroundings.

Imaging the subcellular physiology of developing embryos

Much of our knowledge of cellular physiology comes from studies of immortalized cells cultured onto flat substrates. However, to understand the true physiological state of a cell, it must be studied within the multicellular environment in which it evolved. This is possible with lattice light-sheet microscopy, at least in the superficial layers of developing embryos where sample-induced aberrations are minimal. We demonstrated this in two model systems: the nematode *Caenorhabditis elegans* (Fig. 6, A and B) and the fruit fly *Drosophila melanogaster* (Fig. 6, C to F).

One challenge in such studies is that many subcellular processes occur on the time scale of seconds to minutes, whereas development from fertilization to hatching occurs over many hours to several days. However, even with the minimal invasiveness of our method, it is not possible to acquire the tens to hundreds of thousands of 3D volumes needed to follow fast subcellular dynamics over the full course of development without bleaching or damaging the specimen.

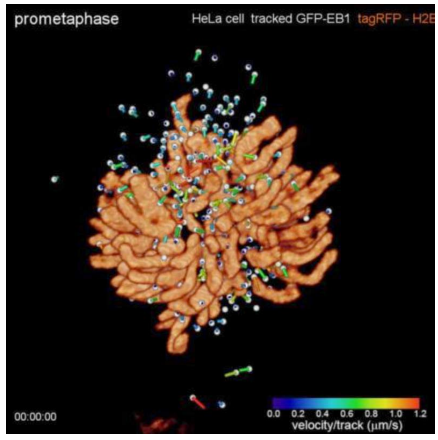

Movie 5. Measured GFP-EB1 trajectories denoting growing microtubule endpoints, color-coded by velocity, and TagRFP-H2B highlighting chromosomes, at five different stages during the division of a single HeLa cell.

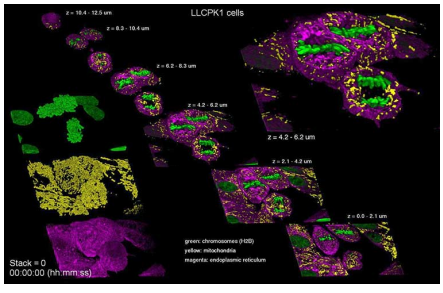

Movie 6. Chromosomes (green, mCherry-H2B), mitochondria (yellow, mitotracker–deep red), and ER (magenta, mEmerald-calnexin) in a field of dividing LLC-PK1 cells. Compare with Fig. 4B. (**Left**) Individual volume renderings. (**Center**) Three-color overlay, with the imaging volume sliced in ~2-μm-thick slabs to facilitate the visualization of the internal arrangement of the features. (**Right**) Magnified view of one such slab, showing mitochondrial fragments nestled in ER cisternae.

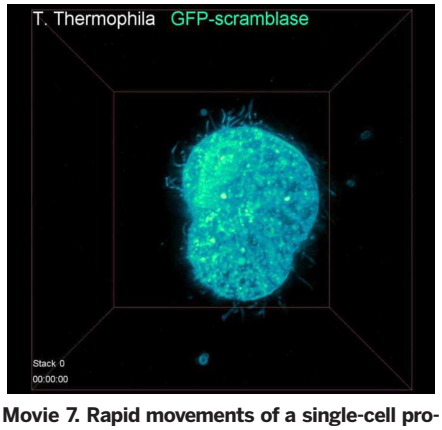

Movie 7. Rapid movements of a single-cell protozoan *T. thermophila* expressing GFP-scramblase and confined in a small pocket in agarose. Compare with Fig. 4C. Rapid translational movements present in the movie represent a recentering of the organism within the microscope field of view. Bounding box, 53 μm by 53 μm by 51 μm.

Hence, it is necessary to carefully select the exact developmental stage and imaging interval to match the process of interest at the time of interest. For example, we imaged a GFP-tagged version of the Aurora B kinase homolog AIR-2, a chromosomal passenger complex protein essential for cytokinesis in *C. elegans*, at 1-min intervals in order to follow its localization during cell division (Fig. 6A and Movie 11). As seen previously in embryos (*42*, *43*), AIR-2 localizes to metaphase chromosomes, followed by midbody microtubules in anaphase, and eventually in a persistent midbody remnant after cytokinesis. However, the thinness of our lattice light sheet allowed us to follow this process in 4D at high SNR in live embryos with remarkable detail (fig. S12). AIR-2 first associated with the chromosomes in prophase. By anaphase, it was indeed most concentrated at the spindle midzone microtubules, but some remained at the chromosomes, some at the centrosomes, and a faint residue outlined the astral microtubules. In late cytokinesis, AIR-2 was observed on the midbody remnant between the daughter cells. Although the localization of AIR-2 has been well studied in fixed samples or single 2D slices (*43*, *44*), high spatiotemporal analysis of the 3D localization of different populations of AIR-2 may provide new insight into how it regulates cell division in developing embryos.

Other dynamic processes in *C. elegans* require higher time resolution. At the threefold stage, just before hatching, muscle contractions make it difficult to follow specific features continuously over time, although we have recorded two color 3D snapshots across the entire embryo at 2.6-s intervals. At the other end of the developmental spectrum, we imaged the 3D distribution of GFP-Lifeact at 4.8-s intervals for over 300 time points from the single-cell pseudocleavage stage through the division of the AB cell in an uncompressed embryo (Fig. 6B, fig. S13, and Movie 12). We observed an initial enrichment of actin generating the pseudocleavage furrow, which progressively relaxed to create a smooth round embryo in maintenance phase. At this stage, actin became concentrated into long, bright, bundled filaments in the anterior half of the embryo. Before the formation of the first contractile ring, actin again spread across the entire embryo in dim filaments and bright punctae before becoming concentrated in the cleavage furrow during the first embryonic division. Just before the division of the AB cell, actin became enriched in the anterior portion of the P1 cell. This actin then migrated to the interface between the P1 and the ABp cells after AB division. Throughout the imaging, extremely actin-dense comets would occasionally appear and move rapidly through the cytosol. Although these comets and other stages of the cortical actin distribution have been observed previously in live embryos by spinning disk confocal microscopy (*45*), higher 4D resolution of both the actin dynamics and the shape of the embryo such as we demonstrate here will aid in developing physical models of how actomyosin forces lead to morphological changes in the early embryo (*46*), without the potential

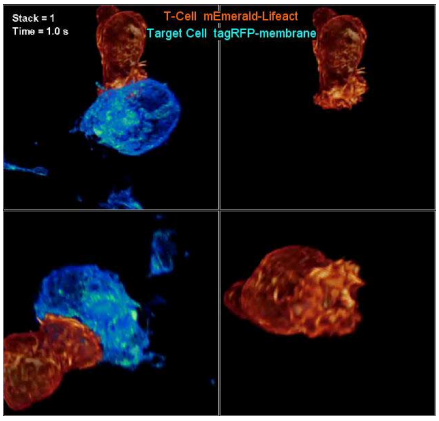

Movie 8. T cell and its target cell. Two-color volume rendering seen from two different orientations of the interaction of a T cell expressing mEmerald-Lifeact (orange) with a target cell expressing a plasma membrane marker fused to TagRFP (blue) over 430 time points at 1.3-s intervals. The target cell has been made invisible in the views in the right column (compare with Fig. 5, A to C, for a second example).

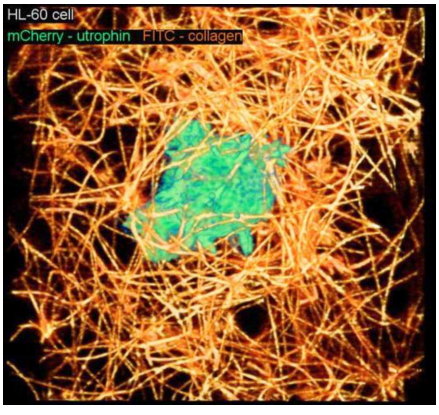

Movie 9. Cell movement through a matrix. Two-color volume rendering of a neutrophilic HL-60 cell expressing mCherry-utrophin migrating through a 3D collagen matrix labeled with FITC over 250 time points at 1.3-s intervals (compare with Fig. 5, D to F).

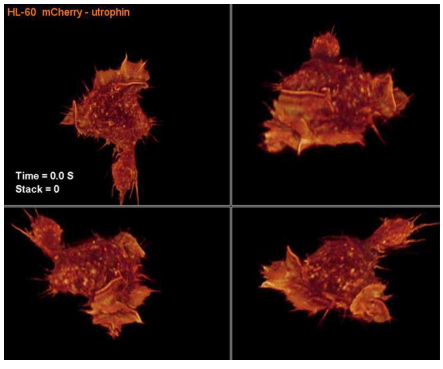

Movie 10. Cell migration in two dimensions. Volume rendering from four different viewing angles of a neurophilic HL-60 cell expressing mCherry-utrophin migrating on a 2D glass substrate over 150 time points at 1.1-s intervals.

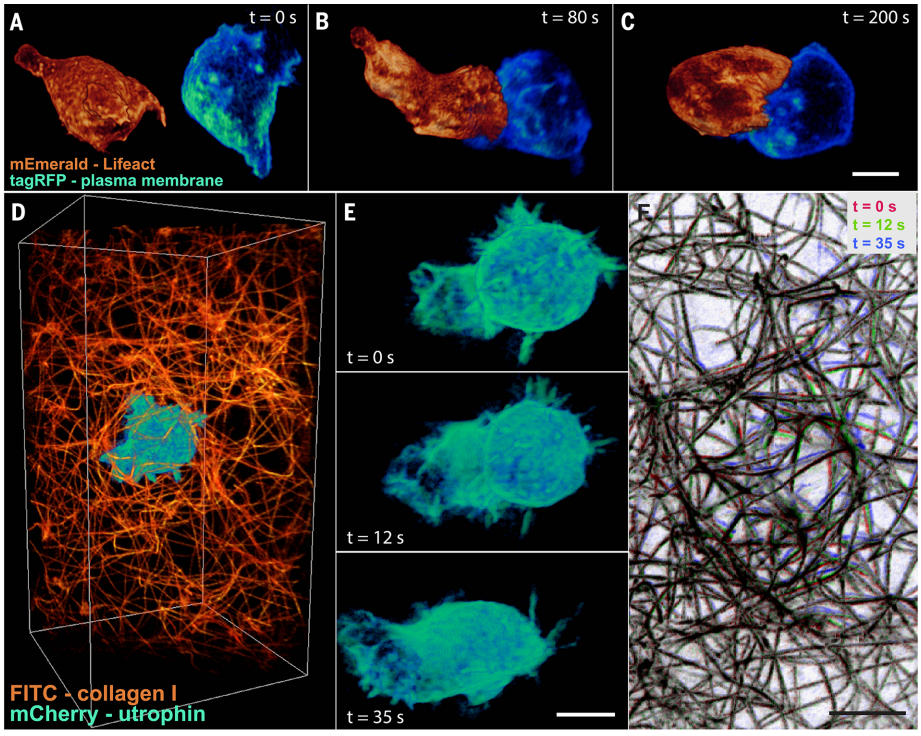

Fig. 5. Imaging cell-cell and cell-matrix interactions. (**A**) T cell expressing mEmerald-Lifeact (orange) approaching a target cell expressing a plasma membrane marker fused to TagRFP (blue), as seen from the side. (**B**) Initial contact. (**C**) The two cells, after immunological synapse formation. These data represent three time points from a 4D, two-color data set spanning 400 time points. Scale bars, 4.0 μm. Other cell-cell interactions, such as the aggregation-starved *D. discoideum* cells, can likewise be studied for extended periods (compare with movie S14). (**D**) Neutrophil-like human HL-60 cell expressing mCherry-utrophin in a fluorescently labeled collagen matrix. (**E**) Volume renderings of the cell at three time points extracted from a 4D, two-color data set of the cell and the matrix covering 250 time points (compare with Movie 9). Scale bar, 5.0 μm. (**F**) Overlaid MIPs in three different colors of the collagen at the same three time points. Colored regions highlight local displacements of the matrix by the cell. Scale bar, 5.0 μm.

artifacts introduced by the embryo compression typically applied when using spinning disk confocal microscopy.

On a larger scale, we also studied the process of dorsal closure in *D. melanogaster*, the point in embryogenesis where two lateral sheets of epithelial cells converge over an eye-shaped opening to cover the amnioserosa, a thin layer of squamous cells. In embryos expressing GFP-labeled *DE*-cadherin to mark cell boundaries, apical shape oscillations and ingression of amnioserosa cells have been previously quantified in 2D models of the curved surface extracted from 3D spinning disk data (*47*). However, with lattice light-sheet microscopy, we could study this process (Fig. 6C) in 4D up to twice as fast and at five times finer z sampling in uncompressed embryos throughout the thickness of the amnioserosa and beyond. We have also imaged embryos expressing GFP-tagged myosin (Fig. 6D and Movie 13) or sGMCA (Fig. 6E), a marker of filamentous actin at the plasma membrane, and observed contractile oscillations of the cytoskeleton temporally correlated to cell shape changes at the basal as well as the apical surface (Fig. 6F). Taken together, such data may facilitate the development of 4D models of the collective dynamics of dorsal closure as driven by forces in the amnioserosa and in the encroaching epithelium, with its actomyosin-rich purse string that resides near their mutual boundary.

Discussion

One limitation of lattice light-sheet microscopy is that, like all forms of optical microscopy, its performance degrades increasingly with depth because of sample-induced aberrations. Thus, depending on the optical heterogeneity of the specimen of interest, imaging beyond 20 to 100 μm will likely require combining the technique with adaptive optics (*48*) in both excitation and detection pathways to compensate for these aberrations.

The chief benefit of lattice light-sheet excitation for in vivo imaging is its exceptionally low photobleaching and phototoxicity—each of the 4D data sets presented here was distilled from tens to hundreds of thousands of raw 2D images acquired from each specimen. This is about an order of magnitude more images per specimen than we achieved with linear Bessel beam plane illumination (*7*, *8*) and nearly two orders of magnitude more than in typical confocal data sets of similar specimens at similar expression levels. Thus, although excitation with a line (Bessel) is better than a point (confocal), a plane (lattice) is better than a line. The implication is that, although the total light dose delivered to the

specimen is an important factor dictating its health, an even more important metric may be the peak intensity delivered to the specimen. In retrospect, this is not surprising, because photodamage mechanisms that scale supralinearly with peak intensity have been identified for both visible (*49*) and two-photon (*50*) excitation. Given that confocal and lattice light-sheet microscopy operate at similar 1- to 100-μW power levels in live cells yet distribute this power over areas that differ by 10^4 to 10^5 times in the focal plane, these mechanisms should be expected to yield vastly greater phototoxicty in the confocal case.

Indeed, seen in this context, confocal microscopy is far from an optimal tool for in vivo imaging—not only do the incoming and outgoing cones of excitation create premature bleaching and damage outside the focal plane, at the focal plane itself an actinic spot of light is created that leaves destruction in its wake as it sweeps through the specimen. Although this damage is ameliorated in spinning disk confocal microscopes that use many foci in parallel, peak intensities are still far higher than in lattice light-sheet microscopy, out-of-focus excitation remains a problem, and pinhole cross-talk can lead to artifacts and poor SNR in thick fluorescent specimens (*51*).

Another key advantage of our method is its speed. At 200 to 1000 planes per second, it is typically an order of magnitude faster than with linear Bessel beam excitation and two orders of magnitude faster than in typical spinning disk confocal systems applied to comparable specimens. This is critical, because if we wish to follow physiological processes throughout the 3D volume of the specimen with the same or better temporal resolution as in prior 2D studies, we must image at least *N*-fold faster, where *N* is the

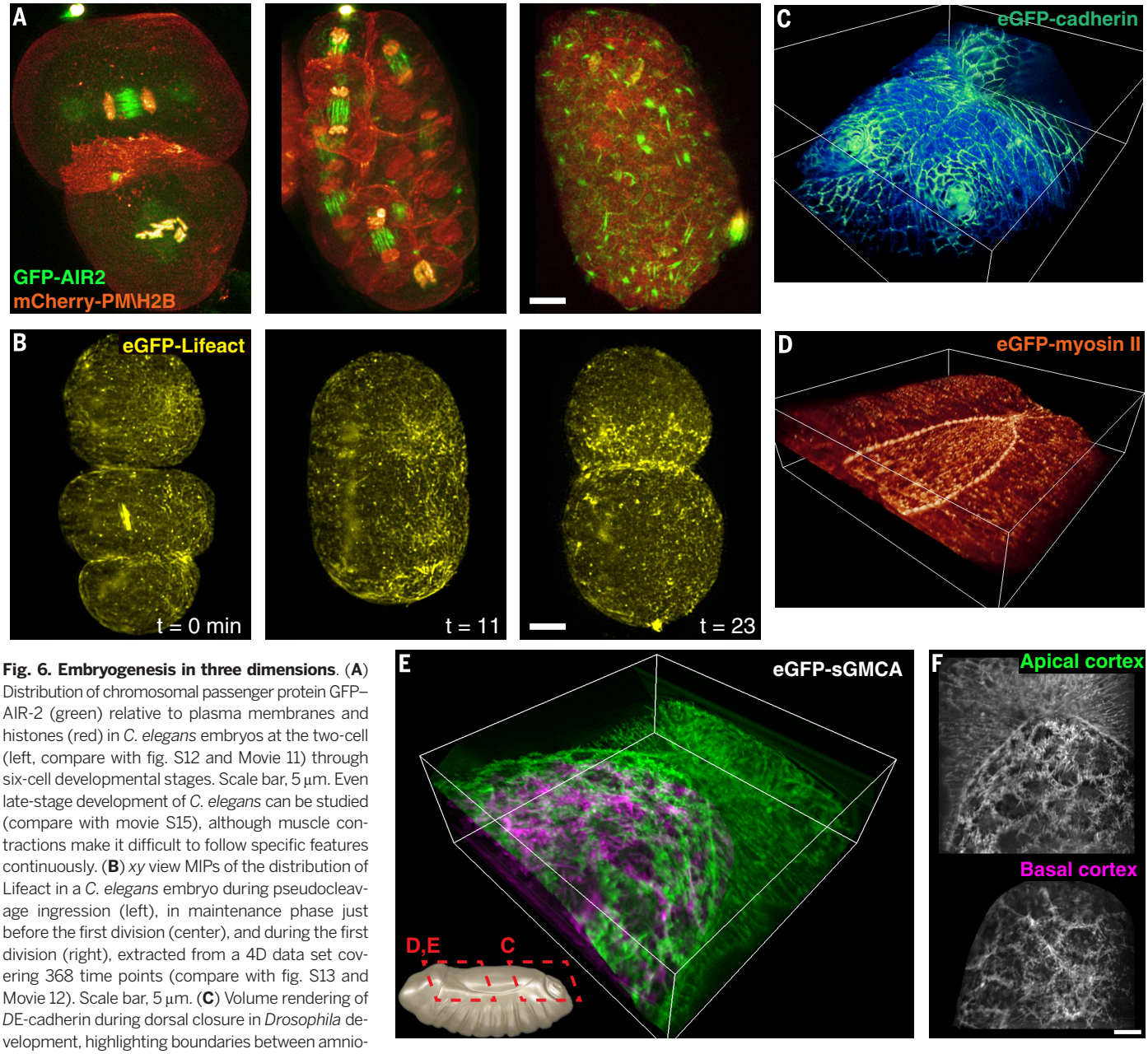

Fig. 6. Embryogenesis in three dimensions. (**A**) Distribution of chromosomal passenger protein GFP–AIR-2 (green) relative to plasma membranes and histones (red) in *C. elegans* embryos at the two-cell (left, compare with fig. S12 and Movie 11) through six-cell developmental stages. Scale bar, 5 μm. Even late-stage development of *C. elegans* can be studied (compare with movie S15), although muscle contractions make it difficult to follow specific features continuously. (**B**) *xy* view MIPs of the distribution of Lifeact in a *C. elegans* embryo during pseudocleavage ingression (left), in maintenance phase just before the first division (center), and during the first division (right), extracted from a 4D data set covering 368 time points (compare with fig. S13 and Movie 12). Scale bar, 5 μm. (**C**) Volume rendering of *D*E-cadherin during dorsal closure in *Drosophila* development, highlighting boundaries between amnioserosa cells and the formation of spiracles, from a 4D data set containing 840 time points (compare with movie S16); bounding box, 86 μm by 80 μm by 31 μm. (**D**) Myosin II during dorsal closure, highlighting the myosin-rich purse string at the interface between the outer epithelium and the amnioserosa, from a 4D data set covering 1000 time points (compare with Movie 13); bounding box, 80 μm by 80 μm by 26 μm. (**E**) sGMCA during dorsal closure, from a 4D data set covering 639 time points (compare with movie S17); bounding box, 73 μm by 73 μm by 26 μm. (**F**) MIPs highlighting cortical actin at the apical and basal surfaces of the amnioserosa, extracted from (E). Scale bar, 10 μm.

number of 2D images comprising each 3D stack. In spinning disk confocal systems, speed limitations often make it necessary to undersample N, trading axial resolution for temporal. However, with our approach, we can image many specimens in 3D at subsecond intervals, even though $N \sim 100$ to 200 planes per time point are required by the Nyquist criterion to recover the full axial resolution of which our microscope is capable (~370 nm in the dithered mode, 280 nm in the SIM mode). Achieving such high axial and temporal resolution simultaneously (which is not possible under either the spinning disk confocal or Gaussian light-sheet paradigms) is essential: When imaging in 4D, the results are often only as strong as the weakest dimension; high-resolution information from certain dimensions is lost when smeared across the poor resolution of others.

Together, high speed and low phototoxicity position lattice light-sheet microscopy not only at the forefront of live cell fluorescence imaging but also as a key enabler to bring recent advances in biology and microscopy into mainstream application. For example, genome-edited cells (*52*) expressing endogenous levels of a targeted protein allow specimens to be studied closer to their native physiological state; however, expression levels can be far lower than in conventionally transfected specimens. This requires proportionally higher excitation intensities to yield comparable SNR at comparable speed when imaging in vivo and will severely limit their applications with conventional microscopy. High speed also expands the application space for structured illumination microscopy, which, to reconstruct artifact-free images, requires that the specimen move by less than the reconstructed voxel size in the time it takes to record the raw images contributing to that voxel. Because the elimination of out-of-focus background permits us to use shorter exposures to achieve the same SNR, we can image 3D processes that evolve at least 10 times faster by lattice light-sheet SIM than is possible with widefield SIM, albeit at somewhat lower resolution. In addition, we can image these processes far longer because of the elimination of out-of-focus photobleaching and photodamage and lower total light dose per time point. Last, for other physiological processes that evolve slowly compared with the speed of our microscope, the extra bandwidth can be expended in a fifth dimension to image in more colors. Indeed, typical cells are composed of more than 10,000 unique proteins, yet they are usually imaged in vivo only one or two at a time. By using spectral unmixing (*53*) and/or combinatorial labeling (*54*–*56*), it may prove possible with our system to study the 4D interplay of a dozen or more proteins in the same cell at the same time and to understand how they orchestrate complex cellular functions such as membrane trafficking or mitosis.

Materials and methods

Microscope optics

Seven collinear but individually modulated circular laser beams ranging in wavelength from 405 to 647 nm were passed through two pairs of cylindrical lenses to illuminate a thin stripe across the width of a ferroelectric spatial light modulator (fig. S4A, Forth Dimension Displays, SXGA-3DM). The SLM has a large number of pixels (1280 pixels by 1024 pixels) and a fast (<1 ms) switching time, the latter essential for rapid coregistered multicolor imaging. The remainder of the excitation optical path serves to create a demagnified image of the SLM (81.6-nm pixels) at the focal plane of the excitation objective, so that the pattern projected on the SLM (e.g., fig. S5C) creates a corresponding lattice light sheet of the desired properties (e.g., fig. S5G) within the specimen. First, a lens is used in a 2F configuration to create a diffraction pattern at its front focal plane (e.g., fig. S5D) that is the Fourier transform of the electric field reflected from the SLM. A custom opaque mask with transmissive annuli (e.g., fig. S5E; Photo-Sciences Incorporated) is placed at this plane, and a specific annulus is chosen to remove the unwanted diffraction orders and enforce a limit on the minimum field of view in y. The electric field transmitted through the mask (e.g., fig. S5F) is then imaged in series onto each of a pair of galvanometers (Cambridge Technology, model 6215H) and the rear pupil plane of the excitation objective. The galvanometers serve to translate the light sheet through the specimen in x and z. Last, the field is reverse-transformed by the excitation objective to create the desired lattice light sheet at its front focal plane.

The fluorescence generated within the specimen is collected by a detection objective [Nikon, CFI Apo LWD 25XW, 1.1 NA, 2-mm working distance (WD)] whose focal plane is coincident with the light sheet. Its high NA is essential to maximize the xy resolution and to optimize the light collection for single-molecule detection. The excitation objective (Special Optics, 0.65 NA, 3.74-mm WD) was custom-designed to fill the remaining available solid angle above the cover slip (Fig. 1, E and F), in order to optimize the z resolution, as well as the x resolution in the SIM mode, under this constraint.

A tube lens images the fluorescence from the illuminated slice within the specimen onto an sCMOS camera (Hamamatsu Orca Flash 4.0 v2) capable of frame rates down to 1 ms. A 3D image is produced from a stack of such 2D slices, either by moving the light sheet and detection objective together through the specimen [the former with the z galvo, the latter with a piezoelectric stage (Physik Instrumente, P-621.1CD)] or, far more commonly, by translating the specimen with a second piezo stage through the stationary light sheet along an axis s in the plane of the specimen cover slip (Fig. 1F and movie S2). The latter approach permits the use of more tightly confined light sheets for specimens that are thinner than they are long, such as single cultured cells. The specimen holder and specimen piezo are mounted on a trio of closed-loop micropositioning stages (Physik Instrumente M-663 for horizontal motion in the cover slip plane, M-122.2DD for vertical travel). In conjunction with an epifluorescence view-finding objective from below (fig. S4A, Olympus LUMPLFLN40XW, 0.8 NA, 3.3-mm WD), these are used to position the desired region of interest within the field of view of the

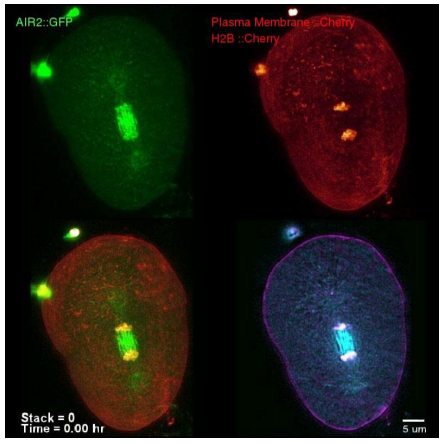

Movie 11. Protein localization in early embryo. Localization of the chromosomal passenger protein AIR-2 during the first few cell divisions of the early *C. elegans* embryo (compare with Fig. 6A and fig. S12).

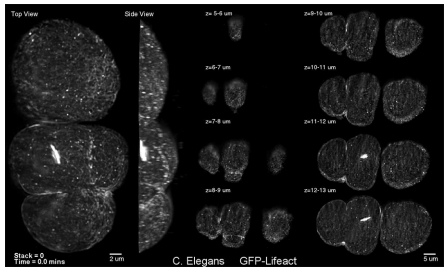

Movie 12. Actin distribution in early embryo. Various maximum intensity projections of the distribution of actin in the upper longitudinal half of a *C. elegans* embryo expressing GFP-Lifeact over 360 time points at 4.8-s intervals, from a few minutes after fertilization to just after the division of the AB cell. Left, top view. Middle, side view. Right, MIPs in eight consecutive longitudinal slabs through the data set, designed to help distinguish cortical from cytosolic actin (compare with Fig. 6B and fig. S13).

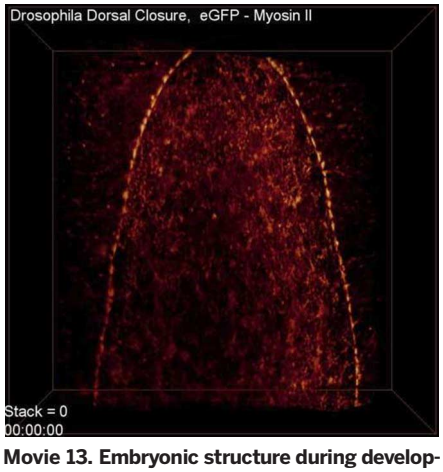

Movie 13. Embryonic structure during development. Volume rendering and orthoslices of myosin II highlighting the myosin-rich purse string during dorsal closure in a *D. melanogaster* embryo, over 1000 time points at 6.0-s intervals (compare with Fig. 6D). Bounding box, 80 μm by 80 μm by 26 μm.

light sheet. They also permit larger fields of view to be tiled together from multiple image subvolumes or multiple specimens to be imaged on the same cover slip in a repetitive loop for those cases where the dynamics occur on a time scale slow compared with the 3D imaging speed.

Complete details regarding the optical design are given in supplementary note 3. Certain aspects of the design are derived from our earlier Bessel beam work, so these earlier publications (*7*, *8*, *57*) remain valuable resources as well.

Control electronics

All analog/digital input/output signals are calculated and controlled by custom LabVIEW software (Coleman Technologies, Incorporated, National Instruments) and a field-programmable gate array card (FPGA, fig. S14, National Instruments, PCIe-7852R Virtex-5 LX50 R series). Analog outputs (AOs) controlling galvos and piezos were conditioned by individual scaling amplifiers (SRS, SIM983, and SIM900 mainframe) to match their 16-bit resolution to the control range of each device. Instrument control and data analysis were performed on independent Supermicro workstations (Supermicro X8DTG-QF) running Windows 7 Professional 64 bit (Microsoft), each equipped with two Intel Hexa-CoreXeon X5680 processors, 96 GB of RAM, and an NVIDIA GeForce GTX TITAN graphics card.

The SLM runs under internal timing and serves as the master clock for image acquisition. A series of SLM images known as a Running Order (fig. S15) is loaded into the SLM, and a hardware start signal from the FPGA triggers execution of the Running Order (fig. S16). A digital LED Enable output from the SLM is read by the FPGA and mirrored as an output sent to the scientific complementary metal-oxide semiconductor (sCMOS) camera (which operates in external trigger, rolling shutter mode), in order to synchronize the image acquisition to the positive/negative display states of the SLM (fig. S17). The number of transitions of LED Enable is counted to determine which SLM image in the Running Order is currently displayed, so the FPGA can send the appropriate outputs to control the acousto-optic tunable filter (AOTF), galvos, and piezos (fig. S18). The acceleration and flyback speeds of the latter two can be adjusted independently (fig. S19) to match their intrinsic response times. Control sequences exist to run the microscope in single or multiple colors in any one of four versions: objective scan, dithered mode (fig. S20); objective scan, SIM mode (fig. S21); sample scan, dithered mode (fig. S22); or sample scan, SIM mode (fig. S23). More complete details can be found in supplementary note 4.

Sample preparation and imaging conditions

Specimens are cultured or mounted on 5-mm-diameter cover slips (Warner Instruments, 64-0700) cleaned before use according to our earlier protocol (*7*). The cover slip is clipped to the end of a long extension of the sample holder (orange, fig. S4D). This end is dipped in a shallow media-filled bath (translucent yellow, fig. S4D), while the opposite end is bolted to the sample piezo. The bath has inlet and output ports for perfusion of the media. A subassembly with the excitation and detection objectives and their translation stages is lowered from above until the ends of the objectives are dipped in the media at the distance from the cover slip appropriate for creating a lattice light sheet near its upper surface.

For operation away from room temperature (particularly for live mammalian cells at 37°C), heated or chilled water from a remote temperature-controlled reservoir is pumped through self-contained channels cut in the base of the bath, unconnected to the bowl that contains the imaging media. Asymmetric heating or cooling of the ends of the objectives creates substantial optical aberrations that affect the microscope performance, as does convection of the media because of temperature gradients in the bath. Thus, additional heating/cooling blocks (translucent green and red, fig. S4D) with self-contained water channels are bolted around and close to the objectives, but not in contact. These are supplied with water from a second reservoir to maintain a circularly symmetric, uniform temperature around the objectives that matches the temperature of the bath. The temperatures of the two reservoirs needed to attain a given specimen temperature differ but can be determined empirically.

Preparation conditions specific to each specimen are given in the supplementary note 5. Imaging conditions specific to each specimen, including maximum and minimum excitation NA, excitation power, imaging time, image and voxel sizes, imaging mode, fluorophores, and proteins, etc., are given in table S1.

Image processing and visualization

Unless otherwise noted, all data acquired in the dithered mode were deconvolved by using a Richardson-Lucy algorithm adapted to run on a graphics processing unit (GPU) (NVIDIA, GeForce GTX TITAN), using an experimentally measured PSF for each emission wavelength. All data acquired in the SIM mode were reconstructed with an implementation of the algorithm for 3D-SIM (*9*) previously adapted for Bessel beam–structured plane illumination microscopy (*8*, *57*), running on the same GPU, using an OTF calculated from an experimentally measured PSF for each emission wavelength. All 3D data sets acquired via sample scan in the x, y, and s coordinated system were transformed ("deskewed") to the more conventional x, y, and z coordinates in the GPU before visualization. Where noted (table S1), data sets were corrected for photobleaching and hot pixels by using either built-in Image J functions (histogram matching or exponential fitting) or by rescaling the maximum display value such that about 0.1% of all voxels (99.9th percentile) at any given time point were saturated. Last, processed data sets were imported into Amira (FEI) for 5D volumetric rendering.

Single-molecule tracking and 3D PALM imaging

Single-molecule tracking within mouse embryonic stem cell spheroids (Fig. 3, A to E, and movies S8 and S9) was performed by using the particle-tracking software Diatrack (v3.03, Semasopht) as described previously (*58*). Briefly, the software fits intensity spots with fixed-width symmetric 2D Gaussian functions. A map of local apparent diffusion coefficients was generated with code written in Igor 6.3.4 (WaveMetrics). The local apparent diffusion coefficients were evaluated in 40 nm–by–40 nm grids and calculated from the mean square displacements originating from within a radius of 150 nm of each grid point over a time scale of 10 ms (Fig. 3C). The single-molecule trajectories were further analyzed by calculating mean square displacements (MSDs) for all possible time intervals and cumulative distribution functions (CDFs) of all 10-ms displacements in the sample plane (Fig. 3, D and E). The fit data from each CDF were best fit by a linear combination of two exponential functions, $P(r) = 1-[\exp(-r^2)/4D_{app}\Delta t]$, where D_{app} is the apparent diffusion coefficient and t is time, corresponding to both fast and slow components.

PALM was performed with a cylindrical lens of 1000-mm focal length (Thorlabs, LJ1516RM-A) placed 40 mm before the imaging camera, to enable axial localization via the resulting astigmatism (*27*). The sample was scanned 31,000 times in 61 steps of 500 nm each (270 nm in the z direction), for a total of 1.83×10^6 raw 2D single-molecule images. For each such image, single molecules were identified and localized in 3D by using a custom-written maximum likelihood estimator algorithm, an experimentally measured calibration curve (for z-axis fitting), and a Levenberg-Marquardt optimization. Each 3D fit was offset by the sample-piezo position at the time of acquisition and assembled into a composite 3D image. Because a molecule could be localized at multiple image planes and across multiple image volumes, an algorithm was used to link repeated localizations of the same molecule, as determined by a minimum spatial/temporal separation, into a single higher-precision localization event in the final reconstructed image. The initial localization, fit refinement, and linking were implemented on a GPU by using custom-written Matlab and CUDA code (NVIDIA). For visualization of the final data set, a 3D Gaussian with standard deviations determined by the 3D localization precision was plotted at the centroid of each localization. The voxel size of the final reconstructed image (Fig. 3, G and H, and movie S10) was 10 nm by 10 nm by 20 nm.

Tracking plus ends of microtubules during mitosis

Microtubule trajectories and velocities (Fig. 4A, Movie 5, figs. S8 and S9, and movies S11 and S12) were determined from the centroids of EB1 spots in each 3D data set by using a watershed algorithm and linked between time points using a version of plusTipTracker (*31*) that was custom-modified to accept our 4D data sets. The computed trajectories were then imported into Amira and color-coded by track velocity using the Spatial Graph data class.

REFERENCES AND NOTES

1. D. B. Murphy, M. W. Davidson, *Fundamentals of Light Microscopy and Electronic Imaging* (Wiley-Blackwell, Hoboken, NJ, ed. 2, 2013).
2. D. J. Stephens, V. J. Allan, Light microscopy techniques for live cell imaging. *Science* **300**, 82–86 (2003). doi: 10.1126/science.1082160; pmid: 12677057
3. J. Huisken, D. Y. Stainier, Selective plane illumination microscopy techniques in developmental biology. *Development* **136**, 1963–1975 (2009). doi: 10.1242/dev.022426; pmid: 19465594
4. J. Huisken, J. Swoger, F. Del Bene, J. Wittbrodt, E. H. Stelzer, Optical sectioning deep inside live embryos by selective plane illumination microscopy. *Science* **305**, 1007–1009 (2004). doi: 10.1126/science.1100035; pmid: 15310904
5. U. Krzic, S. Gunther, T. E. Saunders, S. J. Streichan, L. Hufnagel, Multiview light-sheet microscope for rapid in toto imaging. *Nat. Methods* **9**, 730–733 (2012). doi: 10.1038/nmeth.2064; pmid: 22660739
6. R. Tomer, K. Khairy, F. Amat, P. J. Keller, Quantitative high-speed imaging of entire developing embryos with simultaneous multiview light-sheet microscopy. *Nat. Methods* **9**, 755–763 (2012). doi: 10.1038/nmeth.2062; pmid: 22660741
7. T. A. Planchon *et al*., Rapid three-dimensional isotropic imaging of living cells using Bessel beam plane illumination. *Nat. Methods* **8**, 417–423 (2011). doi: 10.1038/nmeth.1586; pmid: 21378978
8. L. Gao *et al*., Noninvasive imaging beyond the diffraction limit of 3D dynamics in thickly fluorescent specimens. *Cell* **151**, 1370–1385 (2012). doi: 10.1016/j.cell.2012.10.008; pmid: 23217717
9. M. G. Gustafsson *et al*., Three-dimensional resolution doubling in wide-field fluorescence microscopy by structured illumination. *Biophys. J.* **94**, 4957–4970 (2008). doi: 10.1529/biophysj.107.120345; pmid: 18326650
10. R. Gräf, J. Rietdorf, T. Zimmermann, Live cell spinning disk microscopy. *Adv. Biochem. Eng. Biotechnol.* **95**, 57–75 (2005). doi: 10.1007/b102210; pmid: 16080265
11. E. Betzig, Sparse and composite coherent lattices. *Phys. Rev. A* **71**, 063406 (2005). doi: 10.1103/PhysRevA.71.063406
12. K. I. Petsas, A. B. Coates, G. Grynberg, Crystallography of optical lattices. *Phys. Rev. A* **50**, 5173–5189 (1994). doi: 10.1103/PhysRevA.50.5173; pmid: 9911519
13. I. Bloch, Ultracold quantum gases in optical lattices. *Nat. Phys.* **1**, 23–30 (2005). doi: 10.1038/nphys138
14. M. Campbell, D. N. Sharp, M. T. Harrison, R. G. Denning, A. J. Turberfield, Fabrication of photonic crystals for the visible spectrum by holographic lithography. *Nature* **404**, 53–56 (2000). doi: 10.1038/35003523; pmid: 10716437
15. E. Betzig, Excitation strategies for optical lattice microscopy. *Opt. Express* **13**, 3021–3036 (2005). doi: 10.1364/OPEX.13.003021; pmid: 19495199
16. I. Tikhonenko, D. K. Nag, D. N. Robinson, M. P. Koonce, Microtubule-nucleus interactions in *Dictyostelium discoideum* mediated by central motor kinesins. *Eukaryot. Cell* **8**, 723–731 (2009). doi: 10.1128/EC.00018-09; pmid: 19286984
17. G. Jung, M. A. Titus, J. A. Hammer 3rd, The *Dictyostelium* type V myosin MyoJ is responsible for the cortical association and motility of contractile vacuole membranes. *J. Cell Biol.* **186**, 555–570 (2009). doi: 10.1083/jcb.200810147; pmid: 19687255
18. S. Diez, G. Gerisch, K. Anderson, A. Müller-Taubenberger, T. Bretschneider, Subsecond reorganization of the actin network in cell motility and chemotaxis. *Proc. Natl. Acad. Sci. U.S.A.* **102**, 7601–7606 (2005). doi: 10.1073/pnas.0408546102; pmid: 15894626
19. M. Coelho, N. Maghelli, I. M. Tolić-Nørrelykke, Single-molecule imaging in vivo: The dancing building blocks of the cell. *Integr. Biol.* **5**, 748–758 (2013). doi: 10.1039/c3ib40018b; pmid: 23525260
20. J. G. Ritter, R. Veith, J. P. Siebrasse, U. Kubitscheck, High-contrast single-particle tracking by selective focal plane illumination microscopy. *Opt. Express* **16**, 7142–7152 (2008). doi: 10.1364/OE.16.007142; pmid: 18545417
21. M. Tokunaga, N. Imamoto, K. Sakata-Sogawa, Highly inclined thin illumination enables clear single-molecule imaging in cells. *Nat. Methods* **5**, 159–161 (2008). doi: 10.1038/nmeth1171; pmid: 18176568
22. J. Chen *et al*., Single-molecule dynamics of enhanceosome assembly in embryonic stem cells. *Cell* **156**, 1274–1285 (2014). doi: 10.1016/j.cell.2014.01.062; pmid: 24630727
23. J. C. Gebhardt *et al*., Single-molecule imaging of transcription factor binding to DNA in live mammalian cells. *Nat. Methods* **10**, 421–426 (2013). doi: 10.1038/nmeth.2411; pmid: 23524394
24. E. Betzig, Proposed method for molecular optical imaging. *Opt. Lett.* **20**, 237–239 (1995). doi: 10.1364/OL.20.000237; pmid: 19859146
25. F. Cella Zanacchi *et al*., Live-cell 3D super-resolution imaging in thick biological samples. *Nat. Methods* **8**, 1047–1049 (2011). doi: 10.1038/nmeth.1744; pmid: 21983925
26. M. Speidel, A. Jonás, E. L. Florin, Three-dimensional tracking of fluorescent nanoparticles with subnanometer precision by use of off-focus imaging. *Opt. Lett.* **28**, 69–71 (2003). doi: 10.1364/OL.28.000069; pmid: 12656488
27. H. P. Kao, A. S. Verkman, Tracking of single fluorescent particles in three dimensions: Use of cylindrical optics to encode particle position. *Biophys. J.* **67**, 1291–1300 (1994). doi: 10.1016/S0006-3495(94)80601-0; pmid: 7811944
28. E. Betzig *et al*., Imaging intracellular fluorescent proteins at nanometer resolution. *Science* **313**, 1642–1645 (2006). doi: 10.1126/science.1127344; pmid: 16902090
29. J. Ellenberg *et al*., Nuclear membrane dynamics and reassembly in living cells: Targeting of an inner nuclear membrane protein in interphase and mitosis. *J. Cell Biol.* **138**, 1193–1206 (1997). doi: 10.1083/jcb.138.6.1193; pmid: 9298976
30. Y. Mimori-Kiyosue, N. Shiina, S. Tsukita, The dynamic behavior of the APC-binding protein EB1 on the distal ends of microtubules. *Curr. Biol.* **10**, 865–868 (2000). doi: 10.1016/S0960-9822(00)00600-X; pmid: 10899006
31. K. T. Applegate *et al*., plusTipTracker: Quantitative image analysis software for the measurement of microtubule dynamics. *J. Struct. Biol.* **176**, 168–184 (2011). doi: 10.1016/j.jsb.2011.07.009; pmid: 21821130
32. A. Khodjakov, C. L. Rieder, Imaging the division process in living tissue culture cells. *Methods* **38**, 2–16 (2006). doi: 10.1016/j.ymeth.2005.07.007; pmid: 16343936
33. N. Taguchi, N. Ishihara, A. Jofuku, T. Oka, K. Mihara, Mitotic phosphorylation of dynamin-related GTPase Drp1 participates in mitochondrial fission. *J. Biol. Chem.* **282**, 11521–11529 (2007). doi: 10.1074/jbc.M607279200; pmid: 17301055
34. L. Lu, M. S. Ladinsky, T. Kirchhausen, Cisternal organization of the endoplasmic reticulum during mitosis. *Mol. Biol. Cell* **20**, 3471–3480 (2009). doi: 10.1091/mbc.E09-04-0327; pmid: 19494040
35. D. Wloga, J. Frankel, From molecules to morphology: Cellular organization of *Tetrahymena thermophila*. *Methods Cell Biol.* **109**, 83–140 (2012). doi: 10.1016/B978-0-12-385967-9.00005-0; pmid: 22444144
36. A. T. Ritter, K. L. Angus, G. M. Griffiths, The role of the cytoskeleton at the immunological synapse. *Immunological Reviews* **256**, 107–117 (2013). doi: 10.1111/imr.12117; pmid: 24117816
37. D. Dormann, C. J. Weijer, Imaging of cell migration. *EMBO J.* **25**, 3480–3493 (2006). doi: 10.1038/sj.emboj.7601227; pmid: 16900100
38. P. H. Wu, A. Giri, S. X. Sun, D. Wirtz, Three-dimensional cell migration does not follow a random walk. *Proc. Natl. Acad. Sci. U.S.A.* **111**, 3949–3954 (2014). doi: 10.1073/pnas.1318967111; pmid: 24594603
39. P. Friedl, S. Borgmann, E. B. Bröcker, Amoeboid leukocyte crawling through extracellular matrix: Lessons from the *Dictyostelium* paradigm of cell movement. *J. Leukoc. Biol.* **70**, 491–509 (2001). pmid: 11590185
40. A. B. Hauert, S. Martinelli, C. Marone, V. Niggli, Differentiated HL-60 cells are a valid model system for the analysis of human neutrophil migration and chemotaxis. *Int. J. Biochem. Cell Biol.* **34**, 838–854 (2002). doi: 10.1016/S1357-2725(02)00010-9; pmid: 11950599
41. W. R. Legant *et al*., Measurement of mechanical tractions exerted by cells in three-dimensional matrices. *Nat. Methods* **7**, 969–971 (2010). doi: 10.1038/nmeth.1531; pmid: 21076420
42. J. N. Bembenek, K. J. Verbrugghe, J. Khanikar, G. Csankovszki, R. C. Chan, Condensin and the spindle midzone prevent cytokinesis failure induced by chromatin bridges in *C. elegans* embryos. *Curr. Biol.* **23**, 937–946 (2013). doi: 10.1016/j.cub.2013.04.028; pmid: 23684975
43. J. M. Schumacher, A. Golden, P. J. Donovan, AIR-2: An Aurora/Ipl1-related protein kinase associated with chromosomes and midbody microtubules is required for polar body extrusion and cytokinesis in *Caenorhabditis elegans* embryos. *J. Cell Biol.* **143**, 1635–1646 (1998). doi: 10.1083/jcb.143.6.1635; pmid: 9852156
44. M. Carmena, W. C. Earnshaw, The cellular geography of aurora kinases. *Nat. Rev. Mol. Cell Biol.* **4**, 842–854 (2003). doi: 10.1038/nrm1245; pmid: 14625535
45. N. Velarde, K. C. Gunsalus, F. Piano, Diverse roles of actin in *C. elegans* early embryogenesis. *BMC Dev. Biol.* **7**, 142 (2007). doi: 10.1186/1471-213X-7-142; pmid: 18157918
46. S. W. Grill, Growing up is stressful: Biophysical laws of morphogenesis. *Curr. Opin. Genet. Dev.* **21**, 647–652 (2011). doi: 10.1016/j.gde.2011.09.005; pmid: 21982413
47. A. Sokolow, Y. Toyama, D. P. Kiehart, G. S. Edwards, Cell ingression and apical shape oscillations during dorsal closure in *Drosophila*. *Biophys. J.* **102**, 969–979 (2012). doi: 10.1016/j.bpj.2012.01.027; pmid: 22404919
48. K. Wang *et al*., Rapid adaptive optical recovery of optimal resolution over large volumes. *Nat. Methods* **11**, 625–628 (2014). doi: 10.1038/nmeth.2925; pmid: 24727653
49. G. Donnert, C. Eggeling, S. W. Hell, Major signal increase in fluorescence microscopy through dark-state relaxation. *Nat. Methods* **4**, 81–86 (2007). doi: 10.1038/nmeth986; pmid: 17179937
50. N. Ji, J. C. Magee, E. Betzig, High-speed, low-photodamage nonlinear imaging using passive pulse splitters. *Nat. Methods* **5**, 197–202 (2008). doi: 10.1038/nmeth.1175; pmid: 18204458
51. T. Shimozawa *et al*., Improving spinning disk confocal microscopy by preventing pinhole cross-talk for intravital imaging. *Proc. Natl. Acad. Sci. U.S.A.* **110**, 3399–3404 (2013). doi: 10.1073/pnas.1216696110; pmid: 23401517
52. J. D. Sander, J. K. Joung, CRISPR-Cas systems for editing, regulating and targeting genomes. *Nat. Biotechnol.* **32**, 347–355 (2014). doi: 10.1038/nbt.2842; pmid: 24584096
53. T. Zimmermann, J. Rietdorf, R. Pepperkok, Spectral imaging and its applications in live cell microscopy. *FEBS Lett.* **546**, 87–92 (2003). doi: 10.1016/S0014-5793(03)00521-0; pmid: 12829241
54. J. Livet *et al*., Transgenic strategies for combinatorial expression of fluorescent proteins in the nervous system. *Nature* **450**, 56–62 (2007). doi: 10.1038/nature06293; pmid: 17972876
55. E. Lubeck, L. Cai, Single-cell systems biology by super-resolution imaging and combinatorial labeling. *Nat. Methods* **9**, 743–748 (2012). doi: 10.1038/nmeth.2069; pmid: 22660740
56. A. M. Valm *et al*., Systems-level analysis of microbial community organization through combinatorial labeling and spectral imaging. *Proc. Natl. Acad. Sci. U.S.A.* **108**, 4152–4157 (2011). doi: 10.1073/pnas.1101134108; pmid: 21325608
57. L. Gao, L. Shao, B. C. Chen, E. Betzig, 3D live fluorescence imaging of cellular dynamics using Bessel beam plane illumination microscopy. *Nat. Protoc.* **9**, 1083–1101 (2014). doi: 10.1038/nprot.2014.087; pmid: 24722406
58. B. P. English *et al*., Single-molecule investigations of the stringent response machinery in living bacterial cells. *Proc. Natl. Acad. Sci. U.S.A.* **108**, E365–E373 (2011). doi: 10.1073/pnas.1102255108; pmid: 21730169

ACKNOWLEDGMENTS

We thank L. Gao, now at Stony Brook University, for technical expertise; the Shared Resource teams at Janelia for their skill and dedication in specimen handling and preparation; and the Instrument Design and Fabrication team for their manufacturing expertise. B.-C.C., W.R.L., K.W., L.S., Z.L., B.P.E., and E.B. are funded by the Howard Hughes Medical Institute (HHMI). We also gratefully acknowledge the support of the Janelia Visitor Program. C.J. is supported by NIH grant R01GM080370. X.S.W. and J.A.H. are funded by the Division of Intramural Research, National Heart, Lung, and Blood Institute, NIH. Y.M.-K. is supported by the Japan Society for the Promotion of Science–NEXT program LS128, the Uehara Memorial Foundation, the Takeda Science Foundation, the Kurata Memorial Hitachi Science and Technology Foundation, and an intramural grant from the RIKEN Center for Developmental Biology. A.T.R. and J.L.S. acknowledge G. M. Griffiths of the University of Cambridge as the doctoral cosupervisor of A.T.R., who provided technical expertise with CTL experiments. These experiments are a collaboration with GMG. L.F.L. and R.D.M. were supported by NIH grant RM01-GM61010 and HHMI. A.-C.R. is supported by the Human Frontier Science Program LT000926/2012. S.W.G. acknowledges support from the European Research Council starting grant 281903. J.T.W. and G.S. are supported by NIH R01HD37047. G.S. is also an HHMI Investigator. U.S.T. and D.P.K. are supported by NIH grant GM33830. All data in the manuscript are available upon request. Researchers can apply to access the microscope as visitors through the Advanced Imaging Center at Janelia Farm (www.janelia.org/aic). Documentation for the construction of a copy of the microscope is available after execution of a research license with HHMI. Portions of the technology described herein are covered by U.S. Patent 7,894,136 issued to E.B. and assigned to Lattice Light, LLC of Ashburn, VA; U.S. Patent 8,711,211 issued to E.B. and assigned to HHMI; and U.S. Patent application 13/844,405 filed by E.B. and K.W. and assigned to HHMI.

SUPPLEMENTARY MATERIALS

www.sciencemag.org/content/346/6208/1257998/suppl/DC1
Supplementary Text
Figs. S1 to S26
Table S1
References (*59*–*73*)
Movies S1 to S18

27 June 2014; accepted 3 September 2014
10.1126/science.1257998

RESEARCH ARTICLE SUMMARY

DNA REPLICATION

Cdc48 and a ubiquitin ligase drive disassembly of the CMG helicase at the end of DNA replication

Marija Maric,* Timurs Maculins,* Giacomo De Piccoli, Karim Labib†

INTRODUCTION: Chromosome replication is initiated by a universal mechanism in eukaryotic cells. This mechanism entails the assembly and activation at replication origins of the DNA helicase known as CMG (Cdc45-MCM-GINS), which is essential for the progression of replication forks. The replisome is built around the CMG helicase, which associates stably with DNA replication forks until the termination of DNA synthesis. The mechanism by which CMG is disassembled was unknown until now but is likely to represent a key regulated step at the end of chromosome replication.

RATIONALE: The CMG helicase exists only at DNA replication forks but can be isolated from extracts of S-phase budding yeast cells, after digestion of chromosomal DNA. We screened for posttranslational modifications of the CMG helicase that might regulate its function.

RESULTS: Here we show that the CMG helicase is ubiquitylated during the final stages of chromosome replication in *Saccharomyces cerevisiae*, specifically on its Mcm7 subunit. The F-box protein Dia2 is essential in vivo for ubiquitylation of CMG, and the SCF^{Dia2} ubiquitin ligase is also required to ubiquitylate CMG in vitro on its Mcm7 subunit in extracts of S-phase yeast cells. Ubiquitylated CMG exists only transiently in vivo, as it is rapidly disassembled in a reaction that is independent of the proteasome but requires the Cdc48/p97 segregase, which associates with ubiquitylated CMG. Consistent with these data, we show that Dia2 is essential for disassembly of the CMG helicase at the end of S phase in budding yeast. Rather than causing dissolution of the active helicase, Dia2 specifically induces the disassembly of terminated CMG complexes, which suggests that the helicase undergoes a change at the end of DNA replication, predisposing it for disassembly.

ON OUR WEB SITE

Read the full article at http://dx.doi.org/10.1126/science.1253596

CONCLUSION: Our findings indicate that the end of chromosome replication in eukaryotes is controlled in a similarly complex fashion to the much-better-characterized initiation step. Our findings indicate that replisome disassembly is driven by the regulated dissolution of the stable CMG helicase, which uses its hexameric ring of Mcm2-7 proteins to encircle the parental DNA at replication forks. Our data identify two key features of helicase disassembly in budding yeast: First, there is an essential role for the F-box protein Dia2, which drives ubiquitylation of the CMG helicase on its Mcm7 subunit. Second, the Cdc48 segregase is required to break ubiquitylated CMG into its component parts. Once separated from GINS and Cdc45, the Mcm2-7 hexamer is less stable, so that all of the subunits of the CMG helicase are lost from the newly replicated DNA. Just as the main features of helicase assembly have been conserved across evolution from yeasts to humans, we envisage that disassembly of the CMG helicase will also involve a universal mechanism in eukaryotic cells, by which Cdc48/p97 drives disassembly of ubiquitylated CMG at the end of DNA replication. ■

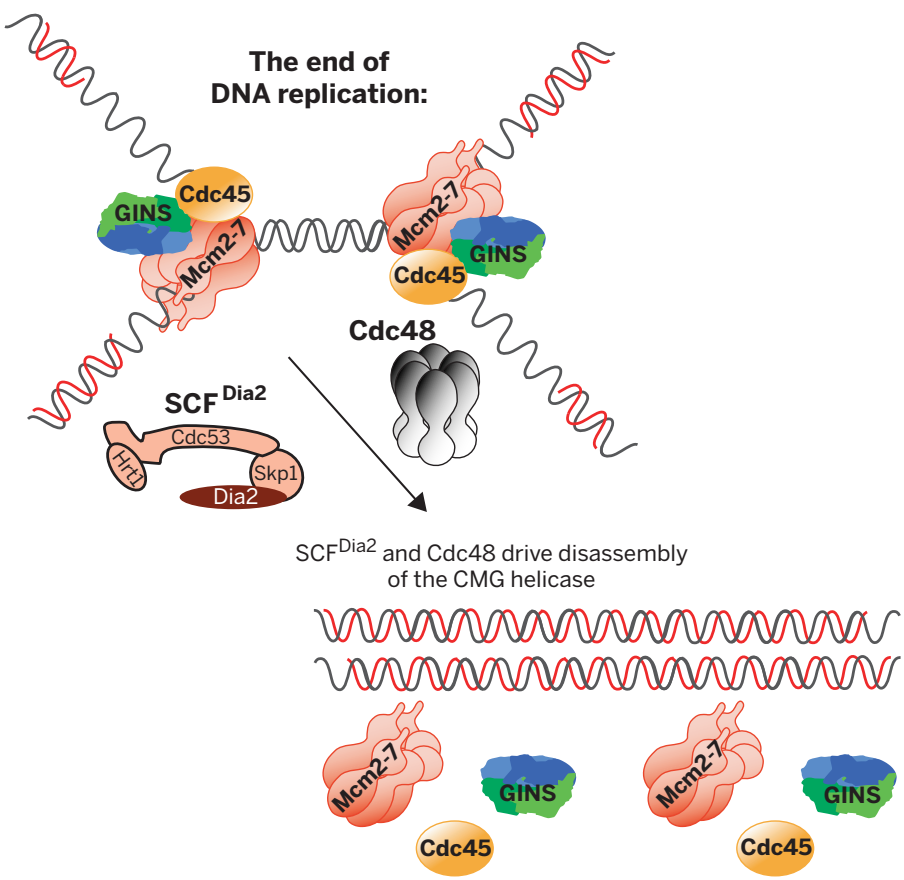

Regulated disassembly of the CMG helicase at the end of chromosome replication in budding yeast. It is very important that the CMG helicase is not displaced from replication forks during elongation, because it cannot be reloaded. When replication terminates, however, the ubiquitin ligase SCF^{Dia2} and the Cdc48 segregase induce disassembly of the CMG helicase, leading to dissolution of the replisome.

RELATED ITEMS IN *SCIENCE*

S. P. Bell, Terminating the replisome. *Science* **346**, 418–419 (2014).
S. Priego Moreno *et al.*, Polyubiquitylation drives replisome disassembly at the termination of DNA replication. *Science* **346**, 477–481 (2014).

The list of author affiliations is available in the full article online.
*These authors contributed equally to this work.
†Corresponding author. E-mail: kpmlabib@dundee.ac.uk
Cite this article as M. Maric *et al.* *Science* **346**, 1253596 (2014); DOI: 10.1126/science.1253596

Published by AAAS

RESEARCH ARTICLE

DNA REPLICATION

Cdc48 and a ubiquitin ligase drive disassembly of the CMG helicase at the end of DNA replication

Marija Maric,[1,2]* Timurs Maculins,[2]*† Giacomo De Piccoli,[2]‡ Karim Labib[1]§

Chromosome replication is initiated by a universal mechanism in eukaryotic cells, involving the assembly and activation at replication origins of the CMG (Cdc45-MCM-GINS) DNA helicase, which is essential for the progression of replication forks. Disassembly of CMG is likely to be a key regulated step at the end of chromosome replication, but the mechanism was unknown until now. Here we show that the ubiquitin ligase known as SCF^{Dia2} promotes ubiquitylation of CMG during the final stages of chromosome replication in *Saccharomyces cerevisiae*. The Cdc48/p97 segregase then associates with ubiquitylated CMG, leading rapidly to helicase disassembly. These findings indicate that the end of chromosome replication in eukaryotes is controlled in a similarly complex fashion to the much-better-characterized initiation step.

The initiation of chromosome replication involves a set of conserved and highly regulated factors, which recruit Cdc45 and the GINS complex to the Mcm2-7 helicase core at origins of replication, producing the active DNA helicase that contains 11 subunits and is known as CMG (Cdc45-MCM-GINS) (*1*, *2*), around which the replisome is built (*3*–*5*). Helicase assembly represents the key regulated step during the initiation of chromosome replication (*3*), and the CMG helicase then gets a single opportunity to unwind the parental DNA duplex in each region of the genome (*6*), thus ensuring that every chromosome is copied just once. Whereas the Mcm2-7 helicase core can be loaded around DNA only during the G_1 phase of the cell cycle (*7*–*9*), as an inactive double hexamer of two Mcm2-7 rings, the missing helicase subunits known as Cdc45 and GINS can be recruited only when cells enter S phase (*4*, *5*). This produces active CMG complexes that each contains a single Mcm2-7 hexamer (*1*).

Once assembled, the CMG helicase stably encircles the parental DNA and must remain continuously associated with each DNA replication fork (*6*), whatever barriers are encountered during the elongation phase of DNA replication (*10*, *11*), because CMG cannot normally be reloaded after initiation. Nevertheless, the convergence of two replication forks leads rapidly to disassembly of the CMG helicase, and thus of the entire replisome, by a mechanism that until now has remained enigmatic.

[1]MRC Protein Phosphorylation and Ubiquitylation Unit, Sir James Black Centre, College of Life Sciences, University of Dundee, Dow Street, Dundee DD1 5EH, UK. [2]Cancer Research UK Manchester Institute, University of Manchester, Wilmslow Road, Manchester M20 4BX, UK. *These authors contributed equally to this work. †Present address: Postdoctoral Research Programme, Discovery Sciences, Astrazeneca, Alderley Park, Cheshire SK10 4TG, UK. ‡Present address: Division of Biomedical Cell Biology, Warwick Medical School, University of Warwick, Coventry CV4 7AL, UK. §Corresponding author. E-mail: kpmlabib@dundee.ac.uk

Results

CMG is ubiquitylated on its Mcm7 subunit

In native extracts of S-phase budding yeast cells, we discovered a modification of the Mcm7 protein (fig. S1), which was specifically detected in the small fraction of Mcm7 that associates with GINS and Cdc45 at DNA replication forks, as part of the CMG helicase (*1*). The modification of Mcm7 was more evident above neutral pH, and above of pH 8.5 we found that almost all of the Mcm7 protein that associated with GINS was present as a ladder of modified forms (fig. S1A). Several lines of evidence demonstrated that the modification corresponded to ubiquitylation of Mcm7 (Fig. 1A and fig. S1C), involving the addition of K48-linked ubiquitin chains (Fig. 1B and fig. S1D).

To confirm that Mcm7 was only ubiquitylated when it formed part of the CMG helicase, we isolated Mcm2-7 complexes that had been released from chromatin into yeast cell extracts by deoxyribonuclease (DNase) digestion. These comprised the inactive Mcm2-7 helicase core that is loaded at origins of replication before the initiation of chromosome replication (*12*, *13*), and also the active CMG helicase that is present at DNA replication forks (*1*, *2*)—these are the only two stable forms of the budding yeast Mcm2-7 complex under these extract conditions (*14*). Ubiquitylation of Mcm7 was only detected in isolated Mcm2-7 complexes and only upon entry into S phase (Fig. 1C, *Control*). Moreover, ubiquitylation was not detected if assembly of CMG was blocked by prior depletion of degron-tagged Cdc45 during G_1 phase (Fig. 1C, *cdc45-td*). These findings define a ubiquitylation of the CMG helicase, which is specific for the Mcm7 subunit (Fig. 1D).

SCF^{Dia2} is required for ubiquitylation of CMG in yeast extracts

Ubiquitylation of CMG was independent of the various E3 ubiquitin ligases and E2 ubiquitin conjugating enzymes that are known to regulate DNA replication and DNA repair in response to DNA damage [such as Rad18, Rad5, and Ubc13 that ubiquitylate PCNA (*15*, *16*); the cullin Rtt101 and its partner Mms22 (*17*); and the SUMO-directed ubiquitin ligase Slx5-Slx8 (*18*, *19*) (fig. S2)]. In contrast, ubiquitylation of CMG was completely blocked in the absence of the F-box protein known as Dia2 (fig. S2). The Dia2 protein maintains genome integrity and forms the substrate-targeting component of the SCF^{Dia2} ubiquitin ligase (*20*–*22*), which associates with the "replisome progression complex" that assembles around the CMG helicase at replication forks (*23*).

In principle, the high efficiency of CMG ubiquitylation in these experiments could have had several very different explanations. One possibility was that almost all CMG complexes at DNA replication forks in vivo were ubiquitylated by SCF^{Dia2}. Alternatively, the yeast extract under these particular conditions might serve as an efficient and highly specific in vitro system, in which SCF^{Dia2} drives ubiquitylation of the Mcm7 subunit of CMG helicase complexes that were derived from DNA replication forks in S-phase cells. In support of the latter idea, ubiquitylation of the helicase was blocked by an increased salt concentration in the extract (Fig. 2A, 700 mM salt), which does not affect the stability of CMG but prevents its association in vitro with dynamic partners (*1*, *24*), including SCF^{Dia2} (*23*). To prove that SCF^{Dia2} was required for in vitro ubiquitylation of CMG, we developed an assay involving two yeast strains that were grown in parallel to each other. The first represented a recipient strain for the in vitro ubiquitylation assay and had a TAP tag on the Sld5 subunit of GINS, to allow the isolation of CMG helicase from the recipient yeast cell extracts. The second was a donor strain that provided the source of Dia2 for in vitro ubiquitylation of CMG. The recipient and donor strains were synchronized in S phase, before the two cultures were mixed in equal proportions and used to generate a common cell extract, from which recipient CMG was isolated by immunoprecipitation of TAP-Sld5. As controls, we showed that ubiquitylation of CMG was observed when both recipient and donor strains contained Dia2 (Fig. 2B, sample 1), but not if both strains lacked Dia2 (Fig. 2B, sample 2). Critically, we found that in vitro ubiquitylation of CMG complexes from *dia2*Δ recipient cells was partially restored when the donor strain contained wild-type levels of Dia2 (Fig. 2B, sample 3; note that the concentration of Dia2 was reduced twofold by the 1:1

mixture of *DIA2* donor cells with *dia2*Δ recipient cells). Moreover, ubiquitylation was fully restored if the donor strain overexpressed *DIA2* (Fig. 2B, sample 4). Finally, we showed that the addition of purified Dia2 was able to rescue the ubiquitylation of CMG in extracts of *dia2*Δ cells (Fig. 2C). These findings indicate that Dia2 promotes the ubiquitylation of CMG in yeast cell extracts.

The SCF represents a family of E3 ubiquitin ligases, of which each uses a different F-box protein to recruit substrates but all share a common scaffold comprising the cullin that in budding yeast is known as Cdc53. We showed that in vitro ubiquitylation of CMG was blocked by inactivation of Cdc53, but not by inactivation of the essential F-box protein Cdc4, which produces an equivalent arrest to cell cycle progression [Fig. 2D, (a)]. Similarly, we found that in vitro ubiquitylation of CMG was prevented by inactivation of the Cdc34 E2 enzyme, which ubiquitylates substrates of the SCF, and the defect could be rescued by addition of purified Cdc34 [Fig. 2D, (b)]. These findings demonstrate that SCF^{Dia2} either ubiquitylates directly the Mcm7 subunit of the CMG helicase in yeast cell extracts or else is required for CMG to be ubiquitylated by another unknown ligase.

Dia2-dependent ubiquitylation links CMG to Cdc48 in vivo

To search for in vivo ubiquitylation of the CMG helicase at DNA replication forks, we isolated CMG complexes from high-salt extracts that blocked the in vitro ubiquitylation reaction (as shown in Fig. 2A). Ubiquitylated CMG helicase was not detected when cells entered S phase, even in the presence of DNA damage, or upon activation of the S-phase checkpoint by depletion of deoxynucleotide triphosphates (Fig. 3A). One possible explanation was that ubiquitylated CMG might exist only very transiently in vivo, either due to proteasomal degradation of ubiquitylated Mcm7, or else due to a disassembly reaction that could require the Cdc48/p97 segregase (*25*, *26*). Inactivation of the Rpt6/Cim3 proteasome subunit blocks completion of the cell cycle (*27*), but the CMG helicase complex disappeared upon shifting an asynchronous culture of *cim3-1* cells to 37°C (Fig. 3B) rather than accumulating in a ubiquitylated form. The disappearance of CMG was probably due to helicase disassembly at the end of S phase, because *cim3-1* cells in S phase are able to finish DNA replication when the proteasome is inactivated at 37°C (fig. S3).

In contrast, in vivo ubiquitylation of the Mcm7 subunit of CMG was detected, even at the permissive temperature of 24°C in *cdc48-3* cells, and accumulated still further at the restrictive temperature of 37°C (Fig. 3C). Whereas similar amounts of GINS could be immunoprecipitated from control and *cdc48-3* cells, more of the Cdc45 and Mcm2-7 proteins associated with GINS in the mutant, suggesting that the CMG helicase complex had accumulated in cells with defective Cdc48/p97 (Fig. 3C, also see below). These findings indicated that ubiquitylated CMG helicase exists in vivo but is normally a transient species that is rapidly processed in a reaction that requires the Cdc48 adenosine triphosphatase (ATPase).

To explore the regulation of CMG by ubiquitylation in vivo, we generated a degradable allele of Cdc48 (Fig. 3D) by fusion of the endogenous

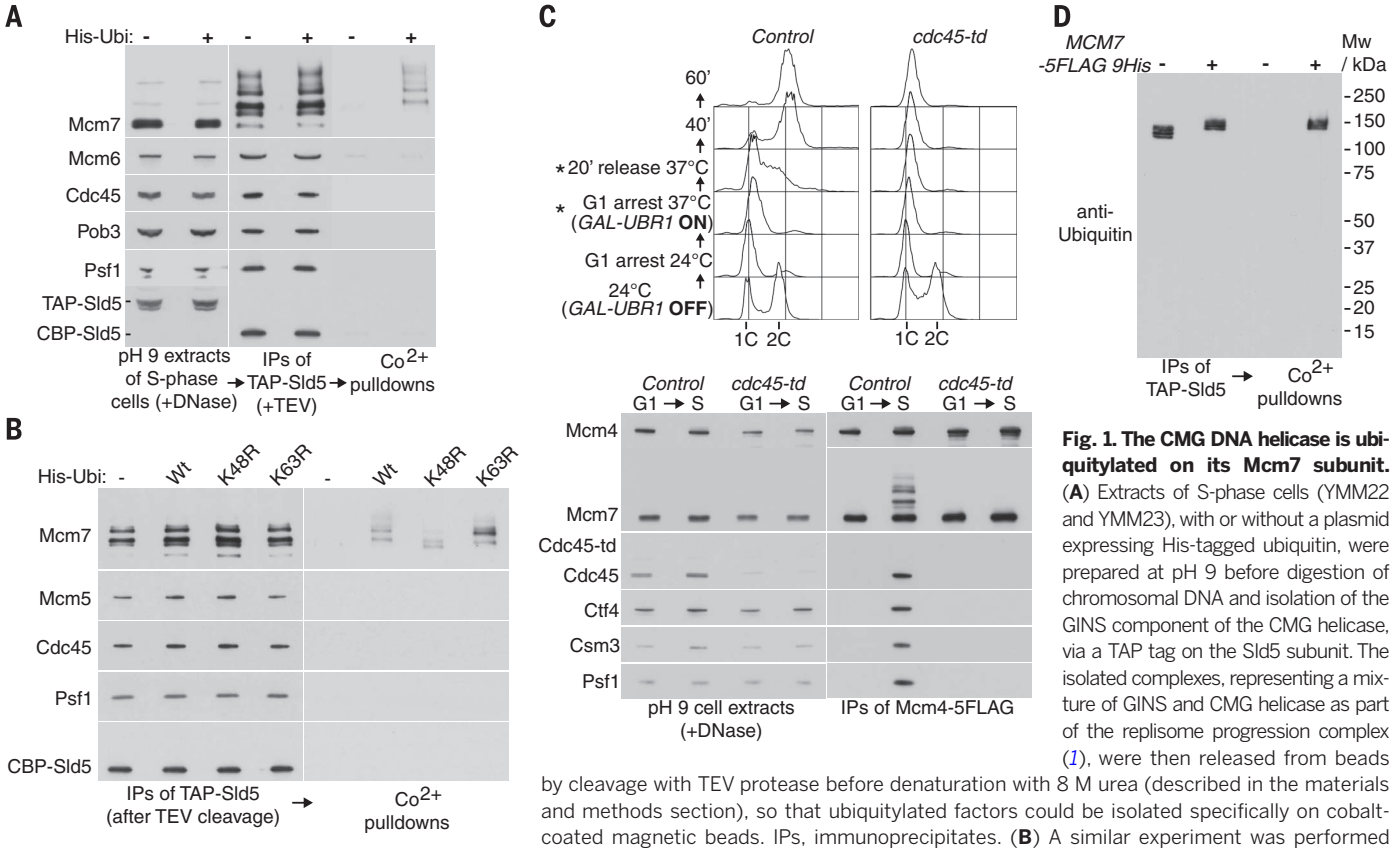

Fig. 1. The CMG DNA helicase is ubiquitylated on its Mcm7 subunit. (**A**) Extracts of S-phase cells (YMM22 and YMM23), with or without a plasmid expressing His-tagged ubiquitin, were prepared at pH 9 before digestion of chromosomal DNA and isolation of the GINS component of the CMG helicase, via a TAP tag on the Sld5 subunit. The isolated complexes, representing a mixture of GINS and CMG helicase as part of the replisome progression complex (*1*), were then released from beads by cleavage with TEV protease before denaturation with 8 M urea (described in the materials and methods section), so that ubiquitylated factors could be isolated specifically on cobalt-coated magnetic beads. IPs, immunoprecipitates. (**B**) A similar experiment was performed with control cells (YMM22) or cells expressing wild-type (YMM23) ubiquitin, K48R ubiquitin (YMM89), or K63R ubiquitin (YMM90). (**C**) Control (YSS184) and *cdc45-td* (YMM74) cells were arrested in G_1 phase at 24°C, before inactivation of Cdc45-td and release into S phase for 20 min, as described in the materials and methods. DNA content was measured by flow cytometry (asterisks denote samples that were used to prepare cell extracts). After digestion of chromosomal DNA in cell extracts, the Mcm4 subunit of the Mcm2-7 helicase core was then isolated by immunoprecipitation. This enriched specifically for two forms of Mcm2-7 complex, each of which are bound to chromatin (*14*): the inactive double hexamer at origins and the active CMG helicase at forks, the latter of which is the substrate for ubiquitylation on its Mcm7 subunit. (**D**) A similar experiment to that shown in (A) was performed with control cells (YASD375) or cells with tagged Mcm7 (YGDP483). The isolated material was resolved in a 4 to 12% gradient gel, before immunoblotting with anti-ubiquitin antibody (P4D1). Mw, molecular weight. Additional flow cytometry data for the experiments depicted in this figure can be found in fig. S14.

CDC48 gene to the auxin-inducible degron (*28*). Ubiquitylated CMG helicase was not detected in an asynchronously growing culture of *cdc48-aid* cells, but addition of auxin to the culture led to accumulation of CMG with ubiquitylated Mcm7 (Fig. 3E). Consistent with our in vitro data, in vivo ubiquitylation of the CMG helicase required Dia2 (Fig. 3F) but was independent of Rad5, Rad18, Ubc13, Slx5-Slx8, or Rtt101 (fig. S4). These data indicate that SCF^{Dia2} drives CMG ubiquitylation in vivo, leading rapidly to Cdc48-dependent disassembly.

Dia2 is required for CMG disassembly

The CMG helicase is assembled during the initiation of chromosome replication and then remains associated with DNA throughout the elongation phase, until the convergence of two replication forks terminates DNA synthesis, and leads to helicase disassembly. Whereas the CMG helicase is not present before S phase in control cells (*1*), we found that *dia2*Δ cells contained stable CMG complexes even during G_1 phase (Fig. 4 and fig. S5). This phenotype was not observed in the absence of other E3 ubiquitin ligases that regulate chromosome replication (fig. S6, A and B), or upon deletion of genes encoding other factors that preserve genome integrity at DNA replication forks, such as the Rrm3 helicase, the Blooms helicase Sgs1, Topoisomerase 3,

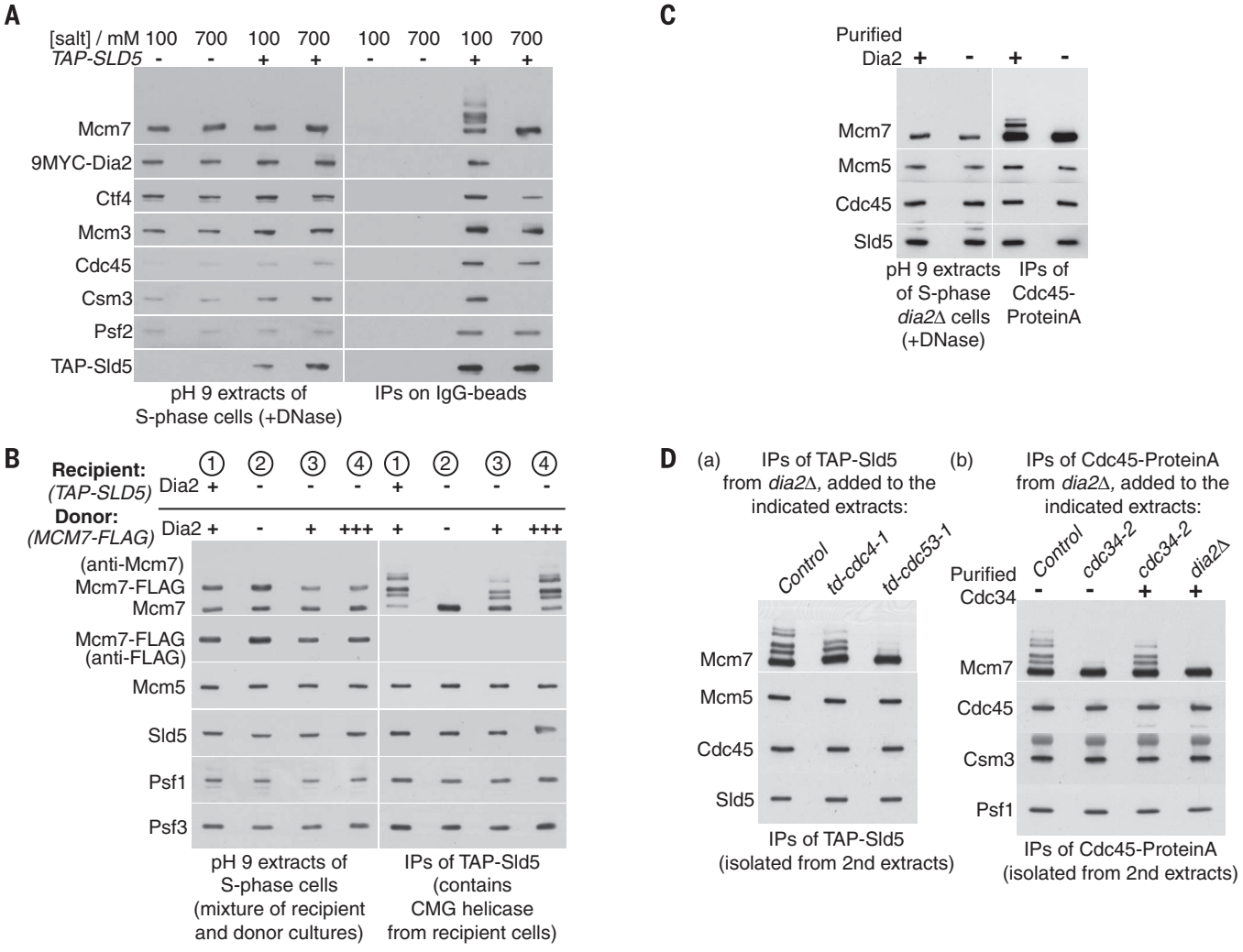

Fig. 2. SCF^{Dia2} drives in vitro ubiquitylation of CMG in yeast cell extracts. (**A**) Control (YHM117) and *TAP-SLD5* cells (YHM132) were processed as above, except that the extracts were made in the presence of 700 mM salt where indicated. Note that the CMG helicase is still stable in the presence of 700 mM salt but does not associate with other replisome components such as Csm3 or Dia2. (**B**) To demonstrate that Dia2 promotes the in vitro ubiquitylation of CMG, we synchronized the indicated *TAP-SLD5* recipient strains (1, YASD375; 2 to 4, YHM130) and *MCM7-5FLAG* donor strains (1 to 4, YTM305, YTM306, YTM305, and YTM312, respectively) in S phase at 30°C. Each of the indicated pairs of recipient and donor cultures were then mixed and used to prepare a single-cell extract at pH 9 (see materials and methods). After digestion of chromosomal DNA, the CMG helicase from recipient cells was isolated and monitored by immunoprecipitation of its TAP-Sld5 subunit. (**C**) *dia2*Δ *CDC45-Protein A* cells (YTM415) were synchronized in S phase, as above, and used to prepare a cell extract at pH 9. Purified Dia2 (from YTM532; see materials and methods) was added to the cell extracts as indicated, before immunoprecipitation of Cdc45-Protein A and detection of the associated CMG components by immunoblotting. (**D**) (a) Material containing CMG complexes was isolated from extracts of S-phase *dia2*Δ cells (YHM130) by immunoprecipitation of TAP-tagged Sld5 on IgG beads. The beads were then added to pH 9 extracts of control cells (YTM330), *td-cdc4-1* cells (YTM445), or *td-cdc53-1* cells (YTM444), which had been grown initially at 24°C, before shifting to 37°C for 60 min to inactivate Td-cdc4-1 and Td-cdc53-1 (see materials and methods for details). After reisolation of the beads, the indicated proteins were detected by immunoblotting. (b) Analogous experiments were performed with CMG-containing material that was isolated by immunoprecipitation of Cdc45-Protein from *dia2*Δ cells (YTM415). In this case, the beads were added to pH 9 extracts of control cells (YTM330), *cdc34-2* cells (YTM376), or *dia2*Δ cells (YMM90), which were then shifted from 24° to 37°C for 60 min. As indicated, the extracts were supplemented with purified Cdc34, which was isolated on IgG beads from an extract of *CDC34-TAP* cells (YTM396) and then liberated with TEV protease.

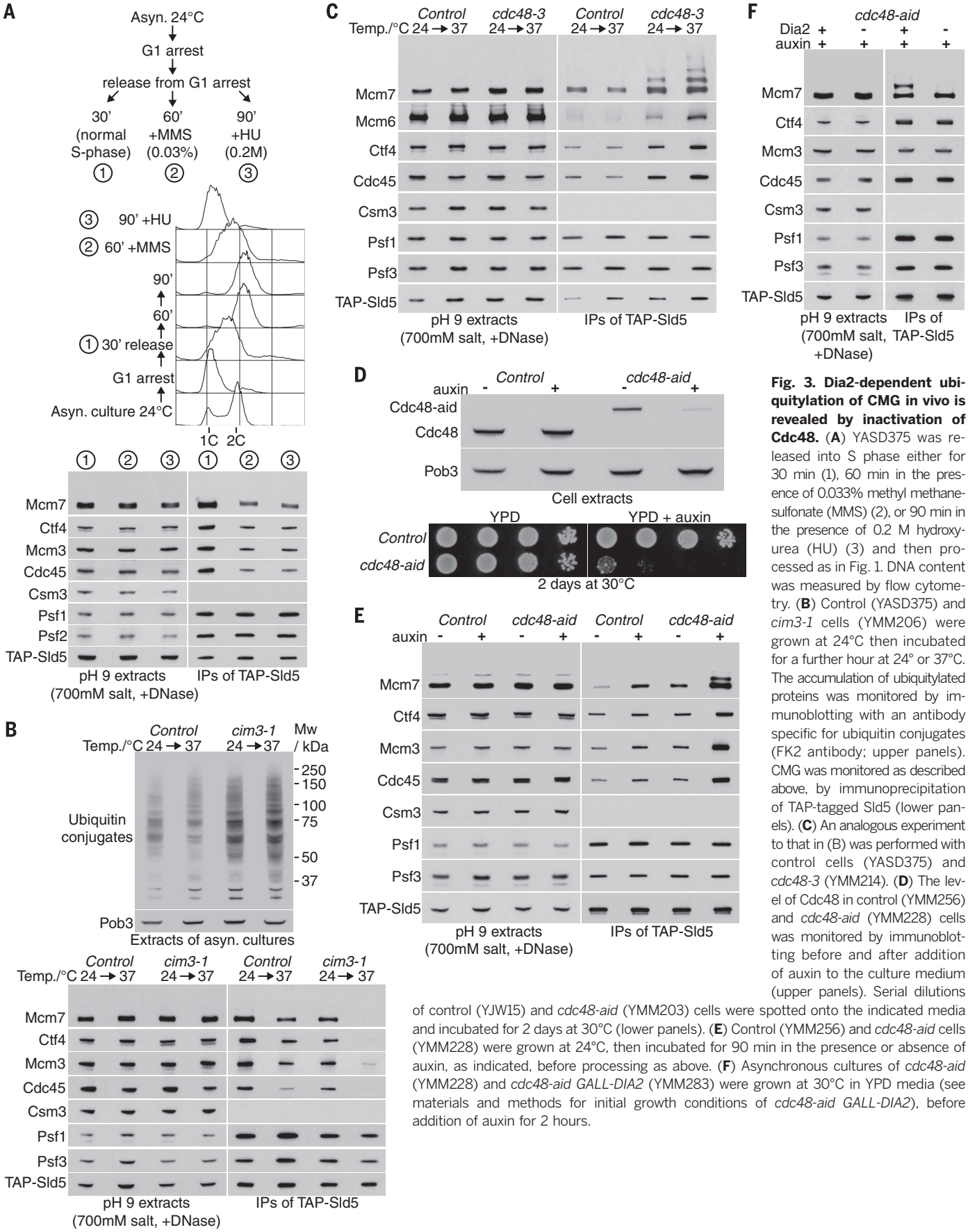

Fig. 3. Dia2-dependent ubiquitylation of CMG in vivo is revealed by inactivation of Cdc48. (**A**) YASD375 was released into S phase either for 30 min (1), 60 min in the presence of 0.033% methyl methanesulfonate (MMS) (2), or 90 min in the presence of 0.2 M hydroxyurea (HU) (3) and then processed as in Fig. 1. DNA content was measured by flow cytometry. (**B**) Control (YASD375) and *cim3-1* cells (YMM206) were grown at 24°C then incubated for a further hour at 24° or 37°C. The accumulation of ubiquitylated proteins was monitored by immunoblotting with an antibody specific for ubiquitin conjugates (FK2 antibody; upper panels). CMG was monitored as described above, by immunoprecipitation of TAP-tagged Sld5 (lower panels). (**C**) An analogous experiment to that in (B) was performed with control cells (YASD375) and *cdc48-3* (YMM214). (**D**) The level of Cdc48 in control (YMM256) and *cdc48-aid* (YMM228) cells was monitored by immunoblotting before and after addition of auxin to the culture medium (upper panels). Serial dilutions of control (YJW15) and *cdc48-aid* (YMM203) cells were spotted onto the indicated media and incubated for 2 days at 30°C (lower panels). (**E**) Control (YMM256) and *cdc48-aid* cells (YMM228) were grown at 24°C, then incubated for 90 min in the presence or absence of auxin, as indicated, before processing as above. (**F**) Asynchronous cultures of *cdc48-aid* (YMM228) and *cdc48-aid GALL-DIA2* (YMM283) were grown at 30°C in YPD media (see materials and methods for initial growth conditions of *cdc48-aid GALL-DIA2*), before addition of auxin for 2 hours.

or the recombination factors Rad51 and Rad52 (fig. S6, C and D).

To monitor directly the assembly and disassembly of the CMG helicase during a single cell cycle, we arrested control and *dia2*Δ cells in G_1 phase and then expressed a tagged version of the Psf2 subunit of GINS (in addition to the endogenous *PSF2* gene) before allowing the cells to enter S phase and complete chromosome replication (Fig. 5A). When control cells entered S phase, tagged Psf2 was incorporated into CMG complexes that subsequently disappeared when replication was completed [Fig. 5B, (a)]. In contrast, newly formed CMG complexes were assembled on schedule when *dia2*Δ cells entered S phase, but CMG disassembly did not occur at the end of S phase [Fig. 5B, (b); see Psf2-5FLAG]. We observed the same result when a tagged version of Cdc45 was expressed from G_1 phase onward in equivalent experiments (fig. S7), and it appears that the CMG persists into the next cell cycle in cells lacking Dia2, with much of the complex still associated with chromatin (fig. S8). Moreover, the persistence of CMG after S phase in *dia2*Δ cells did not reflect the unscheduled assembly of new CMG complexes (fig. S9). These findings demonstrate that Dia2 is essential for the disassembly of the CMG helicase, when budding yeast cells complete chromosome replication.

To begin to study how the role of Dia2 in CMG disassembly is regulated in vivo, we generated a yeast strain in which expression of the endogenous *DIA2* gene was controlled by a weakened *GALL* version of the *GAL1* promoter (*29*, *30*). Whereas *GALL-DIA2* behaved like control cells in medium containing galactose, repression of *GALL-DIA2* led to the persistence of "old" CMG complexes in G_1 phase (Fig. 6, A and B, stage 1), even upon prolonged incubation (Fig. 6, A and B, stage 2). Critically, however, reexpression of *DIA2* in G_1 phase led to efficient disassembly of these CMG complexes from previous cell cycles (Fig. 6, A and B, stage 3). Nevertheless, expression of *GALL-DIA2* did not interfere with the assembly of new CMG complexes when cells entered the subsequent S phase (Fig. 6, A and B, stage 4). These data indicate that Dia2 plays a direct role in CMG disassembly but is only able to induce the disassembly of the terminated helicase complexes that are produced when cells complete chromosome replication.

Dia2 drives CMG ubiquitylation during the completion of DNA replication

The action of SCF^{Dia2} is likely to be a key regulated step in the dissolution of the CMG helicase, leading rapidly to Cdc48-dependent disassembly. To establish whether ubiquitylated CMG is a transient form of the helicase that is generated throughout S phase, or else is induced by specific signals, we examined the consequences of inactivating Cdc48-aid in early S phase. When the progression of DNA replication forks was inhibited by addition of hydroxyurea to the culture medium, inactivation of Cdc48-aid did not reveal ubiquitylation of CMG (Fig. 7A, stage 1), even after prolonged incubation (Fig. 7A, stage 3) or in combination with DNA damage (Fig. 7A, stage 4). In contrast, washing cells into fresh medium lacking hydroxyurea allowed them to complete DNA replication and led to the accumulation of ubiquitylated CMG (Fig. 7A, stage 2; also see fig. S10). This was not due to inhibition of ubiquitylation by the S phase checkpoint pathway (Fig. 7B), and instead these data indicate that ubiquitylation of CMG is linked to a late step in DNA replication. In similar experiments, we examined all 11 subunits of CMG in immunoprecipitates of GINS or Mcm2-7 and found that Mcm7 was the predominant target for ubiquitylation in vivo (fig. S11), mirroring the in vitro ubiquitylation reaction that occurs in yeast cell extracts (Fig. 1).

Cdc48-dependent CMG disassembly when replication terminates

In favor of Cdc48 playing a direct role in the disassembly of CMG, we found that Cdc48

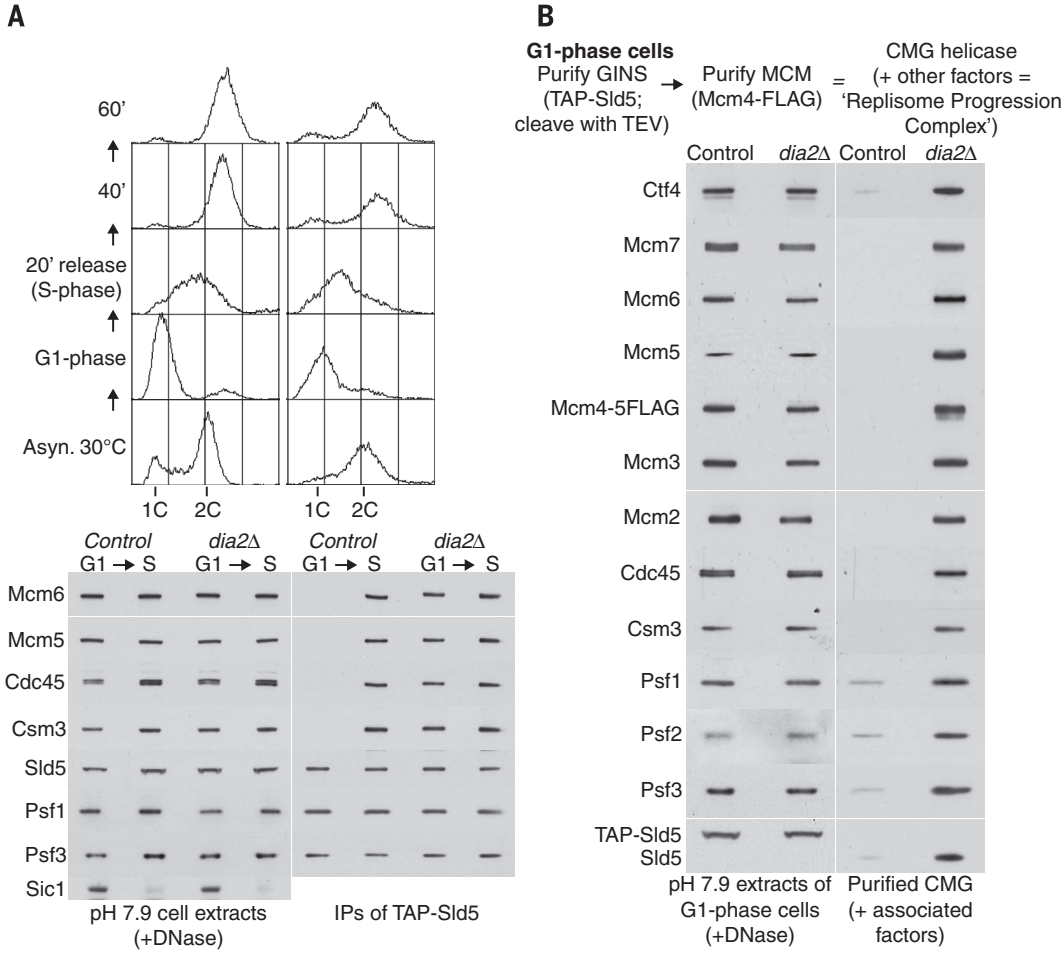

Fig. 4. CMG is present during the G_1 phase of the cell cycle in the absence of Dia2. (**A**) Control (YASD375) and *dia2*Δ (YHM130) cells were grown at 30°C, synchronized in G_1 phase by addition of mating pheromone, and then released into S phase. Samples were taken at the indicated times (S phase, 20-min sample) and processed for flow cytometry (top panels) or else used to make cell extracts (containing 100 mM salt), before digestion of chromosomal DNA and immunoprecipitation of the TAP-tagged Sld5 subunit of GINS (lower panels). The association of GINS with Cdc45 and Mcm2-7, as well as with other components of the replisome progression complex such as Csm3 and Ctf4 (*1*), was monitored by immunoblotting of the indicated proteins. (**B**) Cell extracts were generated as above, from G_1 phase control (YAG230-3) and *dia2*Δ (YTM687) cells. To screen for the presence of the CMG helicase, GINS was isolated as above, before release of the purified material from beads by cleavage with TEV protease and immunoprecipitation of Mcm4 (*1*). The final material was analyzed by immunoblotting, along with the cell extracts.

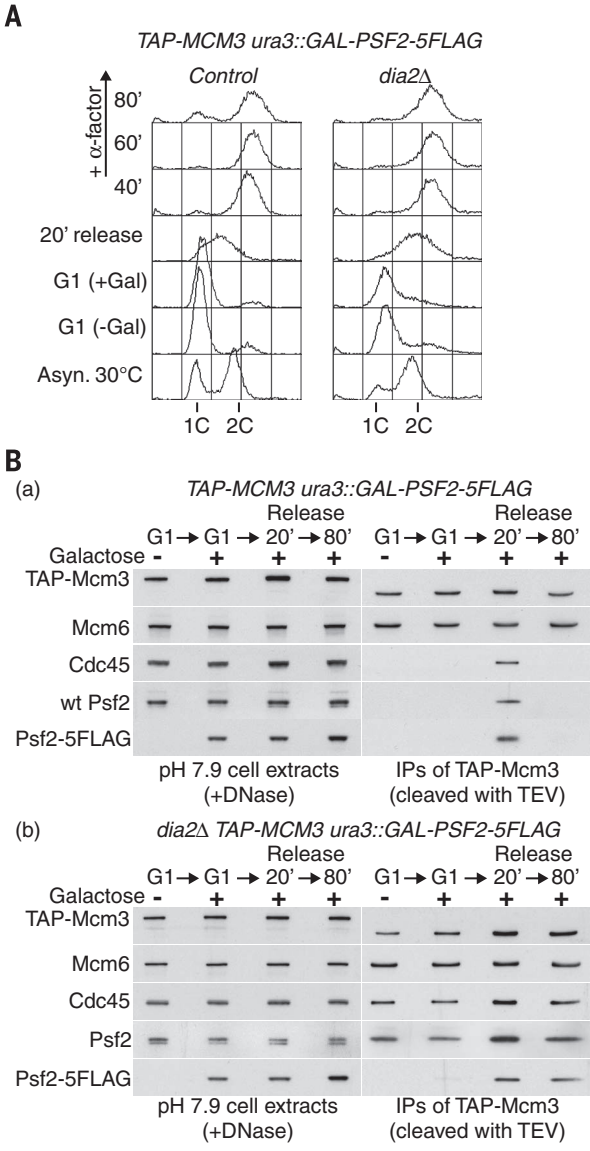

Fig. 5. Disassembly of the CMG helicase at the end of S phase requires Dia2. (**A**) A plasmid containing the *GAL-PSF2-5FLAG* construct was integrated at the *ura3* locus in control (YTM593) and *dia2*Δ (YTM592) cells, which were then synchronized at 30°C in G_1 phase with mating pheromone, in medium lacking galactose. Cells were held in G_1 phase for a further 60 min in the presence of galactose to induce expression of Psf2-5FLAG, before release for the indicated times in medium lacking mating pheromone. Alpha factor mating pheromone was added again from 40 min onward to prevent nuclei from entering into the next round of S phase, and DNA content was measured throughout the experiment by flow cytometry. (**B**) Cell extracts from the same experiment as depicted in (A) were treated with DNase before immunoprecipitation of TAP-tagged Mcm3. The material was released from beads with TEV protease before immunoblotting, to prevent TAP-Mcm3 from interfering with the similarly sized Mcm6 protein.

copurified with ubiquitylated CMG helicase from extracts of control S-phase cells, but the association was lost in extracts of *dia2*Δ cells (Fig. 8A). To determine the consequences of ubiquitylating the CMG helicase during late S phase, we monitored the completion of S phase upon release from hydroxyurea arrest, either in control cells or after inactivation of Cdc48-aid. Both strains reached a 2C DNA content with similar kinetics [Fig. 8B, (a)], indicating that the progression of DNA replication forks was not prevented by depletion of Cdc48-aid. In control cells, CMG briefly accumulated upon release from hydroxyurea arrest and then disappeared completely as cells completed DNA replication [Fig. 8B, (b), *Control*], reflecting the normal process of helicase disassembly at the end of S phase. In marked contrast, helicase disassembly was completely blocked in the absence of Cdc48, and instead progression through DNA replication led to a progressive accumulation of the CMG helicase, coupled to ubiquitylation of its Mcm7 subunit [Fig. 8B, (b), *cdc48-aid*]. Isolation of the ubiquitylated CMG helicase from cell extracts was still dependent on digestion of the parental DNA (fig. S12), indicating that the ubiquitylation and disassembly of CMG normally occur when the helicase is still present on chromatin at the end of DNA replication. Together, these findings demonstrate that Cdc48 is essential for disassembly of the CMG helicase, when budding yeast cells complete chromosome replication. In addition to its recently identified roles in the cellular response to DNA damage and defective DNA synthesis (*31*–*37*), our results identify Cdc48 as a key player in the final stages of eukaryotic chromosome replication.

Discussion

The encounter of two converged DNA replication forks leads locally to the termination of DNA synthesis in that particular region of the chromosome and to dissolution of the replisome at each fork. Our findings indicate that replisome dissolution is driven by the regulated disassembly of the stable CMG helicase, which uses its hexameric ring of Mcm2-7 proteins to encircle the parental DNA at replication forks. Our data identify two key features of helicase disassembly in budding yeast: First, there is an essential role for the F-box protein Dia2, which forms part of the E3 ligase SCF^{Dia2} and drives ubiquitylation of the CMG helicase on its Mcm7 subunit. Second, the Cdc48 segregase is required to break ubiquitylated CMG into its three component parts. Once separated from GINS and Cdc45, the Mcm2-7 hexamer is much less stable (fig. S13), so that all three components of the CMG helicase are lost from the newly replicated DNA.

These data raise a series of questions regarding the final stages of chromosome replication in eukaryotes. The mechanisms by which CMG is first ubiquitylated at the end of chromosome replication and then disassembled in a Cdc48-dependent process remain to be elucidated in future studies. It will be interesting to determine how other factors, such as the MCM binding protein (MCM-BP) that is not found in budding yeasts (*38*, *39*), might contribute to this process. Another candidate is the Pif1/Rrm3 family of helicases that is required for the timely resolution of converged DNA replication forks during termination (*40*, *41*), although we found that budding yeast cells lacking Rrm3 are still able to disassemble the CMG helicase before the end of the cell cycle (fig. S6C). By analogy with the extensive studies over the past decade of CMG assembly during the initiation of chromosome replication, it will not only be necessary to define the list of factors that are required for helicase disassembly, but will also be important to develop experimental systems with which each step of the reaction can be recapitulated in vitro. Ultimately, the reconstitution of each step of CMG disassembly with purified components would then allow a more detailed exploration of the underlying mechanisms.

Much also remains to be learned about how cells ensure that the CMG helicase is never disassembled before replication terminates in each section of the genome, and yet is always disassembled when two DNA replication forks meet each other. Considering budding yeast, our data indicate that Dia2 specifically induces the disassembly of terminated CMG complexes in vivo (Fig. 6), but in yeast cell extracts is able to ubiquitylate CMG complexes that are derived from active forks (e.g., Fig. 1 and fig. S1) under in vitro conditions that presumably override some of the normal controls that act at DNA replication forks.

It seems likely that the ubiquitylation of CMG only occurs in vivo when two replication forks converge, although this remains to be demonstrated directly. A major challenge for future studies will be to identify which features of replication termination provide the signal for CMG ubiquitylation. It is possible that the CMG helicase undergoes a structural change or is otherwise modified during the latter stages of replication, in a manner that controls recruitment of

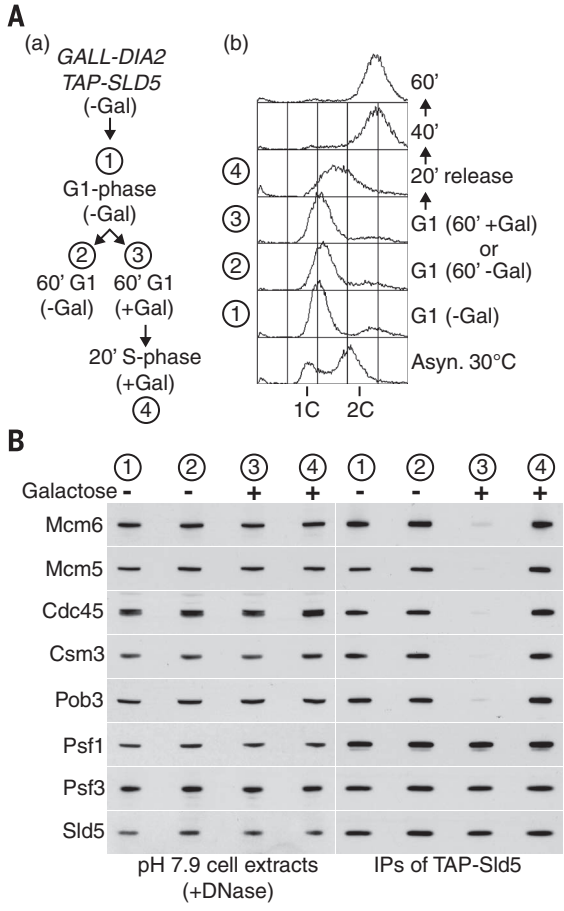

Fig. 6. Dia2 induces disassembly of terminated CMG complexes but does not prevent assembly of active CMG complexes. (**A**) (a) Cells in which the endogenous *DIA2* gene had been placed under the control of the weak and inducible *GALL* promoter (YTM568) were grown at 30°C in medium lacking galactose (*GALL-DIA2* OFF) and then synchronized in G_1 phase by addition of mating pheromone (stage 1). The cells were then held for a further 60 min in G_1 phase, either in the continued absence of galactose (*GALL-DIA2* OFF, stage 2), or in the presence of galactose (*GALL-DIA2* ON, stage 3) before subsequent release for 20 min into S phase (*GALL-DIA2* ON, stage 4). (b) DNA content was monitored by flow cytometry. (**B**) Cell extracts were prepared, treated with DNase, and then used to isolate GINS as above, before monitoring of the associated factors by immunoblotting as indicated.

the ubiquitin ligase and/or Cdc48. It is also conceivable that the latter factors are regulated independently of CMG during the termination of replication, although our data show that both Dia2 and Cdc48 can induce the disassembly of terminated CMG complexes, even during G_1 phase (Fig. 6), suggesting that the cell cycle stage is not a key determinant of the disassembly reaction. Further outstanding questions include how the ubiquitylation of CMG is restricted to its Mcm7 subunit, and how ubiquitylation of Mcm7 is limited to the small fraction of this protein that is present at replication forks in the CMG complex. We note that our data do not address whether SCF^{Dia2} or Cdc48 play any role in the removal of inactive Mcm2-7 complexes from the path of progressing replication forks.

Just as the main features of helicase assembly have been conserved across evolution from yeasts to humans, we envisage that disassembly of the CMG helicase will also prove to involve a universal mechanism in eukaryotic cells. In this case, a major challenge will be to identify the ubiquitin ligase(s) that ubiquitylate CMG in other species. The fission yeast Pof3 protein appears to be orthologous to budding yeast Dia2 (*42*), although it remains to be determined whether SCF^{Pof3} controls disassembly of CMG. It is unclear whether homologs of Dia2 are also present in higher eukaryotes, and it is possible that other ligases might control disassembly of the CMG helicase at the end of chromosome replication.

We anticipate that the role of Cdc48/p97 in CMG disassembly will be conserved in all eukaryotes. Consistent with this view, inhibition of p97/Cdc48 in early embryos of *Caenorhabditis elegans*, or in extracts of *Xenopus laevis* eggs, was found to cause the persistence of GINS on mitotic chromatin (*43*). Although it was thought that this phenomenon was due to a failure to degrade the Cdt1 loading factor of the Mcm2-7 helicase core (*43*), our results suggest that these data might instead reflect a conserved role for p97 in the disassembly of ubiquitylated CMG helicase at the end of chromosome replication. Accordingly, Mcm7 is ubiquitylated on chromatin during chromosome replication in extracts of *Xenopus* eggs, and the removal of CMG subunits from chromatin is dependent on p97/Cdc48 (*44*). It will be important to determine which adaptors of Cdc48/p97 are required for helicase disassembly in different eukaryotic species. A better understanding of the CMG disassembly pathway in human cells might help to explain the potential efficacy in antitumor therapies of small-molecule inhibitors of the p97/Cdc48 ATPase (*45*).

Materials and methods

Yeast strains and plasmids

The budding yeast *Saccharomyces cerevisiae* strains that were used in this study are listed in table S1. A standard one-step polymerase chain reaction (PCR) approach was applied to generate yeast strains harboring individual gene deletions or with epitope tags at the C or N terminus of the target protein (*46*). All the modifications were initially made in the diploid W303-1, before derivation of haploids by tetrad analysis. The *cdc48-aid* allele was constructed by transformation of cells with a PCR product containing the auxin inducible degron tag (*28*) and the *hphNT* marker (*29*). The resultant *cdc48-aid* haploid cells were then crossed to cells expressing the rice Tir1 E3 ligase from the *ura3* locus (a generous gift from K. Nishimura and M. Kanemaki). Deletions of the *RAD5*, *RAD18*, and *UBC13* genes were obtained by transformation of a PCR cassette containing the *hphNT* marker (*29*). A similar approach was used to make the *GALL-DIA2* strain (*29*), which allows very low expression of *DIA2* in medium lacking galactose, due to point mutations in the TATA box of the *GAL1* promoter (*30*). To generate alleles of *CDC53* and *CDC4* that would allow very efficient inactivation of protein function at 37°C, we tagged existing temperature-sensitive alleles with the heat-inducible degron cassette, as described previously (*47*). In this way, we inserted the degron cassette (*48*) into the corresponding genomic locus in *cdc53-1* and *cdc4-1* cells, producing the alleles *td-cdc53-1* and *td-cdc4-1*. DNA fragments expressing Psf2-5FLAG, Cdc45-5FLAG9His, 5FLAG-Dia2, and ProteinA-3TEV-sites-Dia2 were cloned downstream of the *GAL1* promoter in the pRS series of plasmids (*49*). The resultant vectors were then linearized within the marker sequence and integrated into the *ura3* or *leu2* locus of the corresponding yeast strains. The plasmid pRS423-*CUP*-His7-Ubi was a gift from H. Ulrich and was used to make the derivatives pRS423-*CUP*-His7-UbiK48R and pRS423-*CUP*-His7-UbiK63R by site-directed mutagenesis involving three-step PCR reactions.

Growth of yeast cells

Yeast cells were grown at 24°, 30°, or 37°C in YP medium supplemented with sugar. The composition of YP medium is 1% (w/v) yeast extract (Becton Dickinson, 212750) and 2% (w/v) bacteriological peptone (Oxoid, LP0037B). The medium was then supplemented with 2% glucose (YPD), 2% raffinose (YPRaff), or 2% galactose (YPGal). All experiments with *dia2*Δ cells were performed at 30°C because the cells are sensitive to cold (*23*). To synchronize the cells in G_1 phase, we added α-factor mating pheromone (Pepceuticals Limited) to log-phase cell cultures (cell density: 7×10^6 cells/ml) to a final concentration of 7.5 μg/ml. When cells were grown at 24°C, additional aliquots of 2.5 μg/ml (for *cdc48-aid* cells, 5 μg/ml) were added after an hour and a half and then every 30 min until more than 90% of cells were unbudded and had formed "shmoos." When cells were grown at 30°C, additional aliquots of 2.5 μg/ml (for *dia2*Δ cells, 5 μg/ml) of α-factor were added every 15 min after 1 hour until ~90% cells were unbudded.

To release from G_1-phase arrest, cells were washed twice with fresh medium lacking α-factor. To arrest cells in early S phase upon release from mating pheromone arrest, cells were washed twice in YPD medium containing 0.2 M hydroxyurea (H8627, Sigma-Aldrich, and 10872383, Molekula). For the

experiment shown in fig. S3, an asynchronous culture of *cim3-1* cells was arrested in early S phase by incubation for one generation time in medium containing 0.2 M hydroxyurea (*cim3-1* cells are resistant to arrest in G_1 phase with mating pheromone).

To arrest cells in G_2-M phase, the medium was supplemented with nocodazole (Sigma-Aldrich, M1404) at 5 μg/ml. The cells were then incubated until ~90% had large buds. To induce DNA damage during S phase, cells were released into S phase in the presence of 0.033% methyl methanesulfonate [(MMS), M4016, Sigma-Aldrich]. To induce degradation of proteins fused to the auxin-inducible degron, we added 3-indolacetic acid (I3750, Sigma-Aldrich) to the culture medium at a final concentration of 0.5 mM.

For the experiment shown in Fig. 1C, involving depletion of Cdc45-td, cells were first grown at 24°C in YPRaff medium containing 0.1 mM $CuSO_4$, before induction of *GAL-UBR1* for 45 min in YPGal medium at 24°C (*6*). For the experiment in Fig. 2D, where Cdc53 and Cdc4 were inactivated, cells were grown at 24°C in YPRaff medium with 0.1 mM $CuSO_4$, before induction of *GAL-UBR1* for 35 min. For the experiment shown in Fig. 3F, *GALL-DIA2 cdc48-aid* cells were grown overnight at 30°C in YP medium supplemented with 2% sucrose and 0.1% galactose, to allow cells to grow well but also to minimize the initial expression level of Dia2. The culture was then switched to YPD medium for 8 hours at 30°C to repress *GALL-DIA2* (we confirmed that cells would still have been able to grow for one more generation time), before addition of auxin to inactivate Cdc48-aid.

Analyzing cell growth by serial dilution on solid medium

Fresh colonies of yeast cells were grown on YPD plates, and serial 10-fold dilutions of cells were then made in phosphate-buffered saline, before plating cells in spots ranging from 5×10^4 to 5×10 cells. Cells were incubated at the indicated temperature, and the plates were scanned each day for 3 days.

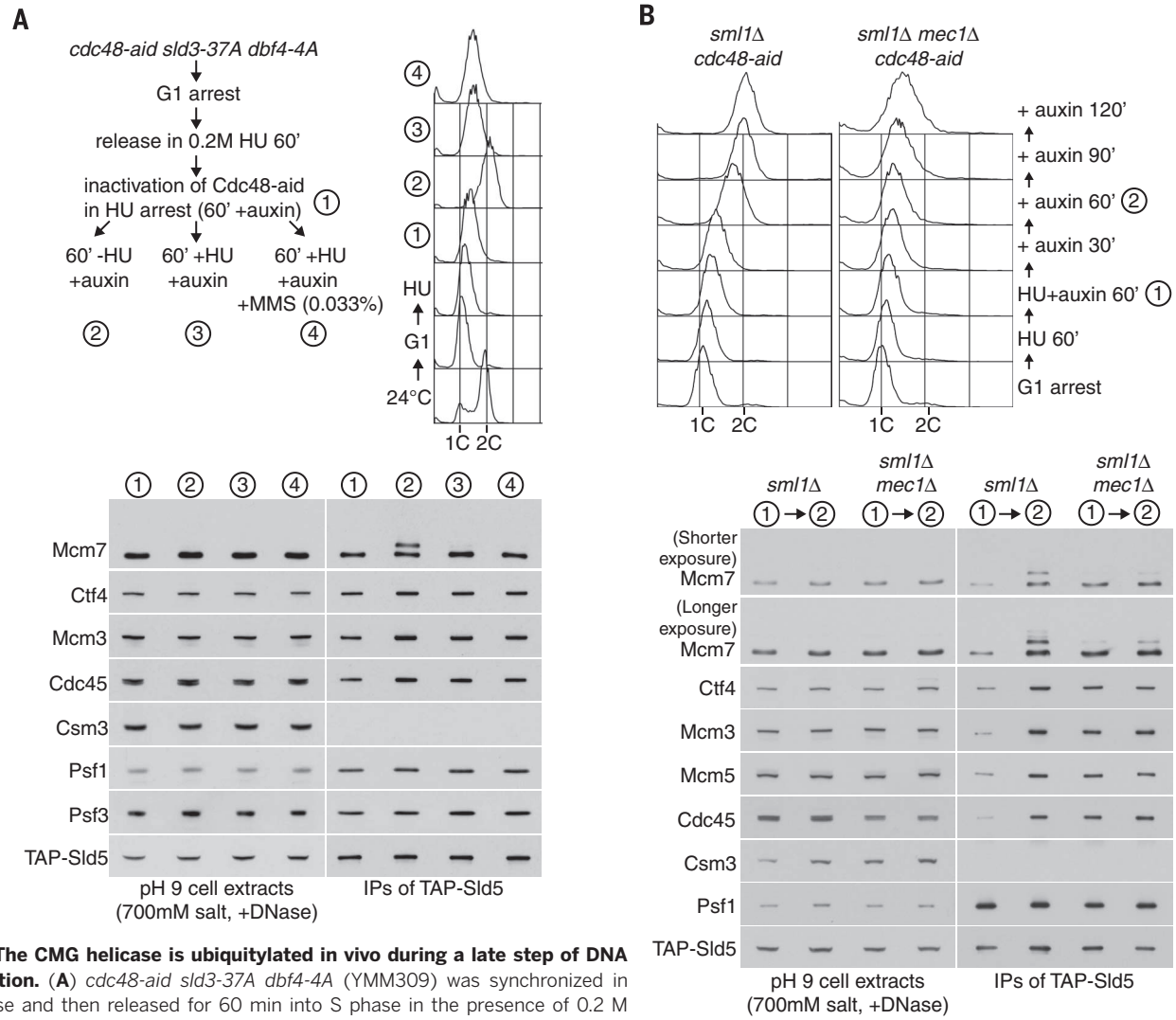

Fig. 7. The CMG helicase is ubiquitylated in vivo during a late step of DNA replication. (**A**) *cdc48-aid sld3-37A dbf4-4A* (YMM309) was synchronized in G_1 phase and then released for 60 min into S phase in the presence of 0.2 M hydroxyurea (HU) to allow early and late origins to fire (*55*). Auxin was then added to inactivate Cdc48-aid (1) before the culture was split and cells were released for 60 min in fresh medium lacking HU (2), held for a further 60 min in the presence of HU (3), or subjected to DNA damage (by addition of 0.033% MMS) in the continued presence of HU (4). The *sld3-37A dbf4-4A* background was used to allow late origins to fire in the HU arrest, thus ensuring that cells would have a similar number of CMG complexes both before and after release from HU arrest, making easier the comparison of the Mcm7 subunit of CMG in the two cases. DNA content was measured by flow cytometry. (**B**) A similar experiment was performed with control cells (YMM366, *sml1Δ cdc48-aid ADH-TIR1*) and *mec1Δ* (YMM368, *mec1Δ sml1Δ cdc48-aid ADH-TIR1*) strains. Inactivation of Cdc48-aid in hydroxyurea HU-arrested cells did not cause efficient accumulation of ubiquitylated CMG helicase in either control or *mec1Δ* cells, consistent with the notion that ubiquitylation only occurs during a late step of DNA replication. When cells were washed into fresh medium lacking hydroxyurea HU, completion of DNA replication in control cells led to the accumulation of ubiquitylated CMG helicase, but this was much less efficient in *mec1Δ* cells, in which the replisome is stable but is unable to resume remain functional after DNA replication stress (*52*).

Flow cytometry

Fixed cells for the measurement of DNA content were prepared as described previously (*50*). Samples were then analyzed using a FACSCalibur flow cytometer and FACSCanto II flow cytometer (Becton Dickinson), and the profiles were analyzed by CellQuest software (Becton Dickinson) or FlowJo software (TreeStar).

Preparation of denatured cell extracts containing trichloroacetic acid

For the experiments shown in Fig. 3, B (upper panel) and D, ~10^8 cells were used to generate

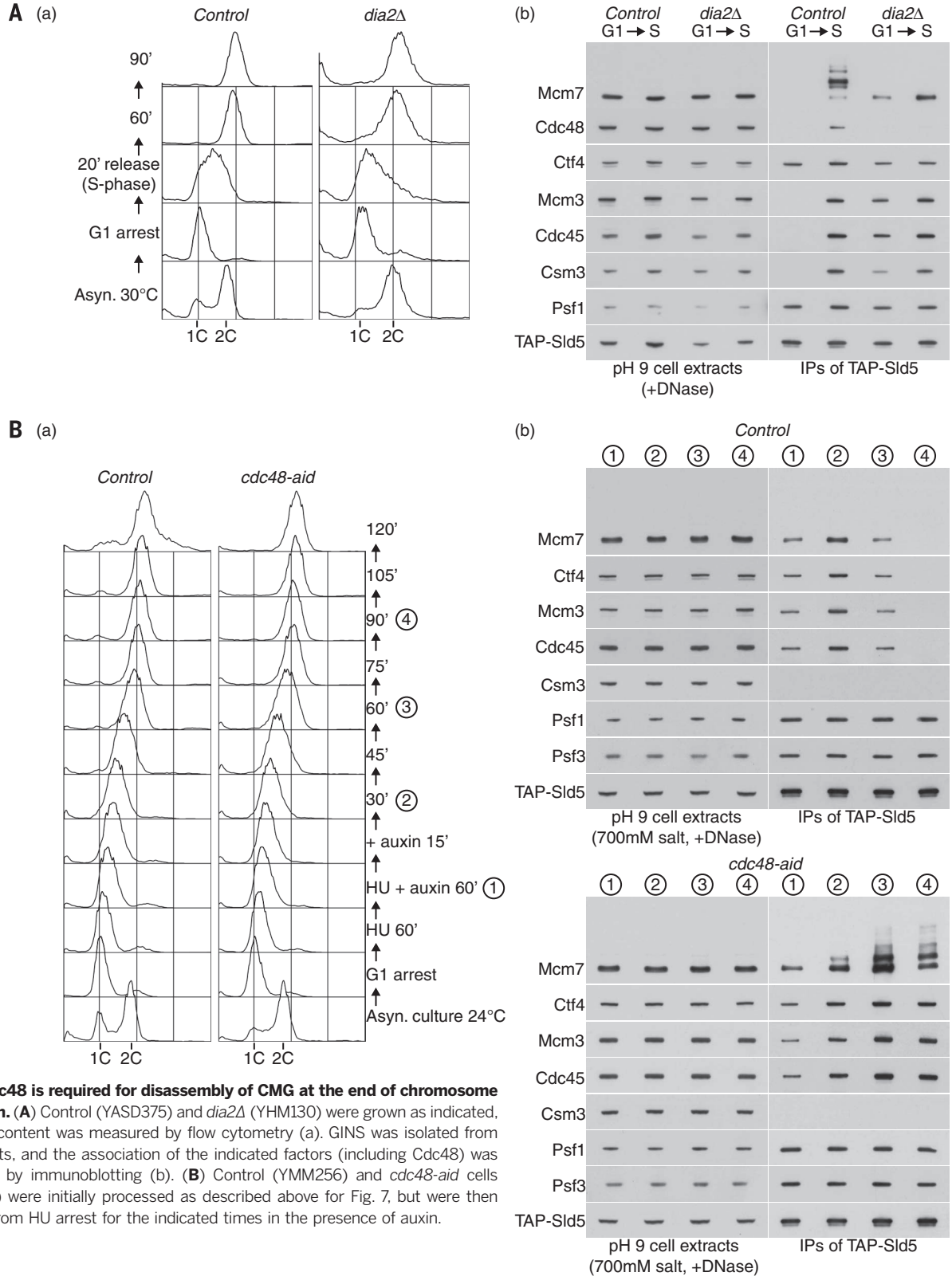

Fig. 8. Cdc48 is required for disassembly of CMG at the end of chromosome replication. (**A**) Control (YASD375) and *dia2Δ* (YHM130) were grown as indicated, and DNA content was measured by flow cytometry (a). GINS was isolated from cell extracts, and the association of the indicated factors (including Cdc48) was monitored by immunoblotting (b). (**B**) Control (YMM256) and *cdc48-aid* cells (YMM228) were initially processed as described above for Fig. 7, but were then released from HU arrest for the indicated times in the presence of auxin.

total protein extracts in the presence of trichloroacetic acid to inactivate proteases, as described previously (*51*).

Immunoprecipitation of protein complexes from yeast cell extracts

Standard cell extracts (pH 7.9)

The preparation of cell extracts from frozen yeast cells, as well as the immunoprecipitation of protein complexes from extracts, was based on previously described methods (*1*, *23*, *52*). Briefly, 250 ml of a cell culture was pelleted at 200 × g for 3 min. Cells were washed once in 50 ml of 20 mM HEPES-KOH pH 7.9 buffer and once in 10 ml of lysis buffer (100 mM HEPES-KOH pH 7.9, 50 mM potassium acetate, 10 mM magnesium acetate, 2 mM EDTA) and then resuspended in three volumes of lysis buffer (1 g of cell pellet was taken as being equivalent to 1 ml of buffer) supplemented with 2 mM sodium fluoride, 2 mM sodium β-glycerophosphate pentahydrate, 1 mM dithiothreitol (DTT), 1% Protease Inhibitor Cocktail (P8215, Sigma-Aldrich), and 1× Complete Protease Inhibitor Cocktail (05056489001, Roche; one tablet dissolved in 1 ml water makes a 25× stock solution) before freezing dropwise in liquid nitrogen. We ground ~2.5 g of frozen yeast cells in a SPEX SamplePrep 6780 Freezer/Mill. After thawing, we measured the volume of the extract and then added one-quarter of the volume of glycerol mix buffer, comprising lysis buffer plus 50% glycerol, 300 mM potassium acetate, 0.5% detergent IGEPAL CA-630 (18896, Sigma-Aldrich), inhibitors, and DTT at the concentrations mentioned above, such that the extract contained 10% glycerol, 100 mM potassium acetate, and 0.1% IGEPAL CA-630. Chromosomal DNA was then digested by addition of 800 U/ml Benzonase Nuclease (71206, Merck) or 400 U/ml Pierce Universal Nuclease (123991963, Fisher) and incubation for 30 min at 4°C. Insoluble cell debris was pelleted in two high-speed centrifugation steps (at 25000 × g for 30 min and then at 100000 × g for 1 hour). To analyze cell extracts subsequently, 100 µl of concentrated Laemmli buffer (1.5 x) was added to 50 µl of cell extract [final concentration of Laemmli buffer corresponds to 6.66% (v/v) glycerol, 715 mM β-mercaptoethanol, 3% (w/v) sodium dodecyl sulfate, 62.5 mM Tris-HCl pH 6.9, and 0.00416% (w/v) Bromophenol Blue]. Cell extracts with added Laemmli buffer were then heated at 95°C for 5 min and stored at −80°C.

The remaining fraction of each cell extract (~2 ml) was then split into two aliquots, each of which was incubated for 2 hours at 4°C with 1.7 × 10^9 magnetic beads (Dynabeads M-270 Epoxy; 14302D, Life Technologies) that had been coupled to rabbit immunoglobulin G (IgG) (S1265, Sigma-Aldrich) or M2 anti-FLAG monoclonal antibody (F3165, Sigma-Aldrich). After the incubation, protein complexes bound on antibody-coupled magnetic beads were washed four times with 1 ml of wash buffer [100 mM HEPES-KOH pH 7.9, 100 mM potassium acetate, 10 mM magnesium acetate, 2 mM EDTA, 0.1% IGEPAL CA-630, 2 mM sodium fluoride, 2 mM sodium β-glycerophosphate pentahydrate, 1% Protease Inhibitor Cocktail (Sigma-Aldrich), and 1× Complete Protease Inhibitor Cocktail (Roche)]. The bound proteins were then eluted by heating at 95°C for 5 min in 50 µl Laemmli buffer and stored at −80°C.

pH 9 cell extracts and high-salt cell extracts

For the experiment in fig. S1A, all respective buffers for immunoprecipitation were made as indicated, with either HEPES-KOH (at pH 7.0, pH 7.9, and pH 8.5) or Tris-acetate (at pH 9). Buffers at pH 7.9 were used in experiments shown in Figs. 4 to 6 and figs. S5 to S9, S12, and S13. For all the other experiments, we used Tris-acetate buffers at pH 9. For the experiments in Figs. 1, 2, 4 to 6, and 8A, as well as figs. S1, S2, S6 to S9, and S13, the lysis buffer and wash buffers contained a final concentration of 100 mM potassium acetate. In other experiments, the buffers all contained 700 mM potassium acetate. In Fig. 2A and fig. S10, both 100 and 700 mM potassium acetate buffers were used, respectively.

More concentrated cell extracts from 1-liter cultures

Some experiments required more concentrated cell extracts, to improve visualization of ubiquitylated forms of Mcm7. In these experiments (Figs. 1, A, B, and D; and 3, C, E, and F; and figs. S1, C and D; S4; and S10), cell extracts were made from 1-liter cell cultures. After washing, the cells were finally resuspended in one-quarter of a volume of lysis buffer supplemented with 8 mM sodium fluoride, 8 mM sodium β-glycerophosphate pentahydrate, 4 mM DTT, 4% Protease Inhibitor Cocktail (Sigma-Aldrich), and 4× Complete Protease Inhibitor Cocktail (Roche). After grinding of the cells, we added 1 ml of lysis buffer (with the appropriate pH and salt concentration) supplemented with 2 mM sodium fluoride, 2 mM sodium β-glycerophosphate pentahydrate, 1 mM dithiothreitol, 1% Protease Inhibitor Cocktail (Sigma-Aldrich), and 1× Complete Protease Inhibitor Cocktail (Roche) to the thawing extracts. The extracts were then adjusted by addition of one-quarter of the volume of the appropriate glycerol mix as above, before digestion of chromosomal DNA with 3200 U/ml of Benzonase Nuclease or 1600 U/ml of Pierce Universal Nuclease.

Isolation of His-tagged ubiquitylated Mcm7

For the experiments in Fig. 1, A, B, and D; and fig. S1D, material containing CMG was isolated as described above, by immunoprecipitation of TAP-Sld5 at pH 9 and with 100 mM potassium acetate from 1-liter cell cultures. Both aliquots of magnetic beads with bound complexes were then washed three times with 1 ml of pH 9 wash buffer (100 mM Tris-acetate pH 9, 100 mM potassium acetate, 10 mM magnesium acetate, 0.1% IGEPAL CA-630, 2 mM sodium fluoride, 2 mM sodium β-glycerophosphate pentahydrate) and once with 1 ml of pH 7.9 wash buffer (100 mM HEPES-KOH pH 7.9, 100 mM potassium acetate, 10 mM magnesium acetate, 0.1% IGEPAL CA-630, 2 mM sodium fluoride, 2 mM sodium β-glycerophosphate pentahydrate) before resuspending in 50 µl of TEV cleavage buffer (100 mM HEPES-KOH pH 7.9, 100 mM potassium acetate, 10 mM magnesium acetate, 0.1% IGEPAL CA-630). Protein complexes were then released from the magnetic beads by the addition of 1 µl (10 U) of AcTEV protease (12575015, Life Technologies) to each aliquot and incubation at 24°C for 2 hours with agitation. Released protein complexes were then denatured by the addition of 450 µl of denaturation buffer per 50 µl [8.88 M urea, 555 mM sodium chloride, 0.11 mM sodium dihydrogen phosphate, 2.22% (v/v) Triton X-100, 11.1 mM Tris-HCl pH 8.0] and incubated with Dynabeads His-tag Isolation and Pulldown (10103D, Life Technologies) for 2 hours at 4°C (we used 100 µl of magnetic bead slurry per isolation). The His-tagged proteins isolated via cobalt-affinity chromatography were then eluted from the magnetic beads by boiling for 5 min at 95°C in Laemmli buffer containing 200 mM imidazole, 5% (w/v) sodium dodecyl-sulfate, 150 mM Tris-HCl pH 6.7, 30% glycerol, 715 mM β-mercaptoethanol, and 0.0125% Bromophenol Blue.

Lambda protein phosphatase assay

Immunoprecipitates of TAP-Sld5 were treated with lambda phosphatase (Lambda PP, P0753, New England Biolabs) as follows: Magnetic beads with bound complexes were washed twice with buffer comprising 100 mM Tris-acetate pH 9.0, 100 mM potassium acetate, 10 mM magnesium acetate, 0.1% IGEPAL CA-630, and 1× Complete Protease Inhibitor Cocktail (Roche). The beads were then washed a further two times with ice-cold phosphatase buffer (New England Biolabs; 1× buffer: 50 mM HEPES, 10 mM sodium chloride, 2 mM dithiothreitol, 0.01% Brij 35, pH 7.5 at 25°C) supplemented with 1× Complete Protease Inhibitor Cocktail (Roche). The beads with bound complexes were then resuspended in 47 µl of phosphatase buffer with 1 mM manganese chloride and 1× Complete Protease Inhibitor Cocktail (Roche). In the sample where phosphatase inhibitors were added, the reaction buffer was supplemented with 50 mM sodium fluoride and 10 mM sodium orthovanadate. We then added 1200 units of lambda phosphatase per sample (3 µl in a total reaction volume of 50 µl) and incubated the reactions for 30 min at 30°C. Magnetic beads with bound complexes were then washed twice with wash buffer [100 mM Tris-acetate pH 9, 100 mM potassium acetate, 10 mM magnesium acetate, 2 mM EDTA, 0.1% IGEPAL CA-630, 2 mM sodium fluoride, 2 mM sodium β-glycerophosphate pentahydrate, 1% Protease Inhibitor Cocktail (Sigma-Aldrich) and 1× Complete Protease Inhibitor Cocktail (Roche)], and the proteins were eluted from the magnetic beads by the addition of Laemmli buffer and boiling.

Purification of Cdc34 or Dia2 for in vitro complementation experiments

Cdc34-TAP or TAP-Dia2 was isolated from 2.5 g of frozen yeast as described above, using magnetic beads coupled to rabbit IgG. After a two-hour incubation with yeast extracts at 4°C, the

IgG-coated beads were washed twice with 1 ml of pH 9 wash buffer supplemented with phosphatase and protease inhibitors, once with 1 ml of pH 7.9 wash buffer and once with 1 ml of TEV cleavage buffer. The magnetic beads were then incubated with agitation for 1 hour at 24°C in 80 μl of TEV cleavage buffer supplemented with 4 μl (40 U) of AcTEV protease. After elution, the supernatant was removed, and 40 μl of supernatant was added to each milliliter of the recipient cell extract (see below for details).

Purification of CMG material from dia2Δ cells for in vitro assays

For the experiment in Fig. 2D, (a), TAP-Sld5 was isolated with associated factors from 2.5 g of S phase *dia2Δ* cells, as described above. After immunoprecipitation, 1.7×10^9 of beads per sample were washed four times with 1 ml of pH 9 wash buffer supplemented with phosphatase and protease inhibitors. The beads were then added to 1 ml of a second cell extract (after the removal of insoluble cell debris) from control, *cdc34-2*, or *dia2Δ* cells and were incubated for 2 hours at 4°C before washing and analysis as above. A similar approach was taken for the experiment in Fig. 2D, (b), except that CMG-containing material was isolated from extracts of S-phase *dia2Δ* cells by immunoprecipitation of Cdc45-ProteinA.

Immunoblotting

Protein samples were resolved on SDS–polyacrylamide gel electrophoresis (PAGE) gels (various concentrations of polyacrylamide used from 5 to 12%) or NuPAGE Novex 4 to 12% Midi Bis-Tris gels (NP0301, Life Technologies) with NuPAGE MOPS SDS buffer (NP000102, Life Technologies). Molecular weight markers used were SDS-PAGE Molecular Weight Standards, Broad Range (161-0317, Bio-Rad) and Precision Plus Protein Kaleidoscope Standards (161-0375, Bio-Rad). Resolved proteins were transferred onto either nitrocellulose membrane Hybond-ECL (Amersham, GE Healthcare) or polyvinylidene difluoride membrane Hybond-P (Amersham, GE Healthcare) with a Trans-Blot SD Semi-Dry Transfer Cell (Bio-Rad) or to a nitrocellulose iBlot membrane (Life Technologies) with the iBlot Dry Transfer System (Life Technologies).

Polyclonal antibodies against replisome components have been described previously (*1*, *53*, *54*). Tagged proteins were detected with polyclonal anti-FLAG antibody (F-7425, Sigma-Aldrich), monoclonal anti-MYC (9E10; Cancer Research UK), or peroxidase-anti peroxidase complex (P1291, Sigma-Aldrich). Ubiquitin conjugates were detected with either the monoclonal P4D1 anti-ubiquitin antibody (3936, Cell Signaling) or the monoclonal FK2 antibody (BML-PW8810, Enzo Life Sciences) that preferentially recognizes polyubiquitylated conjugates. In addition, specific chain linkages of ubiquitin were detected with monoclonal antibodies raised against di-ubiquitin molecules with K48 linkage (Apu2; 05-1307, Millipore) or K63 linkage (Apu3; 05-1308, Millipore). A polyclonal antibody specific to the yeast SUMO protein Smt3 was kindly donated by H. Ulrich. A polyclonal antibody against Cdc48 was raised in sheep against the N-terminal 25-kD portion of the protein, which was expressed as a recombinant His-tagged protein in *Escherichia coli*. Conjugates to horseradish peroxidase of anti-sheep IgG from donkey (Sigma, A3415), anti-rabbit IgG from rabbit (Fisher, GZNA93401ML), or anti-mouse IgG from horse (PI-2000 Vector Labs) were used as secondary antibodies before the detection of chemoluminescent signals on Hyperfilm ECL (Amersham, GE Healthcare) using ECL Western Blotting Detection Reagent (GE Healthcare).

REFERENCES AND NOTES

1. A. Gambus *et al*., GINS maintains association of Cdc45 with MCM in replisome progression complexes at eukaryotic DNA replication forks. *Nat. Cell Biol.* **8**, 358–366 (2006). doi: 10.1038/ncb1382; pmid: 16531994
2. S. E. Moyer, P. W. Lewis, M. R. Botchan, Isolation of the Cdc45/Mcm2-7/GINS (CMG) complex, a candidate for the eukaryotic DNA replication fork helicase. *Proc. Natl. Acad. Sci. U.S.A.* **103**, 10236–10241 (2006). doi: 10.1073/pnas.0602400103; pmid: 16798881
3. Y. Li, H. Araki, Loading and activation of DNA replicative helicases: The key step of initiation of DNA replication. *Genes Cells* **18**, 266–277 (2013). doi: 10.1111/gtc.12040; pmid: 23461534
4. D. Boos, J. Frigola, J. F. Diffley, Activation of the replicative DNA helicase: Breaking up is hard to do. *Curr. Opin. Cell Biol.* **24**, 423–430 (2012). doi: 10.1016/j.ceb.2012.01.011; pmid: 22424671
5. K. Labib, How do Cdc7 and cyclin-dependent kinases trigger the initiation of chromosome replication in eukaryotic cells? *Genes Dev.* **24**, 1208–1219 (2010). doi: 10.1101/gad.1933010; pmid: 20551170
6. K. Labib, J. A. Tercero, J. F. X. Diffley, Uninterrupted MCM2-7 function required for DNA replication fork progression. *Science* **288**, 1643–1647 (2000). doi: 10.1126/science.288.5471.1643; pmid: 10834843
7. R. Y. Samson, S. D. Bell, MCM loading—an open-and-shut case? *Mol. Cell* **50**, 457–458 (2013). doi: 10.1016/j.molcel.2013.05.008; pmid: 23706815
8. T. J. Takara, S. P. Bell, Putting two heads together to unwind DNA. *Cell* **139**, 652–654 (2009). doi: 10.1016/j.cell.2009.10.037; pmid: 19914158
9. H. Yardimci, J. C. Walter, Prereplication-complex formation: A molecular double take? *Nat. Struct. Mol. Biol.* **21**, 20–25 (2014). doi: 10.1038/nsmb.2738; pmid: 24389553
10. A. Calzada, B. Hodgson, M. Kanemaki, A. Bueno, K. Labib, Molecular anatomy and regulation of a stable replisome at a paused eukaryotic DNA replication fork. *Genes Dev.* **19**, 1905–1919 (2005). doi: 10.1101/gad.337205; pmid: 16103218
11. M. Pacek, A. V. Tutter, Y. Kubota, H. Takisawa, J. C. Walter, Localization of MCM2-7, Cdc45, and GINS to the site of DNA unwinding during eukaryotic DNA replication. *Mol. Cell* **21**, 581–587 (2006). doi: 10.1016/j.molcel.2006.01.030; pmid: 16483939
12. C. Evrin *et al*., A double-hexameric MCM2-7 complex is loaded onto origin DNA during licensing of eukaryotic DNA replication. *Proc. Natl. Acad. Sci. U.S.A.* **106**, 20240–20245 (2009). doi: 10.1073/pnas.0911500106; pmid: 19910535
13. D. Remus *et al*., Concerted loading of Mcm2-7 double hexamers around DNA during DNA replication origin licensing. *Cell* **139**, 719–730 (2009). doi: 10.1016/j.cell.2009.10.015; pmid: 19896182
14. F. van Deursen, S. Sengupta, G. De Piccoli, A. Sanchez-Diaz, K. Labib, Mcm10 associates with the loaded DNA helicase at replication origins and defines a novel step in its activation. *EMBO J.* **31**, 2195–2206 (2012). doi: 10.1038/emboj.2012.69; pmid: 22433841
15. S. Bergink, S. Jentsch, Principles of ubiquitin and SUMO modifications in DNA repair. *Nature* **458**, 461–467 (2009). doi: 10.1038/nature07963; pmid: 19325626
16. H. D. Ulrich, H. Walden, Ubiquitin signalling in DNA replication and repair. *Nat. Rev. Mol. Cell Biol.* **11**, 479–489 (2010). doi: 10.1038/nrm2921; pmid: 20551964
17. I. W. Zaidi *et al*., Rtt101 and Mms1 in budding yeast form a CUL4(DDB1)-like ubiquitin ligase that promotes replication through damaged DNA. *EMBO Rep.* **9**, 1034–1040 (2008). doi: 10.1038/embor.2008.155; pmid: 18704118
18. M. C. Geoffroy, R. T. Hay, An additional role for SUMO in ubiquitin-mediated proteolysis. *Nat. Rev. Mol. Cell Biol.* **10**, 564–568 (2009). doi: 10.1038/nrm2707; pmid: 19474794
19. A. M. Sriramachandran, R. J. Dohmen, SUMO-targeted ubiquitin ligases. *Biochim. Biophys. Acta* **1843**, 75–85 (2014). doi: 10.1016/j.bbamcr.2013.08.022; pmid: 24018209
20. D. Blake *et al*., The F-box protein Dia2 overcomes replication impedance to promote genome stability in *Saccharomyces cerevisiae*. *Genetics* **174**, 1709–1727 (2006). doi: 10.1534/genetics.106.057836; pmid: 16751663
21. D. M. Koepp, A. C. Kile, S. Swaminathan, V. Rodriguez-Rivera, The F-box protein Dia2 regulates DNA replication. *Mol. Biol. Cell* **17**, 1540–1548 (2006). doi: 10.1091/mbc.E05-09-0884; pmid: 16421250
22. X. Pan *et al*., A DNA integrity network in the yeast *Saccharomyces cerevisiae*. *Cell* **124**, 1069–1081 (2006). doi: 10.1016/j.cell.2005.12.036; pmid: 16487579
23. H. Morohashi, T. Maculins, K. Labib, The amino-terminal TPR domain of Dia2 tethers SCF(Dia2) to the replisome progression complex. *Curr. Biol.* **19**, 1943–1949 (2009). doi: 10.1016/j.cub.2009.09.062; pmid: 19913425
24. S. Sengupta, F. van Deursen, G. de Piccoli, K. Labib, Dpb2 integrates the leading-strand DNA polymerase into the eukaryotic replisome. *Curr. Biol.* **23**, 543–552 (2013). doi: 10.1016/j.cub.2013.02.011; pmid: 23499531
25. D. Finley, H. D. Ulrich, T. Sommer, P. Kaiser, The ubiquitin-proteasome system of *Saccharomyces cerevisiae*. *Genetics* **192**, 319–360 (2012). doi: 10.1534/genetics.112.140467; pmid: 23028185
26. H. Meyer, M. Bug, S. Bremer, Emerging functions of the VCP/p97 AAA-ATPase in the ubiquitin system. *Nat. Cell Biol.* **14**, 117–123 (2012). doi: 10.1038/ncb2407; pmid: 22298039
27. M. Ghislain, A. Udvardy, C. Mann, *S. cerevisiae* 26S protease mutants arrest cell division in G2/metaphase. *Nature* **366**, 358–362 (1993). doi: 10.1038/366358a0; pmid: 8247132
28. K. Nishimura, T. Fukagawa, H. Takisawa, T. Kakimoto, M. Kanemaki, An auxin-based degron system for the rapid depletion of proteins in nonplant cells. *Nat. Methods* **6**, 917–922 (2009). doi: 10.1038/nmeth.1401; pmid: 19915560
29. C. Janke *et al*., A versatile toolbox for PCR-based tagging of yeast genes: New fluorescent proteins, more markers and promoter substitution cassettes. *Yeast* **21**, 947–962 (2004). doi: 10.1002/yea.1142; pmid: 15334558
30. D. Mumberg, R. Müller, M. Funk, Regulatable promoters of *Saccharomyces cerevisiae*: Comparison of transcriptional activity and their use for heterologous expression. *Nucleic Acids Res.* **22**, 5767–5768 (1994). doi: 10.1093/nar/22.25.5767; pmid: 7838736
31. K. Acs *et al*., The AAA-ATPase VCP/p97 promotes 53BP1 recruitment by removing L3MBTL1 from DNA double-strand breaks. *Nat. Struct. Mol. Biol.* **18**, 1345–1350 (2011). doi: 10.1038/nsmb.2188; pmid: 22120668
32. S. Bergink *et al*., Role of Cdc48/p97 as a SUMO-targeted segregase curbing Rad51-Rad52 interaction. *Nat. Cell Biol.* **15**, 526–532 (2013). doi: 10.1038/ncb2729; pmid: 23624404
33. E. J. Davis *et al*., DVC1 (C1orf124) recruits the p97 protein segregase to sites of DNA damage. *Nat. Struct. Mol. Biol.* **19**, 1093–1100 (2012). doi: 10.1038/nsmb.2394; pmid: 23042607
34. M. Meerang *et al*., The ubiquitin-selective segregase VCP/p97 orchestrates the response to DNA double-strand breaks. *Nat. Cell Biol.* **13**, 1376–1382 (2011). doi: 10.1038/ncb2367; pmid: 22020440
35. A. Mosbech *et al*., DVC1 (C1orf124) is a DNA damage-targeting p97 adaptor that promotes ubiquitin-dependent responses to replication blocks. *Nat. Struct. Mol. Biol.* **19**, 1084–1092 (2012). doi: 10.1038/nsmb.2395; pmid: 23042605
36. J. Mouysset *et al*., Cell cycle progression requires the CDC-48UFD-1/NPL-4 complex for efficient DNA replication. *Proc. Natl. Acad. Sci. U.S.A.* **105**, 12879–12884 (2008). doi: 10.1073/pnas.0805944105; pmid: 18728180
37. M. Raman, C. G. Havens, J. C. Walter, J. W. Harper, A genome-wide screen identifies p97 as an essential regulator of DNA damage-dependent CDT1 destruction. *Mol. Cell* **44**, 72–84 (2011). doi: 10.1016/j.molcel.2011.06.036; pmid: 21981919
38. M. Jagannathan *et al*., A role for USP7 in DNA replication. *Mol. Cell. Biol.* **34**, 132–145 (2014). doi: 10.1128/MCB.00639-13; pmid: 24190967
39. A. Nishiyama, L. Frappier, M. Méchali, MCM-BP regulates unloading of the MCM2-7 helicase in late S phase. *Genes Dev.* **25**, 165–175 (2011). doi: 10.1101/gad.614411; pmid: 21196493
40. D. Fachinetti *et al*., Replication termination at eukaryotic chromosomes is mediated by Top2 and occurs at genomic loci containing pausing elements. *Mol. Cell* **39**, 595–605 (2010). doi: 10.1016/j.molcel.2010.07.024; pmid: 20797631

41. R. Steinacher, F. Osman, J. Z. Dalgaard, A. Lorenz, M. C. Whitby, The DNA helicase Pfh1 promotes fork merging at replication termination sites to ensure genome stability. *Genes Dev.* **26**, 594–602 (2012). doi: 10.1101/gad.184663.111; pmid: 22426535
42. S. Katayama, K. Kitamura, A. Lehmann, O. Nikaido, T. Toda, Fission yeast F-box protein Pof3 is required for genome integrity and telomere function. *Mol. Biol. Cell* **13**, 211–224 (2002). doi: 10.1091/mbc.01-07-0333; pmid: 11809834
43. A. Franz *et al*., CDC-48/p97 coordinates CDT-1 degradation with GINS chromatin dissociation to ensure faithful DNA replication. *Mol. Cell* **44**, 85–96 (2011). doi: 10.1016/j.molcel.2011.08.028; pmid: 21981920
44. S. Priego Moreno, R. Bailey, N. Campion, S. Herron, A. Gambus, Polyubiquitylation drives replisome disassembly at the termination of DNA replication. *Science* **346**, 477–481 (2014).
45. P. Magnaghi *et al*., Covalent and allosteric inhibitors of the ATPase VCP/p97 induce cancer cell death. *Nat. Chem. Biol.* **9**, 548–556 (2013). doi: 10.1038/nchembio.1313; pmid: 23892893
46. M. Knop *et al*., Epitope tagging of yeast genes using a PCR-based strategy: More tags and improved practical routines. *Yeast* **15**, 963–972 (1999). doi: 10.1002/(SICI)1097-0061(199907)15:10B<963::AID-YEA399>3.0.CO;2-W; pmid: 10407276
47. M. Kanemaki, K. Labib, Distinct roles for Sld3 and GINS during establishment and progression of eukaryotic DNA replication forks. *EMBO J.* **25**, 1753–1763 (2006). doi: 10.1038/sj.emboj.7601063; pmid: 16601689
48. A. Sanchez-Diaz, M. Kanemaki, V. Marchesi, K. Labib, Rapid depletion of budding yeast proteins by fusion to a heat-inducible degron. *Sci. STKE* **2004**, pl8 (2004).pmid: 15010550
49. R. S. Sikorski, P. Hieter, A system of shuttle vectors and yeast host strains designed for efficient manipulation of DNA in *Saccharomyces cerevisiae*. *Genetics* **122**, 19–27 (1989). pmid: 2659436
50. K. Labib, J. F. X. Diffley, S. E. Kearsey, G1-phase and B-type cyclins exclude the DNA-replication factor Mcm4 from the nucleus. *Nat. Cell Biol.* **1**, 415–422 (1999). doi: 10.1038/15649; pmid: 10559985
51. M. Foiani, F. Marini, D. Gamba, G. Lucchini, P. Plevani, The B subunit of the DNA polymerase α-primase complex in *Saccharomyces cerevisiae* executes an essential function at the initial stage of DNA replication. *Mol. Cell. Biol.* **14**, 923–933 (1994). pmid: 8289832
52. G. De Piccoli *et al*., Replisome stability at defective DNA replication forks is independent of S phase checkpoint kinases. *Mol. Cell* **45**, 696–704 (2012). doi: 10.1016/j.molcel.2012.01.007; pmid: 22325992
53. A. Gambus *et al*., A key role for Ctf4 in coupling the MCM2-7 helicase to DNA polymerase α within the eukaryotic replisome. *EMBO J.* **28**, 2992–3004 (2009). doi: 10.1038/emboj.2009.226; pmid: 19661920
54. M. Foltman *et al*., Eukaryotic replisome components cooperate to process histones during chromosome replication. *Cell Reports* **3**, 892–904 (2013). doi: 10.1016/j.celrep.2013.02.028; pmid: 23499444
55. P. Zegerman, J. F. Diffley, Checkpoint-dependent inhibition of DNA replication initiation by Sld3 and Dbf4 phosphorylation. *Nature* **467**, 474–478 (2010). doi: 10.1038/nature09373 pmid: 20835227

ACKNOWLEDGMENTS

We thank Cancer Research UK, the Medical Research Council, and the Wellcome Trust (references 097945/B/11/Z for flow cytometry and 102943/Z/13/Z for an award to K.L.) for funding our work. We are grateful to M. Foltman for assistance in the early stages of the project; H. Ulrich, M. Foltman, and S. Sengupta for plasmids; R. Deshaies, M. Kanemaki, H. Morohashi, K. Nasmyth, K. Nishimura, P. Zegerman, and S. Sengupta for providing strains; A. Gambus for helpful discussions; I. Hagan and C. Wilkinson for their support during the latter stages of this work; and all members of our group for helpful discussions.

SUPPLEMENTARY MATERIALS

www.sciencemag.org/content/346/6208/1253596/suppl/DC1
Supplementary Text
Figs. S1 to S14
Table S1
References

19 March 2014; accepted 26 August 2014
10.1126/science.1253596

REPORTS

SOLAR CELLS

Fulleropyrrolidine interlayers: Tailoring electrodes to raise organic solar cell efficiency

Zachariah A. Page,* Yao Liu,* Volodimyr V. Duzhko,† Thomas P. Russell,† Todd Emrick†

A major challenge in organic solar cell design is the trade-off between oxidative stability and work function of the metal cathode. We found that in single-junction polymer solar cells, this problem can be surmounted by solution-based incorporation of fulleropyrrolidines with amine (C_{60}-N) or zwitterionic (C_{60}-SB) substituents as cathode-independent buffer layers. Specifically, a thin layer of C_{60}-N reduced the effective work function of Ag, Cu, and Au electrodes to 3.65 electron volts. Power conversion efficiency values exceeding 8.5% were obtained for organic photovoltaics independent of the cathode selection (Al, Ag, Cu, or Au). Such high efficiencies did not require precise control over interlayer thickness, as devices prepared with C_{60}-N and C_{60}-SB layers ranging from 5 to 55 nanometers performed with high efficiency.

Recent improvements in the design and fabrication of bulk heterojunction (BHJ) polymer-containing solar cells (PSCs) have produced devices with power conversion efficiency (PCE) values exceeding 9% (*1*–*5*). However, achieving such high efficiencies often requires increasingly complex polymer synthesis and device architectures (e.g., tandem devices). In addition, the most common metal used as the device cathode, aluminum, is prone to rapid oxidation and cannot be processed from solution. More stable metals such as silver, copper, and gold can be deposited from solution, but their high work function (Φ) limits attainable open circuit voltage (V_{OC}), short-circuit current density (J_{SC}), and fill factor (FF) because of a low built-in electrostatic potential difference across the device (*6*–*8*). To circumvent this limitation, a thin buffer layer, inserted between the active layer and cathode, tailors the interface to maximize V_{OC} and minimize contact resistance. Numerous inorganic buffer layers have been studied, such as Ca and LiF, whereas organic interlayers are often better suited to solution-based device fabrication (*9*–*11*). Conductive interlayers such as Ca, advantageous for their intrinsically low Φ, suffer from their sensitivity to oxygen and water. Polar organic interlayers permit layer-by-layer solution deposition but often have poor adhesion to active layers with low surface energy (*12*), thus limiting their utility in conventional device architectures (as fabricated from anode to cathode). Furthermore, buffer layers are typically very thin (<5 nm) so as to prevent charge build-up due to large injection barriers at the active layer–buffer layer interface or slow charge transport through the buffer layer. However, from a processing standpoint, the need to reproduce precise interlayer thickness at the nanometer to subnanometer level is in itself problematic.

An ideal cathode design for organic photovoltaics (OPVs) might consist of a metal with a high intrinsic work function to provide stability, and a readily tailored surface to lower the effective work function for the sake of device performance. We show that functionalized fullerenes bearing tertiary amine (C_{60}-N) or sulfobetaine (C_{60}-SB) groups are easy to process from solution, manifest excellent adhesion to the photoactive layer, and afford OPV devices with outstanding PCE values even when using metals with high Φ values as cathodes.

Buffer layers, or interlayers, positioned at the active layer–cathode interface lower the Φ value of the cathode, with a magnitude frequently described as an interfacial dipole (Δ) (*13*), where large negative Δ values have produced some of the most effective reported OPVs. For example, solution-processed, tertiary amine–substituted polyfluorene (PFN) yielded a maximum PCE of 9.21% in an inverted device (*1*), and poly(ethyleneimine) (PEI) and its derivatives enabled all–solution-processed inverted devices with maximum PCE values of 8.9% (*14*, *15*). In each case, the amine functionality of the interlayer is responsible for the large negative Δ values (< −0.5 eV) (*14*). However, these interlayers have their own drawbacks: The PFN backbone is intrinsically p-type, whereas PEI is insulating and exhibits poor adhesion to the active layer. Interest is thus emerging in fullerene-based interlayers that can transport electrons and promote π-π interactions with the active layer for enhanced adhesion (*5*, *16*–*24*); these favorable properties hold promise for eliminating the undesirable effects often associated with interlayers.

With respect to electrode selection, recent reports of BHJ PSCs using a bathocuproine (BCP) interlayer with a Ag cathode achieved PCEs of 7.7% (*25*) and 8.1% (*26*), representing benchmark values to date for standard single-junction PSCs containing Ag cathodes. However, BCP requires a thermal deposition step and a precisely defined interlayer thickness (3.5 nm) (*26*). We recently reported conjugated polymer zwitterions (CPZs) that show large negative Δ values (−0.5 to −0.9 eV) on metals (*27*–*29*). Spin-coating CPZs and the active-layer polymer from orthogonal solvents

Polymer Science and Engineering Department, University of Massachusetts, Amherst, MA 01003, USA.
*These authors contributed equally to this work. †Corresponding author. E-mail: tsemrick@mail.pse.umass.edu (T.E.); russell@mail.pse.umass.edu (T.P.R.); duzhko@mail.pse.umass.edu (V.V.D.)

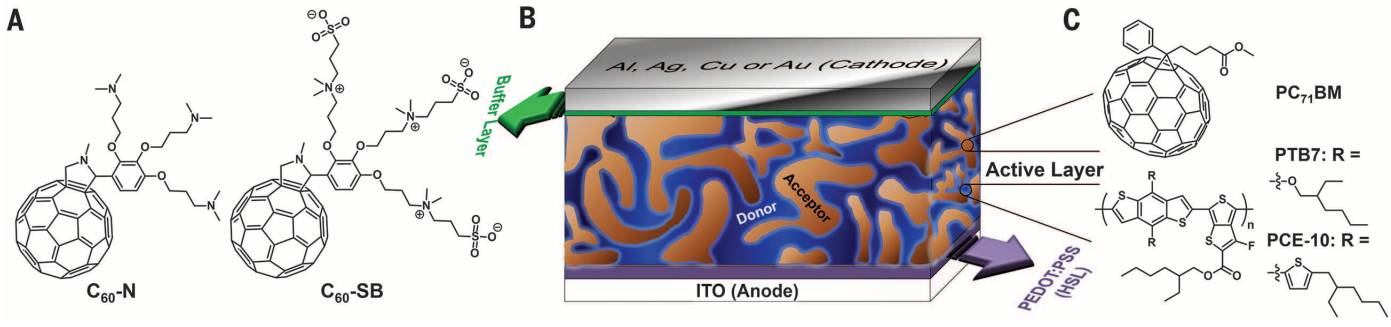

Fig. 1. Solar cell components and architecture. (**A**) Chemical structures of the two fulleropyrrolidines (C_{60}-N and C_{60}-SB) used as cathode modification layers. (**B**) Device configuration, consisting of indium tin oxide (ITO), poly(ethylenedioxythiophene):poly(styrene sulfonate) (PEDOT:PSS), an active layer, a buffer layer, and a cathode, where PEDOT:PSS is the hole selective layer (HSL) and anode modifier, and Al, Ag, Cu, or Au is the cathode. (**C**) Active-layer components, with $PC_{71}BM$ as the acceptor and PTB7 or PCE-10 as the donor.

(i.e., exclusively dissolving only one of the components) provides good control over interlayer thickness with little disruption of the underlying surface. To date, CPZs have demonstrated effectiveness as interlayers in OPV devices over a thickness range of ~5 to 10 nm; however, thicker films are not useful because of the p-type characteristics of the selected polymers (*28*).

Here we report the synthesis, characterization, and use of two trisubstituted polar fulleropyrrolidines as highly effective interlayer materials in polymer-based solar cells. The tris(dimethylamino) (C_{60}-N)–substituted and tris(sulfobetaine) (C_{60}-SB)–substituted fullerenes were prepared by connecting the corresponding trisubstituted phenyl groups through a pyrrolidine ring (Fig. 1A; more detail in scheme S1 and figs. S1 to S8). For C_{60}-N, Mitsunobu coupling (*30*) gave a tris[3-(dimethylamino)propoxy] benzaldehyde that was connected through the Prato reaction (*31*, *32*) to fullerene C_{60}. C_{60}-N served as a precursor to C_{60}-SB through use of the tertiary amines in ring opening of 1,3-propanesultone. These syntheses proved rapid and efficient, and obviated the need for methanofullerene derivatives prepared through unstable diazo intermediates (*33*).

Single-junction OPVs were fabricated with a BHJ active layer containing a blend of [6,6]-phenyl C_{71}-butyric acid methyl ester ($PC_{71}BM$) as the acceptor, and a low–band gap conjugated polymer—thieno[3,4-*b*]thiophene-*a*-benzodithiophene with either 2-(ethylhexyl)oxy (PTB7) (*34*) or 2-(ethylhexyl) thienyl (PCE-10) side chains—as the donor (Fig. 1, B and C). In a device, C_{60}-N or C_{60}-SB was deposited by spin-coating onto the active layer from trifluoroethanol (TFE), followed by deposition of the metal cathode (Al, Ag, Cu, or Au). A device fabricated in this fashion, containing a C_{60}-N/Ag cathode, was examined and certified by the National Renewable Energy Laboratory (NREL) at a PCE of 8.91% (fig. S9), identical to the efficiency obtained in our laboratories for that particular device (fig. S10). We subsequently optimized further the donor/acceptor ratio and interlayer thickness, giving devices with even higher PCE values. The optimized PCE-10:$PC_{71}BM$ OPV devices fabricated with bare Ag cathodes (control devices, no cathode modification layer) gave a PCE of 2.76 ± 0.59% (maximum PCE 3.72%), whereas devices with C_{60}-N or C_{60}-SB interlayers yielded PCE values of 9.35 ± 0.13% (maximum PCE 9.78%) and 8.57 ± 0.15% (maximum PCE 8.92%), respectively (Fig. 2A and table S1). This large efficiency improvement stems from higher V_{OC} and FF values. Devices with bare Ag cathodes suffer from the high Φ value of Ag and the resultant weak built-in electrostatic potential difference. Figure 2A shows that devices fabricated with C_{60}-N interlayers outperform those with C_{60}-SB interlayers, owing to higher V_{OC} (0.75 to 0.78 V) and FF (68 to 71%) values. Devices were also fabricated using a standard Ca/Al cathode, giving PCE values of 8.36 ± 0.21% (table S1). Comparable PCE values were obtained for devices with C_{60}-N/Al and C_{60}-SB/Al, with averages of 8.65 ± 0.11% and 8.29 ± 0.11%, respectively, thus eliminating the need for thermal deposition of Ca. Devices with a PTB7:$PC_{71}BM$ active layer performed similarly, albeit with smaller PCEs (fig. S11 and table S2).

OPV devices fabricated with Cu or Au cathodes, omitting a cathode-modifying interlayer, had low PCE values of 1.29 ± 0.06% and 0.99 ± 0.05%, respectively, as expected from the high Φ values of Cu (4.7 eV) and Au (5.1 eV). However, by casting a ~15-nm layer of C_{60}-N onto the active layer before cathode deposition, the V_{OC} increased to 0.75 V for Cu and 0.76 V for Au, producing devices with PCE values of 8.67 ± 0.17% (PCE_{max} = 8.88%) and 8.56 ± 0.21% (PCE_{max} = 8.83%), respectively. The higher PCE values obtained for Ag-cathode devices stem from their higher J_{SC} values: 16.83 mA/cm^2 for Ag, 16.01 mA/cm^2 for Cu, and 15.75 mA/cm^2 for Au. In addition, the large FF (~70%) obtained, independent of the metal cathode, underscores the universal nature of these C_{60}-N interlayers. Although LiF/Al and Ca/Al are common cathode configurations, Ag, Cu, or Au with LiF or Ca layers give significantly lower PCE values (fig. S12 and table S3). In combination with C_{60}-N interlayers, devices with Ag, Cu, or Au cathodes not only yielded higher PCE relative to devices with LiF/Al or Ca/Al cathodes, but also exhibited improved stability in air (fig. S13). These high-Φ metals not only have the important advantage of increased device lifetime, they also offer a pathway to all-solution processing that can be translated to roll-to-roll (R2R) techniques wherein devices are printed from solution onto a flexible substrate such as a metal foil or plastic.

Seven different interlayer thicknesses were investigated, ranging from 5 to 55 nm (Fig. 2C, figs. S16 and S17, and table S4). Both C_{60}-N and C_{60}-SB produced peak PCE devices at an interlayer thickness of ~15 nm. For C_{60}-N, V_{OC} and FF plateaued at ~0.75 V and 70%, respectively, in accord with interlayer thickness, whereas C_{60}-SB devices maintained a constant V_{OC} (~0.75 V) and a slight decline in FF (from 68 to 65%) for films thicker than ~15 nm, and a decrease in J_{SC} from ~17 mA/cm^2 (thickness ≤15 nm) to ~13 mA/cm^2 (thickness ~55 nm). Thus, these interlayers offer substantial advantages over other interlayers, such as the CPZs we previously reported, in which thickness must be controlled and interlayers thicker than 10 nm produced S-shaped *J-V* curves and reduced PCE (*28*). Unlike the CPZ interlayers, these fulleropyrrolidine interlayers afford efficient devices even when the film thickness exceeds 50 nm.

The interactions of C_{60}-N and C_{60}-SB layers with metal surfaces were investigated and compared to interlayers consisting of 2,3,4-tris(hexyloxy)fulleropyrrolidine (C_{60}-alkyl), which lacks amine or sulfobetaine functionality (scheme S2 and figs. S18 to S22). These three fullerenes exhibited similar optoelectronic properties, with ultraviolet absorption onset indicating optical band gaps (E_g) of ~1.8 eV for each (fig. S16), and cyclic voltammetry (CV) giving electron affinity (E_A) values of 3.8 to 3.9 eV (fig. S23). The high– and low–binding energy onsets measured by ultraviolet photoelectron

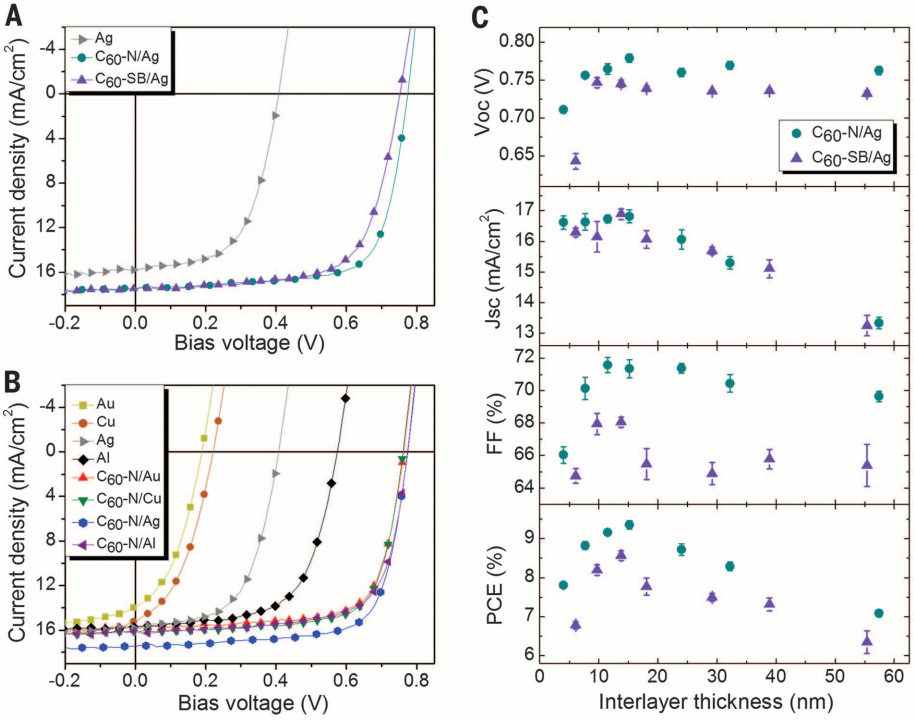

Fig. 2. OPV device performance for ITO/PEDOT:PSS/PCE-10:$PC_{71}BM$/fulleropyrrolidine/cathode architecture. (**A**) Representative *J-V* curves for OPVs with bare Ag cathodes and ~15-nm C_{60}-N and C_{60}-SB interlayers. (**B**) Representative *J-V* curves showing the effect of cathode work function on V_{OC} for the bare metal devices, and impact on OPVs containing a thin layer (~15 nm) of C_{60}-N between the active layer and top cathode. (**C**) Device metrics obtained at varying interlayer thickness (~5 to 55 nm). Error represents ±1 SD over six devices.

spectroscopy (UPS) showed that the ionization potential (I_P) for the fulleropyrrolidines ranged from 5.6 to 5.7 eV (Fig. 3A). E_g values, calculated from the difference between E_A and I_P, correlated closely to the E_g values determined by ultraviolet-visible (UV-Vis) absorbance spectroscopy (~1.8 ± 0.1 eV). The similarities of the E_A values of these fullerenes to that of $PC_{71}BM$ suggest that there is little to no energy barrier for electron transfer at the active layer–interlayer interface. An appreciable energy barrier at this interface would reduce FF as a result of interfacial charge build-up; as such, these substituted fullerenes combine the benefits of unhindered electron transfer with polar, surface-interacting functionality for improved device performance.

The high–binding energy region of the UV photoelectron spectrum provides interfacial dipole (Δ) values that reflect the difference in the high–binding energy onsets, E_{SEC}, of bare versus coated metals. UPS characterization of C_{60}-N, C_{60}-SB, and C_{60}-alkyl on freshly prepared Ag substrates revealed C_{60}-N to have the largest Δ value (Fig. 3A), which remained constant for films thicker than 8 nm and declined for very thin films (in keeping with the reduced V_{OC} values for those devices; see table S5). The larger Δ for C_{60}-N relative to C_{60}-SB accounts for the higher V_{OC} in those devices, as this increases the built-in electrostatic potential difference in the device, improving charge extraction and reducing recombination losses, consistent with higher J_{SC} and FF values for devices with C_{60}-N relative to C_{60}-SB. The difference in Φ value of the electrodes coated with C_{60}-alkyl and C_{60}-SB (0.24 eV) arises from a permanent dipole due to interaction between the zwitterionic sulfobetaine groups with the metal surfaces (*28*). The larger Δ value for C_{60}-N is likely due to electron transfer from the nitrogen lone pair of the tertiary amines to the metal substrate (*35*–*37*), a mechanism not available to the nitrogen of the sulfobetaine groups.

The magnitude of Δ for C_{60}-N films on metal substrates depended critically on film thickness (Fig. 3B). However, for ultrathin films (nominal thickness 1 nm) of C_{60}-N on Ag, Cu, or Au, the effective Φ value remained constant at 3.9 eV, independent of the metal composition. Observing

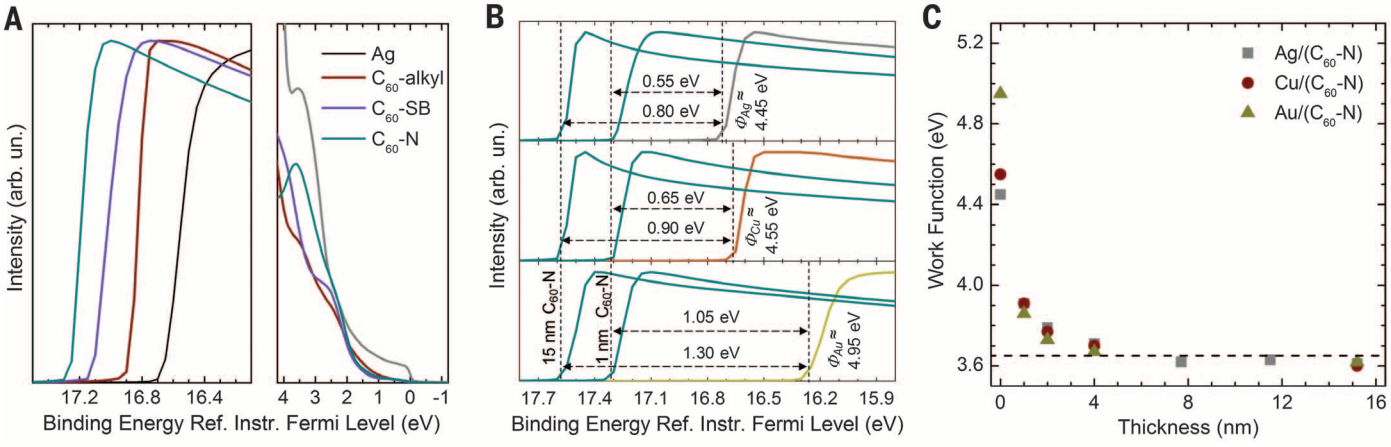

Fig. 3. Ultraviolet photoelectron spectra of fulleropyrrolidine layers on metal substrates. (**A**) Spectra of C_{60}-alkyl, C_{60}-N, and C_{60}-SB (~1-nm layers) on Ag. Δ values extracted from the high–binding energy region near the E_{SEC} (left) are −0.54 eV for C_{60}-N, −0.39 eV for C_{60}-SB, and −0.15 eV for C_{60}-alkyl. The low–binding energy region provides I_P values for C_{60}-alkyl, C_{60}-N, and C_{60}-SB of 5.70 eV, 5.62 eV, and 5.72 eV, respectively. Binding energies are given with reference to the instrument Fermi level. (**B**) Representative high–binding energy region spectra for C_{60}-N films on freshly prepared Ag, Cu and Au, substrates that pin the work function of each modified metal surface at ~3.9 eV or ~3.65 eV for 1-nm and 15-nm films, respectively. (**C**) Work function modification of Ag, Cu, and Au with C_{60}-N films of various thicknesses. Pinning of the effective work function is observed for very thin films (nominally 1 nm), and large modification of work function (to 3.65 eV) is achieved for interlayers greater than 4 nm.

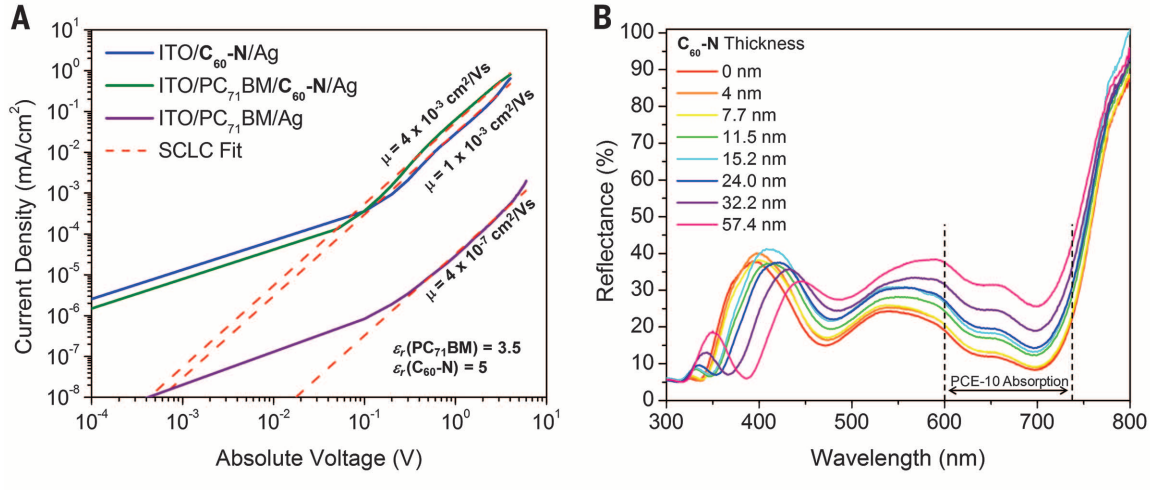

Fig. 4. Probing the effects of fulleropyrrolidine layers on electron mobility and optical absorption. (**A**) Representative *J*-*V* curves for electron-only devices with $PC_{71}BM$, $PC_{71}BM/C_{60}$-N, and C_{60}-N layers in between ITO and Ag electrodes, revealing that C_{60}-N removes the barrier for electron injection from Ag into the bulk organic layer, forming ohmic contact. The dashed lines show fits to the Mott-Gurney law in the range of a SCLC regime of device operation. (**B**) UV-Vis reflectance spectroscopy of OPV devices with C_{60}-N interlayer thicknesses varying from 4 to 57 nm (as well as a control device with no interlayer). The increased reflectance from 600 to 740 nm for devices containing interlayers thicker than 7.7 nm is direct evidence of an optical spacer effect, which explains the reduced J_{SC} for OPV devices with thicker interlayers.

this effect for such thin films indicates that pinning of Φ originates at the metal–C_{60}-N interface, although the exact mechanism of this interaction is not fully understood (*38*). With increasing C_{60}-N thickness, Φ values saturated at 3.65 eV on Ag, Cu, or Au (Fig. 3C). Such a gradual change of Δ within ~5 nm of the interface indicates a narrow space charge region in C_{60}-N films, similar to a depletion region at the metal–doped semiconductor interface. The formation of a positive space charge in C_{60}-N is consistent with electron transfer from tertiary amines to the metal (equation S1), whereas the Δ values for C_{60}-alkyl gave no indication of electron transfer (fig. S24) (*35*–*37*, *39*). This effect is independent of the metal substrate, yielding an effective Φ value of 3.65 eV for C_{60}-N–modified Ag, Cu, and Au electrodes (Fig. 3C). This observation in turn suggests that C_{60}-N provides ohmic contact for electron injection, as well as a large built-in electrostatic potential difference for efficient charge extraction in OPVs. The effect of these fullerenes on different metals confirms not only the general utility of these interfacial layer materials, but also the success of interfacial tailoring independent of the work function inherent in each metal electrode.

Although device efficiency exceeded 6% for interlayers ranging from 5 to 55 nm, optimum PCE values were obtained at a thickness of ~15 nm, followed by a gradual decline in efficiency for thicker interlayers (Fig. 2C). To better understand the role of these polar fullerene interlayers, we prepared single-carrier devices to determine electron mobility using the modified Mott-Gurney law $J = \gamma(^9/_8\varepsilon_r\varepsilon_0\mu)(V^2/L^2)$ (where $\gamma \leq 1$ is the contact non-ideality factor, ε_r is the dielectric constant, and μ is electron mobility) for the space charge–limited current (SCLC) regime of device operation (Fig. 4A and fig. S25). Electron-only devices were constructed using an ITO bottom electrode and Ca/Al top electrode with $PC_{71}BM$, C_{60}-N or C_{60}-SB as the bulk transport material. UPS suggests that hole injection from ITO to the HOMO of C_{60}-N is negligible due to a high energy barrier at the ITO/C_{60}-N interface (fig. S26). Assuming that Ca/Al electrodes provide ohmic contact ($\gamma = 1$) for electron injection, electron mobilities of 1.3×10^{-3}, 1.8×10^{-3}, and 1.0×10^{-5} $cm^2\ V^{-1}\ s^{-1}$ were estimated for $PC_{71}BM$, C_{60}-N, and C_{60}-SB, respectively (values of ε_r were determined by impedance spectroscopy to be 3.5 for $PC_{71}BM$ and 5.0 for C_{60}-N and C_{60}-SB; see figs. S27 to S29). The higher electron mobility of C_{60}-N relative to C_{60}-SB explains its higher efficiency as thicker interlayers in OPVs; less efficient electron extraction through C_{60}-SB interlayers imparts a series resistance that reduces FF and J_{SC}.

To determine whether Ag forms an ohmic contact with $PC_{71}BM$ directly and whether a C_{60}-N interlayer improves its properties, we fabricated devices with a Ag top electrode and a $PC_{71}BM$, $PC_{71}BM$/C_{60}-N, or C_{60}-N electron transport layer (Fig. 4A). Devices with only $PC_{71}BM$ showed evidence of a Schottky barrier, resulting in a $\gamma \times \mu$ product of 4.0×10^{-7} $cm^2\ V^{-1}\ s^{-1}$, where $\gamma \leq 0.001$ (more than three orders of magnitude lower than diodes with Ca/Al electrodes). This is consistent with the high Φ value of Ag (4.45 eV) relative to the lowest unoccupied molecular orbital of $PC_{71}BM$ (3.9 eV). Inserting a layer of C_{60}-N (13 nm, 25 nm, or 48 nm) between $PC_{71}BM$ and Ag improved mobility by four orders of magnitude, to 4.0×10^{-3} $cm^2\ V^{-1}\ s^{-1}$, suggesting an ohmic contact for C_{60}-N/Ag that promotes electron injection into $PC_{71}BM$. With OPVs, a lower potential barrier for electron injection at ohmic contact translates to larger built-in potential, faster electron extraction, and thus higher J_{SC} and FF. Additionally, single-carrier devices with only C_{60}-N as the bulk transport material and top Ag electrodes gave electron mobility values (1.1×10^{-3} $cm^2\ V^{-1}\ s^{-1}$) approximately equal to those measured using Ca/Al electrodes. Because the electron mobility of $PC_{71}BM$ is independent of C_{60}-N interlayer thickness and is comparable to the electron mobility in C_{60}-N itself, electron transport through C_{60}-N does not lead to an increased series resistance in OPV devices, and thus is not likely responsible for compromised PCE at greater interlayer thickness.

We further probed OPV devices fabricated with C_{60}-N interlayers on Ag (Fig. 4B) by UV-Vis reflectance spectroscopy, measured through the ITO substrate at 5° with respect to the surface normal. Devices with interlayers thicker than 7.7 nm exhibited higher reflectance (reduced absorption) from 600 to 740 nm, where PCE-10 absorbs most strongly and C_{60}-N does not absorb. This represents direct evidence of an optical spacer effect (*40*), where C_{60}-N redistributes the optical field within the device. The reduced absorption in the photoactive layer from 600 to 740 nm explains the reduced J_{SC} and lower PCE for OPV devices having thicker interlayers. In addition, UV-Vis reflectance spectroscopy of bare metal cathodes (fig. S30A) revealed that the lower PCE obtained for devices with Cu (8.67 ± 0.17%) or Au (8.56 ± 0.21%) cathodes, relative to Ag (9.35 ± 0.13%) cathodes, can be attributed to the lower reflectivity of Au and Cu. Direct correlation between the metal reflectivity below 550 nm and external quantum efficiency of devices with different metal cathodes, both with and without C_{60}-N interlayers (fig. S30, B and C), indicates that metal reflectivity is responsible for lower short-circuit current densities in devices with Au and Cu cathodes relative to devices with Al or Ag cathodes.

Because of the synthetic accessibility of C_{60}-N and C_{60}-SB, their ability to modify the electronic properties of metal substrates, and the resultant high efficiency OPV devices using C_{60}-N and C_{60}-SB as interlayers, these fulleropyrrolidines represent an excellent platform for electrode modification in OPVs as well as organic electronic devices in general.

REFERENCES AND NOTES

1. Z. He *et al.*, *Nat. Photonics* **6**, 591–595 (2012).
2. J. You *et al.*, *Nat. Commun.* **4**, 1446 (2013).
3. Y. Liu *et al.*, *Sci. Rep.* **3**, 3356 (2013).
4. J. You *et al.*, *Adv. Mater.* **25**, 3973–3978 (2013).
5. K. Yao *et al.*, *Adv. Energy Mater.* **4**, 1400206 (2014).
6. F. C. Krebs, *Sol. Energy Mater. Sol. Cells* **93**, 465–475 (2009).
7. F. C. Krebs, S. Gevorgyan, J. A. Alstrup, *J. Mater. Chem.* **19**, 5442–5451 (2009).
8. F. Guo *et al.*, *Adv. Energy Mater.* **3**, 1062–1067 (2013).
9. H.-L. Yip, A. K.-Y. Jen, *Energy Environ. Sci.* **5**, 5994–6011 (2012).
10. C. Duan, K. Zhang, C. Zhong, F. Huang, Y. Cao, *Chem. Soc. Rev.* **42**, 9071–9104 (2013).
11. C. Gu *et al.*, *Adv. Energy Mater.* **4**, 1301771 (2014).
12. Z. Zhang *et al.*, *J. Mater. Chem. A* **1**, 9624–9629 (2013).
13. B. J. Worfolk *et al.*, *Adv. Energy Mater.* **2**, 361–368 (2012).
14. Y. Zhou *et al.*, *Science* **336**, 327–332 (2012).
15. S. Woo *et al.*, *Adv. Energy Mater.* **4**, 1301692 (2014).
16. K. M. O'Malley, C.-Z. Li, H.-L. Yip, A. K.-Y. Jen, *Adv. Energy Mater.* **2**, 82–86 (2012).
17. X. Yang *et al.*, *Adv. Energy Mater.* **3**, 666–673 (2013).
18. C. Chueh *et al.*, *Adv. Energy Mater.* **3**, 417–423 (2013).
19. Q. Mei *et al.*, *ACS Appl. Mater. Interfaces* **5**, 8076–8080 (2013).
20. S. Li *et al.*, *Adv. Energy Mater.* **3**, 1569–1574 (2013).
21. Y.-Y. Lai *et al.*, *ACS Appl. Mater. Interfaces* **5**, 5122–5128 (2013).
22. X. Li, W. Zhang, Y. Wu, C. Min, J. Fang, *J. Mater. Chem.* **1**, 12413–12416 (2013).
23. C. Duan, C. Zhong, C. Liu, F. Huang, Y. Cao, *Chem. Mater.* **24**, 1682–1689 (2012).
24. Q. Wei, T. Nishizawa, K. Tajima, K. Hashimoto, *Adv. Mater.* **20**, 2211–2216 (2008).
25. R. Betancur *et al.*, *Nat. Photonics* **7**, 995–1000 (2013).
26. A. Martínez-Otero, X. Elias, R. Betancur, J. Martorell, *Adv. Optical Mater.* **1**, 37–42 (2013).
27. Z. A. Page, V. V. Duzhko, T. Emrick, *Macromolecules* **46**, 344–351 (2013).
28. F. Liu, Z. A. Page, V. V. Duzhko, T. P. Russell, T. Emrick, *Adv. Mater.* **25**, 6868–6873 (2013).
29. Z. A. Page, F. Liu, T. P. Russell, T. Emrick, *Chem. Sci.* **5**, 2368–2373 (2014).
30. O. Mitsunobu, M. Yamada, *Bull. Chem. Soc. Jpn.* **40**, 2380–2382 (1967).
31. M. Maggini, G. Scorrano, M. Prato, *J. Am. Chem. Soc.* **115**, 9798–9799 (1993).
32. M. Prato, M. Maggini, *Acc. Chem. Res.* **31**, 519–526 (1998).
33. J. C. Hummelen *et al.*, *J. Org. Chem.* **60**, 532–538 (1995).
34. Y. Liang *et al.*, *Adv. Mater.* **22**, E135–E138 (2010).
35. B. Bröker *et al.*, *Appl. Phys. Lett.* **93**, 243303 (2008).
36. L. Lindell *et al.*, *Appl. Phys. Lett.* **92**, 163302 (2008).
37. L. Lindell *et al.*, *Chem. Mater.* **18**, 4246–4252 (2006).
38. B. S. Braun, W. R. Salaneck, M. Fahlman, *Adv. Mater.* **21**, 1450–1472 (2009).
39. S. M. Sze, K. K. Ng, *Physics of Semiconductor Devices* (Wiley, New York, 2007).
40. J. Y. Kim *et al.*, *Adv. Mater.* **18**, 572–576 (2006).

ACKNOWLEDGMENTS

Supported by the Polymer-Based Materials for Harvesting Solar Energy (PHaSE), an Energy Frontier Research Center funded by the U.S. Department of Energy (DOE), Office of Basic Energy Sciences, under award DE-SC0001087, and an award from the DOE Office of Science Graduate Fellowship Program (DOE SCGF) (Z.A.P.). The DOE SCGF Program was made possible in part by the American Recovery and Reinvestment Act of 2009. The DOE SCGF program is administered by the Oak Ridge Institute for Science and Education (ORISE) for the DOE. ORISE is managed by Oak Ridge Associated Universities (ORAU) under DOE contract number DE-AC05-06OR23100. All opinions expressed in this paper are those of the authors and do not necessarily reflect the policies and views of DOE, ORAU, or ORISE. We thank PHaSE and the NSF-MRSEC on Polymers at UMass (DMR-0820506) for facilities support. A provisional U.S. patent, including some of the contents of this work, has been filed (no. 61/990,305).

SUPPLEMENTARY MATERIALS

www.sciencemag.org/content/346/6208/441/suppl/DC1
Materials and Methods
Schemes S1 and S2
Figs. S1 to S30
Tables S1 to S5
Equation S1

8 May 2014; accepted 3 September 2014
Published online 18 September 2014;
10.1126/science.1255826

ULTRAFAST DYNAMICS

A photoinduced metal-like phase of monoclinic VO_2 revealed by ultrafast electron diffraction

Vance R. Morrison,[1] Robert. P. Chatelain,[1] Kunal L. Tiwari,[1] Ali Hendaoui,[3] Andrew Bruhács,[2] Mohamed Chaker,[3] Bradley J. Siwick[1,2]*

The complex interplay among several active degrees of freedom (charge, lattice, orbital, and spin) is thought to determine the electronic properties of many oxides. We report on combined ultrafast electron diffraction and infrared transmissivity experiments in which we directly monitored and separated the lattice and charge density reorganizations that are associated with the optically induced semiconductor-metal transition in vanadium dioxide (VO_2). By photoexciting the monoclinic semiconducting phase, we were able to induce a transition to a metastable state that retained the periodic lattice distortion characteristic of the semiconductor but also acquired metal-like mid-infrared optical properties. Our results demonstrate that ultrafast electron diffraction is capable of following details of both lattice and electronic structural dynamics on the ultrafast time scale.

The central problem of condensed matter physics involves determining the pathways through which microscopic interactions lead to the emergent properties of materials. Collective phases affected by multiple collaborating or competing interactions (*1*–*3*) have provided a great challenge in this respect. Understanding the properties of such phases depends on the development of methods to address and separate the roles of several active interacting degrees of freedom. Here, we demonstrate that recent improvements in ultrafast electron diffraction (UED) instrumentation (*4*–*7*) provide such a capability by exploring the nature of the semiconductor-to-metal transition in VO_2 (*8*).

At ~343 K, VO_2 undergoes a first-order transition between two crystalline phases (Fig. 1A). This structural phase transition (SPT) is accompanied by a marked change in conductivity (fig. S3), as much as five orders of magnitude in high-quality single crystals (*9*). The high-temperature phase (Fig. 1A, left) is metallic with a rutile crystalline structure (*R*, $P4_2/mnm$). The low-temperature phase (Fig. 1A, right) is characterized by semiconducting electronic behavior (with a band gap energy $E_g \approx 0.6$ eV) and monoclinic structure (*M*1, $P2_1/c$). The SPT may be understood roughly as the formation of a charge density wave (CDW) along the rutile *c* axis with wave vector $2\mathbf{c}_R$, which leads to a doubling of the unit cell along this direction. This periodic lattice distortion (PLD) dimerizes vanadium atoms along the $\mathbf{c}_R$ direction, spaced by 2.85 Å in the high-temperature phase, into alternating V-V separations of 2.62 Å and 3.16 Å. The dimers are also rotated slightly with respect to $\mathbf{c}_R$.

A challenge to understanding this semiconductor-to-metal transition has been to determine the relative contributions of electron-lattice interactions (lattice and charge order) and electron-electron interactions (dynamical correlations and orbital selection) to the change in properties and the nature of the semiconducting phase (*10*–*15*). Here, we interrogated both structure and electronic properties by making use of the beam brightness enhancement provided by radio-frequency compressed ultrafast electron diffraction (*16*–*18*) in combination with time-resolved infrared (IR) transmittance measurements. The combined approach makes it possible to map the reorganization of the VO_2 unit cell during the optically induced transition (*19*, *20*) while simultaneously determining the electronic properties of the material. The results demonstrate a photoinduced transformation to a long-lived state with metal-like mid-IR optical properties and the PLD (or CDW order) of the semiconducting *M*1 phase intact. This metastable state differs from the equilibrium rutile metal crystallographically, and only involves a one-dimensional (1D) reorganization of charge density rather than a transition to the isotropic 3D electronic state of the high-temperature phase (*21*, *22*).

In these experiments, polycrystalline VO_2 films grown by pulsed laser deposition (Fig. 1, B and C) (*23*), initially in the low-temperature *M*1 phase (at ~310 K), are subject to optical (800 nm) excitation with 35-fs laser pulses. The time dependence of the changes in structure and electronic properties after optical excitation of the material are determined using pump-probe UED and time-resolved IR transmittance measurements (*24*). Raw (background-subtracted) ultrafast powder electron diffraction data taken in a transmission geometry (fig. S1) exhibit several weak reflections ($30\bar{2}$, $12\bar{2}$, and $31\bar{3}$), indicated by vertical red lines in Fig. 2A. These peaks are allowed in the *M*1 phase, thanks to the PLD and the doubling of the unit cell along $\mathbf{c}_R$, but not in the *R* phase. At this intermediate pump fluence of 20 mJ/cm^2, the intensity of these peaks clearly decreases with time after photoexcitation, indicative of the optically induced SPT that occurs in some of the

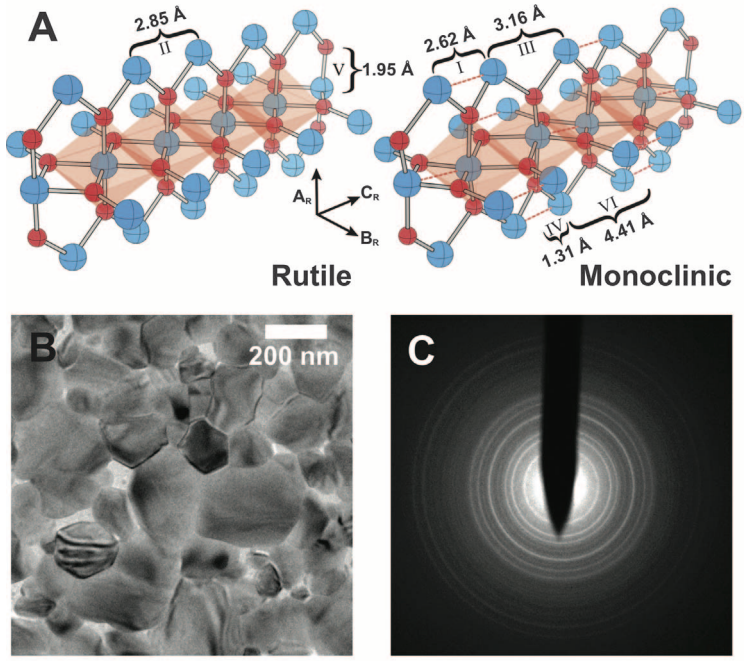

Fig. 1. Structure of VO_2. (**A**) The structure of rutile VO_2 (left) and monoclinic VO_2 (right). (**B**) Transmission electron microscopy image of the pulsed laser deposition–grown VO_2 sample used in these studies. (**C**) Example of electron powder diffraction pattern of the monoclinic phase.

[1]Department of Physics, Center for the Physics of Materials, McGill University, Montreal, Quebec H3A 2T8, Canada. [2]Department of Chemistry, McGill University, Montreal, Quebec H3A 0B8, Canada. [3]Institut National de la Recherche Scientifique, Centre Énergie Matériaux et Télécommunications, Université du Québec, Varennes, Quebec J3X 1S2, Canada.
*Corresponding author. E-mail: bradley.siwick@mcgill.ca

(polycrystalline) sample. Similar observations were made in previous ultrafast structural measurements on VO_2, which identified a time scale of <500 fs for aspects of the SPT (*25*, *26*).

Beyond these specific peaks, however, photoexcitation induces changes in diffracted intensity over the entire scattering vector range shown. This is clearly evident in Fig. 2B, which shows the time-dependent difference in diffracted intensity with respect to negative pump-probe delays (i.e., before photoexcitation). The presence of multiple time scales can be seen clearly in Fig. 2C, which shows the time-dependent intensity of several diffraction features labeled in Fig. 2A. After photoexcitation at 20 mJ/cm^2, there is a fast (time constant 310 ± 160 fs) decrease in the intensity of diffraction peaks associated with the PLD (e.g., $30\bar{2}$), followed by a slow increase (time constant 1.6 ± 0.2 ps) in the intensity of most peaks in the range s < 0.45 Å^{-1} that are present for both phases (e.g., the 220 and 200 features). These are the only two ultrafast time constants observed in the data up to 10 ps.

The amplitudes of these two qualitatively distinct diffraction signatures each scale linearly with fluence, but they have different slopes and threshold fluences: 9 mJ/cm^2 for fast pump-induced changes to peaks associated with the PLD in the *M*1 phase, and 2 mJ/cm^2 for the slow changes. At pump fluences below ~9 mJ/cm^2 (hatched region in Fig. 2D), there is no change in the intensity of diffraction peaks associated with the PLD in the *M*1 phase. The inset in Fig. 2D shows time-resolved IR transmittance curves at 5 μm (0.25 eV) for the VO_2 film at several pump fluences below 9 mJ/cm^2. These curves show a persistent decrease in IR transmissivity that increases with pump fluence and reaches an amplitude of >99% by 3.7 mJ/cm^2. This observation is in quantitative agreement with previous experiments using multi-THz spectroscopy on VO_2 films grown by pulsed laser deposition (*27*, *28*) and is indicative of a (partial) transition to a state with metal-like ac conductivity at a threshold pump fluence of ~2 mJ/cm^2.

We isolated the full spectrum of diffracted intensity changes that correspond to the fast and slow components in the time domain by choosing reference time points for computing the intensity differences that separate these dynamics: t = –1 ps in Fig. 2E (fast dynamics) and t = 2 ps in Fig. 2F (slow dynamics). Unlike the fast dynamics in Fig. 2E, the slow dynamics are dominated by increases in peak intensity over a limited range of scattering vectors (s < 0.45 Å^{-1}) for which electron scattering is known to be particularly sensitive to the valence charge distribution (*29*, *30*). In addition, these slow dynamics are absent for reflections whose reciprocal lattice vector is perpendicular to $\mathbf{c}_R$. That is, peaks with a zero first index in the monoclinic system ($[h_M k_M l_M] = [0k_M l_M]$) as indicated by gray vertical lines in Fig. 2. This observation establishes that electron structure factors orthogonal to $\mathbf{c}_R$ are largely unaffected by the slow process. The slow process corresponds to a 1D modification of the electrostatic crystal potential in the octahedrally coordinated vanadium chains oriented along $\mathbf{c}_R$.

The two diffraction signatures described above represent qualitatively distinct structural reorganizations within VO_2 after photoexcitation. This can be understood by computing the pump-induced changes to the radial pair distribution function (PDF) (*31*) directly from the observed changes in diffracted intensity shown in Fig. 2, E and F. These curves (Fig. 3, A and B) represent the time-dependent difference in the radial autocorrelation function of the crystal potential with respect to the reference time point. The computed difference PDF for the fast dynamics (Fig. 3A) provides a straightforward structural interpretation

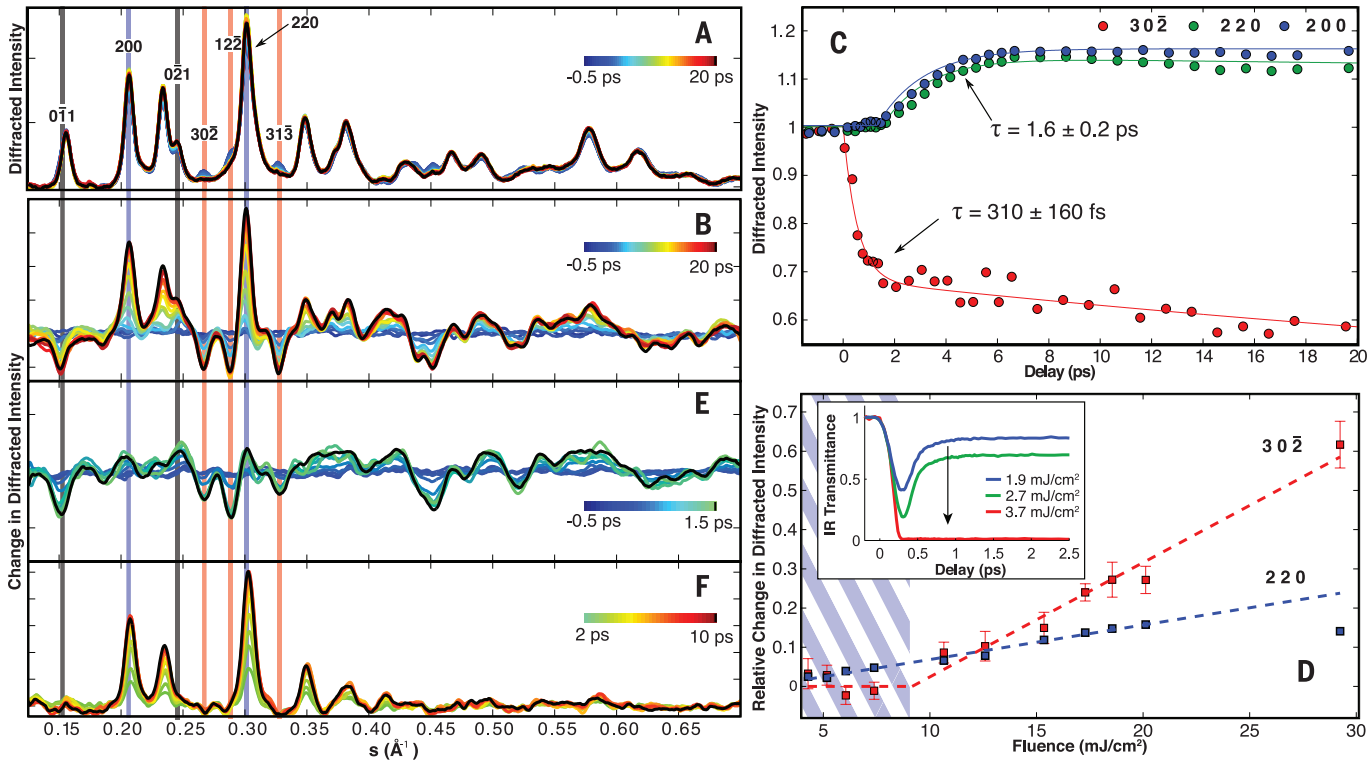

Fig. 2. Structural dynamics during the semiconductor-to-metal transition in VO_2. (**A**) Raw, background-subtracted UED data from 0 to 20 ps. Red vertical lines indicate several weak reflections allowed in the *M*1 phase but not allowed in the *R* phase. Blue vertical lines indicate several peaks present in both equilibrium phases. Gray vertical lines indicate peaks for which h_M = 0, that are only affected by structural changes orthogonal to $\mathbf{c}_R$. (**B**) Overall diffraction difference spectrum from –0.5 to 20 ps. (**C**) Time-resolved diffraction peak intensity showing fast (~300 fs) and slow (~1.6 ps) dynamics, respectively, for peaks indicated by red and blue vertical lines in the diffraction spectra in (A), (B), (E), and (F). (**D**) Fluence dependence of the fast and slow signal amplitudes as measured for the ($30\bar{2}$) and (220) peaks shown in (C). The range of fluences for which no SPT is observed is indicated by the hatched region. Inset: Time-resolved IR (5 μm, 0.25 eV) transmissivity in the hatched fluence region displays a persistent decrease to a very long-lived plateau (>100 ps). The amplitude of this decrease reaches >99% at 3.7 mJ/cm^2, indicating a closing of the semiconducting gap and a transition to a metallic-like state. (**E**) Diffraction difference spectrum for the fast dynamics from –0.5 to 1.5 ps. The change in diffracted intensity is plotted with respect to –1 ps. (**F**) Diffraction difference spectrum for the slow dynamics. The change in diffracted intensity from 2 to 10 ps (referenced to 2 ps) is shown.

for this signal. The positive growing feature (II) corresponds to increased correlation at the *R*-phase V-V bond length, 2.85 Å, while the adjacent negative features (I, III) represent a reduction at the dimer (2.62 Å) and unpaired (3.16 Å) distances of the *M*1 phase (Fig. 1). Thus, the fast dynamics correspond to nonthermal melting of the PLD in a fluence-dependent fraction of crystallites. In these crystallites, the vanadium atomic positions relax to their equilibrium *R*-phase separation on a time scale of 300 fs (*26*). Extrapolating the linear scaling of these dynamics with fluence indicates that ~43 mJ/cm^2 is required to melt the PLD (CDW order) in the entire film. Pump fluences less than ~9 mJ/cm^2 are insufficient to initiate this nonthermal SPT in any crystallites, and leave the PLD and *M*1 crystal structure completely intact. Below this ~9 mJ/cm^2 threshold, only the slow dynamics are observed (Fig. 2F and fig. S4). The diffraction signature of these dynamics is identical below and above the SPT threshold, demonstrating that the slow and fast components represent distinct transitions occurring in different crystallites as a result of the heterogeneity of these pulsed laser deposition–grown samples.

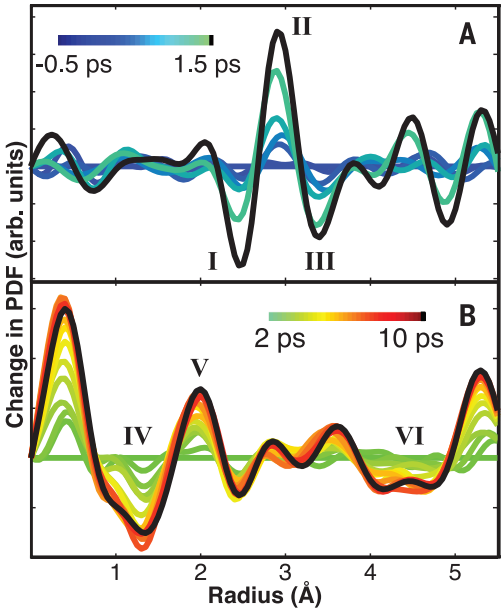

Fig. 3. Difference pair distribution functions for fast and slow dynamics. (**A**) Difference PDF from −0.5 ps to 1.5 ps, referenced to −0.5 ps. (**B**) Difference PDF from 2 ps to 10 ps, referenced to 2 ps. The roman numerals correspond to the distances labeled in Fig. 1.

In contrast to the above, the slower dynamics do not correspond to a structural rearrangement of the lattice (which result in a conservation of diffracted intensity like that seen for the fast dynamics in Fig. 2E). The difference PDF (Fig. 3B) for the slow changes is dominated by negative features at 1.3 Å (IV) and 4.4 Å (VI), equal to half the V-V dimer bond length and the undimerized V-V separation plus half the V-V dimer bond length, respectively (Fig. 1A). Positive changes are also observed at around 1.9 Å (V), the average V-O separation in the octahedron, and at <0.8 Å. These observations are consistent with a collective reorganization of valence charge density in the *M*1 phase that increases the electron density in the vanadium dimer bonds while decreasing the electrostatic potential on primarily the oxygen atoms—an effective modification of the atomic scattering factors.

Previous theoretical work on VO_2 has focused on the behavior and occupancy of the three bands formed from hybridized V-3d/O-2p states of t_{2g} symmetry (Fig. 4A) as the determining factor in its electronic properties (*10*, *13*–*15*). Figure 4B shows the orientation of the localized d orbitals from which these bands are formed. The d_{xy} (also referred to as $d_{||}$) and d_{xz} orbitals mediate σ- and π-type interactions between vanadium atoms along $\mathbf{c}_R$, respectively. The d_{yz} orbital is oriented orthogonal to $\mathbf{c}_R$. There is broad agreement (*13*–*15*) that in the high-temperature phase these three bands almost completely overlap at the Fermi level (Fig. 4A, i). This results in roughly equal occupancy in these bands and a nearly isotropic electronic state (*21*, *22*). It has been suggested that the PLD in the *M*1 phase splits the $d_{||}$ states into bonding and antibonding combinations sufficiently to open an insulating gap (*10*), but density functional theory calculations using the local density approximation maintain density of states at the Fermi level in the *M*1 phase (*13*, *14*), as shown in Fig. 4A, ii (*32*, *33*).

Recent work using cluster dynamical mean-field theory points to dynamical electron-electron correlations acting in collaboration with the PLD as being responsible for the insulating properties of the *M*1 phase (Fig. 4) (*14*, *15*). Our results support this view. We have demonstrated that optical excitation can induce a long-lived state

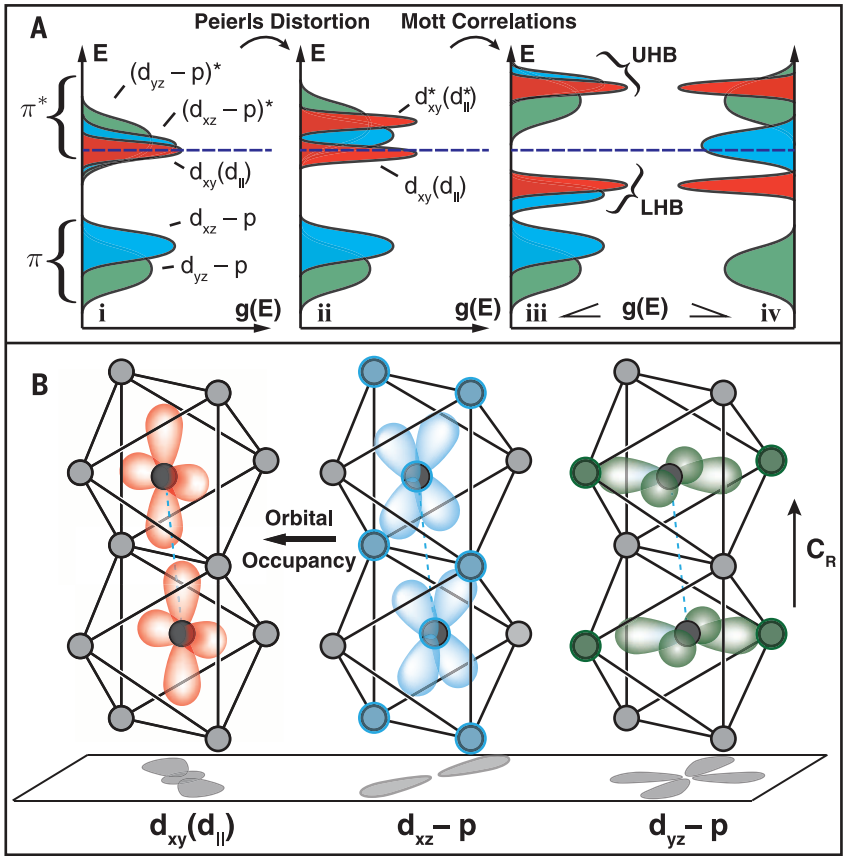

Fig. 4. Effective band diagrams for states of t_{2g} symmetry. (**A**) i: Band diagram for the rutile, metallic phase. ii: Band diagram modified as a result of the PLD. iii: The effect of electron-electron correlations as described in (*15*). UHB and LHB are upper and lower Hubbard bands, respectively. iv: Schematic band diagram indicating partial Mott melting of the d_{xz} band. (**B**) Illustrations of the d_{xy}, d_{xz}, and d_{yz} molecular orbitals.

with IR transmissivity like that of the metallic phase (i.e., collapse of the optical band gap to below 0.25 eV) even without melting the CDW order. In this state the PLD of the insulating phase remains intact, but the valence charge distribution is altered. The nature of the changes in charge density can be understood from the symmetry of the changes in diffraction (Fig. 2F), the orbitals (Fig. 4B), and the difference PDF (Fig. 3B). The negative features at 1.3 Å and 4.4 Å in Fig. 3B suggest an increase in the filling of the d_{xy} subshell that contributes most strongly to the CDW along $\mathbf{c}_R$. The positive features at 0.8 Å and 1.9 Å suggest reduced filling of the d_{xz} subshell, which reduces charge density on the V and O atoms in the octahedral chains. The d_{yz} states oriented orthogonal to $\mathbf{c}_R$, which are understood to be unoccupied in semiconducting VO_2 (*15*, *22*), remain unchanged. Thus, optical excitation with fluences below the threshold required to melt the PLD drives a 1D redistribution of occupancy in the d_{xy} and d_{xz} subshells, not a transformation to the isotropic state of the equilibrium metal. Suppression of correlation-induced splitting into upper (UHB) and lower (LHB) Hubbard bands, either preferentially in the d_{xz} band (Fig. 4A, iv) or in both d_{xz} and d_{xy} shells (Fig. 4A, ii), could lead to such a reorganization. The first case represents an optically induced orbital-selective transition with a mixture of localized (d_{xy}) and itinerant (d_{xz}) behavior (*34*).

The picosecond time scale of this transformation, in addition to its long-lived nature, suggests that the increased vibrational excitation of the lattice due to carrier relaxation (electron-phonon coupling) is a key factor in both inducing and maintaining the reorganization. The nonequilibrium population of excited carriers relaxes within 1 ps in thin VO_2 films grown by pulsed laser deposition (*27*). However, our measurements cannot rule out the possibility of other mechanisms affecting this stability, including kinetic trapping of the valence charge reorganization. Earlier work identified metal-like phases of VO_2 with properties distinct from that of the rutile, high-temperature metal. This includes nanoscale correlated metallic domains with unidentified lattice structure that were observed near the transition temperature (*35*, *36*), as well as the observation that the thermally initiated semiconductor-to-metal transition and the SPT can occur noncongruently, suggesting the presence of a metal-like *M*1 phase of VO_2 (*37*). The correlated metallic state observed in the thermally activated phase transition and the *M*1 metastable state accessed optically here may be related.

The profound decoupling of the semiconductor-to-metal transition in mid-IR optical properties and the SPT induced through optical excitation indicates that the PLD of the *M*1 phase is insufficient to fully explain the semiconducting gap. From the perspective of the striking change in electronic properties, the principal role of the PLD is to alter the accessibility of the bands formed by states of d_{xy} symmetry. With the PLD in place, these states are depopulated, and the highest-energy occupied bands have a 1D character and are susceptible to further electronic ordering. The isotropic electronic character of the equilibrium rutile metal (*22*) cannot be realized with the PLD intact. Finally, the large threshold excitation fluence for the SPT relative to that for the observed electronic reorganization demonstrates that the latent heat of the first-order phase transition at ~340 K is dominated by the SPT rather than by the electronic transition.

Our study shows that UED is able to provide deep insights into the nature of other strongly correlated materials through the disparate concurrent responses of active degrees of freedom in the time domain. Further, our results have relevance to the study of the interplay between valence charge and lattice structure in molecular and materials chemistry.

REFERENCES AND NOTES

1. M. Imada, A. Fujimori, Y. Tokura, *Rev. Mod. Phys.* **70**, 1039–1263 (1998).
2. E. Dagotto, *Science* **309**, 257–262 (2005).
3. P. A. Lee, X.-G. Wen, *Rev. Mod. Phys.* **78**, 17–85 (2006).
4. B. J. Siwick, J. R. Dwyer, R. E. Jordan, R. J. D. Miller, *Science* **302**, 1382–1385 (2003).
5. C.-Y. Ruan, Y. Murooka, R. K. Raman, R. A. Murdick, *Nano Lett.* **7**, 1290–1296 (2007).
6. G. Sciaini, R. J. D. Miller, *Rep. Prog. Phys.* **74**, 096101 (2011).
7. M. Gao *et al.*, *Nature* **496**, 343–346 (2013).
8. L. Whittaker, C. J. Patridge, S. Banerjee, *J. Phys. Chem. Lett.* **2**, 745–758 (2011).
9. C. Berglund, H. Guggenheim, *Phys. Rev.* **185**, 1022–1033 (1969).
10. J. Goodenough, *J. Solid State Chem.* **3**, 490–500 (1971).
11. A. Zylbersztejn, N. Mott, *Phys. Rev. B* **11**, 4383–4395 (1975).
12. R. M. Wentzcovitch, W. W. Schulz, P. B. Allen, *Phys. Rev. Lett.* **72**, 3389–3392 (1994).
13. V. Eyert, *Ann. Phys.* **11**, 650–704 (2002).
14. S. Biermann, A. Poteryaev, A. I. Lichtenstein, A. Georges, *Phys. Rev. Lett.* **94**, 026404 (2005).
15. C. Weber *et al.*, *Phys. Rev. Lett.* **108**, 256402 (2012).
16. T. van Oudheusden *et al.*, *J. Appl. Phys.* **102**, 093501 (2007).
17. R. P. Chatelain, V. R. Morrison, C. Godbout, B. J. Siwick, *Appl. Phys. Lett.* **101**, 081901 (2012).
18. M. Gao *et al.*, *Opt. Express* **20**, 12048–12058 (2012).
19. A. Cavalleri, T. Dekorsy, H. Chong, J. Kieffer, R. Schoenlein, *Phys. Rev. B* **70**, 161102 (2004).
20. S. Wall *et al.*, *Phys. Rev. B* **87**, 115126 (2013).
21. T. C. Koethe *et al.*, *Phys. Rev. Lett.* **97**, 116402 (2006).
22. M. W. Haverkort *et al.*, *Phys. Rev. Lett.* **95**, 196404 (2005).
23. A. Hendaoui, N. Émond, S. Dorval, M. Chaker, E. Haddad, *Curr. Appl. Phys.* **13**, 875–879 (2013).
24. See supplementary materials on *Science* Online.
25. A. Cavalleri *et al.*, *Phys. Rev. Lett.* **87**, 237401 (2001).
26. P. Baum, D.-S. Yang, A. H. Zewail, *Science* **318**, 788–792 (2007).
27. A. Pashkin *et al.*, *Phys. Rev. B* **83**, 195120 (2011).
28. T. L. Cocker *et al.*, *Phys. Rev. B* **85**, 155120 (2012).
29. J. M. Zuo, *Rep. Prog. Phys.* **67**, 2053–2103 (2004).
30. J.-C. Zheng, Y. Zhu, L. Wu, J. W. Davenport, *J. Appl. Crystallogr.* **38**, 648–656 (2005).
31. A. M. M. Abeykoon *et al.*, *Z. Kristallogr.* **227**, 248–256 (2012).
32. A. S. Belozerov, M. A. Korotin, V. I. Anisimov, A. I. Poteryaev, *Phys. Rev. B* **85**, 045109 (2012).
33. R. Sakuma, T. Miyake, F. Aryasetiawan, *J. Phys. Condens. Matter* **21**, 064226 (2009).
34. Y. Yao *et al.*, *Mod. Phys. Lett. B* **27**, 1330015 (2013).
35. M. M. Qazilbash *et al.*, *Phys. Rev. B* **83**, 165108 (2011).
36. M. M. Qazilbash *et al.*, *Science* **318**, 1750–1753 (2007).
37. J. Nag, R. F. Haglund, E. A. Payzant, K. L. More, *J. Appl. Phys.* **112**, 103532 (2012).

ACKNOWLEDGMENTS

Supported by Natural Sciences and Engineering Research Council of Canada (NSERC), the Canada Foundation for Innovation, the Canada Research Chairs program, NSERC PGS-D and CGS-D fellowships (R.P.C. and V.M.), and Fonds de Récherche du Québec–Nature et Technologies. We thank C. Weber for insightful discussion regarding the contemporary theoretical treatment of the electronic structure of VO_2.

SUPPLEMENTARY MATERIALS

www.sciencemag.org/content/346/6208/445/suppl/DC1
Materials and Methods
Figs. S1 to S4
References (*38*, *39*)

24 March 2014; accepted 19 September 2014
10.1126/science.1253779

VALLEYTRONICS

Detecting topological currents in graphene superlattices

R. V. Gorbachev,[1,2]* J. C. W. Song,[3,4]* G. L. Yu,[1] A. V. Kretinin,[2] F. Withers,[2] Y. Cao,[1] A. Mishchenko,[1] I. V. Grigorieva,[2] K. S. Novoselov,[2] L. S. Levitov,[3]* A. K. Geim[1,2]†

Topological materials may exhibit Hall-like currents flowing transversely to the applied electric field even in the absence of a magnetic field. In graphene superlattices, which have broken inversion symmetry, topological currents originating from graphene's two valleys are predicted to flow in opposite directions and combine to produce long-range charge neutral flow. We observed this effect as a nonlocal voltage at zero magnetic field in a narrow energy range near Dirac points at distances as large as several micrometers away from the nominal current path. Locally, topological currents are comparable in strength with the applied current, indicating large valley-Hall angles. The long-range character of topological currents and their transistor-like control by means of gate voltage can be exploited for information processing based on valley degrees of freedom.

Berry curvature is a physical field intrinsic to some crystal lattices, which can dramatically affect the transport properties of materials (*1*–*6*). Topological effects, although known for some time (*7*), have gained attention recently in connection with the discovery of topological insulators (*8*–*11*). In these materials, topological bands lead to new phenomena such as topologically protected edge-state transport in zero magnetic field (*12*–*14*). No less striking,

however, is the expected impact of Berry curvature on bulk transport, leading to topological currents flowing perpendicular to the applied electric field E (*5*, *6*). The nondissipative nature of these currents, ensured by their transverse character, resembles that of Hall currents. However, topological currents can arise in the absence of magnetic field B and even without breaking time-reversal symmetry (TRS). In contrast to cyclotron orbits in a magnetic field drifting perpendicular to E, topological currents originate from perfectly straight trajectories that skew left or right relative to E (Fig. 1A). In materials whose electronic structure has more than one valley (*4*, *15*, *16*), topological currents in different valleys have opposite signs and, if intervalley scattering is weak, can add up to produce long-range topological charge-neutral currents.

Graphene placed on top of hexagonal boron nitride (G/hBN) (Fig. 1) affords an exceptional venue for inducing and manipulating topological bulk currents at $B = 0$ for the following reasons. First, graphene's band structure possesses a nonzero Berry's phase (*17*), which is a prerequisite for the existence of Berry curvature. Second, if crystallographic axes of graphene and hBN are aligned, global A/B sublattice asymmetry is introduced (*18-20*). This gives rise to broken inversion symmetry and a finite Berry curvature. Third, the high electronic quality of graphene protects topological currents against intervalley scattering, allowing them to propagate away from the applied current path. The valley-Hall effect (VHE) creates an electrical response in remote regions, which can be exploited to detect the presence of topological currents experimentally. The nonlocal response is expected whenever the Fermi level in graphene is tuned into one of the Berry curvature hot spots (Fig. 1B). This approach, besides offering a direct probe of topological currents, provides a precision tool for mapping out the Berry curvature in G/hBN Bloch bands. So far, it has proven challenging to probe bulk topological currents without applying B. In particular, this was the case for the anomalous Hall effect in magnetic metals, which was previously perhaps the cleanest system available by which to study topological bands (*6*).

Experimentally, we studied G/hBN superlattices (in which the graphene and hBN lattices were aligned) fabricated following the procedures described in (*21*). Fifteen superlattice devices similar to the one shown in the inset of Fig. 1B were investigated. The charge carrier mobilities μ varied from 40,000 to 80,000 $cm^2 V^{-1} s^{-1}$, and the longitudinal and Hall resistivities (ρ_{xx} and ρ_{xy}, respectively) exhibited essentially the same behavior as reported previously (*18*, *19*, *21*, *22*). Namely, pronounced peaks in ρ_{xx} were observed at the main neutrality point (NP) and at carrier density $n \approx \pm 3 \times 10^{12}$ cm^{-2} (Fig. 1B and fig. S1). The peaks in ρ_{xx} were accompanied by a sign reversal of ρ_{xy} indicating the emergence of new NPs in the valence and conduction bands of graphene (*18–22*). Both encapsulated and nonencapsulated structures were investigated, with the former having an additional hBN crystal placed on top of a G/hBN superlattice to protect it from the environment (*20*, *21*). Some of the latter showed activation behavior at the main NP (fig. S2), yielding a bandgap 2Δ of 350 ± 40 K (*20*), which is in agreement with earlier transport (*18*, *19*) and spectroscopy (*23*) measurements. Our encapsulated devices, despite higher electronic quality, exhibited no activation behavior at the main NP, with the ρ_{xx} value saturating at <10 kilohm for temperatures T below 50 K (*19*, *21*). Although this behavior remains to be understood, it is likely that devices that do not show activation behavior in transport properties still have a bandgap (*20*). In this regard, observing the activation behavior usually relies on midgap impurity states that pin the Fermi level inside the gap (*20*). However, few midgap states are expected in high-quality G/hBN devices. Alternatively, spatial charge inhomogeneity can "short-circuit" the activation behavior by allowing current to circumnavigate the insulating regions. This would also obscure the activation behavior, leading to metallic-like transport in ρ_{xx}. However, charge inhomogeneity is expected to have relatively little effect on the VHE; being a non–sign-changing function of density (Fig. 1B, inset), it should not average out. Therefore, the activation behavior is not essential for observing topological currents (*20*). Indeed, both encapsulated and nonencapsulated graphene were found to exhibit very similar nonlocal response.

The central result of our study is shown in Fig. 1B. The nonlocal resistance R_{NL} was determined by applying current between, contacts 4 and 8 and measuring voltage between contacts 3 and 9 (Fig. 1B, micrograph). R_{NL} exhibits large sharp peaks at the main and hole-side NPs (unless stated otherwise, all the presented data refer to zero B). A striking feature of the observed

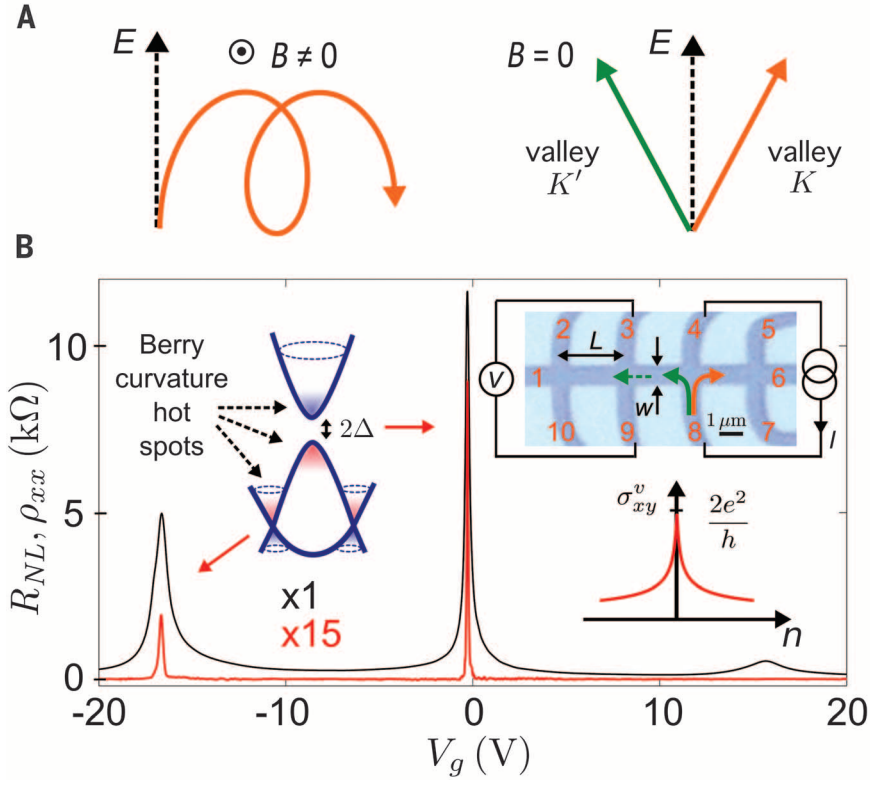

Fig. 1. Detection of long-range valley transport due to topological currents. (**A**) Nontopological and topological Hall currents. (Left) Drifting cyclotron orbits give rise to Hall currents of the same sign for valleys K and K'. (Right) Skewed motion induced by Berry curvature. Trajectories are straight lines directed at nonzero angles to the longitudinal field, having opposite signs for valleys K and K'. The net transverse current, which is charge-neutral, creates a nonlocal charge response via a reverse VHE. (**B**) Nonlocal resistance in graphene superlattices (red curve) and longitudinal resistance (black curve) measured in G/hBN superlattices [graphene aligned on hBN (*18–23*)]. The back gate voltage V_g was applied through a ≈130-nm-thick dielectric (SiO_2 plus hBN); $T = 20$ K. (Top right inset) Optical micrograph of our typical G/hBN device and the nonlocal measurement geometry; $L \approx 3.5$ μm, $w \approx 1$ μm. Shown schematically are valley K and K' currents and the long-range response mechanism. (Left inset) Schematic band structure of graphene superlattices, with Berry curvature hot spots arising near the gap opening and avoided band crossing regions (*20*, *25*). (Bottom right inset) Valley Hall conductivity modeled for gapped Dirac fermions as a function of carrier density.

[1]Centre for Mesoscience and Nanotechnology, University of Manchester, Manchester M13 9PL, UK. [2]School of Physics and Astronomy, University of Manchester, Oxford Road, Manchester M13 9PL, UK. [3]Department of Physics, Massachusetts Institute of Technology, Cambridge, MA 02139, USA. [4]School of Engineering and Applied Sciences, Harvard University, Cambridge, MA 02138, USA.
*These authors contributed equally to this work. †Corresponding author. E-mail: levitov@mit.edu (L.S.L.); geim@manchester.ac.uk (A.K.G.)

nonlocality is its narrow range in n (Figs. 1B and 2A). Unlike ρ_{xx}, which follows the $1/n$ dependence typical for graphene and remains sizeable (>100 ohm) over the entire range of accessible n (Figs. 1 and 2 and fig. S1), R_{NL} decays rapidly with n and completely disappears under noise for densities $>10^{11}$ cm^{-2} away from the NPs. The dependence can be approximately described by $R_{NL} \propto 1/|n|^{\alpha}$, with $\alpha \approx 2.5$ to 3 (Fig. 2B). A nonlocal voltage can also appear because of stray charge currents, described by the van der Pauw relation $R_{NL} \sim \rho_{xx} \exp(-\pi L/w)$, where L is the distance between the current path and voltage probes and w is the device width (Fig. 1B, micrograph) (*24*). For typical aspect ratios $L/w \approx 4$, the formula yields ≈0.01 ohm. The magnitude of this contribution and its n dependence, which follows $\rho_{xx}(n)$, are clearly incompatible with the observed nonlocal response.

We have also investigated how R_{NL} depends on L and found an exponential dependence $\exp(-L/\xi)$ with $\xi \approx 1.0$ μm (Fig. 2C). This ξ value is close to w and much larger than the elastic mean free path of ≈0.1 μm estimated from μ for the range of n where R_{NL} appears. Furthermore, R_{NL} exponentially decreases with increasing temperature T so that no nonlocal signal is detected above 150 K, whereas ρ_{xx} remains large at this T at the main NP (figs. S2 and S3). Nonencapsulated devices exhibited practically the same behavior of R_{NL} as a function of n and T (fig. S4), but the absolute value of R_{NL} was somewhat smaller than that in encapsulated devices (*20*). In addition, we investigated the effect of charge inhomogeneity δn on R_{NL}, which was controlled by sweeping to progressively larger gate voltages V_g beyond the hole-side NP (*20*). When δn was increased by a factor of ≈2, R_{NL} could sometimes change by more than an order of magnitude (*20*). The inhomogeneity enhanced R_{NL} at the main NP and suppressed it at the hole-side NP (fig. S5). The difference is attributed to a narrow energy width of the secondary Dirac spectrum (*20*).

To confirm the key role played by Berry curvature, we verified that the nonlocal response was absent in G/hBN systems without alignment and, accordingly, with no detectable superlattice effects (*18*–*22*). This is illustrated in Fig. 2A, which shows R_{NL} for aligned and nonaligned devices with the same μ and in the same geometry. In the nonaligned devices (>20 measured), no nonlocal signal could be observed even at our maximum resolution of ~0.1 ohm (Fig. 2A, blue curve). Therefore, the observed R_{NL} cannot be explained by charge-neutral flow of spin and/or energy, which are indifferent to crystal alignment. The latter flows also require broken TRS and completely disappear in zero B, as reported previously (*24*–*26*). In our superlattice devices, a contribution of spin/energy flows becomes appreciable only for $B > 0.1$ T (fig. S6), leading to rapid broadening of the R_{NL} peaks, which is in agreement with (*24*).

We have also considered the possibility that the observed nonlocality at $B = 0$ may originate from an edge transport mechanism. For example, topological materials can support gapless edge modes that coexist with the gapped bulk. Such modes could in principle mediate nonlocal charge transport. However, our experiments provide no evidence for metallic conductivity along the device edges. First, the measured nonlocal response was similar for all our devices, independent of whether they exhibited metallic or insulating behavior in ρ_{xx}. Second, atomic force microscopy studies show that the moiré pattern associated with the alignment extends all the way to the device edges, and there are no distinct edge regions (*19*). Third, extrapolating the dependence in Fig. 2C to small L, we found that the edge transport scenario would require metallic conductivity along edges of $\approx 2e^2/h$ over distances of $L > 1$ μm. This would imply perfect edge-state transport, which is unlikely at such length scales in the presence of strong intervalley scattering expected at microscopically rough edges.

Proceeding with the analysis, the aligned superlattices are comprised of hexagonal unit cells, each representing a commensurate graphene/hBN region of ~10 nm in size, which is surrounded by a strained boundary (*19*). All unit cells are characterized by A/B sublattice asymmetry of the same sign, giving a preferred chirality over the entire structure (*19*, *20*, *25*). For our typical $n < 10^{11}$ cm^{-2}, Fermi wavelengths are larger than 100 nm, which exceeds the superlattice periodicity by a factor of ~10. This large wavelength/period ratio renders contributions from spatially varying couplings insubstantial.

We will show below that the observed nonlocality features are consistent with bulk topological currents expected for a gapped Dirac spectrum. The mechanism by which Berry curvature generates topological currents can be elucidated by the semiclassical equations of motion (*5*)

$$\hbar\dot{k} = eE + ev(k) \times B,$$

$$v(k) = \frac{1}{\hbar}\frac{\partial \epsilon(k)}{\partial k} + \dot{k} \times \Omega(k) \qquad (1)$$

where Ω is the Berry curvature density and $v(k)$ is the group velocity of Bloch electrons. The Lorentz force term $ev \times B$ describes the conventional Hall effect. Berry curvature gives rise to an "anomalous velocity," $k \times \Omega(k)$, which is of the same structure as the Lorentz term but in momentum space and leads to transverse currents (Fig. 1A). Such currents may appear in zero B [without breaking TRS that requires $\Omega(k) = -\Omega(-k)$] as long as inversion symmetry is broken, $\Omega(k) \neq \Omega(-k)$, as is the case of our aligned devices with globally broken A/B sublattice symmetry (*19*). For $B = 0$, transverse currents arise solely from $\Omega(k)$, yielding Hall-like conductivity σ_{xy} given by the sum of Berry fluxes for all occupied states in the Fermi sea (*3*)

$$\sigma_{xy} = 2\frac{e^2}{\hbar}\int \frac{d^2k}{2\pi}\Omega(k)f(k) \qquad (2)$$

with $f(k)$ being the Fermi function and the factor of 2 accounting for spin degeneracy. Because Berry

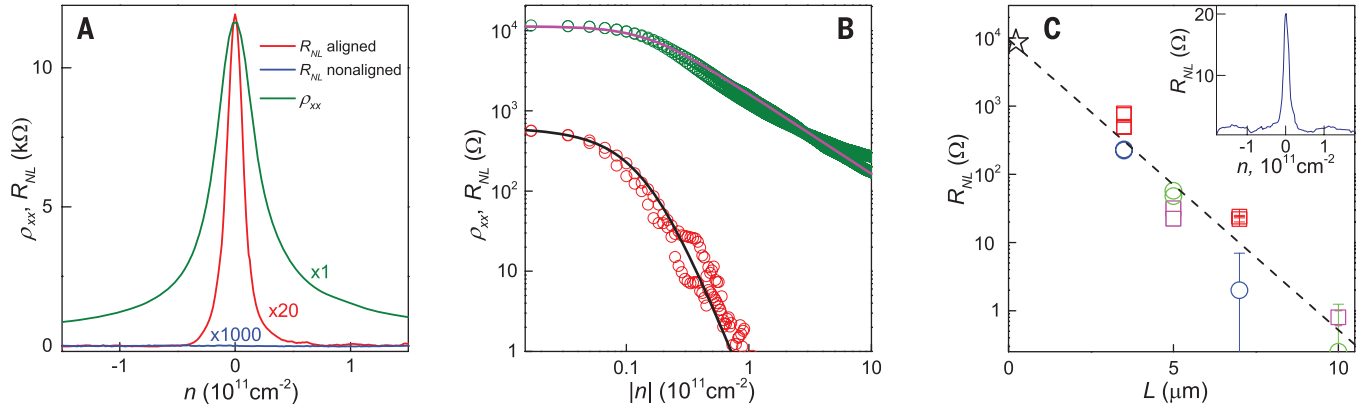

Fig. 2. Density and distance dependences for nonlocal valley currents. (**A**) Behavior of ρ_{xx} and R_{NL} near the main NP in superlattice devices (green and red, respectively). The blue curve is for a nonaligned, reference device (≈10° misalignment between graphene and hBN crystal axes). $L \approx 3.5$ μm; $w \approx 1$ μm; $T = 20$ K. (**B**) The same data as (A) on a logarithmic scale. Away from the NP, ρ_{xx} exhibits the conventional $1/n$ dependence (green symbols) and can be described by $\rho_{xx}(n) \propto 1/(n^2 + \delta n^2)^{1/2}$, where $\delta n \approx 1.5 \times 10^{10}$ cm^{-2} accounts for charge inhomogeneity (light purple line). Measured R_{NL} (red symbols) and the Berry curvature model (black curve, Eq. 3). Model uses the above δn and bandgap $2\Delta = 360$ K found from local measurements (*18*–*20*). (**C**) Nonlocal signal decays exponentially with increasing L. Color refers to similar devices with the same L or the same device with two different L; $w \approx 1$ μm, 20 K; 10 devices in total. The black star is the anomalous contribution to ρ_{xx} observed in the bend geometry, which is consistent with strong topological currents induced locally (*20*). (Inset) R_{NL} remains sizeable at $L \approx 7$ μm.

curvature is odd in energy (*20*), σ_{xy} has the same sign for both electrons and holes. This contrasts with the conventional Hall conductivity that is sign-changing under carrier-type reversal. As a result, σ_{xy} given by Eq. 2 is less susceptible to smearing by inhomogeneity. This mechanism yields a nonzero R_{NL} whenever the Fermi level is tuned through Berry curvature hot spots. Their extent in energy is given by half the bandgap $\Delta \approx 180$ K, which translates into $n \approx 2 \times 10^{10}$ cm^{-2} and agrees well with the ultranarrow width of our R_{NL} peaks.

Because of TRS, the electric field generates topological currents (Eq. 1) with opposite transverse components in graphene's two valleys, K and K' (Fig. 1A), to create the charge-neutral VHE, $J_v = J_K - J_{K'} = \sigma^v_{xy}E$, where $\sigma^v_{xy} = 2\sigma_{xy}$. As illustrated in the inset to Fig. 1B, topological currents can result in a VHE conductivity of $\approx 2e^2/h$. In the absence of intervalley scattering, the charge-neutral currents can persist over extended distances and mediate nonlocal electrical signals (*24*–*28*). The resulting nonlocal resistance R_{NL} can be understood as originating from the VHE and a reverse VHE (*20*), by analogy with nonlocal transport mediated by charge-neutral spin or energy flow (*24*–*28*). Yet unlike the latter, the VHE-induced nonlocality appears without TRS breaking—that is, at zero B. This behavior, as well as the narrow range of n over which R_{NL} is observed, is a telltale sign of bulk topological currents. The analysis outlined above yields the model expression (*20*)

$$R_{NL} = (w/2\xi)(\sigma^v_{xy})^2\rho^3_{xx}\exp(-L/\xi) \qquad (3)$$

The peak in $R_{NL}(n)$ can be described by Eq. 3 with no fitting parameters (Fig. 2B).

The measured spatial decay with $\xi \approx 1.0$ μm is consistent with intervalley scattering occurring at graphene edges and/or at atomic-scale defects (*20*). The large values of R_{NL} at L of several micrometers also imply extremely strong topological currents locally, within the path of the applied current. By extrapolating the observed L dependence to $L < 1$ μm, Fig. 2C yields R_{NL} ~10 kilohm. According to Eq. 3, this translates into $\sigma^v_{xy} \approx 2e^2/h$ and order-one Hall angles, which is in agreement with the VHE expected for weak intervalley scattering. Furthermore, similar to classical magnetotransport, changes in the direction of current flow can lead to additional resistivity. For $\sigma_{xy}\rho_{xx} \sim 1$, the classical magnetoresistance reaches a value of $\sim\rho_{xx}$ when carriers of opposite sign are involved. A valley analog of this extra resistance may explain anomalous contributions of ~10 kilohm in ρ_{xx}, which are observed at short distances $L \approx w$ by using the bend geometry (fig. S7). Parenthetically, the intrinsic VHE mechanism discussed above, which provides excellent agreement with our experimental results, may coexist with extrinsic VHE mechanisms such as skew scattering and side jumps (*6*). Although their role in graphene superlattices remains to be examined, such mechanisms also originate from Berry curvature and arise under the same symmetry conditions as the intrinsic contribution.

Last, sharp changes in R_{NL} with V_g (130-nm-thick dielectric) (Figs. 1 and 2) amount to a transistor-like response with a slope of ≈100 mV/dec—that is, the detected voltage changes by a factor of 10 by varying V_g by ≈100 mV. Although the peaks in R_{NL} broaden with increasing T and disappear above 100 K (because of the relatively small Δ), one can envision electronic devices based on the valley degrees of freedom (*29*), which would become practical if larger bandgap values are achieved. To explore this further, we fabricated a superlattice device with a short top gate (15-nm dielectric) placed between the current and voltage contacts used for nonlocal measurements (fig. S8). Valley currents in this case could be switched on and off, similar to the case of a field effect transistor, by a gate voltage of ≈10 mV at 20 K (*20*). It is feasible to further reduce the thickness of the top gate hBN dielectric down to 2 nm, which would translate into a gate response down to <2 mV/dec at this T. Although further analysis is necessary, these results may indicate that subthreshold slopes better than those achievable for conventional charge-based processing devices (*30*) are possible.

REFERENCES AND NOTES

1. W. Kohn, J. M. Luttinger, *Phys. Rev.* **108**, 590–611 (1957).
2. G. Sundaram, Q. Niu, *Phys. Rev. B* **59**, 14915–14925 (1999).
3. F. D. M. Haldane, *Phys. Rev. Lett.* **93**, 206602 (2004).
4. D. Xiao, W. Yao, Q. Niu, *Phys. Rev. Lett.* **99**, 236809 (2007).
5. D. Xiao, M.-C. Meng, Q. Niu, *Rev. Mod. Phys.* **82**, 1959–2007 (2010).
6. N. Nagaosa, J. Sinova, S. Onoda, A. H. MacDonald, N. P. Ong, *Rev. Mod. Phys.* **82**, 1539–1592 (2010).
7. J. Zak, *Phys. Rev. Lett.* **62**, 2747–2750 (1989).
8. C. L. Kane, E. J. Mele, *Phys. Rev. Lett.* **95**, 226801 (2005).
9. B. A. Bernevig, T. L. Hughes, S. C. Zhang, *Science* **314**, 1757–1761 (2006).
10. L. Fu, C. L. Kane, E. J. Mele, *Phys. Rev. Lett.* **98**, 106803 (2007).
11. R. Roy, *Phys. Rev. B* **79**, 195322 (2007).
12. M. König *et al.*, *Science* **318**, 766–770 (2007).
13. C. Z. Chang *et al.*, *Science* **340**, 167–170 (2013).
14. D. Hsieh *et al.*, *Science* **323**, 919–922 (2009).
15. D. Xiao, G. B. Liu, W. Feng, X. Xu, W. Yao, *Phys. Rev. Lett.* **108**, 196802 (2012).
16. K. F. Mak, K. L. McGill, J. Park, P. L. McEuen, *Science* **344**, 1489–1492 (2014).
17. T. Ando, T. Nakanishi, R. Saito, *J. Phys. Soc. Jpn.* **67**, 2857–2862 (1998).
18. B. Hunt *et al.*, *Science* **340**, 1427–1430 (2013).
19. C. R. Woods *et al.*, *Nat. Phys.* **10**, 451–456 (2014).
20. Materials and methods are available as supplementary materials on *Science* Online.
21. L. A. Ponomarenko *et al.*, *Nature* **497**, 594–597 (2013).
22. C. R. Dean *et al.*, *Nature* **497**, 598–602 (2013).
23. Z. G. Chen *et al.*, *Nat. Commun.* **5**, 4461 (2014).
24. D. A. Abanin *et al.*, *Science* **332**, 328–330 (2011).
25. J. C. W. Song, P. Samutpraphoot, L. S. Levitov, Topological bands in G/hBN heterostructures. http://arxiv.org/abs/1404.4019 (2014).
26. J. Renard, M. Studer, J. A. Folk, *Phys. Rev. Lett.* **112**, 116601 (2014).
27. M. Titov *et al.*, *Phys. Rev. Lett.* **111**, 166601 (2013).
28. D. A. Abanin, A. V. Shytov, L. S. Levitov, B. I. Halperin, *Phys. Rev. B* **79**, 035304 (2009).
29. A. Rycerz, J. Tworzydlo, C. W. J. Beenakker, *Nat. Phys.* **3**, 172–175 (2007).
30. S. M. Sze, K. K. Ng, *Physics of Semiconductor Devices* (Wiley, New York, 2007), chap. 6.

ACKNOWLEDGMENTS

This work was supported by the European Research Council, the Royal Society, the Office of Naval Research, the Air Force Office of Scientific Research, the Engineering and Physical Sciences Research Council (UK), and the National Science Foundation.

SUPPLEMENTARY MATERIALS

www.sciencemag.org/content/346/6208/448/suppl/DC1
Materials and Methods
Supplementary Text
Figs. S1 to S8
References (*31*–*37*)

17 April 2014; accepted 29 August 2014
Published online 11 September 2014;
10.1126/science.1254966

ASYMMETRIC CATALYSIS

Room-temperature enantioselective C–H iodination via kinetic resolution

Ling Chu, Kai-Jiong Xiao, Jin-Quan Yu*

Asymmetric carbon-hydrogen (C–H) activation reactions often rely on desymmetrization of prochiral C–H bonds on the same achiral molecule, using a chiral catalyst. Here, we report a kinetic resolution via palladium-catalyzed enantioselective C–H iodination in which one of the enantiomers of a racemic benzylic amine substrates undergoes faster aryl C–H insertion with the chiral catalysts than the other. The resulting enantioenriched C–H functionalization products would not be accessible through desymmetrization of prochiral C–H bonds. The exceedingly high relative rate ratio (k_{fast}/k_{slow} up to 244), coupled with the subsequent iodination of the remaining enantiomerically enriched starting material using a chiral ligand with the opposite configuration, enables conversion of both substrate enantiomers into enantiomerically pure iodinated products.

A wide range of C–H activation reactions have emerged as promising tools for organic synthesis over the past two decades. However, the development of enantioselective C–H activation reactions has met with limited success in terms of efficiency and scope (*1*). Enantioselective carbene insertions into prochiral methylene C–H bonds adjacent to heteroatoms have been achieved in synthetically useful enantioselectivity (*2*). Asymmetric nitrene insertion has also been demonstrated in both diastereoselective and enantioselective

manners (*3*–*6*). Development of asymmetric C–H activation reactions involving a metal insertion step has also witnessed limited but encouraging progress. Combining C–H activation with subsequent asymmetric carbometalation onto double bonds elegantly connects C–H functionalization reactions to asymmetric catalysis (*7*, *8*). An early example of atropselective alkylation in moderate enantioselectivity [49% enantiomeric excess (ee)] was reported (*9*). Recently, Pd-catalyzed desymmetrization of prochiral C–H bonds has been achieved with excellent levels of enantioselectivity (*10*–*14*) (Fig. 1A). However, the requirement for the presence of two chemically identical groups necessarily limits the structural diversity of the chiral products, preventing the broad application of this method in asymmetric synthesis. An effort to overcome this limitation by developing enantioselective C–H activation of racemic mixtures via a regiodivergent pathway has been reported with an intramolecular reaction (*15*).

Chiral amines are one of the most prevalent motifs in bioactive natural products, drug compounds, and chiral catalysts. Despite remarkable progress in the development of catalytic enantioselective methods for synthesis of chiral amines (*16*), chiral auxiliaries (*17*), classical resolution by crystallization of chiral salts, and enzymatic kinetic resolution (*18*, *19*) are more often used in practice. Nonenzymatic kinetic resolution of amines by asymmetric acyl transfer catalysts remains a substantial challenge when compared to the analogous kinetic resolution of alcohols (*20*–*22*). In our efforts to develop alternative methods for the asymmetric synthesis of chiral amines, we recently achieved the enantioselective C–H iodination of triflyl-protected benzylamines by desymmetrization (*11*). This ligand-controlled reaction has recently been modified to achieve an atropselective C–H iodination through kinetic resolution in promising selectivity ($s \leq 27$) (*23*). To access a wide range of chiral α-branched benzylamines that do not contain two identical aryl groups, we embarked on the development of a kinetic resolution process through an enantioselective C–H iodination of arylalkylamines. Practically, this type of process would not only lead to the resolution of racemic amines but also concomitantly introduce a new functional handle for the further elaboration of the product. Conceptually, the chiral recognition required in kinetic resolution is fundamentally different from that in the desymmetrization process. The catalyst must preferentially recognize one of the enantiomeric substrates in kinetic resolution rather than one of the prochiral groups within the same substrate as in desymmetrization. We were inspired in this context by the landmark success in kinetic resolution of Jacobsen's cobalt-salen–catalyzed epoxide opening process (*24*). The Pd(II)-catalyzed asymmetric oxidation of racemic alcohols (*25*, *26*) has also been demonstrated. However, kinetic

The Scripps Research Institute, 10550 North Torrey Pines Road, La Jolla, CA 92037, USA.
*Corresponding author. E-mail: yu200@scripps.edu

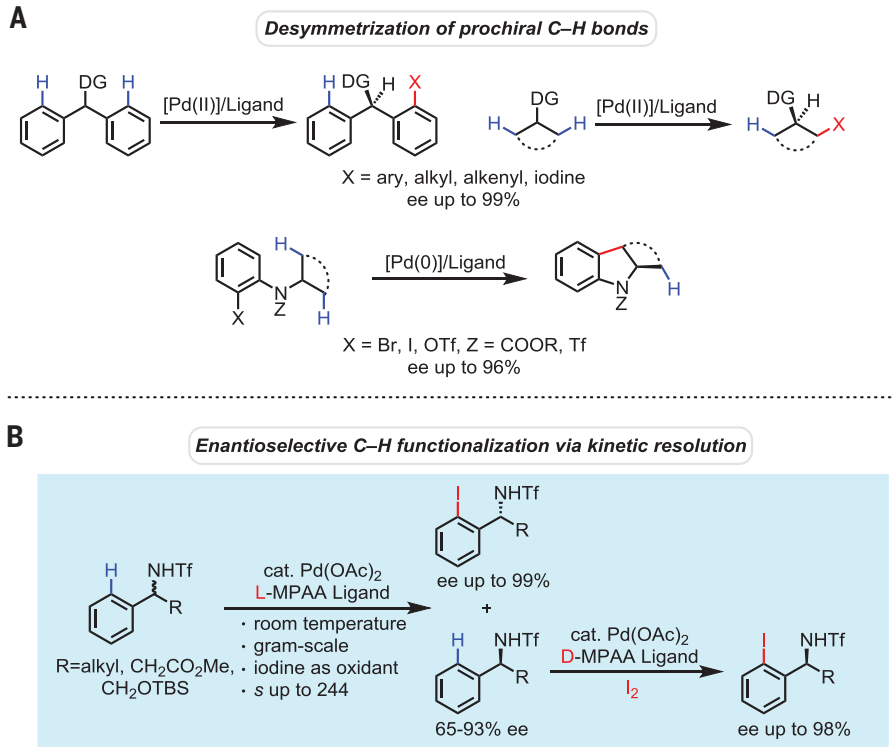

Fig. 1. Enantioselective C–H activation reactions. (**A**) Desymmetrization of prochiral C–H bonds. (**B**) Enantioselective C–H activation through kinetic resolution.

Table 1. Enantioselective C–H iodination of benzylamines.

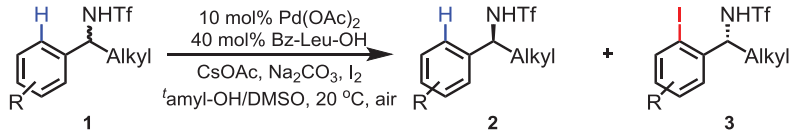

entry	1	Ar	Alkyl	time (h)	conv.* (yield, %)†	ee(%)‡ 2	ee(%)‡ 3	s§
1‖	**1a**	2-Me-Ph	Me	24	51 (48)	93	91	73.6
2	**1b**	2-Me-Ph	Et	24	50 (49)	91	91	67.3
3	**1c**	2-Me-Ph	^{n}Bu	48	47 (45)	77	87	32.9
4	**1d**	2-Me-Ph	^{i}Bu	48	51 (49)	83	81	25.0
5	**1e**	2-Me-Ph	Bn	48	47 (44)	67	75	13.8
6	**1f**	2-Me-Ph	cyclopropyl	24	42 (42)	70	95	83.5
7	**1g**	2-OMe-Ph	Me	24	49 (46)	93	97	240
8	**1h**	2-F-Ph	Me	24	48 (47)	89	96	148
9	**1i**	2-Me,4-Cl-Ph	Me	24	51 (49)	97	93	113
10	**1j**	3-Me-Ph	Me	24	45¶ (42, mono:di=3:1)	78	92#	99.5
11	**1k**	4-Me-Ph	Me	48	45 (35)	78	95	91.7
12	**1l**	2-naphthyl	Me	48	41 (37)	67	95	76.0
13**	**1m**	Ph	^{n}Bu	48	42¶ (40, mono:di=1:1.4)	70	87# (99††)	124
14	**1n**	Ph	^{i}Pr	48	33 (30)	45	90	34.5

*Calculated conversion, c = ee_2 / (ee_2 + ee_3). †Isolated yield of the iodinated product. ‡Determined by chiral HPLC analysis. §Selectivity(*s*) = (rate of fast-reacting enantiomer) / (rate of slow-reacting enantiomer). ‖Reaction also proceeds with 2 mol% $Pd(OAc)_2$ (see Table S1 in supplementary materials for details). ¶Determined by crude ^{1}H-NMR. #ee for the mono product. **3 equiv. I_2 was added after 24 h. ††ee for the di product.

resolution via a Pd-catalyzed C–H activation reaction involving chiral C(sp^3) centers remains to be established.

Here, we report the discovery of a highly efficient kinetic resolution of chiral amines by Pd-catalyzed C–H iodination with selectivities reaching up to 244 (Fig. 1B). In addition to simple arylalkylamines, a wide range of β-amino acids and β-amino alcohols are compatible with this reaction. The use of ambient temperature provides a major operational advantage over nonenzymatic acylative kinetic resolution reactions, which often require low temperature conditions. We further demonstrate that the remaining starting material can subsequently be iodinated using a chiral ligand with opposite configuration to give ortho-iodinated amines in high ees, thus rendering this method capable of converting both enantiomers of the racemic amines into ortho-iodinated chiral benzylamines. The newly introduced ortho-iodides are a useful functional handle, allowing conversion of the products into a broad range of chiral amines.

Our experimental design was based on a previous finding that a mono-protected amino acid ligand (MPAA) can effectively control the stereochemistry in Pd-catalyzed asymmetric insertion into prochiral C–H bonds on different carbon centers, leading to desymmetrization (*10*). This led us to hypothesize that the chiral catalyst assembled from the amino acid ligand and Pd(II) species could preferentially recognize one enantiomer of a racemic substrate during the C–H activation step. If successful, a wide range of C–H activation reactions could potentially be developed into practical tools for asymmetric catalysis through kinetic resolution. Due to its compatibility with low reaction temperatures, we selected our recently developed C–H iodination as a model reaction to investigate the feasibility of achieving kinetic resolution of α-branched benzylamines at room temperature. Thus, 1-(*o*-tolyl) ethylamine, protected by a triflyl group (**1a**), was subjected to our iodination conditions in the presence of various mono-protected amino acid ligands (see table S1). We found that using benzoyl-protected L-2-aminopentanoic acid (norvaline) as the chiral ligand, Pd(II)-catalyzed iodination of **1a** proceeded with promising selectivity (table S1, entry 1, s = 17.6). A minor increase in steric hindrance on the side chain when leucine was used improved the selectivity to 50 (table S1, entries 2 and 3). However, further tuning the steric bulkiness of the side chain only afforded lower selectivity (table S1, entries 4 to 6). Extensive efforts to improve the selectivity by using a substituted *N*-benzoyl protecting group were unsuccessful (table S1, entries 7 to 12). We also found that acetyl, trifluoroacetyl, and Boc protecting groups were inferior to benzoyl-type protecting groups (table S1, entries 13 to 15). We further found that an increase in the reaction concentration improved the selectivity to 62.0 (table S1, entry 16). Finally, an optimum selectivity of 78.8 was obtained by running the reaction in a 5:2.2 ratio of ^{t}amyl alcohol and dimethyl sulfoxide (table S1, entry 17). In this case, both the iodinated product and the recovered starting material were obtained with high enantioselectivity (92% ee) at 50% conversion. The reaction also proceeded with 2 mole percent Pd catalyst to reach a selectivity of 51.2, albeit at longer reaction times (table S1, entry 17). Reducing the ratio of ligand/Pd from 4:1 to 2:1 in the iodination of **1a** resulted in a significant drop of selectivity (s = 33), which can be attributed to competitive binding of the substrate versus ligands (table S1, entry 18).

To examine whether this method could be applied to prepare a broad range of chiral ortho-iodinated benzylamines, we subjected amines **1b** to **1l** to the optimized conditions (Table 1). Iodination of benzylamines **1a** to **1c** gave good to excellent selectivity, whereas the bulkier α-isobutyl and benzyl groups in **1d** and **1e** led to decreases in the selectivity factor to 25.0 and 13.8, respectively (Table 1, entries 1 to 5). Iodination of benzylamine **1f** containing a cyclopropyl group proceeded with an excellent selectivity factor (entry 6, s = 83.5). Arenes containing ortho-methoxy and fluoro groups were also iodinated with outstanding selectivity (entries 7 and 8, s = 148 and 240, respectively). The presence of a para-chloro group on the aryl fragment in **1i** was well tolerated (entry 9, s = 113). Meta- and para-methyl substituted arenes **1j** and **1k** were more suitable substrates than the ortho-methylarene **1a** affording excellent selectivity (entries 10 and 11, s = 99.5 and 91.7, respectively). Iodination of **1l** containing 2-naphthyl group also proceeded with synthetically useful selectivity (entry 12, s = 76). In general, the iodinated products were obtained with high levels of enantioselectivity (91 to 97% ee), with the exception of entries 3 to 5. To investigate whether the decrease of enantioselectivity with these substrates containing bulkier α-alkyls (entries 3 to 5) was a general phenomenon, we subjected **1m** containing α-butyl to the standard iodination conditions. The reaction proceeded with high selectivity (entry 13, s = 124), thus suggesting that the observed adverse effect of the bulky α-alkyl group was partially due to the ortho-methyl groups in substrates **1a** to **1e**. However, the presence of an even bulkier α-*i*-propyl in substrate **1n** also reduced the selectivity to 34.5 (entry 14). Replacing the α-*i*-propyl with α-*t*-butyl resulted in a loss of reactivity under current conditions.

Table 2. Enantioselective C–H iodination of β-amino acids and amino alcohols.

A

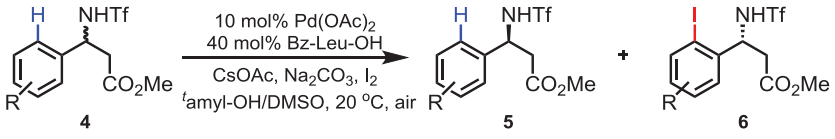

entry	4	Ar	time (h)	conv.* (yield, %)†	ee(%)‡ 5	ee(%)‡ 6	s§
1	**4a**	Ph	48	47‖ (44, mono:di=2:1)	85	96¶	128
2	**4b**	2-Me-Ph	24	49 (49)	93	96	168
3	**4c**	3-Me-Ph	48	50 (44)	93	94	112
4	**4d**	4-OMe-Ph	48	46‖ (43, mono:di=3:1)	82	98¶	134
5#	**4e**	4-F-Ph	48	48 (41)	90	98	244
6#	**4f**	4-Cl-Ph	48	49 (40)	92	97	152
7#	**4g**	4-CF_3-Ph	48	40 (38)	65	99	155

*Calculated conversion, c = ee_5 / (ee_5 + ee_6). †Isolated yield of the iodinated product. ‡Determined by chiral HPLC analysis. §Selectivity(s) = (rate of fast-reacting enantiomer) / (rate of slow-reacting enantiomer). ‖Determined by crude ^{1}H-NMR. ¶ee for the mono product. #3 equiv. I_2 was added after 24 h.

B

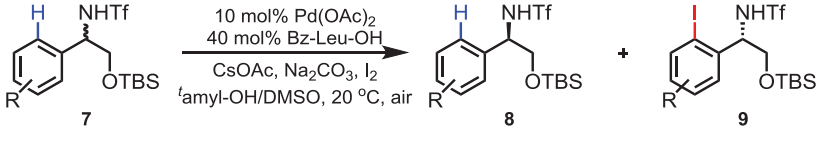

entry	7	Ar	time (h)	conv. (yield, %)	ee(%) 8	ee(%) 9	s
1	**7a**	Ph	48	43* (40, mono:di=1:1)	71	87† (99‡)	88.0
2	**7b**	2-Me-Ph	48	50 (49)	91	92	77.2
3	**7c**	2-F-Ph	48	41 (41)	68	99	188
4	**7d**	2-naphthyl	48	43 (40)	72	96	112

*Determined by crude ^{1}H-NMR. †ee for the mono product. ‡ee for the di product.

We next investigated whether our enantioselective iodination could be applied to the production of iodinated chiral β-amino acids (Table 2A). In spite of a number of highly creative asymmetric methods for making enantioenriched β-amino acids (*27*), resolution is still frequently used in practice because of the ease of preparing racemic β-amino acids by the Rodionov reaction. The development of highly efficient catalysts to resolve racemic β-amino acids continues to attract considerable attention (*28*–*30*). Using our methodology, β-phenyl-β-amino acid **4a** was iodinated under the standard conditions to give **6a** with excellent selectivity (*s* = 128). Substrates containing electron-donating groups at the ortho, meta and para positions of the β-phenyl groups were all iodinated with high selectivity factors ranging from 112 to 168 (Table 2A, entries 2 to 4). Electron-withdrawing groups on the β-phenyl rings were also compatible with this transformation affording selectivity factors as high as 244 (entries 5 to 7). In all cases, the iodinated amino acid derivatives were obtained with high levels of enantioselectivity (94 to 99% ee).

We were pleased to find that this enantioselective C–H activation method was also suitable for preparing ortho-iodinated chiral β-amino alcohols (Table 2B). 2-Phenyl amino alcohol **7a** was iodinated with a practically useful selectivity (*s* = 88). The ortho-methyl group in **7b** led to a slight decrease in the selectivity factor (*s* = 77.2), whereas 2-(ortho-fluoro)-phenyl and 2-naphthyl-amino alcohols were iodinated with excellent selectivity (*s* = 188 and 112, respectively).

To further demonstrate the versatility of this kinetic resolution process, we developed a protocol to convert both enantiomers of the racemic amine substrates to the chiral-iodinated amines in high enantiomeric purity. Thus, 1.0 g of **1l** was subjected to the standard reaction conditions using the L-amino acid ligand to give 37% iodinated product **3l** (maximum 50% yield) with 95% ee (Fig. 2A). The absolute configuration of **3l** determined by x-ray crystallography should also facilitate future establishment of a stereomodel for kinetic resolution by C–H activation. The recovered starting material **2l** with 69% ee was then iodinated using the D-amino acid ligand to give chiral amine **3l′** in 98% ee (Fig. 2A). The use of ligands possessing the opposite configuration to enantioselectively iodinate the enantiomerically enriched starting material could prove extremely useful when the selectivity factor is lower than 50 and the ee of the starting material is lower than 90%. To render this reaction synthetically useful, triflyl-protected amine **3l** was readily deprotected and converted to benzoyl-protected amine **10** under mild conditions without racemization (Fig. 2B). Finally, the chiral-iodinated amine **3l** was converted to a diverse range of amines, illustrating the broad utility of this method to access a diverse range of chiral amines (Fig. 2C).

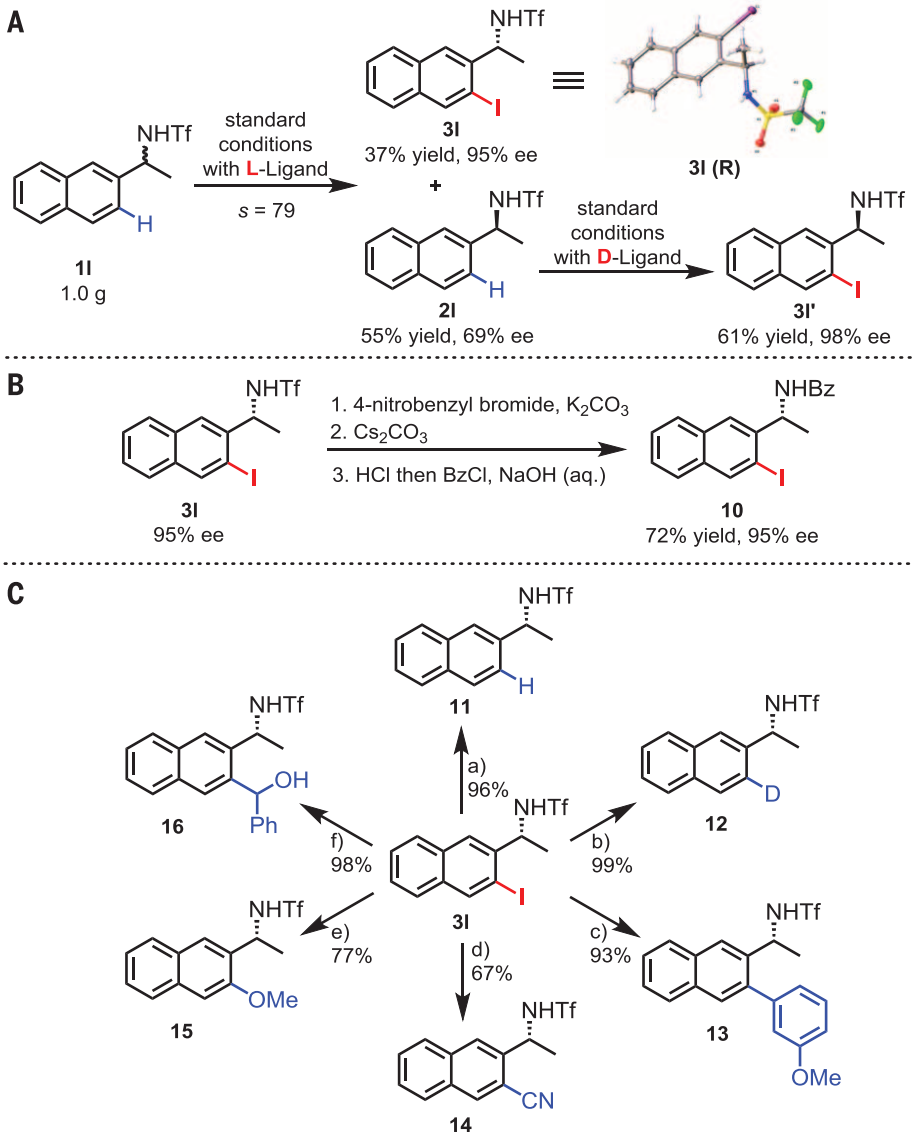

Fig. 2. Enrichment and elaboration of products. (**A**) Gram-scale synthesis, reaction with D-amino acid ligand and x-ray crystallography of **3l**. (**B**) Deprotection of the triflyl protecting group. (**C**) Functionalization of iodinated chiral amine **3l**. Reaction conditions: a) 5 mol% $Pd(PPh_3)_4$, HCO_2Na, dimethylformamide (DMF), 110°C; b) 1) ^{i}PrMgCl-LiCl, tetrahedrofuran (THF), 0°C, 2) D_2O; c) 2.5 mol% $Pd(OAc)_2$, 5 mol% 2-dicyclohexylphosphino-2′,6′-dimethoxybiphenyl (S-Phos), 3-anisole-boronic-acid, K_2CO_3, acetonitrile/H_2O, 100°C; d) CuCN, L-proline, DMF, 120°C; e) 20 mol% CuI, 40 mol% 1,10-phenanthroline, Cs_2CO_3, MeOH, 110°C; f) 1) ^{i}PrMgCl-LiCl, THF, 0°C, 2) PhCHO, 0°C to room temperature.

REFERENCES AND NOTES

1. R. Giri, B.-F. Shi, K. M. Engle, N. Maugel, J.-Q. Yu, *Chem. Soc. Rev.* **38**, 3242–3272 (2009).
2. M. P. Doyle, R. Duffy, M. Ratnikov, L. Zhou, *Chem. Rev.* **110**, 704–724 (2010).
3. R. P. Reddy, H. M. L. Davies, *Org. Lett.* **8**, 5013–5016 (2006).
4. C. Liang *et al.*, *Angew. Chem. Int. Ed.* **45**, 4641–4644 (2006).
5. D. N. Zalatan, J. Du Bois, *J. Am. Chem. Soc.* **130**, 9220–9221 (2008).
6. E. Milczek, N. Boudet, S. Blakey, *Angew. Chem. Int. Ed.* **47**, 6825–6828 (2008).
7. T. K. Hyster, L. Knörr, T. R. Ward, T. Rovis, *Science* **338**, 500–503 (2012).
8. B. Ye, N. Cramer, *Science* **338**, 504–506 (2012).
9. F. Kakiuchi, P. L. Gendre, A. Yamada, H. Ohtaki, S. Murai, *Tetrahedron Asymmetry* **11**, 2647–2651 (2000).
10. B.-F. Shi, N. Maugel, Y.-H. Zhang, J.-Q. Yu, *Angew. Chem. Int. Ed.* **47**, 4882–4886 (2008).
11. L. Chu, X.-C. Wang, C. E. Moore, A. L. Rheingold, J.-Q. Yu, *J. Am. Chem. Soc.* **135**, 16344–16347 (2013).
12. M. Nakanishi, D. Katayev, C. Besnard, E. P. Kündig, *Angew. Chem. Int. Ed.* **50**, 7438–7441 (2011).
13. S. Anas, A. Cordi, H. B. Kagan, *Chem. Commun.* **47**, 11483–11485 (2011).
14. T. Saget, S. J. Lemouzy, N. Cramer, *Angew. Chem. Int. Ed.* **51**, 2238–2242 (2012).
15. D. Katayev, M. Nakanishi, T. Bürgi, E. P. Kündig, *Chem. Sci.* **3**, 1422–1425 (2012).
16. F. Schmidt, R. T. Stemmler, J. Rudolph, C. Bolm, *Chem. Soc. Rev.* **35**, 454–470 (2006).
17. M. T. Robak, M. A. Herbage, J. A. Ellman, *Chem. Rev.* **110**, 3600–3740 (2010).
18. J. Paetzold, J. E. Bäckvall, *J. Am. Chem. Soc.* **127**, 17620–17621 (2005).
19. M. Breuer *et al.*, *Angew. Chem. Int. Ed.* **43**, 788–824 (2004).
20. S. Arai, S. Bellemin-Laponnaz, G. C. Fu, *Angew. Chem. Int. Ed.* **40**, 234–236 (2001).
21. C. K. De, E. G. Klauber, D. Seidel, *J. Am. Chem. Soc.* **131**, 17060–17061 (2009).

22. B. S. Fowler, P. J. Mikochik, S. J. Miller, *J. Am. Chem. Soc.* **132**, 2870–2871 (2010).
23. D.-W. Gao, Q. Gu, S.-L. You, *ACS Catal.* **4**, 2741–2745 (2014).
24. M. Tokunaga, J. F. Larrow, F. Kakiuchi, E. N. Jacobsen, *Science* **277**, 936–938 (1997).
25. D. R. Jensen, J. S. Pugsley, M. S. Sigman, *J. Am. Chem. Soc.* **123**, 7475–7476 (2001).
26. E. M. Ferreira, B. M. Stoltz, *J. Am. Chem. Soc.* **123**, 7725–7726 (2001).
27. J. Song, Y. Wang, L. Deng, *J. Am. Chem. Soc.* **128**, 6048–6049 (2006).
28. A. Berkessel, F. Cleemann, S. Mukherjee, *Angew. Chem. Int. Ed.* **44**, 7466–7469 (2005).
29. V. D. Bumbu, V. B. Birman, *J. Am. Chem. Soc.* **133**, 13902–13905 (2011).
30. S. Zhou *et al.*, *Angew. Chem. Int. Ed.* **53**, 7883–7886 (2014).

ACKNOWLEDGMENTS

We gratefully acknowledge The Scripps Research Institute and NIH (National Institute of General Medical Sciences, 2R01GM084019) for financial support. J.-Q. Y. and L.C. conceived the concept. L.C. developed the enantioselective C–H iodination. L.C. and K.-J.X. synthesized the amine substrates. J.-Q.Y. directed the project. We thank J. Spangler for constructive suggestions. Metrical parameters for the structures of **3l** are available free of charge from the Cambridge Crystallographic Data Centre under reference number CCDC-1021096.

SUPPLEMENTARY MATERIALS

www.sciencemag.org/content/346/6208/451/suppl/DC1
Materials and Methods
Supplementary Text
Tables S1 and S2
References (*31*–*35*)

9 July 2014; accepted 5 September 2014
10.1126/science.1258538

METALLOPROTEINS

Structural basis for organohalide respiration

Martin Bommer,[1]* Cindy Kunze,[2]* Jochen Fesseler,[1] Torsten Schubert,[2] Gabriele Diekert,[2]† Holger Dobbek[1]†

Organohalide-respiring microorganisms can use a variety of persistent pollutants, including trichloroethene (TCE), as terminal electron acceptors. The final two-electron transfer step in organohalide respiration is catalyzed by reductive dehalogenases. Here we report the x-ray crystal structure of PceA, an archetypal dehalogenase from *Sulfurospirillum multivorans*, as well as structures of PceA in complex with TCE and product analogs. The active site harbors a deeply buried norpseudo-B_{12} cofactor within a nitroreductase fold, also found in a mammalian B_{12} chaperone. The structures of PceA reveal how a cobalamin supports a reductive haloelimination exploiting a conserved B_{12}-binding scaffold capped by a highly variable substrate-capturing region.

Anaerobic microorganisms use alternative terminal electron acceptors during respiration, such as nitrate, sulfate, iron(III), or even organohalides. The accumulation of polluting organohalides such as perchloroethylene (PCE, also tetrachloroethene) and trichloroethene (TCE) in the environment, which have been heavily used for dry cleaning and degreasing, is problematic because of their toxicity; however, microbial organohalide respiration can transform these compounds into less toxic forms. Organohalide respiration requires reductive dehalogenases (RDases) for the central reduction step (*1*). In contrast to terminal reductases that contain prosthetic heme groups, molybdopterin, or flavins as cofactors, RDases harbor a corrinoid cofactor and two Fe/S clusters (*2*). RDases are able to convert some of the most noxious environmental pollutants, including halogenated phenols, dioxins, biphenyls, and aliphatic hydrocarbons. RDase genes were identified in distantly related bacterial genera belonging to the chloroflexi; firmicutes; gamma-, delta-, and epsilonproteobacteria; and even archaea (*3*).

[1]Institut für Biologie, Strukturbiologie/Biochemie, Humboldt-Universität zu Berlin, Unter den Linden 6, 10099 Berlin, Germany. [2]Institut für Mikrobiologie, Friedrich-Schiller-Universität Jena, Lehrstuhl für Angewandte und Ökologische Mikrobiologie, Philosophenweg 12, 07743 Jena, Germany.
*These authors contributed equally to this work. **†Corresponding author. E-mail: holger.dobbek@biologie.hu-berlin.de (H.D.); gabriele.diekert@uni-jena.de (G.D.)**

Several hundred RDase gene sequences deposited in databases await testing for functionality and determination of the substrate spectrum. Low growth yields and the oxygen sensitivity of the RDases have hindered large-scale purification and biochemical characterization of RDases (*1*). Genetic manipulation of the bacterial isolates has thus far been difficult, and only recently was functional heterologous production of RDases reported, but it remains challenging (*4*). Structural data will help to resolve how RDases evolved, function, and specifically select the many different substrates, some of which have been present in the biosphere for less than a century.

Here we report the crystal structure of a reductive dehalogenase, PceA (*5*), of the microaerophilic epsilonproteobacterium *Sulfurospirillum multivorans* (formerly *Dehalospirillum multivorans*) (*6*) (i) in an empty state; (ii) in the presence of TCE; (iii) in the presence of the *cis*-dichloroethene (*cis*-DCE) (product) analog *cis*-dibromoethene (*cis*-DBE); and (iv) in the presence of iodide, a substitute for the leaving chloride, at a maximum resolution of 1.6 Å (*7*). *S. multivorans* was isolated in the mid-1990s from activated sludge and possesses a flexible catabolism integrating numerous terminal reductases encoded in its genome (*8*). *S. multivorans* is able to couple the reductive dechlorination of PCE, TCE, or dibromoethene (DBE) to growth (*9*, *10*) through its prototypical RDase PceA.

The 464 amino acids of PceA are structured in a compact α/β fold domain (Fig. 1A). The structure can be divided into an N-terminal unit (residues 1 to 138), a norpseudo-B_{12} binding core (residues 139 to 163 and 216 to 323), an insertion unit (residues 164 to 215), an iron-sulfur cluster binding unit (residues 324 to 394) and a C-terminal unit (residues 395 to 464) (fig. S1). Two protomers in the $P4_1$ asymmetric unit interact tightly to form a dimer with a twofold noncrystallographic symmetry. Two α helices of the norpseudo-B_{12} binding core and one α helix of the N-terminal unit form a helical bundle with their symmetry mates. Along with extensive loop regions in the N- and C-terminal units, these bundles create the dimer interface. The interface covers 20% of the accessible surface area of the protomer, supporting a compact and stable dimeric arrangement. Using gel filtration, an apparent molecular mass of 89 kD (fig. S2) was determined for PceA purified from the membrane fraction, which agrees with a dimeric rather than a monomeric structure as reported previously for the soluble wild-type enzyme (*5*).

RDases lack obvious sequence similarities to other enzyme families, and the fold of PceA is unlike that of known corrinoid-dependent methyltransferases (*11*) or mutases (*12*). The most similar protein with clear homology found was methylmalonic aciduria *cblC* type with homocysteinuria (MMACHC) (*13*) (fig. S3). MMACHC is a B_{12}-trafficking chaperone essential for the formation of adenosyl- or methylcobalamin in humans by catalyzing the reductive removal of the upper axial ligands from cyanocobalamin and alkylcobalamins. Structural homology is limited to the B_{12}/norpseudo-B_{12}–binding core, which resembles the nitroreductase family fold (*14*) (fig. S3). Consequently, RDases and MMACHC most likely evolved from a common ancestral B_{12}-binding protein.

In addition to the norpseudo-B_{12} cofactor, PceA also harbors two [4Fe-4S] clusters. Short distances between the two [4Fe-4S] clusters and the proximal [4Fe-4S] cluster and the Co bound to the corrin ring are expected to allow for a rapid electron transfer within a protein monomer (*15*) (Fig. 1B). The proximal [4Fe-4S] cluster is in van der Waals (vdW) contact distance to the C83 carboxamide side chain and C8 of the corrin ring [for atom numbering, see (*2*)], with the carboxamide N84 being in hydrogen bond distance to a μ3-sulfido ligand of the [4Fe-4S] cluster. The two active sites of the PceA dimer are at a Co-Co distance of 42 Å without cofactors between them, indicating two independent catalytic units per dimer (Fig. 1A).

Both [4Fe-4S] clusters are within 6 Å of the enzyme surface, whereas norpseudo-B_{12} is deeply buried in the structure. Most interactions between the cobalamin cofactor's ring system and the protein matrix are due to hydrogen bonds between the cofactor and the norpseudo-B_{12}–binding core of PceA (Fig. 2). Binding of the phosphate and parts of the adenine group of norpseudo-B_{12} is mediated by a loop in the iron-sulfur cluster binding unit. Co is not coordinated by adenine (base off), and the conformation of the linker is curled rather than extended as is typical for base-off B_{12} (*14*, *16*). Compared to the base-on conformation of isolated norpseudovitamin B_{12} (*2*), several conformational changes, including a 90° rotation around the bond between phosphate and the C3′ of ribose and flip of the ribose, are needed to convert the base-on conformation into the base-off conformation found in PceA (Fig. 2). In comparison to the dimethylbenzimidazole moiety of B_{12}, the adenine moiety of norpseudo-B_{12} has several hydrogen-bond acceptor and donor functions, which in addition to anchoring the cofactor allows solvent accessibility (Fig. 2, inset). C176 of the nucleotide loop packs closely against the adjacent β sheet, and the methyl group found in B_{12} at this position would force the loop to adopt a different conformation, which might explain the preference for norpseudo-B_{12}.

PceA contains Co^{II} in the as-isolated state (*2*), for which an axial ligand is typically observed. Additional density is found above the β face of Co, with a Co-X distance of 2.5 Å. The density has been tentatively assigned to a water molecule. Reduction to the catalytically relevant super-reduced Co^{I} is probably facilitated by the weak axial ligation, making Co effectively tetracoordinated in the protein, and agrees with the elevated midpoint potential of the Co^{II}/Co^{I} transition of −380 mV (pH 7.5, versus a standard hydrogen electrode) (*2*).

Substrate access to the active site is restricted by a selection filter with the shape of a 3 × 5.5 Å "letterbox," a gap made up of side chains from

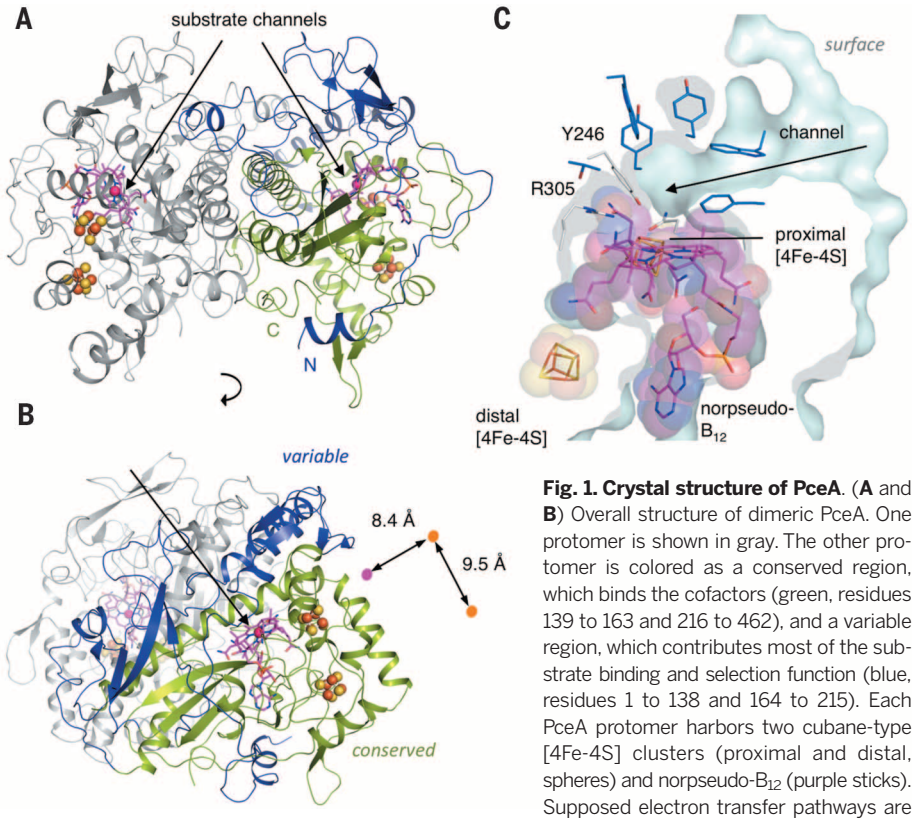

Fig. 1. Crystal structure of PceA. (**A** and **B**) Overall structure of dimeric PceA. One protomer is shown in gray. The other protomer is colored as a conserved region, which binds the cofactors (green, residues 139 to 163 and 216 to 462), and a variable region, which contributes most of the substrate binding and selection function (blue, residues 1 to 138 and 164 to 215). Each PceA protomer harbors two cubane-type [4Fe-4S] clusters (proximal and distal, spheres) and norpseudo-B_{12} (purple sticks). Supposed electron transfer pathways are indicated in (B), along with distances between the closest Fe atoms of the [4Fe-4S] clusters and Co of norpseudo-B_{12}. (**C**) Active-site cavity of PceA. Conserved polar residues in proximity to the axial position of Co are depicted as white sticks, hydrophobic residues of the second ligand sphere as blue sticks. A 12 Å–long channel was identified as the substrate entry site to the active-site dome.

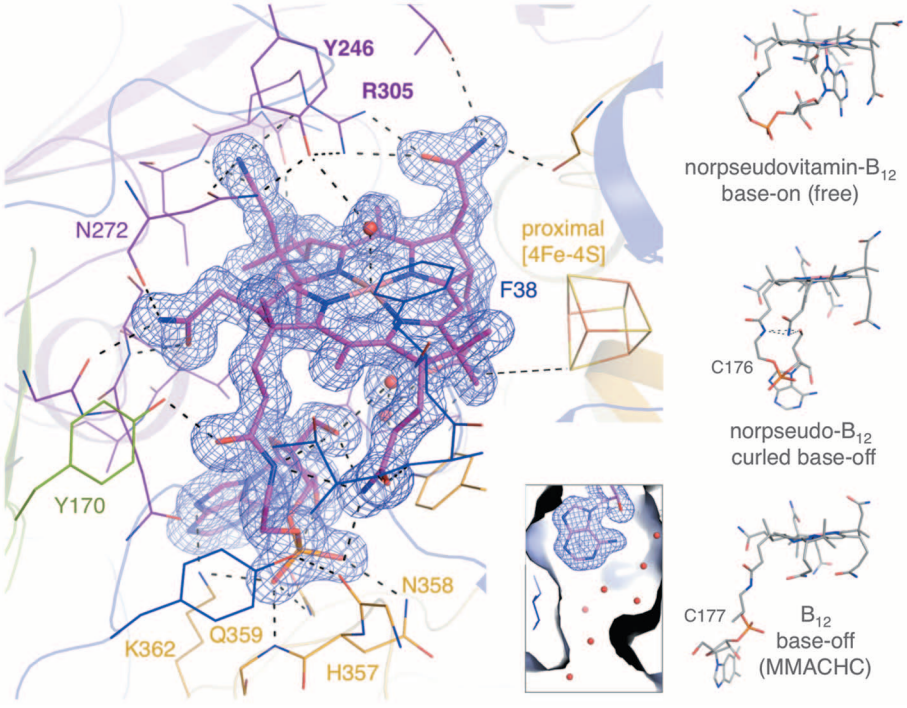

Fig. 2. Norpseudo-B_{12} binding. Potential hydrogen-bonding residues are colored according to their position within PceA: blue, N-terminal (residues 1 to 138); purple, norpseudo-B_{12}–binding core (residues 139 to 163 and 216 to 323); green, insertion unit (residues 164 to 215); yellow, [4Fe-4S]-cluster coordinating loop (residues 324 to 394). The 1σ 2_mFo-$_DFc$ electron density map for norpseudo-B_{12} and water molecules is shown as mesh. The inset shows the solvent-accessible adenine moiety. A comparison of corrinoid linker geometries is shown on the right: free norpseudovitamin B_{12} (*2*), base on (Cambridge Crystallographic Data Centre: 217274, top), norpseudo-B_{12} bound to PceA (middle), and base-off B_{12} in MMACHC (*14*) (Protein Data Bank: 3SOM, bottom). The β ligand is omitted for clarity.

the N-terminal and insertion units (fig. S4). After the filter, PCE and TCE have to pass through a 12 Å–long hydrophobic channel isolating the active site inside the core of the protein (Fig. 1C, arrow). The channel then expands to create the amphiphilic active site pocket at the β face of the corrin ring, where access to the cofactor itself is further restricted by a ring fence of side chains (fig. S4A). The cavity is predominantly lined by tryptophan and tyrosine residues, which define its shape and volume. Three adjacent polar residues, namely Tyr^{246}, Arg^{305}, and Asn^{272} from the B_{12}-binding core, are highly conserved (Figs. 2 and 3C). Of these Tyr^{246} is invariant, whereas some RDases have functionally conserved replacements with a lysine residue in place of Arg^{305} (fig. S5). Asn^{272} is conserved in a subset of RDases. The residues are close to the corrin ring and point with their side chains into the active site pocket, positioning the phenolic hydroxyl group of Tyr^{246} in hydrogen-bonding distance to the guanidinium group of Arg^{305} (Fig. 3C).

To further analyze how substrate specificity and regioselectivity are determined by the protein structure, we analyzed the structure of PceA with its substrate TCE and the tribromoethene dehalogenation product *cis*-DBE. After soaking with TCE, additional density matching the shape of TCE was found in the active site pocket above the corrin ring (Fig. 3), concomitant with a reduction in the occupancy of the close-by water ligand. TCE binds with the dichlorinated carbon (C1) facing the corrin ring. Judged by the shape of the electron density, TCE bound in two orientations with the lone chloride in cis and trans to the Co-facing chloride (Fig. 3A). The PCE/TCE binding pocket is restricted by vdW contacts to the surrounding aromatic side chains (fig. S4). Tyr^{246} is within hydrogen-bonding distance to the Cl substituent of TCE nearest to Co.

Reductive dehalogenation of TCE produces *cis*-DCE, whose binding site and orientation we revealed using *cis*-DBE. *cis*-DBE was used because the stronger anomalous scattering of Br as compared to Cl allowed identification of *cis*-DBE also at low occupancy. Two strong patches of density were observed in the same place as two Cl atoms in the minor orientation of TCE, marking the position of *cis*-DBE. The chloride atom of TCE nearest to Co and Tyr^{246} is unoccupied in the product complex (Fig. 3B and fig. S6).

The side chains in the substrate-binding pocket are tightly packed with little conformational freedom and probably disfavor the binding of molecules significantly larger than PCE or TCE by steric exclusion. Thus, the binding pocket provides a second gate for substrate selection. In contrast to the variable residues forming the channel entrance, aromatic residues within the pocket are partially conserved between different RDases but are dispersed in sequence (fig. S5). Two layers of control over substrate selection (the "letterbox" and the active site) could achieve the necessary selectivity within the wide range of organohalides converted by distinct RDases, which often exist within the same organism (*3*).

PceA is attached to the periplasmic side of the cytoplasmic membrane in *S. multivorans* cells (*17*). For both PceA monomers to function independently, the twofold noncrystallographic symmetry axis of the dimer should be perpendicular to the membrane plane in the PceA-PceB complex. This would agree with two principal orientations of our PceA structure on the membrane. Amino acid residues 411 to 431 (Fig. 4, red ribbon) show high flexibility in all crystals and could only be modeled in one out of six protomers in an alternative ($P2_1$) crystal form, where α-helix 15 (fig. S1) is stabilized by a crystal contact. The disordered helices in both monomers are on the same face of the structure, and we speculate that this is the site of interaction with the PceB membrane anchor that is destabilized after complex dissociation in the purification process. Our proposed arrangement would locate the two electron entrance ports close to the membrane and the substrate channel pointing toward the periplasmic space (Fig. 4).

RDase catalysis involves a transfer of two electrons and a proton, while accommodating the dissociation of a chloride ion from the substrate. The initial step in dechlorination of PCE probably involves a dissociative electron transfer from Co^{I} to PCE, resulting in the formation of a trichlorovinyl radical (*18*, *19*) by chloride elimination, while the cofactor is returned to the Co^{II} state (*18*, *20*, *21*). The distance for this electron transfer between Co and C1 of TCE is 5.8 Å in our structure (Fig. 4).

The intermittent water (Fig. 3A) is depopulated in the TCE-bound active site only, suggesting that the β-ligand water, 2.2 Å from the proximal chloride, is displaced by TCE. The same position was identified as a weak halide-binding site by a strong anomalous signal for iodide at 0.5 M concentration (fig. S6D) but the absence of such a signal at lower chloride concentrations. This would qualify the proximal chloride at C1 over the tightly enclosed distal chloride as the leaving group, ultimately yielding *cis*-DCE from the minor orientation of TCE displayed in Fig. 3A, consistent with the data obtained with the *cis*-DBE product analog.

Recombination of the trichlorovinyl radical with Co^{II}, forming an organometallic intermediate as proposed for free B_{12} (*22*), is an attractive next step but would be disfavored in PceA because of

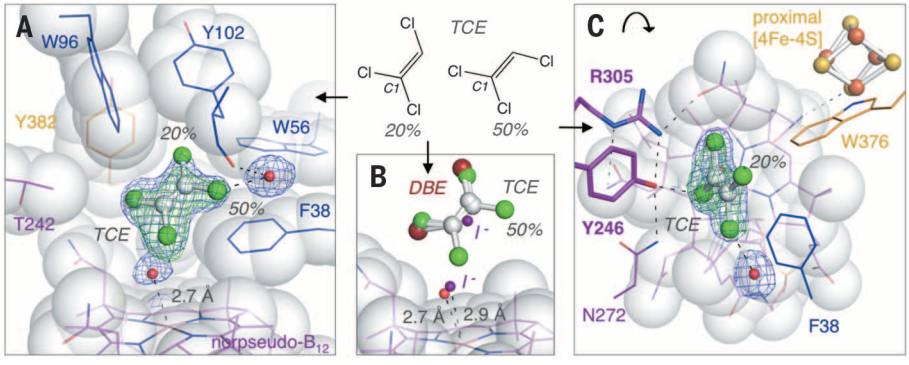

Fig. 3. Substrate/product–analog binding. (**A** and **C**) TCE, overlayed in a high- and low-occupancy (50 and 20% as modeled in the structure) orientation, as indicated in the chemical sketch. Electron density maps are shown for TCE, the β ligand, and water: $1\sigma\ 2_mFo\text{-}_DFc$ (blue) and $4\sigma\ _mFo\text{-}_DFc$ (green). (**B**) Overlay of the active site with TCE, *cis*-DBE, iodide, and the coordinated water (empty structure). Side chains forming the hydrophobic pocket are shown as sticks and are colored according to their position in PceA using the same scheme as in Fig. 2. Hydrogen bonding distances from Tyr^{246}: 2.8 Å (Asn^{272}), 2.9 Å (Arg^{305}), and 2.5 Å (TCE).

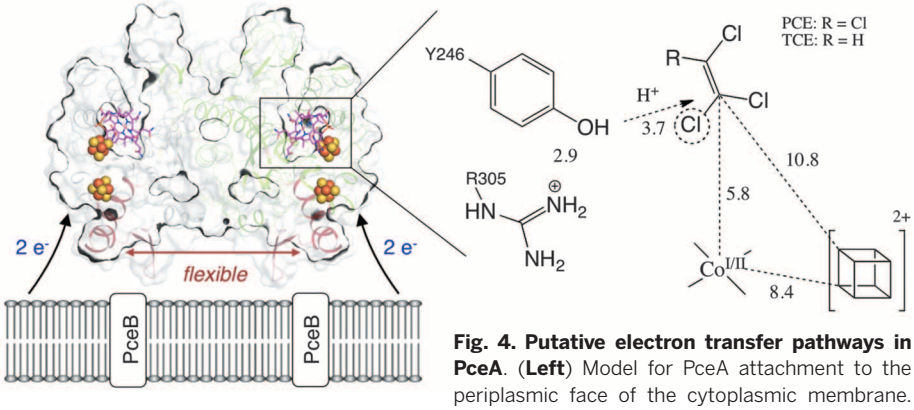

Fig. 4. Putative electron transfer pathways in PceA. (**Left**) Model for PceA attachment to the periplasmic face of the cytoplasmic membrane. The red helix/loop represents structure only observed (helix) or well defined (β sheet/loop) in the presence of a crystal contact in the $P2_1$ crystal form. (**Right**) Distances (in angstroms) for putative electron (dashed lines) and proton (arrow) transfers onto the substrate. The figure shows the geometry observed in the TCE bound crystal.

the dense packing above the β face of the corrin ring (fig. S4A). The same steric constraints would disable an initial nucleophilic attack of Co^{I} on PCE. Instead, the short substrate-cofactor distances would allow the second electron transfer to occur either directly from the proximal [4Fe-4S] cluster or via the Co ion (Fig. 4). The strictly conserved Tyr^{246} is pointing with its phenolic hydroxyl group toward C1 and could donate the required proton to neutralize the carbanion (*20*). Deprotonation of Tyr^{246} could be stabilized by the neighboring positive charge of Arg^{305}. Equally, a role of Tyr^{246} in a radical route (*18*) cannot be excluded.

REFERENCES AND NOTES

1. C. Holliger, G. Wohlfarth, G. Diekert, *FEMS Microbiol. Rev.* **22**, 383–398 (1998).
2. B. Kräutler *et al.*, *Helv. Chim. Acta* **86**, 3698–3716 (2003).
3. L. A. Hug *et al.*, *Philos. Trans. R. Soc. London Ser. B* **368**, 20120322 (2013).
4. A. Mac Nelly, M. Kai, A. Svatoš, G. Diekert, T. Schubert, *Appl. Environ. Microbiol.* **80**, 4313–4322 (2014).
5. A. Neumann, G. Wohlfarth, G. Diekert, *J. Biol. Chem.* **271**, 16515–16519 (1996).
6. H. Scholz-Muramatsu, A. Neumann, M. Messmer, E. Moore, G. Diekert, *Arch. Microbiol.* **163**, 48–56 (1995).
7. Materials and methods are available on *Science* Online
8. T. Goris *et al.*, *Environ. Microbiol.* 10.1111/1462-2920.12589 (2014).
9. E. Miller, G. Wohlfarth, G. Diekert, *Arch. Microbiol.* **166**, 379–387 (1996).
10. L. Ye, A. Schilhabel, S. Bartram, W. Boland, G. Diekert, *Environ. Microbiol.* **12**, 501–509 (2010).
11. C. L. Drennan, S. Huang, J. T. Drummond, R. G. Matthews, M. L. Ludwig, *Science* **266**, 1669–1674 (1994).
12. F. Mancia *et al.*, *Structure* **4**, 339–350 (1996).
13. J. Kim, C. Gherasim, R. Banerjee, *Proc. Natl. Acad. Sci. U.S.A.* **105**, 14551–14554 (2008).
14. D. S. Froese *et al.*, *Biochemistry* **51**, 5083–5090 (2012).
15. H. B. Gray, J. R. Winkler, *Proc. Natl. Acad. Sci. U.S.A.* **102**, 3534–3539 (2005).
16. T. Svetlitchnaia, V. Svetlitchnyi, O. Meyer, H. Dobbek, *Proc. Natl. Acad. Sci. U.S.A.* **103**, 14331–14336 (2006).
17. M. John, R. P. H. Schmitz, M. Westermann, W. Richter, G. Diekert, *Arch. Microbiol.* **186**, 99–106 (2006).
18. J. Shey, W. A. van der Donk, *J. Am. Chem. Soc.* **122**, 12403–12404 (2000).
19. R. P. H. Schmitz *et al.*, *Environ. Sci. Technol.* **41**, 7370–7375 (2007).
20. G. Glod, W. Angst, C. Holliger, R. P. Schwarzenbach, *Environ. Sci. Technol.* **31**, 253–260 (1997).
21. W. Schumacher, C. Holliger, A. J. Zehnder, W. R. Hagen, *FEBS Lett.* **409**, 421–425 (1997).
22. K. M. McCauley *et al.*, *J. Am. Chem. Soc.* **127**, 1126–1136 (2005).

ACKNOWLEDGMENTS

H.D. acknowledges support by the Cluster of Excellence "Unifying Concepts in Catalysis (UniCat)." G.D. and T.S. were supported by the Deutsche Forschungsgemeinschaft (DFG) (Research Unit FOR 1530). M.B. was funded by the DFG through grant SFB 1078-A5. We are grateful for the funding of C.K. by the Ernst Abbe Foundation; in addition, we thank the staff at the Helmholtz-Zentrum Berlin (HZB) MX beamlines and DESY PETRA III beamline P11 for their assistance. We acknowledge access to beamlines of the BESSY II storage ring (Berlin, Germany) via the Joint Berlin MX-Laboratory. The authors thank O. Einsle for critical reading of the manuscript. Structure factors and models have been deposited in the Protein Data Bank under accession numbers 4UQU (empty), 4UR0 (TCE bound), 4UR1 (*cis*-DBE bound), 4UR2 (iodide bound), and 4UR3 ($P2_1$ crystal form).

SUPPLEMENTARY MATERIALS

www.sciencemag.org/content/346/6208/455/suppl/DC1
Materials and Methods
Figs. S1 to S6
Table S1
References (*23*–*35*)

30 June 2014; accepted 18 September 2014
Published online 2 October 2014;
10.1126/science.1258118

WORKING MEMORY

Medial prefrontal activity during delay period contributes to learning of a working memory task

Ding Liu,[1,2]* Xiaowei Gu,[1,2]* Jia Zhu,[1,2]* Xiaoxing Zhang,[1] Zhe Han,[1,2] Wenjun Yan,[1,2] Qi Cheng,[1,2] Jiang Hao,[1]† Hongmei Fan,[1] Ruiqing Hou,[1] Zhaoqin Chen,[1] Yulei Chen,[1] Chengyu T. Li[1]‡

Cognitive processes require working memory (WM) that involves a brief period of memory retention known as the delay period. Elevated delay-period activity in the medial prefrontal cortex (mPFC) has been observed, but its functional role in WM tasks remains unclear. We optogenetically suppressed or enhanced activity of pyramidal neurons in mouse mPFC during the delay period. Behavioral performance was impaired during the learning phase but not after the mice were well trained. Delay-period mPFC activity appeared to be more important in memory retention than in inhibitory control, decision-making, or motor selection. Furthermore, endogenous delay-period mPFC activity showed more prominent modulation that correlated with memory retention and behavioral performance. Thus, properly regulated mPFC delay-period activity is critical for information retention during learning of a WM task.

Working memory (WM) is essential for cognition by allowing active retention of behaviorally relevant information over a short duration known as the delay period (*1*–*3*). Previous studies have shown that the prefrontal cortex (PFC) is crucial for WM, because perturbation of PFC activity impaired WM (*3*) and WM-related activity was observed during the delay period in neurons of dorsal-lateral PFC (DL-PFC) in primates and medial PFC (mPFC) in rodents (*3*–*10*). Nevertheless, the functional role of PFC delay-period activity in WM remains unclear. Memory retention and attentional control are leading candidates (*2*, *3*, *11*). However, PFC is also critical for other brain functions (*3*, *12*, *13*) and has been suggested to be important for inhibitory control (*14*), decision-making (*15*), or motor selection (*16*). These roles cannot be distinguished by a delayed-response task, in which decision-making precedes the delay period (*3*, *12*). In addition, traditional methods for perturbing neural activity (*3*), including transcranial magnetic stimulation (*17*) and electrical stimulation (*18*), do not provide the temporal resolution and cell-type specificity required for delineating the functional role of PFC delay-period activity in WM. We addressed these issues by using a WM task with a delay period designed to temporally separate memory retention from other functions (*5*, *6*, *19*, *20*) and optogenetic approaches (*21*) to bidirectionally manipulate mPFC activity of excitatory and inhibitory neurons during the delay period.

Head-fixed mice were trained to perform an olfactory delayed nonmatch to sample (DNMS) task (Fig. 1, A and B; fig. S1; and movie S1), a modified version of the behavioral paradigms previously used in rats (*19*, *20*). For each trial, an olfactory stimulus (ethyl acetate, EA, or 2-pentanone, 2P) was presented as the sample, followed by a delay period (4 to 5 s) and then a testing olfactory stimulus, either matched or nonmatched to the sample. Water-restricted mice were rewarded with water if they licked within a response time window in the nonmatch but not match trials (Fig. 1B and fig. S2). During the delay period, mice need to retain the information associated with the odor sample. The performance correct rate (referred to hereafter as performance), correct rejection rate, discriminability (d'), and lick efficiency steadily increased throughout the training, but there was a ceiling effect for the hit rate (Fig. 1, C and D, and fig. S3). The potential involvement of visual, auditory, or somatosensory cues was excluded (fig. S4A). The performance decreased with increasing duration of the delay period (fig. S4B), a typical hallmark of WM paradigms (*1*, *3*). For a genuine WM task, subjects should be able to perform beyond two cues (*19*, *20*), which was indeed observed (fig. S4C). We next expressed hM4Di, a designer receptor exclusively activated by designer drug (DREADD) (*22*), in mPFC with adeno-associated virus (AAV). Suppression of neural activity (fig. S5) by intraperitoneal injection of clozapine-N-oxide (CNO) significantly impaired the performance of the mice during the learning phase (days 1 to 5, Fig. 1E; statistics shown in table S1).

It is essential that mice were using WM instead of residual odor during the delay period to perform the task. Photoionization detector (PID)

[1]Institute of Neuroscience and Key Laboratory of Primate Neurobiology, Shanghai Institutes for Biological Sciences, Chinese Academy of Sciences, Shanghai 200031, China. [2]University of Chinese Academy of Sciences, Beijing 100049, China.
*These authors contributed equally to this work. †Present address: Friedrich Miescher Institute for Biomedical Research, Maulbeerstrasse 66, 4058 Basel, Switzerland. ‡Corresponding author.
E-mail: tonylicy@ion.ac.cn

measurements were used to ensure minimal residual odor in the construction of the olfactometry system (fig. S6A). In addition, a behavioral control experiment (nonmatch to long duration sample, NMLS) was performed to further exclude possible involvement of residual odor undetectable by PID. In this task, odor samples were provided during a period corresponding to the delay period in the standard DNMS task to simulate potential delay-period residual odor (fig. S6B). The sample concentration for the chance level performance of the NMLS task was well above the PID-detected residual level during the delay period in the standard DNMS task (fig. S6C).

We then suppressed the delay-period activity of pyramidal neurons with optogenetic methods. It was first achieved through activating γ-aminobutyric acid–releasing (GABAergic) inhibitory neurons expressed with channel rhodopsin (ChR2). We stereotactically and bilaterally injected AAV carrying a Cre-inducible gene encoding ChR2 [pAAV-Ef1a-DIO-ChR2(H134R)-mCherry (*21*); referred hereafter as DIO-ChR2] or mCherry (pAAV-Ef1a-DIO-mCherry, hereafter DIO-mCherry) into mPFC of vesicular GABA transporter (VGAT)–Cre transgenic mice (*23*). Expression and activity-suppression efficiency were verified by immunostaining and op-tetrode recording (fig. S7 and Fig. 2B). Optogenetic manipulation could influence neurons within 1.4 mm from an optical fiber (fig. S8) and affect all subregions of mPFC (fig. S7). Behavioral and optogenetic experiments were performed in a blind design. Step laser illumination (473 nm, 2 mW) was applied in the last 4 s of the 5-s delay period in all trials throughout the learning (Fig. 2A). Suppressing the delay-period activity of mPFC pyramidal neurons in the learning phase impaired behavioral performance, as manifested by the deficits in performance, correct rejection rate, *d'*, lick efficiency, number of trials to criterion (performance above 80% for consecutive 40 trials), and consecutive false choice (Fig. 2, A and B; figs. S9 and S10; and table S2), but not hit rate (Fig. 2B). Optogenetic suppression of mPFC delay-period activity failed to impair WM performance in well-trained mice (based on the averaged results from day 8, Fig. 2, A and B, and table S2), although session-based analysis revealed a small degree of relearning at the initial sessions, which was significantly influenced by suppressing delay-period activity (fig. S11). The results were consistent with the suggested role of PFC in performing novel and attention-demanding, rather than routine and well-rehearsed, tasks (*2*, *3*, *12*, *24*).

To directly suppress activity of mPFC pyramidal neurons, we expressed halo-rhodopsin (NpHR) (*21*) or enhanced yellow fluorescent protein (eYFP) in pyramidal neurons by injecting AAV-CaMKIIα-eNpHR3.0-eYFP or AAV-CaMKIIα-eYFP into mPFC. The expression and functionality of NpHR were verified by immunostaining and op-tetrode recording (fig. S12 and Fig. 2D). Direct suppression of delay-period activity of pyramidal neurons in mPFC by step laser illumination (532 nm, 10 mW) impaired WM performance during the learning phase but not after the mice were well trained (Fig. 2, C and D; figs. S13 and S14; and table S3).

To examine whether optogenetic manipulation influenced WM on a trial-by-trial basis, we suppressed mPFC delay-period activity in an interleaved laser on/off design (Fig. 2E). Performance was indeed impaired in laser-on trials (Fig. 2, E and F; fig. S15; and table S4). To examine the regional specificity of the behavioral effects of optogenetic manipulation, we suppressed delay-period activity in somatosensory cortex (S1) and found no impairment in WM performance (fig. S16).

To further determine whether elevating activity of mPFC pyramidal neurons during the delay period could affect the learning of a WM task, we expressed AAV-CaMKIIα-ChR2-mCherry or AAV-CaMKIIα-mCherry in mPFC of wild-type mice (Fig. 3A and fig. S17). We then applied step laser illumination (473 nm, 0.8 mW) throughout learning. When optogenetic activation was performed during the learning phase, CaMKIIα-ChR2 mice performed worse than the control group (Fig. 3A and table S5). Both hit and correct rejection rates were modulated (Fig. 3B). By contrast, optogenetic activation during the well-trained phase had no effect on the performance, although the correct rejection rate was significantly decreased. Similar results were obtained by enhancing mPFC

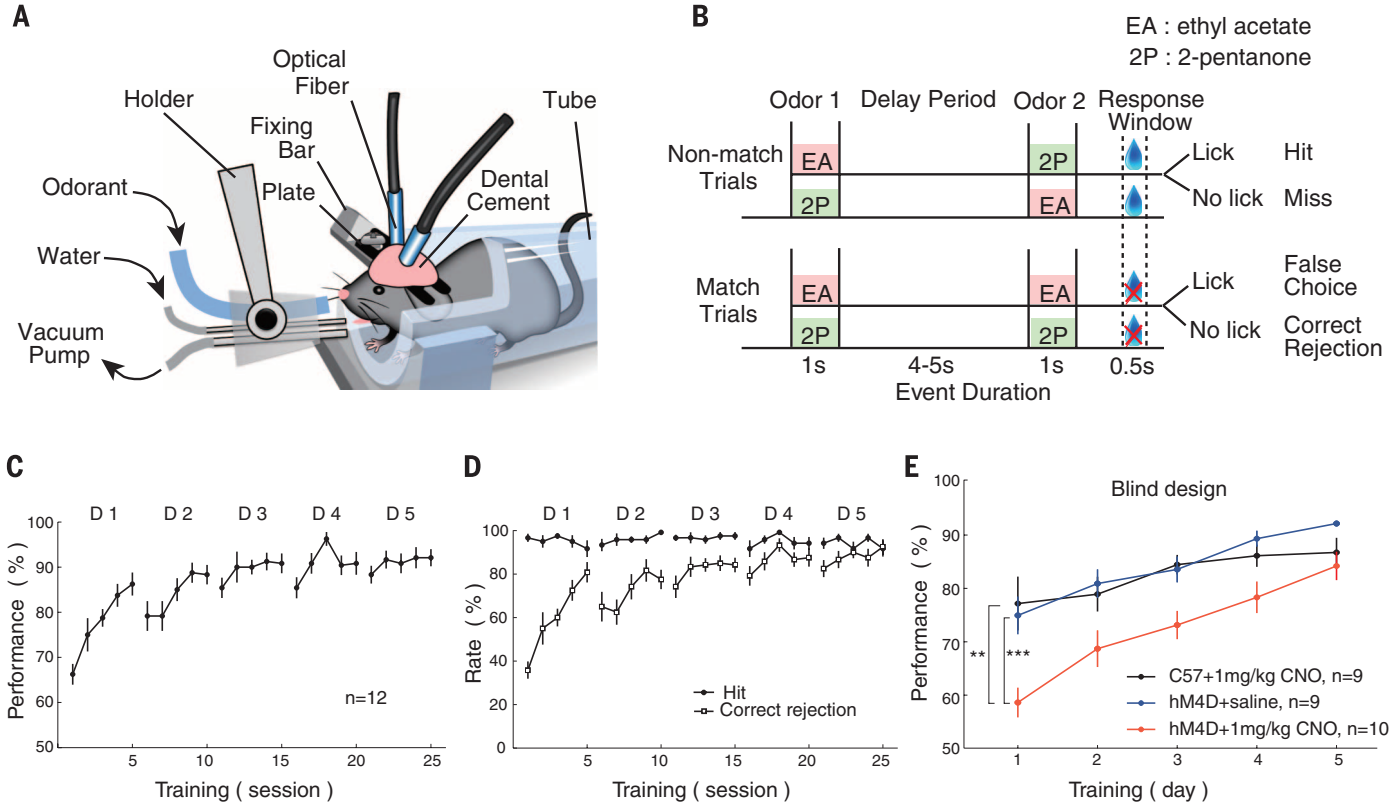

Fig. 1. WM paradigm. (**A** and **B**) Behavioral diagram. (**C**) Performance during learning. Five sessions per day, 20 trials per session. Error bars indicate SEM unless stated otherwise. (**D**) Hit rates and correct rejection rates in learning. (**E**) Performance in experiments of suppressing mPFC activity by hM4Di. $^{**}P$ = 0.003; $^{***}P < 0.001$; two-way analysis of variance with mixed design (Tw-ANOVA-md).

delay-period activity with laser illumination in an odor-sample specific manner (fig. S18). Thus, elevating mPFC activity during the delay period interfered with the learning of the WM task.

In further experiments, we suppressed mPFC activity through NpHR in the second odor-delivery period, during which decision-making behavior occurred. Behavioral performance was unaffected early in learning (days 1 and 2) but was impaired after day 3 (fig. S19). Therefore, the contribution of mPFC delay-period activity in learning of the WM task was temporally specific, a result distinct from but not contradictory to the previous findings of behavioral deficits in well-trained subjects using classic techniques to perturb mPFC activity (*3*, *15*).

To study the functional specificity of optogenetic manipulation, we used behavioral experiments of a nonmatch to sample task without the delay period (NMS-WD, Fig. 3C) and a go/no-go odor discrimination task (GNG, Fig. 3E). Both tasks required sensory encoding, inhibitory control, decision-making, and motor selection (fig. S20A) but not memory retention. In the NMS-WD task, laser illumination covered the entire period for odor perception, decision-making, and motor selection (Fig. 3C). In the GNG task with random intertrial intervals, laser illumination was applied after a trial-starting cue and before the decision-making behavior occurred (Fig. 3E),

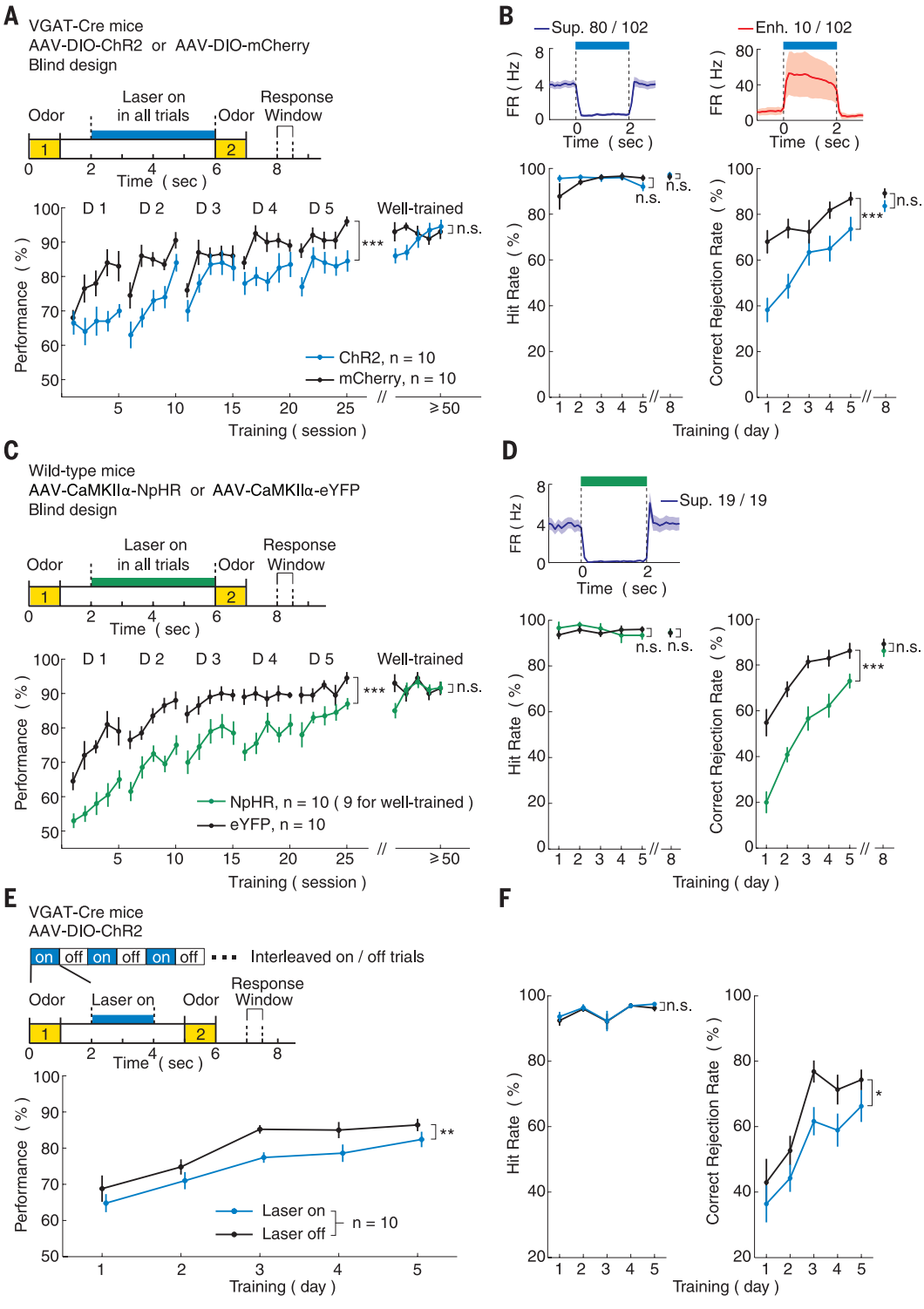

Fig. 2. Suppressing mPFC delay-period activity impaired performance in learning of the WM task. (**A** and **B**) Performance, hit rates, and correct rejection rates for experiments, in which activity of pyramidal neurons was suppressed by activating GABAergic neurons. Top in (A): paradigm information. Top in (B): activity-suppression efficiency revealed by awake op-tetrode recording in vivo. FR, firing rate. (**C** and **D**) As in (A) and (B) with NpHR in pyramidal neurons. (**E** and **F**) As in (A) and (B) with interleaved laser on/off design. *P = 0.016; **P = 0.003; ***P < 0.001; n.s., not significant; learning: Tw-ANOVA-md; well-trained: Mann-Whitney U test.

simulating the delay period in the DNMS task (fig. S20B). We found that behavioral performance was not affected by laser illumination in all trials, in either the NMS-WD (Fig. 3, C and D, and table S6) or GNG (Fig. 3, E and F, and table S7) task. In separate sets of experiments with an interleaved laser on/off design, the same results were obtained (figs. S21 and S22). Therefore, mPFC delay-period activity appeared to be more important in memory retention than sensory encoding, inhibitory control, decision-making, and motor selection.

To examine the neural correlates throughout learning the WM task, we recorded single-unit activity of mPFC by using custom-made tetrodes (Fig. 4, A to C, and figs. S23 and S24). By lowering recording electrodes each day, we recorded 564 neurons during the learning phase (days 1 to 5) from 15 mice and 95 neurons from seven well-trained (days 10 to 15) mice. Similar results were obtained from 636 neurons of nine mice without daily lowering of electrodes (figs. S25 to S28). The delay-period activity was more prominently modulated during the learning than the well-trained phase (Fig. 4D and fig. S29). The delay-period firing rates during the learning phase were significantly higher for neurons with enhanced delay-period activity and lower for suppressed neurons, as compared with those in the well-trained phase (Fig. 4E and table S8).

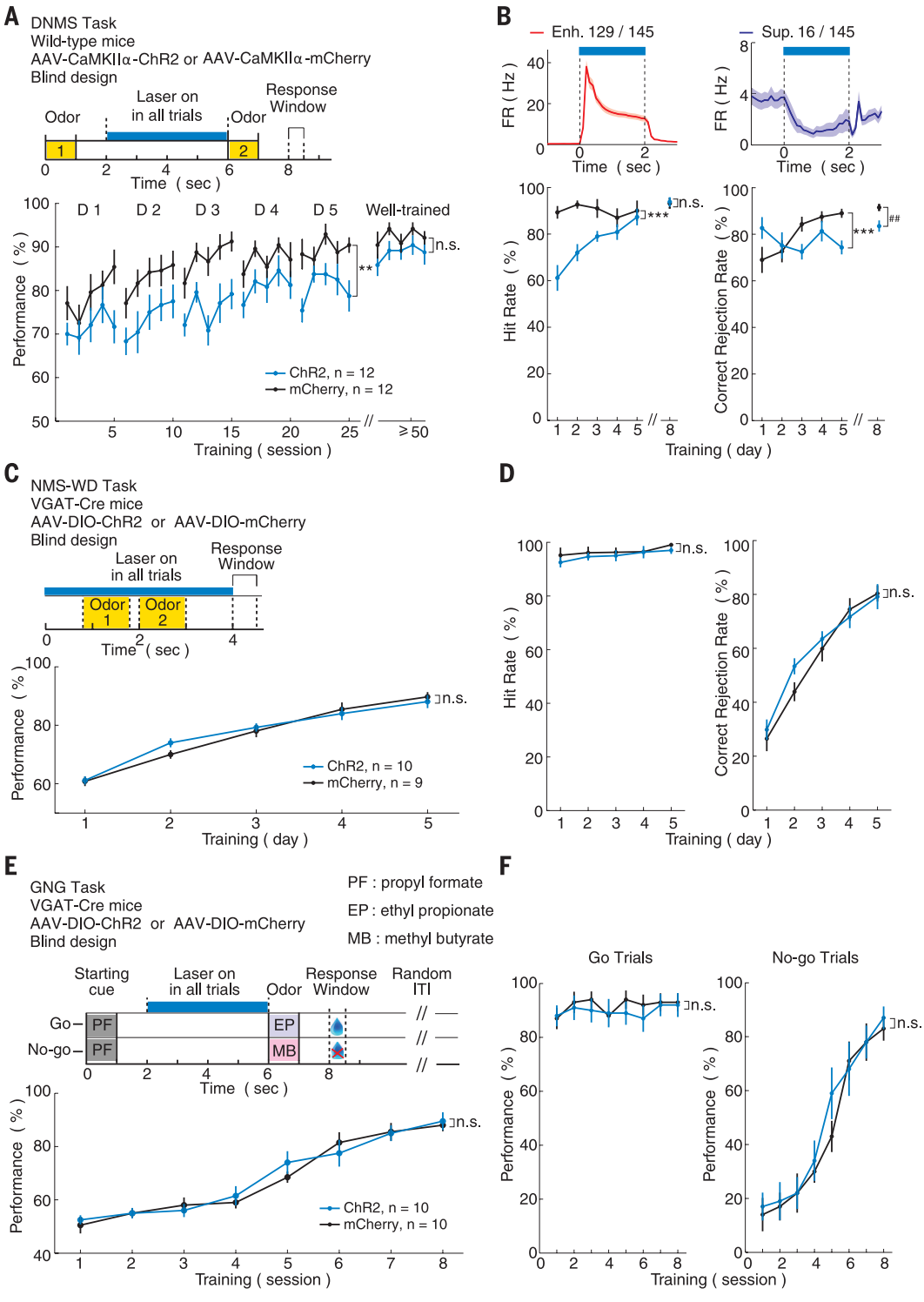

Fig. 3. Importance of properly regulated mPFC delay-period activity and its functional role in the WM task. (**A** and **B**) Performance, hit rates, and correct rejection rates in experiments with elevated mPFC activity during the delay period. (**C** and **D**) Paradigm and performance for NMS-WD experiments with suppressed mPFC activity. (**E** and **F**) As in (C) and (D) for the GNG task. $^{**}P = 0.002$; $^{***}P < 0.0001$; learning: Tw-ANOVA-md. $^{\#\#}P = 0.0048$; well-trained: Mann-Whitney U test.

To retain odor-related information, delay-period population activity should be different after distinct odor samples. We therefore visualized population activity by principal component analysis (PCA) (*25*). The first three PCs captured the majority of variance (72%). The trajectories during the delay period after two different odor samples were separated during the learning but not the well-trained phase (Fig. 4F, fig. S30, and movie S2), as quantified by the trajectory distance (Fig. 4G). The results remained robust by only using half of the neurons (fig. S31). We further analyzed the sensitivity of delay-period population trajectories to behavioral outcome and found that trajectories in correct trials were more separated than in error trials during the learning but not well-trained phase (fig. S32). In decoding analysis (*26*), delay-period activity

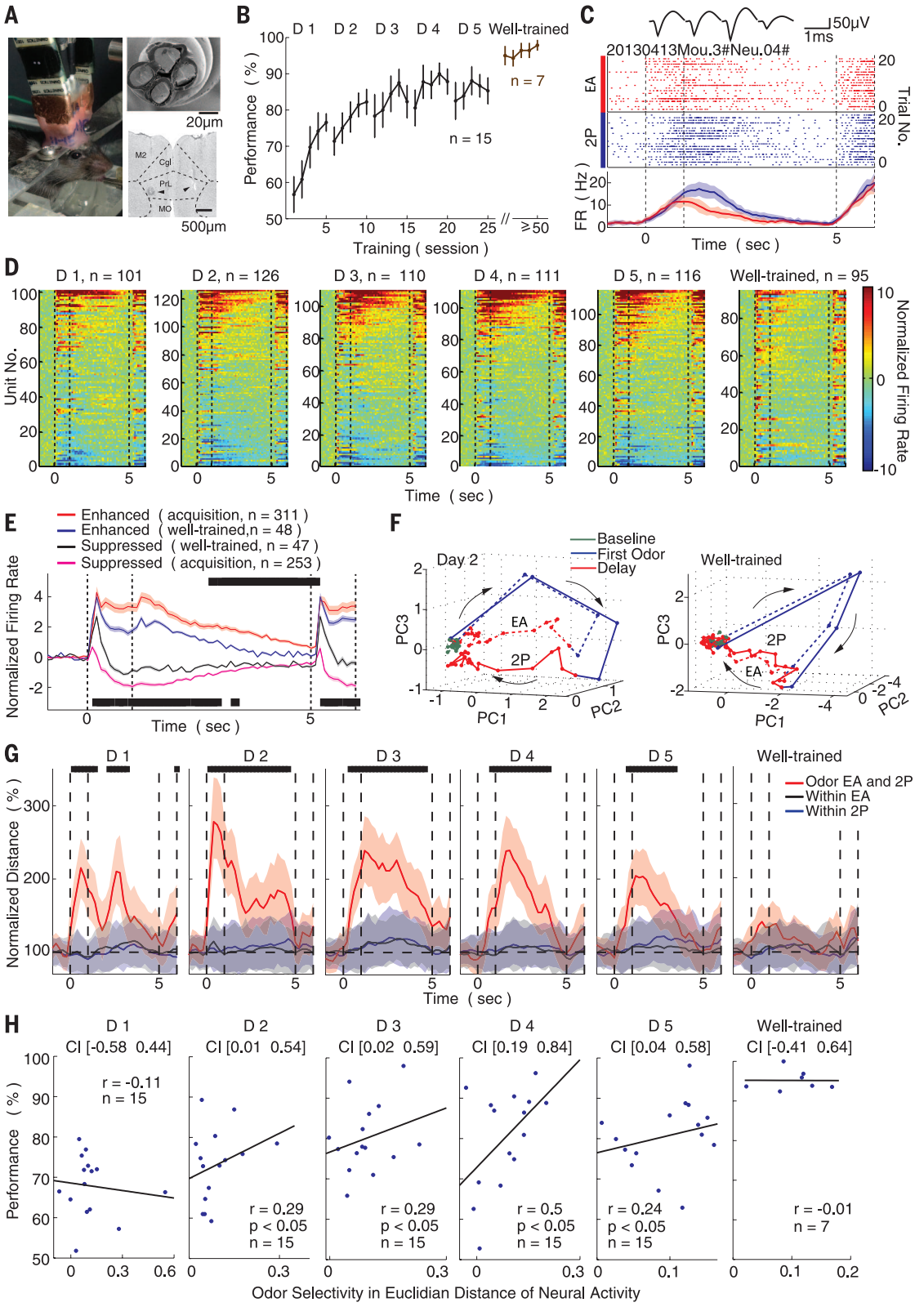

Fig. 4. Modulation of mPFC delay-period activity in learning the WM task. (**A**) Images of microdrive (left), tetrode (right top, electron microscopy), and recording sites (right bottom, indicated by arrowheads). M2, secondary motor area; Cg1, cingulate cortex, area 1; PrL, prelimbic cortex; MO, medial orbital cortex. (**B**) Performance for the recorded mice, 40 trials per session. (**C**) Spike-raster and peristimulus time histogram of an example neuron; trials sorted by odor samples. (Top) Spike waveforms. Shadows indicate SEM. (**D**) Modulation of population activity, which was normalized in *Z*-score and averaged across all trials for each neuron. Results from all the mice recorded with daily lowering of electrodes were presented in (D) to (H). (**E**) Averaged firing rates for neurons with enhanced and suppressed delay-period activity (bin of 100 ms). Black blocks indicate bins with enhanced delay-period activity and significant difference between learning and well-trained phases, $P < 0.05$, Mann-Whitney U test. Black blocks below indicate significant bins for neurons with decreased delay-period activity. Shadows, SEM. (**F**) PCA trajectories of population activity after different odor samples (bin of 200 ms). Arrows: time. (**G**) Distance in PCA trajectories. Shadows indicate 95% confidence interval (CI) from bootstrap of 100 times. (**H**) Correlations between behavioral performance and neuronal odor selectivity. Each dot represents averaged results from one mouse. Statistics: 95% CI from bootstrap of 100 times.

during the learning phase exhibited higher decoding power for odor samples than in the well-trained phase (fig. S33), which critically depended on the neurons with significant delay-period activity (fig. S34).

We then analyzed whether the delay-period odor selectivity of neurons is correlated with the behavioral performance of mice. The Euclidean distance between delay-period activity after different odor samples was calculated for a given neuron and then averaged for all neurons simultaneously recorded to represent neuronal selectivity for each mouse in one day. Although only 2 to 13 neurons (median of 8) were simultaneously recorded each day from a mouse, significant correlation between behavioral performance and neuronal selectivity was observed during the learning (days 2 to 5) but not well-trained phase (Fig. 4H and fig. S35).

The importance of mPFC delay-period activity in the learning phase of a WM task is consistent with its central role in flexible cognitive control in changing environments (*2*, *3*, *12*). However, the DL-PFC activity in primates is important in WM tasks after subjects are well trained (*3*, *12*). Because mPFC appeared earlier than DL-PFC during evolution (*12*), the functional difference between mPFC and DL-PFC suggests that memory retention in novel situations may represent an evolutionarily more primitive function. It is not clear which brain region in rodents is homologous or analogous to DL-PFC in primates (*3*, *12*), but delay-period activity in brain regions other than mPFC (*3*, *5*, *19*, *27–30*) could mediate WM in well-trained mice. Activity of mPFC in other periods during the behavioral task may underlie inhibitory control (*14*), decision-making (*15*), and motor selection (*16*). Nevertheless, the present finding underscores the notion that properly regulated delay-period activity of mPFC is critical for memory retention in attention-demanding WM tasks in novel situations.

REFERENCES AND NOTES

1. A. D. Baddeley, *Working Memory* (Oxford Univ. Press, Oxford, 1986).
2. E. K. Miller, J. D. Cohen, *Annu. Rev. Neurosci.* **24**, 167–202 (2001).
3. J. M. Fuster, *The Prefrontal Cortex* (Academic Press, London, ed. 4, 2008).
4. J. M. Fuster, G. E. Alexander, *Science* **173**, 652–654 (1971).
5. E. K. Miller, C. A. Erickson, R. Desimone, *J. Neurosci.* **16**, 5154–5167 (1996).
6. R. Romo, C. D. Brody, A. Hernández, L. Lemus, *Nature* **399**, 470–473 (1999).
7. E. H. Baeg *et al*., *Neuron* **40**, 177–188 (2003).
8. S. Fujisawa, A. Amarasingham, M. T. Harrison, G. Buzsáki, *Nat. Neurosci.* **11**, 823–833 (2008).
9. J. C. Erlich, M. Bialek, C. D. Brody, *Neuron* **72**, 330–343 (2011).
10. E. M. Meyers, X. L. Qi, C. Constantinidis, *Proc. Natl. Acad. Sci. U.S.A.* **109**, 4651–4656 (2012).
11. R. Desimone, *Proc. Natl. Acad. Sci. U.S.A.* **93**, 13494–13499 (1996).
12. R. E. Passingham, S. P. Wise, *The Neurobiology of the Prefrontal Cortex: Anatomy, Evolution, and the Origin of Insight* (Oxford Univ. Press, Oxford, ed. 1, 2012).
13. S. H. Wang, R. G. Morris, *Annu. Rev. Psychol.* **61**, 49–79, C1–C4 (2010).
14. R. Dias, J. P. Aggleton, *Eur. J. Neurosci.* **12**, 4457–4466 (2000).
15. D. R. Euston, A. J. Gruber, B. L. McNaughton, *Neuron* **76**, 1057–1070 (2012).
16. K. Matsumoto, W. Suzuki, K. Tanaka, *Science* **301**, 229–232 (2003).
17. E. A. Allen, B. N. Pasley, T. Duong, R. D. Freeman, *Science* **317**, 1918–1921 (2007).
18. S. Sobotka, M. D. Diltz, J. L. Ringo, *J. Neurophysiol.* **93**, 128–136 (2005).
19. T. Otto, H. Eichenbaum, *Hippocampus* **2**, 323–334 (1992).
20. X.-C. M. Lu, B. M. Slotnick, A. M. Silberberg, *Physiol. Behav.* **53**, 795–804 (1993).
21. L. Fenno, O. Yizhar, K. Deisseroth, *Annu. Rev. Neurosci.* **34**, 389–412 (2011).
22. B. N. Armbruster, X. Li, M. H. Pausch, S. Herlitze, B. L. Roth, *Proc. Natl. Acad. Sci. U.S.A.* **104**, 5163–5168 (2007).
23. H. T. Chao *et al*., *Nature* **468**, 263–269 (2010).
24. S. B. Ostlund, B. W. Balleine, *J. Neurosci.* **25**, 7763–7770 (2005).
25. M. Rabinovich, R. Huerta, G. Laurent, *Science* **321**, 48–50 (2008).
26. E. M. Meyers, D. J. Freedman, G. Kreiman, E. K. Miller, T. Poggio, *J. Neurophysiol.* **100**, 1407–1419 (2008).
27. M. Stopfer, G. Laurent, *Nature* **402**, 664–668 (1999).
28. C. D. Harvey, P. Coen, D. W. Tank, *Nature* **484**, 62–68 (2012).
29. Z. V. Guo *et al*., *Neuron* **81**, 179–194 (2014).
30. J. Yamamoto, J. Suh, D. Takeuchi, S. Tonegawa, *Cell* **157**, 845–857 (2014).

ACKNOWLEDGMENTS

We thank M. P. Stryker for communication on head-fixed mice preparation; Z. F. Mainen and N. Uchida for communication on behavioral design; G. Laurent for communication on population analysis; L. P. Wang for help in optogenetics; L. N. Lin for help in tetrode drive manufacturing; H. L. Hu for help in electrophysiological recordings; Y. Dan and J. F. Erlich for communication on spike sorting; H. Y. Zoghbi for VGAT-Cre mice; B. L. Roth for DREADD vectors; Z. L. Qiu, H. L. Hu, and X. Yu for help on AAV virus packaging and transgenic mice; A. K. Guo for help in PID experiments; Q. Hu for help in imaging experiments; Y. G. Sun for histochemistry experiments; Y. F. Li for help in drawing diagrams; and M. M. Poo and R. Desimone for critical comments on the manuscript. The work was supported by Chinese 973 Program (2011CBA00406), the State Key Laboratory of Neuroscience, and Chinese Academy of Sciences Hundreds of Talents Program (to C.T.L.). All the behavioral, optogenetic, electrophysiological, and histochemical data are archived in Institute of Neuroscience, Shanghai Institutes for Biological Sciences, Chinese Academy of Sciences.

SUPPLEMENTARY MATERIALS

www.sciencemag.org/content/346/6208/458/suppl/DC1
Materials and Methods
Figs. S1 to S35
Tables S1 to S8
References (*31–42*)
Movies S1 and S2

27 May 2014; accepted 16 September 2014
10.1126/science.1256573

EVOLUTIONARY BIOLOGY

Rapid evolution of a native species following invasion by a congener

Y. E. Stuart,[1]*†‡ T. S. Campbell,[2]* P. A. Hohenlohe,[3] R. G. Reynolds,[1,4] L. J. Revell,[4] J. B. Losos[1]

In recent years, biologists have increasingly recognized that evolutionary change can occur rapidly when natural selection is strong; thus, real-time studies of evolution can be used to test classic evolutionary hypotheses directly. One such hypothesis is that negative interactions between closely related species can drive phenotypic divergence. Such divergence is thought to be ubiquitous, though well-documented cases are surprisingly rare. On small islands in Florida, we found that the lizard *Anolis carolinensis* moved to higher perches following invasion by *Anolis sagrei* and, in response, adaptively evolved larger toepads after only 20 generations. These results illustrate that interspecific interactions between closely related species can drive evolutionary change on observable time scales.

In their classic paper, Brown and Wilson (*1*) proposed that mutually negative interactions between closely related species could lead to evolutionary divergence when those species co-occurred. In the six decades since, this idea has been debated vigorously, with support that has vacillated, depending on the latest set of theoretical treatments and comparative studies [reviewed in (*2–5*)]. However, tests of interaction-driven evolutionary divergence have been slow to capitalize on the growing recognition that evolutionary change can occur rapidly in response to strong divergent natural selection [but see (*6–9*)]; thus, evolutionary hypotheses about phenomena once thought to transpire on time scales too long for direct observation can be tested in real time while using replicated statistical designs.

An opportunity to study such real-time divergence between negatively interacting species has been provided by the recent invasion of the Cuban brown anole lizard, *Anolis sagrei*, into the southeastern United States, where *Anolis carolinensis* is the sole native anole. These species have potential to interact strongly [e.g., (*10*)], being very similar in habitat use and ecology (*11*). We investigated the eco-evolutionary consequences of this interaction on islands in Florida (*12*) using an *A. sagrei* introduction experiment, well-documented natural invasions by *A. sagrei*, genomic analyses of population structure, and a common garden experiment. This multifaceted approach can rule against several of the most

[1]Museum of Comparative Zoology and Department of Organismic and Evolutionary Biology, Harvard University, Cambridge, MA, USA. [2]Department of Biology, University of Tampa, Tampa, FL, USA. [3]Department of Biological Sciences and Institute for Bioinformatics and Evolutionary Studies, University of Idaho, Moscow, ID, USA. [4]Department of Biology, University of Massachusetts, Boston, MA, USA.
*These authors contributed equally to this work. **†Corresponding author. E-mail: yestuart@utexas.edu** ‡Present address: Department of Integrative Biology, University of Texas, Austin, TX, USA.

difficult alternative hypotheses [e.g., plasticity, ecological sorting, environmental gradients (*2*, *5*)] while directly testing two predictions for how *A. carolinensis* responds to its congeneric competitor.

Typical of solitary anoles (*13*), *A. carolinensis* habitat use spans ground to tree crown (*14*). However, where *A. carolinensis* and *A. sagrei* (or their close relatives) co-occur elsewhere, *A. carolinensis* perches higher than *A. sagrei* (*13*–*16*). Thus, we used an introduction experiment to test Collette's prediction (*14*) that competitive interactions with *A. sagrei* should drive an increase in *A. carolinensis* perch height. In early May 1995, we chose six islands that contained resident populations of *A. carolinensis* and collected pre-introduction perch height data from undisturbed lizards (*12*). Later that month, we introduced small populations of *A. sagrei* to three treatment islands, leaving three control islands containing only *A. carolinensis* (*12*). From May to August 1995–1998, we measured perch heights for both species. The *A. sagrei* populations grew rapidly [table S1; (*17*)], and by August 1995, *A. carolinensis* on treatment islands already showed a significant perch height increase relative to controls, which was maintained through the study [Fig. 1, fig. S1, and table S2; (*12*)].

We next predicted, following (*14*), that this arboreal shift by *A. carolinensis* would drive the evolution of larger toepads with more lamellae (adhesive, setae-laden, subdigital scales). Toepad area and lamella number (body-size corrected) correlate positively with perch height among anole species (*14*, *18*–*20*), and larger and better-developed toepads improve clinging ability (*20*), permitting anoles to better grasp unstable, narrow, and smooth arboreal perches. We tested the prediction in 2010 on a set of islands partially overlapping those used in 1995–1998 (*12*). We surveyed 30 islands and found that *A. sagrei* had colonized all but five (*12*). We compared *A. carolinensis* populations on these five islands without the invader (hereafter "un-invaded") to *A. carolinensis* populations on six islands that, on the basis of 1994 surveys, were colonized by *A. sagrei* sometime between 1995 and 2010 (hereafter "invaded") [Fig. 2; (*12*)].

From May to August 2010, we measured perch height for undisturbed lizards and found that, as in the 1995 introduction experiment, *A. carolinensis* perch height was significantly higher on invaded islands [fig. S2 and table S3; (*12*)]. We then tested whether the perch height shift had driven toepad evolution by measuring toepad area and lamella number of the fourth toe of each hind-leg for every *A. carolinensis* captured (*12*). We found that *A. carolinensis* on invaded islands indeed had larger toepads and more lamellae [traits corrected for body size; Fig. 3, A and C, and table S3; (*12*)]).

This morphological change occurred quickly. Assuming, conservatively, that *A. sagrei* reached all six invaded islands in 1995, *A. carolinensis* populations on invaded and un-invaded islands have diverged at mean rates of 0.091 (toepad area) and 0.077 (lamellae) standard deviations per generation [haldanes (*21*); rates > zero, each one-tailed $P < 0.02$; (*12*)], comparable to other examples of rapid evolution (*21*) such as soapberry bug beak length (*22*) or guppy life history (*23*).

We tested several alternative processes that could have generated the observed divergence. First, we used a common garden experiment to investigate possible posthatching, developmental responses to physical challenges imposed by arboreality during growth (i.e., phenotypic plasticity). We took gravid *A. carolinensis* females from four invaded and four un-invaded islands in July 2011, collected their eggs in the laboratory, and raised the offspring in identical conditions (*12*). The effect of *A. sagrei* invasion on *A. carolinensis* toepad characteristics persisted in the common garden [Fig. 3, B and D,

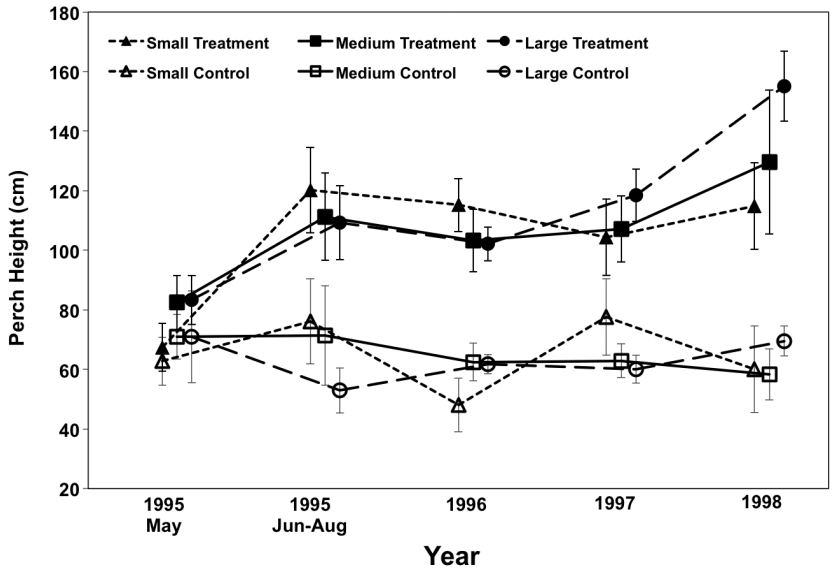

Fig. 1. Perch height shift by *A. carolinensis* after the experimental introduction of *A. sagrei*. We introduced *A. sagrei* to one small, one medium, and one large island (treatment; closed symbols) in 1995, keeping three similarly sized control islands (open symbols). Island means (±1 SE) are shown for perch height. *Anolis sagrei* introduction corresponds with a significant perch height increase by *A. carolinensis* (linear mixed models: treatment × time interactions, all $P < 0.001$ [(*12*)]; tables S1 and S2].

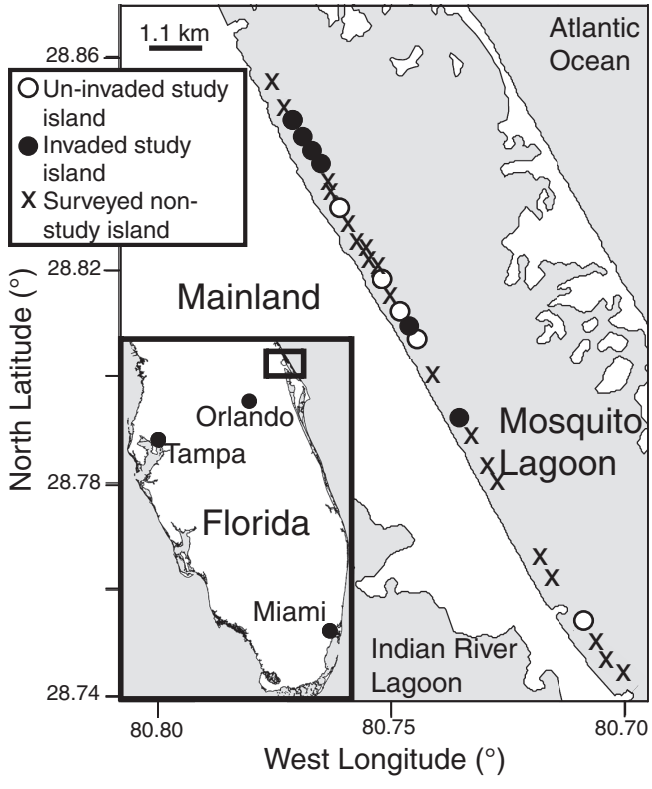

Fig. 2. 2010 study islands along the Intracoastal Waterway. *Anolis carolinensis* inhabits all study islands. Six study islands were invaded by *A. sagrei* sometime between 1995 and 2010 (closed circles), and five study islands remain un-invaded today (open circles). Nineteen additional non–study islands were surveyed ["x"; (*12*)]; 17 of these contained *A. carolinensis* and were invaded by *A. sagrei*; and two were empty of both species.

and table S4; (*12*)], suggesting genetically based divergence in nature (though we cannot rule out transgenerational plasticity).

Second, observed divergence in *A. carolinensis* could have arisen through nonrandom migration of individuals with large toepads among invaded islands, instead of arising independently on each island. Thus, we tested whether relatedness among *A. carolinensis* populations is independent of *A. sagrei* invasion. In 379 *A. carolinensis* individuals from four un-invaded and five invaded islands, we genotyped 121,973 single-nucleotide polymorphisms across the genome [table S5, (*12*)]. Individuals from the same island were closely related, and islands were largely genetically independent (pairwise-F_{ST} 0.09–0.16; table S6). We found no evidence that population relatedness in *A. carolinensis* was correlated with whether an island had been colonized by *A. sagrei* [Fig. 4; (*12*)] or with distance between islands (Mantel test; $P > 0.25$), suggesting that gene flow is relatively limited among islands and that island populations were independently founded from the mainland.

Third, toepad changes could have been generated by adaptation to environmental differences among islands that are confounded with the presence of *A. sagrei* [e.g., (*24*)]. However, invaded and un-invaded islands do not differ in characteristics important to perching or arboreal locomotion [e.g., vegetated area, plant species richness, or available tree heights; table S7; (*12*)]. Fourth, toepad changes could have arisen through ecological sorting, wherein *A. sagrei* was only able to colonize those islands on which the existing *A. carolinensis* population was already sufficiently different. However, *A. sagrei* seems capable of successfully colonizing every island it reaches, regardless of resident *A. carolinensis* ecology or morphology: All 10 *A. sagrei* populations introduced in 1994–1995 are still extant (*12*), and *A. sagrei* inhabits nearly every other island surveyed in the lagoon (Fig. 2). Finally, toepad changes observed in *A. carolinensis* in 2010 could be unrelated to interactions with *A. sagrei* if the latter's invasion merely missed the five islands with the lowest *A. carolinensis* perch heights (fig. S2) by chance; however, this would occur only one time in 462. In sum, alternative hypotheses of phenotypic plasticity, environmental heterogeneity, ecological sorting, nonrandom migration, and chance are not supported; our data suggest strongly that interactions with *A. sagrei* have led to evolution of adaptive toepad divergence in *A. carolinensis*.

Brown and Wilson called evolutionary divergence between closely related, sympatric species "character displacement" (*1*), and our data constitute a clear example of this. Resource competition has been the interaction suggested most often as the source of divergent selection during character displacement [sometimes specifically called "ecological character displacement" (*1–3*)]. For *A. carolinensis* and *A. sagrei*, resource competition for space likely is important: Allopatric *A. carolinensis* and *A. sagrei* overlap in their use of the habitat (*12–14*, *16*); moreover, when they co-occur, the two species interact agonistically (*10*), and our experimental data show a rapid spatial shift by *A. carolinensis* following *A. sagrei* introduction. The two species also overlap in diet and thus may compete for food (*17*). Competition for food is strong among co-occurring *Anolis* and has been shown to be mitigated by differences in perch height (*11*). Evolutionary divergence may also arise, however, from selection to reduce

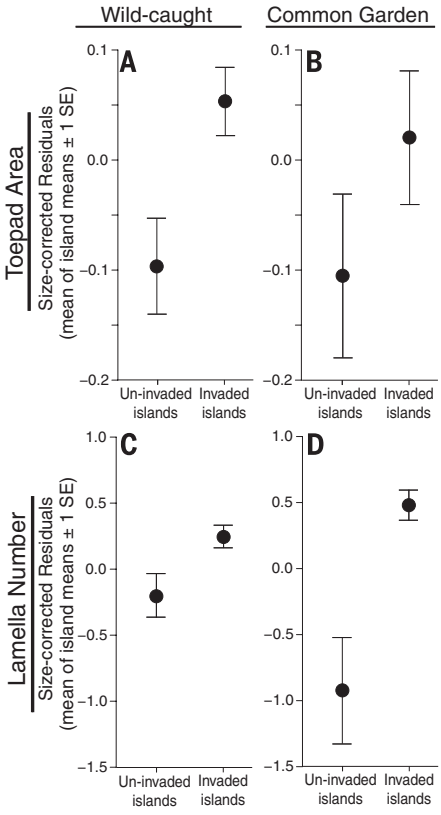

Fig. 3. Divergence in wild-caught and common garden *A. carolinensis*. Mean-of-island-means size-corrected residuals (±1 SE) are shown. The invasion of *A. sagrei* corresponds to a significant increase in both traits for wild-caught lizards (**A** and **C**) in 2010 [five islands un-invaded, six invaded; linear mixed models (LMM); (A) toepad area, $\beta_{invaded} = 0.15$, $t_9 = 2.7$, $P = 0.012$; (C) lamella number, $\beta_{invaded} = 0.54$, $t_9 = 3.1$, $P = 0.009$]. (**B** and **D**) Common garden offspring from invaded islands had significantly larger toepad characteristics [four un-invaded islands; four invaded; LMM; (B) toepad area, $\beta_{invaded} = 0.14$, $t_6 = 2.1$, $P = 0.043$; (D) lamella number, $\beta_{invaded} = 1.45$, $t_6 = 3.6$, $P = 0.006$]. All *P* values are one-tailed.

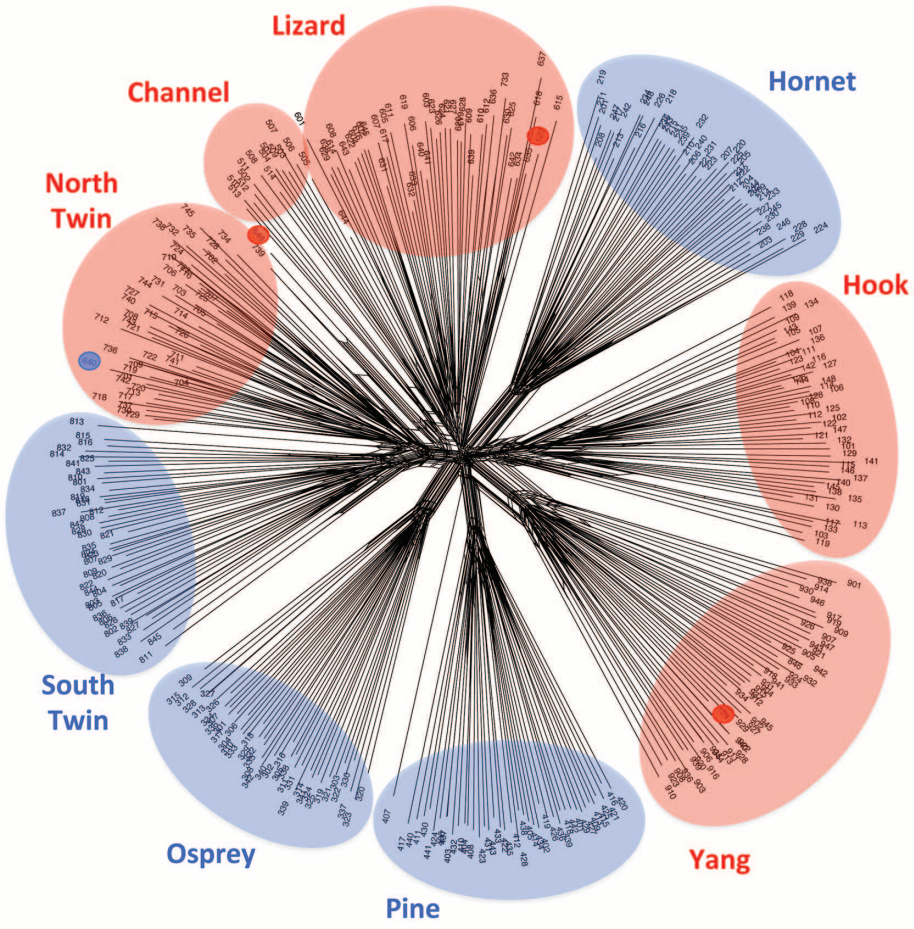

Fig. 4. Neighbor-net analysis of genetic distance for *A. carolinensis* individuals from invaded (red) and un-invaded (blue) islands (*12*). Small shaded areas enclose individuals that do not cluster with their own island; the color of these areas represents invasion status of their home islands.

interspecific hybridization; yet, such "reproductive character displacement" (*4*) seems an unlikely explanation for our results, as *A. carolinensis* and *A. sagrei* already differ markedly in species-recognition characteristics, males of both species nearly exclusively ignore heterospecific females in staged encounters (*25*), and the species have never been reported to successfully produce hybrids. We note, finally, that other mutually negative interactions such as apparent competition (*26*) and intraguild predation (*27*) could also produce divergence among overlapping species. These remain to be explored in this system, though some evidence exists for at least the latter (*17*).

Here, we have provided evidence from a replicated, natural system to support the long-held idea (*4*) that interspecific interactions between closely related species are an important force for evolutionary diversification (*2*). Moreover, we show that evolutionary hypotheses such as character displacement can be rigorously tested in real time following human-caused environmental change. Our results also demonstrate that native species may be able to respond evolutionarily to strong selective forces wrought by invaders. The extent to which the costs of invasions can be mitigated by evolutionary response remains to be determined (*28*), but studies such as this demonstrate the ongoing relevance of evolutionary biology to contemporary environmental issues.

REFERENCES AND NOTES

1. W. L. Brown, E. O. Wilson, *Syst. Zool.* **5**, 49–64 (1956).
2. D. Schluter, *The Ecology of Adaptive Radiation* (Oxford Univ. Press, Oxford, UK, 2000).
3. T. Dayan, D. Simberloff, *Ecol. Lett.* **8**, 875–894 (2005).
4. D. W. Pfennig, K. S. Pfennig, *Evolution's Wedge* (Univ. of California Press, Berkeley, 2012).
5. Y. E. Stuart, J. B. Losos, *Trends Ecol. Evol.* **28**, 402–408 (2013).
6. P. R. Grant, B. R. Grant, *Science* **313**, 224–226 (2006).
7. J. G. Tyerman, M. Bertrand, C. C. Spencer, M. Doebeli, *BMC Evol. Biol.* **8**, 34 (2008).
8. L. M. Bono, C. L. Gensel, D. W. Pfennig, C. L. Burch, *Biol. Lett.* **9**, 20120616 (2013).
9. M. L. Taper, in *Bruchids and Legumes: Economics, Ecology, and Coevolution*, K. Fujii, A. Gatehouse, C. D. Johnson, R. Mitchel, T. Yoshida, Eds. (Kluwer, Dordrecht, Netherlands, 1990), pp. 289–301.
10. J. R. Edwards, S. P. Lailvaux, *Biol. J. Linn. Soc. Lond.* **110**, 843–851 (2013).
11. J. B. Losos, *Lizards in an Evolutionary Tree: Ecology and Adaptive Radiation of Anoles* (Univ. of California Press, Berkeley, 2009).
12. Information on materials and methods is available on *Science* Online.
13. T. W. Schoener, *Ecol. Monogr.* **45**, 233–258 (1975).
14. B. B. Collette, *Bull. Mus. Comp. Zool.* **125**, 137–162 (1961).
15. L. R. Schettino *et al*., *Breviora* **520**, 1–22 (2010).
16. J. R. Edwards, S. P. Lailvaux, *Ethology* **118**, 494–502 (2012).
17. T. S. Campbell, thesis, University of Tennessee, Knoxville (2000).
18. D. Glossip, J. B. Losos, *Herpetologica* **53**, 192–199 (1997).
19. T. E. Macrini, D. J. Irschick, J. B. Losos, *J. Herpetol.* **37**, 52–58 (2003).
20. J. Elstrott, D. J. Irschick, *Biol. J. Linn. Soc. Lond.* **83**, 389–398 (2004).
21. A. P. Hendry, M. T. Kinnison, *Evolution* **53**, 1637–1653 (1999).
22. S. P. Carroll, C. Boyd, *Evolution* **46**, 1052–1069 (1992).
23. D. N. Reznick, F. H. Shaw, F. H. Rodd, R. G. Shaw, *Science* **275**, 1934–1937 (1997).
24. S. Meiri, D. Simberloff, T. Dayan, *J. Anim. Ecol.* **80**, 824–834 (2011).
25. R. R. Tokarz, J. W. Beck Jr., *Anim. Behav.* **35**, 722–734 (1987).
26. R. D. Holt, *Theor. Popul. Biol.* **12**, 197–29 (1977).
27. G. A. Polis, C. A. Myers, R. D. Holt, *Annu. Rev. Ecol. Syst.* **20**, 297–330 (1989).
28. R. Shine, *Evol. Appl.* **5**, 107–116 (2012).

ACKNOWLEDGMENTS

We thank A. Kamath, C. Gilman, A. Algar, J. Allen, E. Boates, A. Echternacht, A. Harrison, H. Lyons-Galante, T. Max, J. McCrae, J. Newman, J. Rifkin, M. Stimola, P. VanMiddlesworth, K. Winchell, C. Wiench, K. Wollenberg, and three reviewers; M. Legare and J. Lyon (Merritt Island National Wildlife Refuge), J. Stiner and C. Carter (Canaveral National Seashore); and Harvard University, Museum of Comparative Zoology, University of Massachusetts Boston, University of Tennessee Knoxville, University of Tampa, NSF (DEB-1110521), and NIH (P30GM103324) for funding. Y.E.S., T.S.C., and J.B.L. designed the study; Y.E.S., T.S.C., P.A.H., L.J.R, and R.G.R. collected the data; Y.E.S., T.S.C., and P.A.H. analyzed the data; all authors contributed to the manuscript. Data are accessioned on datadryad.org: doi:10.5061/dryad.96g44.

SUPPLEMENTARY MATERIALS

www.sciencemag.org/content/346/6208/463/suppl/DC1
Materials and Methods
Supplementary Acknowledgments
Figs. S1 and S2
Tables S1 to S7
References (*29*–*45*)

5 June 2014; accepted 15 September 2014
10.1126/science.1257008

NEW WORLD ARCHAEOLOGY

Paleoindian settlement of the high-altitude Peruvian Andes

Kurt Rademaker,[1,2,8]* Gregory Hodgins,[3] Katherine Moore,[4] Sonia Zarrillo,[5] Christopher Miller,[6,7] Gordon R. M. Bromley,[8] Peter Leach,[9] David A. Reid,[10] Willy Yépez Álvarez,[11] Daniel H. Sandweiss[1,8]

Study of human adaptation to extreme environments is important for understanding our cultural and genetic capacity for survival. The Pucuncho Basin in the southern Peruvian Andes contains the highest-altitude Pleistocene archaeological sites yet identified in the world, about 900 meters above confidently dated contemporary sites. The Pucuncho workshop site [4355 meters above sea level (masl)] includes two fishtail projectile points, which date to about 12.8 to 11.5 thousand years ago (ka). Cuncaicha rock shelter (4480 masl) has a robust, well-preserved, and well-dated occupation sequence spanning the past 12.4 thousand years (ky), with 21 dates older than 11.5 ka. Our results demonstrate that despite cold temperatures and low-oxygen conditions, hunter-gatherers colonized extreme high-altitude Andean environments in the Terminal Pleistocene, within about 2 ky of the initial entry of humans to South America.

Human settlement of high-altitude mountains and plateaus is among the most recent of our species' biogeographic expansions. Earth's highest-altitude lands, located in the Tibetan and Andean regions, pose numerous physiological challenges, including hypoxia (low-oxygen conditions), high solar radiation, cold temperatures, and high energetic costs of subsistence (*1*). These conditions are especially prevalent in the treeless landscapes higher than 4000 meters above sea level (masl), with little fuel for campfires, twice the sea-level caloric intake needed to maintain normal metabolic function (*2*), and O_2 partial pressure less than 60% that at sea level (*1*). Current archaeological models (*3*) emphasize these challenges to explain a lack of pre-Holocene [>11.5 thousand years ago (ka)] (*4*) archaeological evidence above 4000 masl on the Tibetan (*5*) and Andean (*6*) Plateaus.

In the Andes, human biogeographic expansion to high-altitude lands likely stemmed from adjacent areas in Peru (*6*), Chile (*7*), and Argentina (*8*) (Fig. 1A). By ~13.5 to 12.1 ka or earlier, foragers had settled the Pacific Coast (*9*–*13*) and the Southern Cone (*14*), and by ~12.7 to 11.3 ka groups occupied caves at ~2600 masl in central Peru (*15*, *16*) and up to 3300 masl in the Atacama Desert of northern Chile (*17*, *18*). In northwest Argentina, multiple sites at 3400 to 3800 masl date to ~12.0 ka, possibly as early as ~12.8 ka (*8*), although most pre-Holocene occupations have only single, unreplicated radiocarbon ages. Above 4000 masl, the earliest known Andean sites (table S1) date from the first millennium of the Holocene (*19*), with widespread occupation after ~9 ka (*6*–*8*) and earliest year-round settlement after ~7.1 ka (*20*).

Whether genetic adaptations or environmental amelioration were necessary for high-altitude

[1]Department of Anthropology, South Stevens Hall, University of Maine, Orono, ME 04469-5773, USA. [2]Department of Early Prehistory and Quaternary Ecology, Schloß Hohentübingen, Burgsteige 11, 72070 Tübingen, Germany. [3]Accelerator Mass Spectrometry Laboratory, Department of Physics and School of Anthropology, University of Arizona, Tucson, AZ 85721, USA. [4]University of Pennsylvania Museum, 3260 South Street, Philadelphia, PA 19104, USA. [5]Department of Anthropology and Archaeology, Earth Sciences Building, Room 806, 844 Campus Place Northwest, Calgary, British Columbia, Canada. [6]Institute for Archaeological Sciences, University of Tübingen, Rümelinstrasse 23, 72070 Tübingen, Germany. [7]Senckenberg Centre for Human Evolution and Paleoenvironment, University of Tübingen, Rümelinstrasse 23, 72070 Tübingen, Germany. [8]Climate Change Institute, Bryand Global Sciences Center, University of Maine, Orono, ME 04469, USA. [9]Department of Anthropology, 354 Mansfield Road, University of Connecticut, Storrs, CT 06269-1176, USA. [10]Department of Anthropology, University of Illinois at Chicago, Behavioral Sciences Building, 1007 West Harrison Street, Chicago, IL 60607-7139, USA. [11]Arequipa, Peru.
*Corresponding author. E-mail: kurt.rademaker@umit.maine.edu

human settlement remains poorly understood. High-altitude regions are among the most remote and least archaeologically studied lands on the planet. Here, we report initial data from Terminal Pleistocene archaeological sites at nearly 4500 masl in the Peruvian Andes, the highest Pleistocene sites yet identified anywhere in the world. These sites extend the residence time of humans above 4000 masl by nearly a millennium, implying more moderate late-glacial Andean environments and greater physiological capabilities for Pleistocene humans than previously assumed.

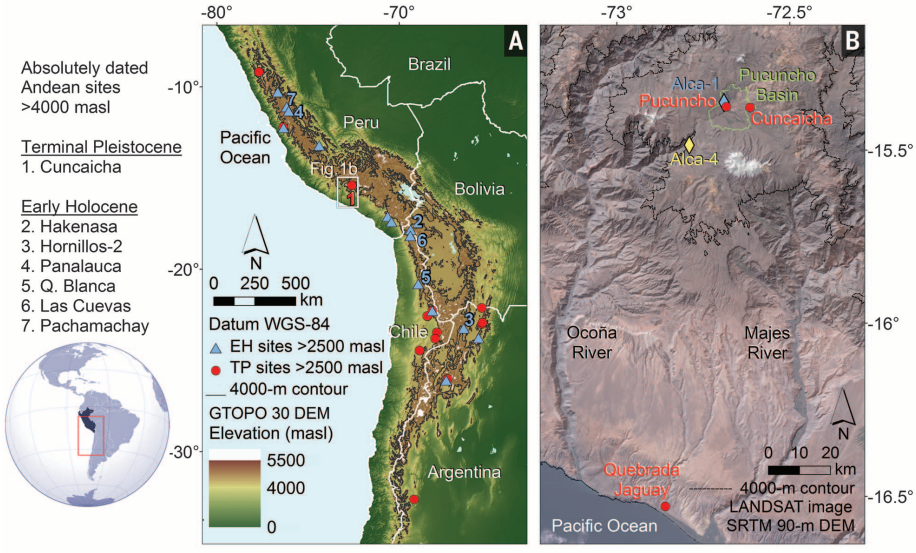

Fig. 1. Project area maps. (**A**) Andes showing Terminal Pleistocene and Early Holocene sites >2500 masl and >4000 masl (also see table S1). (**B**) Study area.

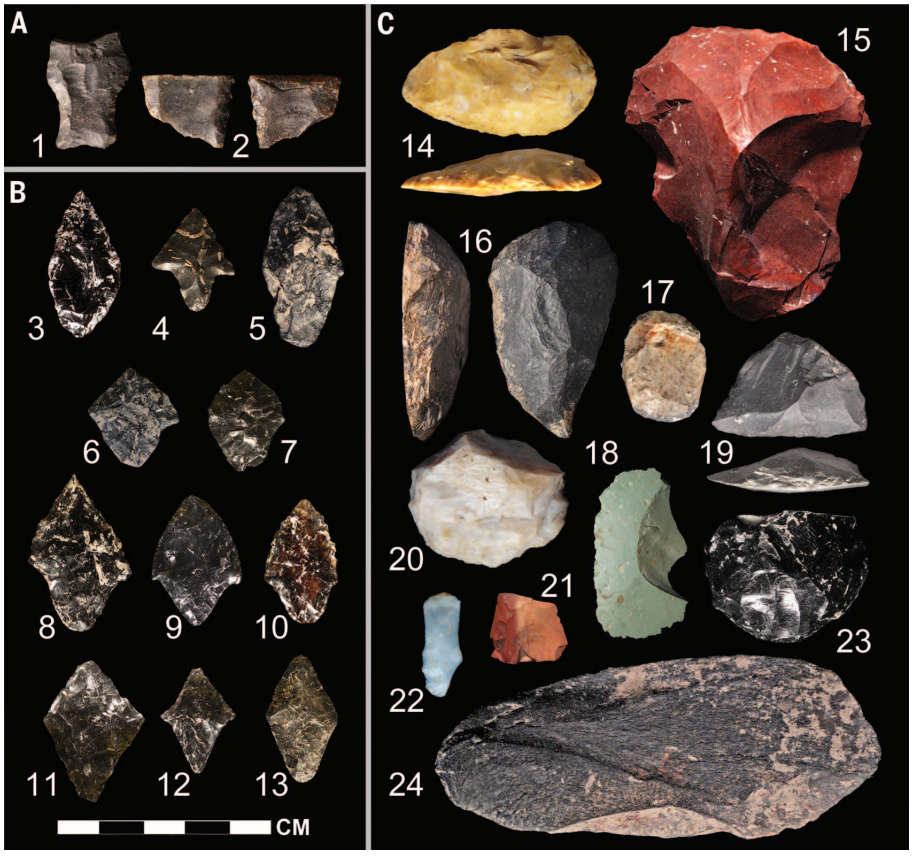

Fig. 2. Terminal Pleistocene lithic artifacts. From (**A**) Pucuncho workshop (1 and 2) and (**B** and **C**) Cuncaicha rock shelter (3 to 24) (also see table S4). (B) Projectile points (3 to 13) illustrated in stratigraphic order. (C) Selected tools and debitage (14 to 24) illustrating diverse forms and raw materials.

We discovered the Pucuncho and Cuncaicha archaeological sites (Fig. 1B and fig. S1) after mapping of the Alca obsidian source (*21*), predictive modeling (*22*), and systematic reconnaissance of the volcanic plateau bounded by the Cotahuasi and Colca canyons of southern Peru (*23*). In the heart of this plateau, the 132-km^2 Pucuncho Basin contains grassland and wetland habitats and thousands of domesticated camelids. The modern annual mean temperature at Pucuncho is 3°C, and prevailing easterly airflow maintains a semiarid climate, with 600 to 800 mm of annual precipitation primarily during the December to March wet season (*24*).

The Pucuncho open-air workshop site (4355 masl) on the basin's west edge was situated to exploit Alca-1 and Alca-5 obsidian pyroclasts eroding from an alluvial fan. The workshop includes debitage and 260 formal tools, including projectile points and nondiagnostic bifaces, unifacial scrapers, and other tools. Two fluted fishtail projectile point bases made of local fine-grained andesite and Alca-5 obsidian (Fig. 2A) are diagnostic to ~12.8 to 11.5 ka (*25*); the Pucuncho fishtails are the highest fluted points yet discovered in the Americas. Pucuncho likely provided the Alca-1 obsidian in contexts dated ~13.4 to 10.2 ka at Quebrada Jaguay, a Terminal Pleistocene fishing settlement ~150 km south on the Pacific Coast (*9*) (Fig. 1B). Because no geologic mechanism can transport Alca-1 obsidian to the coast, Quebrada Jaguay's inhabitants either visited the source or obtained obsidian via exchange.

Seven km east of the Pucuncho site, the Cuncaicha workshop site (4445 masl) occupies an alluvial fan where Alca-5 and Alca-7 obsidian pyroclasts crop out. This surface palimpsest contains debitage and more than 500 projectile points and nondiagnostic bifaces, scrapers, and other unifacial tools, representing thousands of years of episodic occupation. Above the alluvial fan is Cuncaicha rock shelter (4480 masl), comprising two north-facing alcoves formed by slab exfoliation of the andesite bedrock. Both alcoves exhibit sooted ceilings, rock art, and anthropogenic floor sediments, indicating use as campsites. The rock shelter is protected from westerly winds and offers a commanding view of wetland and grassland habitats.

Our investigations at Cuncaicha rock shelter sampled the minimum volume needed to document the stratigraphy and establish a precise absolute chronology of occupation. Ground-penetrating radar revealed collapsed roof slabs and depth of sediments to bedrock, allowing targeted excavations. Sediments are ~1.2 m deep, both within the shelter and outside the drip line over ~150 m^2. We excavated 5.5 m^2 (<4%) of these deposits in 2010 and 2012 (fig. S2).

We dated the Cuncaicha sequence using large-mammal bone specimens in direct association with abundant, unequivocal artifacts. Faunal and other organic remains exhibit outstanding preservation in this cold, dry setting. Moreover, dating large bone specimens avoided the risk of sampling remains vertically translocated by rodent bioturbation, a process shown to affect Andean rock

shelters elsewhere (*15*). Geoarchaeological analysis indicates only small-scale cryo- and bioturbation of deposits (*26*) (fig. S4).

We obtained 35 accelerator mass spectrometry (AMS) ages at three laboratories using distinct pretreatment protocols on bone collagen (*26*) (table S2). Dates on split samples at multiple laboratories are statistically indistinguishable. The AMS-dated bone specimens are in correct stratigraphic order, without reversals. Cuncaicha rock shelter contains occupation components corresponding with five distinct strata (fig. S3). Hiatuses correspond with clear stratigraphic signatures and are well constrained with AMS ages (Table 1 and table S2).

Feature 12-4 (an organic-rich pit containing artifacts) yielded the oldest reproduced ages, ~12.4 to 11.8 ka (n = 2 AMS ages). Stratum 5 is composed largely of carbonates, likely derived from anthropogenic burning of plants, including the local, resinous *Azorella compacta* (*26*) (fig. S5). Terminal Pleistocene-age deposits lack visible stratigraphic divisions. We grouped and averaged AMS ages by excavation level (Table 1). The positive age-depth relationship (Fig. 3) suggests episodic deposition ~12.4 to 11.4 ka (n = 19 AMS ages). The upper contact of stratum 5 is sharp and distinct, likely formed during an occupation hiatus ~11.4 to 9.5 ka. Stratum 4 corresponds to a brief, robust Early Holocene occupation ~9.5 to 9.3 ka (n = 6 AMS ages), followed by a ~3.6 thousand year (ky) mid-Holocene hiatus. Stratum 3 includes distinct late-Middle Holocene occupations dated ~5.7 to 5.5 ka (n = 3 AMS ages) and ~5.5 to 5.1 ka (n = 3 AMS ages). Strata 1 and 2 represent brief, episodic uses of the shelter within the past ~2.2 ky (n = 2 AMS ages) (table S2).

Cuncaicha contains a rich assemblage of ceramics; chipped-stone tools, cores, and debitage; faunal material; bone beads and quartz crystals; and fragments of red ochre (table S3). Ceramics, which locally date <4 ka (*27*), were found only in Late Holocene strata 1 and 2. Temporal affiliations for the 153 projectile points found throughout the stratigraphy (*23*, *28*) are consistent with the AMS chronology. A complete lithic operational chain is present at Cuncaicha shelter and the workshop below. Most lithic tools and debitage at Cuncaicha are made from locally available Alca-1, -5, and -7 obsidian, andesite, and jasper. Lithic tools indicate hunting and butchering activities, consistent with the limited subsistence options on the plateau.

The inhabitants of Cuncaicha hunted vicuña (*Vicugna vicugna mensalis*), guanaco (*Lama guanaco*), and taruka (*Hippocamelus antisensis*) (tables S5 and S6). Preliminary analysis of camelid age profiles suggests predation at the end of the rainy season when vicuña are born (March and April) and possibly during the dry season (May to November) when vicuña bands aggregate (*29*). The even representation of mammal fore- and hindlimb elements indicates dismembering of whole carcasses at the shelter. First and second phalanges are abundant, and the skinning of animals to the toes attests to careful processing of all animal foods, including meat and fat within the bone.

We recovered small, fragmented charred plant remains from sediments (*26*). Most abundant are woody twigs, stems, and root wood, consistent with burning small shrubs and *Azorella compacta*. Also present are charred fragments of parenchymous storage tissue (fig. S6). Their vitreous appearance indicates that these are starchy roots and/or tubers (*30*), likely gathered from lower elevations and brought to the site for consumption (*26*).

Cuncaicha is ~40 to 50 km from elevations ≤2500 masl, so it is unlikely that the site was merely a logistical station for the collection and processing of lithic material, meat, and hides for transport to low-elevation base camps. Together, the quantity and diversity of early tool types; the emphasis on local lithic materials, animals, and combustible fuel; the presence of starchy roots and/or tubers; and the location in the heart of the plateau suggest that Cuncaicha was a base camp.

The Pucuncho Basin constituted a high-altitude oasis ideal for a specialized hunting (and later, herding) adaptation. Vicuña births coinciding with the end of the wet season and maintenance of permanent territories by vicuña bands (*29*) would have permitted predictable scheduling of subsistence activities and year-round plateau residence (*31*). However, wet-season storms and the risk of hypothermia, as well as maintenance of extended

Table 1. Average AMS ages from Cuncaicha rock shelter. Component abbreviations: LMH, Late-Middle Holocene; EH, Early Holocene; TP, Terminal Pleistocene. Two Late Holocene AMS ages were not averaged and are reported in table S2. Stratigraphic abbreviations: L, Level; F, Feature. CALIB 7.0.0 (*39*) reports the test statistic T for a series of uncalibrated ^{14}C ages from the same stratigraphic context (n) having a X^2 distribution with $n - 1$ degrees of freedom (df) under the null hypothesis of no difference with respect to a threshold of $\alpha = 0.05$ (*40*). Weighted means were calculated for statistically indistinguishable groups of stratigraphically equivalent ages and calibrated using SHCal13 (*41*). ^{14}C yr B.P., radiocarbon years before the present. 68%/95% cal B.P., 68% and 95% probability age range in calendar years before the present.

Component	Context	*n*	df	*T*	0.05	^{14}C yr B.P.	68% cal B.P.	95% cal B.P.
LMH-II	30–33 cm	3	2	1.2	6.0	4614 ± 36	5446–5302	5466–5088
LMH-I	40–45 cm	3	2	0.8	6.0	4867 ± 37	5644–5586	5660–5484
EH	50–62 cm	6	5	2.0	11.1	8420 ± 34	9486–9432	9525–9324
TP	L.8-8b, 77–79 cm	3	2	0.5	6.0	10,074 ± 57	11,764–11,406	11,964–11,346
TP	L.9, 79–83 cm	3	2	0.2	6.0	10,073 ± 49	11,760–11,408	11,958–11,357
TP	L.11, 90–98 cm	2	1	0.1	3.8	10,182 ± 50	11,982–11,769	12,067–11,641
TP	L.12, 98–108 cm	2	1	0.8	3.8	10,191 ± 32	11,980–11,822	12,036–11,761
TP	L.13, 108–115 cm	7	6	7.8	12.6	10,228 ± 18	11,953–11,809	12,004–11,759
TP	F.12-4 base	2	1	0.2	3.8	10,345 ± 71	12,386–11,953	12,411–11,822

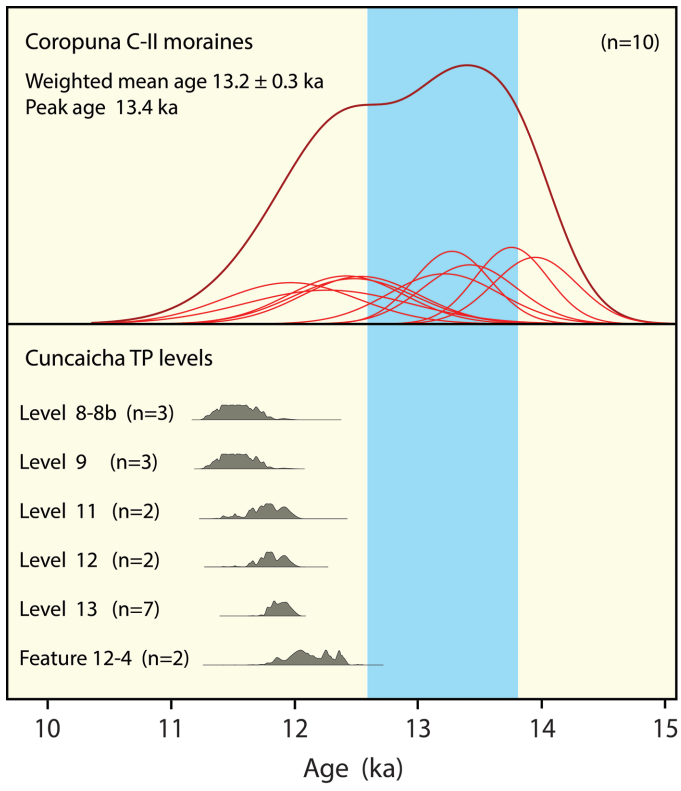

Fig. 3. Nevado Coropuna ^{3}He ages from C-II moraines and average AMS ages from Cuncaicha rock shelter Terminal Pleistocene levels. Blue bar shows 95% range of C-II weighted mean age.

social networks and collection of edible plant resources, may have encouraged regular descents to lower elevations.

Lithic tools and debitage of nonlocal fine-grained rocks, some with stream-polished cortex (Fig. 2C), suggest that Terminal Pleistocene and Early Holocene plateau residents ventured periodically to high-energy rivers below the plateau. Formal tools of Alca-4 obsidian at Cuncaicha originated in outcrops near the plateau edge ~22 km southwest (*21*) (Fig. 1B). Contemporary sites at Quebrada Jaguay on the Pacific Coast contain Alca-1, -4, and -5 obsidian tools and debitage (*9*, *23*); the only source of these three obsidians is the Pucuncho Basin and surrounding plateau (*21*). The oldest dates at Quebrada Jaguay and Cuncaicha overlap at two standard deviations. These sites likely constitute end members in a coast-highland Paleoindian settlement system.

Pleistocene glaciers did not present a barrier to human migration and settlement of the Pucuncho Basin. Glacial-geologic records from adjacent Nevado Coropuna (*32*) suggest that local glaciers reached their late-Pleistocene maxima ~25 to 20 ka and even then did not encroach into the basin. After a relatively minor readvance ~13.4 ka (*26*) (Fig. 3 and table S7), glaciers again receded. Southward displacement of the intertropical convergence zone ~13.0 to 11.5 ka (*33*) probably resulted in increased wet-season precipitation. The arrival of humans to the Pucuncho Basin coincided with a period of warming climate and enhanced primary productivity in plateau habitats.

Our data do not support previous hypotheses, which suggested that climatic amelioration and a lengthy period of human adaptation were necessary for successful human colonization of the high Andes. The Pucuncho Basin sites postdate the oldest known South American lowland site, Monte Verde (*13*), by only ~2 ky. Because early settlement of high-altitude regions is understudied, additional Terminal Pleistocene sites above 4000 masl likely await discovery. The Pucuncho Basin sites suggest that Pleistocene humans lived successfully at extreme high altitude, initiating organismal selection (*34*), developmental functional adaptations (*35*), and lasting biogeographic expansion in the Andes. As new studies (*36*–*38*) identify potential genetic signatures of high-altitude adaptation in modern Andean populations, comparative genomic, physiologic, and archaeological research will be needed to understand when and how these adaptations evolved.

REFERENCES AND NOTES

1. P. T. Baker, M. A. Little, *Man in the Andes: Multidisciplinary Study of High-Altitude Quechua* (Dowden, Hutchinson, and Ross, Stroudsberg, PA, 1976).
2. B. M. Marriot, S. J. Carlson-Newberry, Eds., *Nutritional Needs in Cold and High-Altitude Environments: Applications for Military Personnel in Field Operations* (National Academy Press, Washington, DC, 1996).
3. M. S. Aldenderfer, *World Archaeol.* **38**, 357–370 (2006).
4. All ages and ranges are two-sigma calibrated (2-σ cal).
5. P. J. Brantingham *et al.*, *Geoarchaeol.* **28**, 413–431 (2013).
6. K. Rademaker, G. R. M. Bromley, D. H. Sandweiss, *Quat. Int.* **301**, 34–45 (2013).
7. C. Méndez Melgar, *Quat. Int.* **301**, 60–73 (2013).
8. L. Prates, G. Politis, J. Steele, *Quat. Int.* **301**, 104–122 (2013).
9. D. H. Sandweiss *et al.*, *Science* **281**, 1830–1832 (1998).
10. S. deFrance, N. Grayson, K. Wise, *J. Field Archaeol.* **34**, 227–246 (2009).
11. D. Jackson, C. Méndez, R. Seguel, A. Maldonado, G. Vargas, *Curr. Anthropol.* **48**, 725–731 (2007).
12. T. D. Dillehay *et al.*, *Quat. Res.* **77**, 418–423 (2012).
13. T. D. Dillehay *et al.*, *Science* **320**, 784–786 (2008).
14. J. Steele, G. Politis, *J. Archaeol. Sci.* **36**, 419–429 (2009).
15. T. F. Lynch, *Guitarrero Cave: Early Man in the Andes* (Academic Press, New York, 1980).
16. E. A. Jolie, T. F. Lynch, P. R. Geib, J. M. Adovasio, *Curr. Anthropol.* **52**, 285–296 (2011).
17. M. Grosjean, L. Núñez, I. Cartajena, *J. Quat. Sci.* **20**, 643–653 (2005).
18. C. M. Santoro, L. Núñez, *Andean Past* **1**, 57–109 (1987).
19. Singular Terminal Pleistocene dates from Peruvian sites Pachamachay, Telarmachay, and PAn 12-58 are problematic (*6*) and generally rejected by the investigators; therefore, they are not included in this discussion.
20. J. W. Rick, K. M. Moore, *Boletín de Arqueología* **3**, 263–296 (1999).
21. K. Rademaker *et al.*, *Geology* **41**, 779–782 (2013).
22. K. Rademaker, D. A. Reid, G. R. M. Bromley, in *Least Cost Analysis of Social Landscapes: Archaeological Case Studies*. D. A. White, S. Surface-Evans, Eds. (University of Utah Press, Salt Lake City, UT, 2012), pp. 32–44.
23. K. Rademaker, thesis, University of Maine, Orono (2012).
24. U. Dornbusch, *Erdkunde* **52**, 41–54 (1998).
25. L. J. Jackson, in *Paleoindian Archaeology: A Hemispheric Perspective*. J. E. Morrow, C. Gnecco, Eds. (University of Florida Press, Gainesville, 2006), pp. 105–122.
26. Materials and methods are available as supporting materials on *Science* Online.
27. L. Perry *et al.*, *Nature* **440**, 76–79 (2006).
28. C. J. Klink, M. S. Aldenderfer, in *Advances in Titicaca Basin Archaeology, vol. 1.* C. Stanish, A. B. Cohen, M. S. Aldenderfer, Eds. (Cotsen Institute of Archaeology at UCLA, Los Angeles, 2005), pp. 25–54.
29. W. L. Franklin, in *Mammalian Biology in South America*, M. A. Mares, H. H. Genoways, Eds. (Volume 6, Special Publication Series, Pymatuning Laboratory of Ecology, University of Pittsburgh, Pittsburgh, 1981), pp. 457–489.
30. J. G. Hather, *Archaeological Parenchyma* (Archetype Publications, London, 2000).
31. J. W. Rick, *Prehistoric Hunters of the High Andes* (Academic Press, New York, 1980).
32. G. R. M. Bromley *et al.*, *Quat. Sci. Rev.* **28**, 2514–2526 (2009).
33. P.-H. Blard *et al.*, *Quat. Sci. Rev.* **30**, 3973–3989 (2011).
34. K. M. Weiss, A. W. Bigham, *Evol. Anthropol.* **16**, 164–171 (2007).
35. A. R. Frisancho, *Am. J. Hum. Biol.* **25**, 151–168 (2013).
36. A. W. Bigham *et al.*, *Am. J. Hum. Biol.* **25**, 190–197 (2013).
37. D. Zhou *et al.*, *Am. J. Hum. Genet.* **93**, 452–462 (2013).
38. C. A. Eichstaedt *et al.*, *PLOS ONE* **9**, e93314 (2014).
39. M. Stuiver, P. J. Reimer, *Radiocarbon* **35**, 215–230 (1993).
40. G. K. Ward, S. R. Wilson, *Archaeometry* **20**, 19–31 (1978).
41. A. G. Hogg *et al.*, *Radiocarbon* **55**, 1889–1903 (2013).

ACKNOWLEDGMENTS

Field work was supported by the Churchill Exploration Fund, National Geographic Society Waitt Foundation, Foundation for Exploration and Research on Cultural Origins, American Philosophical Society, and Lambda Alpha. B. Robinson and B. Hall funded pilot AMS dates. National Science Foundation Dissertation Grant no. 1208748 funded the AMS chronology. Pucuncho Basin pastoralists graciously allowed field work on their lands. A. Chu, R. Hintz, C. Mauricio, A. Ramos, A. Saenz, and E. Zuñiga provided invaluable logistical support. We thank field assistants W. Beckwith, K. Gardella, M. Koehler, T. Labanowski, O. McGlamery, E. Olson, and J. Wertheim and the staff of the Arizona AMS Laboratory. E. Cooper created Fig. 2. T. Koffman and P. Strand calibrated C-II ^{3}He ages for Fig. 3. Two anonymous reviewers provided helpful comments on the manuscript. Additional data are available in the supplementary materials. Artifact collections are curated at the Ministry of Culture in Arequipa, Peru.

SUPPLEMENTARY MATERIALS

www.sciencemag.org/content/346/6208/466/suppl/DC1
Materials and Methods
Figs. S1 to S6
Tables S1 to S7
References (*42*–*88*)

3 July 2014; accepted 16 September 2014
10.1126/science.1258260

PLANT SCIENCE

Antheridiogen determines sex in ferns via a spatiotemporally split gibberellin synthesis pathway

Junmu Tanaka,[1]* Kenji Yano,[1]* Koichiro Aya,[1] Ko Hirano,[1] Sayaka Takehara,[1] Eriko Koketsu,[1] Reynante Lacsamana Ordonio,[1] Seung-Hyun Park,[2] Masatoshi Nakajima,[2] Miyako Ueguchi-Tanaka,[1]† Makoto Matsuoka[1]†

Some ferns possess the ability to control their sex ratio to maintain genetic variation in their colony with the aid of antheridiogen pheromones, antheridium (male organ)–inducing compounds that are related to gibberellin. We determined that ferns have evolved an antheridiogen-mediated communication system to produce males by modifying the gibberellin biosynthetic pathway, which is split between two individuals of different developmental stages in the colony. Antheridiogen acts as a bridge between them because it is more readily taken up by prothalli than bioactive gibberellin. The pathway initiates in early-maturing prothalli (gametophytes) within a colony, which produce antheridiogens and secrete them into the environment. After the secreted antheridiogen is absorbed by neighboring late-maturing prothalli, it is modified in to bioactive gibberellin to trigger male organ formation.

Genetic diversity affords a competitive advantage to a particular species. Homosporous ferns have evolved a mechanism to favor cross-fertilization by controlling the sex ratio among individuals or prothalli within the population with the aid of antheridiogens. Antheridiogens are pheromones released in the aqueous environment by early-maturing fern prothalli in a colony, and they cause neighboring late-maturing prothalli in the colony to

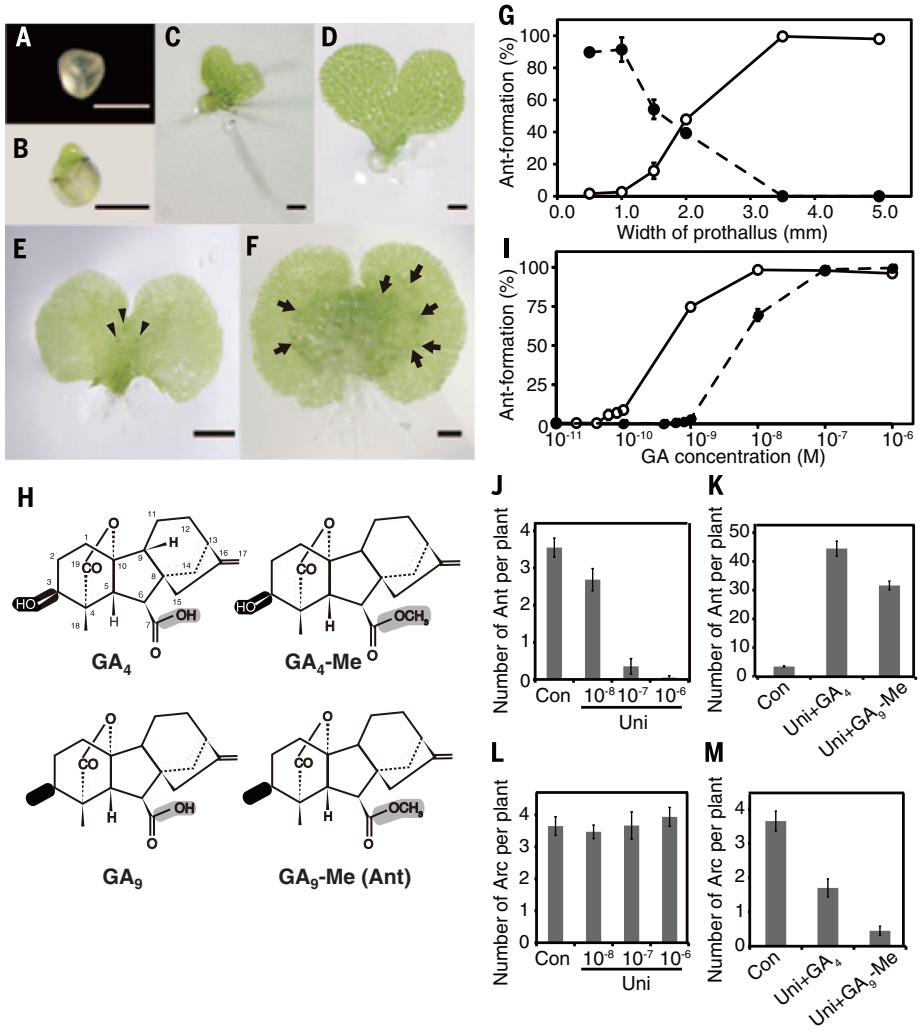

Fig. 1. Antheridiogen production, sensitivity to antheridiogen, effect of GA_4 and GA_9-Me on antheridial formation, and structures of antheridiogen-related compounds used in this study. (**A** to **F**) Prothallus of *L. japonicum* at 0 days after germination (A), 6 days (B), 13 days (~0.5 mm in size) (C), 15 days (~1.0 mm) (D), 19 days (~2.0 mm) (E), and 22 days (~5.0 mm) (F). Arrowheads, archegonia; arrows, antheridia. Scale bars, 0.1 mm [(A) to (D)], 0.5 mm [(E) and (F)]. (**G**) Antheridiogen secretion and sensitivity of prothalli during development. Solid line, secreted antheridiogen level; dashed line, sensitivity to antheridiogens; $n = 8$. (**H**) Chemical structure of antheridiogen-related compounds used in this study. Black shade, presence or absence of OH at C3; gray shade, presence or absence of methyl-esterified group at C6. (**I**) Dose dependence of GA_4 and GA_9-Me action on antheridial (Ant) formation. Solid line, GA_9-Me; Dashed line, GA_4. (**J** and **K**) Effect of Uni (10^{-8}, 10^{-7}, and 10^{-6} M), Uni (10^{-6} M) + GA_4 (10^{-7} M), and Uni (10^{-6} M) + GA_9-Me (10^{-7} M) on antheridial formation; $n = 8$. (**L** and **M**) Effect of Uni, Uni (10^{-6} M) + GA_4 (10^{-7} M), and Uni (10^{-6} M) + GA_9-Me (10^{-7} M) on archegonial (Arc) formation; $n = 8$. Con denotes control (no chemical treatment).

develop male organs (antheridia), thus promoting outcrossing in the colony (*1*–*3*). We first, by bioassay, measured the amount of antheridiogens secreted by prothalli of *Lygodium japonicum* at different developmental stages (Fig. 1, A to F). Prothalli were grown on media to a specified size (0.5 to 5 mm) and then replaced with protonemata (structure prior to prothallus stage). The amount of antheridiogens secreted by the prothalli was estimated by measuring antheridial formation of protonemata (solid line in Fig. 1G). Prothalli larger than 1.5 mm in size gradually started to secrete antheridiogens, and prothalli larger than 3.5 mm secreted enough antheridiogens for protonemata to form 100% antheridia. We also determined the sensitivity of prothalli to antheridiogens by growing prothalli on media under excess amounts of antheridiogens and examined them for antheridial formation (dashed line in Fig. 1G). Young prothalli (≤1 mm) had the greatest tendency to form antheridia, whereas prothalli larger than 3.5 mm were completely insensitive to antheridiogens. These results demonstrate that there is an antiparallel relationship between synthesis/secretion and perception of antheridiogens in adult and young prothalli, respectively.

Antheridiogens in *L. japonicum* (*4*, *5*) share a common *ent*-gibberellane skeleton with gibberellin A_4 (GA_4), the most bioactive gibberellin (GA) in seed plants (Fig. 1H). Although GA_4 is capable of inducing antheridium formation (Fig. 1I), all known natural antheridiogens lack the OH group at C3 that is essential for active GAs. In addition, antheridiogens also possess a methyl-esterified carboxyl group at C6 (Fig. 1H), which hinders GA activity (*6*). In this study, we used GA_9 methyl ester (GA_9-Me) as an antheridiogen, which has 10 times the antheridium-inducing ability of GA_4 (solid line in Fig. 1I). When a GA synthesis inhibitor, uniconazole (Uni) (*7*), was applied, it severely inhibited antheridial formation in prothalli, but not archegonial (female organ) formation (Fig. 1, J and L), whereas cotreatment with uniconazole and 10^{-7} M GA_9-Me or GA_4 promoted antheridial formation but suppressed archegonial formation (Fig. 1, K and M), indicating a dual role of antheridiogens and GA_4 in controlling the sexes (*8*).

The above and previous observations (*5*) indicate that antheridiogens in *L. japonicum* might be synthesized, at least in part, through the GA biosynthetic pathway. Thus, we attempted to isolate *L. japonicum* genes encoding GA synthesis–related enzymes (*9*), specifically *ent*-copalyl diphosphate synthase (CPS), *ent*-kaurene synthase (KS), *ent*-kaurene oxidase (KO), *ent*-kaurenoic acid oxidase (KAO), GA 20-oxidase (GA20ox), and GA 3-oxidase (GA3ox), along with the key components for GA perception (*10*), including the GID1 GA receptor, DELLA protein (a suppressor of GA signaling), and GID2/SLY1 (an F-box protein in GA signaling) (fig. S1). As *L. japonicum* has 58 chromosomes per haploid with more than 1.1×10^9 base pairs (*11*, *12*), we took the RNA sequence strategy for gene isolation. Finally, we cloned and validated the above GA-related genes, and designated them as *Lj_CPS/KS*, *Lj_KO*, *Lj_KAO*, *Lj_GA20ox*, *Lj_GA3ox1* and *2*, *Lj_GID1-1*, *-2*, and *-3*, *Lj_DELLA1* and *2*, and *Lj_GID2* (fig. S2 to S7, table S1, and table S2). Among the genes with two orthologs identified in *L. japonicum*, *Lj_GA3ox1*, *Lj_GID1-1* (*Lj_GID1-3* does not contain the GA receptor activity; see below), and *Lj_DELLA1* were expressed at higher levels in prothalli (fig. S8).

To investigate the molecular events caused by GA_9-Me and GA_4, we first examined their effects

[1]Bioscience and Biotechnology Center, Nagoya University, Nagoya 464-8601, Japan. [2]Department of Applied Biological Chemistry, University of Tokyo, Tokyo 113-8657, Japan.
*These authors contributed equally to this work. †**Corresponding author. E-mail: mueguchi@nuagr1.agr.nagoya-u.ac.jp (M.U.-T.); makoto@nuagr1.agr.nagoya-u.ac.jp (M.M.)**

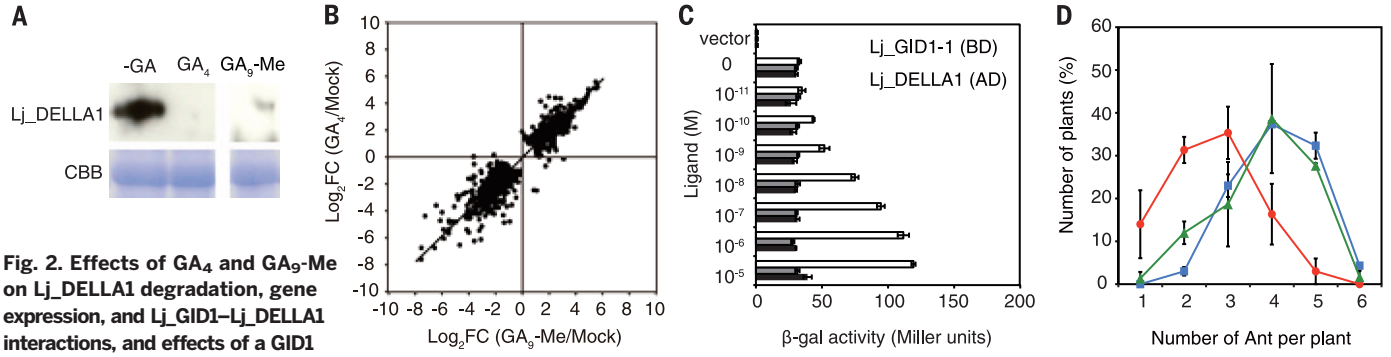

Fig. 2. Effects of GA_4 and GA_9-Me on Lj_DELLA1 degradation, gene expression, and Lj_GID1–Lj_DELLA1 interactions, and effects of a GID1 inhibitor on antheridial formation. (**A**) Degradation of Lj_DELLA1 protein in prothalli after GA_4 and GA_9-Me treatments. (**B**) Comparison of gene expression patterns in prothalli treated with 10^{-6} M GA_4 or 10^{-7} M GA_9-Me for 1 hour. Black line represents the regression line calculated by the least-squares method ($y = 0.9686x - 0.0434$, $R^2 = 0.91081$). (**C**) Yeast two-hybrid assay for the interaction of Lj_GID1-1 as prey and Lj_DELLA1 as bait under various concentrations of GA_4 (white bars), GA_9-Me (gray bars), and GA_4-Me (black bars). The β-gal activity was determined through a liquid assay with yeast (Y187) transformants ($n = 3$). (**D**) Inhibitory effect of TSPC on antheridial formation. Treatment with 10^{-9} M GA_9-Me induced 2 to 6 antheridia per protonema (blue line), whereas co-treatment with 5×10^{-7} M TSPC decreased antheridial formation (red line); 10^{-5} M GA_4 completely counteracted the inhibitory effect of TSPC (green line).

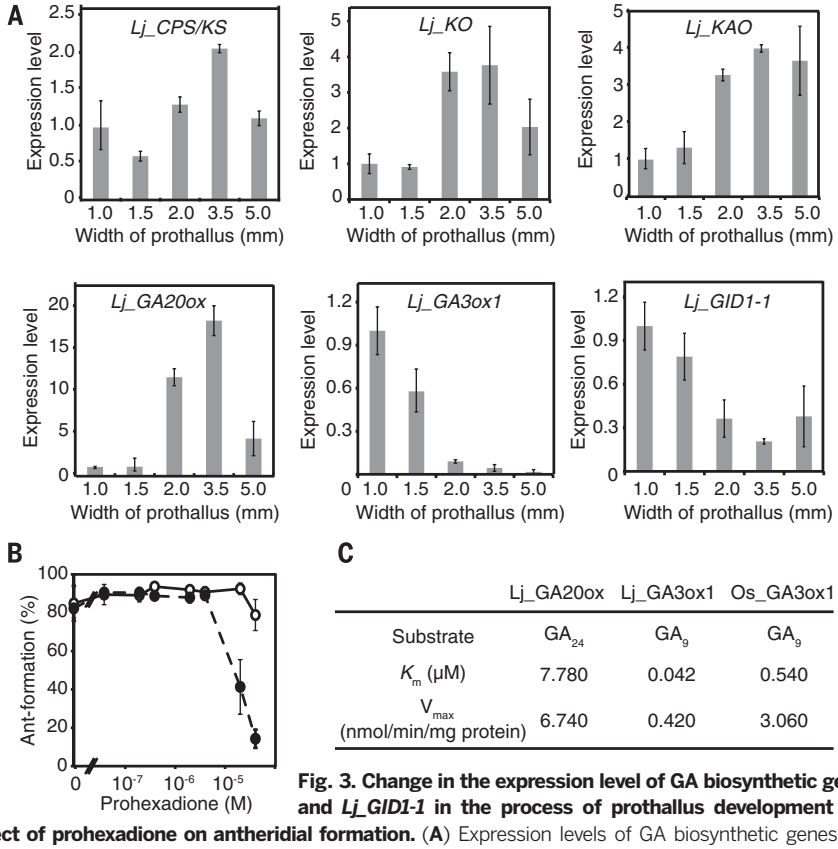

C

	Lj_GA20ox	Lj_GA3ox1	Os_GA3ox1
Substrate	GA_{24}	GA_9	GA_9
K_m (μM)	7.780	0.042	0.540
V_{max} (nmol/min/mg protein)	6.740	0.420	3.060

Fig. 3. Change in the expression level of GA biosynthetic genes and *Lj_GID1-1* in the process of prothallus development and effect of prohexadione on antheridial formation. (**A**) Expression levels of GA biosynthetic genes and *Lj_GID1-1* in prothalli of various sizes. (**B**) Inhibitory effect of prohexadione on antheridial formation in the presence of GA_4 and GA_9-Me. Solid line, 10^{-8} M GA_4; dashed line, 10^{-9} M GA_9-Me. (**C**) Comparisons of K_m and V_{max} (maximum substrate concentration) among Lj_GA20ox, Lj_GA3ox1, and Os_GA3ox1.

on the degradation of the GA signaling repressor DELLA, which is the primary event of GA response (*13*, *14*). By immunoblotting proteins extracted from young prothalli treated with either GA_9-Me or GA_4 for 1 hour, we detected the degradation of Lj_DELLA1 in both treatments (Fig. 2A). Further, we compared the effects of GA_9-Me and GA_4 on gene expression by transcriptome analysis (Fig. 2B). Among the 2213 unigenes differentially expressed between GA_9-Me and the mock treatment at a significant level ($P < 0.001$, false discovery rate <0.01, factor of ≥2 difference) (table S3), almost all were regulated in a similar manner by GA_4, with high correlations. These results indicate that GA_9-Me, like GA_4, elicits GA signaling via the GID1-DELLA system.

To examine whether GA_9-Me is directly perceived by the GID1-DELLA system, we performed a yeast two-hybrid assay to detect the interaction of Lj_GID1-1 and Lj_DELLA1 (Fig. 2C). GA_4 caused a dose-dependent interaction, which was detected even at 10^{-10} M of GA_4, a concentration lower than that required for GID1-DELLA interactions in seed plants by one to two orders of magnitude (*15*, *16*). This indicates that Lj_GID1-1 is especially adapted for detecting and interacting with minute amounts of GA_4. On the other hand, neither GA_9-Me nor GA_4-Me showed any noticeable interactions even at higher concentrations (Fig. 2C). Similar interaction profiles were also seen in other Lj_GID1–Lj_DELLA combinations, with the exception of Lj_GID1-3, which did not interact with any Lj_DELLAs under any conditions (fig. S9). This indicates that GA_9-Me itself cannot bind to Lj_GID1s or elicit GA signaling. We also examined the involvement of GID1 in antheridial formation with the use of a GID1 inhibitor, 3-(2-thienylsulfonyl) pyrazine-2-carbonitrile (TSPC), which is assumed to competitively inhibit GA binding to GID1 (*17*). Treatment with 5×10^{-7} M TSPC inhibited antheridial formation elicited by 10^{-9} M GA_9-Me, whereas cotreatment with 10^{-5} M GA_4 almost rescued the inhibitory effect of TSPC (Fig. 2D). This suggests that antheridial formation by GA_9-Me is mediated by GID1.

Next, we examined the expression pattern of GA biosynthetic genes during prothallus development by quantitative reverse transcription polymerase chain reaction (qRT-PCR) (Fig. 3A). Adult prothalli (3.5 mm) preferentially expressed *Lj_CPS/KS*, *Lj_KO*, *Lj_KAO*, and especially *Lj_GA20ox*, which was expressed at a level 10 to 20 times that in young prothalli. On the other hand, young prothalli (1.0 mm) expressed *Lj_GA3ox1* at a level 10 to 20 times that in adult prothalli, and a similar expression pattern was also observed for *Lj_GID1-1*. Such an antiparallel expression pattern between *Lj_GA20ox* and *Lj_GA3ox1* is very similar to the pattern of antheridiogen synthesis/secretion and antheridiogen sensitivity of prothalli (Fig. 1G). Next, to examine the dependence of antheridial formation on the C3 hydroxylation of antheridiogens by GA3ox, we examined the effect of a GA3ox inhibitor, prohexadione (*18*), on antheridial formation in the presence of 10^{-8} M GA_4 and

10^{-9} M GA_9-Me, which both induce 75% antheridial formation (Fig. 1I). When cotreated with GA_9-Me (which lacks the OH group at C3), prohexadione started to inhibit antheridial formation around 4×10^{-6} M and reduced it to ~10% at 4×10^{-5} M (Fig. 3B). In contrast, in the presence of GA_4 (possessing the OH group at C3), prohexadione did not inhibit at 2×10^{-5} M and caused a decline only at ~4×10^{-5} M. These results demonstrate that the C3 hydroxylation of antheridiogens is essential for antheridial formation, and therefore that antheridiogens are precursors of a compound that induces antheridial formation. This corresponds with the observation that the expression pattern of *Lj_GA3ox1* is similar to that of antheridiogen sensitivity (Fig. 1G). We then compared the enzymatic property of Lj_GA3ox1 produced in *Escherichia coli* to that of rice GA3ox (Os_GA3ox1) (Fig. 3C and fig. S10). The K_m (Michaelis constant) value of Lj_GA3ox1 to the substrate, GA_9, was 42 nM, which was not only lower than that of Os_GA3ox1 (K_m = 540 nM) but also lower than those of GA3oxs from other seed plants, such as *Arabidopsis* At_GA3ox1 (K_m = 1 μM) (*19*) and wheat GA3ox (K_m = 1 μM) (*20*). In contrast, relative to Lj_GA3ox1, the affinity of Lj_GA20ox for its substrate, GA_{24}, was lower by more than two orders of magnitude (K_m = 7.78 μM). These observations demonstrate that Lj_GA3ox1 has an unusual enzymatic property adapted for low substrate concentrations.

If antheridiogens are precursors of an antheridium-inducing compound, GA_4, why do ferns not directly use GA_4 as an antheridiogen? It may be because antheridiogens must be specially adapted for transport across the aqueous environment and have an affinity to, and interaction with, neighboring prothalli. To clarify such possibilities, we incubated young prothalli in a solution containing GA_9, GA_9-Me, GA_4, and GA_4-Me (2 μg/ml each). After removing the prothalli, the remaining GAs in the solution were measured by gas chromatography–mass spectrometry (GC-MS). We observed that GA_9-Me, and to a lesser extent GA_9, were preferentially taken up by prothalli (Fig. 4A). In another experiment, young prothalli preferentially and rapidly absorbed radioactive [^{14}C]GA_9-Me in a concentration-dependent manner, whereas the amount of [^{3}H]GA_4 absorbed was much less and did not reach the level of [^{14}C]GA_9-Me even after a considerable incubation period (Fig. 4B). Both methyl esterification of the carboxyl group and the absence of the hydroxyl group at C3 should result in the hydrophobicity of antheridiogens (Fig. 1H) and hence a higher affinity and faster interaction with hydrophobic materials, such as prothalli in aqueous conditions. Finally, we directly assayed the conversion of GA_9-Me into GA_9 by prothalli (Fig. 4C). The endogenous amount of GA_9 in young (1.0 mm) and adult (5.0 mm) prothalli was similar. Although the GA_9 level in young prothalli increased by a factor of ~3.5 after incubation with GA_9-Me, such an increase did not occur in adult prothalli. This indicates that incorporation and conversion of GA_9-Me into GA_9 occurs in young prothalli but not in adults.

We propose a model for the antheridiogen system that involves a split GA biosynthetic pathway for interindividual communication to regulate the sex ratio in a colony (Fig. 4D). First, early-maturing prothalli in a colony express GA-biosynthetic genes, except *GA3ox*, thus producing a GA_9 intermediate that lacks the OH group at C3. To be effectively transmitted to the surrounding prothalli, GA_9 is modified into an antheridiogen by methyl esterification of its C6 carboxyl group before being secreted to the outside environment. In this transmission process, there is the possible involvement of transporter(s) specific for antheridiogen. Second, antheridiogens are incorporated into neighboring late-maturing prothalli in a colony, which highly express *GA3ox*. Imported antheridiogen is first hydrolyzed to release the methyl group at C6—probably by a methyl esterase, because Lj_GA3ox1 cannot metabolize GA_9-Me into GA_4-Me (fig. S11)—and is then metabolized by GA3ox into GA_4. Finally, GA_4 is perceived by the GID1-DELLA system with the aid of GID2. Activation of the GA signaling pathway causes specific expression to induce and suppress antheridial and archegonial formation, respectively, to maintain an appropriate population of outcrossing male and female prothalli in the colony. To establish this system, GA3ox and GID1, two proteins required for antheridiogen perception, have evolved in *L. japonicum*. Relative to the GID1s of seed plants, the affinity of Lj_GID1-1 for GA_4 was higher by one to two orders of magnitude (Fig. 2C), and Lj_GA3ox1 showed a much higher affinity for its substrate relative to other GA3oxs from seed plants (Fig. 3C). These findings indicate that the two proteins have become attuned to very low concentrations of their substrates within young prothalli.

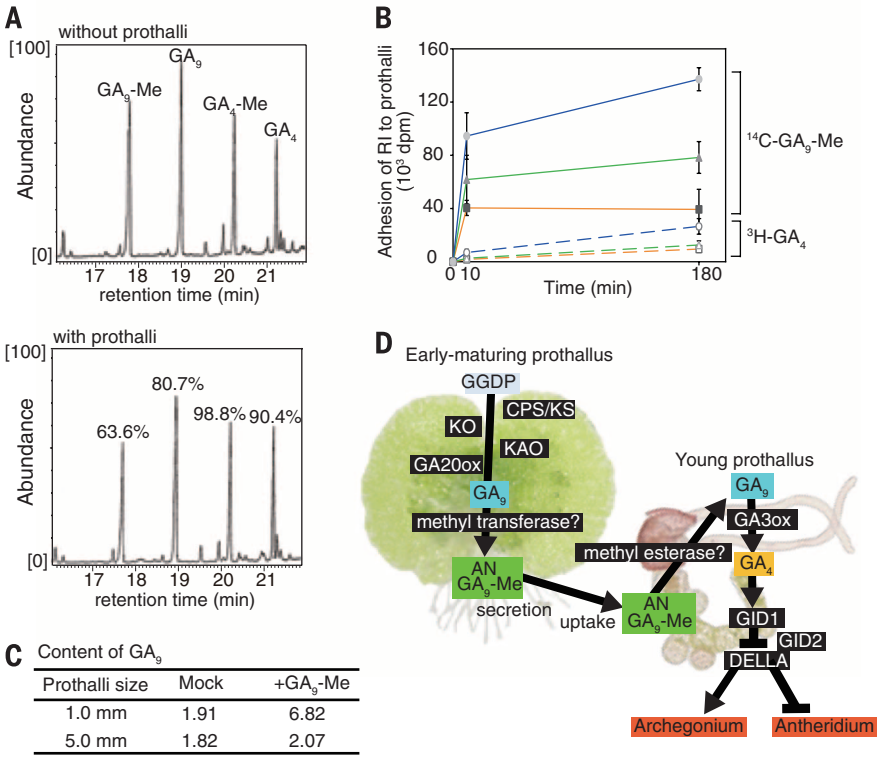

Fig. 4. Uptake of GA_9-Me by prothalli and molecular model of antheridial formation by antheridiogen in *L. japonicum*. (**A**) Uptake of various GAs from solution by young prothalli. Top panel, without prothalli. Bottom panel, with prothalli; percentages of remaining GAs in solution relative to the top panel are shown. (**B**) Accumulation of radioactive GAs in prothalli at different concentrations with respect to incubation time. Dashed lines, [^{3}H]GA_4; solid lines, [^{14}C]GA_9-Me; orange, 5.9 μM; green, 11.8 μM; blue, 23.6 μM. (**C**) GA_9 content (ng/g fresh weight) of young (1.0 mm) and adult (5.0 mm) prothalli with or without incubation with 0.6 mM GA_9-Me for 3 hours. (**D**) Proposed model for fern antheridiogen system.

REFERENCES AND NOTES

1. U. Näf, in *The Experimental Biology of Ferns: Antheridiogens and Antheridial Development*, A. F. Dyer, Ed. (Academic Press, New York, 1979), pp. 436–470.
2. J. J. Schneller, *Biology and Evolution of Ferns and Lycophytes: Antheridiogens* (Cambridge Univ. Press, Cambridge, 2008), pp. 134–158.
3. B. Voeller, E. Weinberg, in *Current Topics in Plant Science: Evolutionary and Physiological Aspects of Antheridium Induction in Ferns*, J. Gunkel, Ed. (Academic Press, New York, 1969), pp. 77–93.
4. H. Yamane, N. Takahashi, K. Takeno, M. Furuya, *Planta* **147**, 251–256 (1979).
5. H. Yamane, *Int. Rev. Cytol.* **184**, 1–32 (1998).
6. P. Hedden, *Nature* **456**, 455–456 (2008).
7. K. Izumi *et al.*, *Plant Cell Physiol.* **26**, 821–827 (1985).
8. K. Takeno, M. Furuya, *Bot. Mag.* **93**, 67–76 (1980).
9. S. Yamaguchi, *Annu. Rev. Plant Biol.* **59**, 225–251 (2008).
10. M. Ueguchi-Tanaka, M. Nakajima, A. Motoyuki, M. Matsuoka, *Annu. Rev. Plant Biol.* **58**, 183–198 (2007).
11. B. Y. S. K. Roy, I. Manton, *New Phytol.* **64**, 286–292 (1965).
12. L. Hanson, I. J. Leitch, *Bot. J. Linn. Soc.* **140**, 169–173 (2002).

13. A. Dill, H. S. Jung, T. P. Sun, *Proc. Natl. Acad. Sci. U.S.A.* **98**, 14162–14167 (2001).
14. H. Itoh, M. Ueguchi-Tanaka, Y. Sato, M. Ashikari, M. Matsuoka, *Plant Cell* **14**, 57–70 (2002).
15. M. Nakajima *et al.*, *Plant J.* **46**, 880–889 (2006).
16. Y. Yamamoto *et al.*, *Plant Cell* **22**, 3589–3602 (2010).
17. J. M. Yoon *et al.*, *Bioorg. Med. Chem. Lett.* **23**, 1096–1098 (2013).
18. I. Nakayama *et al.*, *Plant Cell Physiol.* **31**, 1183–1190 (1990).
19. J. Williams, A. L. Phillips, P. Gaskin, P. Hedden, *Plant Physiol.* **117**, 559–563 (1998).
20. N. E. J. Appleford *et al.*, *Planta* **223**, 568–582 (2006).

ACKNOWLEDGMENTS

We thank M. Kawamura and W. Takase (Nagoya University) for technical assistance and H. Yamane (Teikyo University), M. Hasebe (National Institute for Basic Biology), S. Ooe (Osaka Prefectural Education Center), and T. Yoshimura (Kumiai Chemical Industry Co., Ltd.) for helpful discussions. Supported by Grant-in-Aid for Scientific Research on Innovative Areas no. 23113005 (M.M. and M.N.) and by JSPS through the Funding Program for Next Generation World-Leading Researchers (M.U.-T.). Additional data are in the supplement. DNA Data Bank of Japan (DDBJ) accession numbers: *Lj_CPS/KS*, AB915786; *Lj_KO*, AB915787; *Lj_KAO*, AB915788; *Lj_GA20ox*, AB915789; *Lj_GA3ox1*, AB915790; *Lj_GA3ox2*, AB915791; *Lj_GID1-1*, AB915792; *Lj_GID1-2*, AB915793; *Lj_GID1-3*, AB915794; *Lj_DELLA1*, AB915795; *Lj_DELLA2*, AB915796; *Lj_GID2*, AB915797.

SUPPLEMENTARY MATERIALS

www.sciencemag.org/content/346/6208/469/suppl/DC1
Materials and Methods
Figs. S1 to S11
Tables S1 to S4
References (*21*–*28*)

12 August 2014; accepted 5 September 2014
10.1126/science.1259923

VIRAL CELL BIOLOGY

Influenza A virus uses the aggresome processing machinery for host cell entry

Indranil Banerjee,[1]*† Yasuyuki Miyake,[2] Samuel Philip Nobs,[3] Christoph Schneider,[3] Peter Horvath,[4] Manfred Kopf,[3] Patrick Matthias,[2,5] Ari Helenius,[1]‡ Yohei Yamauchi[1]‡

During cell entry, capsids of incoming influenza A viruses (IAVs) must be uncoated before viral ribonucleoproteins (vRNPs) can enter the nucleus for replication. After hemagglutinin-mediated membrane fusion in late endocytic vacuoles, the vRNPs and the matrix proteins dissociate from each other and disperse within the cytosol. Here, we found that for capsid disassembly, IAV takes advantage of the host cell's aggresome formation and disassembly machinery. The capsids mimicked misfolded protein aggregates by carrying unanchored ubiquitin chains that activated a histone deacetylase 6 (HDAC6)–dependent pathway. The ubiquitin-binding domain was essential for recruitment of HDAC6 to viral fusion sites and for efficient uncoating and infection. That other components of the aggresome processing machinery, including dynein, dynactin, and myosin II, were also required suggested that physical forces generated by microtubule- and actin-associated motors are essential for IAV entry.

Influenza A virus (IAV) is an enveloped virus of great medical impact. With the risk of an influenza pandemic growing, it is increasingly important to understand virus-host interactions in detail and to develop new antiviral strategies (*1*). IAV has a single-stranded, negative-sense RNA genome divided between eight subgenomic RNA molecules. These are individually packaged into helical viral ribonucleoproteins (vRNPs) that contain a viral polymerase complex and multiple copies of the nucleoprotein, NP. In the virus, the vRNPs form a stable, capsid-like, supramacromolecular complex with the matrix protein, M1, which forms a shell around the vRNPs (*2*). During IAV entry into a host cell (Fig. 1A, top), the uncoating process is initiated in early endosomes where the mildly acidic pH triggers the opening of the M2 channel in the viral envelope leading to influx of protons and potassium ions (*3*–*5*). A conformational change occurs that renders the capsid uncoating-competent. When the pH drops further in late endosomes (LEs), the membrane fusion function of the hemagglutinin (HA) is activated, and the capsid is transferred to the cytosol (*6*, *7*). The M1 disperses, and the vRNPs are imported into the nucleus through nuclear pore complexes (*8*–*11*).

While analyzing the role of HDAC8 and HDAC3 in endosome maturation and IAV penetration (*12*), we noticed that another histone deacetylase, HDAC6, was also required for infection. A cytosolic enzyme responsible for deacetylation of tubulin and some other substrates, it also serves as a key component in ubiquitin (Ub)–dependent aggresome formation and disassembly (*13*, *14*). We found that HDAC6 depletion by RNA interference (RNAi) in A549 cells (a human bronchial epithelial cell line) reduced infection by half (fig. S1, A and H). In HDAC6 knock-out (KO) mouse embryonic fibroblasts (MEFs), infection was reduced to 30%, and viral titers to 48%, compared with wild-type (WT) MEFs (fig. S1, B, C, and H). When WT and HDAC6 KO mice (*15*) were infected intratracheally with IAV strains PR8 and X31 in HDAC6 KO mice, lung viral titers were reduced to 48% and 31%, respectively, at day 5 compared with controls (fig. S2, A and B). The antiviral immune responses were comparable when tested in PR8-infected mice (fig. S2, C to E).

When the stepwise IAV entry was analyzed in HDAC6 KO MEFs using quantitative assays (*8*), no significant difference was observed with WT MEFs in endocytic uptake, acid-induced HA conversion, and fusion (Fig. 1A and fig. S1G). However, capsid uncoating and nuclear import of vRNPs were reduced to 22 and 17%, respectively (Fig. 1A). In HDAC6-depleted A549 cells, uncoating was reduced to 21% compared with controls, with no effect on HA acidification or fusion (fig. S1, D to F). It was apparent that HDAC6 played a role in the release of viral capsids from the cytosolic surface of endosomes, the dissociation of M1 from vRNPs, and the dispersion of capsid components in the cytosol.

To confirm that the HDAC6 requirement was postfusion, we induced fusion of the virus directly with the plasma membrane (PM), a process that allows delivery of viral capsids into the cytosol without endocytosis (fig. S3A) (*6*, *7*). Although fusion efficiency was comparable, the M1 was diffusely distributed through the cytoplasm in WT MEFs but remained punctate in HDAC6 KO MEFs (fig. S3, B and C). That uncoating was reduced to 32% in the HDAC6 KO MEFs and to 47% in HDAC6-depleted A549 cells (fig. S3, D and E) compared with control cells confirmed that HDAC6 was required after fusion.

To determine which of the functions of HDAC6 were required for uncoating, we used HDAC6 KO MEFs that had been rescued either with WT HDAC6 (WT^{r}) or with HDAC6s with point mutations either in the two deacetylase domains (HD^{m}) (*16*) or in the zinc-finger domain (ZnF^{m}) (*17*, *18*). The zinc-finger ubiquitin binding domain (ZnF-UBP) is C-terminal and binds Ub. It plays a critical role in aggresome formation and disassembly (*13*, *14*) (Fig. 1B). Whereas most Ub-binding proteins interact with the hydrophobic core of Ub, the ZnF-UBP domain of HDAC6 binds to the C-terminal Gly-Gly residues (*13*, *19*). This means that HDAC6 only binds to Ub and poly-Ub chains that are not coupled to proteins. The point

[1]Institute of Biochemistry, Eidgenossische Technische Hochschule (ETH) Zurich, Switzerland. [2]Epigenetics, Friedrich Miescher Institute for Biomedical Research, Basel, Switzerland. [3]Institute of Molecular Health Sciences, ETH Zurich, Switzerland. [4]Synthetic and Systems Biology Unit, Biological Research Center, Szeged, Hungary. [5]Faculty of Sciences, University of Basel, Basel, Switzerland.
*Present address: Developmental and Molecular Pathways, Novartis Institutes for Biomedical Research, Basel, Switzerland. †Present address: Neural Circuit Laboratories, Friedrich Miescher Institute for Biomedical Research, Basel, Switzerland. ‡**Corresponding author. E-mail: ari.helenius@bc.biol.ethz.ch (A.H.); yohei.yamauchi@bc.biol.ethz.ch (Y. Y.)**

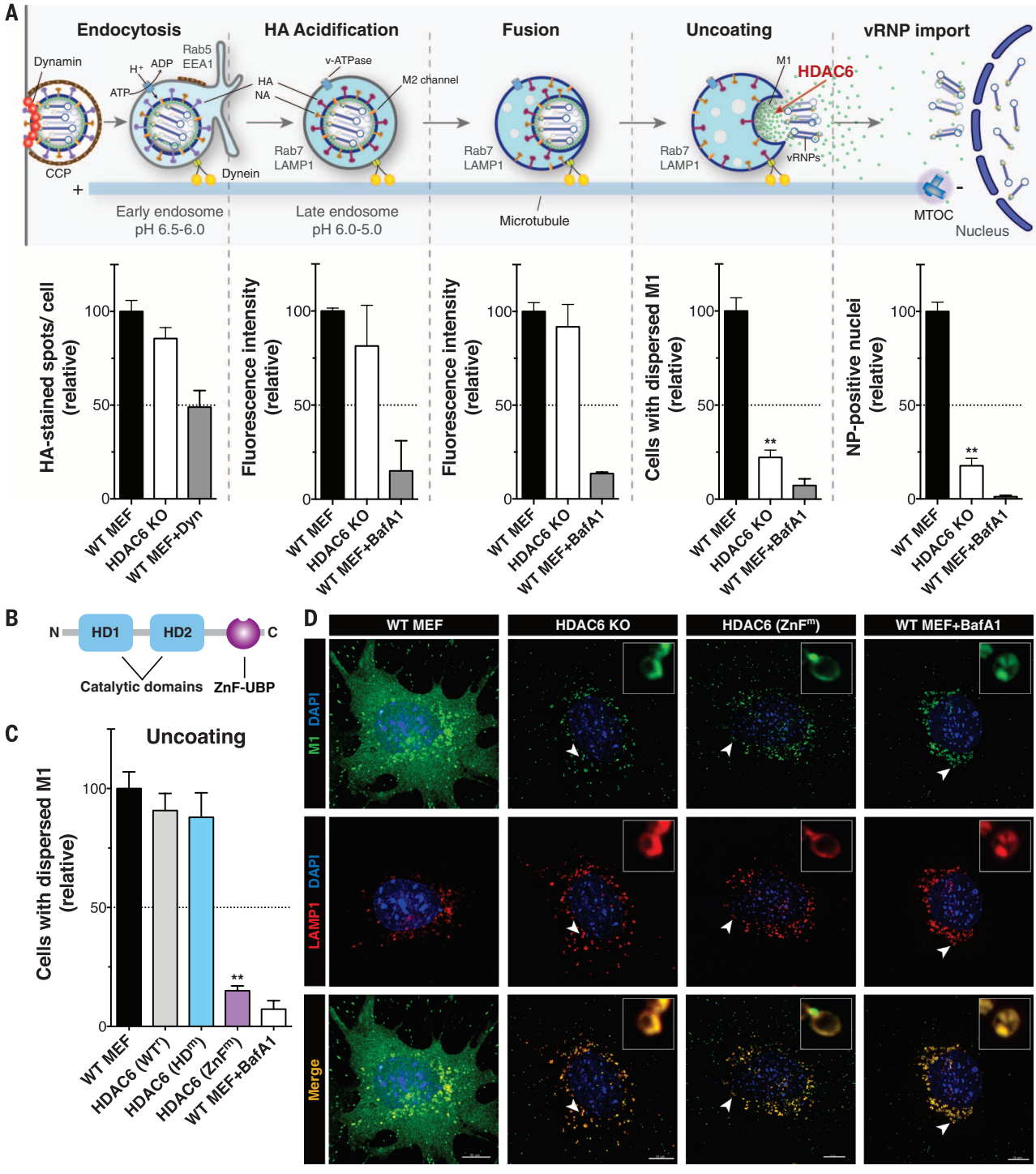

Fig. 1. IAV requires the Ub-binding function of HDAC6 for capsid uncoating. (**A**) (Top) IAV entry steps. The virus particle is endocytosed into early endosomes that undergo dynein-dependent retrograde transport toward the microtubule-organizing center (MTOC). The intraluminal pH drops due to vacuolar adenosine triphosphatase (v-ATPase) activity, inducing HA conformational change and fusion. The capsid disassembles in an HDAC6-dependent manner, followed by vRNP release into the cytosol and import into the nucleus. (Bottom) Quantification of IAV entry assays. Endocytosis: endocytosed IAV particles were detected at 30 min after virus uptake. Dynasore (Dyn) was used at 80 μM to block dynamin-dependent endocytosis. HA acidification: Acidified HA was detected at 1 hour after uptake. Endosome acidification was blocked by 50 nM bafilomycin A1 (BafA1). Fusion: SP-DiOC18(3)/R18–labeled particles were allowed to enter cells for 1.5 hours, and dequenched SP-DiOC18(3) was quantified. Uncoating: M1 uncoating was quantified 2.5 hours after virus uptake. vRNP import: Nuclear NP signal was quantified 4 hours after virus uptake. All assays were performed in the presence of 1 mM cycloheximide to block new synthesis of viral proteins. (**B**) HDAC6 domain organization. (**C**) Uncoating in WT and HDAC6 (WT^r, HD^m, and ZnF^m) MEFs. (**D**) After 2.5 hours of virus uptake into WT, HDAC6 KO, and HDAC6 (ZnF^m) MEFs, M1 (green) and LAMP1-positive (red) endosomes were imaged by confocal microscopy. BafA1 was used to block uncoating. Insets show enlarged images of representative endosomes (arrowhead). All data are represented as mean ± SD. ns, $P > 0.05$; *$P < 0.05$; **$P < 0.01$. Scale bars, 10 μm.

mutations H1094A and H1098A in the HDAC6 (ZnF^m) cells block Ub binding to the ZnF-UBP domain (*20*, *21*).

All three cell lines exhibited normal HA acidification during IAV entry (fig. S4A). However, in the HDAC6 (ZnF^m) cells, uncoating, nuclear import of vRNPs, and infection were reduced to 15, 8, and 17%, respectively (Fig. 1C and fig. S4, B and C). Instead of being dispersed as in WT, M1 was confined to LAMP1-positive vacuoles (Fig. 1D). Uncoating and infection were also blocked after virus fusion with PM (fig. S4, D and E). A point mutation W1182A in the human HDAC6 ZnF-UBP disrupts binding of free Ub chains (*13*). We generated a mutant cell line HDAC6 (ZnF^m-W1116A) with a mutation in the corresponding mouse HDAC6 ZnF-UBP. Uncoating was reduced to 21% in these cells (fig. S4F). However, in the HDAC6 (HD^m) cells, which were devoid of HDAC6 deacetylase activity, uncoating, nuclear import, and infection were normal (Fig. 1C and fig. S4, B and C). An inhibitor of the deacetylase activity of HDAC6, tubastatin A (*22*), had no effect on uncoating (fig. S4G). Thus, the ZnF-UBP domain of HDAC6 was critical for IAV uncoating and infection, whereas the deacetylase activity was not.

Previous mass spectroscopy studies have shown that Ub is present in purified IAV (*23*). Our biochemical analysis confirmed this and showed that virions contained mono- and poly Ub, some of which were unanchored di-, tri-, and tetra-Ub (Fig. 2A). The poly-Ub chains were sensitive to proteinase K digestion only after solubilization of the envelope using Triton X-100, indicating that they were protected (Fig. 2A). In an in vitro pull-down assay, the HDAC6 ZnF-UBP domain associated with Ub molecules present in the virion (Fig. 2, C and D). These were verified as free Ub and poly Ub by immunoblotting with a C-terminal–specific monoclonal antibody (Fig. 2D). Super-resolution microscopy of purified IAV using the same antibody showed free Ub staining in more than half of virus particles (Fig. 2B and fig. S5). The free Ub signal was detected within a boundary defined by the HA signal, indicating that it was inside the particle (Fig. 2B and fig. S5). Viral NP and M1 were also pulled down by HDAC6, but the interaction appeared to be independent of the ZnF-UBP domain (Fig. 2D). When IAV was allowed to enter

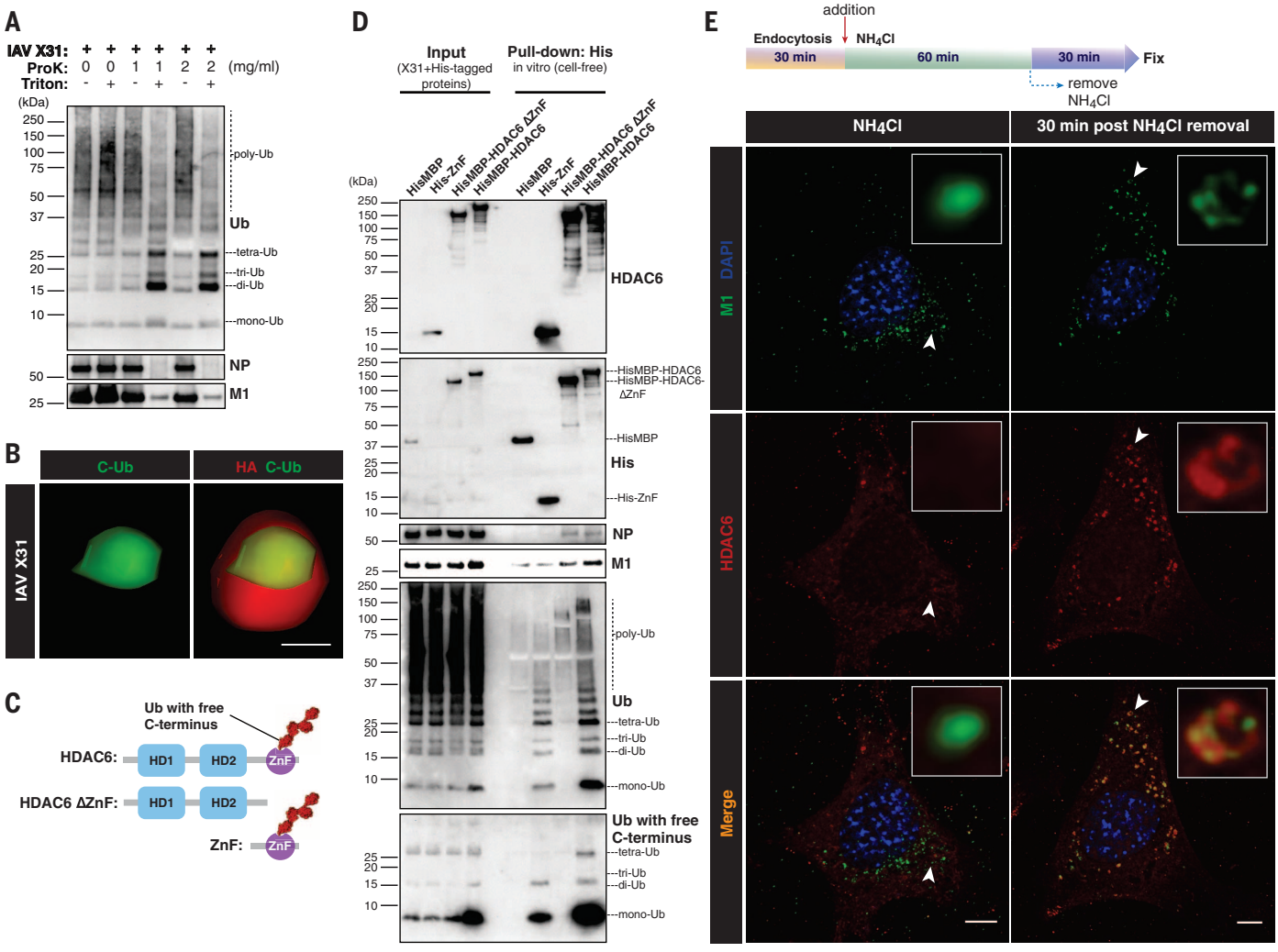

Fig. 2. IAV packages free Ub chains that recruit HDAC6 to LE fusion sites via ZnF-UBP. (**A**) Western blot analyses of Ub, NP, and M1 after proteinase K treatment of purified IAV virions in the presence or absence of Triton X-100. (**B**) Super-resolution microscopy image of purified IAV. Virus particles were bound on the coverslip, followed by incubation in pH 5.5 medium at 37°C for 30 min, and fixed. After permeabilization, the particles were stained with antibodies to C terminus Ub (C-Ub) and HA, followed by appropriate secondary antibody labeled with Alexa Fluor. Images were surface-reconstructed with the Imaris software. Scale bar, 100 nm. (**C**) Schematic representation of different HDAC6 deletion mutants. (**D**) Pull-down assay of purified, His-tagged HDAC6 full-length, and deletion mutants after incubation with purified IAV lysates. Western blotting was done to detect HDAC6, His, NP, M1, Ub, and C-terminus Ub. (**E**) HDAC6 recruitment to M1-positive endosomes after viral fusion. IAV endocytic uptake was allowed for 30 min followed by treatment with 20 mM NH_4Cl for 1 hour. After washout of the drug to allow viral fusion and penetration, cells were fixed, permeabilized, and stained with antibodies to HDAC6 and M1. Before (left) and 30 min after (right) washout. Scale bar, 10 μm.

WT and HDAC6 KO MEFs for 2.5 hours, NP and M1 coimmunoprecipitated with HDAC6 (fig. S4H). In addition, it was observed using indirect immunofluorescence that after ammonium chloride (NH_4Cl) washout to allow penetration of capsids from LAMP1-positive endosomes, the distribution of HDAC6 changed (Fig. 2E). Instead of a diffuse cytosolic staining, HDAC6 now associated with M1-containing vacuoles, where it gave a distinct rim-staining. Association with late endosomal vacuoles was transient and was not observed in the HDAC6 (ZnF^m) cells (fig. S6B).

Via its interaction with dynein and dynactin, HDAC6 acts as an adaptor that mediates retrograde transport of misfolded protein aggregates along microtubules (MTs) to aggresomes (*14*). Consistent with a similar role for HDAC6 in IAV infection, we found that depletion of dynactin 2 (the p50 subunit of the dynactin complex) by RNAi and inhibition of dynein by ciliobrevin D (CilioD) (*24*) reduced uncoating after PM fusion to 51 and 62%, respectively (Fig. 3A). In MEFs in which the HDAC6 lacked the dynein-binding domain (*14*) (fig. S7, A and B) and thus failed to bind dynein (Fig. 3B), uncoating was reduced to 58% compared with WT MEFs (Db^m) (Fig. 3A). Similar loss of uncoating capacity was observed when IAV entered HDAC6 (Db^m) MEFs via the normal endocytic pathway (fig. S7, C and D). Thus, HDAC6 binding to dynein and dynactin promoted IAV uncoating.

Because dynein inhibition alone did not inhibit IAV uncoating completely, we investigated a possible additional role for the actomyosin system. It is known that in aggresomes, free Ub chains are generated by deubiquitination of poly-ubiquitinated proteins. This activates HDAC6 binding and stimulates type II nonmuscle myosin 10 (IIB), which promotes aggresome deaggregation, and clearance (*13*). Using RNAi, we found that uncoating after PM fusion was decreased in myosin 10–depleted but not in myosin 9–depleted A549 cells (to 42% of control) (Fig. 3C). Inhibition of type II myosins with ML-9 and blebbistatin reduced uncoating to 38 and 48%, respectively (Fig. 3C). HDAC6 was, moreover, found to interact both with myosin 10 and actin (Fig. 3D). When actin filaments were depolymerized with cytochalasin D (CytoD) and MTs by nocodazole (Noc), uncoating after PM fusion dropped to 17 and 64%, respectively. Uncoating was, however, blocked completely when both drugs were used together (Fig. 3E).

Finally, we established that dynein, myosin II, MTs, and actin were also involved in uncoating when IAV entered by endocytosis. After virus uptake for 30 min in A549 cells, acid-activated penetration by fusion was prevented by addition of NH_4Cl. Different drugs were now added, the NH_4Cl was washed out to allow penetration, and the effect of the added drugs on uncoating was analyzed after 60 min. The results showed that inhibitors of dynein, myosin II, actin, and MT assembly all reduced uncoating significantly (Fig. 3F). Inhibition of proteasome activity by MG132, or importin-β–mediated nuclear import

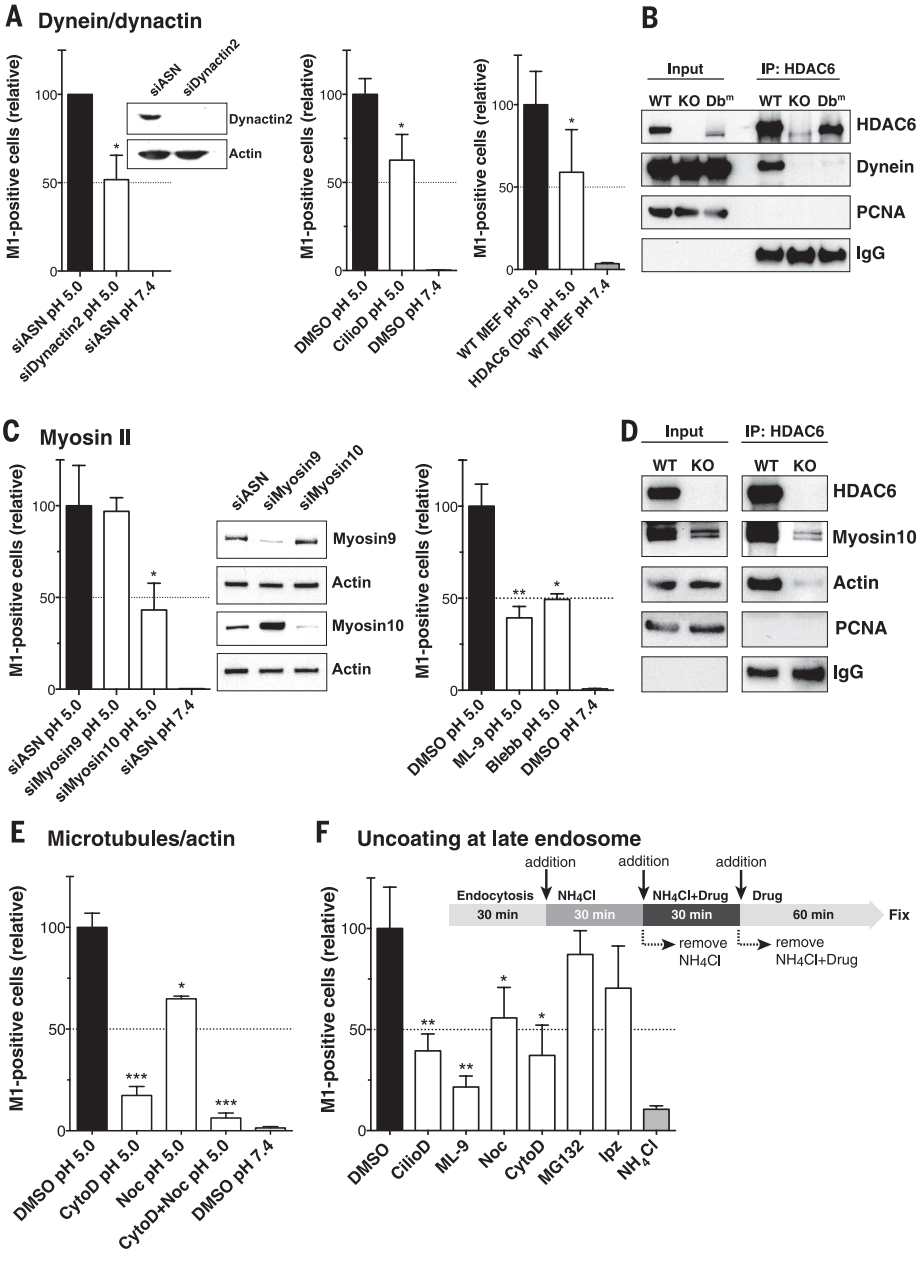

Fig. 3. Dynein/dynactin, myosin II, MTs, and actin promote IAV uncoating. (**A**) Quantification of PM-fused uncoating in A549 cells treated with AllStars negative (ASN) and dynactin 2 small interfering RNAs (siRNAs), A549 cells pretreated with 100 μM of ciliobrevin D (CilioD) 1 hour before and during the assay to block dynein motor activity, and WT and HDAC6 (Db^m) MEFs. Depletion of dynactin 2 was confirmed by Western blotting. Actin was used as a loading control. (**B**) Coimmunoprecipitation with antibody to HDAC6 using WT, HDAC6 KO, and HDAC6 (Db^m) MEFs treated with 5 μM MG132 for 6 hours. Western blotting was done to detect HDAC6, dynein, and proliferating cell nuclear antigen (PCNA). Immunoglobulin G (IgG) served as a loading control. (**C**) Quantification of PM-fused uncoating in A549 cells treated with ASN, myosin 9 and 10 siRNAs, and A549 cells pretreated with 25 μM ML-9 and 100 μM blebbistatin (Blebb) 1 hour before and during the assay. Depletion of myosin 9 and 10 was confirmed by Western blotting. Actin was used as a loading control. (**D**) Coimmunoprecipitation using antibody to HDAC6 in WT and HDAC6 KO MEFs infected with IAV for 2.5 hours. Western blotting was done to detect HDAC6, myosin 10, actin, and PCNA. IgG served as a loading control. (**E**) Quantification of PM-fused uncoating in A549 cells treated with 10 μM cytochalasin D (CytoD), 30 nM nocodazole (Noc), or both drugs 1 hour before and during the assay. Relevant negative and positive controls were included in each experiment. (**F**) A549 cells were treated with 100 μM CilioD, 25 μM ML-9, 30 nM Noc, 10 μM CytoD, 5 μM MG132, 40 μM Importazole (Ipz), and 20 mM NH_4Cl, as indicated in the experimental scheme. M1 uncoating was quantified by fluorescence-activated cell sorting. All data are represented as mean ± SD. ns, $P > 0.05$; *$P < 0.05$; **$P < 0.01$; ***$P < 0.001$.

by importazole (Ipz) (*25*), had no significant effect (Fig. 3F).

Taken together, our results demonstrated that key components of the aggresome formation and disassembly machinery promote IAV uncoating. Among them, HDAC6 is recruited to LEs by newly penetrated capsids by binding with capsid-associated Ubs via its ZnF-UBP domain. It serves as a linker molecule to cytoskeletal motors that generate opposing physical forces (*26*) to break apart the capsid (fig.S8). This cytoskeleton motor-assisted uncoating program offers potential targets such as myosin 10, dynein, and HDAC6 itself for new antiviral strategies.

REFERENCES AND NOTES

1. A. S. Fauci, *Cell* **124**, 665–670 (2006).
2. T. Noda, Y. Kawaoka, *Proc. Natl. Acad. Sci. U.S.A.* **109**, 8797–8798 (2012).
3. K. Martin, A. Helenius, *Cell* **67**, 117–130 (1991).
4. L. H. Pinto, L. J. Holsinger, R. A. Lamb, *Cell* **69**, 517–528 (1992).
5. S. Stauffer *et al.*, *J. Virol.* (2014).
6. J. White, K. Matlin, A. Helenius, *J. Cell Biol.* **89**, 674–679 (1981).
7. K. S. Matlin, H. Reggio, A. Helenius, K. Simons, *J. Cell Biol.* **91**, 601–613 (1981).
8. I. Banerjee, Y. Yamauchi, A. Helenius, P. Horvath, *PLOS ONE* **8**, e68450 (2013).
9. I. Kemler, G. Whittaker, A. Helenius, *Virology* **202**, 1028–1033 (1994).
10. K. Martin, A. Helenius, *J. Virol.* **65**, 232–244 (1991).
11. R. E. O'Neill, R. Jaskunas, G. Blobel, P. Palese, J. Moroianu, *J. Biol. Chem.* **270**, 22701–22704 (1995).
12. Y. Yamauchi *et al.*, *PLOS Pathog.* **7**, e1002316 (2011).
13. R. Hao *et al.*, *Mol. Cell* **51**, 819–828 (2013).
14. Y. Kawaguchi *et al.*, *Cell* **115**, 727–738 (2003).
15. Y. Zhang *et al.*, *Mol. Cell. Biol.* **28**, 1688–1701 (2008).
16. Y. Zhang, B. Gilquin, S. Khochbin, P. Matthias, *J. Biol. Chem.* **281**, 2401–2404 (2006).
17. C. Boyault *et al.*, *EMBO J.* **25**, 3357–3366 (2006).
18. S. Kwon, Y. Zhang, P. Matthias, *Genes Dev.* **21**, 3381–3394 (2007).
19. H. Ouyang *et al.*, *J. Biol. Chem.* **287**, 2317–2327 (2012).
20. N. R. Bertos *et al.*, *J. Biol. Chem.* **279**, 48246–48254 (2004).
21. D. Seigneurin-Berny *et al.*, *Mol. Cell. Biol.* **21**, 8035–8044 (2001).
22. K. V. Butler *et al.*, *J. Am. Chem. Soc.* **132**, 10842–10846 (2010).
23. M. L. Shaw, K. L. Stone, C. M. Colangelo, E. E. Gulcicek, P. Palese, *PLOS Pathog.* **4**, e1000085 (2008).
24. A. J. Firestone *et al.*, *Nature* **484**, 125–129 (2012).
25. J. F. Soderholm *et al.*, *ACS Chem. Biol.* **6**, 700–708 (2011).
26. K. A. Myers *et al.*, *Traffic* **7**, 1333–1351 (2006).

ACKNOWLEDGMENTS

We thank many current and former members of the Helenius laboratory for helpful discussions, T. Heger for providing us the infection counter algorithm, and ScopeM of ETH Zurich for assistance in microscopy. This work was supported by grants to A.H. from ETH Zurich, the European Research Council, and the Swiss National Science Foundation (SNSF); to C.S. and M.K. from the SNSF and NIH; and to Y.M. and P.M. from the Novartis Research Foundation. The findings of this work are filed under patent no. 14172323.9-1464 "New treatment against influenza virus."

SUPPLEMENTARY MATERIALS

www.sciencemag.org/content/346/6208/473/suppl/DC1
Materials and Methods
Figs. S1 to S8
References (*27*–*29*)

5 June 2014; accepted 11 September 2014
10.1126/science.1257037

DNA REPLICATION

Polyubiquitylation drives replisome disassembly at the termination of DNA replication

Sara Priego Moreno,* Rachael Bailey,* Nicholas Campion, Suzanne Herron, Agnieszka Gambus†

Resolution of replication forks during termination of DNA replication is essential for accurate duplication of eukaryotic genomes. Here we present evidence consistent with the idea that polyubiquitylation of a replisome component (Mcm7) leads to its disassembly at the converging terminating forks because of the action of the p97/VCP/Cdc48 protein remodeler. Using *Xenopus laevis* egg extract, we have shown that blocking polyubiquitylation results in the prolonged association of the active helicase with replicating chromatin. The Mcm7 subunit is the only component of the active helicase that we find polyubiquitylated during replication termination. The observed polyubiquitylation is followed by disassembly of the active helicase dependent on p97/VCP/Cdc48. Altogether, our data provide insight into the mechanism of replisome disassembly during eukaryotic DNA replication termination.

During replication fork termination, the replisomes disassemble by an unknown mechanism, and topoisomerase II resolves the daughter DNA molecules (*1*, *2*). If not resolved efficiently, terminating forks result in genomic instabilities (*3*, *4*). In eukaryotic cells, the Mcm2-7 complex forms the core of the replicative DNA helicase (*5*). Its regulated loading onto chromatin (*6*–*8*) leads to replication origins licensing. The Mcm2-7 complexes stably associate with DNA and require replication progression to unload (*9*). A small proportion of chromatin-loaded Mcm2-7 is activated during S phase by the formation of the CMG complex [with Cdc45 and go ichi ni san (GINS)], which acts as a helicase and as an organizing center for the replisome (*10*, *11*). In higher eukaryotes, mini-chromosome maintenance complex–binding protein (MCM-BP) facilitates the removal of the bulk of Mcm2-7 complexes from chromatin (*12*, *13*), but the mechanism of active helicase disassembly upon termination of replication is unknown.

Our aim was to determine the role of ubiquitylation during DNA replication. Recombinant histidine (His_6)–tagged ubiquitin added to cell-free *Xenopus laevis* egg extract is efficiently used by the extract without affecting the replication process (fig. S1, A to C). To inhibit polyubiquitylation, we used a chain-terminating mutant of ubiquitin, which has all lysine residues mutated to alanine (His_6-UbiNOK). Addition of His_6-UbiNOK to the replicating extract resulted in increased and prolonged association of the active replicative helicase with chromatin, whereas nascent DNA synthesis was not affected (Fig. 1A and figs. S1D and S2D) (*14*). The majority of Mcm2-7 complexes (90 to 95%), which represent the inactive origins, were removed from chromatin with normal timing (fig. S1, D and E), and the accumulated CMG components formed large-molecular-size complexes (fig. S1F).

Polyubiquitylation with ubiquitin chains linked through lysine 48 (K48) and lysine 11 (K11) often drives proteasomal degradation of modified substrates (*15*), yet inhibition of proteasomal degradation with the small-molecule inhibitor bortezomib (*16*) (fig. S2, A and B) did not affect replicative helicase on chromatin (fig. S2, C and D). Ubiquitin-driven proteasomal degradation of Cdt1 is important for preventing rereplication during S phase (*17*). After adding His_6-UbiNOK, we observed only a ~15-min delay of its degradation (fig. S2E), whereas inhibition of proteasome results in complete stabilization of Cdt1 (fig. S2E). The inhibition of polyubiquitylation was thus not complete with His_6-UbiNOK, which explained the temporary effect on helicase chromatin accumulation (Fig. 1A).

We next aimed to establish the underlying reason behind our observation. Addition of His_6-UbiNOK did not affect the efficiency of DNA synthesis (Fig. 1A), the length of individual tracks of nascent DNA (fig. S3, A and B), or induced Chk1 phosphorylation (fig. S3C). These findings suggested that progression of the replicating forks was not affected by blocked polyubiquitylation.

We did not see helicase accumulation upon proteasomal inhibition and complete stabilization of Cdt1 (fig. S2C), but to exclude the possibility of Cdt1-driven rereplication (*18*) upon polyubiquitylation inhibition, we supplemented the extract with the Cdt1 inhibitor geminin shortly after adding DNA sperm and His_6-UbiNOK (*19*). The amount of Mcm2-7 complexes loaded onto chromatin was severely reduced (fig. S3D), whereas CMG subunits still accumulated on chromatin when polyubiquitylation was inhibited (Fig. 1B). Moreover, as the majority of Mcm2-7 complexes became activated under the conditions of minimal

School of Cancer Sciences, University of Birmingham, Vincent Drive, Birmingham B15 2TT, UK.
*These authors contributed equally to this work. **†Corresponding author. E-mail: a.gambus@bham.ac.uk**

licensing and thus behaved similarly to other CMG components, we could now observe also the accumulation of Mcm5 on chromatin (Fig. 1B). Blocking late-origin firing by the addition of a CDK inhibitor, p27(KIP1), in early S phase had no effect on the accumulation of CMG on chromatin when polyubiquitylation was inhibited (fig. S3E), nor was the interorigin distance affected by the addition of His_6-UbiNOK (fig. S3F), which suggested that the number of activated origins was not affected by polyubiquitylation inhibition.

We then asked whether the inhibition of polyubiquitylation resulted in CMG accumulation on chromatin through a defect in helicase disassembly

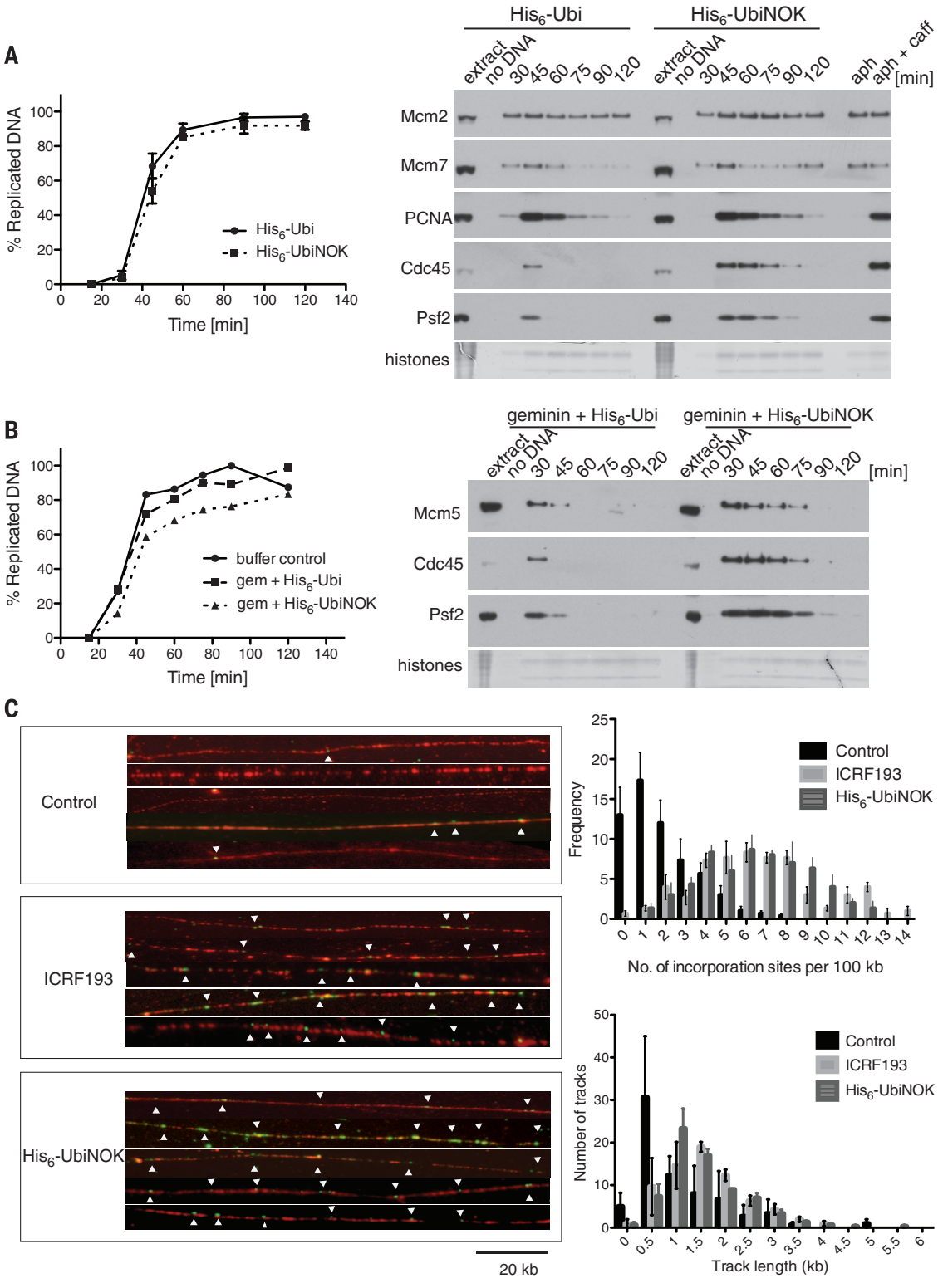

Fig. 1. Partial inhibition of polyubiquitylation leads to active helicase accumulation on chromatin. (**A**) DNA synthesis in interphase extract supplemented with His_6-Ubi or His_6-UbiNOK was assessed at indicated times (left) [average of three experiments in independent extracts with standard error of the mean (SEM)], whereas chromatin was isolated and subjected to Western blotting (right). For comparison, chromatin was also isolated from samples treated with aphidicolin (aph) or aphidicolin and caffeine (aph + caff). (**B**) Cdt1 activity in the extracts supplemented with His_6-Ubi or His_6-UbiNOK was blocked with geminin 3 min after sperm nuclei DNA addition. DNA synthesis in both extracts and in control extract (buffer control with no geminin addition) was assessed (left), whereas isolated minimally licensed chromatin was analyzed by Western blotting (right). (**C**) Extract was supplemented with 5-bromo-2′deoxyuridine 5′-triphosphate (BrdUTP) (visualized in red) and optionally with buffer, His_6-UbiNOK, or ICRF-193. Chromatin was isolated at late S phase (90 min) and incubated in a second extract supplemented with geminin and digoxigenin-11-2′-deoxyuridine 5′-triphosphate (Dig-dUTP) (visualized in green). The number of short green-labeled fragments of replicated DNA (tracks) was scored per 100 kb of DNA (top) and the lengths of 70 green incorporation fragments were measured from three independent experiments each (bottom). The means of three independent experiments were plotted with SEM.

at termination. Unloading of helicase is an irreversible process (*20*), and CMG complexes stably encircle DNA without any dynamic exchange of molecules (fig. S3G), which leads to a requirement for a regulated process to remove them when forks terminate. Blocking polyubiquitylation also led to a replication termination defect as seen by synthesis of short fragments of DNA after release from His_6-UbiNOK inhibition, similar to topoisomerase II inhibition [with the bisdioxopiperazine ICRF-193 (*21*)] replication termination defect (*2*) (Fig. 1C and fig. S3H). This defect did not create long stretches of single-stranded DNA, as Chk1 was not activated (fig. S3C).

Using mutants of ubiquitin containing only one lysine or having all but one lysine mutated, we found that K48 linkage of ubiquitin chains directed the disassembly defect (fig. S4, A to C), although proteasomal degradation was not involved (fig. S2, C and D). The cullin family of ubiquitin ligases was required for this disassembly, as the neddylation inhibitor MLN4924 (fig. S5, A to C) (*22*) also resulted in prolonged CMG association (fig. S5D).

Nickel-mediated pull-down of chromatin-bound proteins modified by His_6-tagged ubiquitin under denaturing conditions showed that Mcm7 was the only CMG subunit detectably modified by multiple ubiquitins during S phase (Fig. 2A). Mcm7 ubiquitylation on chromatin coincided with the presence of replication forks on chromatin (Fig. 2B and fig. S6A) and was represented by mostly polyubiquitylated forms, as addition of His_6-UbiNOK reduced their size (fig. S6A). Mcm7 was polyubiquitylated with K48-linked ubiquitin chains (Fig. 2C), and its ubiquitylation depended on the cullin family of E3s (Fig. 2D).

Any inhibition of replication by DNA damage greatly reduced Mcm7 ubiquitylation (Fig. 3A). Blocking the B family of DNA polymerases with aphidicolin inhibited Mcm7 ubiquitylation, as did the addition of aphidicolin and caffeine combined, which resulted in accumulation of blocked forks on chromatin (Fig. 3B), which in turn suggested that Mcm7 is ubiquitylated only when forks can terminate. Indeed, blocking fork termination with the topoisomerase II inhibitor ICRF-193 (fig. S6B) greatly reduced Mcm7 ubiquitylation (Fig. 3C).

Finally, we wished to establish the mechanism by which polyubiquitylation could drive the disassembly of the replicative helicase during termination. Blocking proteasomal degradation did not affect the level of ubiquitylated Mcm7 on chromatin (fig. S7A). Mass spectrometry analysis of factors interacting with Mcm3 during DNA replication identified 29 peptides of the protein remodeler p97/valosin-containing protein (VCP)/Cdc48 (hereafter, p97). p97 complexes recognize proteins modified with K48 ubiquitin chains and extract them either from endoplasmic reticulum (by endoplasmic reticulum–associated degradation) or chromatin (*23*). We confirmed the interaction of chromatin-associated Mcm3 with p97 during S phase (fig. S7B). Treatment of extracts with MLN4924 leads to the accumulation of the replicative helicase and lower-mobility ubiquitylated forms of Mcm7 on chromatin in later S phase. This treatment also led to an increase in Cdc45 and Psf1 (but not p97) interacting with Mcm3, which suggested that p97 interacted preferentially with fully ubiquitylated helicase (fig. S7B).

To test whether p97 is indeed required for active helicase disassembly during DNA replication termination, we supplemented extract with recombinant wild-type or inactive p97 mutant (*24*). Addition of either protein did not affect nascent DNA synthesis (Fig. 4A) or Cdt1 degradation (fig. S7C). However, supplementation with mutant p97 led to the prolonged association of replicative helicase with chromatin (Fig. 4A), accumulation of the ubiquitylated forms of Mcm7 on chromatin (Fig. 4C and fig. S7D), and replication forks termination defect (Fig. 4D). This suggests that p97-mediated remodeling acts after ubiquitylation of Mcm7 but before disassembly of the replisome at the termination of replication.

p97-deficient *Caenorhabditis elegans* embryos have previously been shown to exhibit persistent chromatin association of Cdc45/GINS during mitosis, which has been suggested as a consequence of Cdt1 stabilization (*25*). However, although p97 plays a role in Cdt1 degradation in specific situations [e.g., mitotic chromatin or after UV irradiation (*25*, *26*)], it is less critical during unperturbed S phase (fig. S7C) (*27*), and the effect it has on the

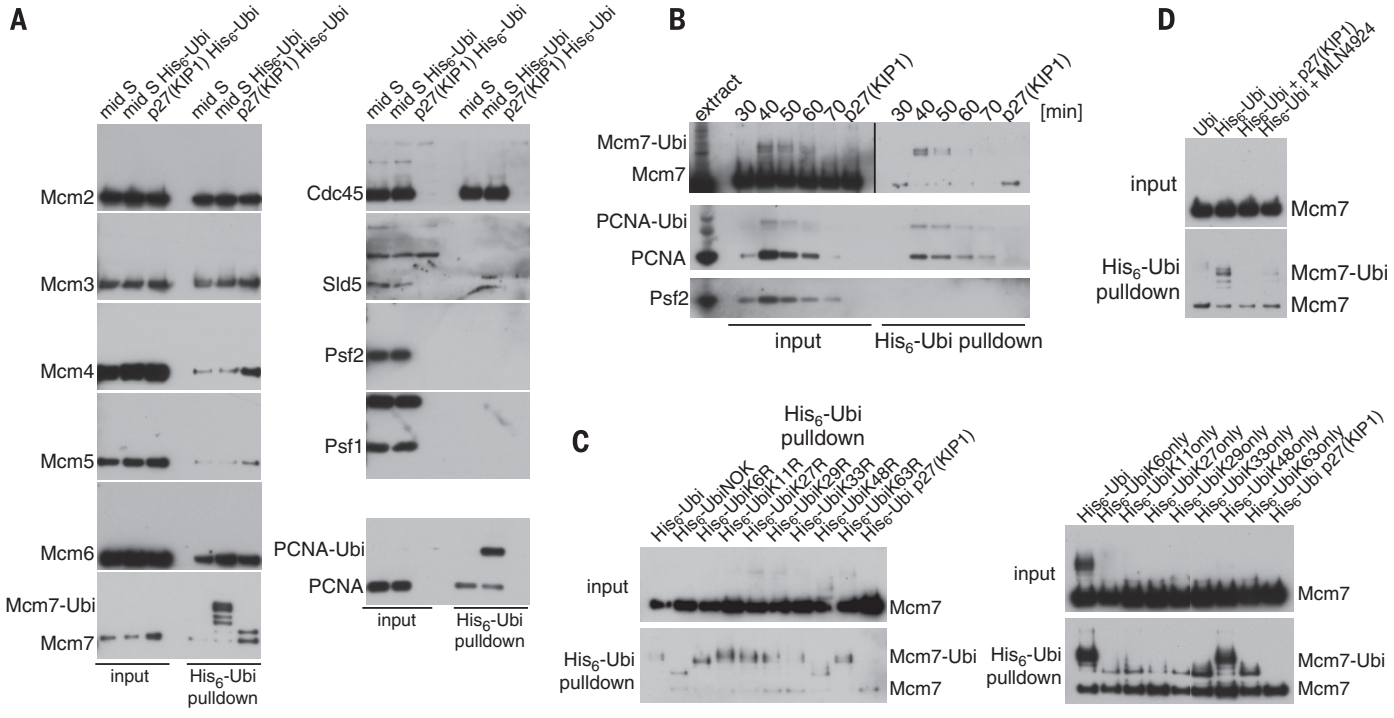

Fig. 2. Mcm7 is polyubiquitylated with K48-linked chains during DNA replication. (**A**) Egg extract was supplemented with His_6-Ubi and optional CDK inhibitor p27(KIP1); ubiquitylated chromatin proteins were pulled down and analyzed by Western blotting. (**B**) Ubiquitylated proteins were pulled down from replicating chromatin as in (A) at indicated times and analyzed by Western blotting. (**C**) Ubiquitylated proteins were pulled down as in (A) from S-phase chromatin, assembled in extract supplemented with indicated His_6-Ubi mutants and analyzed by Western blotting. Two complementary sets of ubiquitin mutants were tested. (**D**) Ubiquitylated proteins were pulled down as in (A) from early S-phase chromatin, assembled in extract supplemented with indicated inhibitors, and analyzed by Western blotting.

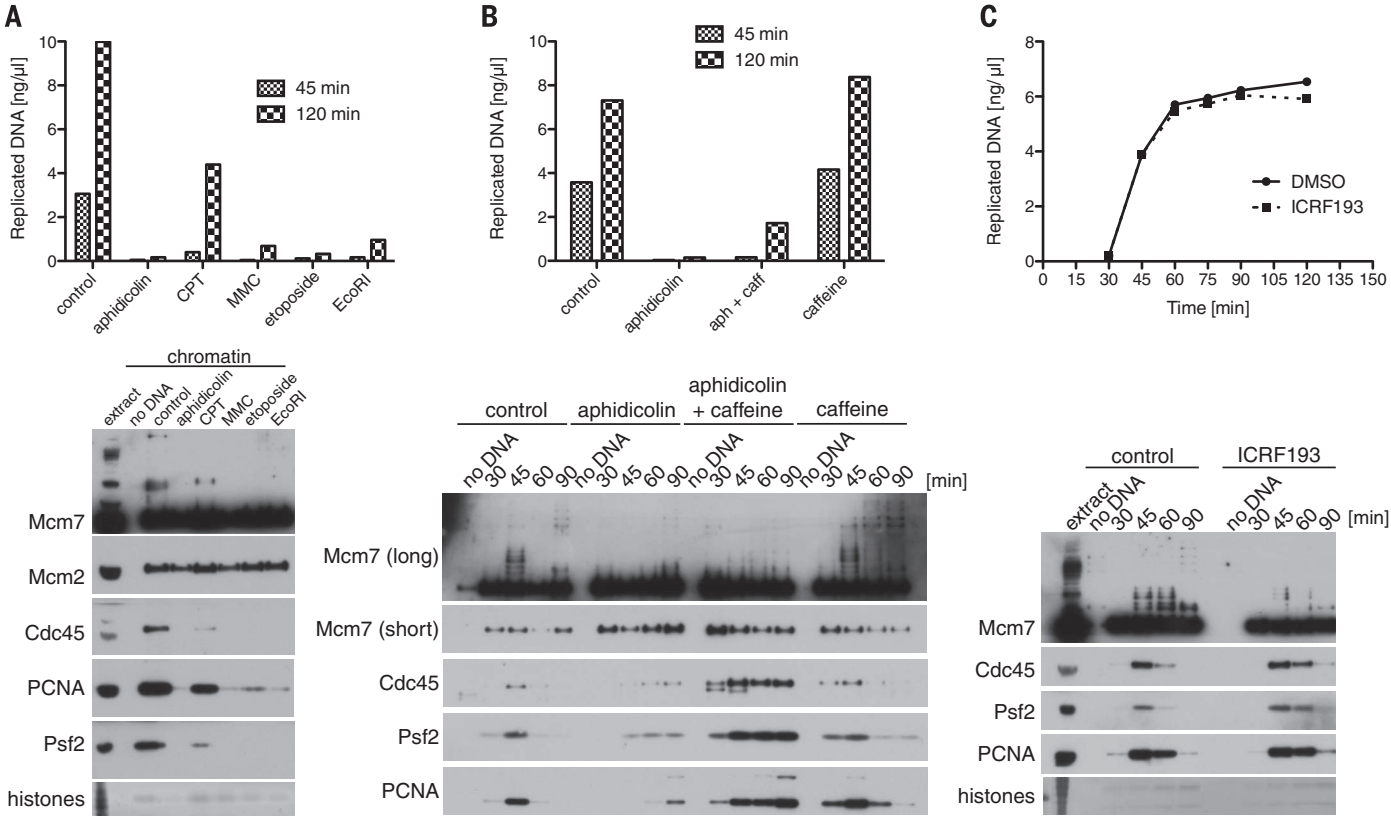

Fig. 3. Mcm7 is ubiquitylated at termination of replication forks. (**A**) Extract was supplemented with indicated inhibitors and DNA damaging agents. The ability of each extract to replicate DNA (top) and chromatin-bound proteins (at 45 min) (bottom) were analyzed. (**B**) Extract was supplemented with indicated inhibitors, and the level of replicated DNA and chromatin-bound proteins were analyzed at indicated times as in (A). (**C**) Extract was supplemented with topoisomerase II inhibitor ICRF-193 or control dimethyl sulfoxide (DMSO) and analyzed as in (A).

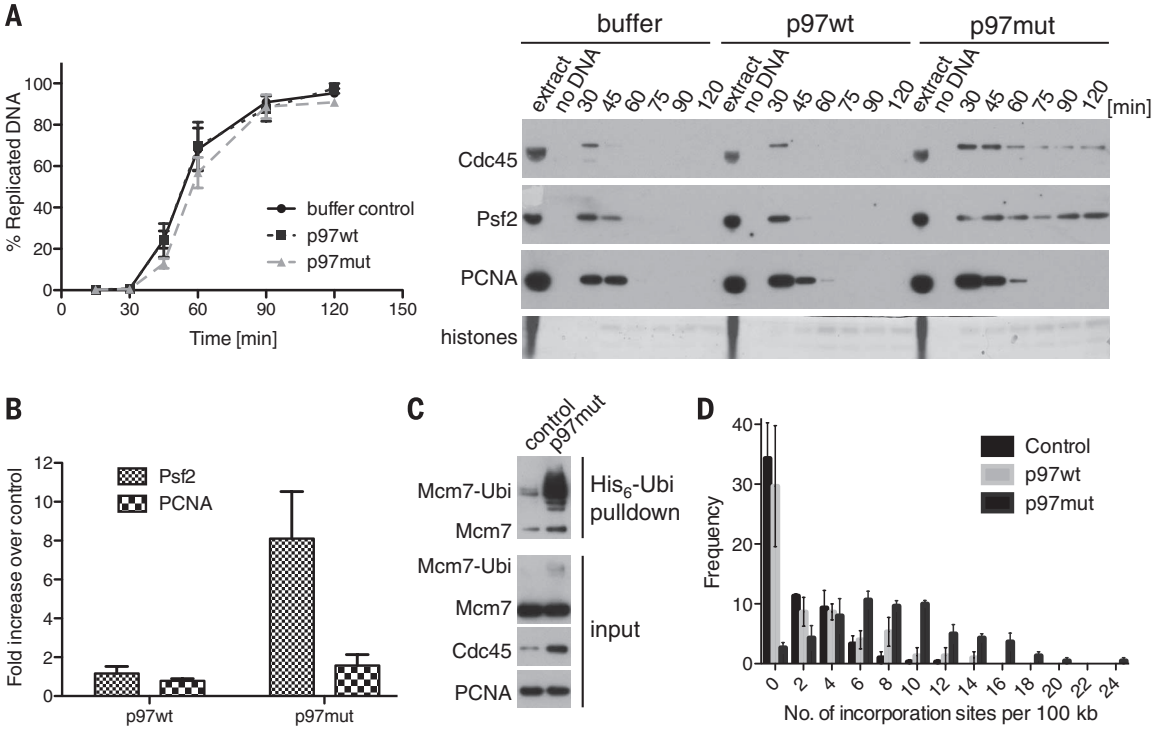

Fig. 4. p97-dependent unloading of active helicase from chromatin. (**A**) Extract was supplemented with recombinant wild-type p97 (p97wt), adenosine triphosphatase (ATPase)–dead p97D1D2 mutant (p97mut) or buffer, and extract's ability to replicate DNA was assessed (left) (average of three experiments), whereas chromatin was isolated at indicated times and analyzed by Western blotting (right). (**B**) The accumulation on chromatin of Psf2 and nonhelicase replisome component proliferating cell nuclear antigen (PCNA) at 90 min was quantified, normalized to loading control, and compared with buffer control (average of three experiments with SEM). (**C**) Extract was supplemented with mutant p97 or buffer; chromatin was isolated in the middle of S phase; and ubiquitylated proteins were pulled down as in Fig. 2A and analyzed by Western blotting. (**D**) Termination fibers were examined as in Fig. 1C but with buffer, p97wt, or p97mut in the first extract. The means of three independent experiments were plotted with SEM.

CMG complex disassembly is not driven through Cdt1 but by direct removal of ubiquitylated helicase from chromatin. Moreover, data obtained from budding yeast presented in the accompanying paper by Maric *et al.* (*28*) indicate that this mechanism of replisome disassembly at the termination of replication is conserved throughout evolution. Polyubiquitylation of Mcm7 has also been observed in human embryonic kidney 293 cells, although a function for it has not yet been reported (*29*).

REFERENCES AND NOTES

1. J. Baxter, J. F. Diffley, *Mol. Cell* **30**, 790–802 (2008).
2. O. Cuvier, S. Stanojcic, J. M. Lemaitre, M. Mechali, *Genes Dev.* **22**, 860–865 (2008).
3. D. Fachinetti *et al.*, *Mol. Cell* **39**, 595–605 (2010).
4. C. J. Rudolph, A. L. Upton, A. Stockum, C. A. Nieduszynski, R. G. Lloyd, *Nature* **500**, 608–611 (2013).
5. K. Labib, J. A. Tercero, J. F. Diffley, *Science* **288**, 1643–1647 (2000).
6. D. Remus *et al.*, *Cell* **139**, 719–730 (2009).
7. C. Evrin *et al.*, *Proc. Natl. Acad. Sci. U.S.A.* **106**, 20240–20245 (2009).
8. A. Gambus, G. A. Khoudoli, R. C. Jones, J. J. Blow, *J. Biol. Chem.* **286**, 11855–11864 (2011).
9. M. A. Kuipers *et al.*, *J. Cell Biol.* **192**, 29–41 (2011).
10. I. Ilves, T. Petojevic, J. J. Pesavento, M. R. Botchan, *Mol. Cell* **37**, 247–258 (2010).
11. A. Gambus *et al.*, *Nat. Cell Biol.* **8**, 358–366 (2006).
12. A. Nishiyama, L. Frappier, M. Méchali, *Genes Dev.* **25**, 165–175 (2011).
13. M. Jagannathan *et al.*, *Mol. Cell. Biol.* **34**, 132–145 (2014).
14. D. T. Mahaffey, C. Gorbea, M. Rechsteiner, *Exp. Cell Res.* **288**, 225–234 (2003).
15. D. Komander, M. Rape, *Annu. Rev. Biochem.* **81**, 203–229 (2012).
16. J. Adams, M. Kauffman, *Cancer Invest.* **22**, 304–311 (2004).
17. J. Jin, E. E. Arias, J. Chen, J. W. Harper, J. C. Walter, *Mol. Cell* **23**, 709–721 (2006).
18. A. Li, J. J. Blow, *EMBO J.* **24**, 395–404 (2005).
19. A. M. Woodward *et al.*, *J. Cell Biol.* **173**, 673–683 (2006).
20. D. Remus, J. F. Diffley, *Curr. Opin. Cell Biol.* **21**, 771–777 (2009).
21. T. Germe, O. Hyrien, *EMBO Rep.* **6**, 729–735 (2005).
22. T. A. Soucy *et al.*, *Nature* **458**, 732–736 (2009).
23. N. P. Dantuma, T. Hoppe, *Trends Cell Biol.* **22**, 483–491 (2012).
24. S. Heubes, O. Stemmann, *J. Cell Sci.* **120**, 1325–1329 (2007).
25. A. Franz *et al.*, *Mol. Cell* **44**, 85–96 (2011).
26. M. Raman, C. G. Havens, J. C. Walter, J. W. Harper, *Mol. Cell* **44**, 72–84 (2011).
27. J. Mouysset *et al.*, *Proc. Natl. Acad. Sci. U.S.A.* **105**, 12879–12884 (2008).
28. M. Maric, T. Maculins, G. De Piccoli, K. Labib, *Science* **346**, 1253596 (2014); DOI: 10.1126/science.1253596.
29. C. Kühne, L. Banks, *J. Biol. Chem.* **273**, 34302–34309 (1998).

ACKNOWLEDGMENTS

We would like to thank K. Labib for sharing his data and critical discussions, J. Blow for support and help with egg extract, R. Hay for advice, O. Stemmann for vectors to express p97, and E. Petermann for help with fibers. A.G. would like to thank D. Tennant for support. This work was supported by U.K. Medical Research Council Career Development Award MR/K007106/1 to A.G. and Cancer Research UK Birmingham Centre award DF/270312 to A.G. S.P.M. was funded by ERASMUS scholarship and Wellcome Trust strategic award ISSFPP47; N.C. was funded by Cancer Research UK Birmingham Centre award CAICS/05/12.

SUPPLEMENTARY MATERIALS

www.sciencemag.org/content/346/6208/477/suppl/DC1
Materials and Methods
Supplementary Text
Figs. S1 to S8
References (*30*–*40*)

19 March 2014; accepted 26 August 2014
10.1126/science.1253585

PROTEIN DESIGN

High thermodynamic stability of parametrically designed helical bundles

Po-Ssu Huang,[1,2]* Gustav Oberdorfer,[1,2,3]* Chunfu Xu,[1,2]* Xue Y. Pei,[4] Brent L. Nannenga,[5] Joseph M. Rogers,[6]† Frank DiMaio,[1,2] Tamir Gonen,[5] Ben Luisi,[4] David Baker[1,2,7]*‡

We describe a procedure for designing proteins with backbones produced by varying the parameters in the Crick coiled coil–generating equations. Combinatorial design calculations identify low-energy sequences for alternative helix supercoil arrangements, and the helices in the lowest-energy arrangements are connected by loop building. We design an antiparallel monomeric untwisted three-helix bundle with 80-residue helices, an antiparallel monomeric right-handed four-helix bundle, and a pentameric parallel left-handed five-helix bundle. The designed proteins are extremely stable (extrapolated ΔG_{fold} > 60 kilocalories per mole), and their crystal structures are close to those of the design models with nearly identical core packing between the helices. The approach enables the custom design of hyperstable proteins with fine-tuned geometries for a wide range of applications.

Coiled coils consisting of two or more α helices supercoiled around a central axis play important roles in biology, and their simplicity and regularity have inspired peptide-design efforts (*1*–*4*). Most studies have used sequence-based approaches, focusing on choosing optimal amino acids at core positions of the coiled-coil heptad repeat (*5*–*7*). The few structure-based efforts have used parametric equations first derived by Francis Crick (*2*) to design peptides that form right-handed coiled coils (*8*) or bind carbon nanotubes (*9*). Here we combine parametric backbone generation with the Rosetta protein-design methodology (*10*) to generate more complex and stable protein structures.

The Crick coiled-coil equation parameters for a bundle of n helices are ω_0, the supercoil twist; ω_1, the α-helical twist; R_0, the supercoil radius; φ_1, φ_2, …, φ_n, the phases of the individual helices; and z_2, …, z_n, their offsets along the superhelical axis relative to the first helix (*2*, *11*, *12*). As shown in the supplementary materials (*12*), successive Cα atoms rotate about the α-helical axis by ~(ω_0 + ω_1), and the protein backbone is strained when this sum deviates from the value of 100° found in ideal helices (which have ω_0 = 0° and ω_1 = 100°) (fig. S1). Hence, supercoil (ω_0) and helical (ω_1) twist are coupled (fig. S1).

Repeating backbone geometries are good targets for design because there are fewer distinct side-chain packing problems to be solved. There are three repeating geometries that require deviation of less than 3° from an ideal unstrained helix. First, if ω_1 is increased to 102.85° from the ideal value of 100.0°, after seven residues the helix has completed two full turns (720°). Second, if ω_1 is reduced to 98.2°, after 11 residues the helix has completed three full turns (1080°) (*8*). Third, if ω_1 is kept at exactly 100°, after 18 residues the helix has completed five full turns (1800°). We refer to these three cases as two-layer, three-layer, and five-layer designs, respectively, corresponding to the number of distinct helix-helix–interacting layers that must be designed. Because of the coupling between ω_0 and ω_1, two-layer designs are left-handed (ω_0 negative), three-layer designs are right-handed (ω_0 positive), and five-layer designs are untwisted (ω_0 close to zero) (*3*).

We explored the design of helix bundles with two-layer, three-layer, or five-layer geometries and different numbers of helices surrounding the supercoil axis. Once the number of helices in the bundle and the layer type were chosen, the Crick equation parameters were sampled on a grid, backbone conformations were generated, and Rosetta sequence design calculations were carried out. Finer grid searches were undertaken in the vicinity of the parameter sets yielding the lowest-energy designs. For the monomeric designs, the helices of the lowest-energy backbone solutions were connected using Rosetta loop modeling (*13*). Rosetta structure prediction calculations were used to investigate the extent to which the final designed sequences encode the desired structure (*14*); if the lowest-energy structures were similar to the design models, the designs were synthesized and experimentally characterized.

We designed antiparallel three-helix bundles with 80-residue helices and an 18-residue repeat unit (ω_1 = 100°). Because a monomeric three-helix bundle contains both parallel and antiparallel helix interactions, we treated each of the three helices independently in the design calculations.

[1]Department of Biochemistry, University of Washington, Seattle, WA 98195, USA. [2]Institute for Protein Design, University of Washington, Seattle, WA 98195, USA. [3]Institute of Molecular Biosciences, University of Graz, Humboldtstrasse 50/3, 8010-Graz, Austria. [4]Department of Biochemistry, University of Cambridge, Cambridge CB2 1GA, UK. [5]Janelia Research Campus, Howard Hughes Medical Institute, Ashburn, VA 20147, USA. [6]Department of Chemistry, University of Cambridge, Lensfield Road, Cambridge CB2 1EW, UK. [7]Howard Hughes Medical Institute, University of Washington, Seattle, WA 98195, USA.
*These authors contributed equally to this work. †Present address: Department of Chemistry, University of Tokyo, Graduate School of Science, 7-3-1, Hongo, Bunkyo, Tokyo 113-0033, Japan.
‡Corresponding author. E-mail: dabaker@u.washington.edu

Hence, there are seven degrees of freedom: the supercoil twist and radius, the phases of each of the three helices, and the displacements along the supercoil axis of the second and third helices relative to the first. Successive grid searches yielded well-packed low-energy models. Following connection of the helices by loop modeling, the lowest-energy structures found in Rosetta@Home structure prediction calculations for the designed sequences had core packing arrangements very similar to those of the design models in the center of the bundle, with small deviations near the turns (fig. S2). Three designs—3H5L_1, 3H5L_2, and 3H5L_4—of four tested were expressed and soluble at high levels in *Escherichia coli* and readily purified. All three proteins had helical circular dichroism (CD) spectra consistent with the design and were stable to thermal denaturation up to 95°C (fig. S3A), and negative-stain electron microscopy showed rodlike shapes with lengths (~12 nm) expected for 80-residue helices (Fig. 1C and fig. S3B).

More detailed thermodynamic characterization showed that 3H5L_2 was exceptionally stable with a denaturation midpoint of 7.5 M guanidinium chloride (GdmCl) at 25°C and 7 M at 80°C (Fig. 1A). Fitting of a two-state model (*15*) yielded a $\Delta G_{D\text{-}N}$ in the absence of denaturant of 61 ± 5 kcal mol^{-1} at 25°C (fig. S4). Because of the long extrapolation, sharp unfolding transition, and the limited unfolded protein CD baseline, the error in $\Delta G_{D\text{-}N}$ may be significantly larger, but the fit m-value ($m_{D\text{-}N}$ = 8.1 ± 0.7 kcal mol^{-1} M^{-1}; 25 °C) is that expected for the size of the protein (*16*). Even at 7.75 M GdmCl, 3H5L_2 unfolded very slowly (k_{unfold} = 7.9 ± 0.3 × 10^{-5} s^{-1} at 25°C) (Fig. 1B).

The 2.8 Å crystal structure of 3H5L_2 (table S2) has the same topology as that of the design model (Fig. 1D) but less superhelical twist; the release of helical strain evidently outweighs the slightly improved packing in the design. Despite this untwisting, the core 18-residue repeat unit is nearly identical in the crystal structure and design [all-atom root mean square deviation (RMSD) 1.1 Å]. Figure 1E shows superpositions of the design and crystal structure for each of the five distinct core packing layers; in each layer, there is tight and complementary side-chain packing, with close agreement between the crystal structure and design model and between different repeats. In several of the layers, close complementary packing of methionine residues identified in the Rosetta combinatorial side-chain packing calculations differs from previously described helix packing motifs. The complexity of the design and hence the necessity for structure-based computer calculations rather than sequence-based rules is highlighted by comparison to classical parallel two-layer (heptad repeat) bundle designs: Whereas the latter have seven unique positions (heptad repeat positions a, b, c, d, e, f, g), every repeat of 3H5L_2 is made up by three unique helix segments each with 18 unique positions, a total of 54 unique positions that must be designed. Further increasing the complexity, each layer involves packing between residues from two parallel helices and one antiparallel helix.

For a second test of the approach, we designed a three-layer connected four-helix bundle with helices 2 and 4 antiparallel to helices 1 and 3. Because of the relaxation of the supercoil twist (ω_0) to a value close to 0°—the ideal value for a

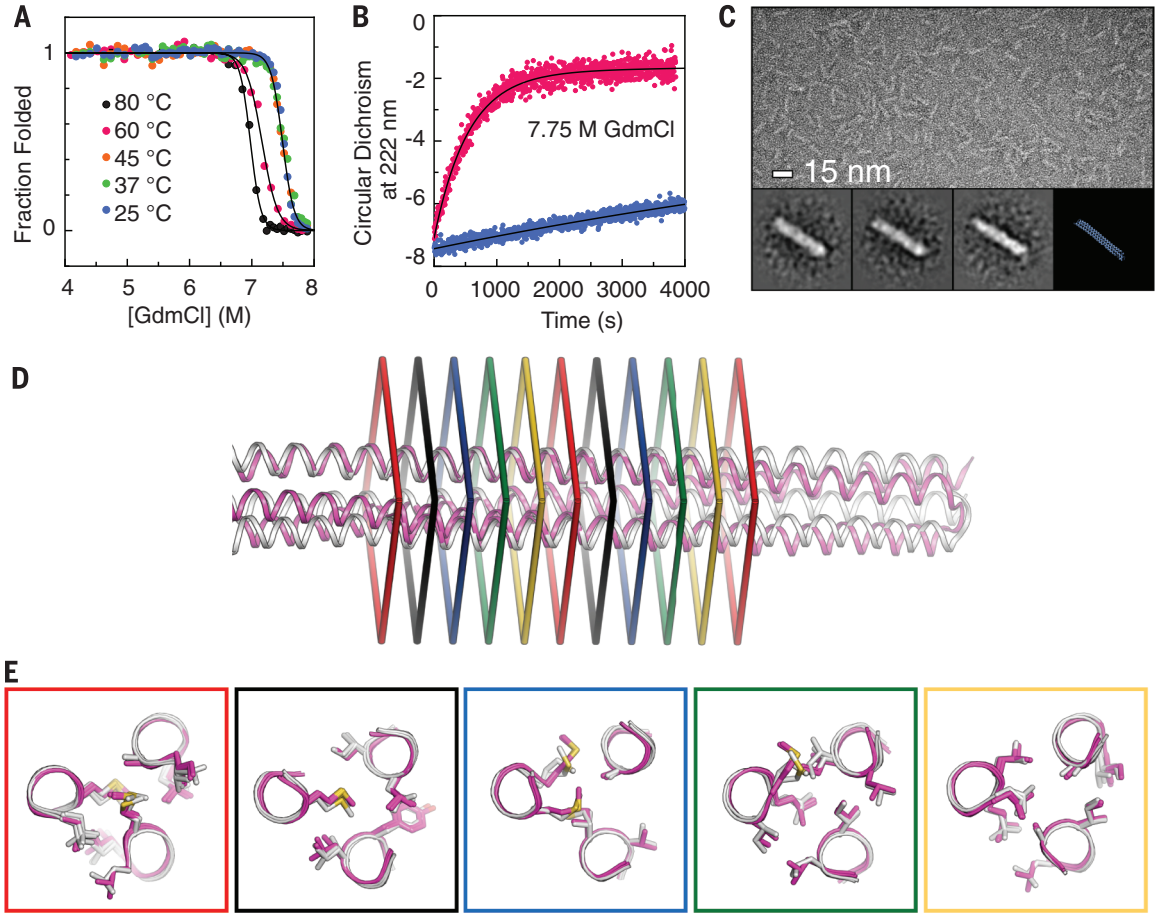

Fig. 1. Stability and structure of designed monomeric three-helix bundle 3H5L_2. (**A**) GdmCl denaturation monitored by CD. At 80°C, the midpoint of the folding transition is ~7 M GdmCl. (**B**) Kinetics of unfolding in 7.75 M GdmCl at 25°C (blue) and 60°C (red). (**C**) Negative-stain electron micrographs of 3H5L_2; particle averages are in the inset. The rods are ~12 nm in length, consistent with the 3H5L_2 design model. (**D**) Superposition of 3H5L_2 crystal structure and design model (RMSD = 3.1 Å over all Cα atoms). Colored rectangles represent the five distinct packing layers in the 18-residue repeat of the structure. (**E**) Side-chain packing arrangements in each of the five unique layers. Magenta, design model; gray, crystal structure. For each layer, the very similar solutions found by Rosetta in the two central 18-residue repeats are shown.

five-layer bundle—observed in the crystal structure of 3H5L_2, we fixed ω_0 at the ideal value given the layer type in subsequent designs. Thus, for the three-layer bundle, the helix twist ω_1 was set to 98.2° and the supercoil twist ω_0 to 1.8°. To reduce the size of the search space, we restricted sampling to *C*2 symmetric conformations in which helices 3 and 4 are related to helices 1 and 2 by a twofold rotation around the *z* axis—the helical phases and offsets for helices 3 and 4 are then identical to those for helices 1 and 2. Iterative grid searches were carried out over the remaining four parameters (the supercoil radius, the phases of helices 1 and 2, and the *z* offset of helix 2). Symmetry between the first two and second two helices was maintained at both the sequence and structure level.

Genes were synthesized for three low-energy designs (4H3L_1 to 4H3L_3) that converged on the designed target structure in Rosetta structure prediction calculations (fig. S2). One of the proteins, 4H3L_3, was solubly expressed as a monomer (fig. S12) at high levels in *E. coli*, had the expected α-helical CD spectrum (Fig. 2A), and was stable to thermal denaturation with almost identical CD spectra at 25° and 95°C (Fig. 2A). No melting transition was observed by differential scanning calorimetry (DSC) at temperatures up to 130°C (fig. S5). The stability to chemical denaturation was even higher than for 3H5L_2: Little or no unfolding was observed in 7.3 M GdmCl up to 130°C (Fig. 2B and fig. S5). In 5 M guanidinium thiocyanate (GdmSCN)—a stronger denaturant than GdmCl—the melting temperature is 97°C (Fig. 2C and fig. S5).

The 1.6 Å structure of 4H3L_3 (table S2) is similar to that of the design model (Fig. 2D) with the predicted right-handed supercoil twist and the 11-residue three-layer repeat geometry. The core packing within individual repeats is virtually identical in the crystal structure and design model with an all-atom RMSD of 0.7 Å over the core repeating units. Superpositions of the side chains in the crystal structure and design model for each of the three unique layers are shown in Fig. 2E. The close and complementary side-chain packing arrangements at each layer are distinct, and the third layer again uses methionine residues.

An advantage of the repeat structure of the parametrically designed bundles is that their length can be readily controlled by varying the number of repeats. 3H5L_2_mini with one 18-residue repeat and 4H3L_3_mini with two 11-residue repeats had CD spectra identical to those of the full-length proteins and were stable for their size (fig. S7).

Both the 3H5L_2 and 4H3L_3 structures deviate from perfect supercoil geometry (Figs. 1D and 2D), and it is likely that the lowest-energy structures for monomeric antiparallel bundles more generally will not be confined to the space spanned by the Crick parameterization near the turns. Rosetta de novo structure prediction calculations are not confined to this space, and for both 3H5L_2 and 4H3L_3 the crystal structures are closer to the lowest-energy predicted structures than to the design models (fig. S2 legend). Hence, a final round of sequence optimization based on lowest-energy predicted structures could increase the accuracy of the design process.

As a third test, we designed parallel five-helix bundles with two-layer geometry (ω_0 = 102.85°). In contrast to the three- and four-helix bundles, which are connected single-chain structures, the five-helix bundles consist of five copies of a single helical peptide arranged with fivefold cyclic symmetry (*C*5). With the *C*5 symmetry, the only degrees of freedom are R_0, ω_0, and φ_1 and hence the parameter space could be scanned in great detail. The energy landscapes following Rosetta sequence design have clear optima at R_0 = 8.7 Å and φ_1 = 43° (fig. S8, A to C). In a five-helix bundle, each helix has two interaction surfaces at 108° from each other; with this solution for φ1, both interfaces have close to optimal packing geometry (fig. S9).

The lowest-energy designs were tested in silico in docking calculations. The lowest-energy *C*5 arrangement sampled was nearly identical to

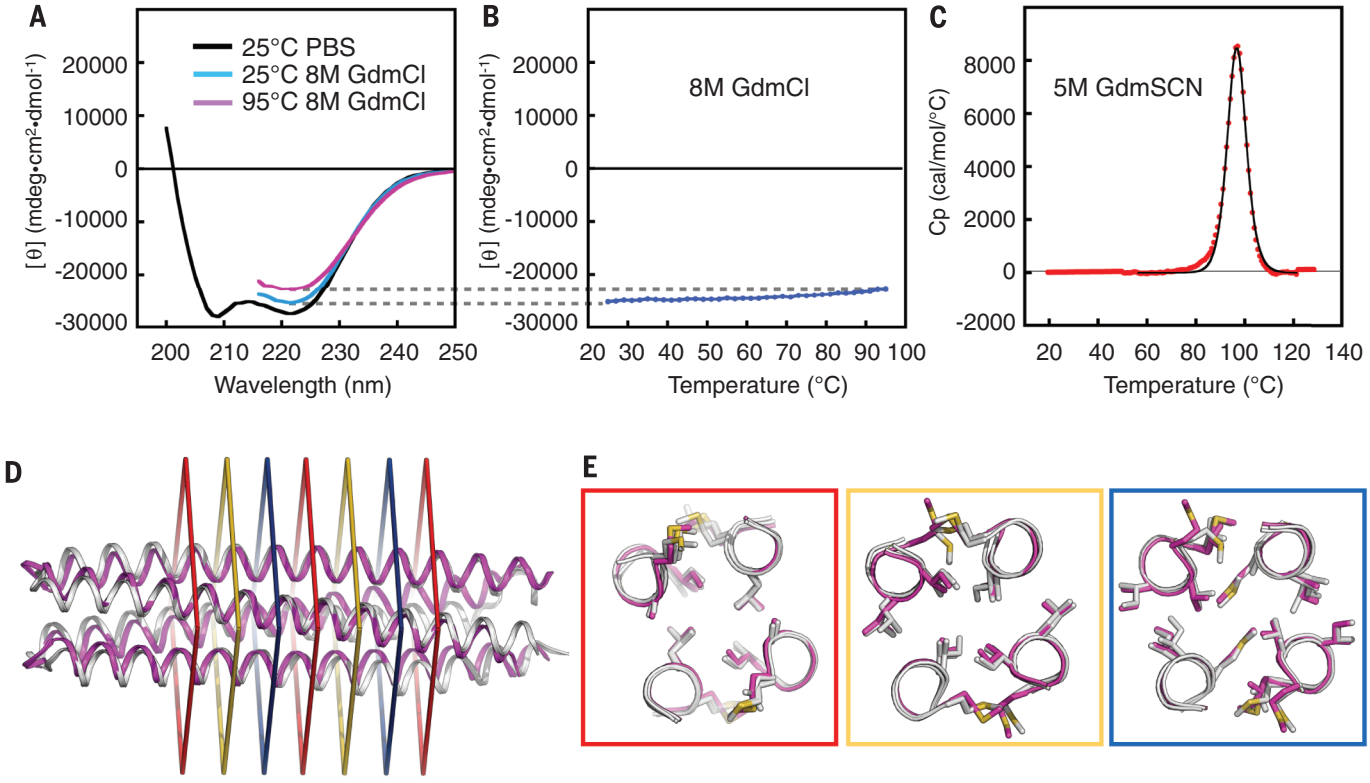

Fig. 2. Stability and structure of designed monomeric four-helix bundle 4H3L_3. (**A**) CD spectra of 4H3L_3 in the presence and absence of GdmCl. (**B**) Temperature dependence of CD signal at 222 nm in 8 M GdmCl. No unfolding transition is observed at temperatures up to 95°C. (**C**) DSC of 4H3L_3 in 5 M GdmSCN. An endothermic transition is observed at 97°C (ΔH = 95 kcal/mol). No transition is observed at temperatures up to 130°C in GdmCl or phosphate-buffered saline (PBS) (fig. S5). (**D**) Superposition of 4H3L_3 crystal structure and design model. At points where the crystal structure deviates from the design model and the helical axis changes direction, peptide backbone carbonyl groups are tipped outward toward the bulk solvent, where they contribute to entrained hydration networks (fig. S6). Colored rectangles indicate the three distinct layers in the 11-residue repeat of the protein. (**E**) Superposition of 4H3L_3 crystal structure and design model for each of the three unique packing layers for both of the central repeats. Magenta, design model; gray, crystal structure.

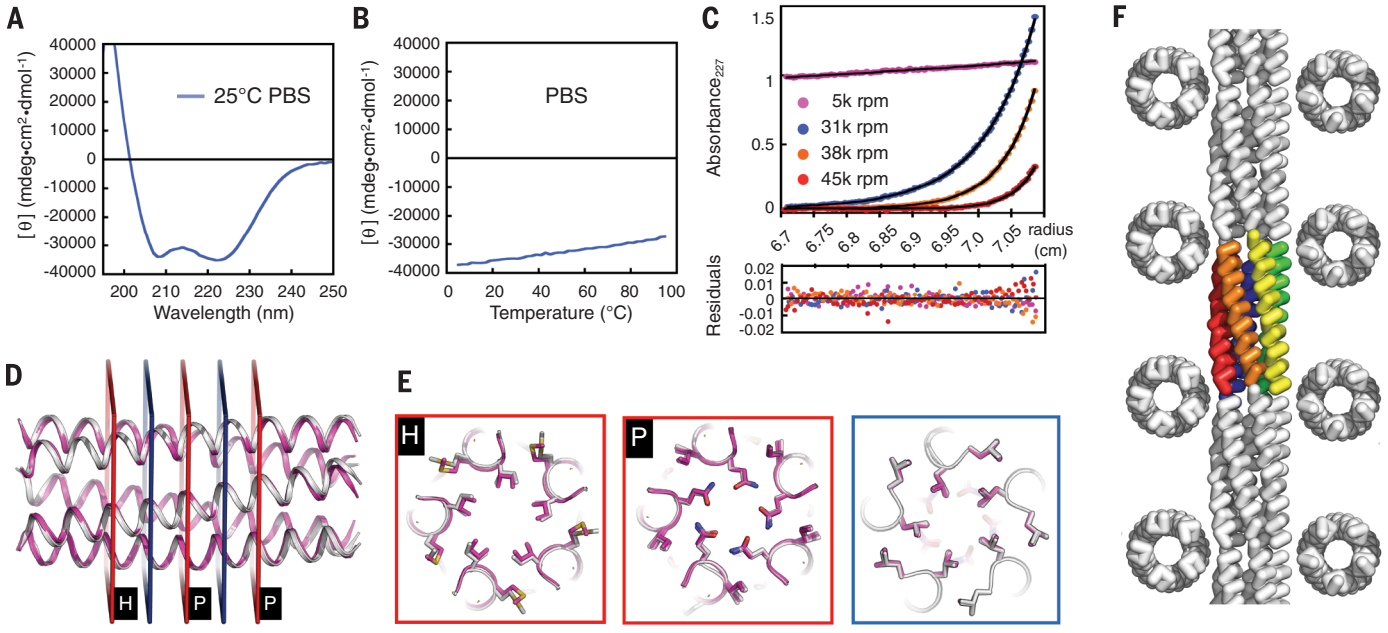

Fig. 3. Stability and structure of designed pentameric five-helix bundle 5H2L_2. (**A**) CD spectrum and (**B**) CD-monitored temperature melt of 5H2L_2 (0.2 mg/ml in PBS, pH 7.4). (**C**) Representative analytical ultracentrifugation sedimentation-equilibrium curves at four different rotor speeds for 5H2L_2 0.5 mg/ml in PBS, pH 7.4. The data fit (black lines) to a single ideal species in solution corresponding to the pentameric complex of 5H2L_2. (**D**) Superposition of backbone of crystal structure and design model. The all-atom RMSD between computational model and experimental structure is 0.4 Å. (**E**) Comparison of side-chain packing in crystal structure (gray) and design model (magenta) at the two unique layers in the 5H2L_2 structure. Two solutions were found for the red layer—a simple aliphatic packing (H) and a polar hydrogen bonding network (P)—and are shown in the two red panels. Both computed solutions were accurately recapitulated in the crystal structure. (**F**) Packing of the pentamers into straight filaments in the crystal. The colored pentamers occupy one asymmetric unit of the crystal, and the gray pentamers are from adjacent units.

that of the design model, and all the *C*4 and *C*6 arrangements had higher energies (fig. S8D). The designed interface also had lower energy than any other interface identified between two monomers in asymmetric docking calculations (fig. S8E). One of two experimentally tested designs, 5H2L_2, was readily soluble in aqueous buffer and was found by CD to have a helical structure (Fig. 3A). 5H2L_2 is stable at 95°C (Fig. 3B) and up to 4 M GdmCl (fig. S10) and sediments as a pentamer in analytical ultracentrifugation experiments (Fig. 3C).

The 1.7 Å crystal structure of 5H2L_2 with a surface substitution to promote crystal growth (5H2L_2.1 in table S1) is nearly identical to that of the design model (0.4 Å all-atom RMSD; Fig. 3D). The two unique core packing layers are shown in Fig. 3E. For the layer indicated in red in Fig. 3D, two distinct packing solutions were found; one involving a hydrogen bond network and the other aliphatic packing. Both are closely recapitulated in the crystal structure. The combination of Leu at the heptad a position and Gln or Ile at the d position is very well packed in the pentamer, and the docking calculations suggest that these residues are not as compatible with other oligomerization states. In the crystal lattice, the helices pack end to end forming long crossing helical tubes, suggesting a route to nanowire design (Fig. 3F).

The stability to chemical denaturation of 3H5L_2 and 4H3L_3 stands out from those of the proteins collected in the ProTherm database (*17*) (Fig. 4 and fig. S11). This is notable given that the sequences and structures of the designs came directly from Rosetta calculations with no human modification or experimental optimization. That hyperstability is relatively easy to achieve by design (two out of nine designs tested), but very rarely observed [an example is described in (*18*)] for naturally occurring proteins, highlights the extent to which function trumped stability during natural evolution. Efforts to design new protein functions will likely move from repurposing native scaffolds to de novo design of hyperstable backbones with geometries optimal for the desired function.

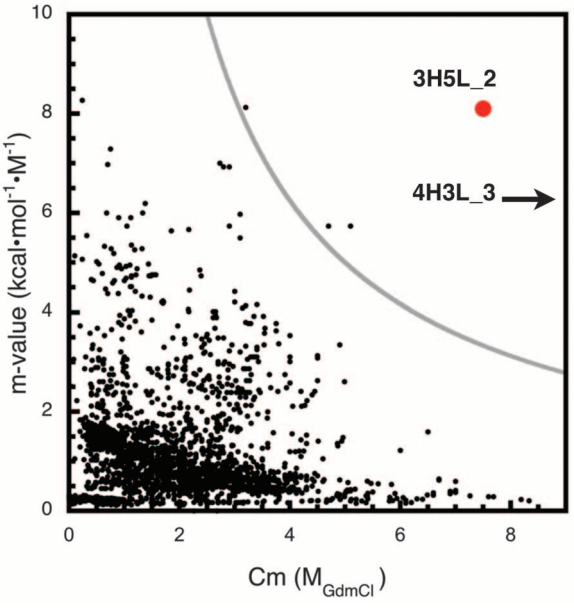

Fig. 4. High thermodynamic stability of 3H5L_2 and 4H3L_3. *X* axis, GdmCl denaturation midpoint (Cm); *y* axis, dependence of folding free energy on GdmCl concentration (*m* value); black dots, data on previously described proteins from ProTherm database (*17*); red circle, 3H5L_2; black arrow, lower bound for 4H3L_3 Cm. The free energy of folding in the absence of denaturant is the product of the *m*-value and the Cm; the curve *m*-value × Cm = 25 kcal/mol (gray) separates almost all native proteins from the two designs. 4H3L_3 does not denature in GdmCl.

Low-energy structures must have unstrained backbone conformations and complementary side-chain packing. The left-handed superhelical twist of the heptad repeat is traditionally attributed to "knobs into holes" side-chain packing; our

approach highlights the less appreciated contribution of backbone strain: The left-handed supercoil compensates for the strain introduced by overtwisting the α helix to achieve two full turns with seven residues. The combination of parametric generation of unstrained backbones and Rosetta combinatorial side-chain optimization should be extendible to the design of other classes of structures (*19*). The ability to readily generate hyperstable proteins with finely tuned geometries without relying on known sequence motifs should contribute to the next generation of designed protein-based nanostructures, therapeutics, and catalysts.

REFERENCES AND NOTES

1. A. L. Boyle, D. N. Woolfson, *Chem. Soc. Rev.* **40**, 4295–4306 (2011).
2. F. H. C. Crick, *Acta Crystallogr.* **6**, 685–689 (1953).
3. M. Gruber, A. N. Lupas, *Trends Biochem. Sci.* **28**, 679–685 (2003).
4. R. B. Hill, D. P. Raleigh, A. Lombardi, W. F. DeGrado, *Acc. Chem. Res.* **33**, 745–754 (2000).
5. P. B. Harbury, T. Zhang, P. S. Kim, T. Alber, *Science* **262**, 1401–1407 (1993).
6. J. Liu *et al.*, *Proc. Natl. Acad. Sci. U.S.A.* **103**, 15457–15462 (2006).
7. N. R. Zaccai *et al.*, *Nat. Chem. Biol.* **7**, 935–941 (2011).
8. P. B. Harbury, J. J. Plecs, B. Tidor, T. Alber, P. S. Kim, *Science* **282**, 1462–1467 (1998).
9. G. Grigoryan *et al.*, *Science* **332**, 1071–1076 (2011).
10. R. Das, D. Baker, *Annu. Rev. Biochem.* **77**, 363–382 (2008).
11. G. Grigoryan, W. F. Degrado, *J. Mol. Biol.* **405**, 1079–1100 (2011).
12. Materials and methods are available as supplementary materials on *Science* Online.
13. P. S. Huang *et al.*, *PLOS ONE* **6**, e24109 (2011).
14. P. Bradley, K. M. S. Misura, D. Baker, *Science* **309**, 1868–1871 (2005).
15. C. N. Pace, *Methods Enzymol.* **131**, 266–280 (1986).
16. C. D. Geierhaas, A. A. Nickson, K. Lindorff-Larsen, J. Clarke, M. Vendruscolo, *Protein Sci.* **16**, 125–134 (2007).
17. M. D. Kumar *et al.*, *Nucleic Acids Res.* **34**, D204–D206 (2006).
18. J. Peters, W. Baumeister, A. Lupas, *J. Mol. Biol.* **257**, 1031–1041 (1996).
19. K. C. Chou, L. Carlacci, G. M. Maggiora, *J. Mol. Biol.* **213**, 315–326 (1990).

ACKNOWLEDGMENTS

We are indebted to G. Grigoryan and W. DeGrado for their paper on coiled-coil geometry and to G. Grigoryan for the CCCP Web server that was used in initial exploratory calculations, and for helpful advice. We thank S. Gordon for protein production, Rosetta@Home volunteers for providing the computing throughput to rigorously test designs by ab initio structure prediction, and the staff at Diamond Light source and at the Advanced Light Source (U.S. Department of Energy contract no. DE-AC02-05CH11231) for access and assistance with x-ray data collection. This work was supported by Howard Hughes Medical Institute, Defense Threat Reduction Agency, and the Wellcome Trust. G.O. is a Marie Curie International Outgoing Fellowship fellow (332094 ASR-CompEnzDes FP7-People-2012-IOF). J.M.R. was supported by a studentship from the Biotechnology and Biological Sciences Research Council. Coordinates and structure factors have been deposited in the Protein Data Bank with the accession codes 4TQL (3H5L_2), 4UOS (4H3L_3), and 4UOT (5L2L_2.1). P.S.H., G.O., C.X., and D.B. designed the research. D.B. wrote the parametric backbone generation code; P.S.H. wrote the loop modeling code; and P.S.H., G.O., C.X., and D.B. carried out design calculations and biophysical analyses. J.M.R. characterized 3H5L_2 and 3H5L_2_mini. With help from G.O. and F.D., X.Y.P. and B.L. solved structures of 4H3L_3 and 5H2L_2, and B.L.N. and T.G. solved the 3H5L_2 bundle structure and did electron microscopy analysis.

SUPPLEMENTARY MATERIALS

www.sciencemag.org/content/346/6208/481/suppl/DC1
Computational Modeling
Materials and Methods
Figs. S1 to S12
Tables S1 and S2
Input Files and Command Lines for Computations
References (*20*–*32*)

16 June 2014; accepted 17 September 2014
10.1126/science.1257481

PROTEIN DESIGN

Computational design of water-soluble α-helical barrels

Andrew R. Thomson,[1]† Christopher W. Wood,[1,2]* Antony J. Burton,[1]* Gail J. Bartlett,[1] Richard B. Sessions,[2] R. Leo Brady,[2] Derek N. Woolfson[1,2]†

The design of protein sequences that fold into prescribed de novo structures is challenging. General solutions to this problem require geometric descriptions of protein folds and methods to fit sequences to these. The α-helical coiled coils present a promising class of protein for this and offer considerable scope for exploring hitherto unseen structures. For α-helical barrels, which have more than four helices and accessible central channels, many of the possible structures remain unobserved. Here, we combine geometrical considerations, knowledge-based scoring, and atomistic modeling to facilitate the design of new channel-containing α-helical barrels. X-ray crystal structures of the resulting designs match predicted in silico models. Furthermore, the observed channels are chemically defined and have diameters related to oligomer state, which present routes to design protein function.

Defining protein sequences that fold into specified three-dimensional structures is called the "inverse protein-folding problem" (*1*). Mostly, this has been applied to mimic existing folds (*2*). However, the design of structures not yet seen in nature can also be considered (*3*). Repeat proteins are of interest here, as extrapolation from known structures can provide geometric parameters and sequence-to-structure relations to guide design (*4*, *5*), and proteins with cyclic symmetry offer possibilities for systematic variation of repeating elements to produce families of proteins (*6*). One example is the α-helical coiled coil (*7*, *8*). Classical coiled coils comprise bundles of two to four α helices, account for >98% of known coiled-coil structures (*9*, *10*), and have well-understood sequence-to-structure relations (*7*, *8*). Unusually for proteins, the conformations of coiled-coil backbones are well described by a small number of parameters (*11*–*14*). Consequently, a relatively large number of successful coiled-coil structures have been designed (*8*), although, with a few exceptions (*8*, *13*), these have largely mimicked natural precedents.

The α-helical barrels present an intriguing subset of coiled coils to move beyond known structures (*15*). These have more-complex helical packing (*15*, *16*), which results in the assembly of five or more α helices into cylindrical bundles with central channels or pores (*15*). The few current examples include natural parallel 5- and 10-helix structures, and antiparallel 10- and 12-helix bundles (*17*–*20*); a de novo parallel hexamer, achieved partly serendipitously (*21*); and a mutant leucine-zipper peptide that forms an unusual staggered parallel 7-helix arrangement (*22*). For these, there is a near-linear relation between lumen size and oligomer state (Fig. 1A), which opens possibilities for designing channel proteins. However, because of the scarcity of α-helical barrels and because these are usually parts of larger membrane-spanning proteins, it is difficult to derive rules to design new examples. To overcome this, we describe a geometrical and computational framework for designing α-helical barrels from first principles and apply this to deliver discrete, water-soluble assemblies with five to seven parallel and identical helices.

First, we required a means to map structural and sequence relations between the new targets and the plentiful examples of classical coiled coils. The latter have heptad sequence repeats, $(\boldsymbol{hxxhxxx})_n$, where $\boldsymbol{h}$ and $\boldsymbol{x}$ are hydrophobic and polar residues, respectively; often labeled ***abcdefg***, this places $\boldsymbol{h}$-type residues at $\boldsymbol{a}$ and $\boldsymbol{d}$. A resulting hydrophobic seam mediates helix association and packing, with the interface often buttressed by polar interactions between $\boldsymbol{e}$ and $\boldsymbol{g}$ (Fig. 1, B and C). These are type-N interfaces, and the residues at the "***gade***" positions determine oligomer state and partner selection (*8*, *23*).

In an α-helical barrel, each helix interacts with two neighbors via independent hydrophobic seams (Fig. 1, D and E). There are three ways to achieve this within a heptad repeat: The two seams can share one residue (type I interfaces); be adjacent (type II) (Fig. 1D); or be separated by an intervening residue (type III) (*15*, *16*). We hypothesized that type II and III interfaces can lead to α-helical barrels, with the oligomer state determined by the angular offset between the two interfaces. Because differences in this contact angle between helices become smaller with increasing oligomeric state (fig. S1A), we anticipated that controlling barrel size would be more tractable for smaller assemblies. Therefore, we concentrated on type II interfaces and "***hhxxhhx***" repeats (read $\boldsymbol{g}$→$\boldsymbol{f}$"), which should define oligomers with five to seven helices.

Also with increasing oligomer state, the helix-helix interfaces in α-helical barrels become more

[1]School of Chemistry, University of Bristol, Cantock's Close, Bristol, BS8 1TS, UK. [2]School of Biochemistry, University of Bristol, Medical Sciences Building, University Walk, Bristol, BS8 1TD, UK.
*These authors contributed equally to this work. **†Corresponding author. E-mail: chzart@bristol.ac.uk (A.R.T.); d.n.woolfson@bristol.ac.uk (D.N.W.)**

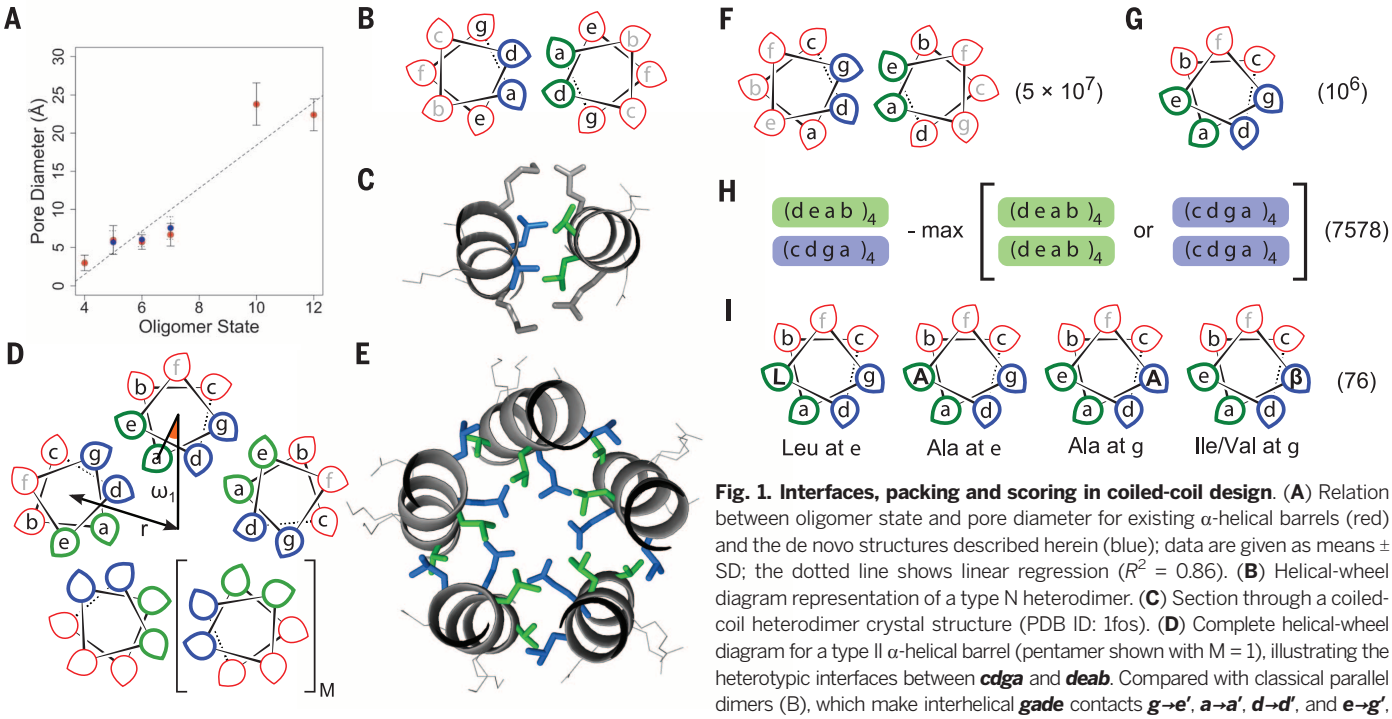

Fig. 1. Interfaces, packing and scoring in coiled-coil design. (**A**) Relation between oligomer state and pore diameter for existing α-helical barrels (red) and the de novo structures described herein (blue); data are given as means ± SD; the dotted line shows linear regression (R^2 = 0.86). (**B**) Helical-wheel diagram representation of a type N heterodimer. (**C**) Section through a coiled-coil heterodimer crystal structure (PDB ID: 1fos). (**D**) Complete helical-wheel diagram for a type II α-helical barrel (pentamer shown with M = 1), illustrating the heterotypic interfaces between ***cdga*** and ***deab***. Compared with classical parallel dimers (B), which make interhelical ***gade*** contacts ***g→e′***, ***a→a′***, ***d→d′***, and ***e→g′***, the approximately equivalent primary contacts in helical α-barrels are ***c→b′***, ***d→e′***, ***g→a′***, and ***a→d′***, respectively. In addition, three of the four geometric parameters required to describe α-helical barrels are shown: coiled-coil radius (*r*), oligomer state (N = M + 4), and helical offset (ω_1). Superhelical pitch, P, is not represented. (**E**) Section through a coiled-coil pentamer crystal structure (PDB ID: 1mz9). (**F**) Helical wheel for an isolated heterodimer-like interface in α-helical barrels. (**G**) Heterodimer-like interfaces in a single sequence with a type II repeat, showing the shared ***a*** and ***d*** positions. (**H**) Calculation of fitness score. (**I**) Designed sequence classes following filtering. Numbers of interaction pairs and/or sequences are shown in brackets at each step for (F) to (I). PyMol (www.pymol.org) was used to create panels (C) and (E).

Fig. 2. Solution-phase biophysical data for the designed peptides. (**A**) CD spectra at 5°C for ILQKIE (red), SLKEIA (green), SIKEIA (green dashes), and ALKEIA (blue). MRE, mean residue ellipticity. (**B**) Thermal denaturation profiles monitored by the change in CD signal at 222 nm. (**C**) Sedimentation velocity c(s) distribution fits at 20°C for ILQKIE, SLKEIA, and ALKEIA. (**D**) Representative sedimentation-equilibrium AUC data (dots) and fitted single-ideal species model curves recorded at 20°C, 280 nm, and 24,000 rpm for ILQKIE, SLKEIA, and ALKEIA, respectively. AU, arbitrary units. Color key: (B) to (D) same as for (A). Conditions: 10 μM (A) and (B); 150 μM (C); and 70 μM (D); peptide concentrations, phosphate-buffered saline (PBS), pH 7.4, except ALKEIA; (C) and (D), tris-buffered saline, pH 7.5.

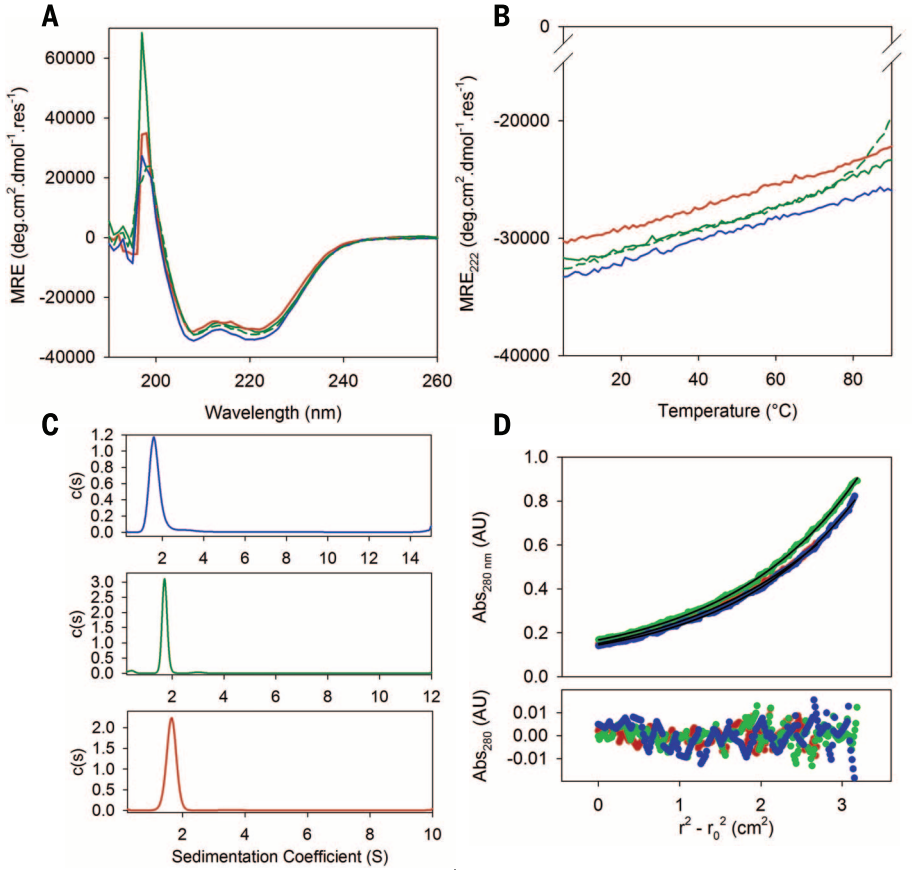

like those of classical coiled-coil dimers, specifically heterodimeric interfaces (fig. S1C and Fig. 1, B and D). Therefore, we devised a scoring system to select sequences encoding two heterotypic hydrophobic seams. This treated each seam as one-half of a heterodimer, with the seams sharing two residues (Fig. 1, F and G). In terms of traditional heptads, these seams comprise residues at ***deab*** and ***cdga***—which are each equivalent to ***gade*** positions in classical parallel dimers—and combine to give a ***gabcde*** repeat. We used the bZIP scoring function (*24*) to assess many ***deab*** plus ***cdga*** interfaces and to identify potential heterotypic pairs. We considered all combinations of A, E, I, K, L, N, Q, R, S, and V residues, which are commonly found in parallel dimers (*10*). Because of the shared residues, the initial screen had 10^6 sequences. For each ***deab*** plus ***cdga*** pair, a "fitness score" was calculated by subtracting the highest homo-paired score from that for the hetero pair (Fig. 1H). The identified pairs were filtered further by the raw bZIP pairing score, to give 7578 hits.

Further screening removed sequences with anticipated destabilizing polar residues at ***a*** and ***d*** positions; selected those with potential ***b***→***c′***, ***b***→***g′***, ***e***→***c′***, or ***e***→***g′*** salt-bridging interactions; and excluded hydrophobic residues at peripheral ***b*** and ***c*** positions. This reduced the set to 370 sequences. Many of these resembled classical tetramers, with Leu at ***a***, Ile at ***d***, and polar residues at ***e*** and ***g***. Thus, to select larger assemblies, we added a requirement for a hydrophobic residue at one or both of ***e*** and ***g***, which reduced the set to 188 sequences. There was some redundancy between Arg and Lys, so we retained only the more readily synthesized Lys-containing sequences. Of the initial 10^6 sequences, 76 met the full selection criteria. Of these, 22 repeats representing sequence diversity in the full set were chosen for further study (Fig. 1I). These were named after their ***gabcde*** repeat and synthesized as four-heptad peptides (table S1).

Next, we developed a software tool, CCBuilder (*25*), to construct in silico models of α-helical coiled coils and barrels. This uses Crick's equations to build coiled-coil backbones (*11*, *12*), adds side chains using SCRWL (*26*) and PyRosetta (*27*), and assesses interhelix packing through implementations of the BUDE force field (*25*, *28*) and SOCKET (*29*). For the 22 sequences, models were generated for each oligomer state with four to eight all-parallel helices. We used a genetic algorithm to search and optimize structural space defined by three independent parameters: radius, pitch, and the rotational offset between helices (Fig. 1D and table S2); note that the number of residues per α-helical turn also varies as it is related to coiled-coil pitch; however, it was constrained within limits known for proteins (3.65 ± 0.07) (*25*). We predicted the preferred association state for each sequence, produced an atomistic model for this, and estimated an energetic difference between it and alternative states.

The most commonly predicted oligomeric state was pentameric (12 sequences) consistent with the angular offset between the two hydrophobic seams in a type II interface (103°) most closely matching the internal angle of a regular pentagon (108°) (fig. S1A). No sequences were predicted to form tetramers, although seven were predicted to form hexamers, two to form heptamers, and one was predicted to form an octamer (table S3).

We synthesized peptides for the 22 targets (table S1 and fig. S2). As judged by circular dichroism (CD) spectroscopy, all of these formed highly α-helical and thermally stable assemblies (Fig. 2, A and B, and fig. S3). Two of the peptides showed low solubility and could not be characterized further. The oligomeric states of the remaining 20 soluble examples were assessed by analytical ultracentrifugation (AUC) (Fig. 2, C and D, fig. S4, and table S3), which indicated assemblies with four to seven peptide chains consistent with the design rationale; specifically, there were two tetramers, four pentamers, six hexamers, and a single heptamer (table S3). In seven cases, a single state could not be identified by AUC. Where determined, the experimental oligomer states matched those predicted using CCBuilder in 8 out of 13 cases (table S3).

High-resolution x-ray crystal structures were determined for four of the peptides (Fig. 3 and fig. S5 to S7, Table 1, and table S4). Structures were solved by molecular replacement with either part of, or intact, CCBuilder predictions (backbone and Cβ atoms only) as initial search models. The structures revealed parallel, blunt-ended α-helical barrels (Fig. 3, A and B), with knobs-into-holes packing confirmed by SOCKET (*29*) and type II interfaces, as designed (Fig. 3C). The experimental and in silico models were closely correlated with low root-mean-square deviations (RMSDs) for backbone and side-chain atoms (Table 1 and fig. S5). The pore sizes of the assemblies are consistent with those expected for each oligomer state (Fig. 1A). To accord with our other de novo coiled coils (*30*), we renamed the sequences CC-Pent, CC-Hex2, CC-Hex3, and CC-Hept (Table 1).

The crystal structure of CC-Pent is the first for a de novo designed pentameric α-helical coiled coil and is one of four pentameric barrels from this study. CC-Hex2, CC-Hex3, and four other sequences are further examples of de novo hexameric coiled-coil barrels (*21*). CC-Hept is the first parallel, blunt-ended heptamer. The repeats for

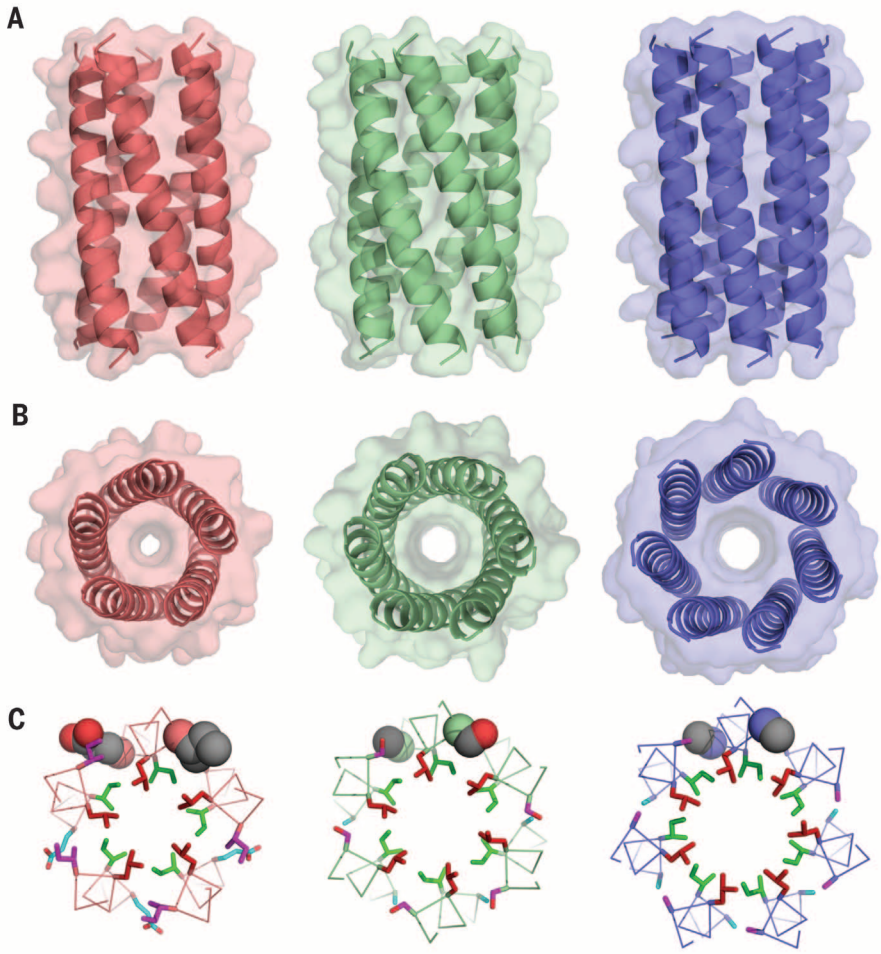

Fig. 3. X-ray crystal structures for three de novo α-helical barrels. (**A**) and (**B**) From left to right, orthogonal views of ILQKIE (CC-Pent, red, PDB ID 4pn8); SLKEIA (CC-Hex2, green, PDB ID 4pn9); and ALKEIA (CC-Hept, blue, PDB ID 4pna). (**C**) Conserved packing of the ***a*** Leu (red) and ***d*** Ile (green) residues and variation of the steric bulk of the ***e*** and ***g*** residues.

Table 1. Modeled and experimental oligomer-state and structural parameters for selected assemblies. Oligomeric state [number of monomers (*n*)] and structural parameters in angstroms (Å): pitch, radius, and pore diameter. Oligomeric state in the second column was taken from AUC sedimentation-equilibrium experiments. Pore diameters were measured with PoreWalker (*32*) and are given as the average pore diameter through the assembly. The coordinates of the experimental and model structures were fitted and the RMSD calculated using the McLachlan algorithm implemented by ProFit (*33*). RMSDs are for all nonhydrogen atoms and are shown in parentheses for Cα coordinates only.

Repeat sequence (*gabcde*) systematic name	Oligomeric state		Crystal structure		
	Model (predicted state, pitch, radius, pore diameter)	Experiment (AUC)	Oligomeric state, pitch, radius, pore diameter	Resolution (Å) and PDB ID	RMSD X-ray vs. model (Å)
ILQKIE CC-Pent	5, 190, 8.2, 5.1	5	5, 183, 8.6, 5.7	2.00, 4pn8	1.61 (0.67)
SLKEIA CC-Hex2	6, 305, 8.6, 5.0	6	6, 162, 9.5, 6.0	2.20, 4pn9	2.47 (1.77)
SIKEIA CC-Hex3	6, 135, 8.8, 5.0	6	6, 132, 9.7, 7.4	2.05, 4pnb	2.36 (1.26)
ALKEIA CC-Hept	7, 280, 9.5, 7.1	7	7, 481, 9.8, 7.6	2.10, 4pna	1.94 (1.17)

CC-Hex2 and CC-Hex3 are point mutants of each other; i.e., SLKEIAx and SIKEIAx, respectively. The former has substantially more favorable raw bZIP and fitness scores. The less-favorable score for CC-Hex3 likely reflects the β-branched residues at the ***a*** positions (fig. S6), which are analogous here to ***d*** positions in type-N, dimeric interfaces where Leu is favored (*10*, *23*). Consistent with this, CC-Hex3 has the beginning of a sharp unfolding transition at high temperatures, whereas CC-Hex2 is highly thermally stable (Fig. 2B). The sequence repeat of CC-Hept, ALKEIAx, has small Ala residues at both ***g*** and ***e***, as seen in the staggered heptamer (*22*). These small residues appear critical to dictate the fold, and a heptamer may be the highest oligomeric state possible on the basis of type II sequences. As mentioned above, one of our designs was predicted to form an octamer, and this also has ***e*** = ***g*** = Ala (table S3). However, AUC measurements were ambiguous, and the peptide did not crystallize. We posit that extending oligomer states past heptamer reliably will require type-III repeats. However, this may prove difficult to achieve because the energetic difference between oligomer states is predicted to diminish with increasing number of helices (fig. S1A), and therefore, single-chain constructs may be needed to direct specific topologies.

In summary, we have developed a geometrical and computational framework for designing α-helical barrels based on one type of complex coiled-coil packing, namely type-II interfaces (*15*). This has produced de novo parallel pentameric, hexameric, and heptameric structures, none of which are commonly observed in nature and with a design success rate of ~36% (8/22). These expand the set of rationally designed coiled-coil assemblies from dimer through to heptamer (*21*, *30*). The CC-Pent, CC-Hex2, and CC-Hept structures are based on a similar sequence framework of ***a*** = Leu plus ***d*** = Ile. Although this constellation appears to be a good general solution in terms of stability, it is not sufficient to confer oligomer-state specificity alone. That requires contributions from the remaining sites of the helical interfaces; i.e., the ***g*** and ***e*** sites, which complete the type II pattern of ***hhxxhhx***, and must have progressively smaller side chains as oligomer state increases. These structures have accessible and chemically defined channels, opening tantalizing prospects for the rational design of channel- and pore-containing protein assemblies with defined internal chemistries and properties (*15*, *21*, *31*).

REFERENCES AND NOTES

1. C. Pabo, *Nature* **301**, 200 (1983).
2. N. Koga *et al.*, *Nature* **491**, 222–227 (2012).
3. B. Kuhlman *et al.*, *Science* **302**, 1364–1368 (2003).
4. E. R. G. Main, A. R. Lowe, S. G. J. Mochrie, S. E. Jackson, L. Regan, *Curr. Opin. Struct. Biol.* **15**, 464–471 (2005).
5. C. Reichen, S. Hansen, A. Plückthun, *J. Struct. Biol.* **185**, 147–162 (2014).
6. K. O. Kopec, A. N. Lupas, *PLOS ONE* **8**, e77074 (2013).
7. A. N. Lupas, M. Gruber, *Adv. Protein Chem.* **70**, 37–38 (2005).
8. D. N. Woolfson, *Adv. Protein Chem.* **70**, 79–112 (2005).
9. E. Moutevelis, D. N. Woolfson, *J. Mol. Biol.* **385**, 726–732 (2009).
10. O. D. Testa, E. Moutevelis, D. N. Woolfson, *Nucleic Acids Res.* **37** (Database), D315–D322 (2009).
11. F. H. C. Crick, *Acta Crystallogr.* **6**, 689–697 (1953).
12. G. Offer, R. Sessions, *J. Mol. Biol.* **249**, 967–987 (1995).
13. P. B. Harbury, J. J. Plecs, B. Tidor, T. Alber, P. S. Kim, *Science* **282**, 1462–1467 (1998).
14. G. Grigoryan, W. F. Degrado, *J. Mol. Biol.* **405**, 1079–1100 (2011).
15. D. N. Woolfson, G. J. Bartlett, M. Bruning, A. R. Thomson, *Curr. Opin. Struct. Biol.* **22**, 432–441 (2012).
16. J. Walshaw, D. N. Woolfson, *Protein Sci.* **10**, 668–673 (2001).
17. V. Koronakis, A. Sharff, E. Koronakis, B. Luisi, C. Hughes, *Nature* **405**, 914–919 (2000).
18. V. N. Malashkevich, R. A. Kammerer, V. P. Efimov, T. Schulthess, J. Engel, *Science* **274**, 761–765 (1996).
19. D. Meusch *et al.*, *Nature* **508**, 61–65 (2014).
20. L. Sun *et al.*, *Nature* **505**, 432–435 (2014).
21. N. R. Zaccai *et al.*, *Nat. Chem. Biol.* **7**, 935–941 (2011).
22. J. Liu *et al.*, *Proc. Natl. Acad. Sci. U.S.A.* **103**, 15457–15462 (2006).
23. P. B. Harbury, T. Zhang, P. S. Kim, T. Alber, *Science* **262**, 1401 (1993).
24. J. H. Fong, A. E. Keating, M. Singh, *Genome Biol.* **5**, R11 (2004).
25. C. W. Wood *et al.*, *Bioinformatics* 10.1093/bioinformatics/btu502 (2014).
26. G. G. Krivov, M. V. Shapovalov, R. L. Dunbrack Jr., *Proteins* **77**, 778–795 (2009).
27. S. Chaudhury, S. Lyskov, J. J. Gray, *Bioinformatics* **26**, 689–691 (2010).
28. S. McIntosh-Smith, T. Wilson, A. A. Ibarra, J. Crisp, R. B. Sessions, *Comput. J.* **55**, 192–205 (2012).
29. J. Walshaw, D. N. Woolfson, *J. Mol. Biol.* **307**, 1427–1450 (2001).
30. J. M. Fletcher *et al.*, *ACS Synth. Biol.* **1**, 240–250 (2012).
31. A. J. Burton *et al.*, *J. Am. Chem. Soc.* **135**, 12524–12527 (2013).
32. M. Pellegrini-Calace, T. Maiwald, J. M. Thornton, *PLOS Comput. Biol.* **5**, e1000440 (2009).
33. Profit, www.bioinf.org.uk/software/profit/

ACKNOWLEDGMENTS

C.W.W. and A.J.B. are supported by the U.K. Biotechnology and Biological Sciences Research Council (BBSRC) South West Doctoral Training Partnership and the Engineering and Physical Sciences Research Council (EPSRC) Bristol Chemical Synthesis Centre for Doctoral Training, respectively. The work was funded by grants from the EPSRC (EP/J001430/1; D.N.W.), BBSRC (BB/J008990/1; D.N.W. and R.L.B.) and the European Research Council (340764; D.N.W.). D.N.W. holds a Royal Society Wolfson Research Merit Award. We thank the Diamond Light Source for access to beamlines I0-3 and I0-4 (award MX8922). We thank N. Zaccai for advice on protein x-ray crystallography, and members of the Brady and Woolfson groups for general discussions. A.R.T. and D.N.W. conceived the research program and approach; A.R.T. designed the peptide sequences; A.R.T., C.W.W., and A.J.B. synthesized the peptides and performed solution-phase characterizations; C.W.W., A.J.B., and R.L.B. solved the x-ray crystal structures; A.R.T., C.W.W., G.J.B., and R.B.S. wrote the computational design and modeling algorithms; A.R.T. and D.N.W. wrote the paper. All authors analyzed the data, and reviewed and contributed to the manuscript. Coordinates and structure factors have been deposited in the Protein Data Bank with the accession codes: CC-Pent, 4pn8; CC-Hex2, 4pn9; CC-Hex3, 4pnb; CC-Hept, 4pna; CC-Pent-variant, 4pnd.

SUPPLEMENTARY MATERIALS

www.sciencemag.org/content/346/6208/485/suppl/DC1
Materials and Methods
Figs. S1 to S7
Tables S1 to S4
References (*34*–*41*)

16 June 2014; accepted 19 September 2014
10.1126/science.1257452

SPE Microelution Plates

A trend in bioanalysis is moving toward methods that require higher levels of sensitivity and reproducibility with decreasing sample volumes. To meet these needs, SOLAμ solid phase extraction (SPE) microelution plates are designed to deliver robust, reproducible processing at elution volumes as low as 25 μL. In company-conducted experiments, the new SPE plates have improved sensitivity over comparable SPE products as much as 20-fold due to improved preconcentration while maintaining high levels of reproducibility. The SOLA macroporous structure is designed for robust, reproducible results with consistent sample and solvent flow through the SPE stationary phase, which can mitigate blockages caused by viscous biological samples. The low elution volumes accommodated by SOLAμ plates can provide a more efficient workflow by removing the blow-down stage of the SPE process. It offers the added benefit of more stability for molecules that are susceptible to adsorption and solvation issues.

Thermo Fisher Scientific
For info: 800-532-4752
www.thermoscientific.com/sola-spe

Atomic Spectroscopy

The new NexION 350 Inductively Coupled Plasma Mass Spectrometer (ICP-MS) and Syngistix for ICP-MS Software, the next generation atomic spectroscopy software platform, are now available. The NexION 350 is designed to empower laboratory professionals with greater efficiency in elemental analyses, specifically delivering the most accurate characterization of nanoparticles in the market. Syngistix for ICP-MS Software is a proprietary workflow-based platform with an intuitive interface and new, automated method setup tools for faster, more efficient implementation. The NexION 350 delivers enhanced instrument uptime and productivity through several technical innovations designed to reduce background and interferences, optimize signal stability, and minimize maintenance requirements and downtime. The combination of these features enable lab professionals to run more samples per unit of time. The NexION 350's data acquisition rates of 100,000 data points per second are ideal for applications that require fast, transient signal analysis, such as nanoparticle characterization, speciation, and laser ablation.

PerkinElmer
For info: 877-754-6979
www.perkinelmer.com

High Precision Microscope Stages

The HLD117 Linear Motor Stages bring a new level of speed and precision to microscope automation. With superior repeatability of 0.15 μm, scanning speeds of up to 300 mm per second and amazingly low-velocity ripple even at speeds down to one micron per second, the HLD117 series of stages is the highest performing stage Prior has ever produced. The innovative low profile, flat top design and ultraquiet operation make the stage especially well suited for high-end OEM and end user applications where performance matters most. The HLD117 series is compatible with Prior's NanoScan Piezo Z stages, PLW20 Well Plate Loaders and Prior's full range of sample holders making the HLD117 the most versatile high-performance stage system available on the market today.

Prior Scientific
For info: 800-877-2234
www.prior.com

Immersion Circulator

A new, highly economical immersion circulator is ideal for basic liquid heating applications. Suitable for use in baths as large as 20 L, LX Immersion Circulator combines simple, intuitive operation with a large digital display to deliver convenient temperature control for a variety of day-to-day laboratory applications. The compact unit has a temperature range of ambient +10°C to 98°C and ±0.07°C temperature stability. The LX Immersion Circulator features a large digital readout that displays both actual bath temperature and set point temperature simultaneously, built-in timer, single-speed pump, and heavy-duty mounting clamp that attaches securely to both flat and rounded tank walls. For added safety and ease of maintenance, the unit has a fully integrated housing that prevents direct contact with the pump and heater, yet provides quick access for inspection and cleaning. The circulator is suitable for use with DIN 12876-1 Class I non-flammable liquids and is compliant with ETL and CE safety requirements.

PolyScience
For info: 800-229-7569
www.polyscience.com

Cytometry Data Acquisition Software

Gallios software combines cutting-edge data acquisition tools with remarkable ease of use to increase efficiency and performance in the cell characterization and analysis workflow of core research laboratories. Researchers at all levels of experience can learn the system quickly using this next generation acquisition software for the Beckman Coulter Gallios cytometer. Users maximize productivity and data output through novel functionalities, such as the ability to set up experimental protocols offline and a Gallios simulator, which facilitates instrument training without running live experiments. The new software combines with Kaluza Analysis, a leading cytometry data analysis program, and together the packages provide a total cytometry data management solution. Kaluza for Gallios features a guided Windows-based drag-and-drop interface that is intuitive and facilitates easy creation of the right setup for accurate plot output. Visual management tools enable tracking of instrument function and experiment progress. Voltage and compensation can be quickly, accurately, and intuitively changed.

Beckman Coulter Life Sciences
For info: 800-526-3821
www.beckmancoulter.com

Electronically submit your new product description or product literature information! Go to www.sciencemag.org/products/newproducts.dtl for more information.

Newly offered instrumentation, apparatus, and laboratory materials of interest to researchers in all disciplines in academic, industrial, and governmental organizations are featured in this space. Emphasis is given to purpose, chief characteristics, and availability of products and materials. Endorsement by *Science* or AAAS of any products or materials mentioned is not implied. Additional information may be obtained from the manufacturer or supplier.

Downloaded from www.sciencemag.org on October 24, 2014

This is the start of something big.

Science Advances | AAAS

Significant research, Global impact

Introducing *Science Advances* – the new, online-only, open-access journal from *Science* and AAAS. Find out how you can be among the first authors published at **scienceadvances.org.**

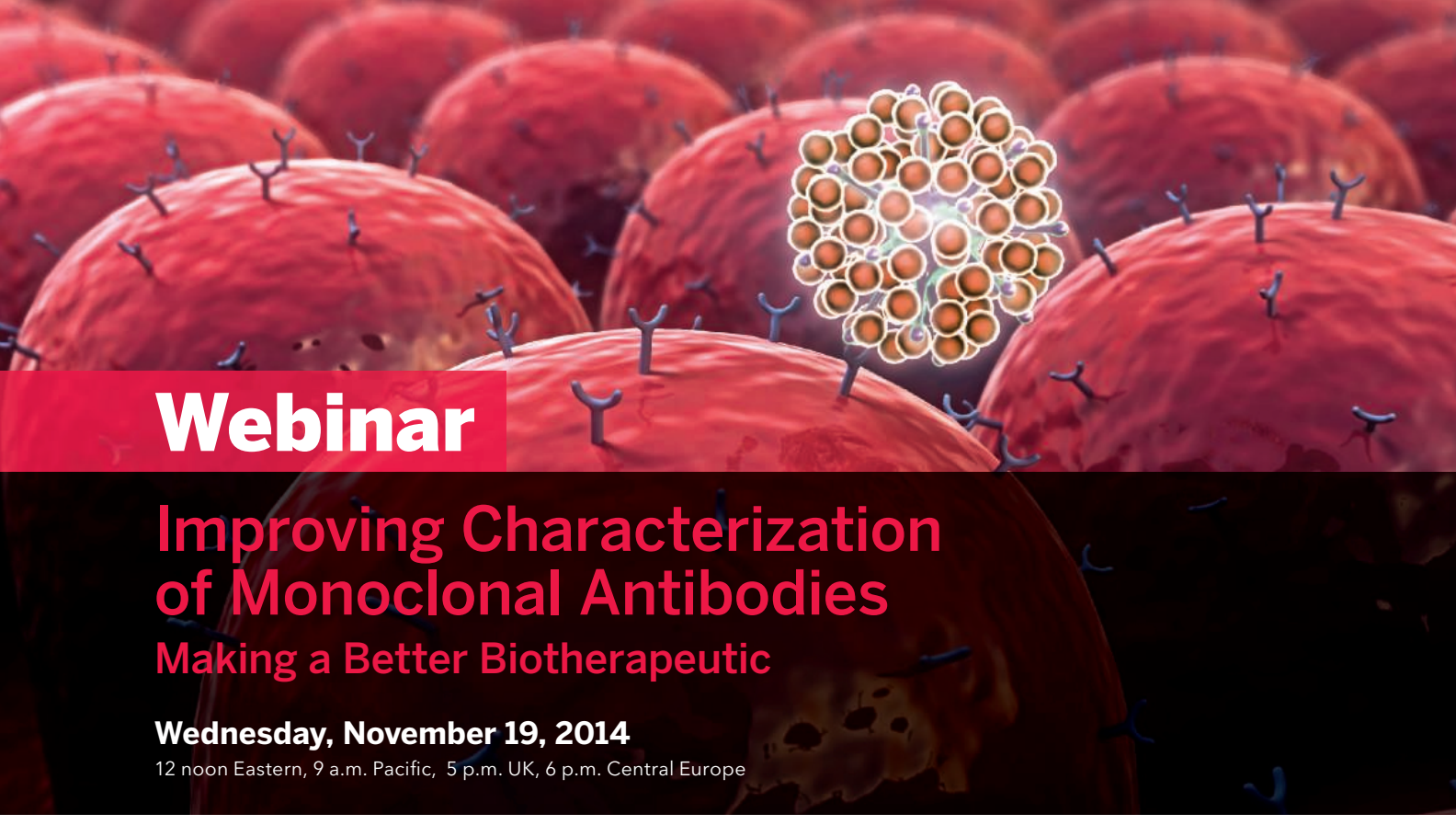

Webinar

Improving Characterization of Monoclonal Antibodies

Making a Better Biotherapeutic

Wednesday, November 19, 2014

12 noon Eastern, 9 a.m. Pacific, 5 p.m. UK, 6 p.m. Central Europe

During the webinar, viewers will:

- Gain a deeper understanding of the factors important in biotherapeutic protein production and characterization
- Learn the fundamentals of microfluidics-based capillary electrophoresis
- Hear how microchip-CE can speed protein analysis, particularly in the drug development pipeline
- Have their questions answered live by the panelists!

Characterization of therapeutic proteins remains labor-intensive and time consuming due to their often complex and heterogeneous structure. This has led to a concerted effort within the biotechnology and biopharmaceutical industry to address these bottlenecks as a means to boost the development of more biotherapeutics. Studies in this vein, such as testing the effect of various cell culture conditions on posttranslational modifications or monitoring the purification process of recombinant proteins, produce large numbers of samples that can easily exceed the capacity of modern analytical laboratories. High throughput analytical platforms with high precision, automation, and ease-of-use are therefore in great demand. To this end, the use of microfluidic analytical platforms such as microchip capillary electrophoresis (CE) have greatly increased the efficiency and reproducibility needed for analyzing proteins intended for therapeutic use. In this webinar, our expert panelists will discuss posttranslational modifications and quality assessment of biotherapeutic proteins for biopharmaceutical development using microfluidic-CE characterization.

REGISTER NOW! **webinar.sciencemag.org**

Speakers

Friederike Winkhaus, Ph.D.
Roche Diagnostics GmbH
Munich, Germany

Niomi Peckham
Alexion Pharmaceuticals
Cheshire, Connecticut

Webinar sponsored by

PerkinElmer
For the Better

Brought to you by the *Science*/AAAS Custom Publishing Office

Science
AAAS

@SciMagWebinars

Dr. Chinyere Kyna Okoro, Branco Weiss fellow since 2013

Know what science will look like tomorrow?
Apply today.

The magnitude of challenges we face today requires people with fresh thinking and novel approaches. To help find new ways forward, Society in Science - The Branco Weiss Fellowship gives extraordinary postdocs and engineers a generous grant to pursue an unconventional project for up to five years anywhere in the world. Have an idea that could change tomorrow? Get in touch with us today!

www.society-in-science.org

ETH zürich

society in science
The Branco Weiss Fellowship

AAAS *Travels*

Panama & Cartagena

January 18-28, 2015

Including the Panama Canal, Canal Train, Parks, Scientific Reserves, and World Heritage Sites!

The Panama Canal has been declared the "Monument of the Millennium" by the American Society of Civil Engineers, and we are celebrating the 100th anniversary of this tremendous achievement. Explore the diversity of Panama around the Canal including a transit of the Canal from Gamboa to the Pacific Ocean. Travel by piragua (dugout canoe) up the Chagres River to the Embera indigenous village and Chagres National Park; visit the Gatun Locks. $3,965 pp + air

For a detailed brochure, call (800) 252-4910
All prices are per person twin share + air

Betchart Expeditions Inc.
17050 Montebello Rd, Cupertino, CA 95014
Email: AAASInfo@betchartexpeditions.com
www.betchartexpeditions.com

Science & Diplomacy

Science & Diplomacy provides an open access forum for rigorous thought, analysis, and insight to serve stakeholders who develop, implement, or teach all aspects of science and diplomacy. Learn more about the latest ideas in science diplomacy and receive regular updates by following @SciDip on Twitter, liking the quarterly's page on Facebook (www.facebook.com/sciencediplomacy), and registering for free at **www.sciencediplomacy.org/user/register**.

www.ScienceDiplomacy.org

Science & Diplomacy is published by the Center for Science Diplomacy of the American Association for the Advancement of Science (AAAS), the world's largest general scientific society.

Science & Diplomacy

AAAS
ADVANCING SCIENCE, SERVING SOCIETY

WHAT DO YOU AND THOMAS EDISON HAVE IN COMMON?

AAAS.

By investing in AAAS you join Thomas Edison and the many distinguished individuals whose vision led to the creation of AAAS and our world-renowned journal, *Science,* more than 150 years ago.

Like Edison, you can create a legacy that will last well into the future through planned giving to AAAS. By making AAAS a beneficiary of your will, trust, retirement plan, or life insurance policy, you make a strong investment in our ability to advance science in the service of society for years to come.

To discuss your legacy planning, contact Juli Staiano, Director of Development, at (202) 326-6636, or jstaiano@aaas.org, or visit www.aaas.org/1848 for more information.

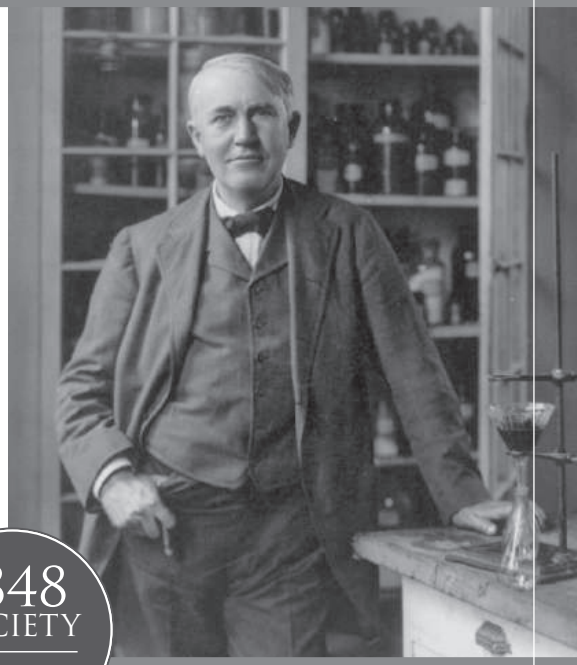

1848 SOCIETY
AAAS

SPE Microelution Plates

A trend in bioanalysis is moving toward methods that require higher levels of sensitivity and reproducibility with decreasing sample volumes. To meet these needs, SOLAμ solid phase extraction (SPE) microelution plates are designed to deliver robust, reproducible processing at elution volumes as low as 25 μL. In company-conducted experiments, the new SPE plates have improved sensitivity over comparable SPE products as much as 20-fold due to improved preconcentration while maintaining high levels of reproducibility. The SOLA macroporous structure is designed for robust, reproducible results with consistent sample and solvent flow through the SPE stationary phase, which can mitigate blockages caused by viscous biological samples. The low elution volumes accommodated by SOLAμ plates can provide a more efficient workflow by removing the blow-down stage of the SPE process. It offers the added benefit of more stability for molecules that are susceptible to adsorption and solvation issues.

Thermo Fisher Scientific
For info: 800-532-4752
www.thermoscientific.com/sola-spe

Atomic Spectroscopy

The new NexION 350 Inductively Coupled Plasma Mass Spectrometer (ICP-MS) and Syngistix for ICP-MS Software, the next generation atomic spectroscopy software platform, are now available. The NexION 350 is designed to empower laboratory professionals with greater efficiency in elemental analyses, specifically delivering the most accurate characterization of nanoparticles in the market. Syngistix for ICP-MS Software is a proprietary workflow-based platform with an intuitive interface and new, automated method setup tools for faster, more efficient implementation. The NexION 350 delivers enhanced instrument uptime and productivity through several technical innovations designed to reduce background and interferences, optimize signal stability, and minimize maintenance requirements and downtime. The combination of these features enable lab professionals to run more samples per unit of time. The NexION 350's data acquisition rates of 100,000 data points per second are ideal for applications that require fast, transient signal analysis, such as nanoparticle characterization, speciation, and laser ablation.

PerkinElmer
For info: 877-754-6979
www.perkinelmer.com

High Precision Microscope Stages

The HLD117 Linear Motor Stages bring a new level of speed and precision to microscope automation. With superior repeatability of 0.15 μm, scanning speeds of up to 300 mm per second and amazingly low-velocity ripple even at speeds down to one micron per second, the HLD117 series of stages is the highest performing stage Prior has ever produced. The innovative low profile, flat top design and ultraquiet operation make the stage especially well suited for high-end OEM and end user applications where performance matters most. The HLD117 series is compatible with Prior's NanoScan Piezo Z stages, PLW20 Well Plate Loaders and Prior's full range of sample holders making the HLD117 the most versatile high-performance stage system available on the market today.

Prior Scientific
For info: 800-877-2234
www.prior.com

Immersion Circulator

A new, highly economical immersion circulator is ideal for basic liquid heating applications. Suitable for use in baths as large as 20 L, LX Immersion Circulator combines simple, intuitive operation with a large digital display to deliver convenient temperature control for a variety of day-to-day laboratory applications. The compact unit has a temperature range of ambient +10°C to 98°C and ±0.07°C temperature stability. The LX Immersion Circulator features a large digital readout that displays both actual bath temperature and set point temperature simultaneously, built-in timer, single-speed pump, and heavy-duty mounting clamp that attaches securely to both flat and rounded tank walls. For added safety and ease of maintenance, the unit has a fully integrated housing that prevents direct contact with the pump and heater, yet provides quick access for inspection and cleaning. The circulator is suitable for use with DIN 12876-1 Class I nonflammable liquids and is compliant with ETL and CE safety requirements.

PolyScience
For info: 800-229-7569
www.polyscience.com

Cytometry Data Acquisition Software

Gallios software combines cutting-edge data acquisition tools with remarkable ease of use to increase efficiency and performance in the cell characterization and analysis workflow of core research laboratories. Researchers at all levels of experience can learn the system quickly using this next generation acquisition software for the Beckman Coulter Gallios cytometer. Users maximize productivity and data output through novel functionalities, such as the ability to set up experimental protocols offline and a Gallios simulator, which facilitates instrument training without running live experiments. The new software combines with Kaluza Analysis, a leading cytometry data analysis program, and together the packages provide a total cytometry data management solution. Kaluza for Gallios features a guided Windows-based drag-and-drop interface that is intuitive and facilitates easy creation of the right setup for accurate plot output. Visual management tools enable tracking of instrument function and experiment progress. Voltage and compensation can be quickly, accurately, and intuitively changed.

Beckman Coulter Life Sciences
For info: 800-526-3821
www.beckmancoulter.com

Electronically submit your new product description or product literature information! Go to www.sciencemag.org/products/newproducts.dtl for more information.

Newly offered instrumentation, apparatus, and laboratory materials of interest to researchers in all disciplines in academic, industrial, and governmental organizations are featured in this space. Emphasis is given to purpose, chief characteristics, and availability of products and materials. Endorsement by *Science* or AAAS of any products or materials mentioned is not implied. Additional information may be obtained from the manufacturer or supplier.

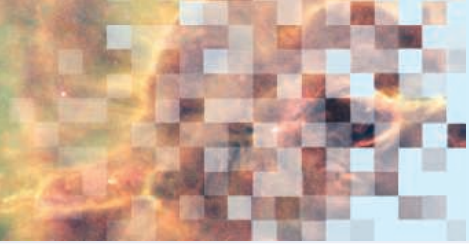

AAAS 2015 ANNUAL MEETING

Join Us in San Jose

Learn about science and technology addressing current and future global challenges.

- Seminars on computing; imaging Earth; infectious disease; and communicating science
- 150+ symposia in 13 disciplinary tracks covering the latest research advances
- Network with colleagues and attend career development workshops

Connect with us

@AAASmeetings #AAASmtg

facebook.com/AAAS.Science

www.aaas.org/meetings

Reporters: The EurekAlert! website hosts the AAAS Annual Meeting Newsroom. For details please visit eurekalert.org/aaasnewsroom/2015

Dear Colleagues:

On behalf of the AAAS Board of Directors, it is my honor to invite you to join us in San Jose, CA for the 2015 AAAS Annual Meeting, 12-16 February. This annual event is one of the most widely recognized global science gatherings, with hundreds of diverse scientific sessions and communication opportunities with broad U.S. and international media coverage.

This year's theme—*Innovations, Information, and Imaging*—will focus on transformation across all disciplines of science and technology brought about by rapid progress in organizing, visualizing, and analyzing data.

Everyone is welcome at the AAAS Annual Meeting. We hope you will join us in San Jose.

Gerald R. Fink, Ph.D.
AAAS President and Program Chair
Margaret and Herman Sokol Professor of Genetics
Massachusetts Institute of Technology

PRESIDENT'S ADDRESS

Gerald R. Fink
AAAS President and Program Chair
Margaret and Herman Sokol
Professor of Genetics,
Massachusetts Institute of Technology

Thursday, 12 February
6:00–7:00 p.m.
San Jose Convention Center, Room 220A

Dr. Gerald Fink's work in genetics, biochemistry, and molecular biology has advanced our understanding of gene regulation, mutation, and recombination. He developed a technique for transforming yeast that allowed researchers to introduce a foreign piece of genetic material into yeast cells and study the inheritance and expression of that DNA. The technique, fundamental to genetic engineering, laid the groundwork for the commercial use of yeast as biological factories for manufacturing vaccines and other drugs, and set the stage for genetic engineering in all organisms. Fink chaired a National Research Council Committee that produced the 2003 report *Biotechnology Research in an Age of Terrorism: Confronting the Dual Use Dilemma,* recommending practices to prevent the potentially destructive application of biotechnology research while enabling legitimate research. A founding member and past director of the Whitehead Institute, he received a Ph.D. in genetics from Yale University and a bachelor's degree in biology from Amherst College. He is a member of the National Academy of Sciences and Institute of Medicine and a fellow of the American Academy of Arts and Sciences and the American Philosophical Society. He has received the National Academy of Sciences Award in Molecular Biology, the Genetics Society of America Medal, the Emil Christian Hansen Award for Microbiology, the George W. Beadle Award, the Gruber Prize in Genetics, and a Guggenheim Fellowship.

PLENARY LECTURES

All plenary lectures will be held in the San Jose Convention Center, Room 220A

Daphne Koller
President and Co-Founder,
Coursera

The Online Revolution: Learning Without Limits

Friday, 13 February
5:00–6:00 p.m.

Karl Deisseroth
D.H. Chen Professor of Bioengineering,
Stanford University

Optical Descontruction of Fully-Assembled Biological Systems

Sunday, 15 February
5:00–6:00 p.m.

David Baker
Professor of Biochemistry,
University of Washington

Post-Evolutionary Biology: Design of Novel Protein Structures, Functions, and Assemblies

Saturday, 14 February
5:00–6:00 p.m.

Neil Shubin
Professor, Organismal Biology and Anatomy,
University of Chicago

Finding Your Inner Fish

Monday, 16 February
8:30–9:30 a.m.

TOPICAL LECTURES

David Altshuler
Professor of Genetics and Medicine, Harvard Medical School
Human Genome Sequence Variation and Disease

Gerbrand Ceder
R.P. Simmons Professor of Materials Science and Engineering, Massachusetts Institute of Technology
Lecture title to come

Sally Davies
Chief Medical Officer and Chief Scientific Adviser,
Department of Health, United Kingdom
Antimicrobial Resistance: A Rising Global Threat

Ann McKee
Professor of Neurology and Pathology,
Boston University School of Medicine
Emerging Concepts in Chronic Traumatic Encephalopathy

Geoffrey Nunberg
Adjunct Professor of Information,
University of California, Berkeley
The Science of Grammar and Vice Versa

Naomi Oreskes
Professor of the History of Science, Harvard University
Science: Why Should They Believe Us?

Naledi Pandor
Minister of Science and Technology, South Africa
Lecture title to come

GEORGE SARTON MEMORIAL LECTURE IN THE HISTORY AND PHILOSOPHY OF SCIENCE
Paul Farber
Distinguished Professor Emeritus, Modern Life Sciences, Intellectual History, Oregon State University
Darwinian Evolution and Human Race

JOHN P. MCGOVERN LECTURE IN THE BEHAVIORAL SCIENCES
Susan Fiske
Eugene Higgins Professor of Psychology and Public Affairs, Princeton University
Humans are Intent Detectors: Implications for Society

SEMINARS

Thursday, 12 February

Communicating Science

Scientific and technological issues may trigger societal conflict when they intersect with personal or political views. Today's scientists and engineers are challenged to communicate and engage with the public, particularly amid pressure on research budgets and related concerns about transparency and accountability. This seminar will share expertise for scientists participating in science communication and public engagement.

Organized by: AAAS Center for Public Engagement with Science and Technology

Scientists Communicating Challenging Issues

MODERATOR: Susanne Moser, Susanne Moser Research and Consulting, Santa Cruz, CA

SPEAKERS:
Noah Diffenbaugh, Stanford University, CA
Kathleen Hall Jamieson, University of Pennsylvania, Philadelphia
Lisa Krieger, *San Jose Mercury News,* CA

Public Engagement for Scientists: Realities, Risks, and Rewards

MODERATOR: Bruce Lewenstein, Cornell University, Ithaca, NY

SPEAKERS:
Elizabeth Babcock, California Academy of Sciences, San Francisco
Heidi Ballard, University of California, Davis
Anthony Dudo, University of Texas, Austin
Nalini Nadkarni, University of Utah, Salt Lake City

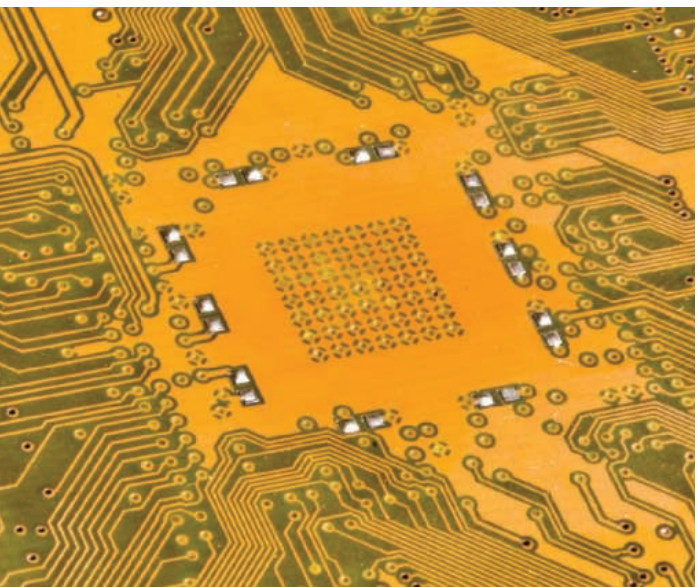

Friday, 13 February

The Future of Computing

New ways of collecting and using information are transforming science, technology, and the fabric of society. This seminar will address some of the most important advances and needs in computing and the internet, including information-centric networking; high-performance computing; artificial intelligence; mobile and wearable devices; and cybersecurity.

Our Computational Foundation Crisis and Life Beyond

Organized by: Jon Candelaria, Semiconductor Research Corporation, Durham, NC; Larry A. Nagahara, National Cancer Institute, Bethesda, MD

SPEAKERS:
Tilak Agerwala, IBM T.J. Watson Research Center, Yorktown Heights, NY
Peter Norvig, Google Inc., Mountain View, CA
Charles Bergan, Qualcomm Inc., San Diego, CA

The Future of the Internet: Meaning and Names or Numbers?

Organized by: Glenn T. Edens, PARC, Palo Alto, CA; J.J. Garcia-Luna-Aceves, University of California, Santa Cruz

SPEAKERS:
Vinton Cerf, Google Inc., Mountain View, CA
David Oran, Cisco Systems, Cambridge, MA
Glenn T. Edens, PARC, Palo Alto, CA

Engineering Information: Adapting Risk and Resilience Frameworks to Cybersecurity

Organized by: Igor Linkov, U.S. Army Engineer Research and Development Center, Concord, MA; Sankar Basu, National Science Foundation, Arlington, VA

SPEAKERS:
Shankar Sastry, University of California, Berkeley
John E. Savage, Brown University, Providence, RI
Ahmad-Reza Sadeghi Sadeghi, Technical University of Darmstadt, Germany
Stephanie Forrest, University of New Mexico, Albuquerque
Ken Heffner, Honeywell International Inc., Clearwater, FL

IMAGE CREDITS: BRAIN IMAGES: COURTESY OF THE LABORATORY OF NEURO IMAGING AND MARTINOS CENTER FOR BIOMEDICAL IMAGING, CONSORTIUM OF THE HUMAN CONNECTOME; TOPOGRAPHIC MAP: ISTOCKPHOTO; JET IN CARINA: PROJECT NASA, ESA, AND THE HUBBLE SM4 ERO TEAM; VIDEO CARD: ISTOCKPHOTO

Saturday, 14 February

Infectious Disease: Monitoring and Response

This seminar will consider how infectious disease can be effectively monitored in order to inform public health response. A discussion about the Ebola virus outbreak in West Africa will feature perspectives from key individuals and organizations involved in monitoring and responding to the public health emergency and provide information on current and future challenges. Another session will review vaccine development and recent advances in genomics, computational and structural biology, and systems biology that address genetic diversity and immune evasion, providing greater probability for success in the next generation of vaccines. The last session will discuss how Earth observation data can be used to predict the spatial and/or temporal distribution of disease in association with environmental factors, resulting in diverse health applications such as support for development of static spatial predictions of disease risk, outbreak early warning systems, and forecasts of climate change health impacts.

Lessons from the Ebola Outbreak: Response and Responsibility

Additional information to follow.

The Human Vaccines Project: Transforming the Future of Vaccine Development

Organized by: Wayne Koff, International AIDS Vaccine Initiative, New York City

SPEAKERS:
Wayne Koff, International AIDS Vaccine Initiative, New York City
Bali Pulendran, Emory Vaccine Center, Atlanta, GA
Peter Kwong, Vaccine Research Center, National Institute of Allergy and Infectious Diseases, Washington, DC

Earth Observation Approaches to Spatial Disease Prediction, Surveillance, and Control

Organized by: Archie C.A. Clements, Australian National University, Canberra

SPEAKERS:
Uriel Kitron, Emory University, Atlanta, GA
Kenneth J. Linthicum, U.S. Department of Agriculture, Gainesville, FL
Archie C.A. Clements, Australian National University, Canberra

Sunday, 15 February

Innovations in Imaging Earth

From Global Positioning System (GPS) mapping devices to internet-connected location tagging, geospatial information permeates society in the modern digital world. This seminar will highlight advances in remote sensing technology, numerical simulations, and computation that enable monitoring of the Earth at high resolution. Big data analysis techniques combined with low cost, high quality data on environmental patterns and processes from satellites, unmanned aircraft, and remote sensor networks provide insights into global change dynamics and how they impact food security, environmental sustainability, and human welfare.

Advances in Earth Observation: Enabling New Insights into Global Environmental Change

Organized by: Lyndon Estes, Princeton University, NJ; Tom Evans, Indiana University, Bloomington

SPEAKERS:
Matt Hansen, University of Maryland, College Park
Kelly Caylor, Princeton University, NJ
Maggi Kelly, University of California, Berkeley

Imaging Earth

Organized by: Ana Barros, Duke University, Durham, NC; Sally McFarlane, U.S. Department of Energy, Washington, DC

SPEAKERS:
Piers Sellers, NASA Goddard Space Flight Center, Greenbelt, MD
Melba Crawford, Purdue University, West Lafayette, IN
William Collins, Lawrence Berkeley National Laboratory, CA

Geospatial Innovations in Imaging Information Intelligently

Organized by: Steven Whitmeyer, James Madison University, Harrisonburg, VA; Declan De Paor, Old Dominion University, Norfolk, VA

SPEAKERS:
David Thau, Google Inc., Mountain View, CA
Barbara Tewksbury, Hamilton College, Clinton, NY
Richard Treves, University of Southampton, United Kingdom
Robert Kolvoord, James Madison University, Harrisonburg, VA
Jennifer Piatek, Central Connecticut State University, New Britain
Declan De Paor, Old Dominion University, Norfolk, VA

SYMPOSIA TRACKS

Organizers are listed under symposia titles.

ANTHROPOLOGY, CULTURE, AND LANGUAGE

Discovering Lost Horizons: People, Land, and Society in Prehistory
George R. Milner, Pennsylvania State University, University Park; Michael Frachetti, Washington University, St. Louis, MO

History Written in Skeletons: Intersections of History, Archaeology, and Biology
Anita Guerrini, Oregon State University, Corvallis

Imaging the Past: Using New Information Technologies To Nurture Historical Analysis
Cecile Menetrey-Monchau and Annekathrin Jaeger, European Research Council, Brussels, Belgium

Radiography of the Past: Revealing the Invisible at Archaeological Sites
Louise Byrne, European Commission, Research Executive Agency, Brussels, Belgium

The Linguistics of Status, Influence, and Innovation: A Computational Perspective
Jacob Eisenstein, Georgia Institute of Technology, Atlanta

The Sense of Smell as a Novel Means to Explore Language, Culture, and Biology
Asifa Majid, Radboud University Nijmegen, Netherlands

Visualizing Verbal Culture: Seeing Language Diversity
John Nerbonne, Rijksuniversiteit Groningen, Netherlands

Worth More Than a Thousand Words: State-of-the-Art Visualization in Cultural Heritage
Francesca Casadio, The Art Institute of Chicago, IL; Marc Walton, Northwestern University, Evanston, IL

BEHAVIORAL AND SOCIAL SCIENCES

Human Mathematical Abilities: From Intuition to the Classroom and Back
James L. McClelland, Stanford University, CA

Human-Made Noise and Nighttime Lighting
Clinton D. Francis, California Polytechnic State University, San Luis Obispo

Innovations in the Family: New Structures, New Challenges
Toni Antonucci, University of Michigan Institute for Social Research, Ann Arbor

Measuring Research Integrity: Survey of Organizational Research Climate
C.K. Gunsalus, National Center for Professional and Research Ethics, Urbana, IL

Social Influences on Health Service Use Following Disasters
Eric Jones, University of North Carolina, Greensboro

Social, Emotional, and Cognitive Bases of Communication: New Analytic Approaches
Judith F. Kroll, Pennsylvania State University, University Park; Cecilia Aragon, University of Washington, Seattle; Laurie Beth Feldman, University at Albany, NY

Virtual Labs: Transforming the Social, Behavioral, and Information Sciences
Michael W. Macy, Cornell University, Ithaca, NY

Visualizing the Experience and Use of Space in the Built Environment
Annekathrin Jaeger and Katja Meinke, European Research Council, Brussels, Belgium

Watching the Brain Think: Naturalistic Approaches To Studying Human Brain Function
Susan Hagen and Jessica F. Cantlon, University of Rochester, NY

BIOLOGY AND NEUROSCIENCE

3D Chemical Imaging: New Frontier Across Disciplines
Barbara Illman, U.S. Forest Service, Madison, WI; Carol Hirschmugl, University of Wisconsin, Milwaukee

Emerging Trends in Visualizing Physical Models and Rapid Prototyping for Biological Systems
Promita Chakraborty and Ronald N. Zuckermann, Lawrence Berkeley National Laboratory, CA

Extracting Evidence From Biological Data: Multiple Disciplines Get In On the Act
Veronica Vieland, The Research Institute at Nationwide Children's Hospital, Columbus, OH

Insights from Social Networks: Visualizing Big Data from Cells to Cell Phones to Societies
Barbara Illman, U.S. Forest Service, Madison, WI; Daniel Rubenstein, Princeton University, NJ

Multisensory Development, Plasticity and Learning: From Basic to Clinical Science
Mark Wallace, Vanderbilt University, Nashville, TN

Neuroimaging: Discoveries from Fetus to Adult
Pat Levitt, University of Southern California, Los Angeles

Neuroscience of Hearing: Brain Implants in the Fight Against Childhood Deafness
Nan Ratner, University of Maryland, College Park

Novel Technologies for Exploring the Uncultivated Microbial Majority
Susannah Tringe and Tanja Woyke, U.S. Department of Energy Joint Genome Institute, Walnut Creek, CA

Proteomics: How Big Data Opens New Vistas in Personalized Medicine
Barbara Wankerl and Patrick Regan, Technical University of Munich, Garching, Germany

Reproducibility of Science: A Roadmap Forward
Pat Levitt, University of Southern California, Los Angeles; Allan R. Sampson, University of Pittsburgh, PA

Searching for Alternative Chemistries of Life on Earth and Throughout the Universe
David G. Lynn, Emory University, Atlanta, GA; Jay T. Goodwin, National Science Foundation, Arlington, VA

To Bug or Not to Bug the Immune System: Benefits and Costs of Altering the Microbiome
Victor J. Johnson, Burleson Research Technologies Inc., Morrisville, NC; Berran Yucesoy, University of Cincinnati College of Medicine, OH

Visualizing Biomedical Data and Processes Across Space and Time Scales
Sean E. Hanlon, National Cancer Institute, Rockville, MD

What Are Race and Sex Doing in Our Genomes? Perspectives on Human "Types"
Sally Lehrman, University of California, Santa Cruz

When Experts Collide: Driving Cross-Cutting Innovation in Biological Imaging and Informatics
Carol Lynn Alpert, Museum of Science, Boston, MA

CLIMATE CHANGE, ENVIRONMENT, AND ECOLOGY

Avoiding Collapse: Human Impacts on the Biosphere
Anthony D. Barnosky, University of California, Berkeley; Paul R. Ehrlich, Stanford University, CA

Climate Change and Big Data
So-Min Cheong, University of Kansas, Lawrence

Climate Intervention and Geoengineering: Albedo Modification
Marcia McNutt, AAAS/Science, Washington, DC

Earth History: Innovative Approaches to Studying Critical Transitions
Dena M. Smith, Geological Society of America, Boulder, CO

Going Negative: Removing Carbon Dioxide From the Atmosphere
Jennifer Milne and Sally Benson, Stanford University, CA

Marine Ecosystems in Hot Water: Some Like It Hot (But Some Do Not)
Frank E. Muller-Karger, University of South Florida, St. Petersburg

Modeling Earth's Interior from Atomic to Global Scale
Renata M. Wentzcovitch, University of Minnesota, Minneapolis; Rob van de Hilst, Massachusetts Institute of Technology, Cambridge; David Bercovici, Yale University, New Haven, CT

Ocean Acidification and Hypoxia: Planning For Regional Action
Michael J. O'Donnell, California Ocean Science Trust, Oakland

Seeing the Invisible: How Sequencing Diverse Eukaryotes Transforms Ocean Science
Jian Guo and Alexandra Z. Worden, Monterey Bay Aquarium Research Institute, Landing Moss, CA; Adam Monier, University of Exeter, United Kingdom

Severe Weather in a Changing Climate: Informing Risk
Michael E. Mann, Pennsylvania State University, University Park; Michael Wehner, Lawrence Berkeley National Laboratory, CA; Donald J. Wuebbles, University of Illinois, Urbana-Champaign

The Atlantic Ocean: Our Unknown Treasure
Marco Weydert and John Bell, European Commission, Research and Innovation, Brussels, Belgium

Visual Cultures of Prediction: Imaging Climate Change Data
Lynda Walsh, University of Nevada, Reno; Birgit Schneider, University of Potsdam, Germany

AAAS 2015 ANNUAL MEETING
INNOVATIONS, INFORMATION, AND IMAGING

Advance Registration Rates

	AAAS Member Rates for members in good standing	New Member Reduced rates if you join AAAS today	Non-Member Rates for all other attendees
Professional	$295	$380	$399
Postdoc	$235	$320	$335
K-12 Teacher	$235	$320	$335
Emeritus	$235	$320	$335
Student	$60	$70	$90

One-day rates are also available. Visit **www.aaas.org/meetings/registration.**

COMMUNICATION AND PUBLIC PROGRAMS

Citizen Science from the Zooniverse: Cutting-Edge Research with 1 Million Scientists
Ramin A. Skibba, University of California, San Diego

Citizen Science: Advancing Innovations for Science, Information, and Engagement
Meg Domroese, Citizen Science Association/Schoodic Institute, Winter Harbor, ME; Jennifer Shirk, Cornell University, Ithaca, NY

Comics, Zombies, and Hip-Hop: Leveraging Pop Culture for Science Engagement
Kishore Hari and Rebecca L. Smith, University of California, San Francisco

Engagement with Intent? Scientists' Views of Communication and Why It Matters
John C. Besley, Michigan State University, East Lansing

From Art to Mathematics: A Visual Mode of Communication
George W. Hart, Stony Brook University, NY

Going Public: Investing in Science Communication for Scientists
Keegan Sawyer, National Academy of Sciences, Washington, DC; Brooke Smith, Communication Partnership for Science and the Sea (COMPASS), Portland, OR; Russ Campbell, Burroughs Wellcome Fund, Research Triangle Park, NC

National Climate Assessment: Resource for Climate Literacy and Making Decisions
Emily Therese Cloyd, U.S. Global Change Research Program, Washington, DC

Public Engagement with Science: What's In It for Scientists?
Katherine Nielsen, University of California, San Francisco, CA

Science Visualization: The Art of Making Data Beautiful
Andy Freeberg, SLAC National Accelerator Laboratory, Menlo Park, CA

Scientific Visualization: Collaborations Between Museums and Scientists
Erika C. Shugart, American Society for Microbiology, Washington, DC

Strategies for Effective Broader Impacts Work
Justin Lawrence and Jennifer Yttri, AAAS Science and Technology Policy Fellow, National Science Foundation, Arlington, VA

Tweet and Shout About Science
Erik Van der Goot and Geraldine Barry, European Commission, Joint Research Center, Brussels, Belgium

Using Cartoons To Convey Science
Yoram Bauman, StandUpEconomist.com, Seattle, WA

EDUCATION AND HUMAN RESOURCES

Assessment in Support of K–12 Science Learning
Natalie Nielsen and Heidi Schweingruber, National Academy of Sciences, Washington, DC

Diversity in the Academic STEM Workforce: Understanding Career Experiences
Julia E. Melkers, Georgia Institute of Technology, Atlanta

Gender in STEM Policy, Practice, and Research: Advances in North America and Europe
Wanda Ward, National Science Foundation, Arlington, VA

Graduate Science Education in Flux: Alternate Pathways to Science Careers
Daryl E. Chubin, Independent Consultant, Savannah, GA; Marilyn J. Suiter, National Science Foundation, Arlington, VA

Inclusive STEM High Schools: Innovative Pathways and Partnerships for Success
Edith Gummer, National Science Foundation, Arlington, VA

Innovations in Broadening Participation and Diversifying the Science Workforce
Jessi L. Smith, Montana State University, Bozeman

Learning from Visualization: Insights from STEM and Cognitive Science Collaboration
Mary Hegarty, University of California, Santa Barbara; Thomas F. Shipley, Temple University, Philadelphia, PA

Learning Science from Scientific Data
Cathryn A. Manduca, Carleton College, Northfield, MN

Next-Generation Learning and Assessment Environments for Science Inquiry Practices
Michael A. Sao Pedro, Worcester Polytechnic Institute, MA

Paving Smoother Pathways for All Students: Systemic Undergraduate STEM Reform
Martin Storksdieck, Oregon State University, Corvallis; Michael Feder, National Research Council, Washington, DC

Preparing Researchers for the Quantitative Biology of the Future
Frederick R. Adler, University of Utah, Salt Lake City; M. Gregory Forest, University of North Carolina, Chapel Hill

The Future of Graduate Education in STEM: Thinking Beyond Disciplines
Jay B. Labov, National Academy of Sciences, Washington, DC

Undergraduate Research at the Community College: Models and Sustainability
James Hewlett, Finger Lakes Community College, Canandaigua, NY

ENGINEERING, INDUSTRY, AND TECHNOLOGY

A New Paradigm for Electron Microscopy: Fast Detectors and Extreme Data Experimentation
Frances M. Ross, IBM TJ Watson Research Center, Yorktown Heights, NY; Jim Ciston and Andrew Minor, University of California, Berkeley

Computer-Aided Design of Catalysts for Sustainable Energy Conversion
Jens Norskov, Stanford University, CA

Correlating Properties of Nano-Building Blocks Via Hyperspectral Nano-Optical Imaging
P. James Schuck and Alexander Weber-Bargioni, Lawrence Berkeley National Laboratory, CA

I See, Therefore I Can
Rene Martins, European Commission, Brussels, Belgium

Integrated Computational Materials Engineering Principles for Additive Manufacturing
Sudarsanam Babu, University of Tennessee/ Oak Ridge National Laboratory, Knoxville

Next-Generation Batteries for Mobile Devices and the Grid
Johanna Nelson Weker and Glennda Chui, SLAC National Accelerator Laboratory, Menlo Park, CA

Revolutionary Vision: Implants, Prosthetics, Smart Glasses, and the Telescopic Contact Lens
Megan Williams, Christian Simm, and Melanie Picard, swissnex, San Francisco, CA

The Business of Innovation: Great Science Is Only the First Step
Fred Ledley, Bentley University, Waltham, MA

The Road to Autonomous Cars
Chris Gerdes, Stanford University, CA

Whole Lotta Shakin': Man-Made Earthquakes and Energy Development
William Savage, Seismological Society of America, Las Vegas, NV; Rex Buchanan, Kansas Geological Survey, Lawrence

GLOBAL PERSPECTIVES AND ISSUES

21st Century Global Food Security and the Environment: Improving or Deteriorating?
Felix Kogan and Alfred M. Powell, National Oceanic and Atmospheric Administration, College Park, MD

Access to Scientific Expertise in Fast Growing African Countries
Max Goldman, Sense About Science, London, United Kingdom

Astrobiology: Expanding Views of Life and Encountering New Societal Questions
Margaret S. Race, SETI Institute, Mountain View, CA; Brian Patrick Green, Santa Clara University, CA

Bounded Gaps Between Prime Numbers: Individual Research Versus Crowdsourcing
Carl Pomerance, Dartmouth College, Hanover, NH; Daniel A. Goldston, San Jose State University, CA

Creationism in Europe
Stefaan Blancke, Ghent University, Belgium; Peter C. Kjærgaard, Aarhus University, Denmark

Earth Observation Systems and Citizen Scientists Tackle Urban Environmental Hazards
Gilles Ollier, European Commission, Directorate General for Research and Innovation, Brussels, Belgium

Gender Equality in the Knowledge Society: Better Analysis Through Better Information
Sophia Huyer, Women in Global Science and Technology, Brighton, Canada

Historical and Philosophical Perspectives on Innovation in Science and Society
Manfred Laubichler, Arizona State University, Tempe

Novel Government Partnerships: Integrating Developing Countries in Global Research
Katherine E. Himes and Cameron D. Bess, U.S. Agency for International Development, Washington, DC

Science Diplomats Tackling Our Lifestyle Killers
Aidan Gilligan, SciCom–Making Sense of Science, Brussels, Belgium; Michel Kazatchkine, United Nations, Geneva, Switzerland

Science for Haiti Reconstruction: Advances in Science and Science Education Capacity
Jorge L. Colón, University of Puerto Rico, San Juan

Solutions for Achieving Gender Equity: International Perspectives
Lynnette D. Madsen, National Science Foundation, Arlington, VA; Catherine Didion, National Academy of Engineering, Washington, DC

Strategies for Pandemic Emergency Response
Eva K. Lee, Georgia Institute of Technology, Atlanta

Ukraine's Scientific Future: International Cooperation and Science Diplomacy
Michela Greco, CRDF Global, Arlington, VA

Unlocking Natural History Collections To Model the Biosphere
Ian Owens, Natural History Museum, London, United Kingdom; Kirk Johnson, National Museum of Natural History, Washington, DC

INFORMATION AND DATA TECHNOLOGY

Advancing University Career Paths in Interdisciplinary Data-Intensive Science
Cecilia Aragon and William Howe, University of Washington, Seattle

Beyond Silicon: New Materials for 21st Century Electronics
Glennda Chui, SLAC National Accelerator Laboratory, Menlo Park, CA

Differential Privacy: Analyzing Sensitive Data and Implications
Salil Vadhan, Harvard University, Cambridge, MA; Cynthia Dwork, Microsoft Research, Mountain View, CA

From the Grid to the Cloud: Computing for Big (and Small) Science
Terry O'Connor, Science and Technology Facilities Council, Swindon, United Kingdom; Vincenzo Napolano, Istituto Nazionale di Fisica Nucleare, Roma, Italy

Holistic Computing Risk Assessment: Privacy, Security, and Trust
L. Jean Camp and Diane Henshel, Indiana University, Bloomington

Improving Quality of Life By Transforming Images to Health Care Decisions
Ram D. Sriram, National Institute of Standards and Technology, Gaithersburg, MD; Ramesh Jain, University of California, Irvine; Donald Henson, Uniformed Services University, Bethesda, MD

Privacy in an Era of Big Data: Directions, Advances, and Reflections
Ersin Uzun, Palo Alto Research Center, CA

Seeing Earth in the "Light" of Gravity: New Views Through Satellite Geodesy
Barbara Wankerl and Patrick Regan, Technical University of Munich, Germany

The Convergence of Massive Data and Complex Control in the Future U.S. Power Grid
Jeffrey Taft, Pacific Northwest National Laboratory, Richland, WA

Visualization Insights from Big Data: Envisioning Science, Engineering, and Innovation
Katy Borner, Indiana University, Bloomington; Joseph E. Sabol, Chemical Consultant, Racine, WI

Wise Computing: Collaboration Between People and Machines
Kazuo Iwano and Yosuke Takashima, Japan Science and Technology Agency, Tokyo; Tateo Arimoto, National Graduate School for Policy Studies, Tokyo, Japan

MEDICAL SCIENCES AND PUBLIC HEALTH

Affordable Diagnostics for All: High-Resolution Medical Imaging for Saving Lives
Comert Kural, Ohio State University, Columbus; Ahmet Yildiz, University of California, Berkeley

Antibiotic Resistance: An Environmental Problem Threatening Global Health Care
Anneli Waara, Uppsala University, Sweden

Bugs Without Borders: A Data-Driven Approach to Tackling Antimicrobial Resistance
Stefania Di Mauro-Nava, British Consulate-General, San Francisco, CA; Lindsay R. Chura, British Embassy, Washington, DC

Cannabis and Medicine: A New Frontier in Therapeutics
Mark Ware and Julie Robert, McGill University Health Center, Montreal, Canada

Challenges in Communicating about Stem Cells
Judy Illes and Julie M. Robillard, University of British Columbia, Vancouver, Canada

Chronic Pain: No Longer an Invisible Disease
Linda Koffmar, Uppsala University, Sweden

E-Cigarettes: Killing Me Softly or Our Greatest Public Health Opportunity?
Aidan Gilligan, CEO, SciCom–Making Sense of Science, Brussels, Belgium; Julian Kinderlerer, European Commission, Brussels, Belgium

Imaging the Future of Cancer Research
Eleni Zika and Sally Donaldson, European Research Council, Brussels, Belgium

Informatics and Bioimaging: New Ways to Better Medicines
Deanna L. Kroetz, University of California, San Francisco

Innovations in Clinical Trial Registers
Victoria Murphy, Sense About Science, London, United Kingdom

Obesity and Microbiome: Concepts and Contradictions
Mary C. Dinauer, Washington University School of Medicine, St. Louis, MO; Shili Lin, Ohio State University, Columbus

Responsible Data Sharing for Clinical Trials
David L. DeMets, University of Wisconsin, Madison

The Digital Human Head: 3D Imaging and the Restoration of Craniofacial Function
Luisa Ann DiPietro, University of Illinois, Chicago

The Human Vaccines Project: Transforming the Future of Vaccine Development
Wayne Koff, International AIDS Vaccine Initiative, New York City

Worldwide Epidemic of Senile Dementias: Challenges of Pre-Clinical Treatment
Edward J. Goetzl, University of California, San Francisco

PHYSICS AND ASTRONOMY

A Science Cycle: From Novel Imaging to Novel Physics, and Vice Versa
Norman Chonacky, Yale University, New Haven, CT

Advancing Solar and Space Physics: Combining Observations, Models, and Analysis
Michael Wiltberger, National Center for Atmospheric Research, Boulder, CO

Building Galaxies: Some Assembly Required
Mark T. Adams, National Radio Astronomy Observatory, Charlottesville, VA

Celebration of 2015: The International Year of Light
Anne Matsuura, The Optical Society, Washington, DC; Anthony Johnson, University of Maryland, Baltimore County; Phil Bucksbaum, Stanford University, CA

Cosmic Neutrinos
Marcela S. Carena, University of Chicago/ Fermi National Accelerator Laboratory, Batavia, IL; Graciela Gelmini, University of California, Los Angeles

Exoplanets: New Worlds Aplenty
William Joseph Borucki and Steve B. Howell, NASA Ames Research Center, Moffett Field, CA

General Relativity at 100: Looking Forward and Looking Back
Beverly Berger, International Society on General Relativity and Gravitation, Livermore, CA; Stanley Whitcomb, California Institute of Technology, Pasadena

Imaging the Unseen: Advanced Adaptive Optics Enabling Scientific Discovery
Lisa A. Poyneer, Lawrence Livermore National Laboratory, CA

Innovations in Accelerator Science
Maria Spiropulu, California Institute of Technology, Pasadena

Scanning the Southern Skies: Harnessing Big Astronomy Data with the Square Kilometer Array
William Garnier, Square Kilometer Array Organization, Macclesfield, United Kingdom; Daan du Toit, South African Science Ministry, Brussels, Belgium

Solar System Exploration by Remote Imaging
Rolf M. Sinclair, University of Maryland, College Park; Fuk K. Li, California Institute of Technology, Pasadena

The Cosmic Microwave Background: Window into New Physics
Glenn E. Roberts, SLAC National Accelerator Laboratory, Menlo Park, CA; Jay Marx, California Institute of Technology, Pasadena

The Hubble Space Telescope: 25 Years of Imaging the Cosmos
Jennifer Wiseman, NASA Goddard Space Flight Center, Greenbelt, MD; Ray Villard, Space Telescope Science Institute, Baltimore, MD

Transformational Opportunities of Quantum Information Technologies
Martin Laforest, University of Waterloo, Canada; Jenny Hogan, National University of Singapore, Malaysia

Wave-Particle Duality of Neutrons, Atoms, and Molecules
Charles W. Clark, Joint Quantum Institute, Gaithersburg, MD

What Can We Expect from the Second Run of LHC in 2015?
James Gillies, European Organization for Nuclear Research (CERN), Geneva, Switzerland; Jon Weiner, Lawrence Berkeley National Laboratory, CA

PUBLIC POLICY

Active SETI: Is It Time To Start Transmitting to the Cosmos?
Jill C. Tarter and David C. Black, SETI Institute, Mountain View, CA

Big Data: Challenges and Social Impacts
Chris Tyler, U.K. Parliamentary Office of Science and Technology, London; Timothy M. Persons, U.S. Government Accountability Office, Washington, DC

Creating and Using New Information To Promote Innovations in Crime and Justice Policy
William Alex Pridemore, Georgia State University, Atlanta

Crisis in Quantitative Training for Biomedical Science
David L. DeMets, University of Wisconsin, Madison

Dementia: Research Milestones and Policy Priorities
Lindsay R. Chura, British Embassy Washington, DC

Developing Data-Driven Policies To Cure and Prevent Age-Related Diseases
Sharotka Simon, AAAS Science and Technology Fellow, Diplomacy Security and Development Program, Washington, DC

Integrity of Science
Thomas Arrison, National Academy of Sciences, Washington, DC

Making Sense of Chaos: A Path to Understanding Environmental Chemicals and Health
Louis J. D'Amico, Kacee Deener, and Samantha J. Jones, U.S. Environmental Protection Agency, Washington, DC

Memories Imaged and Imagined: How the Science of Memory Will Challenge the Law
Henry Greely, Stanford University Law School, CA; Nita Farahany, Duke University, Durham, NC

Metrics for Science Policy and Policy for Metrics
Ismael Rafols, University of Sussex, Brighton, United Kingdom; Michele S. Garfinkel, European Molecular Biology Organization, Heidelberg, Germany

Open Access To Your Emails: Tensions Between Academic Freedom and Open Records Laws
Michael Halpern, Union of Concerned Scientists, Washington, DC

Science During Crisis: Amidst Oil Spills, Hurricanes, and Other Disasters
Gary Machlis, DOI Strategic Sciences Group, Clemson, SC; Kristin Ludwig, U.S. Geological Survey, Reston, VA

Science Policy Professionals in the Era of Big Data: In Honor of Stephen D. Nelson
Susan E. Cozzens, Georgia Institute of Technology, Atlanta

The Human Microbiome: Implications of the Microcosm Within Us
Se Y. Kim and Jennifer Wiseman, AAAS Center for Science, Policy, and Society Programs, Washington, DC

SUSTAINABILITY AND RESOURCE MANAGEMENT

Beyond Intensification: Measuring the "Sustainable" in Sustainable Intensification
Jerry Glover, U.S. Agency for International Development, Washington, DC

Can Our Ocean Commons Be Sustainably Managed? Innovative Strategies for the High Seas
Cassandra M. Brooks and Larry Crowder, Stanford University, CA

Data Infrastructure for Sustainability
Thomas Dietz, Michigan State University, East Lansing; Adam Douglas Henry, University of Arizona, Tucson

Drivers of Tropical Forest Regeneration
Ashwini Chhatre, University of Illinois, Urbana-Champaign

Dynamic Ocean Management: Supporting Ecological and Economic Sustainability
Sara M. Maxwell, Stanford University, CA; Rebecca Lewison, San Diego State University, CA

Ecology, Economics, and Engineering of Nature-Based Coastal Defenses
Jane Carter Ingram, Wildlife Conservation Society, New York City; Michael W. Beck, The Nature Conservancy, Santa Cruz, CA

Feeding 9 Billion+: Information and Imaging for Innovation in Next-Generation Agriculture
Vijaya Gopal Kakani, Oklahoma State University, Stillwater

Information Accelerators: Using Online Tools To Address Sustainability Challenges
Richard Sharp and Rebecca Chaplin-Kramer, The Natural Capital Project, Stanford, CA

Sustainable Intensification in Agriculture: New Scientific Approaches
Karl Zimmerer, Pennsylvania State University, State College

AAAS 2015 ANNUAL MEETING
INNOVATIONS, INFORMATION, AND IMAGING

AAAS, publisher of *Science*, thanks the sponsors and supporters of the 2015 Annual Meeting

European Commission

SUBARU

HELMHOLTZ ASSOCIATION

NANYANG TECHNOLOGICAL UNIVERSITY

the Lemelson foundation
improving lives through invention

AAAS thanks

THE KAVLI FOUNDATION

for its generous support of the Science Journalism Awards

Science Signaling

The Leading Journal for Cell Signaling

Publishing key findings of broad relevance in the multidisciplinary field of cell signaling

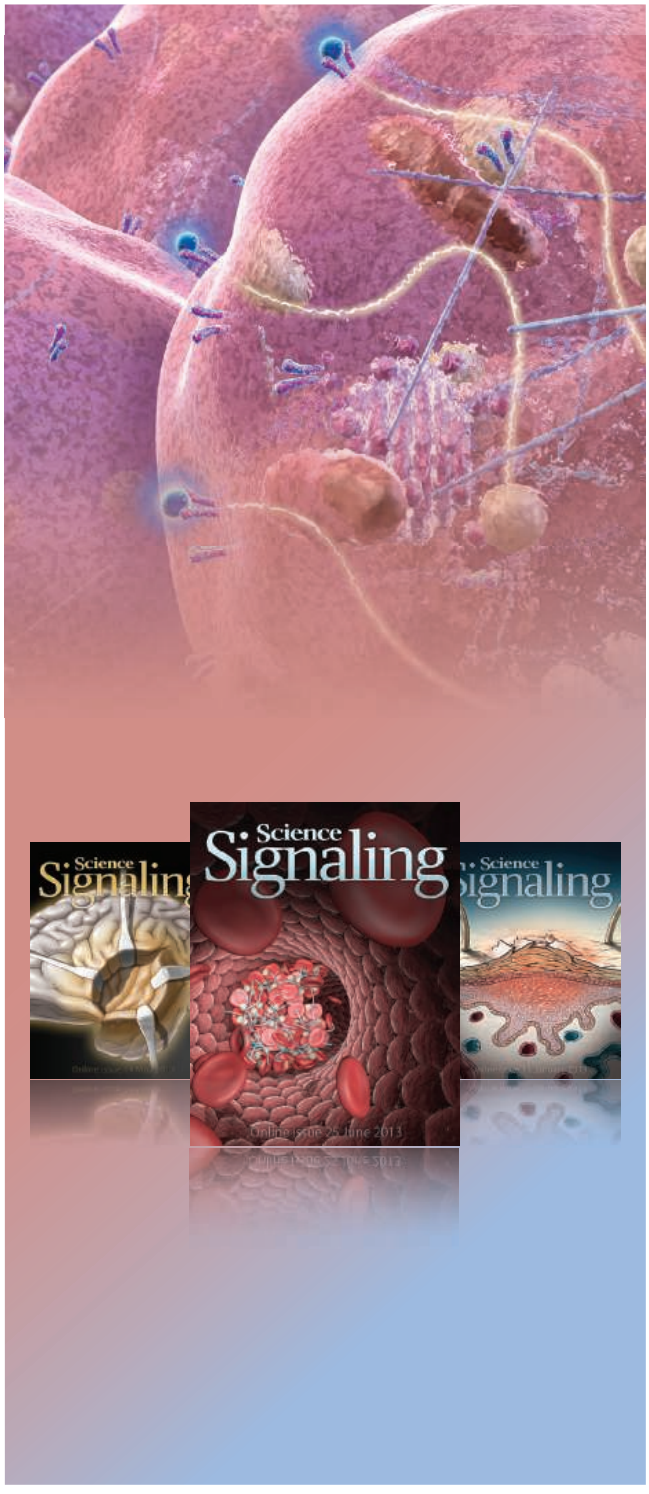

Submit your research

ScienceSignaling.org

Recommend to your library

ScienceOnline.org/recommend

Join the ranks of high-profile papers published in *Science Signaling*:

Cancer Biology
Vemurafenib Potently Induces Endoplasmic Reticulum Stress–Mediated Apoptosis in BRAFV600E Melanoma Cells
D. Beck *et al.* (F. Meier), *Sci. Signal.* **6**, ra7 (2013)

Neuroscience
Requirement for Nuclear Calcium Signaling in *Drosophila* Long-Term Memory
J.-M. Weislogel *et al.* (H. Bading), *Sci. Signal.* **6**, ra33 (2013)

Cell and Molecular Biology
A Nontranscriptional Role for HIF-1α as a Direct Inhibitor of DNA Replication
M. E. Hubbi *et al.* (G. L. Semenza), *Sci. Signal.* **6**, ra10 (2013)

Immunology
Monovalent and Multivalent Ligation of the B Cell Receptor Exhibit Differential Dependence upon Syk and Src Family Kinases
S. Mukherjee *et al.* (A. Weiss), *Sci. Signal.* **6**, ra1 (2013)

Computational and Systems Biology
Cross-Species Protein Interactome Mapping Reveals Species-Specific Wiring of Stress Response Pathways
J. Das *et al.* (H. Yu), *Sci. Signal.* **6**, ra38 (2013)

Chief Scientific Editor
Michael B. Yaffe, M.D., Ph.D.
Massachusetts Institute of Technology

Editor
Nancy R. Gough, Ph.D.
AAAS, Washington, DC

Science Signaling
AAAS

sciencesignalingeditors@aaas.org

NEW ENGLAND BioLabs® Inc.

Expand your toolbox

with NEB's interactive tool, NEBioCalculator™.

Don't let molar ratio calculations slow you down. With NEBioCalculator, quickly and confidently perform scientific conversions and calculations. With NEB®'s online tools, easier experimental design is right at your fingertips.

- To find the right cloning protocol, use our newest NEBtool, **NEBcloner**™.
- Identify the restriction enzyme cut sites within your DNA sequence with **NEBcutter**®.
- Calculate the optimal annealing temperature for your PCR with NEB's **Tm calculator**.

Featured NEB Tool

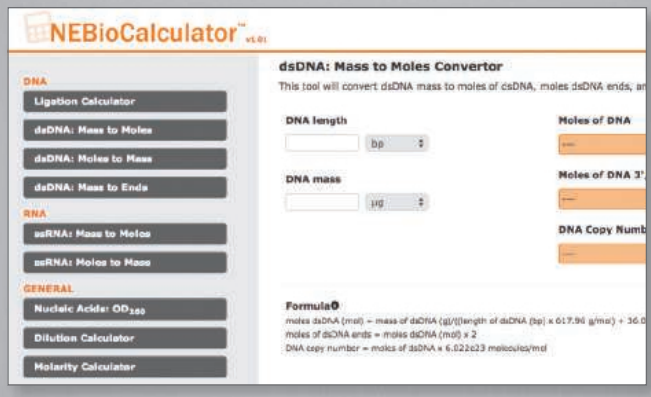

Explore NEB's entire suite of interactive online tools at

www.neb.com/nebtools

NEW ENGLAND BIOLABS®, NEB® and NEBCUTTER® are registered trademarks of New England Biolabs, Inc.
NEBCLONER™ and NEBIOCALCULATOR™ are trademarks of New England Biolabs, Inc.

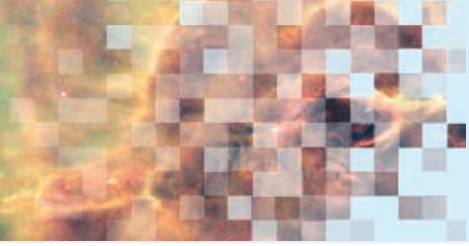

AAAS 2015 ANNUAL MEETING

Join Us in San Jose

Learn about science and technology addressing current and future global challenges.

- Seminars on computing; imaging Earth; infectious disease; and communicating science
- 150+ symposia in 13 disciplinary tracks covering the latest research advances
- Network with colleagues and attend career development workshops

Connect with us

@AAASmeetings #AAASmtg

facebook.com/AAAS.Science

www.aaas.org/meetings

Reporters: The EurekAlert! website hosts the AAAS Annual Meeting Newsroom. For details please visit eurekalert.org/aaasnewsroom/2015

Dear Colleagues:

On behalf of the AAAS Board of Directors, it is my honor to invite you to join us in San Jose, CA for the 2015 AAAS Annual Meeting, 12-16 February. This annual event is one of the most widely recognized global science gatherings, with hundreds of diverse scientific sessions and communication opportunities with broad U.S. and international media coverage.

This year's theme—*Innovations, Information, and Imaging*—will focus on transformation across all disciplines of science and technology brought about by rapid progress in organizing, visualizing, and analyzing data.

Everyone is welcome at the AAAS Annual Meeting. We hope you will join us in San Jose.

Gerald R. Fink, Ph.D.
AAAS President and Program Chair
Margaret and Herman Sokol Professor of Genetics
Massachusetts Institute of Technology

PRESIDENT'S ADDRESS

Gerald R. Fink
AAAS President and Program Chair
Margaret and Herman Sokol Professor of Genetics,
Massachusetts Institute of Technology

Thursday, 12 February
6:00–7:00 p.m.
San Jose Convention Center, Room 220A

Dr. Gerald Fink's work in genetics, biochemistry, and molecular biology has advanced our understanding of gene regulation, mutation, and recombination. He developed a technique for transforming yeast that allowed researchers to introduce a foreign piece of genetic material into yeast cells and study the inheritance and expression of that DNA. The technique, fundamental to genetic engineering, laid the groundwork for the commercial use of yeast as biological factories for manufacturing vaccines and other drugs, and set the stage for genetic engineering in all organisms. Fink chaired a National Research Council Committee that produced the 2003 report *Biotechnology Research in an Age of Terrorism: Confronting the Dual Use Dilemma,* recommending practices to prevent the potentially destructive application of biotechnology research while enabling legitimate research. A founding member and past director of the Whitehead Institute, he received a Ph.D. in genetics from Yale University and a bachelor's degree in biology from Amherst College. He is a member of the National Academy of Sciences and Institute of Medicine and a fellow of the American Academy of Arts and Sciences and the American Philosophical Society. He has received the National Academy of Sciences Award in Molecular Biology, the Genetics Society of America Medal, the Emil Christian Hansen Award for Microbiology, the George W. Beadle Award, the Gruber Prize in Genetics, and a Guggenheim Fellowship.

Downloaded from www.sciencemag.org on October 24, 2014

PLENARY LECTURES

All plenary lectures will be held in the San Jose Convention Center, Room 220A

Daphne Koller
President and Co-Founder,
Coursera

The Online Revolution: Learning Without Limits

Friday, 13 February
5:00–6:00 p.m.

Karl Deisseroth
D.H. Chen Professor of Bioengineering,
Stanford University

Optical Descontruction of Fully-Assembled Biological Systems

Sunday, 15 February
5:00–6:00 p.m.

David Baker
Professor of Biochemistry,
University of Washington

Post-Evolutionary Biology: Design of Novel Protein Structures, Functions, and Assemblies

Saturday, 14 February
5:00–6:00 p.m.

Neil Shubin
Professor, Organismal Biology and Anatomy,
University of Chicago

Finding Your Inner Fish

Monday, 16 February
8:30–9:30 a.m.

TOPICAL LECTURES

David Altshuler
Professor of Genetics and Medicine, Harvard Medical School
Human Genome Sequence Variation and Disease

Gerbrand Ceder
R.P. Simmons Professor of Materials Science and Engineering, Massachusetts Institute of Technology
Lecture title to come

Sally Davies
Chief Medical Officer and Chief Scientific Adviser,
Department of Health, United Kingdom
Antimicrobial Resistance: A Rising Global Threat

Ann McKee
Professor of Neurology and Pathology,
Boston University School of Medicine
Emerging Concepts in Chronic Traumatic Encephalopathy

Geoffrey Nunberg
Adjunct Professor of Information,
University of California, Berkeley
The Science of Grammar and Vice Versa

Naomi Oreskes
Professor of the History of Science, Harvard University
Science: Why Should They Believe Us?

Naledi Pandor
Minister of Science and Technology, South Africa
Lecture title to come

GEORGE SARTON MEMORIAL LECTURE IN THE HISTORY AND PHILOSOPHY OF SCIENCE
Paul Farber
Distinguished Professor Emeritus, Modern Life Sciences, Intellectual History, Oregon State University
Darwinian Evolution and Human Race

JOHN P. MCGOVERN LECTURE IN THE BEHAVIORAL SCIENCES
Susan Fiske
Eugene Higgins Professor of Psychology and Public Affairs, Princeton University
Humans are Intent Detectors: Implications for Society

SEMINARS

Thursday, 12 February

Communicating Science

Scientific and technological issues may trigger societal conflict when they intersect with personal or political views. Today's scientists and engineers are challenged to communicate and engage with the public, particularly amid pressure on research budgets and related concerns about transparency and accountability. This seminar will share expertise for scientists participating in science communication and public engagement.

Organized by: AAAS Center for Public Engagement with Science and Technology

Scientists Communicating Challenging Issues

MODERATOR: Susanne Moser, Susanne Moser Research and Consulting, Santa Cruz, CA

SPEAKERS:
Noah Diffenbaugh, Stanford University, CA
Kathleen Hall Jamieson, University of Pennsylvania, Philadelphia
Lisa Krieger, *San Jose Mercury News,* CA

Public Engagement for Scientists: Realities, Risks, and Rewards

MODERATOR: Bruce Lewenstein, Cornell University, Ithaca, NY

SPEAKERS:
Elizabeth Babcock, California Academy of Sciences, San Francisco
Heidi Ballard, University of California, Davis
Anthony Dudo, University of Texas, Austin
Nalini Nadkarni, University of Utah, Salt Lake City

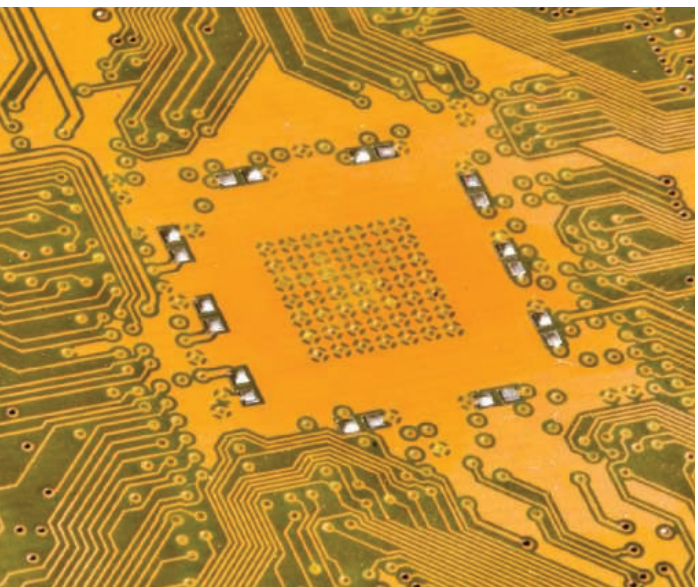

Friday, 13 February

The Future of Computing

New ways of collecting and using information are transforming science, technology, and the fabric of society. This seminar will address some of the most important advances and needs in computing and the internet, including information-centric networking; high-performance computing; artificial intelligence; mobile and wearable devices; and cybersecurity.

Our Computational Foundation Crisis and Life Beyond

Organized by: Jon Candelaria, Semiconductor Research Corporation, Durham, NC; Larry A. Nagahara, National Cancer Institute, Bethesda, MD

SPEAKERS:
Tilak Agerwala, IBM T.J. Watson Research Center, Yorktown Heights, NY
Peter Norvig, Google Inc., Mountain View, CA
Charles Bergan, Qualcomm Inc., San Diego, CA

The Future of the Internet: Meaning and Names or Numbers?

Organized by: Glenn T. Edens, PARC, Palo Alto, CA; J.J. Garcia-Luna-Aceves, University of California, Santa Cruz

SPEAKERS:
Vinton Cerf, Google Inc., Mountain View, CA
David Oran, Cisco Systems, Cambridge, MA
Glenn T. Edens, PARC, Palo Alto, CA

Engineering Information: Adapting Risk and Resilience Frameworks to Cybersecurity

Organized by: Igor Linkov, U.S. Army Engineer Research and Development Center, Concord, MA; Sankar Basu, National Science Foundation, Arlington, VA

SPEAKERS:
Shankar Sastry, University of California, Berkeley
John E. Savage, Brown University, Providence, RI
Ahmad-Reza Sadeghi Sadeghi, Technical University of Darmstadt, Germany
Stephanie Forrest, University of New Mexico, Albuquerque
Ken Heffner, Honeywell International Inc., Clearwater, FL

IMAGE CREDITS: BRAIN IMAGES: COURTESY OF THE LABORATORY OF NEURO IMAGING AND MARTINOS CENTER FOR BIOMEDICAL IMAGING, CONSORTIUM OF THE HUMAN CONNECTOME; TOPOGRAPHIC MAP: ISTOCKPHOTO; JET IN CARINA: PROJECT NASA, ESA, AND THE HUBBLE SM4 ERO TEAM; VIDEO CARD: ISTOCKPHOTO

Saturday, 14 February

Infectious Disease: Monitoring and Response

This seminar will consider how infectious disease can be effectively monitored in order to inform public health response. A discussion about the Ebola virus outbreak in West Africa will feature perspectives from key individuals and organizations involved in monitoring and responding to the public health emergency and provide information on current and future challenges. Another session will review vaccine development and recent advances in genomics, computational and structural biology, and systems biology that address genetic diversity and immune evasion, providing greater probability for success in the next generation of vaccines. The last session will discuss how Earth observation data can be used to predict the spatial and/or temporal distribution of disease in association with environmental factors, resulting in diverse health applications such as support for development of static spatial predictions of disease risk, outbreak early warning systems, and forecasts of climate change health impacts.

Lessons from the Ebola Outbreak: Response and Responsibility

Additional information to follow.

The Human Vaccines Project: Transforming the Future of Vaccine Development

Organized by: Wayne Koff, International AIDS Vaccine Initiative, New York City

SPEAKERS:
Wayne Koff, International AIDS Vaccine Initiative, New York City
Bali Pulendran, Emory Vaccine Center, Atlanta, GA
Peter Kwong, Vaccine Research Center, National Institute of Allergy and Infectious Diseases, Washington, DC

Earth Observation Approaches to Spatial Disease Prediction, Surveillance, and Control

Organized by: Archie C.A. Clements, Australian National University, Canberra

SPEAKERS:
Uriel Kitron, Emory University, Atlanta, GA
Kenneth J. Linthicum, U.S. Department of Agriculture, Gainesville, FL
Archie C.A. Clements, Australian National University, Canberra

Sunday, 15 February

Innovations in Imaging Earth

From Global Positioning System (GPS) mapping devices to internet-connected location tagging, geospatial information permeates society in the modern digital world. This seminar will highlight advances in remote sensing technology, numerical simulations, and computation that enable monitoring of the Earth at high resolution. Big data analysis techniques combined with low cost, high quality data on environmental patterns and processes from satellites, unmanned aircraft, and remote sensor networks provide insights into global change dynamics and how they impact food security, environmental sustainability, and human welfare.

Advances in Earth Observation: Enabling New Insights into Global Environmental Change

Organized by: Lyndon Estes, Princeton University, NJ; Tom Evans, Indiana University, Bloomington

SPEAKERS:
Matt Hansen, University of Maryland, College Park
Kelly Caylor, Princeton University, NJ
Maggi Kelly, University of California, Berkeley

Imaging Earth

Organized by: Ana Barros, Duke University, Durham, NC; Sally McFarlane, U.S. Department of Energy, Washington, DC

SPEAKERS:
Piers Sellers, NASA Goddard Space Flight Center, Greenbelt, MD
Melba Crawford, Purdue University, West Lafayette, IN
William Collins, Lawrence Berkeley National Laboratory, CA

Geospatial Innovations in Imaging Information Intelligently

Organized by: Steven Whitmeyer, James Madison University, Harrisonburg, VA; Declan De Paor, Old Dominion University, Norfolk, VA

SPEAKERS:
David Thau, Google Inc., Mountain View, CA
Barbara Tewksbury, Hamilton College, Clinton, NY
Richard Treves, University of Southampton, United Kingdom
Robert Kolvoord, James Madison University, Harrisonburg, VA
Jennifer Piatek, Central Connecticut State University, New Britain
Declan De Paor, Old Dominion University, Norfolk, VA

SYMPOSIA TRACKS

Organizers are listed under symposia titles.

ANTHROPOLOGY, CULTURE, AND LANGUAGE

Discovering Lost Horizons: People, Land, and Society in Prehistory
George R. Milner, Pennsylvania State University, University Park; Michael Frachetti, Washington University, St. Louis, MO

History Written in Skeletons: Intersections of History, Archaeology, and Biology
Anita Guerrini, Oregon State University, Corvallis

Imaging the Past: Using New Information Technologies To Nurture Historical Analysis
Cecile Menetrey-Monchau and Annekathrin Jaeger, European Research Council, Brussels, Belgium

Radiography of the Past: Revealing the Invisible at Archaeological Sites
Louise Byrne, European Commission, Research Executive Agency, Brussels, Belgium

The Linguistics of Status, Influence, and Innovation: A Computational Perspective
Jacob Eisenstein, Georgia Institute of Technology, Atlanta

The Sense of Smell as a Novel Means to Explore Language, Culture, and Biology
Asifa Majid, Radboud University Nijmegen, Netherlands

Visualizing Verbal Culture: Seeing Language Diversity
John Nerbonne, Rijksuniversiteit Groningen, Netherlands

Worth More Than a Thousand Words: State-of-the-Art Visualization in Cultural Heritage
Francesca Casadio, The Art Institute of Chicago, IL; Marc Walton, Northwestern University, Evanston, IL

BEHAVIORAL AND SOCIAL SCIENCES

Human Mathematical Abilities: From Intuition to the Classroom and Back
James L. McClelland, Stanford University, CA

Human-Made Noise and Nighttime Lighting
Clinton D. Francis, California Polytechnic State University, San Luis Obispo

Innovations in the Family: New Structures, New Challenges
Toni Antonucci, University of Michigan Institute for Social Research, Ann Arbor

Measuring Research Integrity: Survey of Organizational Research Climate
C.K. Gunsalus, National Center for Professional and Research Ethics, Urbana, IL

Social Influences on Health Service Use Following Disasters
Eric Jones, University of North Carolina, Greensboro

Social, Emotional, and Cognitive Bases of Communication: New Analytic Approaches
Judith F. Kroll, Pennsylvania State University, University Park; Cecilia Aragon, University of Washington, Seattle; Laurie Beth Feldman, University at Albany, NY

Virtual Labs: Transforming the Social, Behavioral, and Information Sciences
Michael W. Macy, Cornell University, Ithaca, NY

Visualizing the Experience and Use of Space in the Built Environment
Annekathrin Jaeger and Katja Meinke, European Research Council, Brussels, Belgium

Watching the Brain Think: Naturalistic Approaches To Studying Human Brain Function
Susan Hagen and Jessica F. Cantlon, University of Rochester, NY

BIOLOGY AND NEUROSCIENCE

3D Chemical Imaging: New Frontier Across Disciplines
Barbara Illman, U.S. Forest Service, Madison, WI; Carol Hirschmugl, University of Wisconsin, Milwaukee

Emerging Trends in Visualizing Physical Models and Rapid Prototyping for Biological Systems
Promita Chakraborty and Ronald N. Zuckermann, Lawrence Berkeley National Laboratory, CA

Extracting Evidence From Biological Data: Multiple Disciplines Get In On the Act
Veronica Vieland, The Research Institute at Nationwide Children's Hospital, Columbus, OH

Insights from Social Networks: Visualizing Big Data from Cells to Cell Phones to Societies
Barbara Illman, U.S. Forest Service, Madison, WI; Daniel Rubenstein, Princeton University, NJ

Multisensory Development, Plasticity and Learning: From Basic to Clinical Science
Mark Wallace, Vanderbilt University, Nashville, TN

Neuroimaging: Discoveries from Fetus to Adult
Pat Levitt, University of Southern California, Los Angeles

Neuroscience of Hearing: Brain Implants in the Fight Against Childhood Deafness
Nan Ratner, University of Maryland, College Park

Novel Technologies for Exploring the Uncultivated Microbial Majority
Susannah Tringe and Tanja Woyke, U.S. Department of Energy Joint Genome Institute, Walnut Creek, CA

Proteomics: How Big Data Opens New Vistas in Personalized Medicine
Barbara Wankerl and Patrick Regan, Technical University of Munich, Garching, Germany

Reproducibility of Science: A Roadmap Forward
Pat Levitt, University of Southern California, Los Angeles; Allan R. Sampson, University of Pittsburgh, PA

Searching for Alternative Chemistries of Life on Earth and Throughout the Universe
David G. Lynn, Emory University, Atlanta, GA; Jay T. Goodwin, National Science Foundation, Arlington, VA

To Bug or Not to Bug the Immune System: Benefits and Costs of Altering the Microbiome
Victor J. Johnson, Burleson Research Technologies Inc., Morrisville, NC; Berran Yucesoy, University of Cincinnati College of Medicine, OH

Visualizing Biomedical Data and Processes Across Space and Time Scales
Sean E. Hanlon, National Cancer Institute, Rockville, MD

What Are Race and Sex Doing in Our Genomes? Perspectives on Human "Types"
Sally Lehrman, University of California, Santa Cruz

When Experts Collide: Driving Cross-Cutting Innovation in Biological Imaging and Informatics
Carol Lynn Alpert, Museum of Science, Boston, MA

CLIMATE CHANGE, ENVIRONMENT, AND ECOLOGY

Avoiding Collapse: Human Impacts on the Biosphere
Anthony D. Barnosky, University of California, Berkeley; Paul R. Ehrlich, Stanford University, CA

Climate Change and Big Data
So-Min Cheong, University of Kansas, Lawrence

Climate Intervention and Geoengineering: Albedo Modification
Marcia McNutt, AAAS/Science, Washington, DC

Earth History: Innovative Approaches to Studying Critical Transitions
Dena M. Smith, Geological Society of America, Boulder, CO

Going Negative: Removing Carbon Dioxide From the Atmosphere
Jennifer Milne and Sally Benson, Stanford University, CA

Marine Ecosystems in Hot Water: Some Like It Hot (But Some Do Not)
Frank E. Muller-Karger, University of South Florida, St. Petersburg

Modeling Earth's Interior from Atomic to Global Scale
Renata M. Wentzcovitch, University of Minnesota, Minneapolis; Rob van de Hilst, Massachusetts Institute of Technology, Cambridge; David Bercovici, Yale University, New Haven, CT

Ocean Acidification and Hypoxia: Planning For Regional Action
Michael J. O'Donnell, California Ocean Science Trust, Oakland

Seeing the Invisible: How Sequencing Diverse Eukaryotes Transforms Ocean Science
Jian Guo and Alexandra Z. Worden, Monterey Bay Aquarium Research Institute, Landing Moss, CA; Adam Monier, University of Exeter, United Kingdom

Severe Weather in a Changing Climate: Informing Risk
Michael E. Mann, Pennsylvania State University, University Park; Michael Wehner, Lawrence Berkeley National Laboratory, CA; Donald J. Wuebbles, University of Illinois, Urbana-Champaign

The Atlantic Ocean: Our Unknown Treasure
Marco Weydert and John Bell, European Commission, Research and Innovation, Brussels, Belgium

Visual Cultures of Prediction: Imaging Climate Change Data
Lynda Walsh, University of Nevada, Reno; Birgit Schneider, University of Potsdam, Germany

AAAS 2015 ANNUAL MEETING
INNOVATIONS, INFORMATION, AND IMAGING

Advance Registration Rates

	AAAS Member Rates for members in good standing	New Member Reduced rates if you join AAAS today	Non-Member Rates for all other attendees
Professional	$295	$380	$399
Postdoc	$235	$320	$335
K-12 Teacher	$235	$320	$335
Emeritus	$235	$320	$335
Student	$60	$70	$90

One-day rates are also available. Visit **www.aaas.org/meetings/registration.**

COMMUNICATION AND PUBLIC PROGRAMS

Citizen Science from the Zooniverse: Cutting-Edge Research with 1 Million Scientists
Ramin A. Skibba, University of California, San Diego

Citizen Science: Advancing Innovations for Science, Information, and Engagement
Meg Domroese, Citizen Science Association/Schoodic Institute, Winter Harbor, ME; Jennifer Shirk, Cornell University, Ithaca, NY

Comics, Zombies, and Hip-Hop: Leveraging Pop Culture for Science Engagement
Kishore Hari and Rebecca L. Smith, University of California, San Francisco

Engagement with Intent? Scientists' Views of Communication and Why It Matters
John C. Besley, Michigan State University, East Lansing

From Art to Mathematics: A Visual Mode of Communication
George W. Hart, Stony Brook University, NY

Going Public: Investing in Science Communication for Scientists
Keegan Sawyer, National Academy of Sciences, Washington, DC; Brooke Smith, Communication Partnership for Science and the Sea (COMPASS), Portland, OR; Russ Campbell, Burroughs Wellcome Fund, Research Triangle Park, NC

National Climate Assessment: Resource for Climate Literacy and Making Decisions
Emily Therese Cloyd, U.S. Global Change Research Program, Washington, DC

Public Engagement with Science: What's In It for Scientists?
Katherine Nielsen, University of California, San Francisco, CA

Science Visualization: The Art of Making Data Beautiful
Andy Freeberg, SLAC National Accelerator Laboratory, Menlo Park, CA

Scientific Visualization: Collaborations Between Museums and Scientists
Erika C. Shugart, American Society for Microbiology, Washington, DC

Strategies for Effective Broader Impacts Work
Justin Lawrence and Jennifer Yttri, AAAS Science and Technology Policy Fellow, National Science Foundation, Arlington, VA

Tweet and Shout About Science
Erik Van der Goot and Geraldine Barry, European Commission, Joint Research Center, Brussels, Belgium

Using Cartoons To Convey Science
Yoram Bauman, StandUpEconomist.com, Seattle, WA

EDUCATION AND HUMAN RESOURCES

Assessment in Support of K–12 Science Learning
Natalie Nielsen and Heidi Schweingruber, National Academy of Sciences, Washington, DC

Diversity in the Academic STEM Workforce: Understanding Career Experiences
Julia E. Melkers, Georgia Institute of Technology, Atlanta

Gender in STEM Policy, Practice, and Research: Advances in North America and Europe
Wanda Ward, National Science Foundation, Arlington, VA

Graduate Science Education in Flux: Alternate Pathways to Science Careers
Daryl E. Chubin, Independent Consultant, Savannah, GA; Marilyn J. Suiter, National Science Foundation, Arlington, VA

Inclusive STEM High Schools: Innovative Pathways and Partnerships for Success
Edith Gummer, National Science Foundation, Arlington, VA

Innovations in Broadening Participation and Diversifying the Science Workforce
Jessi L. Smith, Montana State University, Bozeman

Learning from Visualization: Insights from STEM and Cognitive Science Collaboration
Mary Hegarty, University of California, Santa Barbara; Thomas F. Shipley, Temple University, Philadelphia, PA

Learning Science from Scientific Data
Cathryn A. Manduca, Carleton College, Northfield, MN

Next-Generation Learning and Assessment Environments for Science Inquiry Practices
Michael A. Sao Pedro, Worcester Polytechnic Institute, MA

Paving Smoother Pathways for All Students: Systemic Undergraduate STEM Reform
Martin Storksdieck, Oregon State University, Corvallis; Michael Feder, National Research Council, Washington, DC

Preparing Researchers for the Quantitative Biology of the Future
Frederick R. Adler, University of Utah, Salt Lake City; M. Gregory Forest, University of North Carolina, Chapel Hill

The Future of Graduate Education in STEM: Thinking Beyond Disciplines
Jay B. Labov, National Academy of Sciences, Washington, DC

Undergraduate Research at the Community College: Models and Sustainability
James Hewlett, Finger Lakes Community College, Canandaigua, NY

ENGINEERING, INDUSTRY, AND TECHNOLOGY

A New Paradigm for Electron Microscopy: Fast Detectors and Extreme Data Experimentation
Frances M. Ross, IBM TJ Watson Research Center, Yorktown Heights, NY; Jim Ciston and Andrew Minor, University of California, Berkeley

Computer-Aided Design of Catalysts for Sustainable Energy Conversion
Jens Norskov, Stanford University, CA

Correlating Properties of Nano-Building Blocks Via Hyperspectral Nano-Optical Imaging
P. James Schuck and Alexander Weber-Bargioni, Lawrence Berkeley National Laboratory, CA

I See, Therefore I Can
Rene Martins, European Commission, Brussels, Belgium

Integrated Computational Materials Engineering Principles for Additive Manufacturing
Sudarsanam Babu, University of Tennessee/ Oak Ridge National Laboratory, Knoxville

Next-Generation Batteries for Mobile Devices and the Grid
Johanna Nelson Weker and Glennda Chui, SLAC National Accelerator Laboratory, Menlo Park, CA

Revolutionary Vision: Implants, Prosthetics, Smart Glasses, and the Telescopic Contact Lens
Megan Williams, Christian Simm, and Melanie Picard, swissnex, San Francisco, CA

The Business of Innovation: Great Science Is Only the First Step
Fred Ledley, Bentley University, Waltham, MA

The Road to Autonomous Cars
Chris Gerdes, Stanford University, CA

Whole Lotta Shakin': Man-Made Earthquakes and Energy Development
William Savage, Seismological Society of America, Las Vegas, NV; Rex Buchanan, Kansas Geological Survey, Lawrence

GLOBAL PERSPECTIVES AND ISSUES

21st Century Global Food Security and the Environment: Improving or Deteriorating?
Felix Kogan and Alfred M. Powell, National Oceanic and Atmospheric Administration, College Park, MD

Access to Scientific Expertise in Fast Growing African Countries
Max Goldman, Sense About Science, London, United Kingdom

Astrobiology: Expanding Views of Life and Encountering New Societal Questions
Margaret S. Race, SETI Institute, Mountain View, CA; Brian Patrick Green, Santa Clara University, CA

Bounded Gaps Between Prime Numbers: Individual Research Versus Crowdsourcing
Carl Pomerance, Dartmouth College, Hanover, NH; Daniel A. Goldston, San Jose State University, CA

Creationism in Europe
Stefaan Blancke, Ghent University, Belgium; Peter C. Kjærgaard, Aarhus University, Denmark

Earth Observation Systems and Citizen Scientists Tackle Urban Environmental Hazards
Gilles Ollier, European Commission, Directorate General for Research and Innovation, Brussels, Belgium

Gender Equality in the Knowledge Society: Better Analysis Through Better Information
Sophia Huyer, Women in Global Science and Technology, Brighton, Canada

Historical and Philosophical Perspectives on Innovation in Science and Society
Manfred Laubichler, Arizona State University, Tempe

Novel Government Partnerships: Integrating Developing Countries in Global Research
Katherine E. Himes and Cameron D. Bess, U.S. Agency for International Development, Washington, DC

Science Diplomats Tackling Our Lifestyle Killers
Aidan Gilligan, SciCom–Making Sense of Science, Brussels, Belgium; Michel Kazatchkine, United Nations, Geneva, Switzerland

Science for Haiti Reconstruction: Advances in Science and Science Education Capacity
Jorge L. Colón, University of Puerto Rico, San Juan

Solutions for Achieving Gender Equity: International Perspectives
Lynnette D. Madsen, National Science Foundation, Arlington, VA; Catherine Didion, National Academy of Engineering, Washington, DC

Strategies for Pandemic Emergency Response
Eva K. Lee, Georgia Institute of Technology, Atlanta

Ukraine's Scientific Future: International Cooperation and Science Diplomacy
Michela Greco, CRDF Global, Arlington, VA

Unlocking Natural History Collections To Model the Biosphere
Ian Owens, Natural History Museum, London, United Kingdom; Kirk Johnson, National Museum of Natural History, Washington, DC

INFORMATION AND DATA TECHNOLOGY

Advancing University Career Paths in Interdisciplinary Data-Intensive Science
Cecilia Aragon and William Howe, University of Washington, Seattle

Beyond Silicon: New Materials for 21st Century Electronics
Glennda Chui, SLAC National Accelerator Laboratory, Menlo Park, CA

Differential Privacy: Analyzing Sensitive Data and Implications
Salil Vadhan, Harvard University, Cambridge, MA; Cynthia Dwork, Microsoft Research, Mountain View, CA

From the Grid to the Cloud: Computing for Big (and Small) Science
Terry O'Connor, Science and Technology Facilities Council, Swindon, United Kingdom; Vincenzo Napolano, Istituto Nazionale di Fisica Nucleare, Roma, Italy

Holistic Computing Risk Assessment: Privacy, Security, and Trust
L. Jean Camp and Diane Henshel, Indiana University, Bloomington

Improving Quality of Life By Transforming Images to Health Care Decisions
Ram D. Sriram, National Institute of Standards and Technology, Gaithersburg, MD; Ramesh Jain, University of California, Irvine; Donald Henson, Uniformed Services University, Bethesda, MD

Privacy in an Era of Big Data: Directions, Advances, and Reflections
Ersin Uzun, Palo Alto Research Center, CA

Seeing Earth in the "Light" of Gravity: New Views Through Satellite Geodesy
Barbara Wankerl and Patrick Regan, Technical University of Munich, Germany

The Convergence of Massive Data and Complex Control in the Future U.S. Power Grid
Jeffrey Taft, Pacific Northwest National Laboratory, Richland, WA

Visualization Insights from Big Data: Envisioning Science, Engineering, and Innovation
Katy Borner, Indiana University, Bloomington; Joseph E. Sabol, Chemical Consultant, Racine, WI

Wise Computing: Collaboration Between People and Machines
Kazuo Iwano and Yosuke Takashima, Japan Science and Technology Agency, Tokyo; Tateo Arimoto, National Graduate School for Policy Studies, Tokyo, Japan

MEDICAL SCIENCES AND PUBLIC HEALTH

Affordable Diagnostics for All: High-Resolution Medical Imaging for Saving Lives
Comert Kural, Ohio State University, Columbus; Ahmet Yildiz, University of California, Berkeley

Antibiotic Resistance: An Environmental Problem Threatening Global Health Care
Anneli Waara, Uppsala University, Sweden

Bugs Without Borders: A Data-Driven Approach to Tackling Antimicrobial Resistance
Stefania Di Mauro-Nava, British Consulate-General, San Francisco, CA; Lindsay R. Chura, British Embassy, Washington, DC

Cannabis and Medicine: A New Frontier in Therapeutics
Mark Ware and Julie Robert, McGill University Health Center, Montreal, Canada

Challenges in Communicating about Stem Cells
Judy Illes and Julie M. Robillard, University of British Columbia, Vancouver, Canada

Chronic Pain: No Longer an Invisible Disease
Linda Koffmar, Uppsala University, Sweden

E-Cigarettes: Killing Me Softly or Our Greatest Public Health Opportunity?
Aidan Gilligan, CEO, SciCom–Making Sense of Science, Brussels, Belgium; Julian Kinderlerer, European Commission, Brussels, Belgium

Imaging the Future of Cancer Research
Eleni Zika and Sally Donaldson, European Research Council, Brussels, Belgium

Informatics and Bioimaging: New Ways to Better Medicines
Deanna L. Kroetz, University of California, San Francisco

Innovations in Clinical Trial Registers
Victoria Murphy, Sense About Science, London, United Kingdom

Obesity and Microbiome: Concepts and Contradictions
Mary C. Dinauer, Washington University School of Medicine, St. Louis, MO; Shili Lin, Ohio State University, Columbus

Responsible Data Sharing for Clinical Trials
David L. DeMets, University of Wisconsin, Madison

The Digital Human Head: 3D Imaging and the Restoration of Craniofacial Function
Luisa Ann DiPietro, University of Illinois, Chicago

The Human Vaccines Project: Transforming the Future of Vaccine Development
Wayne Koff, International AIDS Vaccine Initiative, New York City

Worldwide Epidemic of Senile Dementias: Challenges of Pre-Clinical Treatment
Edward J. Goetzl, University of California, San Francisco

PHYSICS AND ASTRONOMY

A Science Cycle: From Novel Imaging to Novel Physics, and Vice Versa
Norman Chonacky, Yale University, New Haven, CT

Advancing Solar and Space Physics: Combining Observations, Models, and Analysis
Michael Wiltberger, National Center for Atmospheric Research, Boulder, CO

Building Galaxies: Some Assembly Required
Mark T. Adams, National Radio Astronomy Observatory, Charlottesville, VA

Celebration of 2015: The International Year of Light
Anne Matsuura, The Optical Society, Washington, DC; Anthony Johnson, University of Maryland, Baltimore County; Phil Bucksbaum, Stanford University, CA

Cosmic Neutrinos
Marcela S. Carena, University of Chicago/ Fermi National Accelerator Laboratory, Batavia, IL; Graciela Gelmini, University of California, Los Angeles

Exoplanets: New Worlds Aplenty
William Joseph Borucki and Steve B. Howell, NASA Ames Research Center, Moffett Field, CA

General Relativity at 100: Looking Forward and Looking Back
Beverly Berger, International Society on General Relativity and Gravitation, Livermore, CA; Stanley Whitcomb, California Institute of Technology, Pasadena

Imaging the Unseen: Advanced Adaptive Optics Enabling Scientific Discovery
Lisa A. Poyneer, Lawrence Livermore National Laboratory, CA

Innovations in Accelerator Science
Maria Spiropulu, California Institute of Technology, Pasadena

Scanning the Southern Skies: Harnessing Big Astronomy Data with the Square Kilometer Array
William Garnier, Square Kilometer Array Organization, Macclesfield, United Kingdom; Daan du Toit, South African Science Ministry, Brussels, Belgium

Solar System Exploration by Remote Imaging
Rolf M. Sinclair, University of Maryland, College Park; Fuk K. Li, California Institute of Technology, Pasadena

The Cosmic Microwave Background: Window into New Physics
Glenn E. Roberts, SLAC National Accelerator Laboratory, Menlo Park, CA; Jay Marx, California Institute of Technology, Pasadena

The Hubble Space Telescope: 25 Years of Imaging the Cosmos
Jennifer Wiseman, NASA Goddard Space Flight Center, Greenbelt, MD; Ray Villard, Space Telescope Science Institute, Baltimore, MD

Transformational Opportunities of Quantum Information Technologies
Martin Laforest, University of Waterloo, Canada; Jenny Hogan, National University of Singapore, Malaysia

Wave-Particle Duality of Neutrons, Atoms, and Molecules
Charles W. Clark, Joint Quantum Institute, Gaithersburg, MD

What Can We Expect from the Second Run of LHC in 2015?
James Gillies, European Organization for Nuclear Research (CERN), Geneva, Switzerland; Jon Weiner, Lawrence Berkeley National Laboratory, CA

PUBLIC POLICY

Active SETI: Is It Time To Start Transmitting to the Cosmos?
Jill C. Tarter and David C. Black, SETI Institute, Mountain View, CA

Big Data: Challenges and Social Impacts
Chris Tyler, U.K. Parliamentary Office of Science and Technology, London; Timothy M. Persons, U.S. Government Accountability Office, Washington, DC

Creating and Using New Information To Promote Innovations in Crime and Justice Policy
William Alex Pridemore, Georgia State University, Atlanta

Crisis in Quantitative Training for Biomedical Science
David L. DeMets, University of Wisconsin, Madison

Dementia: Research Milestones and Policy Priorities
Lindsay R. Chura, British Embassy Washington, DC

Developing Data-Driven Policies To Cure and Prevent Age-Related Diseases
Sharotka Simon, AAAS Science and Technology Fellow, Diplomacy Security and Development Program, Washington, DC

Integrity of Science
Thomas Arrison, National Academy of Sciences, Washington, DC

Making Sense of Chaos: A Path to Understanding Environmental Chemicals and Health
Louis J. D'Amico, Kacee Deener, and Samantha J. Jones, U.S. Environmental Protection Agency, Washington, DC

Memories Imaged and Imagined: How the Science of Memory Will Challenge the Law
Henry Greely, Stanford University Law School, CA; Nita Farahany, Duke University, Durham, NC

Metrics for Science Policy and Policy for Metrics
Ismael Rafols, University of Sussex, Brighton, United Kingdom; Michele S. Garfinkel, European Molecular Biology Organization, Heidelberg, Germany

Open Access To Your Emails: Tensions Between Academic Freedom and Open Records Laws
Michael Halpern, Union of Concerned Scientists, Washington, DC

Science During Crisis: Amidst Oil Spills, Hurricanes, and Other Disasters
Gary Machlis, DOI Strategic Sciences Group, Clemson, SC; Kristin Ludwig, U.S. Geological Survey, Reston, VA

Science Policy Professionals in the Era of Big Data: In Honor of Stephen D. Nelson
Susan E. Cozzens, Georgia Institute of Technology, Atlanta

The Human Microbiome: Implications of the Microcosm Within Us
Se Y. Kim and Jennifer Wiseman, AAAS Center for Science, Policy, and Society Programs, Washington, DC

SUSTAINABILITY AND RESOURCE MANAGEMENT

Beyond Intensification: Measuring the "Sustainable" in Sustainable Intensification
Jerry Glover, U.S. Agency for International Development, Washington, DC

Can Our Ocean Commons Be Sustainably Managed? Innovative Strategies for the High Seas
Cassandra M. Brooks and Larry Crowder, Stanford University, CA

Data Infrastructure for Sustainability
Thomas Dietz, Michigan State University, East Lansing; Adam Douglas Henry, University of Arizona, Tucson

Drivers of Tropical Forest Regeneration
Ashwini Chhatre, University of Illinois, Urbana-Champaign

Dynamic Ocean Management: Supporting Ecological and Economic Sustainability
Sara M. Maxwell, Stanford University, CA; Rebecca Lewison, San Diego State University, CA

Ecology, Economics, and Engineering of Nature-Based Coastal Defenses
Jane Carter Ingram, Wildlife Conservation Society, New York City; Michael W. Beck, The Nature Conservancy, Santa Cruz, CA

Feeding 9 Billion+: Information and Imaging for Innovation in Next-Generation Agriculture
Vijaya Gopal Kakani, Oklahoma State University, Stillwater

Information Accelerators: Using Online Tools To Address Sustainability Challenges
Richard Sharp and Rebecca Chaplin-Kramer, The Natural Capital Project, Stanford, CA

Sustainable Intensification in Agriculture: New Scientific Approaches
Karl Zimmerer, Pennsylvania State University, State College

AAAS 2015 ANNUAL MEETING
INNOVATIONS, INFORMATION, AND IMAGING

AAAS, publisher of *Science*, thanks the sponsors and supporters of the 2015 Annual Meeting

European Commission

SUBARU

HELMHOLTZ ASSOCIATION

NANYANG TECHNOLOGICAL UNIVERSITY

the Lemelson foundation
improving lives through invention

AAAS thanks

THE KAVLI FOUNDATION

for its generous support of the Science Journalism Awards

Science Careers Advertising

For full advertising details, go to ScienceCareers.org and click For Employers, or call one of our representatives.

Tracy Holmes
Worldwide Associate Director
Science Careers
Phone: +44 (0) 1223 326525

THE AMERICAS

E-mail: advertise@sciencecareers.org
Fax: 202 289 6742

Tina Burks
Phone: 202 326 6577

Nancy Toema
Phone: 202 326 6578

Marci Gallun
Sales Administrator
Phone: 202 326 6582

Online Job Posting Questions
Phone: 202 312 6375

EUROPE / INDIA / AUSTRALIA / NEW ZEALAND / REST OF WORLD

E-mail: ads@science-int.co.uk
Fax: +44 (0) 1223 326532

Axel Gesatzki
Phone: +44 (0) 1223 326529

Sarah Lelarge
Phone: +44 (0) 1223 326527

Kelly Grace
Phone: +44 (0) 1223 326528

JAPAN

Katsuyoshi Fukamizu (Tokyo)
E-mail: kfukamizu@aaas.org
Phone: +81 3 3219 5777

Hiroyuki Mashiki (Kyoto)
E-mail: hmashiki@aaas.org
Phone: +81 75 823 1109

CHINA / KOREA / SINGAPORE / TAIWAN / THAILAND

Ruolei Wu
Phone: +86 186 0082 9345
E-mail: rwu@aaas.org

All ads submitted for publication must comply with applicable U.S. and non-U.S. laws. *Science* reserves the right to refuse any advertisement at its sole discretion for any reason, including without limitation for offensive language or inappropriate content, and all advertising is subject to publisher approval. *Science* encourages our readers to alert us to any ads that they feel may be discriminatory or offensive.

Science Careers
From the journal *Science* AAAS

ScienceCareers.org

UNIVERSITY OF UTAH SCHOOL OF MEDICINE

Tenure-track Assistant or Associate Professor of Genetics/Genome Sciences

The Department of Human Genetics at the University of Utah School of Medicine (www.genetics.utah.edu) seeks outstanding applicants for tenure-track positions at the level of Assistant or Associate Professor. We are looking for a highly creative scientist who uses genetics to investigate fundamental biological problems. We especially encourage applicants whose research focuses on human and medical genetics using functional, computational, or evolutionary genomics and/or model organisms. As part of a vibrant community of collaborative faculty on campus, the Department of Human Genetics lies at the interface between basic and clinical sciences, creating ample opportunities for interdisciplinary studies (e.g., the newly formed Center for Genetic Discovery). Our institution is set in a unique recreational and geographical landscape that attracts a very diverse and productive scientific community. Successful candidates will receive a generous startup package and enjoy a stimulating research environment that places a strong emphasis on innovation and interaction.

Our submission deadline is **November 14, 2014**. To apply, please see the following website: **http://utah.peopleadmin.com/postings/35937**. For questions regarding this posting or your application, please contact Natalie Johnson at: **njohnson@genetics.utah.edu**

The University of Utah is an Affirmative Action/Equal Opportunity employer and does not discriminate based upon race, national origin, color, religion, sex, age, sexual orientation, gender identity/expression, status as a person with a disability, genetic information, or Protected Veteran status. Individuals from historically underrepresented groups, such as minorities, women, qualified persons with disabilities and protected veterans are encouraged to apply. Veterans' preference is extended to qualified applicants, upon request and consistent with University policy and Utah state law. Upon request, reasonable accommodations in the application process will be provided to individuals with disabilities. To inquire about the University's nondiscrimination or affirmative action policies or to request disability accommodation, please contact: Director, Office of Equal Opportunity and Affirmative Action, 201 S. Presidents Circle, Rm 135, (801) 581-8365.

The University of Utah values candidates who have experience working in settings with students from diverse backgrounds, and possess a [strong or demonstrated] commitment to improving access to higher education for historically underrepresented students.

The University of Utah Health Sciences Center is a patient-focused center distinguished by collaboration, excellence, leadership, and respect. The Health Sciences Center values candidates who are committed to fostering and furthering the culture of compassion, collaboration, innovation, accountability, diversity, integrity, quality, and trust that is integral to the mission of the University of Utah Health Sciences Center.

THE GEORGE WASHINGTON UNIVERSITY
WASHINGTON, DC

Faculty Positions in Computational Biology and Bioinformatics

The newly established Computational Biology Institute at the George Washington University seeks founding faculty members to establish externally funded, internationally recognized, and interdisciplinary research programs in bioinformatics and/or computational biology. There are two open tenure-track faculty positions at any academic level, and we seek applicants concentrating in the areas of genome analysis, biodiversity informatics, translational medicine, and systems biology developing methods to address 'big data' issues from a computational perspective.

Basic Qualifications: Applicants must have an MD or PhD in Bioinformatics, Computational Biology, Computer Science, Mathematics, Genomics, or related discipline, with postdoctoral research experience, evidence of success in obtaining extramural funding, and a solid publication track record.

Successful candidates will enjoy joint appointments at the CBI and an affiliated academic department (e.g., Biochemistry, Biological Sciences, Biophysics, CASHP, Computer Engineering, Computer Science, Integrated Systems Biology, Mathematics, Microbiology, Statistics, etc.) upon approval and have opportunities to establish partnerships with regional research centers of excellence, including Children's National Medical Center, NIST, Janelia Farm, INOVA hospital system, Naval Research Laboratory, the Smithsonian, and the NIH intramural research program.

Application Procedure: Applicants should submit an electronic application, and upload a cover letter emphasizing specific qualifications, a curriculum vitae, a description of research interests, and names and contact information of 3 references at: **http://www.gwu.jobs/postings/24171**. Review of applications will begin on **November 19, 2014** and will continue until positions are filled. Only complete applications will be considered. For further information about the Computational Biology Institute at George Washington University, please see **http://cbi.gwu.edu**. Employment offers are contingent on the satisfactory outcome of a standard background screening. For questions relating to this opportunity, please contact **Keith Crandall, Director, Computational Biology Institute, The George Washington University, kcrandall@gwu.edu**.

The university is an Equal Employment Opportunity/Affirmative Action Employer that does not unlawfully discriminate in any of its programs or activities on the basis of race, color, religion, sex, national origin, age, disability, veteran status, sexual orientation, gender identity or expression, or on any other basis prohibited by applicable law.

LUNDBECK FOUNDATION FELLOWSHIPS

The Lundbeck Foundation hereby invites applications for fellowships within biomedicine and natural sciences which will be granted to especially promising young researchers and their research groups. Within biomedicine, the Foundation has a special focus on neurology, psychiatry and allergology/immune modulation.

The fellowships are awarded for five years and each fellowship amounts to DKK 10 million (approx. Euro 1,3 million).

The subject area should be frontline basic- or applied research within the scope of the Foundation's grant strategy, which can be seen at www.lundbeckfonden.com

This call invites Danish or foreign researchers from abroad who wish to move to Denmark and continue their research here. The call is also open for applicants from Danish universities and university hospitals.

The fellowships are intended for researchers who are qualified to establish or develop their own research groups within the health or natural sciences and who have received their Ph.D. degree within the last 5-7 years.

The application should include an account of the project's research plan, collaborators, budget and how the research group is envisioned to be placed within a Danish research institution. In addition, it should include a letter of intent from a resident researcher at the host institution, who makes him- or herself available as a mentor to facilitate the applicant's establishment of the research group as an integral part of the host institution. Further guidance is provided in the application form.

The application, written in English, should be sent via the Foundation's Electronic Application System for fellowships at www.lundbeckfonden.com no later than December 15, 2014.

Interviews will take place during the weeks of april 13-17 or 20-24, 2015 at the Lundbeck Foundation.

For further information please contact Ulla Jakobsen, Science Manager, phone: 39 12 80 11 or email: application@lundbeckfonden.com

The Lundbeck Foundation has controlling shareholdings in its subsidiaries H. Lundbeck, ALK and Falck. In addition, the Foundation manages financial investments of approx. € 1.7 billion. The Foundation supports research within the medical and natural sciences. In 2013, the Foundation had a profit after tax of approx. € 279 million and made research grants of approx. € 51 million.

Lundbeckfonden
Scherfigsvej 7, DK-2100 Copenhagen Ø
Tel. +45 39 12 80 00
www.lundbeckfonden.com

LUNDBECK FOUNDATION

VCQ
Vienna Center for Quantum Science and Technology

The Vienna Center for Quantum Science and Technology (VCQ) invites applications for the

Vienna Quantum Fellowships

These Fellowships in Experimental or Theoretical Quantum Science will be awarded on the postdoc-level on the basis of an international competition. The appointments are for a three-year duration. Postdoctoral Fellowships carry a competitive annual salary, and offer an annual research expense fund.

The Vienna Quantum Fellowship program has been established with the support from the Austrian Ministry of Science and Research to offer young scientists the best possible opportunity to develop their talents in the environment of the Vienna Center for Quantum Science and Technology (VCQ).

The VCQ faculty provides a broad variety of research opportunities in the areas of Experimental and Theoretical Quantum Science (see **http://vcq.quantum.at**):

- Matter wave interferometry and quantum optics
- Micro and nanoscale quantum optics and quantum optomechanics
- Microoptics and novel quantum states of light
- Cold atoms and degenerate quantum gases
- Many-body quantum physics and quantum simulations
- Entanglement-based quantum communication on Earth and via satellites
- Quantum information and foundations of physics

Information about how to apply and the required application material can be obtained from **http://vcq.quantum.at**

Deadline for the application is **31st December 2014**. Fellowship candidates will automatically be considered for other available postdoctoral positions in their fields of interest.

universität wien · TU WIEN Technische Universität Wien Vienna University of Technology · ÖAW

LOUIS MALASSIS INTERNATIONAL SCIENTIFIC PRIZE

INTERNATIONAL SCIENTIFIC PRIZE FOR AGRICULTURE AND FOOD

Louis Malassis (1918-2007) French agro-economist and educator; and founder of Agropolis.

Created by Agropolis Fondation, the Louis Malassis International Scientific Prize for Agriculture and Food aims to recognize individuals for their exemplary and promising contribution in promoting innovation through research, development and capacity building in order to improve food and agricultural systems sustainability; and contribute to addressing food security and poverty reduction.

3 Categories:

- Distinguished Scientist
- Young Promising Scientist
- Outstanding Career in Agricultural Development

agropolis fondation

The winner in each category will receive € 20,000. Application is open to all stakeholders from the academic or research organization (public or private), the civil society, or the private sector.

OLAM PRIZE FOR INNOVATION IN FOOD SECURITY

OLAM 25 YEARS TRANSCENDING BOUNDARIES

Global agri-business Olam International partners with Agropolis Fondation in awarding the **Olam Prize for Innovation in Food Security** in conjunction with the Malassis Prize.

Open to individuals or research teams, the **Olam Prize** aims to recognize an outstanding innovation for its potential impact on the availability, affordability, accessibility or adequacy of food, as well as to support its further development.

The winner will receive a total of US$50,000 (US$15,000 as a personal award and US$35,000 as a grant for further research).

APPLICATION DEADLINE for both Prizes: 04 DECEMBER 2014, 14:00 (Paris time)

The Award Ceremony will be held during the 3rd Global Science Conference on Climate Smart Agriculture on 16-18 March 2015 in Montpellier, France.

For more information visit:
http://www.agropolis-fondation.fr/uk/our-actions/Malassis-Prize.html
Contact: **malassis-prize2015@agropolis.fr**

THE HONG KONG UNIVERSITY OF SCIENCE AND TECHNOLOGY

Division of Life Science Faculty Positions

The Division of Life Science at The Hong Kong University of Science and Technology seeks applications for tenure-track positions at Assistant Professor and higher ranks.

Applicants should have a doctoral degree and at least 3 years of postdoctoral experience. They will be expected to establish an independent, internationally recognized research program and to contribute to the missions of the Division in undergraduate and graduate education. The Division of Life Science (life-sci.ust.hk) currently has 35 faculty members who come from a range of international backgrounds. Their research covers many different areas of biological sciences, including biotechnology and medicinal biochemistry, cancer biology, cellular regulation and signaling, developmental biology, molecular and cellular neuroscience, macromolecular structure and function, and marine and environmental science. The University has a vibrant research environment and is consistently ranked as one of the top universities in Asia. The medium of instruction is English.

Starting salary will be commensurate with qualifications and experience. Medical/dental benefits and annual leave will be provided. Housing benefits will also be provided where applicable. Initial appointment for Assistant Professor will normally be on a three-year contract, renewable subject to mutual agreement. A gratuity will be payable upon completion of contract.

Application materials including a cover letter, curriculum vitae, statements of a program of research and teaching interests, and contact information of three referees should be submitted to the Chair of Life Science Search and Appointments Committee (**lifssearch@ust.hk**). Review of applications will start in October 2014.

(Information provided by applicants will be used for recruitment and other employment-related purposes.)

THE CHINESE UNIVERSITY OF HONG KONG

Applications are invited for:-

School of Life Sciences
Associate Professor / Assistant Professor

(Ref. 1415/076(665)/2) (Closing date: November 30, 2014)

The School invites applications for an Associate Professorship / Assistant Professorship in food and nutritional sciences. Applicants should (i) have a doctoral degree in a relevant biological science discipline; (ii) demonstrate achievement in any aspect of food and nutritional sciences, particularly experience in applying novel molecular and omics technologies in nutraceutical and functional food research, including experience in metabolomics, the microbiome, food crop genetic engineering, and animal models for metabolic disorders; and (iii) demonstrate potential for excellence in both teaching and research. The appointee will (a) teach undergraduate and postgraduate courses in his/her field of expertise; (b) develop a significant research program with external grant support; (c) provide service for the School and the University. Multidisciplinary research collaborations are encouraged within the School and with other units of the University. Appointment will normally be made on contract basis for up to three years initially commencing January 2016, which, subject to mutual agreement, may lead to longer-term appointment or substantiation later. Assistant Professors will normally be reviewed for advancement and substantiation towards their sixth year of service. Review of applications will begin in December 2014 and will continue until the post is filled.

Salary and Fringe Benefits

Salary will be highly competitive, commensurate with qualifications and experience. The University offers a comprehensive fringe benefit package, including medical care, plus a contract-end gratuity for an appointment of two years or longer, and housing benefits for eligible appointee. Further information about the University and the general terms of service for appointments is available at http://www.per.cuhk.edu.hk. The terms mentioned herein are for reference only and are subject to revision by the University.

Application Procedure

Application forms are obtainable (a) at http://www.cuhk.edu.hk/personnel, or (b) in person/by mail with a stamped, self-addressed envelope from the Personnel Office, The Chinese University of Hong Kong, Shatin, Hong Kong, or (c) by fax polling at (852) 3943 1461.

Please send the completed application form, full curriculum vitae, research plan (in .pdf format) by e-mail to laurenlee@cuhk.edu.hk (subject line: SEARCH2014FNS - name of the applicant). Please also arrange three confidential letters of recommendation forwarded by referees directly to laurenlee@cuhk.edu.hk by the closing date.

The Personal Information Collection Statement will be provided upon request. Please quote the reference number and mark 'Application – Confidential' on cover.

UNIVERSITY of WASHINGTON

Faculty Position
Eukaryotic Cell Biology
Department of Biology

As part of a long-term strategy to enhance strengths in Cell Biology, the Department of Biology is searching to hire a full-time (9-month) Assistant Professor (Job class 0116) for a tenure-track faculty position in eukaryotic cell biology. We seek candidates who integrate perspectives from multiple disciplines, use quantitative approaches, and appreciate the breadth of research encompassed within the Department. We are especially interested in candidates using experimentally tractable plant, animal or protist systems to investigate fields including but not limited to cell homeostasis, signaling, polarity, proliferation, motility, membrane trafficking, interactions between cells and their environments, developmental cell biology, and evolutionary cell biology.

We are looking for individuals with a record of outstanding achievement or strong indications of outstanding future potential. Priority will be given to applications received by **3 November 2014** at: **http://www.biology.washington.edu/faculty/search/**. Applicants must have earned a doctorate by the date of appointment. All University of Washington faculty engage in teaching, research, and service.

The University of Washington is an Affirmative Action, Equal Opportunity Employer. All qualified applicants will receive consideration for employment without regard to, among other things, race, religion, color, national origin, sex, age, status as protected veterans, or status as qualified individuals with disabilities. The University is building a culturally diverse faculty and staff and strongly encourages applications from women, minorities, individuals with disabilities and covered veterans. The University is the 2006 recipient of the Alfred P. Sloan award for Faculty Career Flexibility, and is committed to supporting the work-life balance of its faculty. Our NSF-supported ADVANCE program http://advance.washington.edu/ is dedicated to increasing the participation of women in STEM disciplines.

LSU

MOLECULAR MICROBIOLOGIST
ASSISTANT PROFESSOR (TENURE-TRACK)
DEPARTMENT OF BIOLOGICAL SCIENCES
COLLEGE OF SCIENCE

Responsibilities: This is a tenure-track faculty position and the successful candidate will be expected to establish a vigorous, extramurally funded research program in the areas of Molecular Microbiology at LSU. Biological Sciences is a large and dynamic department, with research ranging across all levels of biological organization from molecules to ecosystems. The successful candidate will complement these strengths, and will be expected to maintain a vigorous, extramurally funded research program, and to contribute to undergraduate and graduate teaching.

Required Qualifications: Ph.D. in Biological Sciences or related field; successful track record of independent research.

Additional Qualifications: Postdoctoral experience is preferred.

An offer of employment is contingent on a satisfactory pre-employment background check. Application deadline is November 18, 2014, or until a candidate is selected. Apply online and view a more detailed ad at: **https://lsusystemcareers.lsu.edu** Position #038253

Quick link at ad URL: **https://lsusystemcareers.lsu.edu/applicants/Central?quickFind=58303**

LSU IS COMMITTED TO DIVERSITY AND IS AN EQUAL OPPORTUNITY/EQUAL ACCESS EMPLOYER

大连理工大学
DALIAN UNIVERSITY OF TECHNOLOGY

“人工光合作用研究所”科研人员招聘

Faculty positions in solar cells and solar fuels

Openings of more than 15 tenure-track positions of Assistant Professor, Associate Professor and Full Professor are now available in the recently established Institute of Artificial Photosynthesis (IAP), Dalian University of Technology (DUT), China. The research fields of these open positions cover dye sensitized solar cells, quantum dots sensitized solar cells, organic polymer solar cells, organic-inorganic hybrid solar cells, catalytic water oxidation, catalytic proton reduction, catalytic CO_2 reduction, functional devices for light driven total water splitting, new type batteries, light to heat conversion at molecular level. Qualified candidates for these open positions should have obtained PhD degree, postdoc research experience, and well documented research achievements in related research fields. DUT will provide for the positions in IAP competitive salaries at international levels. Applicants should send their curriculum vitae, a statement of research plans together with publication list by email to Xue Sun (zhaopin@dlut.edu.cn), indicating in the email subject with “IAP+applicant’s name”. All applications should contain information of related interested positions in certain research fields mentioned above and potential reference persons with corresponding addresses.

Qingdao Technological University Recruits for High-end Talents

Qingdao Technological University is a multiversity includes Science, Engineering, Economics, Management, Literary, Law and Arts. Particularly at Science and Engineering, Civil Construction, Machine Manufacturing, and Environmental Energy.

Enjoys a 60 years history, the university builds a higher education system with undergraduates, masters and doctors. The university now has three campuses: Shibei, Huangdao, and Feixian, which accommodates 19 academic schools, 59 undergraduates programs, 18 level-1 disciplines offering master’s degree programs, 1 first-level discipline offering doctoral degree programs, 7 second-level disciplines offering doctoral degree programs, 2 first-level discipline post-doc research stations, and 25 provincial key disciplines, key labs and engineering technical research centers. Now the University has 2215 faculty and staff members, and over thirty thousand students .

In accordance with the university development, now we are recruiting high-end talents globally.

Disciplines

Civil Engineering, Mechanical Engineering, Environmental Science and Engineering, Architecture, Rural and Urban Planning, Landscape Architecture, Design Planning, Communication and Transportation Engineering, Safety Science and Engineering, Computer Science and Technology, Software Engineering, Information and Communication Engineering, Control Science and Engineering, Materials Science and Engineering, Mechanics, Management science, Business Administration, and Applied Economics.

Requirements

Applicants should have doctorate, also hold the position of assistant professor, associate professor, and professor at leading universities or research institutions overseas. Professionals and talented management at well-known enterprise or financing institution would be acceptable as well.

Contact information

For more information, please check on our main site: http://www.qtech.edu.cn
Tel: +86-0532-85071322
E-mail：qdlgrc@163.com

Job Vacancies in China's Universities

赛尔互联 CERNET

Science Careers From the journal Science AAAS

赛尔互联：《科学》在中国大陆高校人才引进服务独家合作伙伴
CER is Science’s exclusive agent for recruitment advertisement service in mainland China universities and colleges

China's Rapid Development —— More Opportunities

Xi'an Jiaotong University (Xi'an,China)

Faculty positions in Department of Sustainable Energy:
Mission: To pioneer forward-looking education and undertake cutting-edge research in energy science and technologies to support sustainable development.

Faculty Positions in Department of Sustainable Materials:
Mission: To provide a broad-based education in materials science and engineering for sustainability and undertake cutting-edge research in the field to support sustainable development.

Faculty Positions in Department of Sustainable Systems:
Mission: To provide an education and research platform to study interrelationships among eco- nomic and urban development, governance, public policy and regional, national and global ecosystem, focusing on the social and physical systems needed for sustainability.

For further information about JSSD, please visit the following websites: http://jssd.xjtu.edu.cn or http://jssd.ust.hk

Beijing Institute of Technology (Beijing, China)

Open Senior Faculty Positions offered: Equipment Science & Technology Engineering/ Mechanical Engineering/ Information and Communication Engineering/ Mathematics…

Peking University (Beijing, China)

The School of Life Sciences (SLS)at Peking University invites applications for multiple faculty positions at tenure-track assistant professor, associate professor and full professor levels.

For more details, visit http://www.acabridge.cn/

广告联系：赵佳 zhaojia@cernet.com
+86 10 62603373

中国教育在线 www.eol.cn 是赛尔互联旗下品牌

Research Fellows and Senior Research Associates in Atmospheric Science, Jinan University, Guangzhou, South China

百年暨大，诚聘英才
携手暨大，共创未来

We are seeking ***Research Fellows (RF)*** and ***Senior Research Associates (SRA)*** in Atmospheric Science for ***the institute of Atmospheric Environment Safety and Pollution Control (IAESPC), Jinan University (JNU)***, Guangzhou, South China.

JNU is known as the top university for Overseas Chinese and also one of key universities of 'Project 211' in China. The ***IAESPC*** is a newly founded research institute in ***JNU***; the group leader (Prof. Zhen Zhou) was introduced back to China by the National 1000-Talents Program in 2009. Presently, there are 3 research teams in the institute, focusing on atmospheric aerosols, volatile organic compounds and relevant health risk assessment. Besides, the institute also has a super atmospheric monitoring station and a research center on mass spectrometry instrumentation (top one in China). The total area of labs/offices is more than 1000 m^2, and 30+ million has been investigated for the instruments and facilities in the institute.

The requirements for the candidates are specified as follows:

Research Area: Atmospheric Science.

Requirements:

1.Born after 1974.01.01 and 1979.01.01 for ***RF*** and ***SRA***, respectively.

2.PhD from top universities all over the world.

3.For ***RF***, research experience (3+ years)/got an official position/principal investigators in well-known universities/research institutes/companies;

For ***SRA***, post-doc/research associate/key participants in well-known universities/research institutes /companies.

Research Fields: Atmospheric Chemistry, Atmospheric Field Monitoring, Source Appointment of Particulate Matter, Instrumentation on Environmental Analysis (especially mass spectrometry).

Nationalities: All over the world.

Application materials: CV, a list of representative research achievements and a 5-year plan;

Contact:

1.Contact person: Haifeng Fu;

2.Tel: +86 (0)20 85220220;

3.Email: 969852782@qq.com.

Deadline: None.

ILLINOIS
UNIVERSITY OF ILLINOIS AT URBANA-CHAMPAIGN

Open Rank Tenured/Tenure-Track Faculty Positions Department of Comparative Biosciences

The Department of Comparative Biosciences at the College of Veterinary Medicine, University of Illinois at Urbana-Champaign invites applications for two open positions—one in reproductive biology and one in regenerative/stem cell biology—at the Assistant, Associate, or Full Professor level. Candidates must possess a Ph.D., or equivalent degree. Candidates currently at the Associate or Full Professor rank with federal funding are especially encouraged to apply. The successful candidates will participate in the professional and graduate curricula and develop research programs which complement existing department and/or campus strengths in reproductive biology, neuroscience, environmental toxicology and cancer biology. Candidates with research programs related to neuroscience, healthy aging, obesity or cancer are especially encouraged to apply. Full information about the department is available at http://vetmed.illinois.edu/cb/index.html. The positions are regular, full-time, 9-month, tenured or tenure track appointments, and are available August 2015. Salary and rank will be commensurate with qualifications.

Qualified applicants should apply online at https://jobs.illinois.edu. Applications should include a cover letter including a research statement, CV, and contact information for three references. Please indicate on your application which position you are most interested in. Questions may be directed to **Dr. Jodi A. Flaws**, search committee chair, **jflaws@illinois.edu** or **217-333-7933**. In order to ensure full consideration, applications must be received by **December 1, 2014**. Applicants may be interviewed before the closing date; however, no hiring decision will be made until after that date.

Illinois is an Equal Opportunity Employer and all qualified applicants will receive consideration for employment without regard to race, religion, color, national origin, sex, age, status as a protected veteran, or status as a qualified individual with a disability. Illinois welcomes individuals with diverse backgrounds, experiences, and ideas who embrace and value diversity and inclusivity (www.inclusiveillinois.illinois.edu).

SAN DIEGO STATE UNIVERSITY
Leadership Starts Here

Assistant Professor: Innate/Adaptive Immunologist

THE DEPARTMENT OF BIOLOGY AT SAN DIEGO STATE UNIVERSITY invites applications for a tenure-track faculty position in **MOLECULAR** and/or **CELLULAR IMMUNOLOGY** at the Assistant Professor level. We are seeking a candidate whose research is at the forefront of the innate and/or adaptive immune system. The successful candidate will be expected to develop a vigorous, externally funded, independent research program with student participation. The department of Biology is a vibrant environment studying different aspects of biology. Please visit our website at http://www.bio.sdsu.edu/ for more information. Participation in the teaching mission of the Biology department and fair share to University and/or community service is also expected. Applicants must hold a Ph.D. or equivalent degree and have postdoctoral experience.

SDSU is a large, diverse, urban university and Hispanic-Serving Institution with a commitment to diversity, equity, and inclusive excellence. Our campus community is diverse in many ways, including race, religion, color, sex, age, disability, marital status, sexual orientation, gender identity and expression, national origin, pregnancy, medical condition, and covered veteran status. We strive to build and sustain a welcoming environment for all. SDSU is seeking applicants with demonstrated experience in and/or commitment to teaching and working effectively with individuals from diverse backgrounds and members of underrepresented groups. The College of Sciences is host to a large number of federally-funded minority training programs (described at http://www.sci.sdsu.edu/casa/).

Apply via Interfolio at **http://apply.interfolio.com/26940**. Review of applications will begin **December 1, 2014**, and will continue until the position is filled.

The person holding this position is considered a "mandated reporter" under the California Child Abuse and Neglect Reporting Act and is required to comply with the requirements set forth in CSU Executive Order 1083 as a condition of employment. SDSU is a Title IX, equal opportunity employer and does not discriminate against persons on the basis of race, religion, national origin, sexual orientation, gender, gender identity and expression, marital status, age, disability, pregnancy, medical condition, or covered veteran status.

Smithsonian
National Museum of Natural History

ASSOCIATE DIRECTOR FOR SCIENCE

The National Museum of Natural History (NMNH), a science-based museum within the Smithsonian Institution's complex of museums and research organizations, seeks a dynamic scientist to lead its interdisciplinary research, collections programs, specialized laboratories, field stations, and other similar programs and partnerships. The successful candidate will bring extensive experience in science leadership, policy formulation and strategic planning to the NMNH that has 80 scientists and 330 total staff in the fields of biology, botany, entomology, zoology, geology, paleobiology, anthropology and archeology. Working in collaboration with the Sant Director, this high-profile leader will formulate and implement strategic directions for the Science programs of the Museum; assure the quality and breadth of all Science activities; and provide institutional leadership in national and international initiatives.

The National Museum of Natural History is dedicated to understanding and explaining the natural world and is the most visited natural history museum in the world, thus providing an unparalleled venue for science education. With over 128 million specimens and objects, the Museum's collections represent over 90% of the holdings of the Smithsonian. This collections-based research forms the foundation for the extensive public programs of the Museum, including exhibitions, education, training, and outreach.

This is a full-time, permanent position to be filled as: (i) Federal Civil Service (U.S. citizenship required) or (ii) Trust (private sector, U.S. citizenship not required, proof of eligibility to work in the U.S. required). Salary commensurate with experience. The Smithsonian Institution offers a comprehensive package of benefits. For complete requirements and application procedures, please visit: **www.sihr.si.edu** and refer to Announcements **EX-14-24** (Trust) or **EX-14-25** (Federal). Applications must be received online by **December 10, 2014** and must reference the announcement number. Applicants will be notified by email when their applications are received.

We encourage all qualified candidates to apply.

The Smithsonian Institution is an Equal Opportunity Employer.

Introducing the new
***Science* Careers Jobs app** from Science

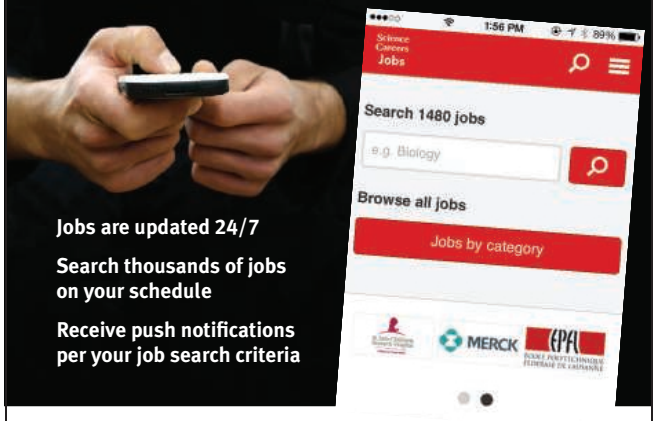

Get a job on the go.
Search worldwide for thousands of scientific jobs in academia, industry, and government. Keep your finger on the pulse of your field—set up an alert for the type of job you are looking for and receive push notifications when jobs are posted that meet your criteria. The application process is seamless, linking you directly to job postings from your customized push notifications.

Scan this code to download app or visit **apps.sciencemag.org** for information.

Science Careers
From the journal *Science* AAAS
ScienceCareers.org

ILLINOIS
UNIVERSITY OF ILLINOIS AT URBANA-CHAMPAIGN

Reengineering Photosynthesis Assistant, Associate or Full Professor

The School of Integrative Biology and the Department of Plant Biology at the University of Illinois, Urbana-Champaign seek an outstanding individual working in the broadly defined fields of bioengineering/synthetic biology/biochemistry, with interest in devising novel strategies and using cutting-edge technologies to improve photosynthetic performance and efficiency of plants. Research areas of interest in reengineering photosynthesis include, but are not limited to: carboxylation chemistry and redesign, synthetic assembly of new photosynthetic processes, installing microbial pathways into plants, and systems engineering of extant photosynthetic metabolism and pathways.

The successful candidate will be expected to develop an externally funded research program, teach at undergraduate and graduate levels, and collaborate with faculty to develop research and education initiatives in plant bioengineering and photosynthetic redesign. A Ph.D. or equivalent in a relevant field is required for appointment. For the Assistant Professor level postdoctoral experience is highly desirable. Appointment as an Associate or Full Professor requires credentials warranting tenure at the University of Illinois.

The University of Illinois provides a highly collaborative and supportive academic environment for cross-disciplinary plant systems research given its strengths in photosynthesis, bioengineering, crop sciences, global change, molecular and cellular biology, genomics, ecology, chemistry and computation. Relevant interacting units include the: Institute for Genomic Biology; Energy Biosciences Institute; National Center for Supercomputer Applications; Bill and Melinda Gates Foundation funded Realizing Improved Photosynthetic Efficiency (RIPE) project; Departments of Biochemistry, Microbiology, Bioengineering, Chemical and Biomolecular Engineering, Crop Sciences and Computer Science.

The appointment is for a full-time, nine-month **Assistant (tenure-track), Associate or Full Professor (tenured)**. Target start date is 16 August 2015. Salary is commensurate with experience.

To ensure full consideration, please create your candidate profile through **http://go.illinois.edu/Photosynthesis** and upload your application letter, curriculum vitae, summary of research and plans, teaching philosophy and experience, and contact information including e-mail addresses for three professional references by **1 December 2014**. After a review of the candidate's record, the search committee may then contact the applicant about soliciting letters of reference.

Applicants may be interviewed before the closing date; however, no hiring decision will be made until after that date. For further information contact Reengineering Photosynthesis Search Chair, **sib@life.illinois.edu**.

Illinois is an Equal Opportunity Employer and all qualified applicants will receive consideration for employment without regard to race, religion, color, national origin, sex, age, status as a protected veteran, or status as a qualified individual with a disability. Illinois is an Affirmative Action /Equal Opportunity Employer and welcomes individuals with diverse backgrounds, experiences, and ideas who embrace and value diversity and inclusivity. (www.inclusiveillinois.illinois.edu).

ILLINOIS
UNIVERSITY OF ILLINOIS AT URBANA-CHAMPAIGN

Harley Jones Van Cleave Professor Host-Parasite Interactions
Department of Animal Biology and School of Integrative Biology

The Department of Animal Biology and the School of Integrative Biology at the University of Illinois, Urbana-Champaign seek a highly qualified candidate for the Harley Jones Van Cleave Professor of Host-Parasite Interactions. This Professorship was made possible by the generous gift of David R. and Margaret Stirewalt Lincicome. This is a full-time faculty position at the rank of Associate or Full Professor with credentials warranting tenure at the University of Illinois. We seek a broadly trained biologist who has a well-established, internationally renowned, externally funded research program in any aspect of host-parasite interactions, including but not limited to coevolutionary interactions, the molecular, physiological, developmental, or immunological bases of such interactions, molecular parasites and genome evolution, effects of parasites on host behavior, life histories, population dynamics, conservation biology, or alterations in such interactions caused by global change. We welcome empirical and theoretical approaches. The successful candidate will have the opportunity to be part of dynamic and well-established communities of integrative biologists with interests spanning a wide range of taxa in the School of Integrative Biology, as well as in a number of interdisciplinary programs across the campus. Responsibilities also include teaching and participation in both undergraduate and graduate training. The successful candidate must have a Ph.D. in biology or related discipline. Salary is commensurate with qualifications and experience. Target start date is August 16, 2015 but is negotiable.

The University of Illinois at Urbana-Champaign is a public land-grant university with more than 40,000 students and provides a highly collaborative and supportive academic environment. There are opportunities for interactions with the Institute of Genomic Biology, the Program in Ecology, Evolution and Conservation Biology, the National Center for Supercomputer Applications, Roy J. Carver Biotechnology Center, the Beckman Institute for Advanced Science and Technology, and the Illinois State Natural History Survey and the Illinois State Geological Survey.

To ensure full consideration, please create your candidate profile through **http://go.illinois.edu/VanCleaveProf** and upload your application letter, curriculum vitae, summary of research and plans, teaching philosophy and experience, and contact information for three professional references by **December 9, 2014**. After a review of the research record, the search committee may then contact the applicant about soliciting letters of reference. Applicants may be interviewed before the closing date; however, no hiring decision will be made until after that date. For further information contact Host-Parasite Interactions Search Chair, s**ib@life.illinois.edu**.

Illinois is an Equal Opportunity Employer and all qualified applicants will receive consideration for employment without regard to race, religion, color, national origin, sex, age, status as a protected veteran, or status as a qualified individual with a disability. Illinois is an Affirmative Action /Equal Opportunity Employer and welcomes individuals with diverse backgrounds, experiences, and ideas who embrace and value diversity and inclusivity. (www.inclusiveillinois.illinois.edu).

Universidad Andrés Bello, Santiago (Chile).

Universidad Andrés Bello (PMI UAB1301) calls for applications for the following job positions:

1. PhD in Chemistry, Pharmacy, Biochemistry or equivalent: Knowledge in preparation of nano and micro capsules for biomedical use in small and medium scale. Required experience in the use of spray drying techniques, double phase emulsion and techniques related to the characterization and pharmacological action of nano micro capsules.

2. Postdoctoral Scholar: PhD in Biology, Biochemistry, Biotechnology or equivalent. Experience with biological and/or fungal models in molecular and physiological aspects. Desirable experience in analytical techniques for establishing independent trials of innovative materials in the area of rot control and plant senescence.

3. Postdoctoral Scholar: PhD in molecular Biology, Biochemistry, Neurosciences, Life Sciences or equivalent. Ample knowledge on chemical modeling and drug design using theoretical and experimental approaches and/or in vivo pharmacology.

Candidates should submit full curriculum vitae to: comunicaciones.dtt@unab.cl

Application period: Until 21 November

Application results: 19 December

University of Missouri - Kansas City

Assistant/Associate Professor (Job 14479)

The School of Biological Sciences at the University of Missouri – Kansas City invites applications for two full-time tenure track faculty positions at the rank of Assistant or Associate Professor. Applicants applying biochemical, genetic, or model systems approaches to neuroscience or computational modeling approaches are preferred, but any qualified applicant employing molecular biological approaches will be considered. The School seeks to attract an active, culturally, and academically diverse faculty of the highest caliber.

The School has strengths in structural biology, molecular genetics, and developmental biology. It has a strong track record in attracting faculty who develop successful research programs with extramural support. The School grants B.S., B.A., M.S., and Ph.D. degrees, the latter in two disciplines, Cell Biology & Biophysics and Molecular Biology & Biochemistry. UMKC has a strong focus in life sciences, with programs in the Schools of Biological Sciences, Medicine, Pharmacy, Dentistry, and Nursing and Health Studies.

For additional details, instructions, and submission of application, visit **http://apptrkr.com/527276** For questions about how to apply, please call 816-235-1621, or if experiencing technical problems, please call 855-524-0002. UMKC is an equal access, equal opportunity, affirmative action employer that is fully committed to achieving a diverse faculty and staff.

IOWA STATE UNIVERSITY

Assistant Professor in Stress Biology

Iowa State University has launched the Presidential High Impact Hires Initiative to support targeted faculty hiring in areas of strategic importance. This position is part of a cluster hire of 5 faculty in four colleges within the strategically important area of Translational Health and is included among the 29 high-impact hires in the second year of the initiative (http://www.biotech.iastate.edu/ISU-HRI/blueprint.html).

The Genetics, Development, and Cell Biology (GDCB) Department seeks applicants for a tenure-track faculty position at the Assistant Professor level who will investigate the cellular networks that mediate responses to stresses in animals, plants or microbes. The successful candidate will establish a vibrant, externally funded research program, work collaboratively with faculty, complementing existing research strengths at ISU, and skillfully contribute to undergraduate and graduate education, including teaching courses in their area(s) of expertise.

Qualified applicants must have a Ph.D. in the life sciences or a related field and demonstrated potential to develop a successful research program. Please visit **www.iastatejobs.com/postings/search** and search for posting number **400059** to view the entire vacancy and apply electronically. For full consideration, applications must be received by **November 30, 2014**.

Iowa State University is an EO/AA Employer. All qualified applicants will receive consideration for employment without regard to race, color, religion, sex, national origin, disability, or protected Vets status.

INSTITUT PASTEUR

Department of Parasites and Insect Vectors

FACULTY POSITIONS IN PARASITES AND INSECT VECTORS

The Institut Pasteur in Paris announces an international call for outstanding candidates at all levels to establish independent research groups in the Department of Parasites and Insect Vectors. Preference will be given to studies of trypanosomes/tsetse flies, *Leishmania*/sandflies, malaria/*Anopheles*, and *Toxoplasma*. We expect to recruit a new faculty member in each of the following areas: (i) field or clinical research emphasizing epidemiology, pathogenesis, intervention studies, transmission, or populations of parasites or vectors, and (ii) laboratory-based studies on all aspects of parasite or vector biology. Attractive start-up and ongoing support includes salary, equipment, and operating costs. In addition, Institut Pasteur provides access to state-of-the-art technology platforms, and to laboratories and research infrastructure in disease-endemic regions through the Pasteur International Network.

The application should comprise the following (in order) in a single pdf file: (i) A brief introductory letter, (ii) CV and full publication list, (iii) A description of past and present research activities (4-5 pages with 1.5 spacing), (iv) The proposed research project (8-10 pages with 1.5 spacing). Separately, provide the names of 3 scientists from whom letters of recommendation can be sought, together with the names of scientists with a potential conflict of interest from whom evaluations should not be requested.

Applications and requests for information should be addressed to **parasitology@pasteur.fr** by **15 January 2015**. Short-listed candidates will be invited for interviews in early 2015 and decisions will be announced by mid-2015.

AAAS is here –

helping scientists achieve career success.

Every month, over 400,000 students and scientists visit ScienceCareers.org in search of the information, advice, and opportunities they need to take the next step in their careers.

A complete career resource, free to the public, *Science* Careers offers a suite of tools and services developed specifically for scientists. With hundreds of career development articles, webinars and downloadable booklets filled with practical advice, a community forum providing answers to career questions, and thousands of job listings in academia, government, and industry, *Science* Careers has helped countless individuals prepare themselves for successful careers.

As a AAAS member, your dues help AAAS make this service freely available to the scientific community. If you're not a member, join us. Together we can make a difference.

To learn more, visit
aaas.org/plusyou/sciencecareers

AAAS + U = Δ

Science Careers

CER

“《科学》职业”已经与赛尔互联(CER)开展合作。中国大陆的高校可以直接联系CER进行国际人才招聘。

请访问

Sciencecareers.org/CER

了解详细信息。

Science

AAAS

UNIVERSITY OF MIAMI

Faculty Position in Evolutionary Developmental Biology

The Department of Biology at the University of Miami, Coral Gables, Florida invites applications for a tenure-track appointment at the Assistant/Associate Professor level in Evolutionary Developmental Biology. We are searching for an outstanding scientist addressing fundamental questions in evo-devo; however, applicants who complement the existing strengths of our department and who can also contribute to a university-wide initiative in Biomaterials are particularly encouraged to apply. Potential areas of research interests include, but are not limited to, regenerative studies with a focus on extracellular matrices, the evolution and development of biomineralized structures, plant cell walls, spider silk or other biological novelties that can potentially be exploited for biologically-inspired materials research. We seek candidates with a Ph.D. and a minimum of two years postdoctoral experience who have demonstrated creativity and productivity in research and have a strong interest in undergraduate and graduate education. The successful candidate will have the opportunity to interact with a growing community of integrative scientists in the Departments of Chemistry, Physics, Math, Computer Science, Biochemistry, and Psychology, as well as the Miller School of Medicine, Rosenstiel School for Marine and Atmospheric Science, Fairchild Tropical Botanic Garden and Abbess Center for Environmental Science & Policy.

Inquiries may be directed to the Search Chair at **evodevo@bio.miami.edu**. Details on the Department of Biology and our strengths and foci can be found at: **http://www.as.miami.edu/biology/**

Applications should include a full curriculum vitae listing all publications and contact information of three references. Copies of three relevant publications and statements of research objectives and teaching interests should also be included. A cover letter outlining how the applicant will complement the current research areas of the Department of Biology, and link with a campus-wide initiative on interdisciplinary approaches to biomaterials should be included.

The position will remain open until filled; priority will be given to those applications received by **November 15, 2014**. Application materials must be uploaded at **http://content.as.miami.edu/biology/about-the-department/apply/**.

The University of Miami is an Equal Opportunity Employer —Females/Minorities/Protected Veterans/Individuals with Disabilities are encouraged to apply. Applicants and employees are protected from discrimination based on certain categories protected by Federal law.

UNIVERSITY OF MIAMI

Faculty Positions in Plant Biology

The Department of Biology at the University of Miami, Coral Gables, Florida, invites applications for two open rank tenure-track positions in the following areas of plant biology.

Plant-Microbial Symbiosis: Outstanding candidates engaged in answering fundamental questions in microbial or mycorrhizal plant symbioses using molecular approaches are encouraged to apply.

Ecosystems Ecologist: Outstanding candidates using experimental or modeling approaches to study nutrient cycles and their impact on processes such as population dynamics, biodiversity or terrestrial productivity are encouraged to apply.

For both positions, we are seeking scientists who will complement the existing strengths of our department and can also contribute to a university-wide initiative to recruit researchers looking at energy problems from different disciplinary perspectives. These individuals will interact with Biology faculty having a broad range of interests such as symbiosis, plant-animal interactions, demography, ecophysiology and evolution. In addition, the Department of Biology has a joint program with the Mathematics Department (Institute of Theoretical and Mathematical Ecology), and has strong interactions with the Abess Center for Ecosystem Science & Policy and the Fairchild Tropical Botanic Garden.

Inquiries may be directed to the Search Chair at plantsearch@bio.miami.edu. Details on the Department of Biology and our strengths and foci can be found at: **http://www.as.miami.edu/biology/**

Candidates must hold a PhD with a minimum of two years of postdoctoral experience. Applications should include a full curriculum vitae, including a listing of all publications and contact information of three references. Copies of three relevant publications, statements of research objectives and teaching interests should also be included. A cover letter outlining how the applicant will complement the current research areas of the Department of Biology and link with a campus-wide initiative on interdisciplinary approaches to research on energy should be included. Application materials for the respective positions must be uploaded to either **http://www.as.miami.edu/biology/plantmicrobialSymbiosis/** or **http://www.as.miami.edu/biology/EcosystemEcologist/** by **November 15, 2014**.

The University of Miami is an Equal Opportunity Employer — Females/Minorities/Protected Veterans/Individuals with Disabilities are encouraged to apply. Applicants and employees are protected from discrimination based on certain categories protected by Federal law.

POSITIONS OPEN

ASSISTANT PROFESSOR
Department of Chemical Engineering
Massachusetts Institute of Technology (MIT)

The MIT Department of Chemical Engineering (**website: http://web.mit.edu/cheme/**) invites candidates for faculty positions starting July 2015 or thereafter. Appointment will be at the assistant or untenured associate professor level. In special cases, a senior faculty appointment may be possible. Candidates must have a Ph.D. in chemical engineering or a related field by the start of their employment. Candidates with research and teaching interests in all areas relevant to the field of chemical engineering will be considered. The successful candidate is expected to advise students, and develop and teach chemical engineering courses at both undergraduate and graduate levels, as well as to develop a sponsored research program and be involved in service to MIT and the profession.

Interested candidates should submit application materials electronically at **website: https://chemefacsrch.mit.edu.** Each application must include: curriculum vitae; the names and addresses of three or more references; a strategic statement of research interests; and a statement of teaching interests. It is the responsibility of the candidate to arrange for reference letters to be uploaded at **website: https://chemefacsrch.mit.edu/letters/.**

Please address questions to **e-mail: cheme-searchmaster@chemefacsrch.mit.edu.** Responses received by December 1, 2014, will be given priority.

With MIT's strong commitment to diversity in engineering education, research, and practice, we especially encourage minorities and women to apply. MIT is an Equal Opportunity/Affirmative Action Employer

---

CURATOR OF INVERTEBRATES AND ASSISTANT PROFESSOR in Ecology & Evolutionary Biology

The University of Colorado Museum of Natural History and Department of Ecology & Evolutionary Biology (EBIO), University of Colorado Boulder, invite applications for a joint, tenure-track appointment as Curator of Invertebrates and Assistant Professor. Primary responsibilities will be to develop an active research program on any non-insect group of invertebrates using molecular systematic approaches, preferably including bioinformatics tools; to curate and develop the Museum's invertebrate collections; and to teach in the Museum and Field Studies and EBIO programs. The successful candidate will be expected to take a leadership position in advancing the role of the collections, particularly in digital and molecular assets. Applicants must have a doctoral degree and strong research, curatorial, teaching, and mentoring credentials. Application materials must be submitted electronically at **website: https://www.jobsatcu.com, Posting #89649,** beginning October 13. The application package should include cover letter, curriculum vitae, representative publications, statements of research, teaching, and curatorial experience and vision, along with names and addresses of four references. Review of applications begins December 1, 2014. Contact **e-mail: christy.mccain@colorado.edu.** *The University of Colorado is an Equal Opportunity/Affirmative Action Employer.*

POSTDOCTORAL FELLOW

Harvard University is seeking applicants to conduct research in the Chem & Chem Bio Department Develop new single-molecule experimental techniques and apply these techniques to answer mechanistic questions in NIH-funded project studying ATP-dependent chromatin remodeling. Experience developing and applying single-molecule experimental techniques in mechanistic biology analyses, and knowledge of optics, fluorescence microscopy, nanofabrication, solid-state physics, computer simulations, molecular biology, and genetics, required. Apply to **Attn: M. Kilroy, Zhuang Grp, Department of Chemistry & Chemical Biology, 12 Oxford St., Cambridge MA, 02138.** *Affirmative Action/Equal Opportunity Employer.*

POSITIONS OPEN

PROFESSOR - CLIMATE, OCEANOGRAPHY
Massachusetts Institute of Technology (MIT)

MIT's Department of Earth, Atmospheric and Planetary Sciences seeks to expand its vibrant and interdisciplinary approach to research and education in climate science. We seek applications from outstanding candidates working in climate related fields. We particularly encourage applicants working in the fields of ocean dynamics, oceans and climate, and/or marine biogeochemical cycles.

Requirements: Applicants must hold a Ph.D. by the start of employment. We seek highly motivated candidates with a strong commitment to excellence in research, teaching, and student advising. A keen interest in relating to complementary research in the Department and/or in the MIT/Woods Hole Joint Program in Oceanography is important.

Preference will be given to appointments at the rank of **ASSISTANT PROFESSOR** but a more senior appointment can be considered for an individual with exceptional qualifications.

Review of applications will begin immediately. To receive consideration, a complete application must be received by December 31, 2014. Applicants should submit curriculum vitae and two-page descriptions of research and teaching plans and arrange for three letters of reference to be submitted directly by professional referees.

Questions regarding the search may be addressed to Professor **Mick Follows**, Search Committee Chair (**e-mail: mick@mit.edu**).

Applications are being accepted at Academic Jobs Online at **website: https://academicjobsonline.org/ajo/jobs/4822.**

Questions regarding the application procedure can be addressed to: **Ms. Karen Fosher, Human Resources Administrator, EAPS, 54-924 Massachusetts Institute of Technology, 77 Massachusetts Avenue, Cambridge, MA 02139**; **e-mail: kfosher@mit.edu; telephone: 617-253-2132.**

MIT is an Equal Opportunity/Affirmative Action Employer. Applications from women, minorities, veterans, older workers, and individuals with disabilities are strongly encouraged.

MOLECULAR TUMOR BIOLOGY

A **POSTDOCTORAL POSITION** is available to study novel molecular targets and signaling pathways in cancer cells and to develop therapeutic strategies in animal models. Recent Ph.D. with background and training in molecular biology and biochemistry, and animal procedures is desirable. Please send curriculum vitae and names of three references electronically to **Usha Kasid,** Ph.D., Professor, Georgetown University Medical Center, Washington DC 20057 (**e-mail: kasidu@georgetown.edu**). *An Equal Opportunity/Affirmative Action Employer.*

More scientists agree—we are the most useful website.

Science Careers
From the journal *Science* AAAS
ScienceCareers.org

POSITIONS OPEN

FACULTY POSITIONS
Department of Materials Science and Engineering
Massachusetts Institute of Technology (MIT)
Cambridge, MA

The Department of Materials Science and Engineering (DMSE) seeks candidates for two open tenure-track faculty positions to begin July 2015 or thereafter. Appointments would be at the **ASSISTANT** or untenured **ASSOCIATE PROFESSOR** level. In special cases, a senior faculty appointment may be possible. Faculty duties include teaching at the graduate and undergraduate levels, research, and supervision of student research.

Candidates should hold a Ph.D. in Materials Science and Engineering or a related field by the start of employment. Candidates with deep knowledge of the core of Materials Science and Engineering are desired. DMSE seeks to broaden its research portfolio in two areas: **Materials chemistry.** Including: surface science and surface chemical reactions, catalysis, corrosion, surface treatment, colloids, chemical assembly of materials, bio-inspired, and biomolecular assembly of materials, polymer science, surface design for novel optical, electronic, or magnetic properties, inorganic-organic interface. **Microstructure and mechanics.** Including: mechanics of heterophase architectures (integrated electronics, advanced composites, etc.), advanced microstructure characterization including in-situ and in-operando methods, computational modeling of materials processing, computational design of materials and microstructure.

However, DMSE has strengths and interests across the full spectrum of materials research, and excellent candidates with expertise in any and all areas of the field are welcomed. For example, DMSE has active programs in electronic, photonic, and magnetic materials, materials for energy and the environment, materials in medicine, biomaterials, structural materials, computational materials science and engineering, materials processing and manufacturing, and archaeological materials.

MIT has a number of Institute-wide initiatives under way or in development, on topics that include Manufacturing, Energy, Environment, and Health. Individuals who can connect to these initiatives are of interest.

Interested candidates should submit application materials electronically at **website: http://dmsefacsrch.mit.edu.** Each application should include curriculum vitae, a statement of research interests, and a statement of teaching interests. We request that each candidate arrange for three letters of reference to be uploaded at **website: http://dmsefacsrch.mit.edu/letters/.** Questions should be addressed to **e-mail: dmse-searchmaster@dmsefacsrch.mit.edu.** Responses received by December 31, 2014, will be given priority. No application received after February 1, 2015 will be considered in this year's search.

We especially encourage minorities and women to apply because of MIT's strong commitment to diversity in engineering education, research, and practice.

Stop searching for a job; start your career today.

Science Careers
From the journal *Science* AAAS
ScienceCareers.org

For your career in science, there's only one Science

A career plan customized *for* you, *by* you.

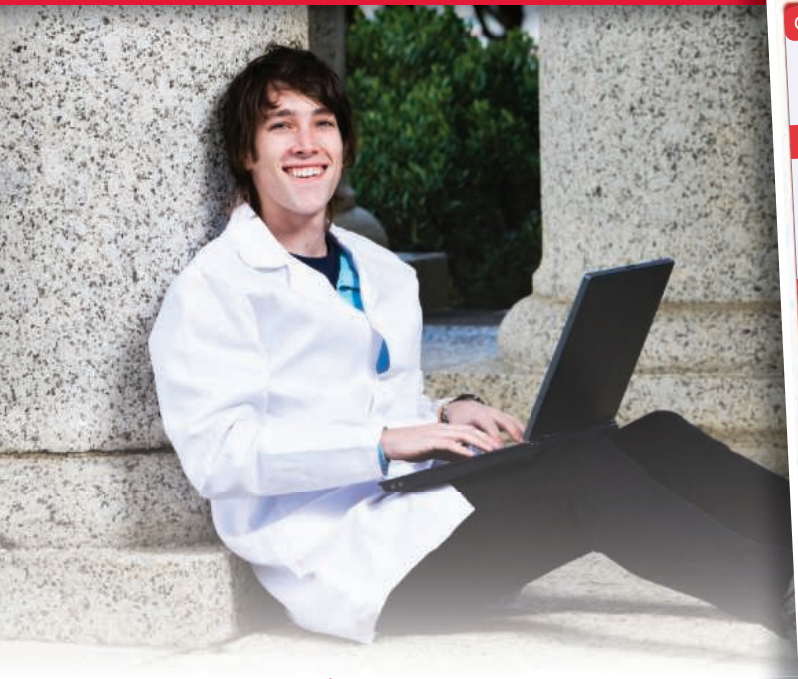

myIDP.sciencecareers.org

Recommended by leading professional societies and endorsed by the National Institutes of Health, an individual development plan will help you prepare for a successful and satisfying scientific career.

my IDP Science Careers

In collaboration with FASEB, UCSF, and the Medical College of Wisconsin and with support from the Burroughs Wellcome Fund, AAAS and *Science* Careers present the first and only online app that helps scientists prepare their very own individual development plan.

Visit the website and start planning today!
myIDP.sciencecareers.org

In partnership with:

advancing the life sciences 1912-2012 FASEB Federation of American Societies for Experimental Biology

UCSF University of California San Francisco

Medical College of Wisconsin

Burroughs Wellcome Fund

By **Huan Wang**

A double dose of advice

In 2006, I flew across the ocean to study molecular biology at the University of Colorado, Boulder. As the top graduate from my program at Zhejiang University in China, I had no problem learning from a textbook or solving equations. Graduate school, however, was not like studying from a book. In graduate school, every student writes her own book, and sometimes there is no equation to follow. I had another challenge, too, a challenge of my choosing: coordinating two labs and two advisers.

Early in graduate school, I did lab rotations in three labs, and I liked two of them. The principal investigators in those labs—Kristi Anseth and Leslie Leinwand—were collaborators, so they agreed to let me take on a collaborative project. My goal was to engineer cardiac valve tissue for patients who need valve replacement surgery. Achieving that could have a big medical payoff, but to make it work, we needed to understand the fundamental interactions between cardiac valve cells and the tissue matrix surrounding them. It was my job to bring together fundamental and applied expertise.

"Co-advised students get twice as many researchers to interact with."

To make co-advising work, everyone needs to play an active role. But you—the graduate student—are the main actor in this movie, so you must take the lead. Here are some things I learned from the experience.

- You need to be open-minded and a little adventurous, and you need to fully embrace a new field—or, in some cases, two new fields. I went to work each day with the attitude that all disciplines are of equal value, each offering advantages but also the risk of narrowing one's thinking. The goal of cross-disciplinary collaboration is to break us out of those boxes and create a new approach that complements traditional disciplines.
- As a co-advised student, you may work in directions that diverge from the main themes of either lab. It is important to be independent and lead. In my early years, I spent more time in the molecular biology lab, but I gradually moved into the biomaterial engineering lab as I got fascinated by the possibilities of combining biomaterials and cell biology. None of this would have been possible if my advisers had not allowed me to lead, with their supervision.
- Co-advised students get twice as many researchers to interact with. Take advantage of that opportunity; interactions with other researchers are necessary for a young researcher to grow. Brilliant ideas may come from formal meetings or casual chats. An idea may be simple, but only a colleague's years of experience can make it viable.
- Being co-advised usually means attending twice as many meetings, interacting with twice as many people, and learning techniques from both labs. So use your time efficiently and spend more time planning. My advisers scheduled their lab meetings on Wednesdays at different times, so for me, Wednesday was the day for summarizing data, planning future experiments, and interacting with people in the groups.
- Communicating well with your advisers will engage them in the progress of your work and invite suggestions. Learn the management, scientific, and communication styles of your advisers, and integrate those styles into your own. Find a comfortable and efficient middle ground for maintaining three-way communication. It takes time, confidence, and sensitivity to learn how to communicate well, but you will use this skill to great advantage for the rest of your career.

The result? I found that culturing cardiac valve cells on synthetic hydrogels preserves their normal properties better than the traditional plastic plates do, and I discovered a signaling pathway connecting the stiffness of the supporting scaffold to the cells' cytoskeletal structure. One laboratory taught me diverse molecular and cellular techniques, and the other trained me to engineer biocompatible scaffolds. The interaction of these disciplines shaped my scientific perspective and focused my career on understanding and engineering organs for clinical applications. I earned my Ph.D. with confidence, a deep appreciation of both disciplines, and gratitude toward my advisers—both of them! ■

Huan (Sharon) Wang is now a postdoc working in the lab of Peter Sorger at Harvard Medical School. For more on life, science, and careers, visit www.sciencecareers.org.

ILLUSTRATION: ROBERT NEUBECKER

Downloaded from www.sciencemag.org on October 24, 2014

Published by AAAS